AFAPL-TR-79-2126

AD A122667

A COLLECTION OF PAPERS IN THE AEROSPACE SCIENCES

Edited By

K. S. Nagaraja, AFWAL/FIMM
J. S. Petty, AFWAL/POTC

June 1982

Approved for Public Release; Distribution Unlimited

DTIC FILE COPY

AERO-PROPULSION LABORATORY
AIR FORCE WRIGHT AERONAUTICAL LABORATORIES
AIR FORCE SYSTEMS COMMAND
WRIGHT-PATTERSON AIR FORCE BASE, OHIO 45433

DTIC
ELECTE
DEC 16 1982
S D
A

82 12 15 073

NOTICE

When Government drawings, specifications, or other data are used for any purpose other than in connection with a definitely related Government procurement operation, the United States Government thereby incurs no responsibility nor any obligation whatsoever; and the fact that the government may have formulated, furnished, or in any way supplied the said drawings, specifications, or other data, is not to be regarded by implication or otherwise as in any manner licensing the holder or any other person or corporation, or conveying any rights or permission to manufacture use, or sell any patented invention that may in any way be related thereto.

This report has been reviewed by the Office of Public Affairs (ASD/PA) and is releasable to the National Technical Information Service (NTIS). At NTIS, it will be available to the general public, including foreign nations.

This technical report has been reviewed and is approved for publication.

James S. Petty

JAMES S. PETTY
Project Engineer

Charles E. Bentz

CHARLES E. BENTZ
Acting Chief, Components Branch

FOR THE COMMANDER

H. I. Bush

HORACE I. BUSH
Director, Turbine Engine Division

"If your address has changed, if you wish to be removed from our mailing list, or if the addressee is no longer employed by your organization please notify AFWAL/POTC, *W-PAFB, OH 45433 to help us maintain a current mailing list".*

Copies of this report should not be returned unless return is required by security considerations, contractual obligations, or notice on a specific document.

COMPONENT PART NOTICE

THIS PAPER IS A COMPONENT PART OF THE FOLLOWING COMPILATION REPORT:

(TITLE): A Collection of Papers in the Aerospace Sciences.

(SOURCE): Air Force Aero Propulsion Laboratory

Wright-Patterson AFB, OH 45433.

TO ORDER THE COMPLETE COMPILATION REPORT USE AD-A122 667.

THE COMPONENT PART IS PROVIDED HERE TO ALLOW USERS ACCESS TO INDIVIDUALLY AUTHORED SECTIONS OF PROCEEDINGS, ANNALS, SYMPOSIA, ETC. HOWEVER, THE COMPONENT SHOULD BE CONSIDERED WITHIN THE CONTEXT OF THE OVERALL COMPILATION REPORT AND NOT AS A STAND-ALONE TECHNICAL REPORT.

THE FOLLOWING COMPONENT PART NUMBERS COMPRISE THE COMPILATION REPORT:

AD#:	TITLE:
P000 315	Electro Fluid Dynamics: The Role of Hans von Ohain.
AD-P000 316	Hans von Ohain's First Legacy: Trends and Research Opportunities.
AD-P000 317	Comments on "Chocked Flow: A Generalization of the Concept and Some Experimental Data".
AD-P000 318	Technological Advances in Airframe - Propulsion Integration.
AD-P000 319	The Energy Balance in Axi-Symmetric Steady Compressible Swirl Flows with Closed Streamlines.
AD-P000 320	Compound-Compressible Nozzle Flow.
AD-P000 321	Co-Axial Dump Combustor Investigations.
AD-P000 322	Military Aircraft Noise.
AD-P000 323	A Note on Adaptive Wind Tunnels with Imperfect Control.
AD-P000 324	The Numerical Solution of Pressure Oscillations In An Open Cavity.
AD-P000 325	Boundary-Layer Transition on Blunt, Slender Cones at Hypersonic Mach Numbers.
AD-P000 326	A Note on the Oscillation of Cavities Coupled to Aerodynamic Flows.
AD-P000 327	On the Structure of Three-Dimensional Shock-Induced Separated Flow Regions.
AD-P000 328	Computational Fluid-Dynamics - An Engineering Tool.
AD-P000 329	Constant Parameter Two Component Channel Flow.
AD-P000 330	The Use of Vortex Generators as Inexpensive Compressor Casing Treatment.
AD-P000 331	Degradation of a Laser Beam By a Turbulent Jet.
AD-P000 332	On The Large Scale Structure of Turbulence In Boundary Layer and Shear Flows.
AD-P000 333	Improved Analytical and Numerical Techniques for Calculating Explosions and Implosions.
AD-P000 334	On Synges Criterion for the Stability of Plane Couette Flow.
AD-P000 335	Mixing of Compressible Flows with Application to Ejector Thrusters.

COMPONENT PART NOTICE (CON'T)

AD#: P000 336	TITLE:	Highlight of an Ejector Analysis.
AD-P000 337		Advances in Ejector Technology - A Tribute to Hans von Chain's Vision.
AD-P000 338		Lifting Surface Theory for Thrust Augmenting Ejectors.
AD-P000 339		A One-Dimensional Procedure for Estimating the Performance of Ejector Nozzles.
AD-P000 340		Effects of Non-Constant Enthalpy Addition on Fan-Nozzle Combinations.
AD-P000 341		Some Advantages of Unsteady Aerodynamics.
AD-P000 342		The Bojarski-Lewis Identity for Elastic Wave Scattering.
AD-P000 343		Thermal Dissociation of Diatomic Molecules.
AD-P000 344		Vibration Analysis of a Spinning Disk Using Image Derotated Holographic Interferometry.
AD-P000 345		Statistical Experimental Designs in Computer Aided Optimal Aircraft Designs.

Accession For	
NTIS GRA&I	☒
DTIC TAB	☐
Unannounced	☐
Justification	
By	
Distribution/	
Availability Codes	
Dist	Avail and/or Special
A	

UNCLASSIFIED
SECURITY CLASSIFICATION OF THIS PAGE (When Data Entered)

REPORT DOCUMENTATION PAGE		READ INSTRUCTIONS BEFORE COMPLETING FORM
1. REPORT NUMBER AFAPL TR 79-2126	2. GOVT ACCESSION NO. AD-A122667	3. RECIPIENT'S CATALOG NUMBER
4. TITLE (and Subtitle) A COLLECTION OF PAPERS IN THE AEROSPACE SCIENCES		5. TYPE OF REPORT & PERIOD COVERED Final Report December 1978 - November 1979 6. PERFORMING ORG. REPORT NUMBER
7. AUTHOR(s) Editors: K. S. Nagaraja (AFWAL/FIMM) J. S. Petty (AFWAL/POTC)		8. CONTRACT OR GRANT NUMBER(s)
9. PERFORMING ORGANIZATION NAME AND ADDRESS AERO PROPULSION LABORATORY (POTC) AIR FORCE WRIGHT AERONAUTICAL LABORATORIES (AFSC) WRIGHT-PATTERSON AIR FORCE BASE OH 45433		10. PROGRAM ELEMENT, PROJECT, TASK AREA & WORK UNIT NUMBERS PE 62203F, ~~AFAPLST1~~
11. CONTROLLING OFFICE NAME AND ADDRESS AERO PROPULSION LABORATORY (POTC) AIR FORCE WRIGHT AERONAUTICAL LABORATORIES (AFSC) WRIGHT-PATTERSON AIR FORCE BASE OH 45433		12. REPORT DATE June 1982 13. NUMBER OF PAGES 685
14. MONITORING AGENCY NAME & ADDRESS(if different from Controlling Office)		15. SECURITY CLASS. (of this report) UNCLASSIFIED 15a. DECLASSIFICATION/DOWNGRADING SCHEDULE
16. DISTRIBUTION STATEMENT (of this Report) Approved for public release; distribution unlimited.		
17. DISTRIBUTION STATEMENT (of the abstract entered in Block 20, if different from Report)		
18. SUPPLEMENTARY NOTES		
19. KEY WORDS (Continue on reverse side if necessary and identify by block number) Propulsion: research trends, compressors, ejectors, combustors, noise, holography, animal flight, propulsion-airframe integration, nozzle flows Fluid dynamics: aerodynamics, computational fluid dynamics, boundary layers, separated flows, unsteady aerodynamics (see reverse)		
20. ABSTRACT (Continue on reverse side if necessary and identify by block number) This document is a collection of thirty-five (35) papers covering a wide range of topics in the aerospace sciences, including propulsion, fluid dynamics, aerodynamics, energy conversion, and mathematical analysis. The introductory paper in this collection is biography of Dr Hans von Ohain, a pioneer in the development of the aircraft jet engine. The other papers, with few exceptions, are technical reports on research in progress or completed. These papers were contributed by individuals both within and outside the Government service.		

DD FORM 1 JAN 73 1473 EDITION OF 1 NOV 65 IS OBSOLETE

UNCLASSIFIED
SECURITY CLASSIFICATION OF THIS PAGE (When Data Entered)

19. Energy conversion: wind turbines, lasers, plasma pnysics, electrofluid-dynamics.

Other: mathematical analysis, numerical analysis, test analysis, wind tunnels, orbital mechanics, computer aided design, biographical.

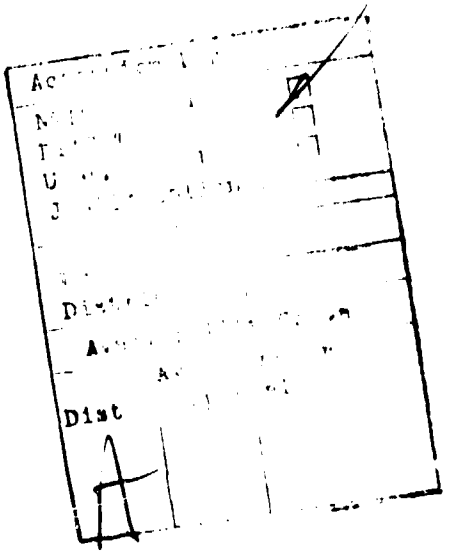

DTIC
COPY
INSPECTED
2

FOREWORD

On 12 January 1979 Dr Hans von Ohain, a pioneer in the development of the aircraft jet engine, retired as Chief Scientist of the Air Force Aero Propulsion Laboratory, ending a 31 year career in the U. S. Government service.

Friends and associates of Dr von Ohain, wishing to commemorate his distinguished career, have contributed the technical papers appearing in this volume. These papers cover a wide range of research areas to which Dr von Ohain has made contributions, including fluid dynamics, aerodynamics, thermodynamics, propulsion and energy conversion.

Papers contributed by individuals employed by the Department of Defense are technical reports on work in progress or completed. The project, task and work unit under which such work was performed is identified on the title page for the paper.

The work reported in papers not so identified was accomplished without cost to the Government.

The authors' affiliations given on the title page for each paper are as of the date the manuscript was received, and so are not necessarily current.

This volume was edited and assembled by Dr K. S. Nagaraja (AFWAL/FIMM) and Dr J. S. Petty (AFWAL/POTC), Air Force Wright Aeronautical Laboratories (AFSC), Wright-Patterson Air Force Base, Ohio 45433.

The editors wish to acknowledge to efforts of Mrs Doris Appel for her assistance with the typing of the title pages and preface pages, and of Ms Ann Gerstner for re-typing several of the manuscripts and for her assistance in handling the numerous small details required to pull everything together.

TABLE OF CONTENTS

		PAGE
Introduction:	Two Ships That Did Not Pass in the Night, E. C. Simpson	1
1.	Hans von Ohain -- Contributions of Excellence, Herman Viets	2
2.	Electro Fluid Dynamics: The Role of Hans von Ohain, Frank Wattendorf and Maurice Lawson	68
3.	Hans von Ohain's First Legacy: Trends and Research Opportunities, Brian Quinn	83
4.	Investigation of the Mixing Region Between the Primary and Secondary Streams of a Two-Dimensional Supersonic Air-Air Ejector System, William C. Robison and James R. Nelson AD-621 018	94
5.	Technological Advances in Airframe - Propulsion Integration, D. Zonars	99
6.	The Energy Balance in Axi-Symmetric Steady Compressible Swirl Flows with Closed Streamlines, K. G. Guderley	116
7.	Compound-Compressible Nozzle Flow, A. Bernstein, C. Hevenor and W. H. Heiser	137
8.	Co-Axial Dump Combustor Investigations, R. R. Craig, J. E. Drewry and F. D. Stull	145
9.	Theory of Wind Turbines with Contrarotation, G. N. Patterson AD-3025 256	157
10.	Military Aircraft Noise, Paul A. Shahady	185
11	A Note on Adaptive Wind Tunnels with Imperfect Control, William R. Sears	191
12.	The Numerical Solution of Pressure Oscillations In An Open Cavity, W. L. Hankey and J. S. Shang	208
13.	Boundary-Layer Transition on Blunt, Slender Cones at Hypersonic Mach Numbers, Kenneth F. Stetson	243
14.	A Note on the Oscillation of Cavities Coupled to Aerodynamic Flows, Alexander H. Flax	293
15.	On tne Structure of Three-Dimensional Shock-Induced Separated Flow Regions, R. H. Korkegi	319
16.	Computational Fluid-Dynamics - An Engineering Tool, John D. Anderson	324

TABLE OF CONTENTS (Cont)

		PAGE
17.	Constant Parameter Two Component Channel Flow, Kenneth R. Cramer	337
18.	The Use of Vortex Generators as Inexpensive Compressor Casing Treatment, C. Herbert Law, Arthur J. Wennerstrom and William J. Buzzell	358
19.	Degradation of a Laser Beam By a Turbulent Jet, G. G. Cudahy, J. T. Van Kuren, and H. E. Wright	372
20.	On The Large Scale Structure of Turbulence In Boundary Layer and Shear Flows, M. A. Badri Narayanan	395
21.	Improved Analytical and Numerical Techniques for Calculating Explosions and Implosions, John W. Goresh and Henry E. Fettis	416
22.	On Synges Criterion for the Stability of Plane Couette Flow, K. F. Lee and Knox Millsaps	448
23.	Mixing of Compressible Flows with Application to Ejector Thrusters, Morton Alperin and Jiunn-Jeng Wu	456
24.	Highlight of an Ejector Analysis, Siegfried Hasinger	478
25.	Advances in Ejector Technology - A Tribute to Hans von Ohain's Vision, K. S. Nagaraja	489
26.	Lifting Surface Theory for Thrust Augmenting Ejectors, P. M. Bevilaqua	518
27.	A One-Dimensional Procedure for Estimating the Performance of Ejector Nozzles, Kervyn D. Mach	540
28.	Effects of Non-Constant Enthalpy Addition on Fan-Nozzle Combinations, Gordon C. Oates and Walter M. Persz, Jr.	556
29.	Some Advantages of Unsteady Aerodynamics, Herman Viets	567
30.	The Bojarski-Lewis Identity for Elastic Wave Scattering, D. A. Lee	586
31.	Effect of Initial Configurations on Libration Point Motion, Lynn E. Wolaver AD-660 771	598
32.	Thermal Dissociation of Diatomic Molecules, W. F. Bailey and A. Garscadden	634
33.	Vibration Analysis of a Spinning Disk Using Image Derotated Holographic Interferometry, J. C. MacBain, J. E. Horner, W. A. Stange, and J. S. Ogg	641

PAGE

34. Statistical Experimental Designs in Computer Aided Optimal Aircraft Designs, K. S. Nagaraja and Ram B. Ram. 648

35. MTBF Confidence Bounds Based on MIL-STD-781C Fixed-Length Test Results, H. Leon Harter AD-A063 047 671

TWO SHIPS THAT DID NOT PASS IN THE NIGHT:

AN INTRODUCTION

E. C. Simpson
Director (Retired)
Turbine Engine Division
Aero Propulsion Laboratory

I realize my contribution to this volume is small and inconsequential to most, but I want to voice my great respect to one who, many years ago, had to be considered an enemy but who, today, I consider a delightful, valued and respected friend.

Back in the days following WWII when I was a Captain in the U. S. Army running wildly around Germany as a member of ATI "hitting intelligence targets", messing with ADIK, 'T' Force, Special Services and such, I first met Hans Von Ohain in Zuffenhausen. His English was better than my German which is not a compliment, but there were two people trying to help us communicate; the first a Heinkel employee in Sales named Wolfe, and the second my jeep driver, Liepold. Hans and I did communicate, but I must say the conversation was less than flowing. At the time, Hans was working on getting the -011 engine into production. Even today, a tour through this design with its designer is a real treat. Many novel features; many problems that a little nickel, chrome and cobalt could cure. I can vouch for its running, having tested it in the BMW altitude facility at Munich (the air supply is now the 'A' air supply at AEDC). The data was shared by the U. S. and U. K. and the parts to build the test hardware were collected from all over Germany by 37 of us chasing them down in the Aug-Sep 1945 time period.

Both Hans and I tried very hard to communicate and did succeed in building trust and respect in each other. The doubts that existed were based on my rather shallow knowledge of the turbine engine which was based on my memory of "Stodola" and Sir Geoffrey Smith's little book purchased at a street book stall in London. I was not sure exactly what Hans had done, but as a result of our conversation in garbled German and broken English, I concluded that one of the things he had not done was stand around twiddling his thumbs. As my knowledge of what he had done grew, I have developed a very deep respect for this man's character, particularly his kindness, understanding and humble demeanor.

Over the years, our relationship has grown. There have been many discussions, usually rounding out and defining an engineering problem like, "Does the J65 have one compressor stage too many?" and other less technical areas like, "In C.B. radio, what is a Beaver?" Occasionally there was disagreement which, without exception, was resolved without rancor. My great respect is based on Han's cleverness, and the determination it took to be the first in a major invention or development. The pioneer is assailed by doubts, failures and uncertainties that assail the mind, numb the senses and urge you to quit over and over, when it would be so easy to do so. A person who has not been through it cannot imagine the elation that comes when you luck out and it works. Hans has never quit or given up, and those of us in the turbine engine business now begin by knowing that with just sweat and work, technical success will follow. Thank you for providing this lesson to so many of our young folks, and thank you for your wise counsel in many things.

Hans von Ohain --

Contributions of Excellence

Hermann Viets

Wright State University

copyright 1979
Hermann Viets
2511 South Patterson Blvd
Kettering, Ohio 45409

FOREWORD

The following pages are an attempt to describe some of the accomplishments of a truly extraordinary man:

- a man whose technical efforts brought him to the forefront of his profession at an age of twenty-seven years with the flight of the world's first turbojet powered aircraft;
- a man who rose in the service of his adopted country to the position of Chief Scientist of two major scientific laboratories;
- and yet a man who consistently offers a kind word, a smile or encouragement to all.

The quotations in the footnotes are his own words.

THE FORMATIVE YEARS

Hans von Ohain was born in Dessau, Germany on the 14th of December, 1911. He was the younger son of Wolf and Kathrine von Ohain. The von Ohain brothers are shown with their parents in Figure 1, on the Baltic Sea Shore. His father was a former military officer who had resigned and operated a wholesale electrical parts business. At about the age of nine years, young Hans moved to Magdeburg with his family. They lived there about a year and then moved to Berlin, where they lived during World War I in a large house shown in Figure 2.

As a child in school, von Ohain did not exhibit much of the intellect which was to serve him so well in later years. In fact, his grades in the earliest school years were not particularly good. He estimates that he was in the lower third of the class in performance. The problem appears to be that he was not at all challenged. Much of the education was drilled by rote and little concern was given to motivating the students. The work was relatively easy for him and thus he did not need to and indeed want to apply himself.

Around the ninth or tenth school year, his grades started to improve and by two years later his grades were excellent. This was true not only in mathematics and physics but also in the other subjects. As a boy he also enjoyed experimenting with chemistry. One of his less successful experiments involved attempting to produce hydrogen by a reaction between acid and a metal. The metal was placed in the acid probably too quickly and the reaction caused some of the acid to land on von Ohain. He quickly washed it away with cold water but it was present long enough to leave some temporary spots on his face. His parents noticed the spots and were less than enthusiastic about his experiment.

Figure 1. Young Hans von Ohain (center) with his family.

Figure 2. The von Ohain home in Berlin.

Another of the young boy's interests was model airplane building, although it certainly did not match his interest in physics and chemistry. No ready made kits were available. All airplanes needed to be built from the construction materials, the main one being bamboo. Each piece needed to be cut out and bent.

His main childhood hero and indeed, a hero to this day, was Albert Einstein. It was absolutely fantastic to von Ohain that a person could go to such depth of understanding and analysis by just thinking and without experiments. We did not, after all, need to explain the Lorenz contraction by means of an ether which always drops out of the computation.

Einstein also had another attribute which was greatly admired by von Ohain and is highly evident in his own work. He was able to give clear physical thoughts without torturing you with a tremendous amount of obscuring mathematics. On the other hand, however, he was also a master of applied mathematics and thus was able to express his physical insight in highly mathematical form. There are few people who can do either one or the other and to find both in one person is indeed rare.

Young von Ohain's interest in science continued, and his father enrolled him at 19 years in the University of Göttingen, the foremost technical university in Germany. His stay there was brief, completing the normal seven years in four and receiving his doctorate. By this time, his ideas on jet propulsion were formulated and partially tested. When he was 26 years old, as he is shown in Figure 3, he was in the midst of a program destined to lead to the first turbojet powered aircraft in the world.

The automobile in Figure 4, is the Opel which von Ohain drove during his university days and which influenced his life by the choice of a parking location.

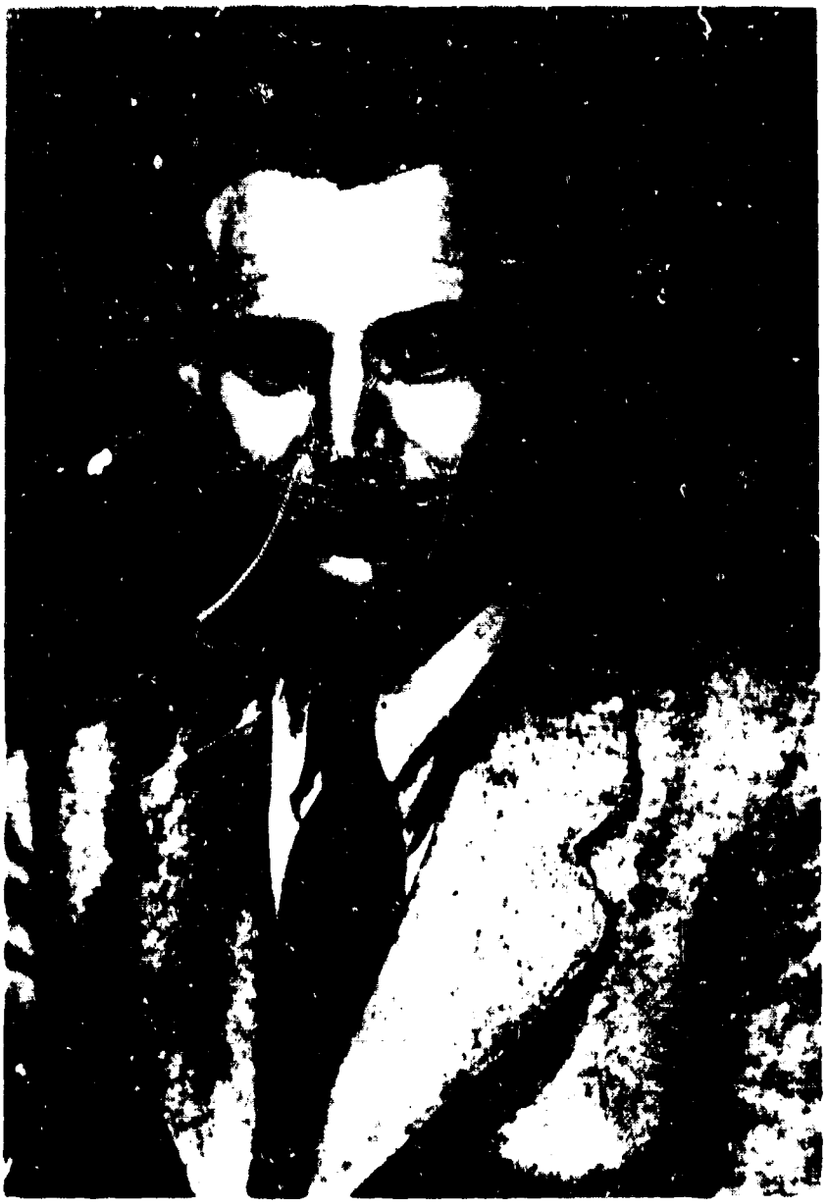

Figure 3. Hans von Ohain at 26 years

Figure 4. The Opel which served to introduce Hans von Ohain and Max Hahn.

THE GÖTTINGEN YEARS

First considerations of jet propulsion -

In the early 1930's, when Hans von Ohain was studying Physics and Aerodynamics at George-August University in Göttingen, Germany, very rapid progress was being made in aircraft systems. This was particularly true of the reciprocating piston engine with a variable pitch propeller. Substantial performance improvements were still forthcoming and no immediate need for a new propulsion system seemed to exist.

However, it occurred to von Ohain, somewhat intuitively, that a steady process with a continuous constant pressure combustion would be superior to the unsteady cyclical process represented by the piston engine. He felt that the combination of piston engine and propeller was inherently less powerful, light, smooth and compatable with future higher speed aircraft than a continuous process.

At first, his approach was to consider a steady aerothermodynamic process with a continuous, constant pressure combustion, in which energy for compressing the fresh air would be extracted from the combustion gas without machinery. This he intended to accomplish by bringing the inflowing fresh air in direct contact with the expanding combustion gas (a kind of ejector process). However, after studying specific processes and configurations, it became apparent to him that such types of processes would have enormous problems with respect to large internal losses and adverse heat transfer effects caused by mixing between the fresh air and the combustor gas. Thus, this idea was put aside for future considerations[1] and he began to investigate a propulsion process in which compression and expansion were separated and carried out by a turbo compressor and turbine respectively.

Investigators in other countries, particularly England, Italy and the United States had followed various paths to arrive at a similar conclusion and starting point.

The various projects were unknown to the young von Ohain and he first became aware of them several years later while in the midst of his own industrial development program.

Searching for an extremely lightweight, compact and simple configuration, he chose a radial outflow compressor rotor back-to-back with a radial inflow turbine rotor. This configuration also promised correct matching simply by providing equal outer diameters for the straight radial outflow compressor rotor and the straight radial inflow turbine rotor. In spite of the fact that radial configuration was chosen, he was aware of the possibility of employing axial flow compressors[2] and turbines. The axial flow configuration was very desirable for future developments from a standpoint of small frontal area, but was too complex and expensive for the early development. In particular, stage matching of a multistage axial flow compressor and matching of axial flow compressor and turbine without component test facilities appeared to be too much of a gamble at this point.

[1] "The idea of a continuous aerothermodynamic propulsion process without machinery and with the capability of operating from zero flight speed on never became entirely dormant. In 1937 Dr. Hilsch, who was during my study years assistant of Prof. Pohl and later became known by his Hilsch-Ranque effect, discussed with me the possibility of employing the fluiddynamic energy exchange process in the "Hilsch Tube" for achieving a continuous static propulsion process. While flow curvature effects seemed to be beneficial for the energy exchange process, theoretical investigations of the internal efficiency did not look promising enough to warrant experiments. In 1948 Dr. E. Knoernchild (formerly D.V.L.) who worked at that time at Wright-Patterson AFB on an aerodynamic theory of the Hilsch Tube revived my interest in the continuous static propulsion cycle. However, the analytical investigations showed that adverse heat exchange between fresh air and combustor gas stubbornly remained the major obstacle. Some French patents on similar ideas were found, but they did not indicate any promising avenue for eliminating or alleviating the problems of adverse heat exchange. A new fluiddynamic process seemed to be needed in which the heat exchange between fresh air and combustion gas is greatly reduced while the effectiveness of fluiddynamic energy transfer is increased."

During 1934 rudimentary design and weight studies were conducted by von Ohain, along with some performance calculations based on a pressure ratio of 3:1 and turbine inlet temperature of about 1400°F. It appeared that at a high flight speed of about 500 miles per hour, an overall efficiency could be obtained which was around 60% of that of an equivalent propeller piston engine. However, the weight of this new propulsion system promised to be only a fraction (quarter of less) of that of an equivalent propeller-piston engine system. At that time, the propulsion system of a fighter aircraft constituted a much greater weight portion than the fuel, and consequently the above trade between fuel weight and propulsion system weight seemed to be very favorable.

Search for a demonstration model

He was encouraged and began patent procedures, but his greatest concern was the choice of an approach for selling the idea of turbojet propulsion. He felt that, in any case, a working model would be most important, and thus decided at the end of 1934, to have a prototype built at his own expense at the auto repair shop and garage "Bartels & Becker" in Göttingen.

The choice of an auto repair shop to build a prototype jet engine seems rather odd, but von Ohain was well acquainted with this repair shop and with the head mechanic and machinist, Max Hahn, long before he thought of jet engines. He had a small Opel car which he parked there, and in this way

---

2"Across from the Institute of Physics, in which I was working at that time, the Institutue for Fluiddynamics of Profs. Prandtl and Betz was located. In this Institute Dipl. Ing. Enke, with whom I later because acquainted, was engaged in research on axial flow compressors (single stage). With respect to multistaging, Enke was very cautious. Several years later, however, he became involved in work on multistaging; he became a consultant to the jet development team of the Junkers Corporation under the direction of Dr. Anselm Franz for the layout of the multistage axial flow compressor of the Jumo 004 engine and the BMW engine."

became acquainted with Hahn. From frequent conversations with him about automobile and other technical subjects, von Ohain, gained the impression that Max Hahn had an outstanding natural engineering talent and was particularly knowleageable in manufacturing methods.

Thus it was natural that the two discussed the manufacturing possibilities and cost of a demonstration model. When Hahn saw the sketches, he made many suggestions for simplification and changes to enable the manufacturing of the model with the machine tools available at the auto repair shop. Hahn's ingenuity and practical mind brought the construction of the model within the realm of von Ohain's financial means. The cost of the prototype was to be borne by some of his savings and some money advanced by his father. Including combustor, the total price estimate was slightly greater than 1000 marks, about the cost of a medium-priced used automobile. The actual final price was somewhat greater, mainly due to some changes. It is difficult to convert 1000 marks' worth of machine-man hours of 1935 in a meaningful manner into dollars of today. If the same model were to be built today, it certainly would cost more than $10,000.

Some of the physical details of the prototype are shown in the Figures. The back to back arrangement of the compressor-turbine combination is illustrated in the photograph of Fig. 5 with the outer shroud removed. The actual combustion chamber was located in the short region between the outflow compressor and inflow turbine. Achieving complete combustion within this chamber was the major difficulty in the early development of the jet engine.

The balancing of the rotary components of the earliest engine was performed on a lathe in the Bartels and Becker repair shop as shown in Figure 6. The rudimentary character of the test is evident in the coupling connecting the engine

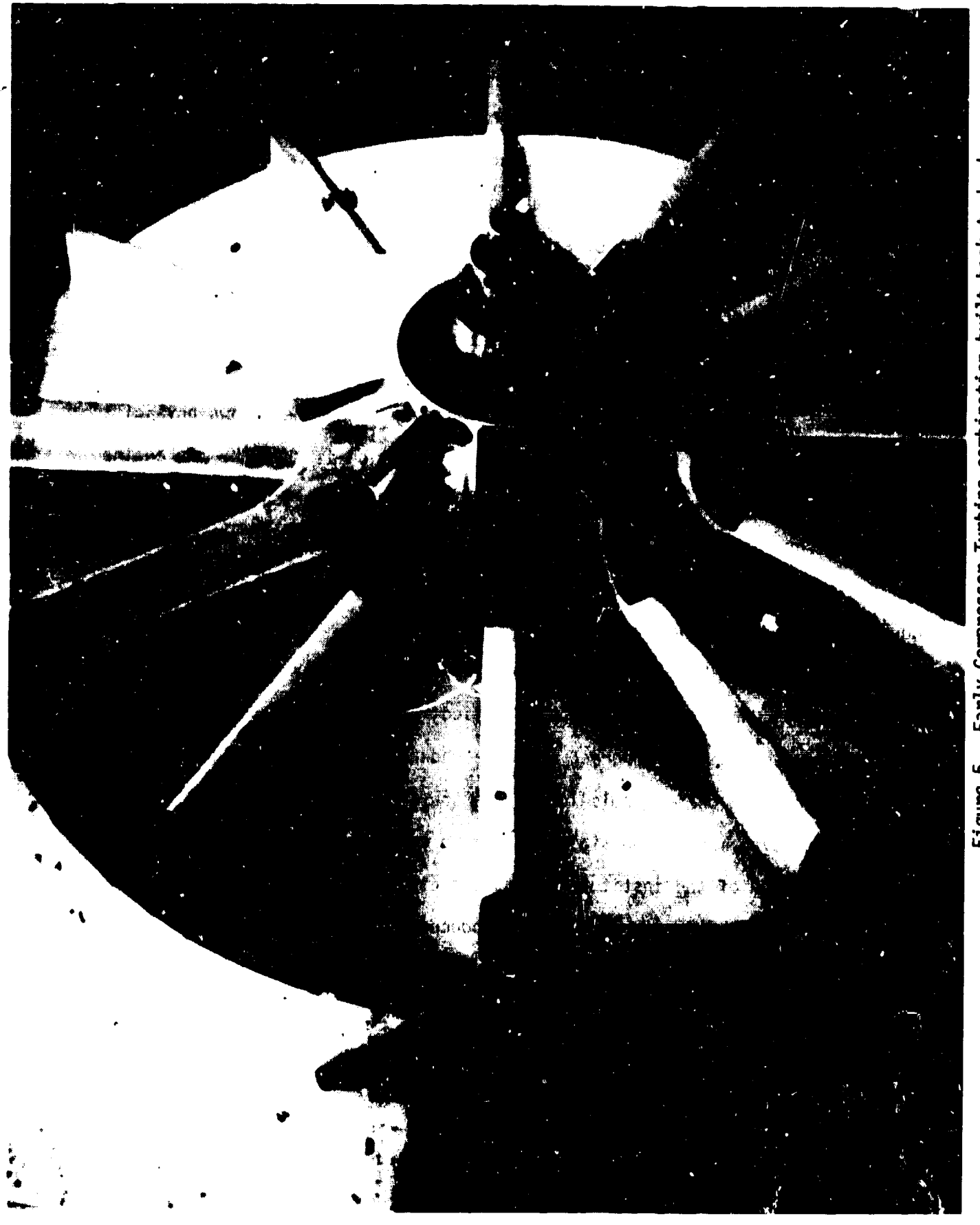

Figure 5. Early Compressor-Turbine combination built back to back.

shaft to the lathe drive on the right. The coupling is nothing more than a piece of hose tied by string to the shafts. The primitive methods employed in the early tests had little to do with experimental method but were driven by the meager support available. Even much later in the development cycle, when financial support was no longer a problem, material support became the main issue due to the lack of certain critical elements such as nickel. Thus the testing took place under some very adverse circumstances.

Prof. R. W. Pohl

During this time, von Ohain was completing his Ph.D. dissertation in the Institute of Physics of the University of Göttingen under the renown physicist Prof. R. W. Pohl. The amazing aspect of this situation is that the jet engine study was not his dissertation but rather only an extra-curricular activity, completely unrelated to his thesis and to the work of the Institute. He showed his theoretical investigations to Prof. Pohl, along with his conclusions and a plan for his working model. To his credit, Prof. Pohl was open minded and reacted positively. Although his own work was strictly theoretical and basic while von Ohain's was definitely applied, he was able to see the value in such a device and indeed agreed with the underlying theoretical bases. He generously gave von Ohain permission to use the Institute's instruments and equipment and even made it possible for him to conduct the actual experiments in a rear section of the institute. Thus the essential measurements of temperature and pressure distribution were made and produced valuable experience for von Ohain.

First Göttingen Experiments

The actual combustion experiments indicated the gasoline combustors were not functioning as planned. The combustion did not appear to take place in the combustor section (see figure 5) but rather inside the radial turbine rotor and

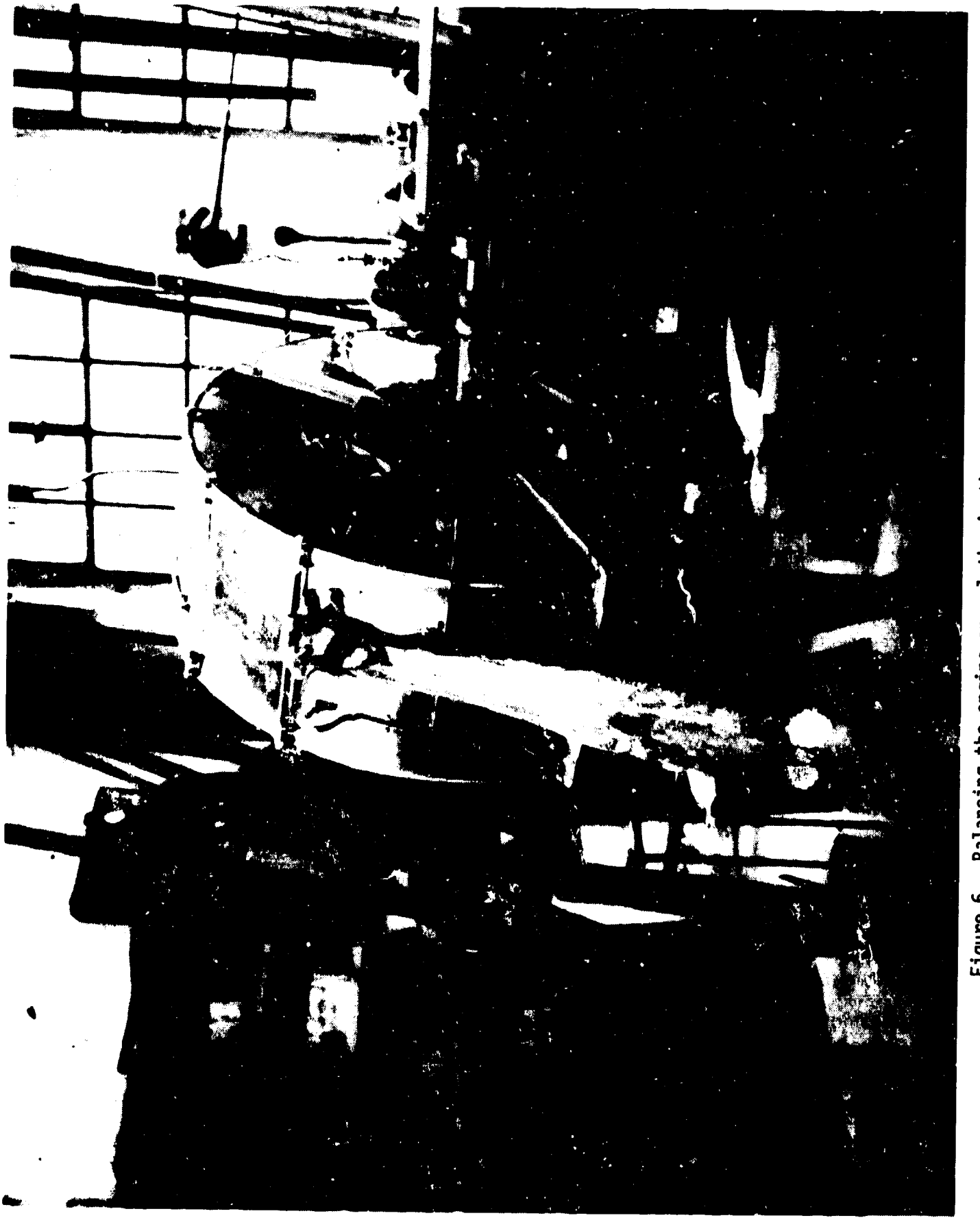

Figure 6. Balancing the engine on a lathe in the auto repair shop.

extended into the exhaust jet. Long yellow flames leaked out of the turbine and the apparatus resembled more a flame thrower than a turbine. The malfunctioning of the combustors was substantiated by temperature indications on the metal surfaces and the formation of lampblack depositions.

The engine was started, as are jets today, by means of a starter engine whose purpose was to raise the rotational speed to a value where the pressure increase produced by the compressor would be sufficient to allow combustion. It was then hoped to remove enough power through the turbine to drive the compressor and have enough left to produce thrust. Although self-sustained operation was not achieved, the starter engine was greatly unloaded, indicating that a significant amount of power was being extracted by the turbine, in spite of the combustion problems.

The lack of total success in the initial experiments had a curious effect on the participants. Von Ohain, a natural optimist (a very useful and to some degree necessary trait for a researcher) was keenly disappointed. Max Hahn, on the other hand, was a dour and normally skeptical man who in this particular instance seemed quite positive and optomistic. He expressed hope and optimism in view of the fact that the drive motor was greatly unloaded and that the flames came out at the right place with seemingly great speed. Whether this change in normal personalities was a natural occurrence or whether it was an effort on the part of Hahn to balance the disappointment of the young von Ohain is not clear. What is clear, however, is that in time of adversity, the pair which originally complemented each other in a technical sense now also seemed to do so in a psychological sense.

Search for development & support

These tests indicated to von Ohain that fundamental combustor investigations and systematic developments were necessary which would require time and money

exceeding his private means. Again, Prof. Pohl came to his rescue. In a very cordial discussion, Pohl declared that he was convinced of the correctness of von Ohain's analysis and of the great future potential of jet propulsion. However, Pohl suggested that industrial support would be necessary and offered to give him a recommendation letter to any company of his choice. Since Pohl was widely respected in German industrial circles, such an offer was not to be taken lightly.

At this point in his career, von Ohain was confronted with the very critical choice of how and where to pursue his ambition of building a jet engine. The manner in which this choice was made provides great insight into the intuitive psychological understanding he possesses, especially since his reasoning was borne out some time later by events.

He chose, not a large engine manufacturer with high powered technical support personnel and the correct expertise to solve the types of problems which were likely to arise in a new engine development, but rather an airplane company which did not even manufacture engines, the Heinkel Corporation. Asked today why he chose an airframe manufacturer over an engine manufacturer to support the development of his new jet, his answer and reasoning are fascinating. "I thought that the engine industry would be negative toward a gas turbine development. I therefore suggested the Heinkel Corporation, since Ernst Heinkel was the sole owner of his airplace company and his unconventional thinking and enormous interest in the development of high speed aircraft were generally known."[3]

---

[3]" I learned later that my belief about a negative attitude of the engine industry toward jet propulsion was very true; even the Air Ministry had great difficulties to persuade the engine industry to accept generous contract offers for jet engine development."

Heinkel was indeed interested in high speed flight. Unknown to von Ohain, Heinkel was already engaged in a development project on a rocket powered airplane led by another young German engineer, Werner von Braun.

Direct contact with Heinkel was also an important aspect of von Ohain's decision. He was concerned about the inertia in large engine companies. Much of the problem was due to the engine companies tremendous investment in tooling that would be upset by a concept such as the gas turbine engine whose construction would be radically different. In the same way, the enormous retooling costs in a modern industry such as the automotive industry causes a natural aversion to innovation. In addition, von Ohain recognized the need to be able to influence high enough company levels to reach the person with authority to make far reaching decisions. In his dealings with Heinkel, he strived to maintain the direct contact to avoid such problems at a later date.

An additional motivation for von Ohain's association with Heinkel was his love for the area near the Baltic Sea. The company was located in Warnemünde at that time and later moved to an area between Warnemünde and Rostock. Von Ohain had spent the summer of 1932 as a student in Rostock and enjoyed it tremendously. The primary motivation for choosing the Heinkel company was, of course, based on the observations mentioned above, but it was fortuitous that his choice of location was simultaneously satisfied.

Prof. Pohl's Letter

True to his offer, Prof. Pohl wrote a letter of recommendation to Dr. Heinkel. In it he referred to von Ohain's "extrodinary ability to apply his physical knowledge to technical application." He pointed out von Ohain's prior success in his dissertation, where he envisioned constructed and tested a device which converted acoustic pressure oscillations into oscillations of

light intensity. This device was patented by von Ohain and subsequently purchased by the firm of Siemans and Halske for application to military signal use.

Having thus identified his student as a practical man, he discussed his latest work. "Now he has developed another idea which I consider to be much more important, namely a discovery to power an airplane without a propeller." Not only that, stated Pohl, but "he has carried through the calculations" and "has taken practical construction into account." The only reason he was writing to Heinkel, Pohl continued, was because he believed that such a development can only be accomplished in industry. Although he conceded that Heinkel must often be bothered by offers of foolish projects, Pohl emphatically pointed out that this one concerns a "physically well founded" concept and it was to make this clear that he, and not von Ohain,wrote the letter.

Ernst Heinkel

Ernst Heinkel, ever ready for new ideas and extremely anxious to be at the forefront of the development of fast aircraft, responded quickly. He invited von Ohain to meet with him at his villa near Warnemünde on the Baltic Sea. After some preliminary discussion Heinkel arranged a conference for von Ohain to present his jet engine proposals to a group of Heinkel's leading engineers. They were to decide the merits of the proposal and report back to Heinkel.

Not surprisingly, the engineers were undecided due to the conflicting positive and negative aspects of the concept. They were dismayed at the fuel consumption rate of the proposed jet engine but the power to weight ratio of the turbo jet was acknowledged to be potentially better than that of the propeller-piston engine. This was very significant due to the large percentage of the overall airplane weight dedicated to the engine.

In addition, Heinkel's two foremost aerodynamic designers, Siegfried and Walter Guenther emphasized the need for high power output per frontal area (more than 2000 equivalent horsepower per square meter of frontal area). They also acknowledged the importance of abolishing the propeller in view of future high-speed aircraft. Thus, it was clear to some that the propeller-piston combination had inherent limitations in terms of speed and that these could potentially be overcome by the proposed jet. Of course the jet had not yet operated so this was considered by others to be wishful thinking.

Von Ohain proposed to the group that the jet engine could also be utilized for the generation of direct lift. That is, instead of accelerating the airplane on a runway until the speed was sufficient to generate the required lift, suppose the engines are installed such that the thrust is vertical. This is attractive in the jet engine case due to the high thrust to weight ratio and especially so for the flat "pancake" shape of the radial compresser-turbine combination because its shape was suitable for installation in the aircraft wing. Heinkel's engineers were not enthusiastic about the direct thrust application of the jet. This is understandable when one considers that a direct thrust vertical take-off aircraft was not operational until the British "Harrier" in the late 1960's.

Contact with Heinkel

Since his engineers did not reject the idea of jet propulsion outright, and, in fact, noted several positive aspects to the proposal, Heinkel decided to gamble on the potential of the concept. He entered into two separate contracts with the young scientist (at von Ohain's insistence). The first was an employment contract, beginning 15 April 1936, while the second was a royalty agreement for a portion of the proceeds from any eventual sale of the engine to be developed.

Von Ohain also wanted Max Hahn to be employed in the development program, although he was by no means certain that Hahn would be willing to leave his stable employment at the Bartels and Becker garage. Hahn's position became somewhat of a stumbling block because Heinkel's Employment Division reasoned that he would be too much of a responsibility for von Ohain, in view of the uncertainty of the outcome of the jet engine development project. Heinkel originally stayed out of this situation. However, when it threatened to affect the project he interceded. He pointed out that the hesitation was ridiculous since his company could always use a good mechanic even if the project were not to prove successful. After these difficulties were resolved, von Ohain approached Hahn, who agreed to join him at Heinkel. It should be pointed out that such changes in position were not taken lightly in mid 1930's Germany. Thus Hahn's decision expressed very significant confidence in the eventual positive outcome of the project.

Heinkel wanted to keep the jet development apart from his aircraft organization with the goal to form a separate gas turbine division in the event that the early phases of jet engine development were successful. For this reason a clause was written into von Ohain's employment contract requiring that he report directly to Heinkel for the jet engine development. For the purposes of security (both company proprietary and national security), the project was called "Sonder-Entwicklung" or "Special Development" and the jet designation dropped. For the same security reasons Heinkel wanted the location of the "Special Development" to be separated from the rest of his company, and so a temporary small building with an adjacent semi-open test stand was erected a considerable distance away from the main building complex. This building provided working space for eight people. Surrounding the building was a wooden board fence about a man's height. There were simple locks at the

gates and, although the arrangement was worked out with the resident military security officer, the facility would have presented little challenge to someone attempting to breach the security precautions. After the building was finished (early June 1936), Heinkel detailed Max Hahn and Dip. Ing. Wilhelm Gundermann and two draftsmen to the project.

Heinkel's desire for internal security was prompted by his objective to be first in the jet propulsion field and, as he explained to von Ohain, that he wanted the jet engine development to remain his own enterprise without government sponsorship. He was extremely anxious to fly with jet propulsion as soon as possible and chose a technical goal of an engine with a thrust of 600 kg (1320 lbs.). He ordered an immediate start on the design of such an engine, including the requirement that it be suitable for flight. Thus the engine could not be an experimental "boiler plate" version (in which the construction materials and their weight would not be significant, only the performance would be measured). Flight compatability required that the engine, in addition to meeting the performance requirement (in terms of thrust) would also need to be lightweight, compact and with a very limited frontal area. In addition, Heinkel decreed that ground testing for the new engine should begin in about one year, resulting in a goal of about June 1937.

A development strategy

Von Ohain recognized immediately that the goals and time limits outlined by Heinkel would not allow for an orderly scientific methods as he had planned. His early tests in Göttingen had clearly demonstrated that a basic difficulty was the poor combustor performance. Since the combustion process was not complete in the combustor but rather proceeded into the turbine region (and for that matter also into the engine exhaust), the full energy was not available

in the turbine flow and therefore the amount necessary to drive the compressor was not being extracted. His original plan had been to first develop a well functioning combustor and,based on that, to begin to design an engine around the combustor.

The original plan had to be scrapped for three reasons; Von Ohain's rather tenuous position in the Heinkel Corporation (his position depended on the ongoing success of the project), the political climate (unemployed men were almost immediately drafted into the army) and, most important of all, the great impatience of Heinkel . However, he realized that to proceed exactly as Heinkel had directed to a flight-worthy engine would be a very poor gamble since another encounter with a poorly functioning combustor would almost certainly mean the end of the turbojet project.

Scientific understanding alone is insufficient to solve such a problem. A successful strategy requires psychological insight, since the major constraints described above drive the technical aspects of the program rather than the other way around. Thus the choice of an approach to the technical problem is as important as the actual solution of the technical problems.

Von Ohain's approach was in two phases; one phase to satisfy the immediate pressures and give himself time for the second phase to be completed in a more systematic manner. The first phase was to build very quickly a simple jet engine which would bypass the problems associated with the combustor and yet demonstrate the jet principle in a very convincing and impressive manner. The second phase was a longer term and systematic gasoline combustor development. The phases overlapped since at the beginning of the project, Phase I received the majority of the attention but the preliminary component tests for Phase II needed to be initiated. Von Ohain was convinced, based on his understanding

of Heinkel, that a successful demonstration of a jet engine (even short of a flight worthy model) would assure him of the necessary time required for the development of a combustor and flight engine.

The hydrogen engine

The chosen design for an engine of low development risk was the combination of radial outflow compressor and radial inflow turbine. This was the same concept as the initial test in Göttingen and was chosen for essentially the same reason; namely to avoid (at least for the time being) the additional development problems associated with an axial flow device, especially the matching of the turbine and compressor and the effects of multiple stages.

The early Göttingen test had shown that the combustion of the gasoline was too slow and thus occurred in the turbine and exhaust as well as the designated combustion chamber. This problem was to be treated in Phase II. For Phase I von Ohain chose gaseous hydrogen as the fuel because of its known properties of a very high diffusion speed and a very wide fuel-air concentration range over which combustion is possible. Thus the risk involved in Phase I was minimized since the hydrogen properties were expected to allow relatively complete combustion before the entrance to the turbine. In this way the full fuel energy would be added before any energy was extracted by the turbine. The turbine energy extraction was therefore expected to be more successful and, in particular, enough energy was expected to be available to drive the compressor and make the engine self-sustaining.

Von Ohain had already conceived a hydrogen combustor which he was sure would function very well and not need any time consuming preliminary tests. It consisted of a large number of hollow vanes with blunt trailing edges placed within the airduct between the compressor stator exit and the turbine stator

inlet as shown in Figure 7. The gaseous hydrogen was ducted into the hollow vanes and was injected through a number of small holes along the blunt trailing edge into the wake behind the vanes.

Von Ohain's attention was primarily occupied by the design calculations for the hydrogen combustion engine and its actual layout as well as the concepts and preliminary design of the gasoline combustion chamber. Gundermann and Hahn worked on a design concept using spin-parts riveted to ring flanges. Spin parts are axisymmetric shapes formed out of sheet metal by turning and forming the metal on a special lathe. This method was commonly used for aircraft fuselage construction. Thus the spin parts, supported by flanges, were to form the shroud and flow ducts of the engine. Gundermann made the detailed mechanical calculations of the sheet metal rotors and discs. The Heinkel Corporation was, as an airframe company, well equipped to quickly produce large spin-parts, but was unable to manufacture the ring flanges and the rotor discs. Because of their size, these parts had to be manufactured in a nearby shipyard. The smaller compressor and turbine parts were produced in the company's machine shops.

During 1936, the highest priority was placed upon the design and construction of the hydrogen demonstration engine, designated the He.S.1 and shown in Figure 7. The completed engine was installed in the test bed about the end of February 1937. The exact date of the first run with hydrogen fuel is not certain. It may have been in late February or early March.[4] Most of the

[4] Heinkel wrote in his memoirs that the first run of the hydrogen engine He.S.1 took place in Sept. 1937. This date is definitely wrong because I remember several comments in which nine months from the beginning to the first run were emphasized. In addition, I recall that water puddles in the vicinity of the jet made the demonstration very impressive. During March and early April we often had night frost, and prior to our first demonstrations to Heinkel's top engineers and important visitors, the test mechanic cracked the thin ice coverage of the puddles."

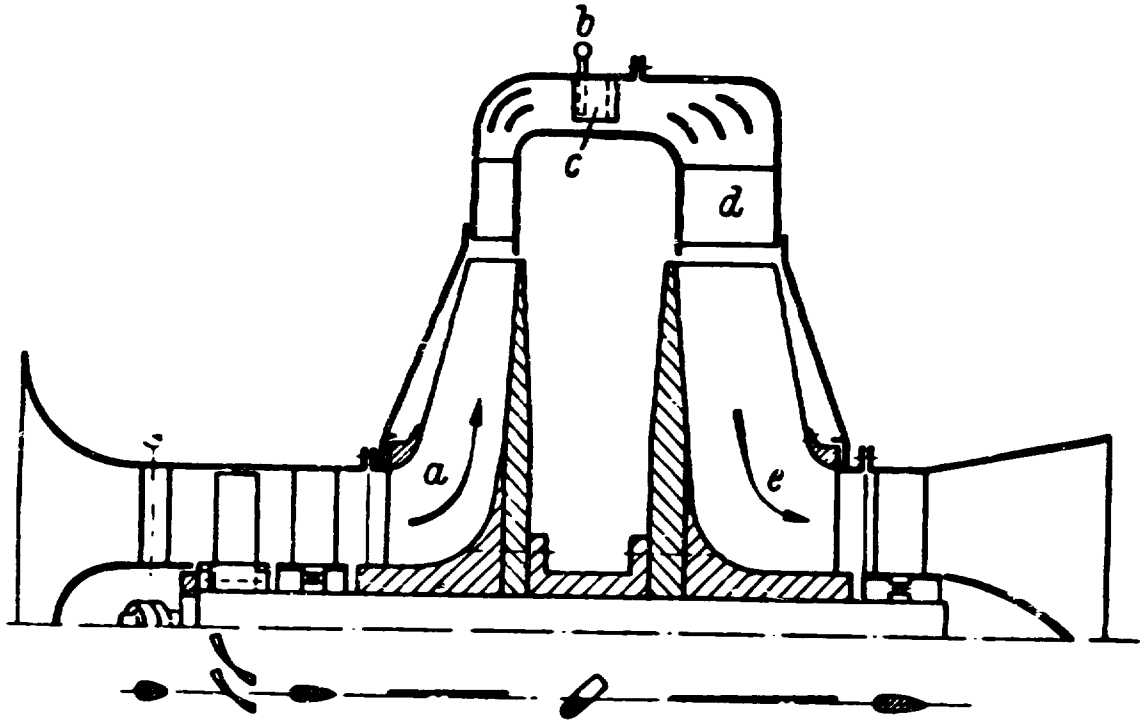

RADIAL TURBOJET (He S-1)
WITH HYDROGEN
(Built in 1936; tested in April 1937)

Radius of rotor - 1'
Thrust - 250#
10,000 RPM

Figure 7. The hydrogen demonstration engine.

hydrogen test runs were completed by April 1937.

The hydrogen engine fully met their expectations and was a great success. It reached the anticipated performance and handled very well in acceleration and deceleration, probably due to the relatively small moment of inertia of the compressor and turbine rotors and the great stability of the hydrogen combustor over a wide operational range. Most important of all, the psychological effect was enormous. Heinkel and his engineers suddenly believed firmly in the feasibility of turbojet propulsion, and von Ohain's position in the company was now very secure. It also was a considerable morale boost to von Ohain, Hahn, Gunderman and the rest of the development team, which at this point numbered only five people plus the construction support at the Heinkel corporation and the nearby shipyard.

The development team

As evidenced by their success, the team of von Ohain, Gundermann and Hahn worked very well together. Each had his particular area of strongest technical interest and competence: Hahn in manufacturing techniques and combustion experimentation; Gundermann in stress analysis and mechanical design. He also was head of the group of draftsmen. Von Ohain gave the overall technical direction, such as utilizing hydrogen for the first test engine and establishing the program for the combustor development. He also made the layouts for the test engines, specifically the thermodynamic analysis and the internal aerodynamics, and became versed in the design techniques of axial flow compressors.

Von Ohain several times attempted to discuss aerodynamics with Gundermann, who expressed no interest in the field although he was very competent in stress analysis. In order to clarify and enlarge on his ideas, von Ohain needed to discuss the aerodynamic problems involved in the gas turbine. This he did with Professor Helmwold, Head of Heinkel's high speed wind tunnel, who was a marine engineer well known for his work in anti-cavitating propellers. This branch of fluid mechanics was really the first to experience problems with compressibility. Due to the combined foreward and rotational speeds, the tips of the propeller reached high speeds and it was there that compressibility effects first appeared. The conversations with Helmwold were very valuable and it was from them that von Ohain learned the tricks of axial flow compressor design.

As pointed out earlier, Hahn had no formal training in his areas and was essentially self taught. Moreover von Ohain, trained as a physicist, had never taken a course in thermodynamics and was completely self taught in that field. He had, however, a minor in aerodynamics and had studied under Professors Prandtl and Betz at Göttingen, the best aerodynamics institute in the world at that time.

Von Ohain had a strong personal relationship with Prandtl in addition to his taking a minor in aerodynamics. They sometimes went skiing together in the Hartz Mountains near Göttingen. Prandtl had tremendous insight into fluid mechanics. He was able to present the information clearly and concisely even though he stuttered and deliberated slowly.

One project in which von Ohain participated with Prandtl was an investigation of why cats always seem to land on their feet. There was some suspicion that it could be an aerodynamic effect. This possibility was

quickly negated by the fact that a cat could land on its feet even when released from an inverted position only a foot or less above the floor. An aerodynamic effect would take far too long for it to be responsible. The suggestion was made that the effect was caused by the swinging of the cat's tail in the opposite direction to the motion. Observation also showed that this was not the cause of the phenomenon. The effect was finally traced to a muscular reaction in the cat's back which caused the cat to twist appropriately in the air.

The very advantage of being outside the aircraft engine establishment, which had led von Ohain into the Heinkel company in the first place, now began to show some negative aspects. Heinkel had the attributes of being farsighted and ambitious for his company. However, he lacked the technical insight required to fully appreciate the difficulty of the jet engine development. Thus he did not clearly see the support necessary for such a project. He had lived and worked through the days of wooden aircraft with fabric wings where very rapid building and rebuilding was possible. This was no longer the case with the jet engine. Any substantial design changes would require far more time to construct and implement.

Heinkel also believed in the principle that one first demonstrates the ability to do something and then asks for more support to achieve further objectives. This stepwise was fine for some projects but in the case of the jet engine development it was inappropriate, as von Ohain and others attempted to tell him. In order to move on with the required speed and attention to detail, they needed more engineers, especially specialists in materials, manufacturing (machining and casting processes) and controls. These people were not available in the Heinkel company and were also very scarce in the

overall economy. Even after Heinkel was convinced, it was several years before he obtained the necessary personnel. Thus the lack of corporate inertia which made it possible for von Ohain to demonstrate the feasibility of the gas turbine engine appeared again as less than the critical mass required for its timely development.

Initial gasoline powered tests

After the successful demonstration of the He.S.1, Heinkel exerted a strong pressure for an accelerated flight engine program. As verified by the hydrogen tests, the basic component required was the gasoline combustor development project which was already underway at a lower priority level than the hydrogen engine. A component test facility was established with the installation of a two horsepower Sirocco blower with controllable bypass so the flow in the combustion chamber could be varied.

Installing segments of annular combustors in what was really a combustion wind tunnel, the effects of various parameters on the combustion process could be determined. The questions to be answered in this facility included:

a. What is the influence of the shape of the chamber on the combustion?
b. Are flame holders required (to reduce the local velocity to a point where the flame will stabilize in one position) and if so what is a good design?
c. How can air be gradually added to the combustion process in order to more precisely control the fuel-air ratio?
d. In what way can the combustor volume be reduced for a given pressure and fuel flow?
e. How can the total pressure drop through the combustor be minimized.

The injection of the fuel into the combustion chamber was, of course, a critical problem. The fuel and the airflow had to mix very rapidly in order to allow combustion to take place in the very limited confines of the combustion chamber. Two methods of introducing the fuel into the combustion

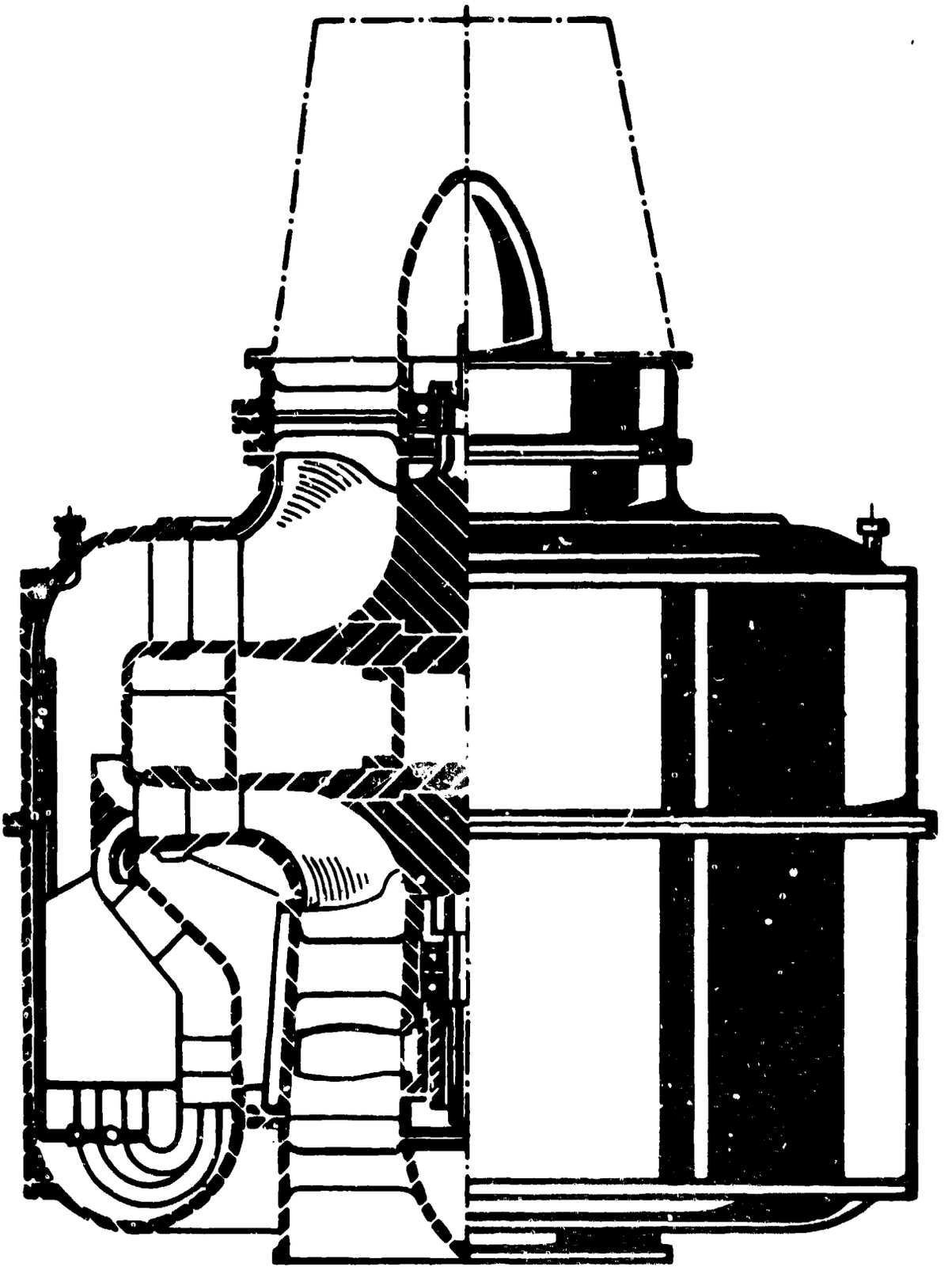

Figure 8. Engine Schematic showing the axial inducer stage.

chamber were investigated. One was the generation of gasoline vapor and its injection into the combustor. This required a high pressure vapor which was produced by an electrically heated pressure boiler. This method appeared promising because the vapor could be expected to diffuse rapidly in the air.

The second method considered was the introduction of gasoline as an atomized liquid through a very small pressurized nozzle. This technique would have the advantage of relative simplicity because it would avoid the necessity for the fuel boiler.

The intensified combustor program, beginning in May 1937, produced an excellent operational combustor in less than a year. By early 1938, a very low pressure drop combustor was available. These combustors worked best, however, with gasified fuel. The tests with atomized liquid fuel still exhibited some difficulties during starting and low-speed operation which were later overcome. Max Hahn's automotive background made his assistance especially effective in the experimental phases of the combustor development program.

Aside from the combustor problems a major difficulty with the flight engine lay in the need for achieving a high mass flow and high component efficiencies of compressor and turbine. The high mass flow was obtained by an unconventionally large ratio of compressor rotor inlet diameter to rotor exit diameter. Normally such a compressor configuration would result in a very large inlet losses caused by excessively high Mach numbers and too large inlet blade curvatures. Von Ohain tried to reduce these losses by means of an axial inducer stage which gave the inlet flow both a precompression and a prerotation, thereby substantially reducing the Mach number and curvature of the rotor inlet blading. The inducer stage, showin in the schematic of Figure 8., is really the first step toward an axial flow compressor. A more detailed view is presented in the engine layout of Figure 9.

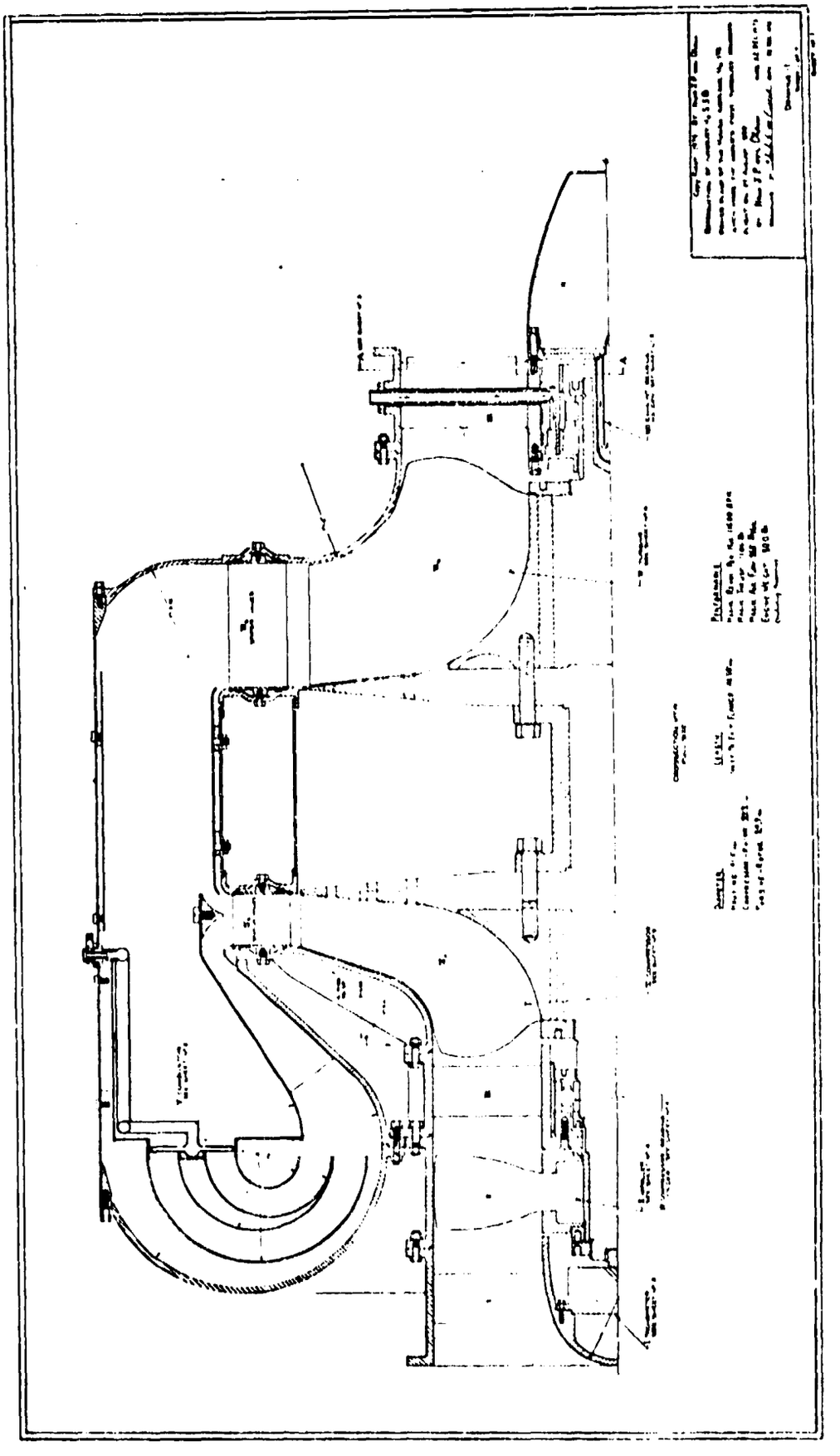

Figure 9. The engine layout.

The performance of this engine, the He.S.3 is shown in Figure10 in terms of thrust and specific fuel consumption as a function of flight velocity. The maximum thrust of 500 kg. (1100 lbs.) was especially significant in view of the engine's weight, also equal to 500 kg.

The front combustor

Comparing the gasoline engine of Figure 8 with the hydrogen powered engine of Figure 7, it is obvious that the combustion chamber has been moved to a new position. This change occurred in late 1937 when von Ohain was working on various layouts of the flight engine and Max Hahn suggested to him an idea of arranging the combustor in the large unused space in front of the radial flow compressor. He pointed out that this would greatly reduce engine length and total weight. Von Ohain considered this to be an excellent idea and could see many additional mechanical and aerodynamical advantages. He incorporated Hahn's suggestion in the layout of the flight engine and worked out the aerodynamics of the air ducts and the mixing of the combustion products with the bypass air.

The front combustor configuration, as it was called, was important since it allowed an increased combustor length without increasing the engine length or frontal area. Von Ohain was especially pleased by the significance of Hahn's contribution. As he recalled, "In view of the initial difficulties I had with Max Hahn's employment, it gave me great satisfaction to notify the Patent Division of Hahn's proposal." The company proceeded with an international patent[5] which appeared with Hahn as the sole inventor. This is another concrete example of Hans von Ohain's character. He certainly would have been justified to add himself as a joint inventor, due to the contributions required of him to transform the concept to an actual workable design. However, he felt strongly that Max Hahn should be recognized in his own right.

Cut away view

Schnittzeichnung

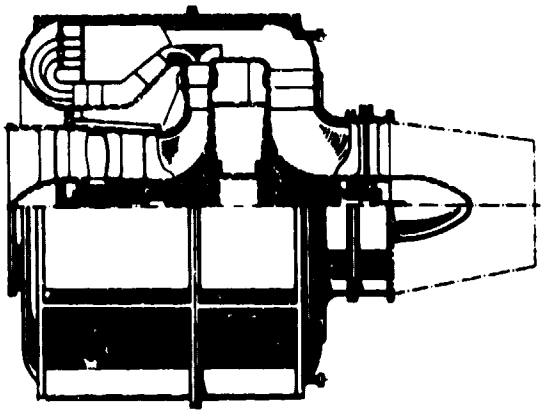

Schaubilder

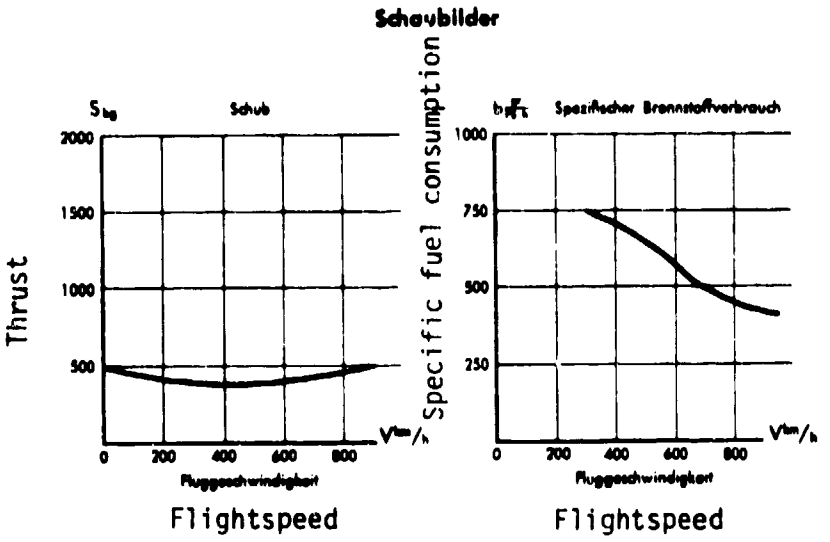

Figure 10. Performance of the He.S.3.

The deadline for the flight engine was set for early spring 1939 and therefore the design had to be frozen (fixed for construction) in about early summer 1938. At that time the combustor with atomized liquid fuel injection was not working entirely satisfactorily; therefore, the internal fuel gasification system was employed for the first flight engines. Its design and layout is shown in Figure 11. An independent accessory drive was planned for the first flight engines. Later engines would use the atomized liquid fuel injection system powered by a mechanical accessory drive operating off the engine and developed by Gundermann.

An early series of test was undertaken with the He.S.3A engine mounted beneath the fuselage of a He118 piston engine experimental bomber. This engine's turbine eventually failed after being exposed to the hot combustion products for many flights. However, the data collected led to an improved design, designated the He.S.3B. This was the engine installed in the world's first turbojet powered aircraft, the He 178.

The Design of the He 178

During the last months of 1937, the Guenthers had begun preliminary design studies of the first jet propelled aircraft and projected a required thrust of (1100 lbs.) 500 kg. This aircraft was, in many respects, an experimental aircraft for demonstration of the principle and the characteristics of jet propulsion but already contained provisions for some armament.

About early 1938,the detailed design of the He 178 began. Gundermann made essential contributions to the shape of the air inlet, and the air

---

5 The Encyclopedia Britannica speaks of a joint patent of Max Hahn and Hans von Ohain. This is incorrect: Hahn was the sole inventor of the "Front Combustor" configuration. The von Ohain patents had been applied for several years prior to Max Hahn's patent application."

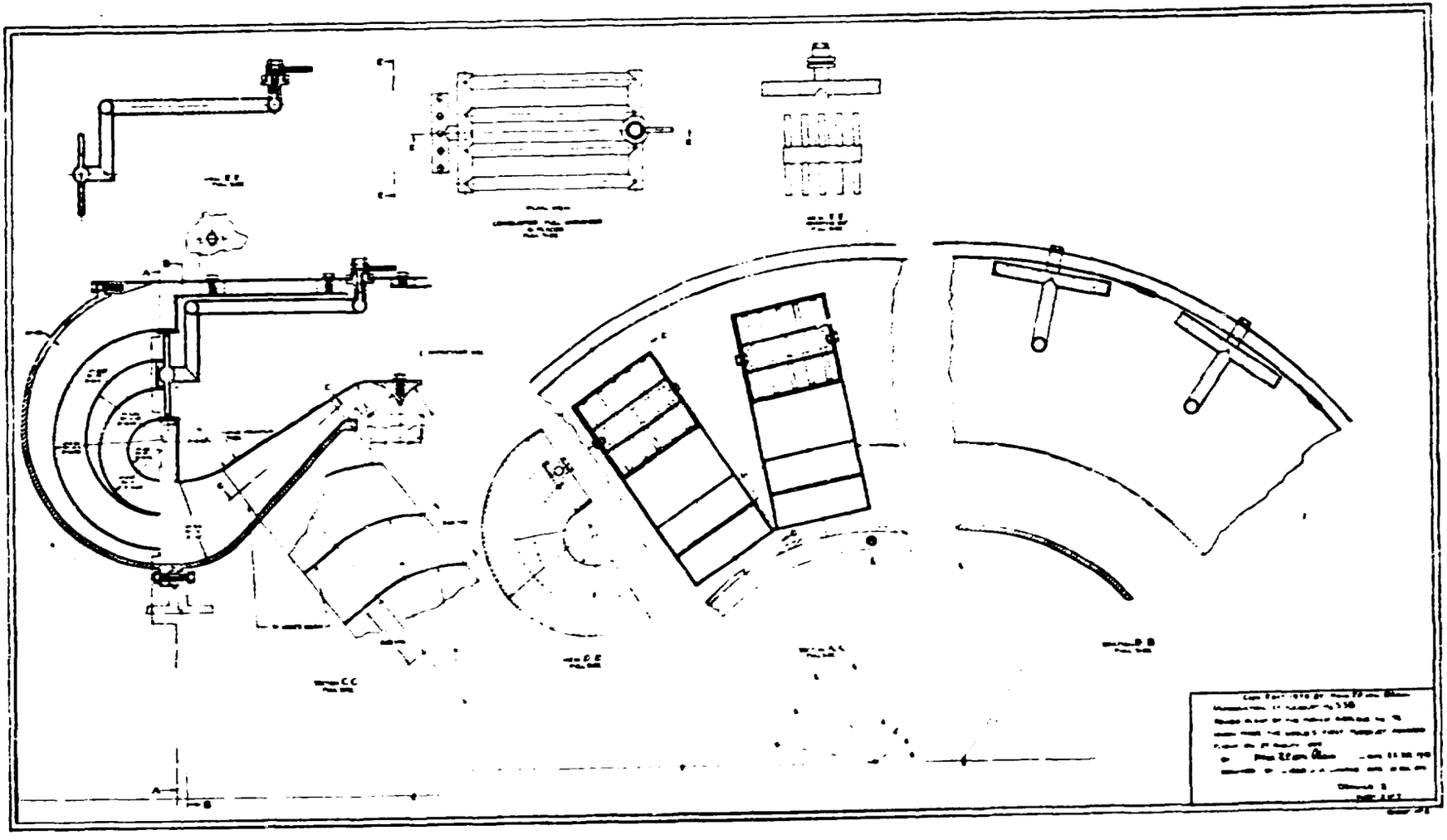

Figure 11. Fuel gasification system for the He.S.3B engine.

and exhaust gas ducts. A schematic of the aircraft showing the duct and engine locations is shown in Figure 12. The engine was in the fuselage with the inlet at the nose of the craft as shown in Figure 13 a side view of the actual aircraft. The inlet air duct passed under the cockpit and then curved up to the engine mounted in the aft section of the craft. In this position the engine frontal area was not a problem since it fit within the fuselage. However, this position resulted in a rather long tailpipe. A single fuel tank was mounted behind the pilot's seat.

The wingspan of the first turbojet aircraft was 23 ft. 7 1/2 in. of basically wooden construction. The fuselage was constructed in a duraluminum monocoque fashion with a length of 24 ft. 6 1/2 inches. The aircraft height was a 6 ft. 10 3/4 inches with a wing surface area of 97.95 sq. ft. Additional views of the He 178 are shown in Figure 14-17.

After the completion of the engine and airframe in the late spring 1939, the net thrust was considerably below the anticipated 500 kg. Therefore, a takeoff from the relatively short company air field was not possible. A number of internal engine adjustments were made, specifically in the exchangeable compressor-diffuser and turbine stator. In August the engine performance reached nearly the anticipated values. On the 27th of August, 1939, Heinkel's test pilot Erich Warsitz, made the first successful flight.

The First Turbojet Flight

The world's first flight of a turbojet aircraft took place shortly after sunrise on a beautiful morning near the Baltic Sea. Captain Erich Warsitz took off from the Marienehe airfield at about 6:00 A.M. The He 178 with its He.S.3B engine rose smoothly and relatively quietly into the air. Although the plane was designed to operate at 450 mph, Warsitz held it below 200 mph

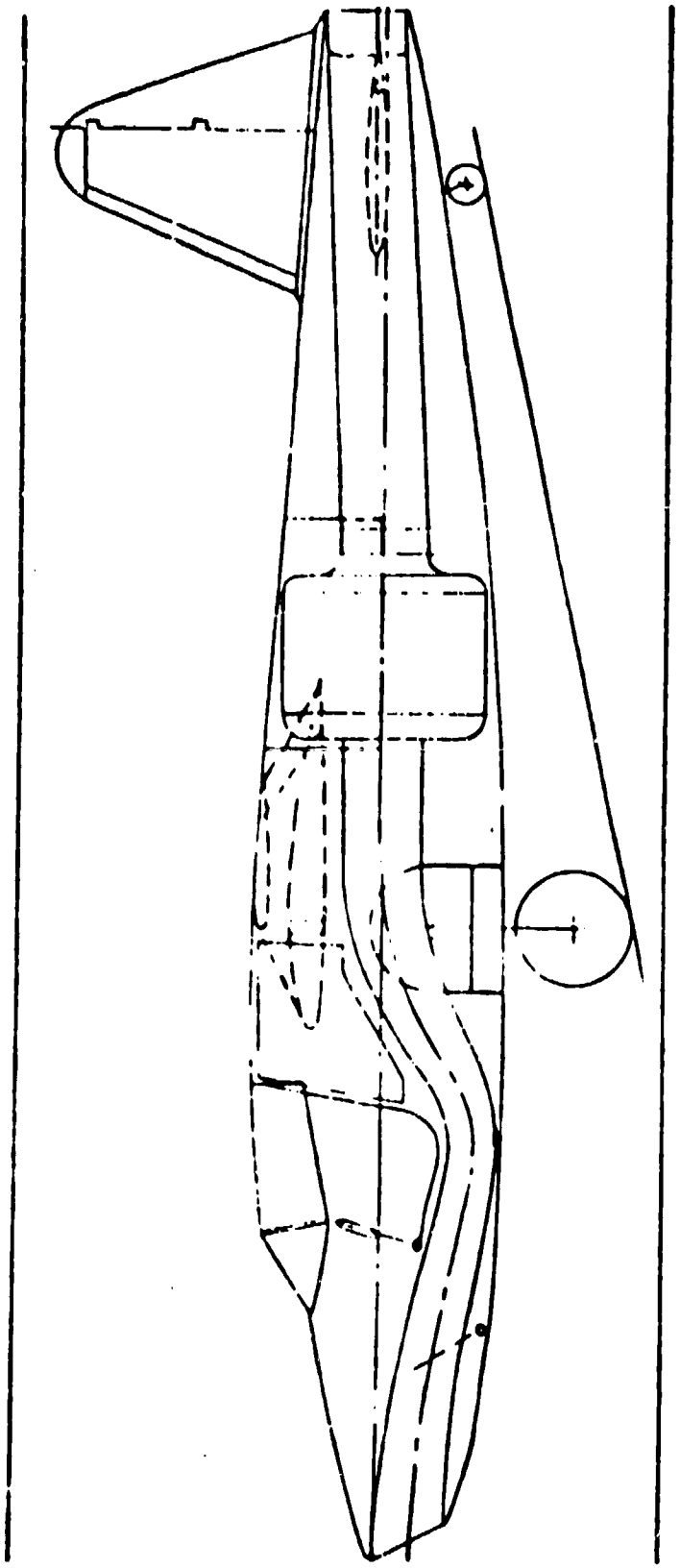

Figure 12. Layout of the Heinkel He178 Aircraft.

The world's first aircraft to fly purely on turbojet power, the Heinkel He 178. Its first true flight was on 27 August, 1939.

Figure 13. Side view of the H3 178

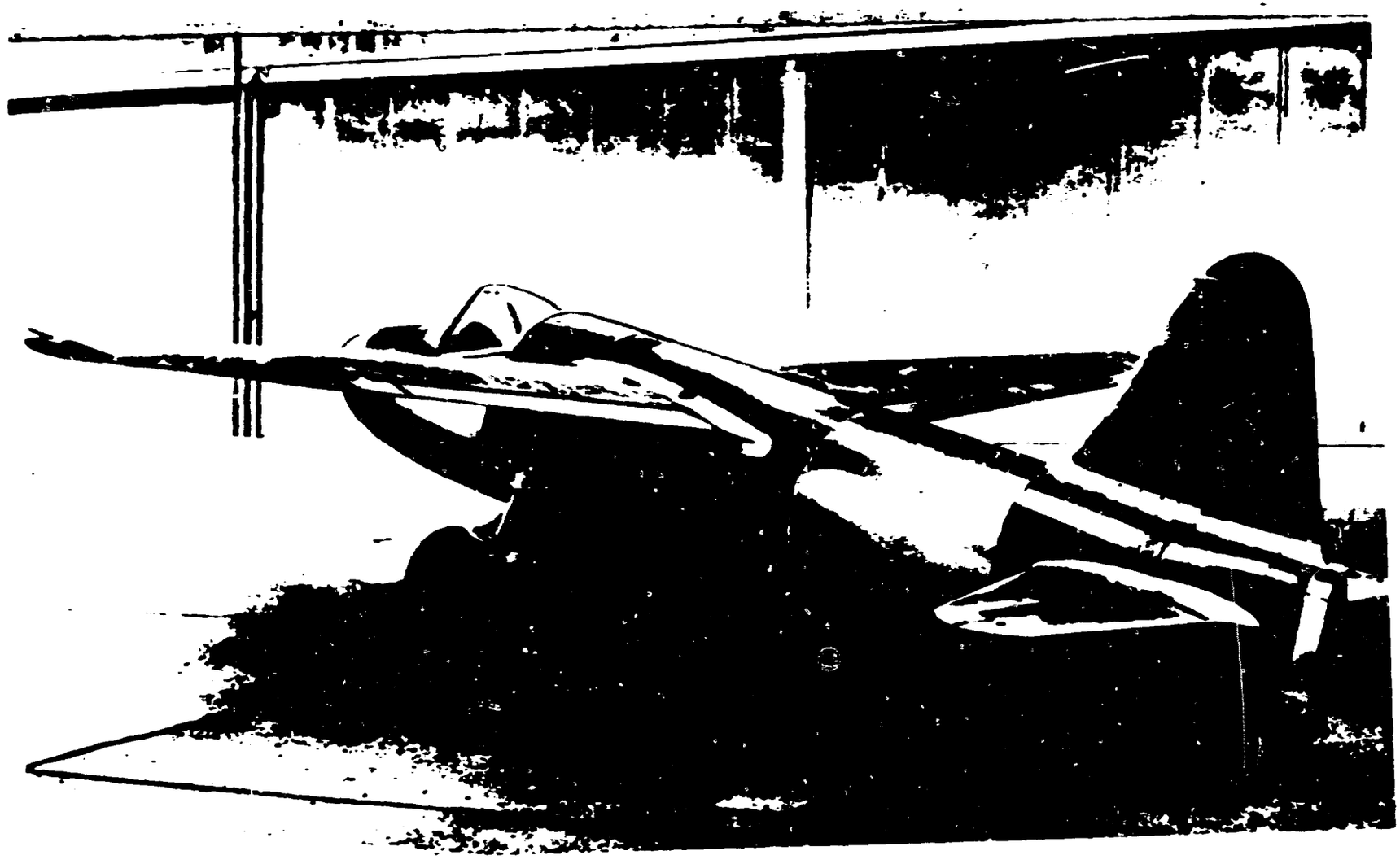

Figure 14. The He 178 showing the access panels covering the engine.

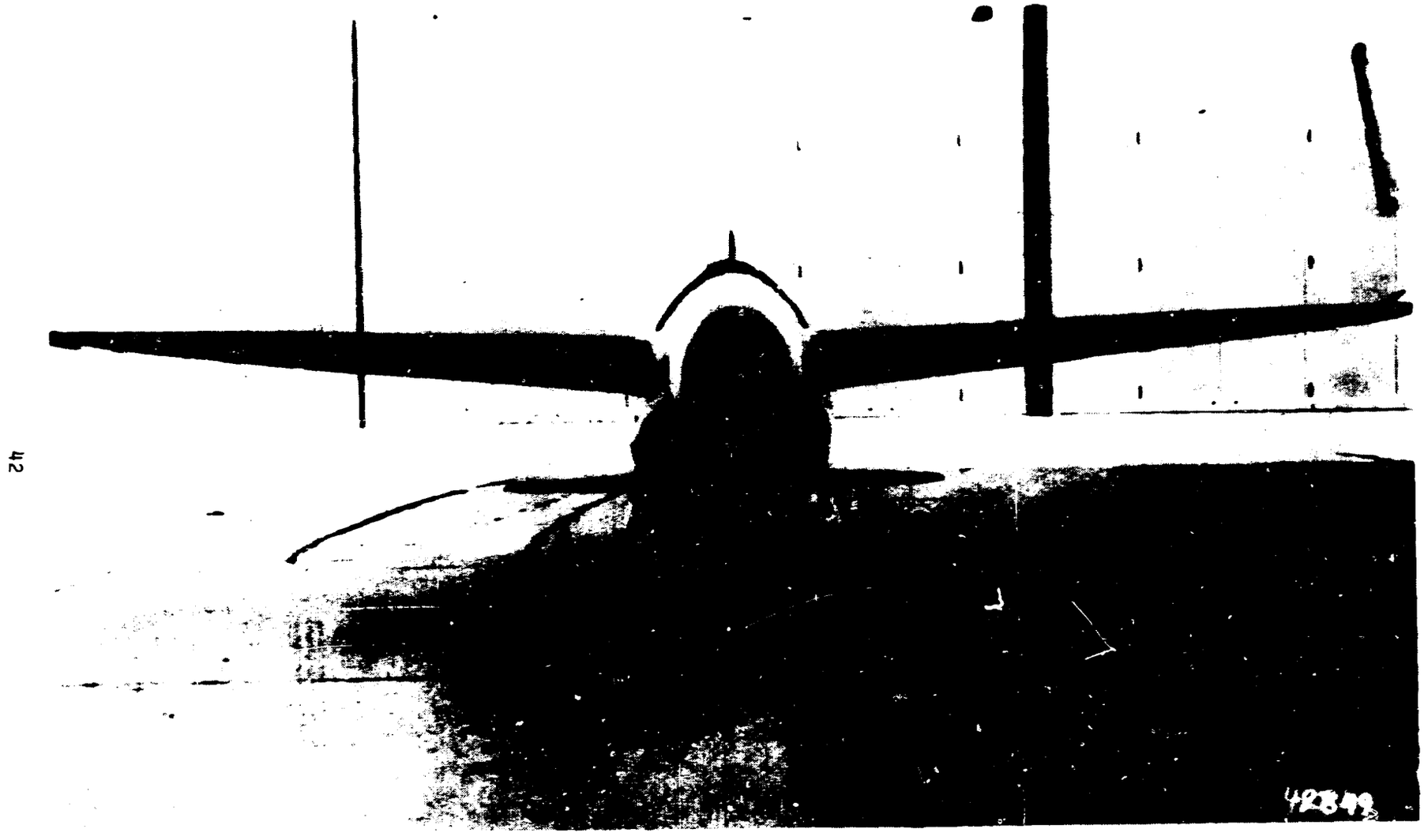

Figure 15. Front view of the He 178

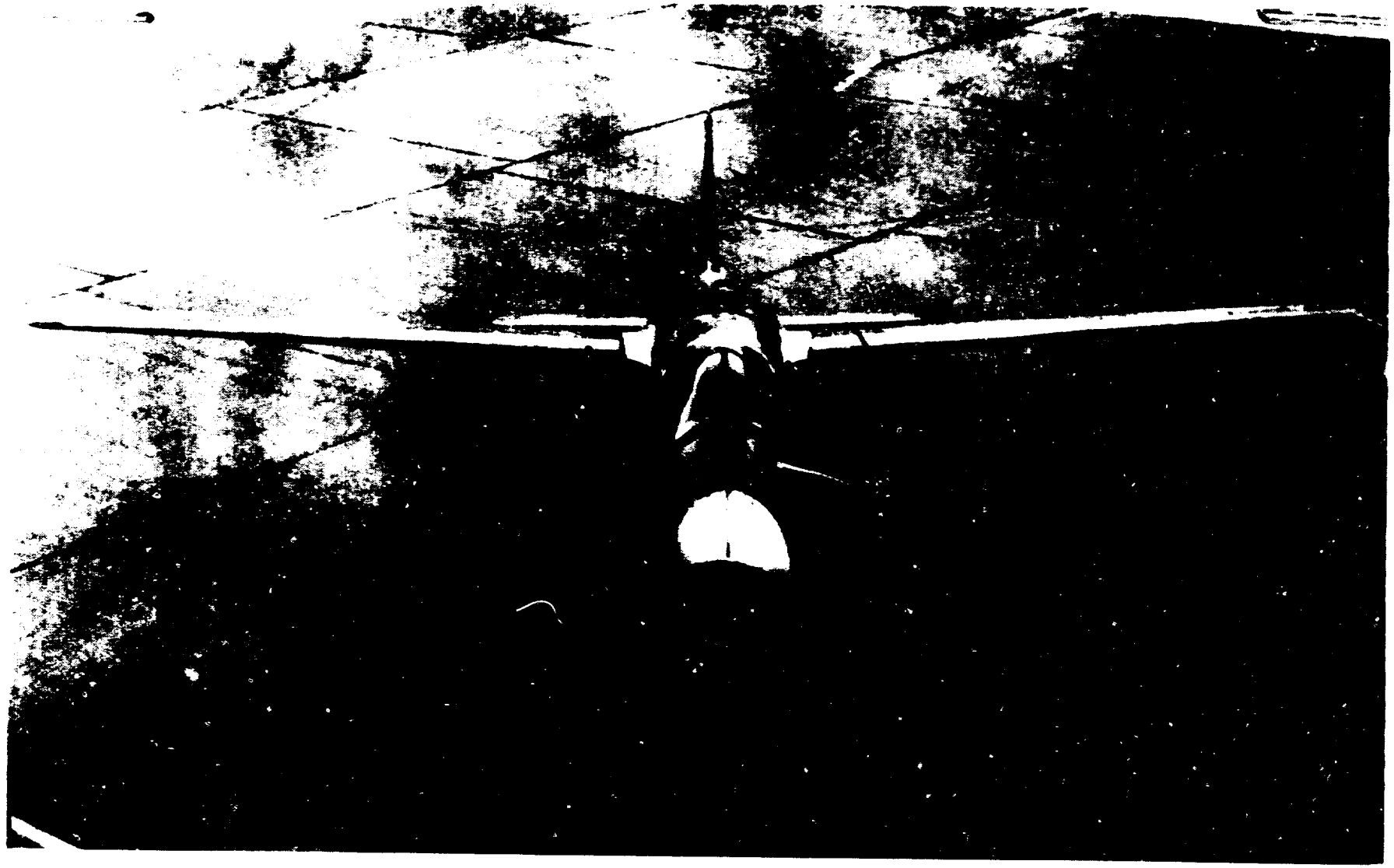

Figure 16. Additional view of the He 178

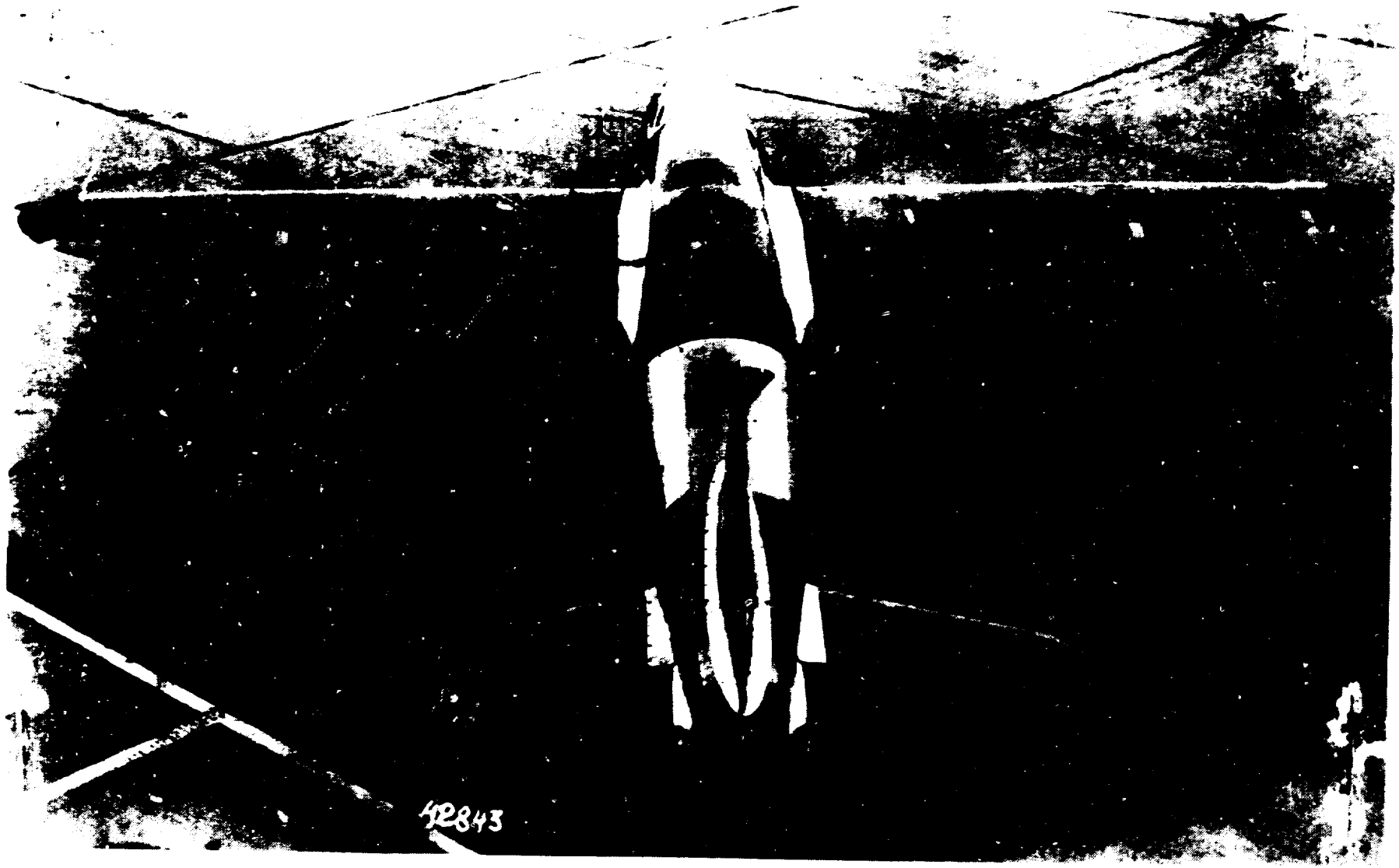

Figure 17. Additional view of the He 178

because he wanted the gas turbine to run as cool as possible. After the flight he said he could have flown much faster, which he later did. The initial flight totaled a distance of roughly 50 miles, mostly at an altitude of between 2.000 and 3,000 feet.

Although the weather was beautiful, there was a heavy early morning fog. The observers of the first flight thought the pilot was enjoying himself because he made several passes at the field. Actually, Warsitz was having trouble trying to get down through the fog. The landing was successful and a pleasant celebration followed for the 50 to 80 people who witnessed the flight.

Von Ohain later learned from Helmut Schelp at the German Air Ministry that German counter-intelligence had determined that an English spy had witnessed the first flight and that the information was available in London two days later. The spy need not have been included in the group watching within the plant. He could simply have seen the airplane flying without propellers and could have, for that matter, lived at the local hotel. The Air Ministry was rather upset that Heinkel had allowed the flight to take place from a non-secure airfield.

Even without the question of spies, the project received a lot of attention within the company. It was listed in the company telephone directory under "Sonder Enwickelung" and thus prompted a substantial curiosity among the other Heinkel employees. In addition, the test stand was near enough for the turbine noise to be heard. The workers didn't know what it was, but guessed that it was involved with power and propulsion. The attention was a source of enjoyment to von Ohain's co-workers.

First Turbojet Debriefing

A substantial amount of information was produced by the first flight, especially in the form of a substantiation of expected behavior. There were no particular surprises and the engine functioned rather closely to expectation. For example, it had been predicted that the turbine inlet temperature would be reduced in flight as compared to ground testing. This was verified and therefore more accurate predictions of future flight performance were possible. The design procedure for the air inlet was also verified by the flight test. The main corrections to be made did not involve the engine at all but rather the airframe itself. There were some problems with the external aerodynamics and some difficulties with the landing gear, including some instabilities.

The pilot's response to the turbojet was very interesting. Von Ohain's group was amused by the fact that Warsitz had a false sense of security due to the lack of the normal shaking and rumbling produced in the cockpit by a reciprocating engine. The absence of vibration and noise -- like an electric motor increased the pilot's comfort and lulled him into a false sense of security. These factors were, of course, to make the jet engine very attractive to commercial aviation in later years. The pilot was also pleased by the fact that the turbojet aircraft did not exhibit the torque that is normally evident in a propeller powered airplane.

In all, the first turbojet flight was a great success. Not only could a jet engine produce enough thrust to power an aircraft but the engine was compatible with the aircraft requirements and indeed produced a smoother, more comfortable flight. Having successfully demonstrated the first turbojet powered aircraft was, however, not enough to gain Heinkel's company the support of the German Air Ministry.

The Air Ministry

In order to understand the reaction to the first successful turbojet flight and the subsequent events it precipitated, it is important to first examine the German Air Ministry's plans and actions. Circa 1937-38, there was no consensus within the German Air Ministry concerning turbojet propulsion possibilities. The position of many of the higher echelons was one of indifference prompted by lack of technical understanding and vision. In contrast, the technical division which dealt with advanced propulsion systems was a strong proponent of turbojet development. This division was first headed by Hans Mauch and later by Helmut Schelp. Both were convinced of the enormous future potential of turbojet propulsion. Both men were aware and kept abreast of Heinkel's efforts -- which certainly were encouraging. However, both were seriously concerned whether Heinkel, who was only an airframe and not an aircraft engine manufacturer, could succeed with production engines. Their concern was due to the fact that the Heinkel Corporation employed insufficient numbers of experienced engineers and designers in the field of aircraft propulsion (especially accessories and controls), and lacked facilities such as engine component test stands, a materials laboratory, foundries, and suitable machine tools.

Mauch and Schelp considered it an intolerable situation that the enormously important turbojet development should be handicapped and delayed by Heinkel's shortcomings, while the aircraft engine industry (Junkers/Dessau, BMW and Daimler-Benz) with its excellent equipment and competence remained uninvolved in turbojet engine development. In their efforts to correct this situation, Mauch and Schelp were faced with one major problem, namely that the aircraft engine industry was not interested in turbojet engine development, presumably because of its low efficiency.

The situation was especially curious since the Air Ministry was perfectly willing to provide very substantial amounts of government funds to encourage the companies to pursue the turbojet. The engine companies, however, were experiencing an extreme shortage of engineering and technical personnel due to the general munitions buildup preceeding World War II. For that reason, they exhibited little enthusiam for devoting their technical resources to a project in which they saw little promise, even if the funding was available.

In 1938, the Air Ministry finally succeeded in their negotiations with Junkers and BMW concerning the development of axial flow turbojets, while Daimler-Benz remained disinterested. These negotiations were not without amusing incidents. For example, Professor Mader, top manager of the Junkers Aircraft Engine Division stated that the "nonsense" of jet engines should never come into his company, and furthermore, he had no turbomachinery competence in his company. The Air Ministry pointed out to Mader that Dr. Anselm Franz, head of his turbo supercharger group,would make an excellent team leader for the turbojet development project.

Therefore, roughly a year before the first turbojet aircraft flew Heinkel already had two very strong competitors, each with a larger team, excellent facilities, and an enormous competence in aircraft engine design.

Reaction to the first turbojet

While the internal company reaction to the flight of the He 178 was enthusiastic, the reaction of the Air Ministry was far more controlled. The technical levels of the Air Ministry were pleased by the success but were still not convinced that the Heinkel Company was the proper choice for the production of a turoojet aircraft. This was due not only to the fact that there still remained a tremendous amount of work to transform the prototype into a production engine

but also that Heinkel did not possess the tooling to go into a full scale engine production. In addition the Junkers and BMW axial flow engines were making rapid progress.

The upper levels of the Air Ministry, personified by General Udet, were even less interested. They did not expect war with England or France and thus saw no need for an aircraft of the turbojet type. Immediately after successful completion of the first flight, Heinkel invited high ranking officials to a demonstration. This demonstration took place in the fall of 1939. The pragmatic and indifferent attitude of his visitors was a very great disappointment to Heinkel, who could not detect even a glimmer from his guests that what they had seen might mean the beginning of a new era in powered flight.

The technical levels in the Air Ministry, especially Shelp, realized that Heinkel could not develop into an engine manufacturer. Moreover, even if it were possible, they did not want another engine manufacturer. They felt Heinkel should receive credit for a major advance but should give up the further development of the gas turbine engine to the engine manufacturers.

Heinkel was a man accustomed to dealing with the upper levels of the Air Ministry. He could not relate well to the technical levels and considered them to be of no consequence. This attitude did not, of course, aid him in this case, since the upper levels were indifferent to the turbojet development and the technical levels were dissatisfied with his engine manufacturing potential. This point was resolved by Heinkel's later acquisition of an engine manufacturer.

Proposal of the He-280

In spite of the fact that the Air Ministry did not look favorably on Heinkel's plans to manufacture an aircraft based on the He 178, the success

of the first turbojet airplane could not be ignored. Heinkel actually had successfully accomplised the first major stepping stone toward his goal; to independently reach a stature in aircraft gas turbine engines and, consequently, acceptance by the Air Ministry. When, in late 1939, Heinkel proposed a new turbojet fighter designated the He 280 with two new HeS8 turbojet engines, the proposal was accepted by the Air Ministry.

The He-280 was the result of long review and planning sessions involving Heinkel's new technical director, Lusser, von Ohain and Heinkel's project office. It was concluded that a single engine turbojet fighter of the He 178 type was much inferior to a twin engine turbojet fighter with the two engines externally mounted under the wing. Heinkel promised the Air Ministry a target date of early 1941 for the beginning of flight testing.

Due to the external engine installation design for the He-280, a small engine frontal area (or diameter) is a requirement. Therefore, the preferrable engine design would be the axial flow type rather than the radial compressor-turbine combination of the He.S.3. However, the target date of early 1941, left only a total time span of about one and one-half years for development and ground testing of the new engine. Meanwhile, Heinkel's two axial flow competitors, Junkers, and BMW, had been working on their development for more than one year.

Development of the He.S.8

Because of the time constraints, von Ohain decided to adapt the He.S.3. design and introduce only those changes absolutely required for a significant reduction in engine diameter. A full development of an axial flow device could not possibly be expected to satisfy the promise of flight tests in early 1941. A perspective, cut-away view of the resulting engine, the He.S.8, is shown in

Figure 18. In this case, the radial flow compressor and diffuser are moved farther apart. The front combustor is abandoned and the combustion chamber fills the space between the compressor and turbine. In order to accomplish combustion, the high velocity behind the compressor must be reduced. This is achieved by a novel axial flow diffuser just after the outflow from the radial compressor. A more detailed view of the impeller, compressor and turbine rotors is shown in Figure 19. The engine installation under the wing is illustrated in Figure 20, including the control linkage from the cockpit.

Ground testing of the He.S.8 began in February 1941, and soon a performance of 1300 lbs. was demonstrated. However, von Ohain's group was plagued for some time with turbine blade fatigue failures near the blade roots at the turbine exit section. Nevertheless, despite the relatively short total operational time, they could predict with reasonable confidence a lifetime of up to ten hours for the engine. And so in April 1941, the He-280 flew for the first time. An artist's conception of the twin engine turbojet in flight is shown in Figure 21 taken from a Heinkel brochure.

During the subsequent two years von Ohain's engine team and Heinkel's airframe group worked on improving the He-280. It was flown and tested by many military and civilian pilots and ultimately considered an excellent fighter aircraft. However, it lost in competition against the Messerschmidt Me-262 with Junkers Jumo 004 engines. The Me-262 was faster (in mid-1944 it flew 624 MPH), and it had heavier weapons[6].

---

[6] "I believe the Me-262 was the first fighter in the world with a slight sweptback wing. The reputation of Junkers as a very capable and reliable engine manufacturer was also an important factor in the final selection. I don't believe it was a loss for Heinkel, however, since large scale manufacturing of turbo-jet engines in his factories would not have been possible at that time.

Strahltriebwerk HeS 8 A

Perspektiv-Teilschnitt

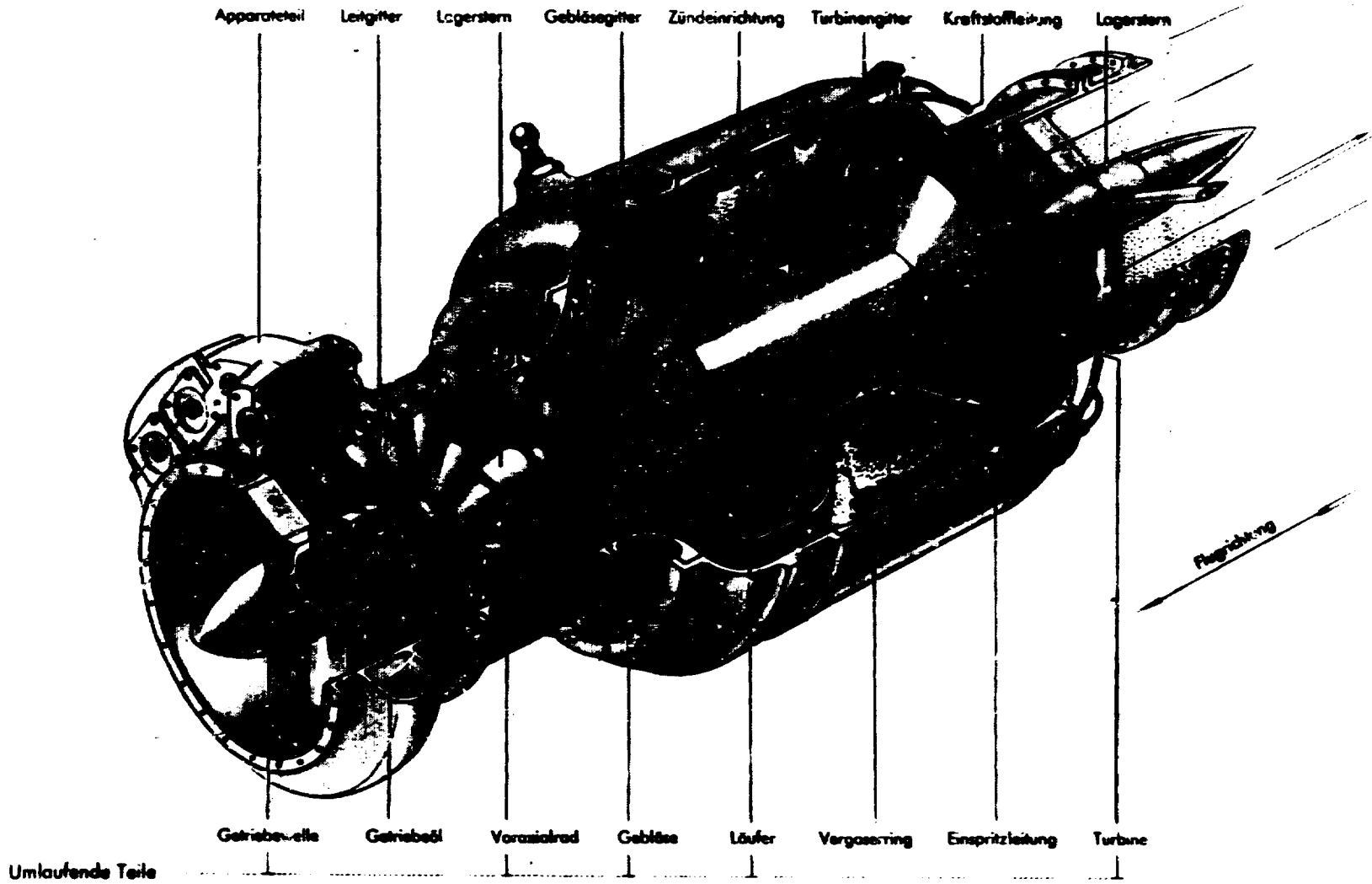

Gegen Flugrichtung gesehen ist in dieser Ansicht das rechte obere Viertel des Gehäuses weggeschnitten.

Figure 18. Cut away view of the Radial Flow HeS8A engine.

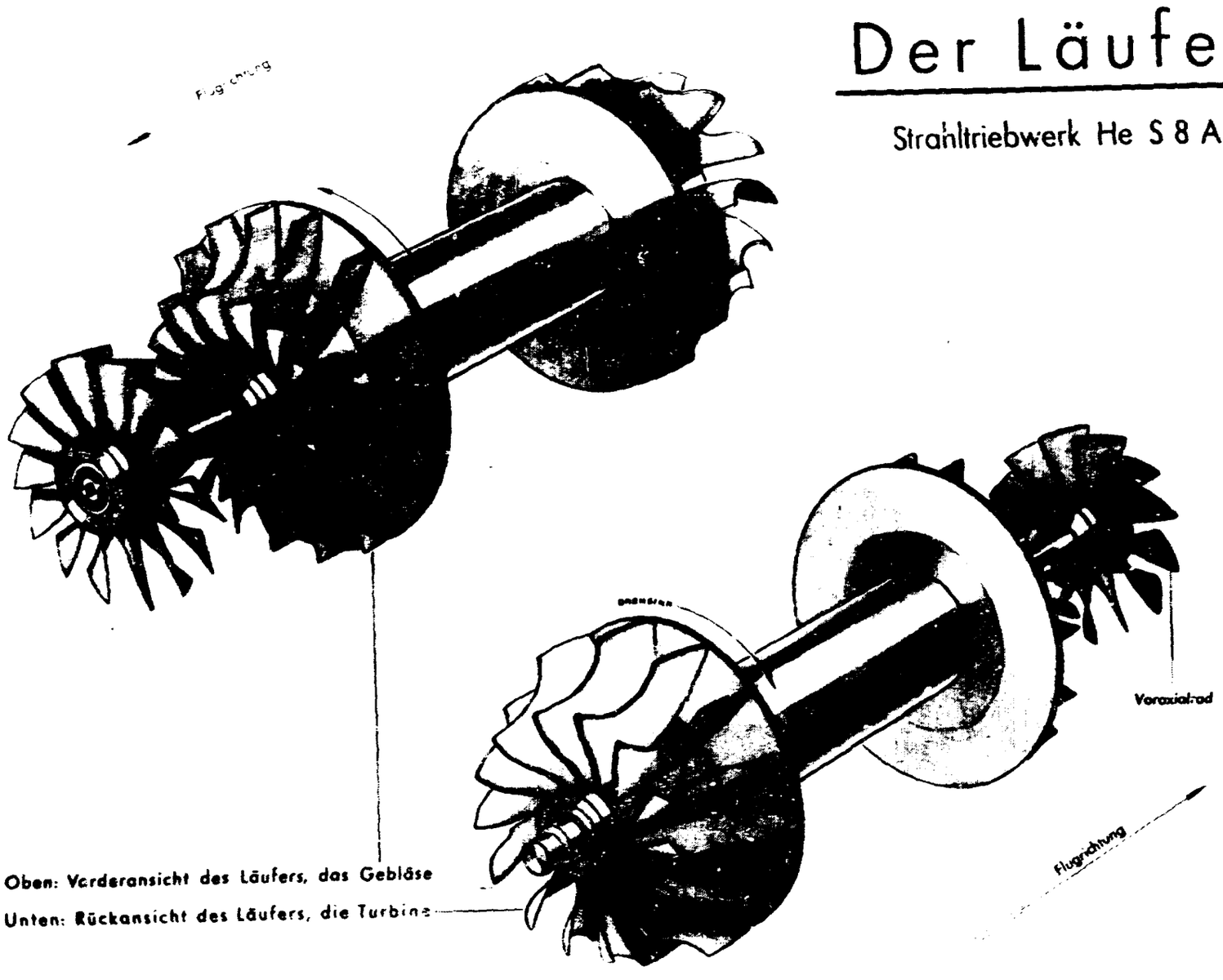

Figure 19. Details of the impeller, compressor and turbine

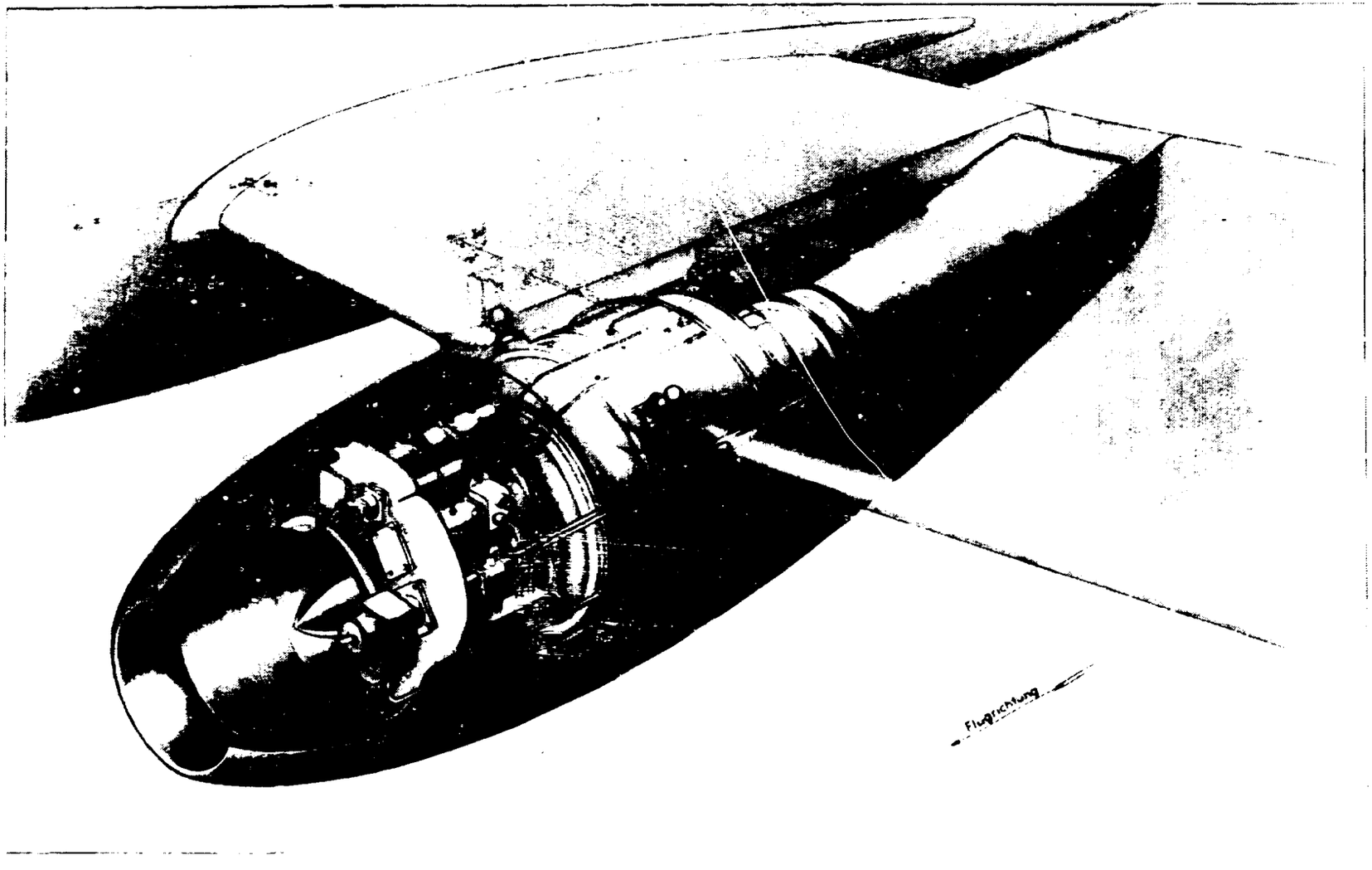

Figure 20. Engine installation under the wing

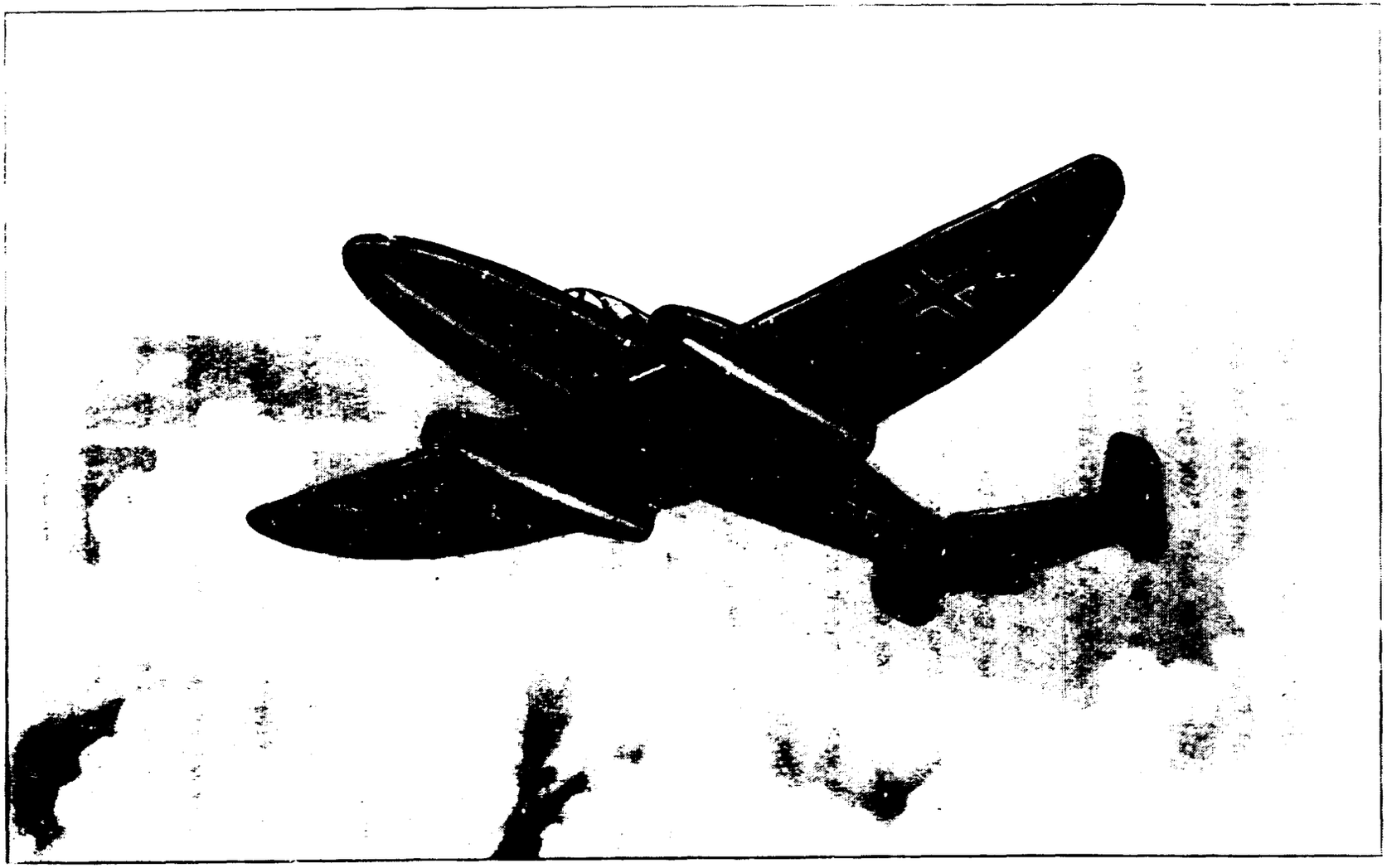

Figure 21. Artist concept of the twin engine He 280

Any comparison between the Heinkel He-280 and the Messerschmidt Me-262 must include the historical perspective. The engine in the Heinkel craft was the He.S.8,a radial flow engine, while the Junkers Jumo 004 engine in the Messerschmidt airplane was an axial flow type. The Jumo engine had the advantage of two extra years of development time, since the development was begun shortly after the successful demonstration of von Ohain's hydrogen powered gas turbine in 1937.

The Junkers group had gone directly into the axial flow configuration due to its reduced frontal area and potential performance improvement in the case of engines mounted outside the fuselage. That the axial flow device was the preferable type was also clear to von Ohain. However, his time constraints were too short to allow the development of an axial flow engine with all the attendant matching problems between the compressor and turbine components.

Acquisition of the Hirth Corporation

Heinkel's ambition to be both an airframe and engine manufacturer had been thwarted in the past by the Air Ministry's reasoning that his corporation did not have the hardware or the experience to build production engines. This was, of course, a double edged sword since they could not obtain the required experience without producing engines. Heinkel, however, was not to be denied. Prior to the development of the He-280, he worked out an agreement with the Air Ministry to allow him to acquire the Hirth Aircraft Engine Corporation, located near Stuttgart, after the first successful flight of the twin engine jet.

The approval of the Air Ministry was essential to the acquisition and from their point of view it made sense. The Hirth Company built small aircraft engines for general aviation and turbo superchargers for larger engines. The owner had died and the sale of the company to Heinkel would encourage more activity and

competition in the engine field. For Heinkel, this was the second and most important step in his attempt to become a gas turbine manufacturer. He would obtain the necessary manufacturing facilities as well as the firm engine technology foundation including experts in the various peripheral design fields. The actual transfer of the corporation took place several days after the He-280 flew. The credit for Heinkel's successful entrance into the aircraft engine business is due primarily to Hans von Ohain. It was his development of the gas turbine engine which led to the acquisition of the Hirth Corporation and especially its engineers and facilities.

Heinkel-Hirth Corporation

In 1942, von Ohain and most members of his team joined the newly created Heinkel-Hirth organization. Integration of the former Heinkel team and leading engineers of the former Hirth corporation proceeded very smoothly thanks to the great skill and personality of plant manager Curt Schif. The new team's strength with respect to the number of people and top engineering talent, highly experienced and dependable support personnel and excellent facilities was for von Ohain an almost unbelievable change from the mode of operation over previous years. For example, Dr. Max Bentele, a recognized expert in aeroelasticity was in charge of component development and testing, including a 2000 hp compressor research facility and Hatenstein was in charge of engine testing with a team of skillful engineers and technicians.

At the young age of 31 years, von Ohain was a Director in the Heinkel Hirth Corporation outside Stuttgart. Contrary to the operations in Warnemunde, he no longer had to worry about every detail. The operation grew more rapidly than he had ever imagined. The engineers and mechanics now often made detailed improvements in the engine without even consulting him. His

increase in responsibility was also reflected in a very rapid increase in salary. However, although his income from salary and patent royalties was very substantial, there was little that he could do with the money other than immediate necessities. The money devalued very quickly and even where the money was available, the consumer goods were not.

Von Ohain had always shown a passion for sports cars. Now that his income was high, he chose a "fantastic" BMW sports car and ordered it. The price was around 8000 Marks, which he paid in cash. Soon he learned that the delivery time was one year. Not long thereafter he was notified that the car was undeliverable and he could have his 8000 Marks back. "That money devaluated very quickly and later on I could buy eight pounds of sugar for it on the black market," he recalls.

The He S 011 Engine

With the combined resources of his former development team and the additional engineers obtained from the Hirth Corporation under his leadership, von Ohain was charged with a new task -- to develop an axial advanced turbojet designated as the 011. The thrust specification was 3000 lbs and was to be obtained with a symmetrically bladed axial compressor with one inducer stage. The design pressure ratio was 5:1. As a reflection of the poor state of affair of raw materials in Germany late in the war, the engine was planned to be built without any alloys containing heat resistant materials such as nickel. Thus the engine needed to have an air cooled turbine and thereby included some of the very techniques which are presently being explored for turbine cooling. The hollow turbine blades, developed by Dr. Bentele, may be clearly seen in Figure 22. The three stage axial compressor is shown in Figure 23 along with the single inducer stage upstream. The overall 011 engine is shown in Figure 24

Figure 22. The hollow turbine blades of the OTI

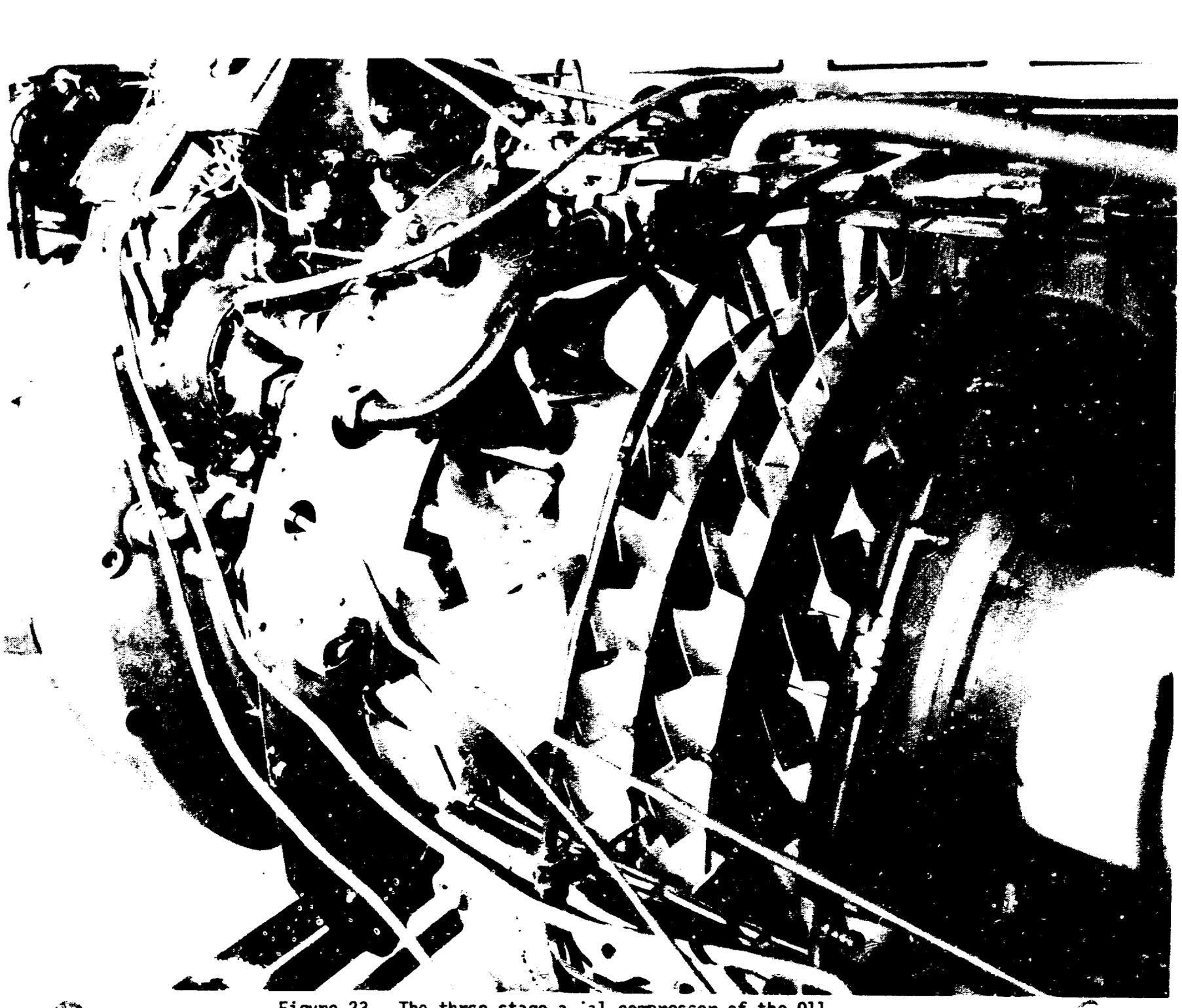

Figure 23. The three stage a ial compressor of the OII.

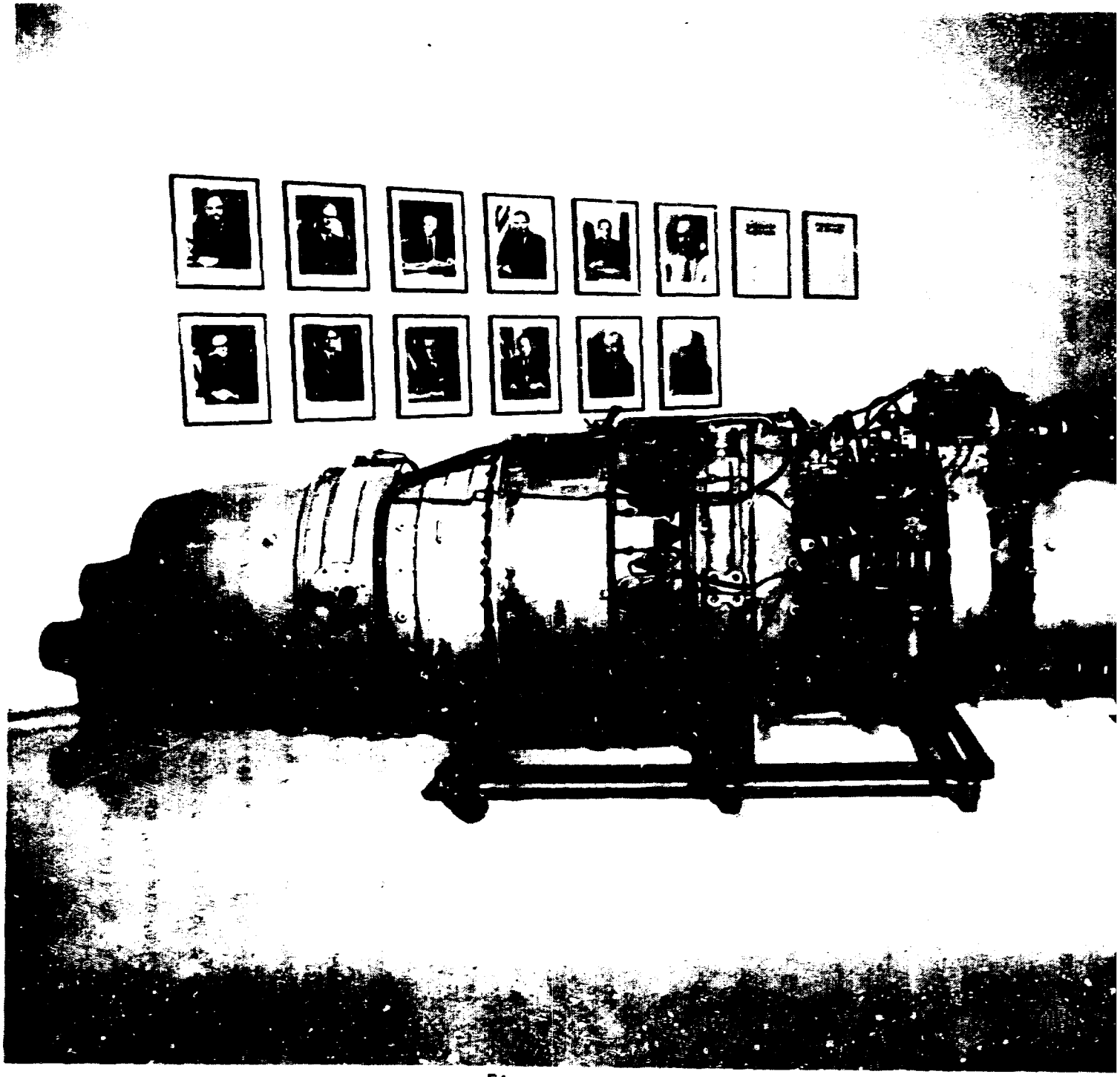

Figure 24. The 011 engine.

By the latter part of 1944, the Oll had met its performance specifications. It was, at this point, the most powerful and advanced engine in the world. Large scale production was planned for Mid-1945. However, the Oll was destined never to be produced in more than prototype quantities. The collapse of the German war machine would spell the end of the gas turbine engine there.

THE POST-WAR YEARS

The End of Hostilities

In early 1945, von Ohain and part of his team were relocated from Stuttgart to Kolbermohr, a small town near Rosenheim. Some empty factories were located in Kolbermohr due to the demise of a spinning business. The aim was to erect a field type test facility for the Oll engine test program. The facility construction only got to the point of choosing test sites and making a very preliminary start on the accumulation of materials.

The group had very strict orders not to let the several Oll engines, which they had brought from Stuttgart, fall into the hands of the Allies. If the enemy were to reach a nearby city, probably Rosenheim, the engines were to be burned. This indeed occurred and von Ohain himself took a hand in the destruction of the Oll engines in their possession.

To the superficial observer, this would appear to be a tragedy. A man being forced to destroy the very devices in which he had invested such a tremendous amount of time and effort. Von Ohain's response is fascinating. Although they really had no choice other than to obey the order due to the presence of devout Nazis, sometimes unknown even to those around them, they would not have avoided burning the engines even if they had the opportunity. "We immediately envisioned the beauty of this situation," he recalls. "We could rebuild the engines later on, possibly in Stuttgart. Thus the destruction

of the engines was the insurance policy von Ohain's group needed.

Arrival of Intelligence Teams

With the end of the war, various intelligence teams passed through the area in search for information. Each of the Allies had their own teams and in some cases even the various services within a single country had their own teams. Von Ohain's group had enough small extra parts and test results to show the visitors, if they wanted to share the information. Such was not always the case.

The quality of the intelligence teams varied widely. Some were extremely arrogant and others threatened force in order to force the German scientists to cooperate. The British teams, in particular, were inept. They were under the impression that one had to shout at a German in order to get through to him. One American Army team tried to intimidate the scientists by having a sergeant carry a rifle beside the interrogator. It was disconcerting to them that von Ohain only grinned because he knew they wouldn't shoot him anyway.

The best intelligence teams came from the U.S. Navy. They arrived in jeeps with a tremendous amount of intelligence information already available to them. They knew who was located in Kolbermohr and what it was they were doing. The initial Navy team was headed by a Bill Bolay, who impressed von Ohain with his technical ability. In addition, the Navy team knew how to treat the German scientists in order to make them enthusiastic to cooperate.

The initial team was followed by one headed by Navy Captain Robinson, who was very enterprising and well liked by the German scientists. The Navy made arrangements with von Ohain and the remnants of his team to have them rebuild the 011 engine under contract to the U.S. Navy. The question was never asked, "Why did you ever burn those beautiful engines." The Navy people understood that the orders were given from above and even at the end of the war they had

to be obeyed.

The rebuilding of the Oll engines began in Kolbermohr but soon moved back to Stuttgart. About this time, von Ohain resigned from the Heinkel Corporation, since he could see that the system was falling apart and he wanted to resign before the resignations were forced. In spite of the situation the Corporation sent him a nice letter thanking him for his services and accepting his resignation. The letter was not, however, from Heinkel himself.

U.S. Navy Consultant

With his resignation, von Ohain became a consultant to the Navy. He set up a little engineering office in Kornthal, a community outside of Stuttgart. Thus, although he was no longer a Heinkel employee, he still had access to the Heinkel-Hirth plant, in order to see what was going on therein. The plant was headed during this time by a military officer, one of whom was the Navy Captain Minter.

Various members of von Ohain's team left to work in other areas. Max Bentele, for example, went to England at the invitation of the British. Bentele had been in charge of component development under von Ohain in Stuttgart. After two years in England, he returned to the Heinkel corporation and did pioneering work on advanced static pressure exchangers. Some of that work still has direct application today in the area of diesel superchargers. He subsequently worked in the United States at Curtis-Wright Corporation on the Wankel engine development and later at Avco Lycoming in conjunction with engines for helicoptors.

Max Hahn, on the other hand, stayed with the Heinkel Corporation. After the end of the war, the Corporation was split into a number of smaller companies because there was no longer a need for aircraft. Hahn became the Head of Manufacturing for one of these off-shoots of the original Heinkel Corporation.

Also around this period, von Ohain was visited by a U.S. Army officer, representing the Army Air Corps, the predecessor of the U.S. Air Force. He wanted to convince von Ohain to come to Wright FIeld in Ohio. This was something that von Ohain really wanted, but the Naval Plant Manager, Captain Miller, intercepted the Army officer and told him in no uncertain terms to go to Hell! He told von Ohain "You stay here, you're under a Navy contract and I'll chase every Army guy out!"

The consultation program came to an abrupt halt when the Russian newspapers printed the information that the Americans were working with the Germans on advanced engines. This was in opposition to the four power agreements reached by the Allies after the conclusion of hostilities. Thus the Navy was directed by Washington to discontinue the program. There were several 011's which had been built and several others which were hastily assembled without being run and shipped to the United States.

Operation Paper Clip

Thus von Ohain was again without support. Very soon, however, another intelligence team arrived from the Army Air Corps. He was asked to come to a certain location in Stuttgart, where they offered him a contract to come to Wright Field, outside of Dayton, Ohio (now Wright-Patterson Air Force Base). He was to be paid a salary in Germany and to be sent to the U.S. on a per diem basis. The per diem was based on that of a junior officer and amounted to roughly $6. per day.

A number of other German scientists were offered similar contracts under the overall plan, Operation Paper Clip. The group was housed in an old Visiting Officer Quarters complex located on the corner of Old Route 4 and Col. Glenn Highway in Fairborn, Ohio. These quarters have since been removed and the land is now part of the Wright State University Campus.

It didn't bother von Ohain to come to the U.S. in a relatively low level position compared with his level as a Director of the Heinkel-Hirth Corporation and a mid-level contractor as opposed to the man in charge of the foremost jet engine development program in the world. By his own reasoning, he was still much better off than he would have been in Germany. Besides that, he felt that since he needed to learn English and become acquainted with the people, the lower level position would allow him more time to do so. The contract arrangement also protected the inflow of German scientists from the competitiveness of the Civil Service System.

For von Ohain, it was good to be in a position to do something for some of his friends in Germany. As he says "You could send something to an old professor or an old girlfriend." As many other people with friends and relatives in Europe, von Ohain spent many weekends wrapping packages for them. One of those who received packages was Ernst Heinkel, whose wife needed coffee as a stimulant for a heart condition. Coffee was practically impossible to obtain in Germany unless you had a friend outside the country.

EPILOGUE

Thus Hans von Ohain embarked on a new career in the United States. Consistent with his fruitful efforts in Germany, the American portion of his career was highly distinguished and continues to this day. Roughly a year after arriving in the United States, he joined the Civil Service at a mid-level (GS-13 roughly) position. He contributed greatly to the planning and facilities design that produced the Arnold Engineering and Development Center in Tullahoma, Tenn. This facility is still the backbone of the Air Force testing program. When Dr. Theodore von Karman and General Hap Arnold called for the establishment of an Air Force research facility to enable the Air Force to be a full partner in the technical areas of their

interest, Hans von Ohain was one of the founders. The Aeronautical (later Aerospace) Research Laboratories filled the void and von Ohain himself contributed greatly with outstanding programs in electrofluiddynamic power generation, a nuclear propulsion system and a thrust augmentation system for vertical take-off and landing aircraft.

As Chief Scientist from 1964 to 1975, he also turned his interest to the wide spectrum of scientific and engineering programs to benefit the U.S. Air Force.

At the Air Force Aero Propulsion Laboratory from 1975 to 1979, he continued his role of advocacy of high quality government programs to complement, the contract research programs. Following his retirement from government service in January 1979, he has continued to work in the areas of propulsion and has, in addition, expanded his efforts into the area of energy which has always been of interest to him, even in the post-war years of interest in very efficient engines.

Hans von Ohain's place in history is secure as the man responsible for the world's first turbojet powered flight. Over the years he has received many awards and honors, including the AIAA Goddard Award and the Air Force Association's Citation of Honor. He has given many important lectures and published numerous technical papers, but Hans von Ohain's claim to lasting fame is his ability to bring an earth changing concept to practical fruition in spite of strong opposition and against tremendous odds.

ELECTROFLUID DYNAMICS: THE ROLE OF HANS VON OHAIN

by

Frank Wattendorf
Maurice Lawson

AD A100315

In the late 1950's, with the advent of space as the new frontier, the United States Air Force, among others, became strongly interested in exploring future potentialities of relevant specific phenomena. At that time, Dr Hans von Ohain was especially concerned with the overall spectrum of energy conversion; especially for regions hitherto relatively unexplored. Of special interest to him was direct conversion of fluid dynamic energy to electricity, without moving parts. This process gave promise of compact, low weight power systems combined with long endurance and low maintenance.

During the summer of 1959, Dr von Ohain presented his views to a high level U.S. Air Force Long Term Scientific Study Group. He showed that in the electromagnetic conversion spectrum involving fluid dynamics, major attention had been given to magnetic phenomena. On the other hand, no comparable systematic effort had been devoted to electrostatic processes, whereby charged particles are transported by fluid flow against an electric potential.

At the 1959 meeting, Dr von Karman, the Chairman of the Study Group, Dr von Ohain, and the two present authors agreed that:

1. Since the term fluid dynamics encompasses both hydrodynamics and gas dynamics, the entire spectrum in question should be referred to as Electromagnetic Fluid Dynamics (EMFD); with the two principal regions called: Magneto Fluid Dynamics (MFD) and Electrofluid Dynamics (EFD).
2. The scientific exploration of the energy spectrum, especially the Electrofluid Dynamic portion should be encouraged.

In accordance with Dr von Ohain's views, and with his guidance and inspiration, a systematic, long term research program was initiated at the Aerospace Research Laboratories, with one of the present authors as consultant and the other as group leader. The main emphasis was: analysis of basic phenomenon; identification of components; parametric studies;

Manuscript Received March 1980.

development of scaling laws; optimization studies of components; optimization of systems with respect to selective goals; verification experiments and exploratory research.

The present paper reviews the progress in Electrofluid Dynamics, recalling principal approaches and results, giving references, and highlighting the creative and inspirational role of Hans von Ohain; to whom it is a pleasure and a privilege to give tribute.

Introduction

The broad field of direct energy conversion has received greatly increased emphasis during recent years; largely due to the new requirements of operations in space, under the ocean, and at remote, unattended locations. Processes employing direct energy conversion do not need moving mechanical parts, and promise significant increases in reliability, compactness, and ability to operate over long periods of time without maintenance or personal attention. Promising applications are for space vehicles, satellites, orbiting laboratories, and lunar bases; for remote, unattended locations such as radar stations, communication links, navigation aids, etc.; also for operations where air pollution is a problem. Research in this field is typically of interdisciplinary nature, being concerned with combined effects and phenomena in such disciplines as physics, chemistry, aerothermodynamics and electrodynamics (including photon interaction and lasing phenomena).

A great deal of attention is being devoted to processes by which enthalpy of a gaseous working medium is directly converted into electrical energy. Such processes can be grouped in two major categories, the electrofluid dynamic (EFD) and the magnetofluid dynamic (MFD) energy conversion processes.

Although the terms electrohydrodynamics (EHD) or electrogasdynamics (EGD), and magnetohydrodynamics (MHD) have been widely used in the literature, the more general terms of EFD and MFD arose during dicussions among Dr. Theodore von Karman, Dr. von Ohain, and the present authors at an Air Force Long Term Scientific Study at Woods Hole, Massachusetts, in the summer of 1959. These particular discussions reviewed the entire energy conversion spectrum, showing that MFD and EFD referred to different but complementary portions of the spectrum, with the EFD portion in a much less developed state.

Phenomena involving the interaction of fluid flow and electrostatic electricity have been known for many years. Armstrong and Faraday reported on such phenomena in the 1840's. Interest in EFD power generation was revived in the 1900's by individual projects in several countries, such as France, Belgium, USSR, and the U.K. In the U.S., Marks and Gourdine were especially active, among others.

However, EFD received much less attention and support than MFD. A major reason for this may be that initial investigations of EFD processes indicated poor conversion efficiencies from fluid dynamic energy into electrical energy. Moreover, the total pressure ratio of the EFD process is inherently very small. indicating very poor conversion efficiencies from heat into fluid dynamic energy. System concepts and systematic research approaches to overcome these shortcomings were the objectives of tne research effort launched by Hans von Ohain.

PART I

COMPARISON OF FUNDAMENTAL CHARACTERISTICS BETWEEN EFD AND MFD CONVERSION PROCESSES

In EFD processes, direct conversion between enthalpy and electrical energy is accomplished by passing an electrically insulating working gas containing electrical charges of one polarity through an electrostatic field. In general, EFD processes are analogous to the process of a Van de Graaff generator in that the mechanically driven belt, which transports surface charges of one polarity, corresponds to the carrier gas flow containing the electric charges of one polarity. The overall compactness of EFD conversion devices promises to be potentially much greater than that of a mechanically driven Van de Graaff generator because fluid flow is volumetric and not speed limited.

In MFD processes, enthalpy is directly converted into electrical energy by passing an electrically conductive working gas across a magnetic field. The principal differences between the fundamental processes of EFD and MFD are summarized in Table 1 below.

Table 1: Synopsis of Complementary Fundamental Characteristics of EFD and MFD

	EFD	MFD
Potential gradient	Order of magnitude 10^5 volts/cm.	10 to 100 volts/cm
Voltage Output	Order of magnitude 10^5 volts and above.	Order of magnitude from 10^2 to 10^4 volts.
Power Scaling	With cross section of conversion channel.	With volume of conversion channel.
Range of Power Output	From about 1 kW up.	From about 1 MW up.
Ionization	One polarity; 10^8 neutrals per elementary charge.	Gross Neutrality about 10^2 neutrals per ion.
Temperature	From room temperature to 2000°R.	Above about 4000°F.
Suitable Energy Sources	Chemical, solar isotope, nuclear reactor.	Mainly chemical.
Suitable Cycles	Open, closed.	Mainly open.

Suitable Energy Sources

For EFD processes, all conceivable major energy sources such as chemical, solar, isotope heat, and nuclear reactor can be employed in principle since the EFD process can operate with moderate temperatures. In contrast, the MFD

process, which requires ultra-high operating temperatures, can only use special chemical energy sources resulting in highly ionized reaction products. It is conceivable that special nuclear reactors that may be built can produce, for short duration, sufficiently high temperature working media.

Suitable Cycles and Applications

EFD energy conversion cycles have no restrictions with respect to using such conventional conversion cycles as the Rankine or Brayton cycles; also, open or closed cycles can be employed. MFD energy conversion processes, in view of their ultra high temperatures, seem to be most suited for open cycles. The potential application areas of MFD processes seem to lie in commercial power plants as topping cycles or standby equipment, also in special short duration power sources where enormous burst powers of perhaps 100 Mw over a few seconds are required. Such power plants, for example, may be utilized for reentry simulation. Capital cost of a conventional power plant would be prohibitive for this purpose. An ultra short duration giant power pulse can be produced by an MFD process employing explosives. EFD is able to satisfy requirements for small power outputs,also for typical closed cycles. This is shown in greater detail in Table 2, below.

Table 2: Potential Applications of EFD Energy Conversion Processes

Power Output	Cycle	Energy Source	Application Area		Voltage
Fraction kW to order of magnitude of 10 kW	Rankine	Solar Isotope Chemical	Telecommunication Power for Remote Areas Vehicle Power	With Power Conditioning	Order of magnitude 10^5 volts
			Electric propulsion (Colloidal) for attitude control		
Order of magnitude 100 kW to 1000 kW	Rankine	Nuclear Reactor	Electric propulsion (Colloidal) for scout vehicles		Order of magnitude 10^5 volts
	Open (Open gas turbine)	Chemical (Nuclear)	Mobile Military Power Power for Remote Areas Standby Equipment	With Power Conditioning	
	Closed Cycle	Fan or Compressor Actuated by Electrical or Chemical Energy	Fluid Dynamic Van De Graff for Research		Order of magnitude 10^7 volts
Order of magnitude 10 MW and above	Open Gas Turbine	Chemical (Nuclear)	High Power Standby		10^6 volts
	Storage Blowdown		Short Duration, High Power Output (hypersonic flow simulation)		10^6 volts and above

Aspects of Conversion from Heat Into Electrical Energy Employing EFD Processes

One important application of EFD processes lies in the field of thermodynamic cycles, by which the heat released from an energy source is converted into electrical energy. A distinction can be made among three major phases of such thermodynamic cycles.

Phase (a) Conversion of heat into fluid dynamic energy.

Phase (b) Conversion of fluid dynamic energy into electrical energy by an EFD conversion process.

Phase (c) Restoration of the initial conditions of the working medium, if required (closed cycle). In this case, the portion of heat energy released by the energy source not converted into electrical energy has to be rejected, e.g., by a radiator, and the pressure of the working medium has to be brought back to its initial value.

As a typical example, let us consider the three phases in a Rankine cycle.

Phase (a) The vapor coming from the boiler is expanded through a nozzle; thereby, a portion of the heat energy released from the source is converted into kinetic energy of the working substance.

Phase (b) This kinetic energy is converted by the EFD process into electrical energy with a conversion efficiency.

Phase (c) The exhaust vapor from the EFD conversion channel is condensed in a heat exchanger and the liquid is pumped back into the boiler. The energy for pumping is taken from the energy of the vapor (e.g., employing the well-known steam ejector pump).

It is very important to note that a high overall conversion efficiency is not necessarily the most important performance parameter. Depending on the intended specific application of the conversion system, the main emphasis may shift between eight major system characteristics:

(a) Overall Compactness
(b) Reliability
(c) Endurance
(d) Total Weight per kW
(e) Capital Cost
(f) Overall Conversion Efficiency
(g) Pollution
(h) Applicability of specific energy sources, e.g., low grade fuel.

In a large variety of thermodynamic cycles (including unconventional ones discussed, e.g., by Lawson, et al.), application of EFD energy conversion processes would be attractive. These cycles differ greatly in temperature and total pressure ratio. But even those cycles which operate efficiently with relatively low pressure ratios (cycles employing internal counterflow heat exchangers) would require far greater pressure ratios than obtainable with a single-stage channel, which would indicate staging.

The major aspects of the integrated EFD injector, shown in Figure 1, are:

1. The gas leaving the diffuser has a sufficiently low speed that it can be returned to the entrance of the EFD conversion duct with negligible aerodynamic losses (analogy to classical subsonic wind tunnels).

2. The medium aspect ratio channel serves a dual purpose: mixing duct for the ejector and, at the same time, EFD conversion channel.

3. From ejector efficiency considerations it follows that the primary vapor injected into the mixing duct should have a velocity which may be 1.2 to 2 times higher than the velocity of the recirculating gas in the conversion channel. This results in transfer efficiencies from the primary to the recirculating gas between approximately 75 to 85 percent. Since there is a wide choice of molecular weight ratios between the recirculating gas and the injected vapor, e.g., hydrogen-mercury or hydrogen-alkali metal vapor or hydrogen-water vapor and others, it will be possible always to obtain a high expansion pressure ratio for the injected vapor. For example, if the recirculating hydrogen has a velocity of about 400 m/sec in the conversion duct, the injected vapor may have a velocity of about 500 to 800 m/sec. With a suitably chosen high molecular weight of the vapor, high expansion pressure ratios can be employed. This shows that combinations of a high thermodynamic efficiency,high transfer efficiency, and high electrofluid dynamic efficiency are, in principle,possible with the integrated EFD ejector.

4. The primary vapor injector nozzle has a multiple purpose: injection of the primary vapor, electric charge production, and finally, by partial vapor condensation, production of charged colloids.

5. The high vapor speed at the nozzle exit prior to mixing is favorable for charge generation. (The high speed for given current and flow cross section reduces locally charge concentration and, thereby, space charge effects.)

6. Charge spreading will proceed with mixing; it will be possible to avoid any charge deposition at the conversion duct walls.

7. The vapor is condensed in the low speed return duct, and the recirculating gas is conditioned to produce effectively charged colloids by mixing with the injected vapor at the entrance to the EFD conversion channel. (The condensate is separated from the recirculating gas and returned into the boiler.)

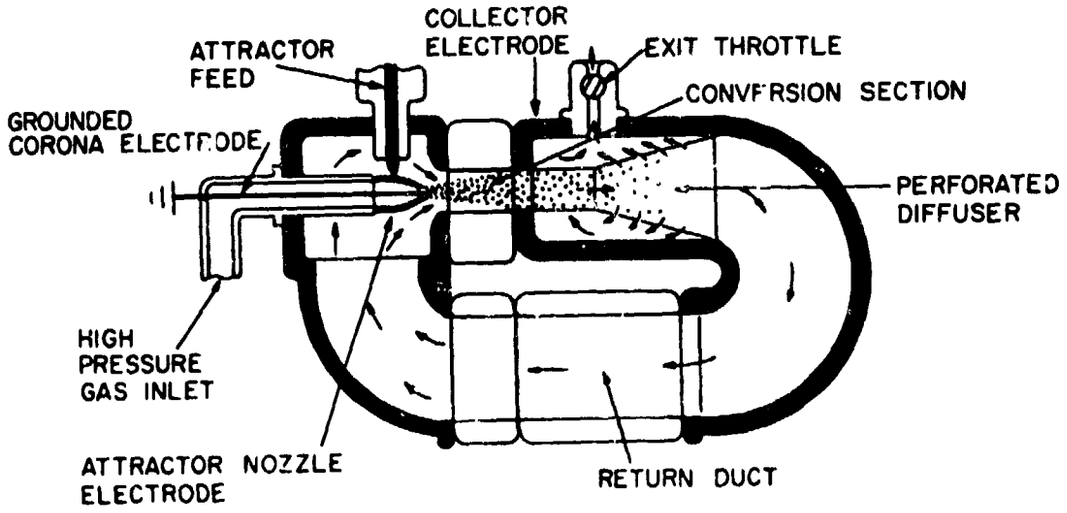

Figure 1. Recirculatory EFD Generator, (Closed Cylce Simulation) Schematic View.

PART II

RESEARCH RESULTS

The major research topics are summarized below, and progress made at the Aerospace Research Laboratory (ARL) in each area will be reviewed in the following.

Scaling and Similarity

The electrical characteristics of similar but different size channels operated at a given temperature and at a given product of pressure times a channel dimension (e.g., diameter) will be the same; that is, the output voltage and current will be the same. This was demonstrated in experiments conducted at ARL and later by TRW Systems, Inc., under U. S. Air Force contract. Three similar channels having diameters of 0.5, 0.167, and 0.0835 inches were tested with respective pressures of 4 atm. absolute, 12 atm., and 24 atm. (i.e., PxD equal 2 atm-inches). Collector output voltages and power were, respectively, 175 KV and 62 watts, 183 KV and 68 watts, and 176 KV and 65 watts. The scaling characteristic provides increased power density and conversion efficiency for small diameter channels, operating at high gas pressure, since the fluid power is directly proportional to the channel diameter.

Working Media

The results of studies performed at the Massachusetts Institute of Technology for the application of mercury as the thermodynamic fluid in the two-fluid EFD ejector cycle demonstrated that for vapor mixtures with helium, nitrogen, and hydrogen, the last-named is by far the most desirable choice for efficient thermal-electric conversion.

Field Structure

Computer solutions for the total electric field structure and electrical performance were developed at the University of Dayton for both axisymmetric and two-dimensional geometries. The computer program permits the detailed study of the electric field structure of EFD generators of rather complex geometry over a wide range of generator variables. Effects of various charge density distributions in the conversion channel can be determined.

Geometry

Major experimental work was conducted at ARL with the cylindrical channel and good agreement was obtained with simplified theoretical analyses as well as with the University of Dayton computer solutions. The conversion section developed in time from a full-length solid wall insulator channel to a free jet channel because of problems associated with charge contamination on the solid insulation walls. The free jet channel also was not limited in field strength by the inherently low values of surface field strength of the solid insulator walls.

Although the research conducted at ARL was incomplete, high mass flow, small radii, ejector type, two-dimension, and radial outflow EFD generators were also investigated. Theoretical emitter currents of 0.03 amperes were produced using a four-inch diameter corona disk edge which was fashioned after a squared-off cylinder emitter electrode of the axisymmetric geometry. However, the charged droplets could not be carried by the flow against high electric fields corresponding to design loads for the generator. Flow studies of two-dimensional generator geometries for a range of ratios, including unity, of primary to secondary velocities should be conducted.

Unipolar Charge Generation

Two major types of charged water drop production were investigated. The first was supersonic expansion of humidified air about various shaped corona electrodes. Supersaturated conditions of about 1000 to 1 were attained such that homogeneous condensation was achieved in the presence of an ion cloud. It was found that the squared-off cylindrical electrode, or the square-edged disk (in the two-dimensional radial outflow geometry) produced design levels of current. The position of the corona electrode in the expanding nozzle was important for producing such current levels.

The second type of charged droplet production means investigated was electro-hydrodynamic spraying. In the cylindrical geometry, it was found that the optimum position of a small tube bearing the water was slightly upstream and centered on the axis of the throat of a Mach 2 nozzle where flow Mach numbers were about 0.6 to 0.8. At this position the dual conditions of very high gas

dielectric strength and high flow velocities existed. These conditions could provide copious amounts of extremely small diameter droplets, which could provide nuclei for condensation of the vapor in the humidified flow. In both types of charge production processes, attention must be paid to field strength levels at the nozzle tip, as space charge levels could be lowered by high frequency breakdown to the tip of the nozzle.

In the radial outflow geometry only the corona discharge process was investigated.

Cycles

As previously discussed in Part I, the ARL research program emphasized the integrated EFD generator ejector process to alleviate the effects of the low pressure ratio characteristic of the EFD generator stage. In the early period of research, electrical pressures that were imposed on the flow were low, about 3 lb/ft^2. Ultimately, electrical performance as well as direct pressure measurements demonstrated values which were about 1000 times greater. Still, this performance expressed as an isentropic pressure of the primary flow was only 1.05, while in comparison a single impulse turbine stage may have a value of about 10.

Experiments were conducted with ejector channels utlizing a single fluid, air, as both the primary fluid and the secondary fluid; while future plans, unrealized, were to experimentally investigate optimized fluid combinations. After the achievement of good correlation between theory and experiments, studies of the proper matching of generator and ejector characteristics were made. For the case of using air as both the primary and secondary fluids and towards the objective of increasing the total enthalpy converted into electrical, this led to the application of high Mach numbers, small nozzle area (relative to the ejector channel area) primary flows. Using an existing combination of nozzle and channel, an experimental value of 5 percent was achieved for a Mach number of 1.5, while theoretical studies indicated limiting values of 8 percent should be attainable for a Mach two nozzle of proper size.

For the case of applying mercury vapor as the primary fluid and hydrogen as the secondary fluid, separate theoretical studies conducted by ARL and TRW Systems, Incorporated, indicated that thermal efficiencies of 40 percent should be achievable. Future work will require research on large area ratio, high Mach number primary flow ejectors, where a low Mach number secondary flow attains nearly the velocity of the primary. Two types of geometries should be investigated, one having the ejector and EFD converter integrated, and the other having the EFD converter following the diffuser of the ejector channel. The first geometry has the advantage that the primary flow can produce directly, without a fluid dynamic energy transfer process, some of the electrical work; the second geometry has the advantage of providing an extremely low subsonic Mach number flow, about 0.05, at the face of the EFD converter, thereby providing a good match of velocity pressure and electrical pressure.

CONCLUSIONS

The systematic research effort at the Aerospace Research Laboratories on EFD power generation, described above, has shown progressive and encouraging improvements. In particular, scaling laws developed and experimentally verified indicate that highest enthalpy removal corresponds to the use of small hydraulic diameter channels operated at high gas density. Generator performance equations show that for high kinetic enthalpy flows either extremely high output voltages or extremely small diameter flows are required.

For the two-fluid generator case, two approaches have been suggested to alleviate this condition. One, by Solbes, to charge drops in the recirculating secondary flow; and the other, by the authors, to place the generator in the low head flow downstream of the ejector diffuser. Both approaches could provide relatively high current levels and low output voltages.

The disestablishment of the Aerospace Research Laboratories terminated the high pressure EFD power generation research described in this paper. However, other aspects of EFD power generation continue elsewhere. For example, two research programs at the University of Dayton Research Institute support, in part, the realization of high enthalpy EFD generators. One is the EFD Wind Generator, sponsored by the Wind Systems Branch, U. S. Department of Energy and by the Solar Energy Research Institute (SERI). New two-dimensional geometries have been investigated which, besides wind application, hold promise for application to the two-fluid ejector system.

The other program is the Rankine Cycle Augmented Light Gas Turbine, sponsored by the U. S. Department of Energy, Division Advanced Energy Projects. This program involves research and development in two-fluid ejectors and is to provide important new knowledge in such ejectors.

Both of the University of Dayton Research Institute programs, briefly described above, are outgrowths of research programs initiated in the early sixties by Dr. von Ohain.

TRIBUTE

Hans von Ohain is creative in thought; exploratory in his approach to new problems; and inspirational in guiding research efforts. The present review of electrofluid dynamic energy conversion has the purpose of exemplifying his role in a typical research area. The present authors are privileged to have been associated with him in various aspects of this research; and use this medium to express our sincere appreciation for his friendship and inspiration. Warmest wishes and best of fortune to Hans von Ohain and his family!

SELECTED REFERENCES

Armstrong, W. G., "On the Electricity of a Jet of Steam Issuing From a Boiler," Phil. Mag., 17, 370, 1840.

Faraday, M., "Experimental Researches in Electricity," Phil. Trans. Roy. Soc., London, 17, 1843.

Babat, G., "Mercury Vapour Electrostatic Generators for D.C. and A.C." Technical Physics of the U.S.S.R., 3, 786, 1936.

Pauthenier, M. and M. Moreau-Hanot, "Generateurs de Haute Tensions à Courants Gazeaux," J. de Physique et le Rad. 8, 193, 1937.

Marks, A. M., Heat-Electrical Power Conversion Through the Medium of a Charged Aerosol. U. S. Patent No. 2, 638, 555, May 1953.

Gourdine, M.C., "The Electrical Wind in a Stationary Gas," Jet Propulsion Laboratories, 1958.

von Ohain, H., Presentation on Direct Energy Conversion to the Air Force Long Term Scientific Study Group, July 1959.

Gourdine, M. C.,"Power Generation by Means of the Electric Wind," Report No. 32-6, Jet Propulsion Laboratories, 1960.

Lawson, M., H von Ohain, and F. Wattendorf, "Performance Potentialities of Direct Energy Conversion Processes Between Electrostatic and Fluid Dynamic Energy," ARL Report 178, (AD 273015), Aerospace Research Laboratories, Wright-Patterson Air Force Base, Ohio, December 1961.

von Ohain, H., Presentation on Dr. Theodore von Karman on Electrostatic Phenomena in Direct Energy Conversion. Aerospace Research Laboratories, Wright-Patterson Air Force Base, Ohio (unpublished), 1962.

Kahn, B. and M. C. Gourdine, "A Basic Study of Slender Channel EGD," ARL-63-205, Aerospace Research Laboratories, Wright-Patterson Air Force Base, Ohio, 1963.

Sutherland, J. P. and J. W. Storr, "The Electrical Characteristics of an Electrohydrodynamic Generator for an Alternating Input," unpublished thesis GA/PHys/63-11, 12, Air Force Institute of Technology, Wright-Patterson Air Force Base, Ohio, sponsored by ARL, August 1963.

Hawes, M., "Experimental Techniques in Electrofluid Dynamic Energy Conversion Research," 6th AGARD Combustion and Propulsion Colloquium, March 16-20, Cannes,France, 1964; ARL Report 64-77, Aerospace Research Laboratories, Wright-Patterson Air Force Base, Ohio, (AGARDograph 81, "Energy Sources and Energy Conversion,"pp 539-630, 1967.

Hasinger, S., "Performance Characteristics of Electro Ballistic Generators," 6th AGARD Combustion and Propulsion Colloquium, Cannes, France, March 1964. ARL Report 64-75, Aerospace Research Laboratories, Wright-Patterson Air Force Base, Ohio, October 1964 (AGARDograph 81, pp 539-630).

Lawson, M.O., "Performance Characteristics of Electrofluid Dynamic Energy Conversion Processes Employing Viscous Coupling," 6th AGARD Combustion and Propulsion Colloquium, Cannes, France; ARL Report 64-74, Aerospace Research Laboratories, Wright-Patterson Air Force Base, Ohio, October 1964; (AGARDograph 81, pp 539-630).

von Ohain, H. and F. Wattendorf, "Potentialities of Direct Electrofluid Dynamic Energy Conversion Processes for Power Generation," 6th AGARD Combustion and Propulsion Colloquium, Cannes, France; ARL Report 64-73, Aerospace Research Laboratories, October 1964, (AGARDograph 81, pp 539-630).

Kahn, B., "A Continuation of the Basic Study of Slender Channel Electrogasdynamics," ARL Report 65-4, Aerospace Research Laboratories, (AD 614907), Wright-Patterson Air Force Base, Ohio, January 1965.

Gourdine, M. C, and D. H. Malcolm, "Feasibility of an EGD High Voltage Power Source," 19th Annual Power Sources Conference, Atlantic City, New Jersey, May 1965.

Wattendorf, F., et al., High Voltage Electrostatic Generator, U. S. Patent No. 3, 225,225, December 21, 1965.

"Selected Topics in Electrofluid Dynamic Energy Conversion (1968)," Invitational Working Electrofluid Dynamic Energy Conversion Conference, Aerospace Research Laboratories, Wright-Patterson Air Force Base, Ohio, May 24-26, 1966 (AGARDograph 122).

Herzog, E., "Electrofluid Dynamic Generator Supplying an A.C. Electric System—A Feasibility Study," Final Report, Contract AF 33(615)-1915, ARL, Wright-Patterson Air Force Base, Ohio, November 1966.

Brandmaier, H., T. H. Dimmick, and B. Kahn, "Research on Power Generation Electrogasdynamic Energy Conversion," ARL Report 67-0005, Aerospace Research Laboratories, Wright-Patterson Air Force Base, Ohio, January 1967.

Decaire, J. and M. Lawson, "Electrofluid Dynamic Power Generation: Trends and Expectations," 8th Symposium on Engineering Aspects of Magnetohydrodynamics, Stanford University, March 28-30, 1967.

Decaire, J. and M. Lawson, "Investigation on Power Generation Using Electrofluid Dynamic Processes," Advances in Energy Conversion Engineering, ASME, New York, 1967, pp 473-483, (1967 Intersociety Conversion Engineering Conference).

Decaire, J. and M. Lawson, "Outlook for Electrofluid Dynamic Power Generation," ASME Paper 67-Pwr-11.

Minardi, John E., "Computer Program for the Calculation of Electric Fields in an Electrofluid Dynamic Generator," ARL 68-0156, August 1968 (final report on Contract AF 33(615)-3203).

Joshi, K. K., "Electrical Charging of Liquid Sprays in High Pressure Gas Flows for Electrofluid Dynamic Processes," Institute of Electrical and Electronic Engineers, International Electron Devices Meeting, Washington, D.C., October 18-20, 1967.

Minardi,J. E., "Computer Study of Electrofluid Dynamic Colloid Generator," Intersociety Energy Conversion Engineering Conference, Boulder, Colorado, August 13-16, 1968.

Trezek, G. and D. France, "The Contribution of Space-Charge in Slender Channel Electrogasdynamics," Energy Conversion, Vol. 9, 1969.

Melcher, J. R. and T. C. Cheng, "Prospects of Electrogasdynamic Power Generation," IEEE Winter Power Meeting, New York, New York, January 25-30, 1970.

Borok, A. M., "Electrogasdynamic Generation with Neutralization of the Space Charge," Soviet High Temperature, Vol. 8, No. 1, January-February 1970.

Lawson, M. and H. von Ohain, "Electrofluid Dynamic Energy Conversion, Present Status and Research Areas," ASME Journal of Engineering for Power, April 1971, ASME Paper No. 70-Ener-A.

Willke, T. and E. F. Fretter, "Description of a High Pressure Electrofluid Dynamic (EFD) Facility," ARL Report 71-0260, Aerospace Research Laboratories, Wright-Patterson Air Force Base, Ohio, November 1971.

Willke, T. L., "Current Production in Cylindrical Geometry Electrofluid Dynamic Generator," ARL Report 71-0245, Aerospace Research Laboratories, Wright-Patterson Air Force Base, Ohio, October 1971.

Musgrove, Peter, "The Prospects for Electrogasdynamic Energy Conversion," Electrical Review, September 17, 1971.

Solbes, A., "Research on Charged Alkali Colloids for Aerospace Vehicle and Ground Based Power Generators," ARL reports 74-0125 and 75-0004, Aerospace Research Laboratories, Wright-Patterson Air Force Base, Ohio, October 1974.

Huberman, M., et al., "Study on Electrofluid Dynamic Power Generation," Interim Report, 23 April 1973 to 22 April 1974, ARL Report 74-0119, Aerospace Research Laboratories, Wright-Patterson Air Force Base, Ohio, October 1974.

Lawson, M., E. F. Fretter, and R. W. Griffith, "Report on Progress in Achieving Direct Conversion of a Major Fraction of Sonic Flow Kinetic Power into Electric Power by Electrofluid Dynamic (EFD) Processes," 9th Intersociety Energy Conversion Engineering Conference, San Francisco, California, August 26-30, 1974.

Huberman, M., et al., "Study on Electrofluid Dynamic Power Generation," Interim Report, 25 April 1974 to 25 April 1975, ARL Report 75-0200, Aerospace Research Laboratories, Wright-Patterson Air Force Base, Ohio, October 1975.

Lawson, M. O., "Injector Generator Matching Characteristics," Lecture presented at TRW Systems, Incorporated, Redondo Beach, California, September 11, 1975.

Griffith, R. W., "Experimental Charge Production in a Two Dimensional Electrofluid Dynamic Test Generator," ARL Report 74-0002, Aerospace Research Laboratories, Wright-Patterson Air Force Base, Ohio, January 1974.

Joshi, K. K., "Single Channel Investigations for 5 kW Clustered Channel EFD Generator," ARL Report 72-0059, Aerospace Research Laboratories, Wright-Patterson Air Force Base, Ohio, April 1972.

Calvert, C., and J. Watson, "Investigation in Energy Transfer and Energy Conversion for Advanced Power and Propulsion Systems," ARL Report 73-0122, Aerospace Research Laboratories, Wright-Patterson Air Force Base, Ohio, October 1973.

Frecter, E. and J. Minardi, "Effect of Sloped Electrodes on P Times D Parameter for EFD Generators," 1976.

Minardi, J. E., M. O. Lawson, and G. Williams, "Electrofluid Dynamic (EFD) Wind Driven Generator," Final Report, COO/4130-77-1, October 1976.

Minardi, J. E. and M. O. Lawson, "Annual Progress Report on the Electrofluid Dynamic Wind Generator," UDRI-TR-77-38, University of Dayton Research Institute, Dayton, Ohio, 22 July 1977.

Minardi, J. E. and M. O. Lawson, "Progress in Electrofluid Dynamic (EFD) Wind Driven Generator Research," Third Biennial Conference and Workshop in Wind Energy Conversion Systems, Washington, D. C., September 19-21, 1977.

Minardi, J. E. and M. O. Lawson, "Electrofluid Dynamic (EFD) Wind Driven Generator Research," Society of Engineering Science, Inc., 14th Annual Meeting, Bethlehem, PA, November 14-16, 1977.

Minardi, J. E. and M. O. Lawson, "Research in the Electrofluid Dynamic (EFD) Wind Driven Generator," IEEE 1978 National Aerospace and Electronics Conference, Dayton, Ohio, pp 869-873, May 16-18, 1978.

Minardi, J. E., M. O. Lawson, and F. L. Wattendorf, "Third Annual Progress Report on the Electrofluid Dynamic Wind Generator," University of Dayton Research Institute, Dayton, Ohio, May 1979.

HANS VON OHAIN'S FIRST LEGACY: TRENDS AND RESEARCH OPPORTUNITIES

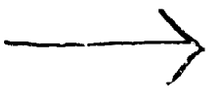

by

Brian Quinn
Director of Aerospace Sciences
Air Force Office of Scientific Research

AIAA-79-0116

To have contributed to a volume paying homage to Hans von Ohain's research and development career in the Air Force honored the author. To have experienced the explosion of ideas, the questioning smile and the curiosity of Dr von Ohain through daily association is to have learned to extract the essential, to have tasted success in science and to have shared his humanity. And, hopefully, to have appreciated the friendship of an especially exciting human being. As comfortable with Hegel as with Heisenbert, finding parallels between minor themes in Antigone and loss mechanisms in ejectors, acquaintances may see Dr von Ohain as a man of contrasts. His friends, on the other hand, readily discern the continuous threads which unify such contrasts within an intellect of vast proportions. So it is that the man who in reviewing a mathematical development once said "At my age, Brian, one no longer integrates," was also the man who years before had so exquisitely integrated not just a mathematical expression but several sciences and technologies into the first jet engine. That engine flew in 1939. Today's refinements continue to shrink our association of time with distance. The following paragraphs examine several areas in which research may further refine Hans von Ohain's technology.

To project the historical trends of a technology is to glean some insight into the research advances necessary for its continued improvement. Such insight suffers somewhat from myopia since it focuses on evolutionary advances and filters the revolutionary results that could radically and abruptly change the technology. Imagine, for example, the effect on engine performance of the unpredicted formulation of a 3500^{O}F turbine material! Managers of research differentiate between evolutionary and revolutionary advances. Wise managers plan to achieve the former and hedge against

Copyright AIAA 1979. Reprinted with Permission.

against their myopia by providing the broad based environment for the latter.

Along with the analysis of trends the manager's basket of planning tools includes the opinions of experts who assist in identifying the research needs important to the organization's mission. Reference 1, called the Research Objectives, is such a consensus, and classifies the research needs of the Air Force in seven technical areas. This paper complements and borrows from the section of that document on air breathing propulsion.

This discussion begins with the history and evolution of selected military engine parameters. Whenever possible, references indicate a particular engine's first flight or its delivery date to the manufacturer. Cross referencing may result, however, in errors as large as five years. It is important to recognize that ten or more years separate an engine's conception from its manufacture. In other words, today's engines are built with advanced technology of the late sixties. The research which sired that technology is even older.

In the present context the work "research" means increasing knowledge and understanding in areas of the physical, chemical, mathematical and engineering sciences related to long term needs. From such a definitive perspective it seems more appropriate to organize the research opportunities described in the intermediate section of this paper along the lines of scientific dsiciplines rather than by components of airbreathing engines. The paper closes with a restatement of key research needs and suggests a mechanism for increasing the probability of revolutionary advances in research related to airbreathing engines.

HANS VON OHAIN'S FIRST LEGACY: TRENDS AND RESEARCH OPPORTUNITIES

Brian Quinn
Director of Aerospace Sciences
Air Force Office of Scientific Research

To have contributed to a volume paying homage to Hans von Ohain's research and development career in the Air Force honored the author. To have experienced the explosion of ideas, the questioning smile and the curiosity of Dr von Ohain through daily association is to have learned to extract the essential, to have tasted success in science and to have shared his humanity. And, hopefully, to have appreciated the friendship of an especially exciting human being. As comfortable with Hegel as with Heisenberg, finding parallels between minor themes in Antigone and loss mechanisms in ejectors, acquaintances may see Dr von Ohain as a man of contrasts. His friends, on the other hand, readily discern the continuous threads which unify such contrasts within an intellect of vast proportions. So it is that the man who in reviewing a mathematical development once said "At my age, Brian, one no longer integrates," was also the man who years before had so exquisitely integrated not just a mathematical expression but several sciences and technologies into the first jet engine. That engine flew in 1939. Today's refinements continue to shrink our association of time with distance. The following paragraphs examine several areas in which research may further refine Hans von Ohain's technology.

To project the historical trends of a technology is to glean some insight into the research advances necessary for its continued improvement. Such insight suffers somewhat from myopia since it focuses on evolutionary advances and filters the revolutionary results that could radically and abruptly change the technology. Imagine, for example, the effect on engine performance of the unpredicted formulation of a 3500°F turbine material! Managers of research differentiate between evolutionary and revolutionary advances. Wise managers plan to achieve the former and hedge against their myopia by providing the broad based environment for the latter.

Along with the analysis of trends the manager's basket of planning tools includes the opinions of experts who assist in identifying the research needs important to the organization's mission. Reference 1, called the Research Objectives, is such a consensus, and classifies the research needs of the Air Force in seven technical areas. This paper complements and borrows from the section of that document on air breathing propulsion.

This discussion begins with the history and evolution of selected military engine parameters. Whenever possible, references indicate a particular engine's first flight or its delivery date to the manufacturer. Cross referencing may result, however, in errors as large as five years. It is important to recognize that ten or more years separate an engine's conception from its manufacture. In other words, today's engines are built with the advanced technology of the late sixties. The research which sired that technology is even older.

In the present context the word "research" means increasing knowledge and understanding in areas of the physical, chemical, mathematical and engineering sciences related to long term needs. From such a definitive perspective it seems more appropriate to organize the research opportunities described in the intermediate section of this paper along the lines of scientific disciplines rather than by components of airbreathing engines. The paper closes with a restatement of key research needs and suggests a mechanism for increasing the probability of revolutionary advances in research related to airbreathing engines.

Technological Trends

The dramatic improvement in jet engine performance over the years can be gleaned from Figure 1 where thrust-to-weight ratio is seen to have doubled, approximately, every fifteen years. Growth is equally attributable to the structural innovations and reduced weight of advanced designs and to a chronic demand for more thrust from smaller engines.

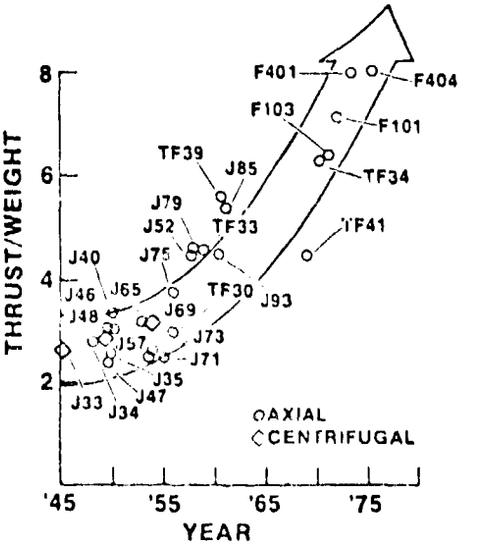

Fig 1. Increasing trend of thrust-to-weight ratio.

The trend reflects two conceptual changes: the dominance of axial compressors after the late forties and the introduction of turbofans in the mid sixties. Otherwise, changes have been more evolutionary than revolutionary, and chronological improvements mostly reflect advances in the design of components. Especially impressive is the improved stage performance of axial flow compressors. With eleven stages, the J34-WE-36 of the

late forties achieved a pressure ratio of nearly 4.4. With just a few more stages, today's engines achieve pressure ratios in the twenties. This trend, shown in Figure 2, has been consistent over the years and gives no hint of having reached a maximum. Indeed, the single stage research compressor designed and tested by Wennerstrom[4] and his colleagues at the Air Force Aeropropulsion Laboratory has already produced pressure ratios around two. Such achievements underscore the continuing progress made in understanding the complex flow fields found in turbomachinery as well as the ability of creative designers to translate research results into practical machines.

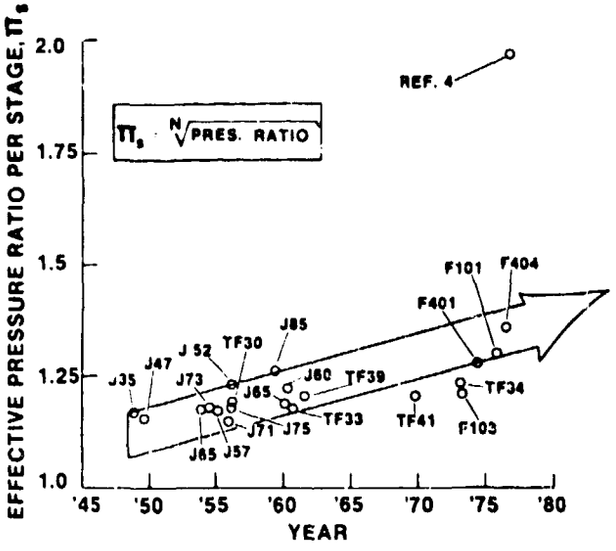

Fig. 2. Increasing trend of effective stage pressure ratio.

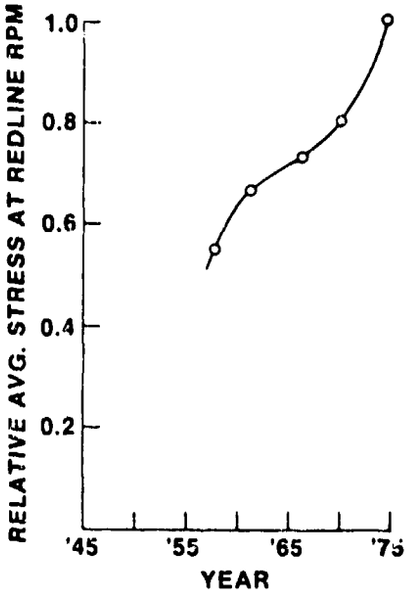

Fig. 3. Increasing trend of average tangential stress in turbine disks.

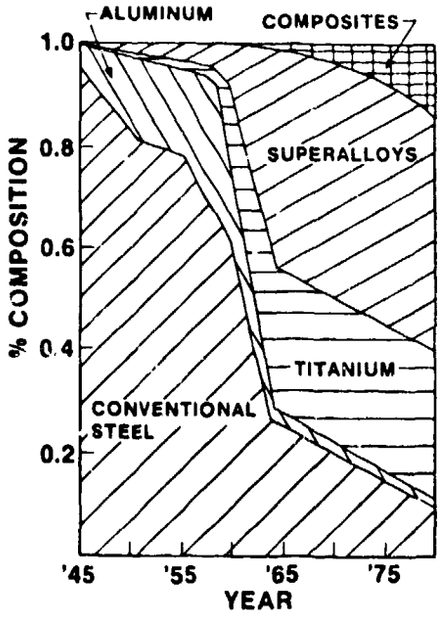

Fig. 4. Material composition of engines over the years.

The designers have been especially aggressive in their pursuit to optimize the strength-to-weight ratio of engine components. The trend toward loading lighter and thinner structures with increasingly intense forces has pushed stresses perilously close to their allowable limits. The point was brought home by Osias, et al[5], from whose paper Figure 3 was obtained. The curve charts average nominal tangential stress of selected turbine disks at maximum operating speed in terms of the like stress on the P&W F100 engine.

Credit for structural improvements is due, in part, to advances in the materials sciences. A pattern of stronger and lighter materials is evident in the brief history of gas turbine engines. Engines put into service during the early forties were made almost entirely from conventional steels. Stainless steel and aluminum made their jet engine debuts in the late forties, but aluminum began to be displaced by titanium in the mid-fifties. The superalloys began to play a dominant role in the mid-sixties, about the same time that the large by-pass ratio fans increased the relative importance of titanium. These trends, together with the recent intrusion of composites as engine materials, have been sketched in Figure 4. Their use, disuse and relative importance to the aircraft engine scene have been motivated by the need to satisfy frequently conflicting objectives: lightweight structures and sufficient strength.

The strength of a material, however, is inseparably tied to its environment. Designers have typically increased the thrust of engines over the years by "turning up the wick," by increasing turbine temperatures and creating inhospitable environments. The trend is clear, as clear as the growing gap between the turbine temperatures and the acceptable operating temperatures of the materials identified in Figure 5.

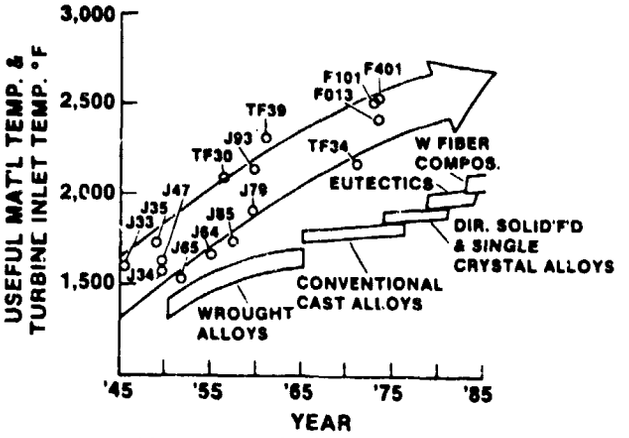

Fig 5. Trend of increasing turbine inlet temperatures.

Active turbine cooling has been the sole successful bridge across the temperature gap. Important figures of jet engine merit, such as pressure ratio, thrust and efficiency all favor higher turbine temperatures and nothing has appeared on the horizon at this time to suggest a turn around in the increasing temperature trend.

Certain high speed aircraft requirements, such as nacelle drag, stealth and volume constraints, have pressured engine manufacturers to install more thrust in smaller packages. So successful have they been in this regard that thrust per square foot of frontal area has about doubled in the past twenty-five years. Engines are also more compact, being considerably shorter now, per pound of thrust, than in former times. Figure 6 describes the trend toward reduced frontal area. The weight of air passing through the engine, rather than thrust, has been used as the reference parameter to emphasize the higher through flows and higher through flow velocities of today's engines. This factor has special and rather obvious meaning to the fluid dynamic processes occurring in the engine's various components.

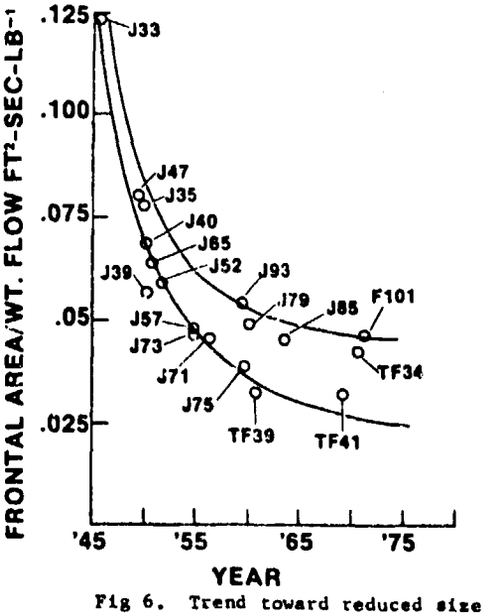

Fig 6. Trend toward reduced size and higher through flows.

Specific fuel consumption (SFC) characterizes engine efficiency or, more properly, engine effectiveness. By relating an engine's thrust to the rate at which it burns fuel, SFC integrates the efficiencies of processes that occur between the inlet and the exhaust nozzle. Figure 7 summarizes the interesting improvements in SFC provided by advancing technologies. While the SFC of pure turbojets progressed through the late fifties, the introduction of fan engines significantly altered that trend for the better.

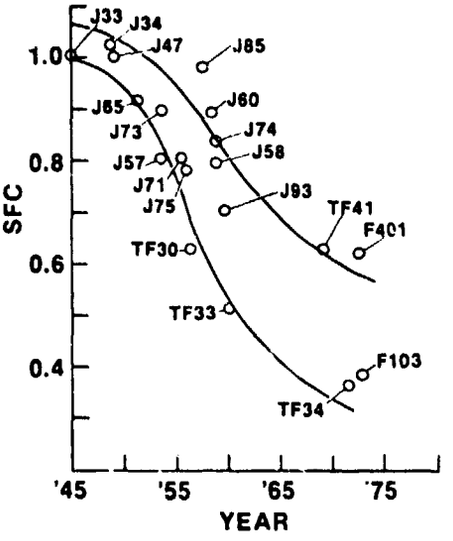

Fig 7. Trend of specific fuel consumption (lb. of fuel per second per lb. of thrust).

There is no need to labor the question of efficiency at a time when fuel consumption and its availability have become critical national issues. While the trend of SFC has been declining, the trend of fuel cost has been increasing at a much faster rate. Their product has also been increasing, resulting in alarming operating costs and a trend which will, no doubt, encourage the redistribution of economic resources toward the immediate needs of a mission oriented agency. The availability of fuel, or the lack thereof, impacts more than price. In an environment of conservation a conscious decision not to allow an agency's consumption of fuel to increase relative to the nation's consumption must surely curtail its operations. The probable adverse effect such a policy would have on the effectiveness of the agency has to be weighed in assigning national priorities. This is a large issue, but within the context of a paper dealing with technological trends and research opportunities, the important observation is that the issue is forced by a trend of increasingly scarce fuel.

Yet another unsatisfactory trend deserves discussion. In estimating the cost of aircraft turbine engines, Large[6] correlated the cost of the thousandth engine in a production run with thrust to the 0.612 power. Costs were indexed to the year 1969. As evident in Figure 8, three distinct regions developed which Large associated with the type of compressor, operating temperature, Mach number and other factors. From this analysis

it would appear that advancing technology in the turbine engine industry is an expensive proposition. Contradistinction with the electronics industry prompts a discussion of capital vs. labor intensiveness, but also raises a question of manufacturing processes, their age and efficiency. In light of the real growth of engine costs, it stands to reason that dollar invested per pound of thrust, or some other economic parameter, will continue to grow in relative importance to other engine performance factors.

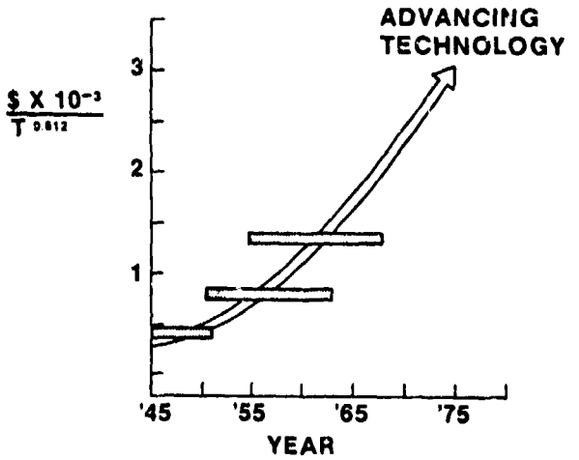

Fig 8. The increasing cost of advanced technology.

More thrust, less weight and smaller dimensions seem to have been the design parameters which pulled technology through the past. The result has been increasing pressures and temperatures, higher through flow velocities and a continuous reassessment of suitable materials. Better efficiency has resulted; higher pressure ratios are now achieved with fewer stages and more thrust is now produced with less fuel. The same trends will most likely persist through the turn of the century, although acquisition and operating costs rather than thrust, weight and size will be the principal source of motivation. In any event, the technologies required in the future will fail to blossom if the science base is not cultivated today. Advances are necessary especially in mechanics, materials, chemistry and mathematics.

Research Opportunities

Fluid Mechanics

One of the oldest fluid dynamic processes continues to perplex modern practitioners except in the most elementary applications. The process is diffusion and the design of devices for effectively accomplishing the process remains, in most cases, a trial and error task. Especially in aircraft turbomachinery the role played by diffusers assumes an importance that belies the apparently simple conversion of kinetic energy to pressure. As a diffuser, the engine inlet attempts to deliver to the fan or to the compressor a uniform flow at a Mach number substantially below its free stream value. In this capacity its efficiency affects overall propulsion efficiency on a one-to-one basis. Nevertheless, mistakes in the design of inlets persist, because very fundamental fluid mechanics problems remain unsolved.

If one considers two-dimensional flows, the boundary layer - shock wave interaction problem can now be handled with reasonable confidence. Add the third dimension of practical inlets, and hope displaces confidence. Designers need experimentally verified three-dimensional analysis techniques capable of handling shock-boundary layer interactions and of providing flow separation criteria. Whereas such criteria alone would be acceptable at this time, longer range thinking will emphasize the need to continue calculations completely through separation in search of reattachment. Moreover, any calculation scheme requiring uniform initial conditions will have very limited value. Military aircraft flying at very high angles of attack, or modest angles of sideslip, produce very nonuniform flows at the entrance to the inlet. Good external aerodynamic techniques must be developed to quantify the degree of nonuniformity and equally good, but intrinsically more difficult, techniques must be developed to follow the evolution of the distortion through the twists, turns and area scheduling of the inlet passage. Equipped with the proper analytical tools, the designer could evaluate the quality of the flow being delivered to the fan or compressor and make the paper changes required to keep it within specified tolerances.

Very similar problems, which were all but insignificant at one time, are now important because of the trend toward higher through flows, Figure 6. This trend, together with the increasing demand for shorter engines, underscores the need to recover more pressure with more compact diffusers. This is hardly a new goal, but its achievement has been hampered or prevented inevitably by flow separation in one form or another. Novel designs, like trapped vortex diffusers, and more conventional boundary layer control techniques have provided a measure of help, but these are still art forms that require much more research before designers confidently use them and before the power they require fails to reduce diffuser efficiency below tolerable levels. To achieve success with compact diffusers and inlets, fundamental research is needed at the heart of the problem: the response of anisotropic flows to rapid rates of strain. Boundary layers, skewed inlet profiles and the wakes shed from the last stage stator blades have in common a structure of large scale eddies whose axes are generally aligned normal to the direction of flow. Depending on how such eddies are strained while passing through the inlet or diffuser, they are intensified or attenuated, and the quality of the flow tends away from or toward uniformity. Experiments have already demonstrated the impact of eddy strain rate on diffuser performance, but much more research will be required before the phenomenon is understood or of use to designers.

The demand for higher efficiency and the trend toward higher stage loadings discussed in connection with Figure 2 have driven tip speeds faster and brought very complex, transonic and mixed-flow aerodynamic problems to axial flow compressors. An appreciation for the complexities of the flow passing through a compressor blade row

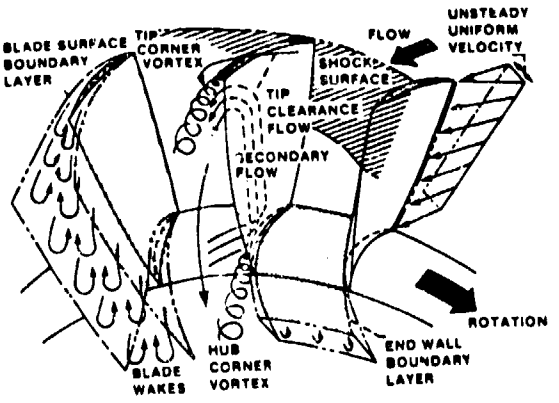

Fig 9. Complex flow structure through a compressor blade row.

can be gleaned from Figure 9, which was taken from a paper by C. H. Hauser et al[7]. The flow first passes through a shock wave whose surface is usually three-dimensional. The "inviscid" flow field in the passage therefore includes strong radial pressure gradients and radial velocity components that are neither insignificant nor uniform. To this must be added the additional complication of an upstream flow field which is either nonuniform because of inlet distortion, or nonuniform and unsteady because of passing through the wakes of upstream stators. Shock wave - boundary layer interactions are once again apparent, as also is a three-dimensional boundary layer which evolves into a streamwise vortex along the juncture of the hub and the suction side of the blade. Another streamwise vortex structure develops as flow leaks from the pressure side to the suction side of the blade through the tip clearance. Both vortex systems, tip and hub, are intimately tied to a secondary field that circulates the flow around the passage. This, together with reflected or residual shocks and the wakes from hub and blades, joins the mainstream in forming very messy inlet conditions for the stator.

The flow described in Figure 9 is usually analyzed subject to a number of simplifying assumptions. Common practice tends to match two-dimensional blade-to-blade characteristics with an axisymmetric hub-to-tip approximation to the mean flow through the blade row passage. Difficulties intrinsic to the real flow all but force analysts to concentrate on a particular aspect of the flow and to exclude other, equally important contributions. Thus, there are solutions to the potential equations which describe the flow through thin, lightly loaded blade rows. Such results are steady, shock free and, perforce, inviscid. Some finite difference solutions allow for weak shocks but they also suffer from the steady, two-dimensional, inviscid assumptions. Other finite difference schemes relax one or another of these assumptions but none has yet calculated the complete physical flow.

In view of the significant advances that have occurred during the past few years in analyzing complex, transonic external flows with imbedded shocks, mathematicians and numerical fluid dynamicists must be encouraged to continue basic research in this area. The problems are essentially non-linear and multidimensional, and research opportunities exist for all advanced computational techniques that promise reliable and economic solutions.

Quite another, but related, activity must proceed hand in glove with techniques for flow field analysis: the design and optimization of compressor and fan blades. What the supercritical wing did for external transonic aerodynamics awaits what an analogous design will do for transonic compressors. Novel means of energizing boundary layers while paying the minimum price in power must be explored. Somewhat related research is required in turbine design where the trend toward higher temperatures, Figure 5, necessitates active cooling. In particular, there is an urgent need for accurate predictions of steady and unsteady film and convective heat transfer coefficients associated with a variety of internal and external flow conditions.

The problems identified in Figure 9 are as much or more of a challenge to experimentalists as they are to theoreticians. Nevertheless, experiments which accurately describe each aspect of that complex flow are perhaps more important at this time than theoretical studies, if only because the latter models the former. But how to map a three-dimensional shock surface, how to measure static pressure gradients, how to measure flows in physically small vortices and tip clearances, and how to measure accurately within rotating turbomachinery are questions that have perplexed many creative minds. Success in similar endeavors has often been the byproduct of a radically new instrument, and it would seem that if the flow through rotating blade rows will ever yield to delineation, then it, too, will require new instrumentation and diagnostic techniques.

Another component for which research into instrumentation and diagnostic methods will produce large payoffs is the combustor. The trend toward more compact engines and, therefore, toward more compact combustors exerts strong pressures on new means of accelerating and concluding the mixing of fuel and air. Studies pertaining to the dynamic interactions between liquid jets and gaseous streams that include two-phase flow aspects are needed to develop the promise of pre-mixing and pre-vaporization. The trend toward higher through-flow velocities adds another dimension of importance to the mixing task. Insofar as mixing within turbomachinery is governed by turbulence, it stands to reason that research and improved understanding of the structure of turbulence will produce appropriate rewards. Similar statements can be said with regard to the impact of a more complete understanding of turbulence on combustion dynamics and of delivering a uniform temperature profile to the turbine. The recent recognition of the role played by large scale turbulent structures offers hope that a new level of understanding is attainable. Its realization will require a comprehensive and well focused series of experiments capable of extracting detailed information from high temperature, reacting flows. Such experiments will also require advanced diagnostic devices.

Structural and Material Mechanics

The structural design of engine components continues to suffer from unreliable prediction methods. Despite designer's "rules of thumb" and "knockdown factors," rather serious problems have developed with a number of modern power plants. Zollinger[8] mentions a few catastrophes, noting that the problems are not unique to any particular manufacturer. In many cases the cause of failure derives from insufficient knowledge of nonlinear material properties and loading responses. The need for research in structural and material mechanics becomes increasingly acute as thrust-to-weight ratios (Figure 1), stress levels (Figure 3), and turbine temperatures (Figure 5) maintain their upward trends.

The transonic and unsteady flows discussed in the preceding section engender severe aeroelastic problems with fan and compressor blades. Designers suffer many handicaps in this area, not the least of which is predicting modes and eigenfrequencies of complex geometries with ill-defined boundary conditions. Although the finite element techniques have succeeded in describing many experimentally observed modes, the success is limited by ill-defined material properties and by geometric constraints on twist or thickness distributions. Only in a few cases have modes been obtained for rotating, but geometrically simple, blades, and these have confirmed an intuited dependence of certain eigenfrequencies on rotation speed. Research must continue to study the mechanisms of wave propagation: experimentalists particularly need to delineate the stress fields in realistic geometries under realistic loads at any frequency while analysts must likewise uncomplicate their codes and, most important, accurately describe real, rarely completely elastic or linear boundary conditions.

Figure 10 provides appreciation for the extent to which flutter in one form or another covers a compressor map. Because of analytical uncertainties in predicting cyclic stress and of the experience of failures associated with flutter, engineers work hard to assure that engines operate free from flutter. While present knowledge warrants such conservatism, it could well be that the flutter-free restriction suboptimizes the fluid

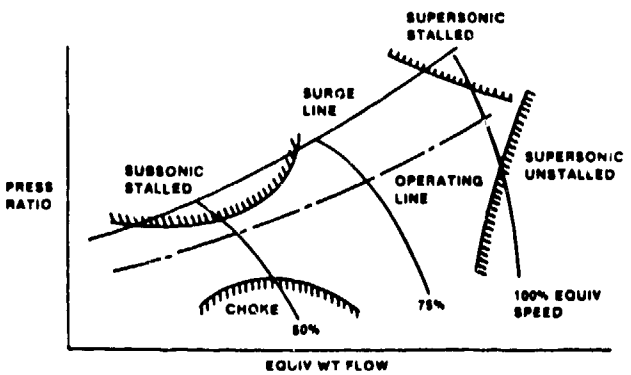

Fig 10. Typical flutter boundaries.

dynamic performance of compressors and fans. A growing body of knowledge has associated increased lift coefficients with oscillating airfoils. Other experiments have identified boundary layer control and drag reduction through the action of unsteady walls. Only research can determine if meaningful performance benefits would accrue to operating compressors in a controlled flutter, and only research can determine if blades would maintain their integrity under the consequent fatigue stresses. Tailoring the anisotropic properties of blades made from composite materials offers the challenging hope of increasing stage loading through purposefully oscillating blades.

Introducing composite materials to the realm of flutter raises the thorny issue of how successfully the existing computational methods predict stress distributions in other than elastic, isotropic materials. Few, if any, of the finite element approaches mentioned above could calculate the resonant modes and frequencies of an anisotropic blade. The problem is two-fold and points to shortcomings in the analytical - numerical schemes and in the characterization of material properties from both macroscopic and microscopic points of view.

In a macroscopic sense, research must identify the response of composite structures to shear and combined loading, to high strain rate impacts from foreign objects and to realistic environmental factors. Failure modes need to be identified for all composites, including the epoxy based materials found on fairings and the titanium matrix materials projected for high temperature applications. Other challenging research opportunities can be found in the characterization of composite materials on the micro scale. Constitutive relationships need to be derived from experimental and theoretical investigations into the strength of fibers, their orientation as a laminate and the characteristics of their interface and interaction with the matrix. At the same time, the properties and failure modes of polymeric resins must be examined and described in light of their intrinsic sensitivity to time. Similar studies must delve into the rheology of adhesives and determine their failure modes before designers can confidently join composite components to other load bearing structures.

The increasing cost of acquiring and maintaining engines has advanced the concept of retirement for cause, a practice wherein components are replaced, because defects impair future use and not because defects are simply present or even presumed to be present. The key to the concept is an accurate prediction of life, under actual operating conditions, that begins with crack initiation and continues through propagation. The basis for predicting the residual life of flawed components is fracture mechanics.

The fracture mechanics of ductile materials essentially remains a planar, elastic discipline, although the heart of the problem lies in the deformation of the plastic region near the crack tip. Research in elastic-plastic and dislocation theories, together with additional test data, are required before plastic responses to loads are accurately predictable. Research must also continue to explore the three dimensional propagation of

entire crack fronts, along surfaces and within the bulk of materials. How elevated temperatures and biaxial loading affect crack propagation also needs to be answered.

The fracture mechanics of composite materials is an infant discipline which, therefore offers a wealth of research opportunities. Similar analysis methods are required, although the lack of plastic behavior produces entirely different crack propagation mechanisms in composites from those in alloys. Residual stresses, matrix properties and the fiber-matrix interfaces appear to play fundamental roles in propagating cracks through composite materials. In this regard, much of the microstructural needs discussed earlier will also benefit fracture mechanics.

The retirement for cause philosophy will fail to succeed, and the science of fracture mechanics will fail to advance if meaningful improvements fail to materialize in nondestructive inspection methods. Lightweight, portable and easy to use devices will be required in the field to locate and assess damage before residual life can be determined. Very accurate devices will be required in laboratories to quantify the development of damage and to relate its advance to precisely defined loading sequences. While electron microscopy and conventional X-ray techniques are invaluable to the characterization of microstructure, the definition of internal stress fields is the real, driving requirement. Very recent studies indicated the feasibility of bulk measurements of residual stress with X-ray diffraction. It seems advisable to pursue these activities and complement them with similar research using higher energy particles. Neutron radiography, for example, has already proved its worth to the turbine engine community by identifying hydrogen embrittlement on turbine blades where other methods failed. The affinity of hydrogen for neutrons suggests the exceptional potential of neutron radiography as a diagnostic tool for composite materials. Immediately obvious is its application to moisture induced damage detection and to fracture and microscale characterization of certain polymeric resins and adhesives.

Ultrasonic methods have been used for many years to detect flaws in engine components. In situ examinations usually rely on a pulse echo technique, but laboratory experiments might also employ resonance, through-transmission or other methods. The potential of ultrasonics to describe interior stress fields derives from two considerations. The first of these is the dependence of the propagation speed of disturbances on the stress within an elastic solid and, therefore, an inference of local stress from measurements of local wave speed. Present methods unfortunately involve the time of flight over prescribed distances and, thereby, integrate local properties to mean values. The second consideration, tomography, may eliminate this shortcoming. The techniques now being developed by radiologists to examine discrete planes in the human body must be studied for their application to the local measurement of stress. The payoff promised by success with tomographic techniques for acquiring local stress measurements associates a high priority with related research activities.

The requirement for engine materials research is driven to a large extent by turbine inlet temperatures, which are now approaching stoichiometric values. Needed are strong thermodynamically stable and oxidation resistant materials with useful strength above 2800°F. The basis for discovering such materials from a rational approach lies in a fundamental understanding of eutectic-eutectoid binary and ternary phase transformations occuring under solid-liquid and solid state conditions. On a general scale, such understanding is presently lacking.

As shown in Figure 5, directional material structures are expected to play a major role in the future. Directionally solidified eutectic alloys and tungsten-fiber-reinforced superalloys are identified in the figure but, whether or not their candidacy leads to operational use depends on the results of research. Unfortunately, directional structures are anisotropic and while their stress axes may be aligned to support the loads of high tip speeds, their tolerance to shear may prove inadequate. This property could lead to failures in turbine blade roots where shear stresses are currently approaching 30 KSI. Metal turbine blades, eutectics and superalloys will also need coatings to protect them from the severe, oxidizing environment. Ceramic coatings serve also as thermal barriers between the blade and the hot gas because of their low conductivities. Fundamental data needed for computing heat loads under operating conditions are rarely available. Conductivity and thermal emittance data are needed, as are radiative property data which will become more important as gas pressures continue their upward trend.

Chemistry

Combustion kinetics and dynamics, fuel synthesis and characterization and composite material characterization on the microscale are a few of the many areas in which the chemical sciences can contribute to airbreathing combustion. Controlling effluents to meet military as well as civilian objectives has motivated many combustion efforts. Especially irritating because of its visibility, smoke continues to stream from jet engines in spite of the resources invested in its elimination. The problem lies in our incomplete knowledge of liquid and solid phase nucleation and condensation processes, especially the former. In the case of carbon soot, its formation prior to the complete consumption of the oxygen in producing carbon monoxide suggests a nonequilibrium process. A number of mechanisms, including ionic and free radical mechanics, have been proposed to explain carbon formation, and each is probably important to different combustion locales. The fact of the matter is that undesirable soot does form in engine combustors and will probably continue in many future turbomachines. Accurate measurements of thermodynamic and emissive properties of hot carbon particles therefore remain of interest to military agencies.

The oxides of nitrogen are other engine emissions which have received attention during the past decade. Lowering flame temperatures reduces NO_x, an observation that encourages burning premixed and very lean mixtures. Because of their high chemical activity, catalytic combustors are well suited to very low fuel-air mixtures and to combustion temperatures less than 1400°C. Catalytic combustors offer many other

advantages but their acceptance and general use in turbomachinery must await the answers to a number of very fundamental questions related to the burning of lean mixtures. Very careful studies are needed to define flame speeds and flammability limits in premixed, prevaporized mixtures and to devise suitable quenching means to inhibit flashback. Other problems directly related to the catalyst must also be resolved; poisons inherent to hydrocarbon fuels need identification and removal; and the chemical activity of catalysts operating for extended periods at combustion temperatures needs verification.

Combustion problems such as those mentioned in the preceding paragraphs stand a good chance of being aggravated by synthetic or alternative fuels. While the constitution of fuels obtained from coal or oil shale defies accurate prediction at this time, it is expected that they will contain less hydrogen and more carbon, water, sulfur, nitrogen and oxygen than present fuels. The physical and rheological characteristics of such fuels will have to be determined and means will have to be devised to alter those properties which exceed tolerance. At the same time, present tolerances on viscosity, density, pour point, freezing point and other physical characteristics will need to be reexamined from the point of view of their necessity and possible relaxation. A hydrocarbon type analysis of fuels derived from coal or shale oil will undoubtedly differ from a similar analysis of JP-4, Jet-A or other modern fuels. Higher order parafins, aromatics, olefins and napthenes will be present, and a firm thermodynamic and kinetic data base will need to be established before oxidation reactions can be predicted.

In an altogether different area, chemistry has played a key role in the development of resin matrix composite materials. Although frequently overlooked, there is a fundamental relation between the chemical structure of a material and its mechanical behavior. This relation affects the constitutive law and also controls processing characteristics and failure modes. For example, Kelley and Williams[9] have shown that an elastic modulus, an engineering property, is directly related to the crosslink density of a polymer network, a chemical structure parameter, through the product of the Boltzman constant and the absolute temperature. Many more interdisciplinary and analogous studies will undoubtedly precede the resolution of the really difficult problems in composite materials, and these should be encouraged.

Mathematics

The pervasive nature of mathematics assures that its advances will eventually accelerate the progress of airbreathing engines. The need for improved analysis methods was mentioned in conjunction with the discussions of fluid and solid mechanics. In those fields, mathematics is an assistant, a vehicle for arriving at a physical result. Yet, there is one area of modern mathematics which could and probably will directly impact the future of airbreathing engines: control theory.

Aircraft engines have been growing more complex as they have been tasked to operate at high performance over growing operating envelopes. Variable cycle engines have been proposed for V/STOL, supersonic cruise and other missions. The exhaustive number of parameters needed to operate such engines over broad envelopes, together with increasing demands for faster response and reliability have driven engine controllers away from hydraulic and mechanical systems and toward digital electronic systems. The operational basis of such systems is control theory. While digital engine controllers have been developed for specific and limited applications, achieving their full potential will require research in several areas.

Statistical techniques must be developed before the outputs of advanced sensors can be compared against control standards with predetermined reliabilities. Economies obtain from rationally selecting from among the many measured variables on the basis of their relative importance. In this regard, research needs exist in the development of search linear models and regression analysis suitable for control problems. Finally, it is also important to continue research in multivariate analysis, including the statistical design and analysis of experiments, since this discipline underlies a system's capability to reject external disturbances and to track essential command inputs. Investments in mathematics research are relatively inexpensive and offer a substantial return to future airbreathing engine technology.

Closure

Having examined the trends of selected engine performance and technology parameters, the foregoing discussion advises certain research activities. Space, time and the author's personal interests limit the discussion to a few research opportunities. Hopefully, their importance bears an inverse relation to their number.

In most instances, the research needs within each discipline are discussed in terms of an applicable trend. Three dimensional, time dependent aerodynamics has a number of critical applications in airbreathing engines, especially in inlets and compressors. An improved understanding of turbulence will impact the efficiency of every engine's major components. Characterization of metallic and non-metallic materials on the microscale is essential for the development of constitutive relations needed in fatigue and fracture analyses and in life cycle predictions. Combustion dynamics and kinetics take on increasingly important roles as new and advanced fuels are synthesized. Such "trend pulled" research assures the evolutionary advances mentioned in the introductory paragraphs. The real objective, however, is revolutionary research results which give birth to new technology and to stepwise trend discontinuities.

Extraordinary advances have been known to spring from intellectually narrow surroundings but this is not usually the case. The common denominator of most important findings is their association with an environment of multidisciplinary excellence. Broad based renaissance savants succeeded within this framework and a similar milieu persists today in some corporate laboratories, especially in the communication and electronics industry. Such interdisciplinary research has all but disappeared from American universities where investigators tend to segregate their perspectives according to teaching departments.

One notable exception that developed during the last decade illustrates the point. Faced with declining aerospace support, some aeronautical engineering professors joined forces with medical researchers in answering fundamental circulatory, cardiovascular and skeletal problems. There is no need to dwell on the extraordinary impact the fresh breath of fluid dynamics has had on medical technology but recognize that artifical heart valves are a functioning reality. Unfortunately, academic researchers in those disciplines that underlie turbomachinery technology have not been similarly motivated to work together.

While the author is a firm believer and strong advocate of individual efforts in basic research, he questions if our present national effort is not hampered by its fragmentation. To the extent that major basic research pertinent to airbreathing combustion is conducted in universities, it appears to suffer from the isolation of many individual efforts, no one of which is of sufficient size to permit effective consolidation of similar theoretical pursuits, integration of related results and, most of all, exploitation of multidisciplinary, and synergistic opportunities. In short, the present size of individual academic research groups is below critical. In contrast are the multidisciplinary and above-critical size turbomachinery research focal points in Germany and in the Soviet Union.

Not every scientific research area lends itself to larger and integrated research endeavors but most do. Activities in fracture mechanics, for example, would very naturally synthesize the efforts of metallurgists, chemists and solid mechanicians. Efforts related to improving compressor and turbine performance would reap benefits from tuning contributions from fluid and structural dynamicists. Real advances in combustors and combustion processes must surely await the combined efforts of chemists and fluid dynamicists. It is also difficult to imagine the development of new instrumentation and diagnostic techniques in the absence of multidisciplinary thinking.

From Leonardo to the Mars landing, history demonstrates the power of multidisciplinary association. In the interest of international preeminence in science, in engine technology and in economics, research management would be remiss in failing to create environments that increase the probability of revolutionary research advances. Managers' portfolios currently emphasize individual research efforts. Including several above-critical size, interdisciplinary and focused activities in their programs is a step in the right direction.

REFERENCES

1. Air Force Systems Command Research Planning Guide, HQ AFSC TR 76-01, May 1976. Obtainable only from Defense Documentation Center, ADA 029310.

2. Jane's All the World's Aircraft, 1956 through 1977 editions, Jane's Yearbooks, London, England.

3. Wilkinson, P.D., Aircraft Engines of the World, 1950 through 1970 editions, published by the author, 225 Varick St., New York, NY 10013.

4. Wennerstrom, A. J. and Frost, G. R., "Design of a 1500 fps Transonic High Flow Through Single Stage Axial Flow Compressor with Low Hub/Tip Ratio," Air Force Aeropropulsion Laboratory Report AFAPL TR-76-59, 1976.

5. Osias, J. R., Meyer, T. G. and Hill, R. J., "Complex Mission History Effects on Low Cycle Fatigue of Disks, in Fatigue Life Technology edited by T. A. Cruse and J. P. Gallagher, ASME Transactions of the 22nd International Gas Turbine Conference, Philadelphia, PA., 27-31 March 1977.

6. Large, J. P., "Estimating Aircraft Turbine Engine Costs," Rand Corporation RM-6384/1-PR, September 1970.

7. Hauser, C. H., et al., "Compressor and Turbine Technology," Aeronautical Propulsion, NASA SP-381, pp 229-288, 13-14 May 1975.

8. Zollinger, J. E., "Structural Integrity for Propulsion Systems," AIAA Journal of Aircraft, Vol 12, Number 4, April 1975, pp 195-197.

9. Kelley, F. N. and Williams, M. L., "The Relation Between Engineering Stress Analysis and Molecular Parameters in Polymeric Materials," Proceedings of the Fifth International Congress of Rheology, Vol 3, pp 185-202, Tokyo, Japan, 1970.

INVESTIGATION OF THE MIXING REGION BETWEEN THE PRIMARY AND SECONDARY STREAMS OF A TWO-DIMENSIONAL SUPERSONIC AIR-AIR EJECTOR SYSTEM

by

William C. Robison
and
James R. Nelson
Commander (Former) Air Force Wright Aeronautical Laboratories

The turbulent mixing region of a two-dimensional, supersonic, air-air ejector system has been experimentally investigated utilizing an interferometer. Density distributions for the two-stream mixing region within the ejector duct were established for 6 different test configurations. Similarity of the density distributions was indicated for mixing region cross sections as close as one nozzle-exit hydraulic diameter from the nozzle. Density profiles at successive downstream duct locations were plotted to show the spread of the mixing region. The effect of normal and oblique shocks on the rate of spread of the mixing region was found to be small. In addition, ejector performance data and techniques for spark lamp photography are presented. It is concluded that the interferometer could be effectively utilized to help determine the transport coefficients of ejector system turbulent mixing processes.

Copyright AIAA 1966. Reprinted with Permission.

COMMENTS ON "CHOKED FLOW: A GENERALIZATION OF THE CONCEPT AND SOME EXPERIMENTAL DATA"

William C. Robison and James R. Nelson
Wright-Patterson Air Force Base, Ohio

AD P000317

In the article by Hoge and Segars[1] the argument is against the ejector model which assumes that the supersonic primary stream and the walls of the mixing tube form a converging channel in which the secondary stream expands to sonic velocity. Recent air ejector studies made at the Air Force Institute of Technology by Nelson[2] confirm that the area variation of the primary stream is insufficient to choke the secondary stream for the test conditions presented in Ref 1 where the ratio of the mixer area to the primary nozzle exit area Am/Ap was 3, and the ratio of the mixer length to its hydraulic diameter L/D was 10.6. We would argue, however, that this result might be altered for higher ratios of primary stream total pressure to secondary stream total pressure P_{op}/P_{os}.

The situation, for example, at an Am/Ap of 2 is quite different. As can be seen from Figures 1 and 2, a primary stream entering the mixer through a diverging nozzle at a Mach number of 2 rapidly expands entrained ambient air to supersonic speeds before an oblique-normal shock system forms. the interferogram (Figure 2) shows that the mixer wall and the alternate expansion and contraction of the nonideally expanded primary jet form a convergent-divergent nozzle. It may be noted also that relatively little mixing occurs until the primary stream is decelerated substantially. It is, therefore, clear that shear and area variation are the dominant factors in the acceleration of the secondary stream.

Other important conclusions from Reference 2, which are of interest to investigators of ejector performance and turbulent mixing, are as follows.

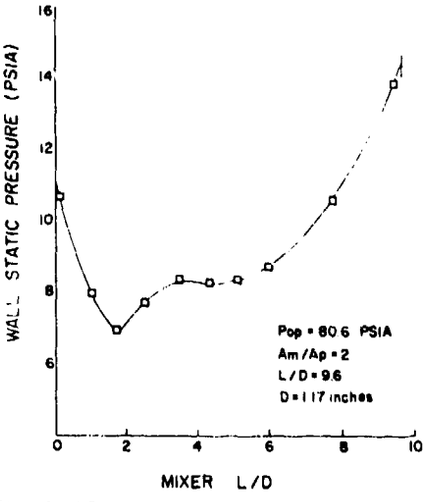

Fig. 1 Mixer wall static pressure profile.

1) Mixer wall static pressure profiles are not an adequate indication of the rate of mixing or completeness of mixing in supersonic ejector systems for cases where the secondary flow is supersonic or where strong shocks are present.

2) Interferograms indicate that the mixing region in a supersonic ejector system does not appear to be changed appreciably in width when passing across shocks that are present in the primary or secondary flow. The mixing region is displaced laterally as it crosses an oblique wave, and the direction of displacement is dependent upon whether its primary stream has been compressed or expanded.

3) It was found that the boundary-layer assumption of $\partial P/\partial y = 0$ across the mixing region was a quite close approximation, but the centerline static pressures were not equal to the wall static pressures. In each region of the primary stream between oblique waves, there is a static pressure variation. However, for the flows to remain separated with a mixing region for a boundary, the pressure gradient indeed must vanish at the boundary.

We believe that this last observation makes a one-dimensional analysis such as that of Reference 1 invalid for an ejector with a supersonic primary stream. The average pressures of the primary and secondary stream legitimately cannot be assumed to be equal. The streams must be allowed to interact to provide equal pressures at the edge of the mixing region. The best analytical effort of this sort that we have seen is that of Chow and Addy.[3]

Fig. 2 Interoferogram of Mixer Flowfield (Am/Ap = 2, Mp = 2)

References

1. H. J. Hoge and R. A. Segars, "Choked Flow: a Generalization of the Concept and Some Experimental Data," AIAA J.3, 2177-2183 (1965).

2. J. R. Nelson, "Investigation of the Mixing Region Between the Primary and Secondary Stream of a Two-Dimensional Supersonic Air-Air Ejector System," M.Sc. Thesis, Air Force Institute of Technology, Wright-Patterson Air Force Base OH (June 1965).

3. W. F. Chow and A. L. Addy, "Interaction Between Primary and Secondary Streams of Supersonic Ejector System and Their Performance Characteristics," AIAA J.2, 686-695 (1964).

TECHNOLOGICAL ADVANCES IN AIRFRAME-PROPULSION INTEGRATION

by

D. Zonars
Deputy Director (Retired), Air Force Flight Dynamics Laboratory
Wright-Patterson Air Force Base, Ohio

AD P000378

F-111A aircraft inlet system and TF-30 engine compatibility is reviewed based on an assessment of time averaged and instantaneous distortion parameters. In addition, recent advances in research on inlet configurations associated with steady-state and dynamic distortions are presented. A complete random data acquisition, editing and processing method is described for accomplishing data analysis as an inlet flow diagnostic tool. Finally, recent afterbody and nozzle research results, which improve the technology base for understanding airframe-nozzle interactions, are reviewed. A basic aircraft configuration incorporating a common forebody, wing, inlet system and a twin engine installation was utilized during high Reynolds number wind tunnel tests to determine the relative merits of a wide spectrum of afterbody-nozzle geometrical variations.

This work was performed at the Air Force Flight Dynamics Laboratory under AFSC direction.

TECHNOLOGICAL ADVANCES IN AIRFRAME-PROPULSION INTEGRATION

D. Zonars, Chief Scientist
Air Force Flight Dynamics Laboratory
Air Force Systems Command
Wright-Patterson Air Force Base, Ohio

Abstract

F-111A aircraft inlet system and TF-30 engine compatibility is reviewed based on an assessment of time averaged and instantaneous distortion parameters. In addition, recent advances in research on inlet configurations associated with steady-state and dynamic distortions are presented. A complete random data acquisition, editing and processing method is described for accomplishing data analysis as an inlet flow diagnostic tool. Finally, recent afterbody and nozzle research results, which improve the technology base for understanding airframe-nozzle interactions, are reviewed. A basic aircraft configuration incorporating a common forebody, wing, inlet system and a twin engine installation was utilized during high Reynolds number wind tunnel tests to determine the relative merits of a wide spectrum of afterbody-nozzle geometrical variations.

I. Introduction

Over the past twenty years, both military and civilian flight vehicle sophistication has drastically increased as a result of the ever proliferating demands for improved performance. This increase in aerospace system sophistication has been possible through new and rapidly emerging technologies including the advent of new design techniques and facility testing methods.

The continuing degree of interest displayed in airframe-propulsion integration is not surprising since this technical domain involves critically important influences which strongly impact vehicle performance. More importantly, this area has been under significant scrutiny due to the difficulties experienced in the operation of tactical type aircraft. The most severe problem has been engine surge or compressor stall due to steady-state and dynamic distortion emanating principally from the inlet. On the other hand, acknowledgment of the excessive drag associated with inlet and nozzle installations has been of a subtle nature with low level attention given to this subject until recently. In both cases, variable geometry systems have been employed to accommodate the wide range of mass flow and pressure ratio characteristics required for matching airframe and propulsion systems.

The transonic flight regime still appears as the most difficult portion of the speed range in which limited analysis methods can be applied to predict airframe-nozzle interactions. By necessity, one must turn to experimental means in order to develop a viable and correct determination of the phenomena involved. The AF Flight Dynamics Laboratory has undertaken a number of programs to investigate the effects of air flows about fuselage and fuselage wing configurations throughout the subsonic, transonic and supersonic speed regimes. A portion of this work is reported herein.

II. F-111 Inlet Flight Experiences

Advanced tactical aircraft are required to perform a number of missions which demand a high degree of airframe propulsion integration including low flow distortion over a much larger range of operating conditions (Mach number, altitude, angle of attack, engine mass flow) than previous supersonic tactical aircraft systems. Requirements for maneuvering flight in a low drag configuration necessarily implies high angle of attack flight attitudes from subsonic to supersonic speeds in excess of Mach number 2.0.

It has been, therefore, quite natural to utilize an inlet design for the F-111A which takes advantage of the flight vehicle fuselage and wing to reduce the effects of angle of attack and angle of yaw during maneuvering flight. The F-111A inlet shown in Figure 1 is an external compression 88 degree segment of an axisymmetric inlet which is integrated with the airframe fuselage-wing root intersection. Locating the inlet in the wing-fuselage flow field also provides precompression for the inlet flow in supersonic flight which means that the inlet capture area is reduced from that required at free stream conditions. Further, a significant vehicle weight savings is realized by integrating the supporting structure of the inlet and relatively short duct with the vehicle structure.

The spike system of the inlet translates fore and aft and the second cone angle varies with flight Mach number and angle of attack to vary the inlet throat area. Each of the inlets is matched to a Pratt and Whitney TF-30-P-3 afterburning turbofan engine. The modulated afterburner improves the tactical ability of the F-111A by providing a variable thrust output in afterburner mode upon demand by the throttle. Therefore, in addition to being closely integrated with the airframe, the F-111A inlet system is closely integrated with the engine to accommodate variations in airflow demand during engine transient operation.

During prototype flight tests of the F-111A, it became apparent that the desired flight envelope was restricted. Maneuverability of the aircraft at high subsonic speeds and supersonic speeds was being limited by a rapid buildup of steady and dynamic inlet flow distortion resulting in engine compressor stall. This incompatibility of the inlet and engine in the F-111A aircraft was the impetus for a comprehensive evaluation of flight test and wind tunnel data to identify the causes of the compressor stalls and define modifications to the inlet system to reduce the incidence of compressor stalls in both steady state and maneuvering flight.

In order to identify problem areas and suggest modifications to improve the inlet system and its compatibility with the engine, the inlet of a prototype airplane was equipped with diagnostic total and static pressure instrumentation in the inlet and engine. In addition, the engine compressor

FIGURE 1. AFT VIEW OF TYPICAL F-111A INLET

face was equipped with 40 total pressure probes in centroids of equal areas to map the total pressure pattern entering the fan and low pressure compressor of the engine. There were eight rakes with five probes per rake.

Initially, a theoretical study was undertaken to determine the anticipated steady state distortion at the compressor face during supersonic flight. The purpose of this study was to compare such information with similar 1/6 scale wind tunnel and actual flight test data and thus provide insight as to trouble areas resulting from specific theoretical-experimental differences. The conditions of Mach number 2.2 and angle of attack of 5.5 degrees with an initial inlet cone angle of 12.5 degrees and second cone angle of 24 degrees was chosen. The theoretical approach first consisted of estimating the Mach number aft of the conical wave system resulting from the fuselage-wing glove intersection. This yielded a Mach number of 2.08 wherein the flow field was assumed to be uniform to the inlet. An exact Taylor-Maccoll solution was developed for the initial cone angle with subsequent use of the method of characteristics to generate the flow field about the second cone. A normal shock was then assumed at the entrance to the cowl lip. The resulting isobars for this 88 degree inlet segment were then uniformly expanded into a circumferential profile at the compressor face. A plane of symmetry was assumed half way between the 88 degree sector of the inlet system. The total pressures resulting from such calculations were plotted and compared with those of the 1/6 scale wind tunnel and flight case. Figure 2 shows such a comparison. The wind tunnel and flight data showed a remarkably similar profile, however the comparison with theory is understandably different due to the absence of viscous effects. More importantly, the main difference stems from a clearly identifiable low energy area on the inboard, lower portion of the compressor face which is quite different than that predicted by the inviscid theory. It was therefore clear that an investigation should be undertaken to survey the oncoming and duct flow relating to this portion of the entire airflow. Values of steady state distortion are also presented as derived from the expression K_{DA} as follows:

$$K_{DA} = \frac{\sum_{i=1}^{5} \left[\frac{P_{t_{av}} - P_{t_{min}}}{P_{t_{av}}} \right]_i \bar{e}_i \bar{C}_i}{\sum_{i=1}^{5} C_i} \times 100 \quad (1)$$

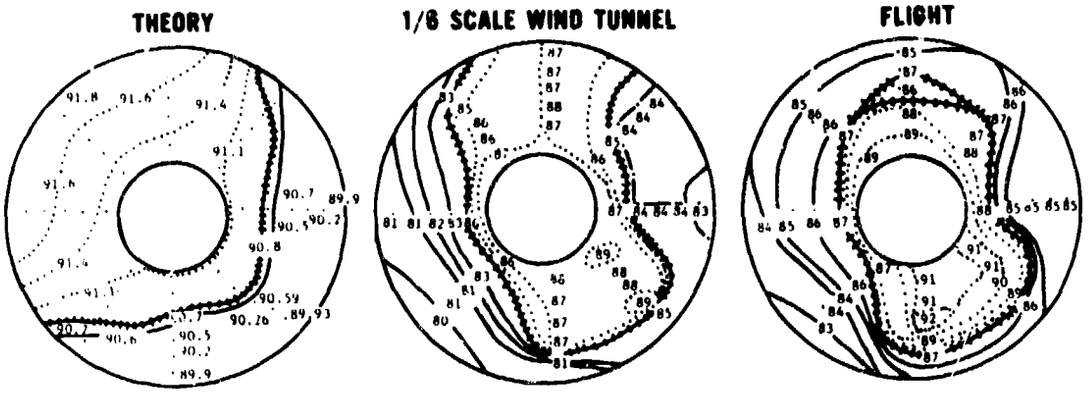

PARAMETER	THEORY	WIND TUNNEL	FLIGHT
AIR FLOW, LBS / SEC.	168	168	162
AVE. RECOVERY PRESSURE RATIO	90.8	85	87
DISTORTION FACTOR, K_{DA}	100	383	428

FIGURE 2. COMPARISON OF F-111A COMPRESSOR FACE TOTAL PRESSURES FOR MACH NUMBER 2.2 and AN ANGLE OF ATTACK OF 5.5 DEGREES

where

C = ratio of compressor inlet radius to ring radius

i = number of ring

θ = largest continuous arc of the ring over which the total pressure is below the ring average pressure

$P_{t_{av}}$ = ring average pressure

$P_{t_{min}}$ = ring minimum total pressure

Here again, the low theoretical K_{DA} value is due to the absence of the low, inboard impact pressures and the inviscid assumptions.

In the analysis of the flight test data taken with this instrumentation, several approaches were employed. First, compressor face total pressure maps were compared, which showed the changes in flow distortion as a compressor stall condition was approached. Although this analysis indicated a low total pressure region on the inboard side, the results were inconclusive and so time variations of data from other sets of instrumentation further upstream in the duct were examined for many stall sequences in order to identify problem areas in the inlet flow field as they developed. From the time sequence plots, selected data for a particular time cut were used to define duct static pressure distributions or boundary layer total pressure profiles. The static pressure distributions were used to locate shock wave positions, indicate boundary layer bleed effectiveness, estimate stream velocities, and indicate regions of separated flow. Total pressure profiles were used to define regions of low energy flow ahead of and in the inlet, and to indicate regions of separated flow. In a parallel study coordinated with this quasi-steady data evaluation, the dynamic pressure fluctuations indicated by traces from the flight telemetry and magnetic tape output of the individual probes were being carefully analyzed. Under certain flight conditions, the traces indicated extreme "turbulence" at the compressor face. This was known to cause a loss in engine stability in other engines as reported by Gabriel, Wallner and Lubick[11] and was felt to be a contributory factor in the stall problems of the F-111A. Although a complete correlation between quasi-steady flow distortion and dynamic pressure fluctuations was not undertaken, it was realized that there was a cause and effect relationship between these two types of distortion and the approach was to address the cause of unsteady and non-uniform flow in the inlet and attempt to eliminate it. A corresponding reduction of the severity of the dynamic-pressure fluctuations (dynamic distortion) would be expected, but it was important to know the relationships between steady and dynamic flow to the limits of the instrumentation signal available.

III. F-111 Inlet Pressure Fluctuation Effects

The effects of transient disturbances, or more specifically, the fluctuating nature of the measured total pressures at the compressor face were considered to have a strong influence in the stall properties of the engine. This influence and corresponding effect were considered to be above the acceptable steady-state distortion which could be accommodated by the engine. The flight regime in which this phenomenon commenced was found to be at low supersonic speeds, with increasing disturbance intensity as a function of increasing Mach number. These disturbances exhibited a wide range

of amplitude-frequency content showing both slow and rapid transients. The slow transients could possibly be compensated for by inlet and engine controls. For such low frequency disturbances, engine performance is basically similar to steady-state operation since normally, the outlet pressures will follow the inlet flow variations in magnitude and phase such that the overall compressor pressure ratio will remain the same. However, the majority of actual transient disturbances and total pressure fluctuations were found to be significantly faster than any of the aforementioned control capabilities. Under these circumstances, specific outlet pressures lag the inlet pressure variations in both amplitude and phase. Consequently, the pressure ratio across the compressor can differ considerably from the steady-state value on the operating line, and conditions can be reached wherein compressor stall margin reduction and even stall will be experienced. Data from reference (1) has shown this to be the case for a simply induced sinusoidal pressure variation input to a compressor.

It is important to note here that the original compressor face total pressure instrumentation on the prototype test aircraft was never intended for the accurate measurement and analysis of transient disturbances. Hence, an effort to correlate transient disturbances with the lower frequency average values of the measured total pressures to the compressor face required special data reduction methods. Total pressure readout from flight magnetic tapes at conditions appropriate to engine stall were first identified and then processed through narrow band pass filters by the Field Measurements Group of the Air Force Flight Dynamics Laboratory. Figure 3 shows two typical frequency spectrums obtained from the filtering process of the flight test data wherein 85.55 inch long pressure carrying lines were provided between the pressure probes and the transducers. At first

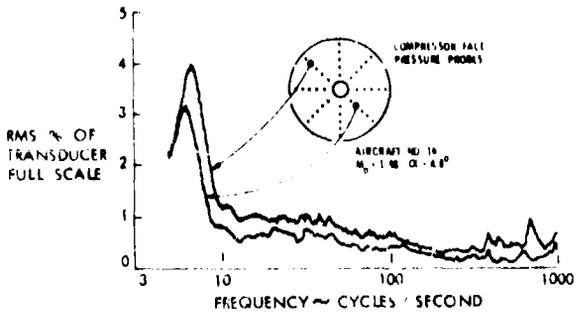

FIGURE 3. TYPICAL F-111A COMPRESSOR FACE PRESSURE AMPLITUDE-FREQUENCY SPECTRUM

glance, the higher amplitude data would appear to occur at the lower frequencies; however, the utilization of 85.55 inch lines (tubulation) for steady state pressure measurements suggested the possibilities of transient signal attenuation to the transducer due to classical acoustic type dissipation. In order to correct for this tubulation effect, an experimental program was undertaken by the Aero-Acoustics Branch of the Air Force Flight Dynamics Laboratory to apply corrections to the measured pressure variations for conditions just prior to engine stall. Theoretical predictions were provided by Air Force Aero Propulsion Laboratory personnel. Figure 4 shows the nature of the amplitude corrections as a function of frequency when examined for an average pressure of 14.7 psi and varying temperature. The experimental data taken at room temperature showed excellent agreement with theory.

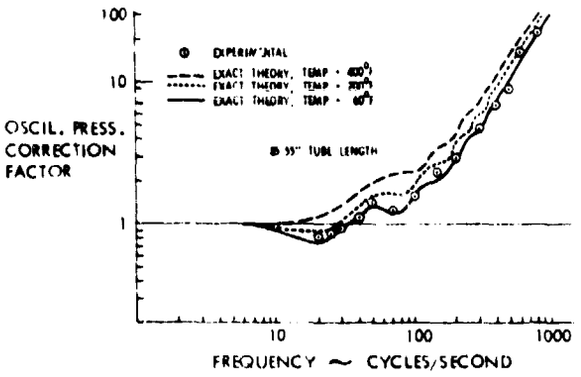

FIGURE 4. F-111A OSCILLATORY PRESSURE TUBULATION CHARACTERISTICS

Many supersonic flight conditions associated with engine stall were examined with specific emphasis on the high frequency aspects of the transient disturbances. Multiplexing of the instrumentation, as is normally accomplished on test aircraft for measuring steady-state parameters, was found to have a strong influence on the high frequency transient data. In an effort to isolate these effects, several flights were performed involving a minimum of multiplexing with a 15 inch line replacing one of the 85.55 inch lines for reduced tubulation effects. A comparison of pressure transients in a 85.55 inch line with multiplexing versus a 15 inch length tubing with minimal multiplexing is shown in Figure 5.

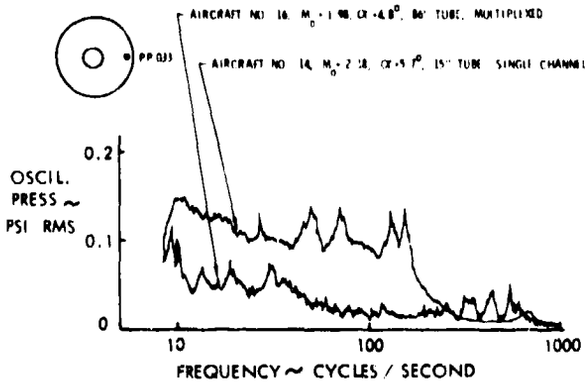

FIGURE 5. COMPARISON OF F-111A TUBULATION

Above approximately 250 cps it can be seen that the high frequency transients recorded with the 85.55 inch line were due to multiplexing, and not present except for some disturbances in the 525-660 cps range. It was, therefore, decided to utilize

0 - 250 cps frequency range for data analysis when transient data was subject to multiplexing, and 0 - 1000 cps for the data with minimal multiplexing.

A specific comparison of steady-state compressor face recovery pressures with corresponding transient disturbance values obtained from flight is shown in Figure 6. The oscillatory or transient pressure data is based on 0 - 250 cps as discussed above. Figure 6 shows, generally, that the high, steady-state recovery pressures corresponded to areas of reduced transient or oscillatory pressures, whereas low recovery pressures related to regions of higher transient values. The region in the lower left-hand corner of the oscillatory pressure map was of particular interest. This area of highest transient disturbance values corresponded directly to the lower left-hand portion of the inlet which was most susceptible to boundary layer ingestion. In addition, the steady state analysis from flight demonstrated the upward spreading of low total pressures from the bottom of the sharp cowl lip with increasing angle of attack. The data of Figure 6 would indicate that, in addition to being of a very low recovery nature, this portion of the flow possessed a high degree of flow unsteadiness sufficient to cause engine stall.

The transient disturbance analysis for all 40 compressor face pressure measurements for a particular stall condition would have required a prohibited expenditure of manhours and it was, therefore, decided to use an available single pitot tube of 15 inch tubulation to examine the fluctuating nature of the duct flow. Figure 7 shows the effect of angle of attack on the dynamic characteristics of this probe at a constant $M_0 = 0.77$. Although many discrete frequencies were identified from the spectrum analyzer output, specific frequencies of 130, 230, and 525 cps appeared to persist with relatively high amplitude for this test condition, which was at a military power engine setting. The amplitudes of these particular frequencies appeared to be fairly constant up to moderate angle of attack with a tendency to converge and further increase in amplitude at higher angles of attack until engine compressor stall was experienced. Also shown on Figure 7 are the effects of first zone afterburner operation for cruise angle of attack. The

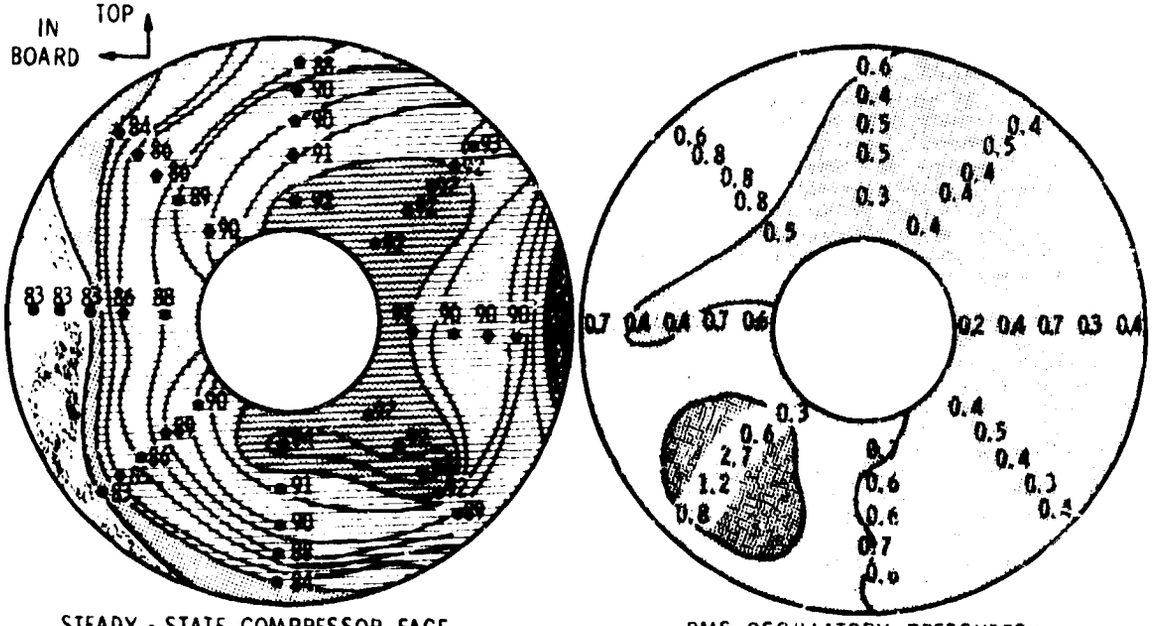

AIRCRAFT 16; $M_0 = 1.98$, $\alpha = 4.8^0$, 0.2 SECONDS BEFORE ENGINE STALL

FIGURE 6. F-111A COMPRESSOR FACE STEADY-STATE AND OSCILLATORY PRESSURES

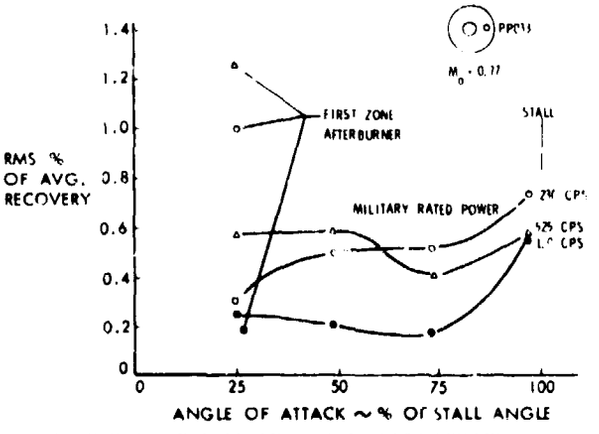

FIGURE 7. F-111A COMPRESSOR FACE PRESSURE FLUCTUATIONS VS. ANGLE OF ATTACK

amplitude associated with 130 cps was found to change a small amount, however, there was a substantial amplitude increase in the 230 and 525 cps frequencies.

The condition of aircraft acceleration for cruise angle of attack at maximum afterburner power was examined with results as presented in Figure 8.

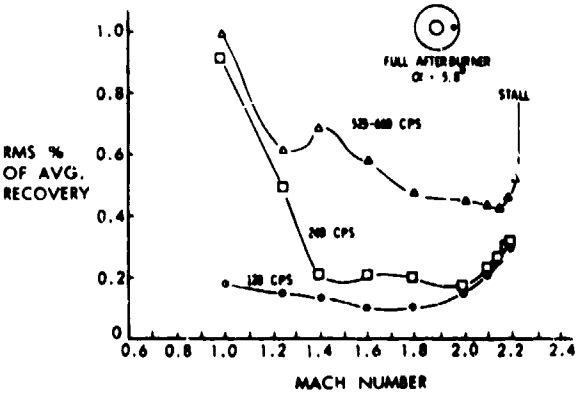

FIGURE 8. F-111A COMPRESSOR FACE PRESSURE FLUCTUATIONS VS. MACH NUMBER

Here again, the influence of afterburner operation is shown in the amplitudes of the 240 and 525 cps frequencies for transonic flight conditions. However, amplitudes at these frequencies decreased with increasing Mach number and corresponding decreases in corrected air flow up to approximately Mach number 2. Beyond Mach number 2, there was a dramatic increase in all three amplitudes up to Mach number 2.2 where engine stall was experienced.

From the quasi-steady and transient disturbance data studied during 1967, it was clear that the engine compressor stall characteristics were strongly influenced by inlet pressure pulsations at high frequencies and this effect must be considered in conjunction with the "steady state" distortion.

IV. Detailed Studies of F-111A Inlet and Engine Air Flow Fluctuation Effects

Subsequent to the initial study of the F-111A inlet engine incompatibility effort discussed in Section III, a limited number of investigations[2-6] have been carried out in order to shed light on this important problem area. A typical example of one of the more significant and recent programs was reported by Plourde and Brimelow[7]. Recently, Burcham and Hughes[8] have modified and utilized the Pratt and Whitney K_{DA} distortion factor for predicting surge. The engine compressor face was sub-divided into 5 equal areas through concentric circles or rings. Probes were placed on rings which were maintained at a constant radii from the compressor centerline. The modified K_{DA} distortion parameter was defined as follows:

$$K_{DM} = \frac{\frac{1}{2}\sum_{i=1}^{5}\left[\frac{P_{t_{max}} - P_{t_{min}}}{P_{t_{av}}}\right]\bar{\theta}_i C_i}{\sum_{i=1}^{5} C_i} \times 100 \qquad (2)$$

where

C = ratio of compressor inlet radius to ring radius

i = number of ring

$\bar{\theta}$ = largest continuous arc of the ring over which the total pressure is below the ring average pressure

$P_{t_{max}}$ = ring maximum total pressure

$P_{t_{av}}$ = ring average pressure

$P_{t_{min}}$ = ring minimum total pressure

In this specific effort a flight test F-111A aircraft was utilized to determine the dynamic nature of inlet pressure fluctuations related to engine operational stability. Derived steady state flow distortion patterns as developed from low response pressure instrumentation were compared with both the K_{DA} and K_{DM} distortion parameters calculated from high response instrumentation. A typical comparison is shown in Figure 9 for the flight case of Mach number 1.6 at an altitude of 45,000 feet with off-design inlet spike position. Here it is clearly seen that the low response data technique functioning at a sampling rate of 50 cuts per second did not yield information indicative of the compressor stall. On the other hand, utilizing the higher response data technique and calculating either the K_{DA} or K_{DM} distortion parameter at 400

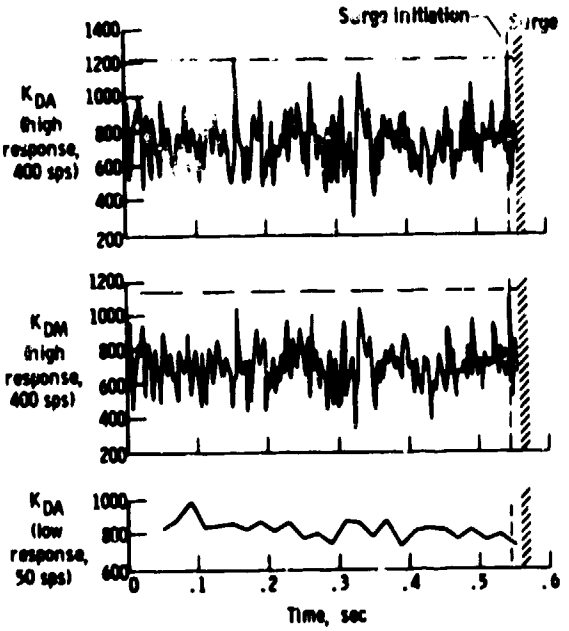

FIGURE 9. COMPARISON OF HIGH AND LOW RESPONSE K_{DA} WITH HIGH RESPONSE K_{DM}. F-111A FLIGHT CONDITIONS; MACH NUMBER = 1.6, ALTITUDE = 45,000 FEET AND OFF-DESIGN SPIKE POSITION

samples per second did yield a substantial peak approximately 15 milliseconds prior to surge. Figure 10 shows a time history of the probe data and distortion factor for Mach number 2.17 and an altitude of 44,000 feet. Probes A and B show increases in pressure as the stall condition is approached whereas probes A^1 and B^1 are decreasing and hence result in a maximum distortion value. It is interesting to note that the instantaneous pressure recovery map shows a larger high pressure area along with a more intense low pressure area.

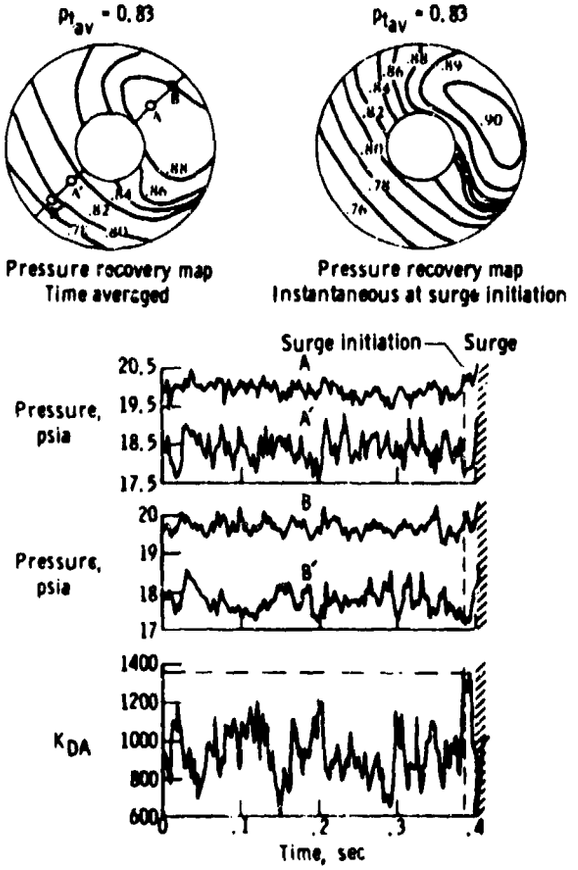

FIGURE 10. COMPARISON OF AVERAGE RECOVERY AND INSTANTANEOUS RECOVERY MAPS WITH K_{DA}. F-111A FLIGHT CONDITIONS: MACH NUMBER = 2.17, ALTITUDE = 44,000 FEET

Figure 11 shows the surge characteristics for transonic flight at Mach number 0.9 and 30,000 feet altitude. This particular stall occurred as a result of the off-design conditions of the inlet cone and is generally recognized as a "drift" type of surge. This is demonstrated by the fact that peak values of the distortion factor occurred several times during the time period examined.

The modified distortion parameter as developed by Burcham and Hughes[8] was found to be approximately 80 percent effective in identifying surge when dynamic conditions prevailed within approximately 90 percent of the maximum steady state distortion value. Needless to say, additional information[9,10] and more exacting methods must be developed to predict engine instability due to dynamic inlet conditions.

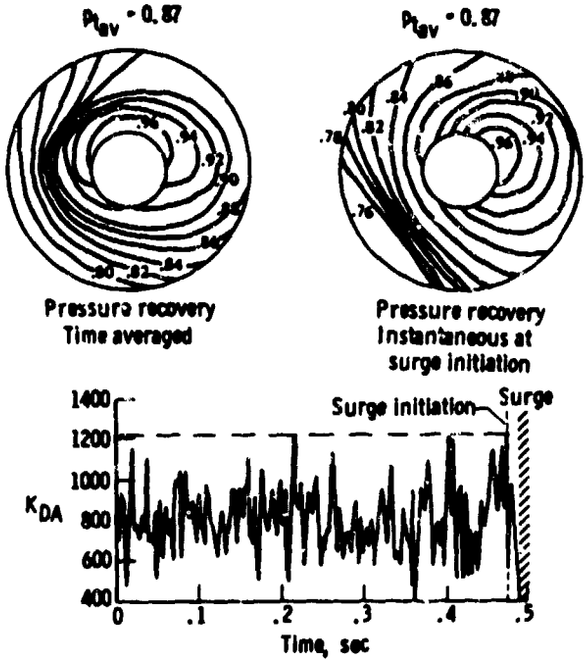

FIGURE 11. COMPARISON OF AVERAGE RECOVERY AND INSTANTANEOUS RECOVERY MAPS WITH K_{DA}. F-111A FLIGHT CONDITIONS; MACH NUMBER = 0.9, ALTITUDE = 30,000 FEET AND OFF-DESIGN SPIKE POSITION

V. Advanced Inlet Configuration Studies

More recently the Air Force Flight Dynamics Laboratory has undertaken a number of programs to investigate flows about fuselage and wing-fuselage combinations throughout the subsonic, transonic and supersonic speed regimes. The objectives of these programs are to develop a clear understanding of inlet-airframe interactions and, more importantly, to attain an experimental data bank and corresponding analytical approach for assessing the dynamic phenomena associated with engines and inlets. The Laboratory has initiated project Tailor-Mate in order to examine the effects of configuration variations on flow field dynamics and related effects to the engine system. Figures 12 and 13 show a typical 1/3 scale wind tunnel model along with various aircraft configurations studied. Configurations A-1 and A-2 are examples of side mounted type inlets whereas A-3 is an example of a fuselage shielded inlet, and wing shielded inlets are shown by configurations B-3 and B-4. One quarter scale fuselage models were constructed for wind tunnel testing purposes with appropriate fuselage static pressure distributions, boundary layer measurements and more importantly, the dynamic nature of the flow fields at the proposed inlet stations. In addition to the flow field measurements made in the area of the entrance to the inlet, two side mounted and two shielded external compression inlets were tailored for the flow fields defined by the forebody as shown in Figure 14. The detailed instrumentation for such a duct system is shown in Figure 15. Instrumentation was utilized to document the inlet performance and included static pressure rakes near the cowl lip, in the diffuser and at the

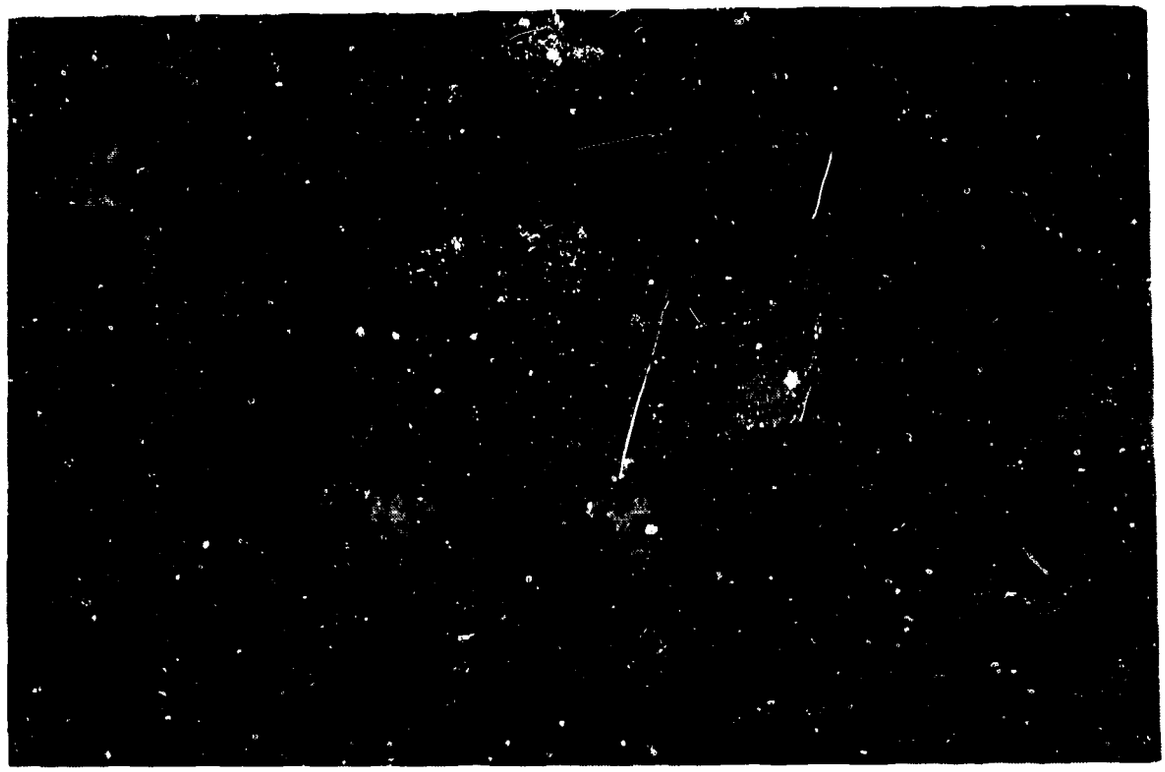

FIGURE 12. TYPICAL 1/3 SCALE TAILOR-MATE WIND TUNNEL MODEL

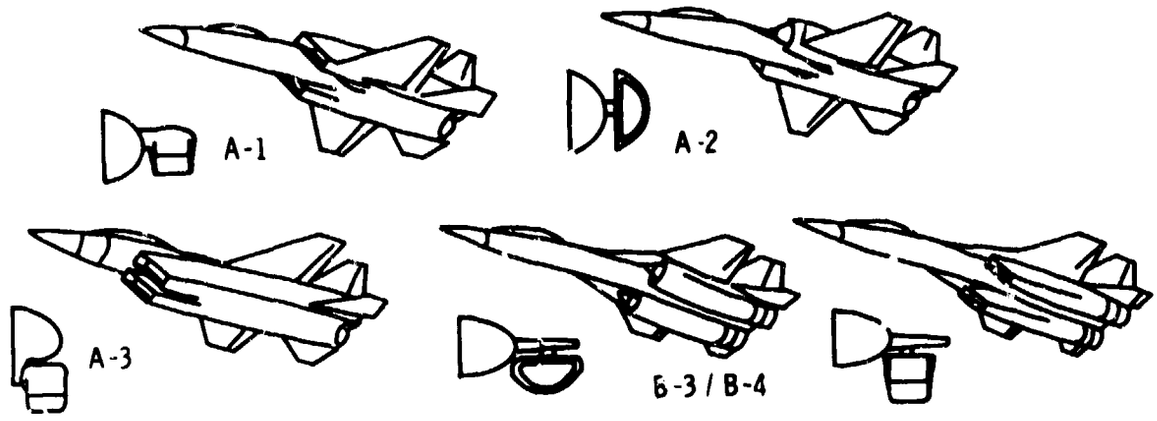

FIGURE 13. REPRESENTATIVE CONFIGURATIONS FOR FOREBODY FLOW FIELD TESTS

simulated compressor face. It is important to note that the compressor face instrumentation contained high response type transducers to identify the fluctuation nature of the inlet flow. Figure 16 shows the results of wind tunnel tests for the four configurations mentioned. These tests were performed at Mach number 2.2 with varying angle of attack. Figure 16 shows both wing shielded inlet systems experienced lower distortion as indicated by the simple distortion index along with low "turbulence" as a function of angle of attack. As might be expected the side mounted type of inlets experienced higher distortion with correspondingly higher indices of "turbulence."

The importance of the flow field generated by the forebody of the fuselage has been pointed out by Surber and Stava[11] and Zonars[12]. An example of such sensitivity is shown in Figure 17 wherein the side mounted 2-dimensional inlet on body A-1 was examined in conjunction with body A-2. This figure shows the vastly different characteristic of distortion vs "turbulence." Surprisingly enough, the small change in contour of the A-2

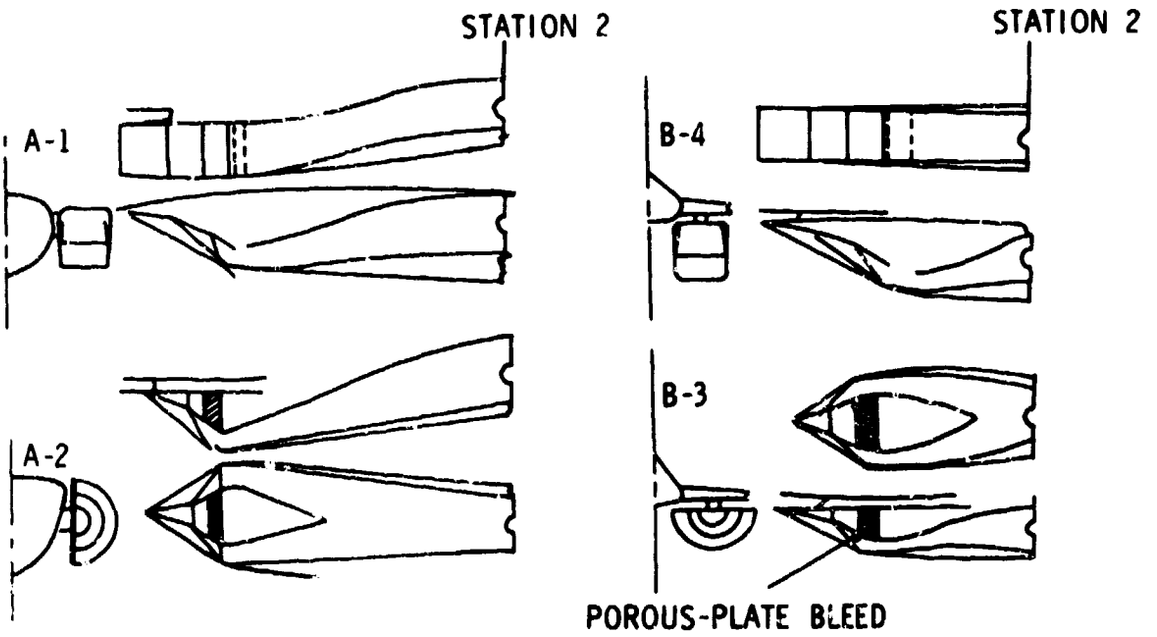

FIGURE 14. NOMENCLATURE AND COMPARISON OF FOUR (4) INLET DESIGNS

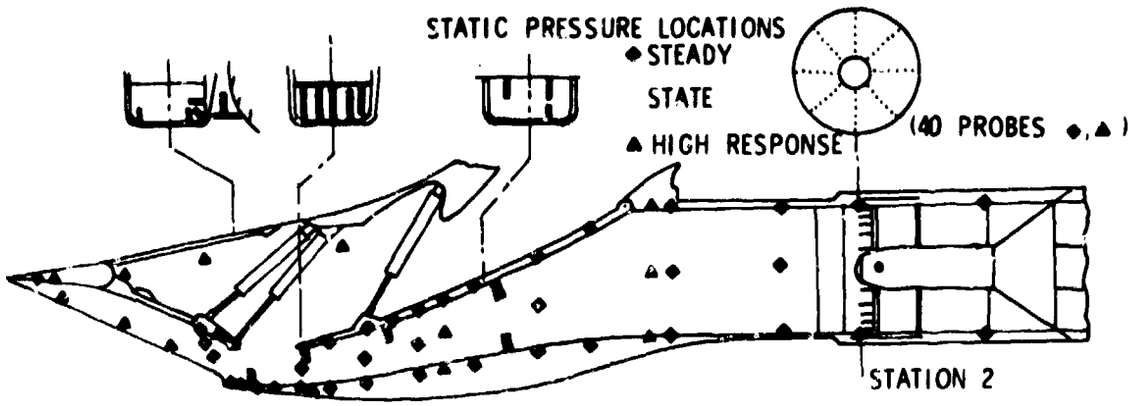

FIGURE 15. TYPICAL INLET INSTRUMENTATION

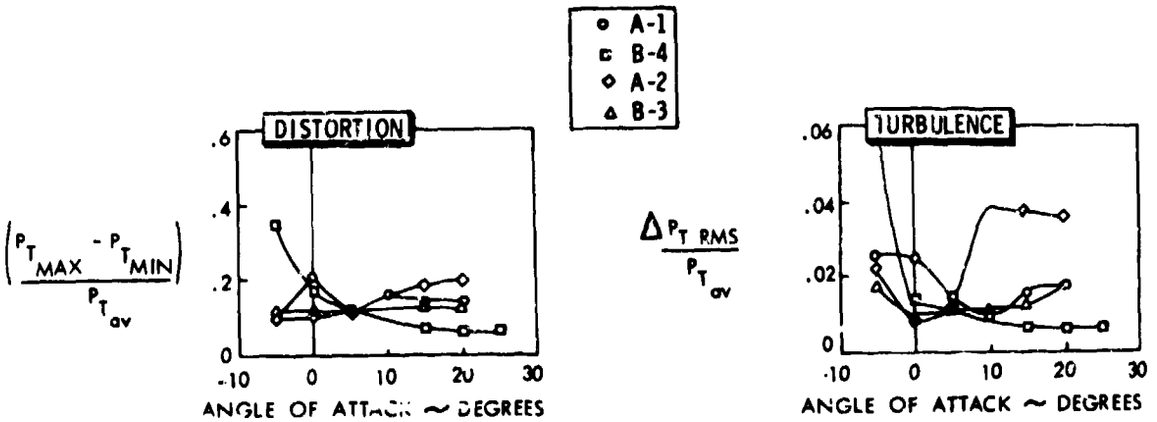

FIGURE 16. COMPARISON OF STEADY-STATE AND DYNAMIC DISTORTION FOR VARIOUS CONFIGURATIONS AT MACH NUMBER 2.5

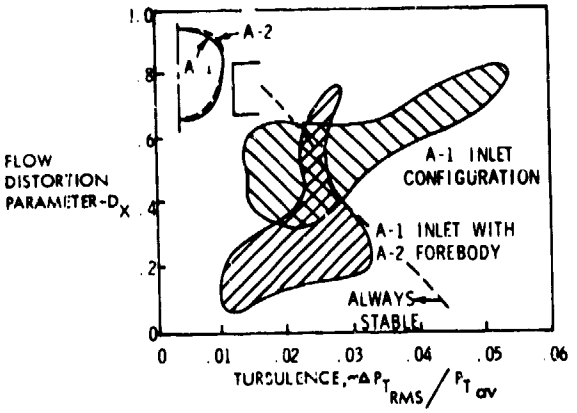

FIGURE 17. INFLUENCE OF FOREBODY CONTOUR ON ENGINE STABILITY AT MACH NUMBER 2.2

fuselage was found to have a substantially better characteristic than A-1. This is undoubtedly due to a lower local outwash and hence a reduced tendency toward flow separation on the inboard side of the inlet. In the event the designer is confined to the A-1 inlet configuration and cannot readjust the body contour as shown by the A-2 characteristics, he must then look for other means by which he can suppress both the steady state and "turbulent" distortion. A longer inlet duct has a surprisingly favorable characteristic as denoted in Figure 18. There is a considerable reduction in both distortion parameters which puts the operational mode of the inlet well within the stable bounds of engine operation.

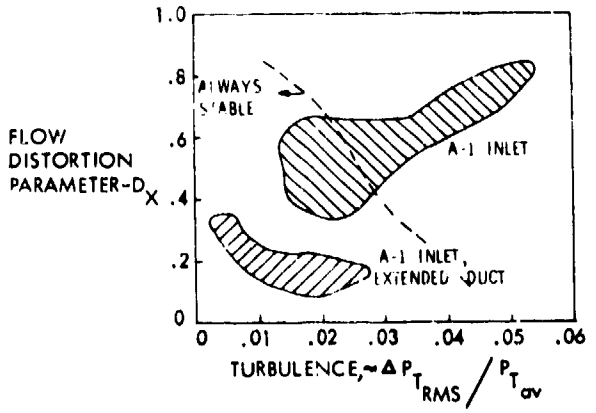

FIGURE 18. EFFECT OF LONGER DUCT ON SUPPRESSING STEADY STATE AND "TURBULENT" DISTORTION

VI. Dynamic Data Handling Technique

Among the problems that exist in handling dynamic data are the tremendous quantities of analog data tapes generated during inlet study and development programs and that past efforts to analyze dynamic data has depended heavily upon what has been seen relative to the behavior of the steady state or average component of compressor face total pressure. As a consequence, only about one percent of the data is actually examined since considerable digitization is required to review one case. More specifically, the area of interest centers on the analysis of the dynamic or fluctuating component of total pressure measured at the compressor face plane of a trisonic type inlet. The pressures are measured by means of fast response instrumentation located in rakes radiating from the hub. This data is recorded on analog tape and represents the beginning of our problem.

The solution to this problem has been to develop an analog editing system for screening and editing inlet dynamic data based on the use of engine distortion parameters. As a result, large quantities of tape can be screened and those parts of the data identified which would have adverse effects on airframe-propulsion compatibility.

A typical Air Force Flight Dynamics Laboratory inlet program consists of 5000 data points wherein one Mach number, angle of attack and yaw, and capture area ratio comprises a single data point. At least 200 feet of tape are used for each data point and as a result, it can be seen that about 100 reels of tape are required for a program of this magnitude. For a more extensive inlet development program, such as associated with advanced flight vehicles, as many as 500 tapes are required. In any event, the data of interest is contained on only about one percent of the tape which is not necessarily the same one percent of tape mentioned previously. The principle question that arises is how does one expeditiously and economically locate the data of interest?

In the development of the analog editing system, certain goals were established. First, it was desirable to utilize parameters involving all the compressor face steady-state and dynamic data which had a direct relationship to engine stability. Second, a scheme was desired that would identify high levels of dynamic flow activity on the tapes and where this event occurred. Third, a fast response capability was a requirement in order to account for model scale. For example, if a particular engine is sensitive to pressure fluctuations up to 200 cycles/second, and the inlet wind tunnel model is one-tenth scale, then valid data out to 2000 cycles/second is required from the model. Model scaling characteristics have been hypothesized by Sherman and Motycka[13]. Fourth, a desirous capability was to use more than one parameter in the screening process to determine which was most meaningful and acceptable and hence avoid tape re-runs. Fifth, the system should be flexible to permit digitization of data and possess a data playback capability at the recorded speed.

Among the parameters selected for data screening was the Pratt & Whitney engine distortion parameters K_θ, K_{RAD} and K_A which have been formulated on the basis of experimental data. The expressions shown below, which in part relates to reference(12), describe the level of distortion associated with a particular compressor face pattern.

$$K_A = K_\theta + bK_{RAD} \tag{3}$$

$$K_{RAD} \left[\frac{1}{Q_{av} \sum_{i=1}^{I} D_i^{-x}} \right] \sum_{i=1}^{I} \left[D_i^{-x} \left(P_{t_{av}} - P_{t_{av,i}} \right) \right] \tag{4}$$

where

b = constant depending on engine design and entrance Mach number

x = weighting factor depending on distortion sensitivity

K_θ describes the influences associated with a circumferential distortion pattern while K_{RAD} describes the pattern variation associated with radial distortion. When a combined pattern exists, which is typically the case, K_θ and K_{RAD} are added together in a weighted manner to form K_A. In addition to the Pratt and Whitney parameters, a set of General Electric engine distortion parameters have been programmed. These expressions are used to identify high levels of dynamic activity in the air flow process. These data are subsequently subjected to further analysis which in turn aids in determining the necessary modifications required to alleviate the compatibility problem.

The dynamic data screening device or system was developed jointly between the Air Force Flight Dynamics Laboratory and the Aeronautical Systems Division Computer Center using a hybrid computer. This program was initiated in January 1970 by Sedlock and Marous [14] with the acquisition of a 72 channel multiplex discriminator system, a 14 track direct playback tape transport, tape search unit peak detectors, and a 48 channel data filtering system. The complete system shown in Figure 19 became operational in July 1971. The system described above is similar to that developed by Crites and Heckart[15], Crites[16], Lynch and Slade[17] except for the added flexibility due to a hybrid computer capability.

The current status of the Air Force Flight Dynamics Laboratory system is that both General Electric and Pratt and Whitney engine distortion parameters have been programmed on the computer and up to five parameters can be tracked simultaneously with an order of priority established for each parameter. The primary requirement of the system is to identify dynamic peaks and the time of occurrence. The resolution of the tape search unit permits identification of the peak value within one millisecond. Center frequencies used in the discriminators have been selected for greatest compatibility with those being used by USAF and contractor facilities. The dynamic data can be filtered from 125 to 9000 cycles/second in six discrete increments in order to account for model scale and filtering of any unwanted high frequency information such as probe resonance. Both the engine distortion parameters and pressure data can be digitized at various sampling rates.

Our past and current efforts have included review of the compatibility points in the B-1 Interface Control Document and the Arnold Engineering Development Center 1/10 scale inlet test data. In addition to continued support of the B-1 program, data from the RA-5C wind tunnel-flight test correlation and Tailor-Mate programs will be reviewed.

McDonnell-Douglas personnel[16] have developed a screening system for use during the F-15 inlet development program. In examining this capability to review dynamic data based on conventional means, it was estimated that six manyears and one million dollars were required to review one percent of a 250 data point program which represented some four million pressure distributions. The development of an analog editing system reduced this task to six weeks with less than 1000 feet of tape to be examined. Our own experience has shown that one reel of tape containing 30 data points can be examined in approximately one hour. To accomplish the same task with a digital computer would require 15 hours to digitize the data and approximately 20 hours of computer time to process the information. This estimate is based on 200 samples per data point. The development described above represents a major step in handling the extremely large amount of data associated with an inlet development program.

A description of how the engine distortion are implemented on the analog/digital computer to accomplish the goal of editing and screening the

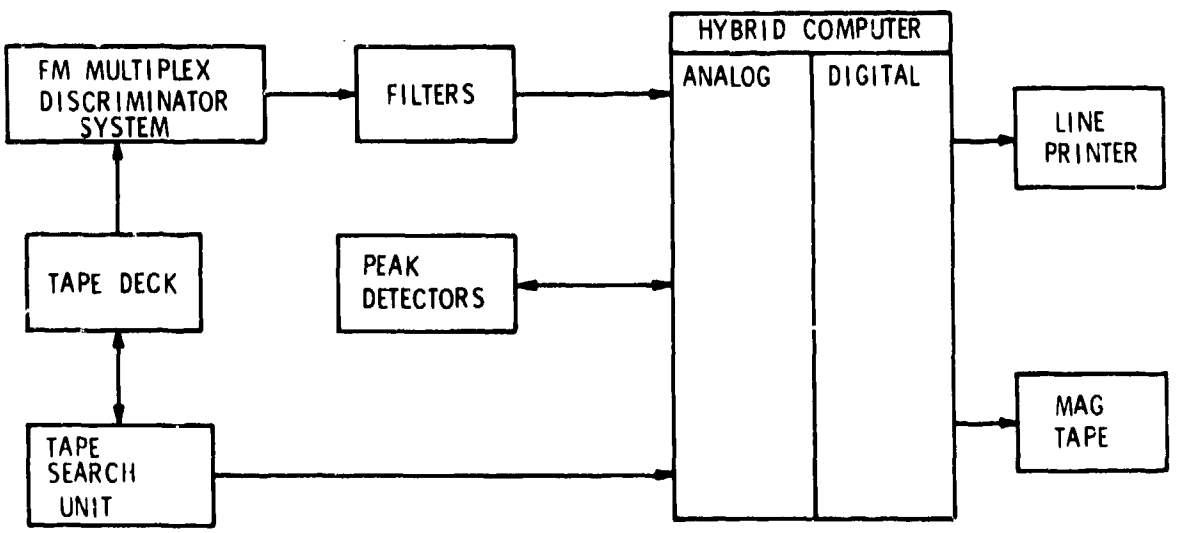

FIGURE 19. DYNAMIC DATA SCREENING AND EDITING SYSTEM

data will now be addressed. This can be accomplished by relating the expression for K_θ to a particular configuration of total pressure probes at the compressor face. In this particular case, consider a configuration that consists of 48 probes with six rings and eight rakes. The implementation of Equation (3) on the analog computer is quite simple. The steady state and gain adjusted fluctuating pressure are summed together to form the total component of pressure. Each pressure is multiplied by its respective sine0 and cosine0, summed around each ring, and then squared. These two terms are added together and then the square root is taken of this summation. Finally, this value is multiplied by the value of the leading term to attain K_θ for one ring. This process is repeated for each ring and then the individual ring K_θ are summed together to form the total K_θ. While the value of this expression is being calculated, a similar process is occurring simultaneously for the other parameters.

The editing process is accomplished by considering the time history of the parameter K_θ, K_θ can be generated as a continuous function since an analog computer is a continuous type of machine. The operator has the ability to set a threshold level for each of the parameters such that only information occurring about that level will be examined. The engineer must know when a peak in K_θ has been experienced and the time of this occurrence. In addition, he is interested in the value of K_θ when it exceeds a given threshold level and when it returns to a lower value. Special peak detector networks are utilized to accomplish these objectives. These peak detectors track an increasing signal to the peak level and maintain that level until it is reset. The peak detectors are normally reset when the value of the parameter drops below the threshold level in order that successive peaks can be detected even through such peaks may be of a lower value than a preceding peak. In addition, the peak detectors can be used as a signal generator that signifies a peak has been detected. Judgement must be made as to identifying both threshold crossings and peaks or peak values alone. When a threshold crossing occurs, an interrupt signal is generated, and the information is transferred from the analog to the digital computer. No on-line manipulation of this information is permitted in order to transfer the data as quickly as possible. The current response time from signal interrupt thru information transfer is 300 microseconds. An important feature of the program is the identification of which parameters triggered the interrupt signal. Whenever the interrupt signal occurs, the peak value of the parameter is stored as well as the value of the other parameters at this particular instant. The next output from the editor is the time when the peak was detected. The time resoltuion is to within one millisecond.

Many electronic components make up the editing system. A 14 track tape transport is used to playback the dynamic data through the discriminator system which de-multiplexes the individual signals. Each pressure signal is filtered before it is sent to the analog computer. Coupled with the tape deck and hybrid computer is the tape search unit. The search unit allows one to find a particular time-pressure history on the tape while it also serves as the time reference frame for the hybrid computer. The peak detectors, mentioned earlier, are coupled to the analog computer. The information stored in the digital computer can be printed out on the line printer or stored on magnetic tape.

VII. Advanced Nozzle Configuration Studies

The Air Force Flight Dynamics Laboratory has undertaken a number of programs[18] to investigate the effects of airframe-nozzle interactions throughout the subsonic, transonic and supersonic speed regimes. The objective of these programs is to develop a clear understanding of nozzle-airframe interactions and hence improve the technology base. A basic aircraft configuration incorporating a common forebody, wing, inlet system, and a twin engine installation shown in Figure 20, was utilized during high Reynolds number ($0.5 - 6 \times 10^6$ per foot) wind tunnel tests to determine the relative merits of a

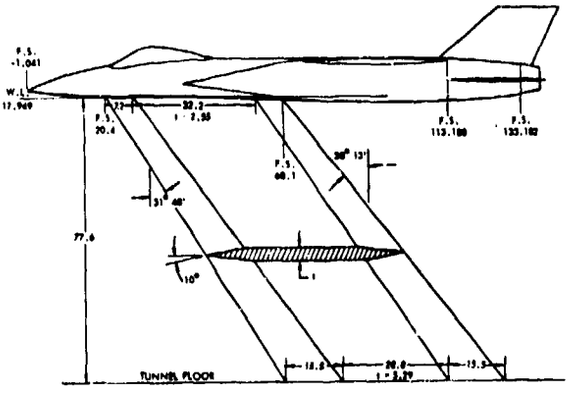

FIGURE 20. BASIC TWIN-ENGINE WIND TUNNEL MODEL; ALL DIMENSIONS IN INCHES

wide spectrum of aft-body nozzle geometrical variations. This figure shows a schematic of the model and the support system required to conduct tests in the 16 foot AEDC Propulsion Transonic and Supersonic Wind Tunnels. Cross-sectional area distributions, including the influence of the support strut system and the effect of nozzle spacing, is shown in Figure 21.

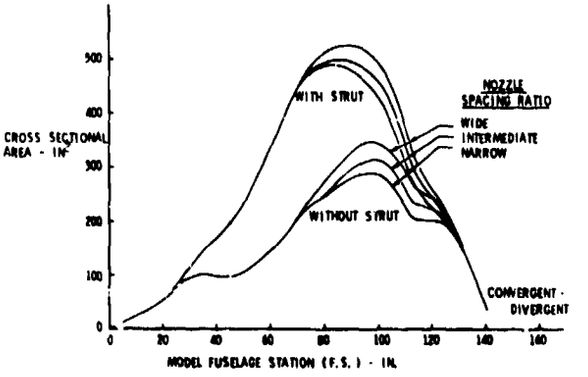

FIGURE 21. WIND TUNNEL MODEL AND SUPPORT SYSTEM CROSS-SECTIONAL AREA CHARACTERISTICS

The same type of area distributions, involving the

effect of wing, tail and the limits of nozzle setting, are shown in Figure 22. The various nozzles,

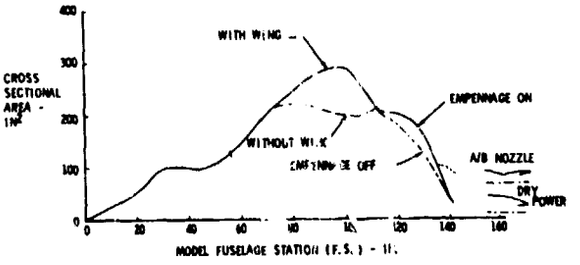

FIGURE 22. WIND TUNNEL MODEL CROSS-SECTIONAL AREA CHARACTERISTICS

which were connected or disconnected at fuselage station 133.182 inches for non-afterburning conditions are shown in Figure 23. Maximum afterburning

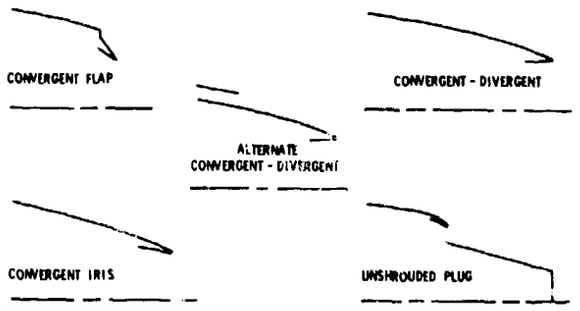

FIGURE 23. SYSTEM OF NON-AFTERBURNING NOZZLES CONFIGURATIONS TESTED

nozzle contours are shown in Figure 24 and were similarly attached to the same fuselage location. The large scale wind tunnel model shown in Figure

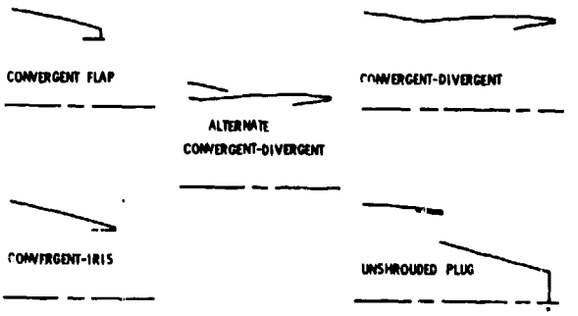

FIGURE 24. AFTERBURNING NOZZLE CONFIGURATIONS TESTED

25 was configured in such a manner as to employ a system of balances which measured both the aft-body boattail drag and the nozzle boattail drag. In addition, a thrust balance was incorporated to measure the internal thrust and nozzle boattail drag. It is important to note that both the horizontal and vertical tail were not included in the drag measurements aforementioned.

The nozzle boattail drag characteristics for the non-afterburning condition is shown in Figure 26 for Mach number 0.9. The drag coefficients displayed in this figure are referenced to the cross-sectional area located at fuselage station 133.182 inches. The convergent-divergent and convergent iris nozzles, which are basically slender in nature,

FIGURE 25. PHOTOGRAPH OF MODEL INSTALLED IN THE 16 FOOT AEDC TRANSONIC PROPULSION WIND TUNNEL

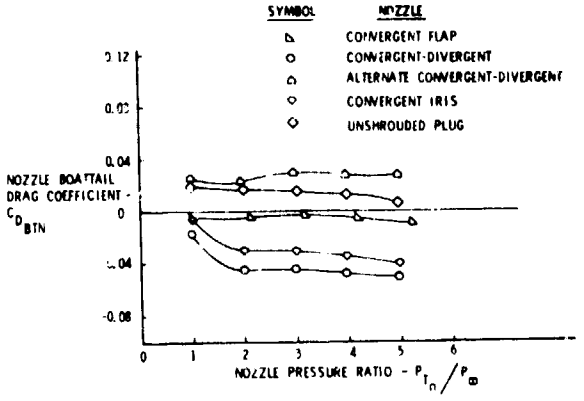

FIGURE 26. NON-AFTERBURNING NOZZLE BOATTAIL DRAG CHARACTERISTICS; MACH NUMBER = 0.9

displayed the lowest drag characteristics. In fact, these two nozzles, along with the convergent flap nozzle, experienced pressurization of the external aft-facing surfaces and, hence, were subjected to a thrust rather than a drag force. The alternate convergent-divergent nozzle experienced the highest drag due to flow separation caused by the rearward facing step between the nozzle and fuselage fairing. The unshrouded plug nozzle also experienced separated flow, which basically prevented pressurization of the external surfaces with correspondingly lower relative drag.

The nozzle boattail drag based on maximum afterburner nozzle position for Mach number 0.9 is shown in Figure 27. The convergent-flap and convergent-iris nozzles show good pressure recovery

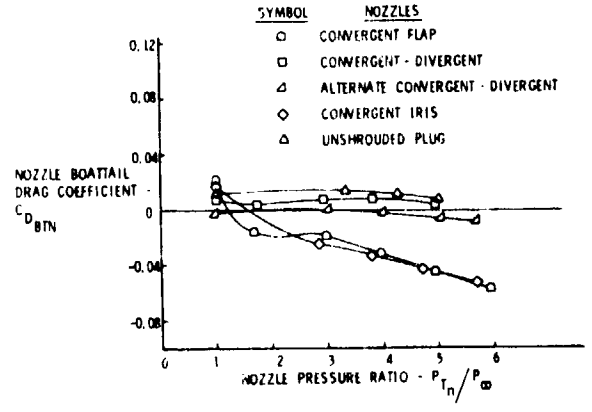

FIGURE 27. AFTERBURNING NOZZLE BOATTAIL DRAG CHARACTERISTICS; MACH NUMBER = 0.9

characteristics, particularly with increased nozzle pressure ratio. The remaining three nozzles yielded higher drag characteristics. The same nozzle boattail drag characteristics associated with the maximum afterburner position for Mach number 1.2 is shown in Figure 28. Here it can clearly be seen that the convergent-flap and convergent-iris nozzles involve a substantial drag penalty due to the large projected frontal area; however, the drag coefficient of these two nozzles diminishes with increased pressure ratio as might be expected with a Mach number

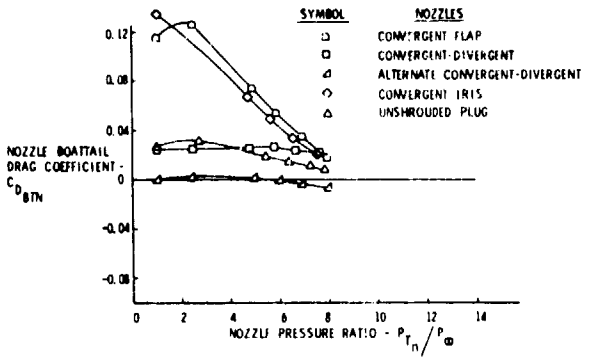

FIGURE 28. AFTER-BURNING NOZZLE BOATTAIL DRAG CHARACTERISTICS; MACH NUMBER = 1.2

1.2 flight requirement. The convergent-divergent and unshrouded-plug nozzles have lower drag characteristics than the two aforementioned nozzles primarily due to the reduced aft-facing surface areas. The alternate convergent-divergent nozzle displayed the best characteristics with very little influence of nozzle exhaust pluming effects.

The aft-body boattail drag coefficient, based upon the cross-sectional area at fuselage station 113.188 associated with the non-afterburning nozzle and afterburning nozzle positions for Mach number 0.9, is shown in Figures 29 and 30. The

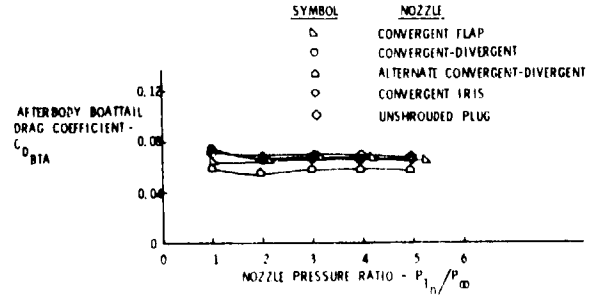

FIGURE 29. AFT-BODY BOATTAIL DRAG CHARACTERISTICS; NON-AFTERBURNING NOZZLES, MACH NUMBER = 0.9

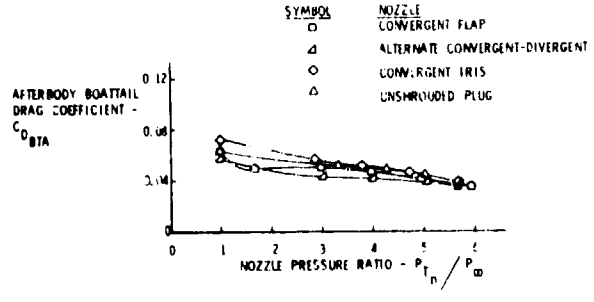

FIGURE 30. AFT-BODY BOATTAIL DRAG CHARACTERISTICS; AFTERBURNING NOZZLES, MACH NUMBER = 0.9

some aerodynamic coefficient for Mach number 1.6 with maximum afterburner nozzle conditions is shown in Figure 31. In all three cases, the afterbody

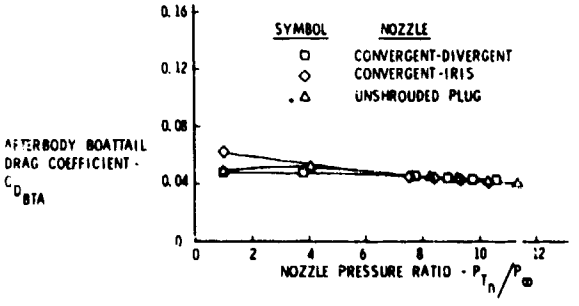

FIGURE 31. AFT-BODY BOATTAIL DRAG CHARACTERISTICS; AFTERBURNING NOZZLES, MACH NUMBER = 1.6

boattail drag was of a positive nature with small differences caused by downstream changes in the nozzle boattail geometry.

The total drag coefficient, i.e., the summation of aft-body boattail drag and nozzle boattail drag, is shown in Figure 32. Here we see that the

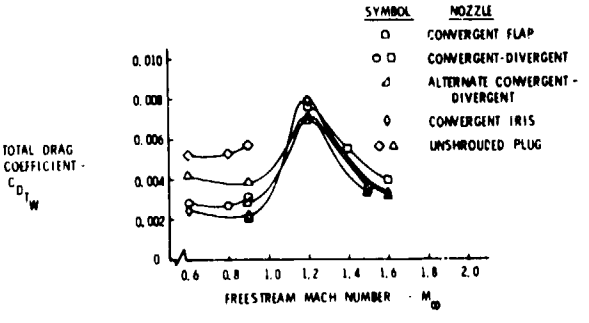

FIGURE 32. TOTAL AFT-END DRAG CHARACTERISTICS

total aft-end drag variations based upon aircraft wing area is principally due to aft-body boattail drag characteristics previously described. Also, one can observe that the total aft-end drag is of a positive nature mainly due to the aft-body boattail section. Variations of this drag are associated with the nozzle boattail drag characteristics.

Reynolds number effects on the total aft-body drag are shown in Figure 33. These results, which show increasing aft-body drag as a function of increasing unit Reynolds number, was unexpected since skin friction effects and separated flow conditions normally improve such circumstances with lower resulting drag. Although not presented in this paper, the Reynolds number effects on the nozzle boattail drag were of an opposite nature.

The nozzle test characteristics and results presented above represent a complex interaction between external and internal flows. The issue is further clouded by viscous considerations. The accurate simulation of all important parameters is very difficult, even to the point where some parameters are not fully defined or identified. A research and development effort is required to define the proper parameters and their associated importance.

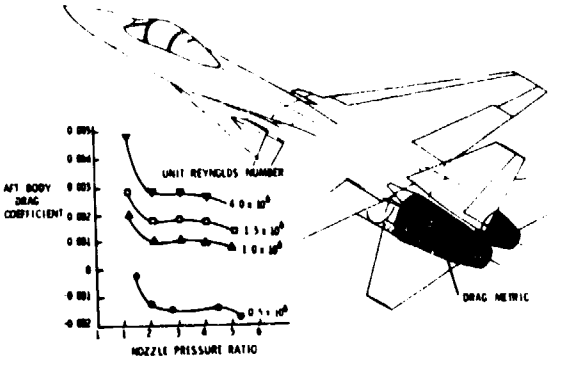

FIGURE 33. AFT-BODY DRAG CHARACTERISTICS AS A FUNCTION OF REYNOLDS NUMBER; MACH NUMBER = 0.9

REFERENCES

1. Gabriel, D.S., Wallner, L.E., and Lubick, R.J., "Some Effects of Transients in Inlet Pressures and Temperatures on a Turbojet Engine," Institute of the Aeronautical Sciences Twenty-Fifth Annual Meeting, (January 1957).

2. Martin, A.W. and Kostin, L.C., "Propulsion System Dynamic Test Results," North American Aviation, Inc., Report No. NA-67-386, (April 1967).

3. Winslow, L.J., et. al., "Inlet Distortion Investigation, Upstream Engine Influence and Screen Simulation," The Boeing Company, Technical Report AFAPL-TR-68-140, (January 1969).

4. Wasserbauer, J.F. and Willoh, R.G., "Experimental and Analytical Investigation of the Dynamic Response of a Supersonic Mixed Compression Inlet," AIAA Preprint 68-651 (1968).

5. Martin, A. and Kostin, L., "Dynamic Distortion at the Exit of a Subsonic Diffuser of a Mixed Compression Inlet," North American Rockwell, Report TFD-69-588 (1969).

6. Oates, G.C., Sherman, D.A., Motycka, D.L., "Experimental Study of Inlet-Generated Pressure Fluctuations," PWA Report 3682 (1969).

7. Plou de, G.A. and Brimelow, B., "Pressure Fluctuations Cause Compressor Instability," Air Force Airframe/Propulsion Compatibility Symposium, (June 1969).

8. Burcham, F.W., Jr. and Hughes, D.L., "Analysis of In-Flight Pressure Fluctuations Leading to Engine Compressor Surge in an F-111A Airplane for Mach Number to 2.17," AIAA Preprint 70-264 (1970).

9. Calogeras, J.E., Burstadt, P.L. and Coltrin, R. E., "Instantaneous and Dynamic Analysis of Supersonic Inlet-Engine Compatibility," AIAA Preprint 71-667 (1971).

10. Jansen, W., "Compressor Sensitivity to Transient and Distorted Transient Flows," AIAA Preprint 71-670 (1971).

11. Surber, L.E. and Stava, D.J., "Supersonic Inlet Performance and Distortion During Maneuvering Flight," AGARD Propulsion and Energetics Panel Specialists' Meeting on "Inlets and Nozzles for Aerospace Engines," AGARD Conference Proceedings CP-91-71, (1971).

12. Zonars, D., "Problems on Inlets and Nozzles," 7th Congress of the International Council of the Aeronautical Sciences, (August 1970).

13. Sherman, D.A., and Motycka, D.L., "Experimental Evaluation of a Hypothesis for Scaling Inlet Turbulence Data," AIAA Preprint 71-669 (1971).

14. Sedlock, D. and Marous, J., private communication, (1972).

15. Crites, R.C. and Heckart, M.V., "Application of Random Data Techniques to Aircraft Inlet Diagnostics," AIAA Preprint 70-597 (1970).

16. Crites, R.C., "The Philosophy of Analog Techniques to the Analysis and High Speed Screening of Dynamic Data, "AIAA Preprint 70-595 (1970).

17. Lynch, F.R. and Slade, C.J., "Data Acquisition and Automated Editing Techniques for Engine-Inlet Tests," AIAA Preprint 70-596 (1970).

18. Air Force Flight Dynamics Laboratory, "Experimental and Analytical Determination of Integrated Airframe-Nozzle Performance," Interim Report (1972).

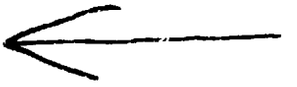

THE ENERGY BALANCE IN AXISYMMETRIC STEADY COMPRESSIBLE SWIRL FLOWS WITH CLOSED STREAMLINES

by

K. G. Guderley

AD P000319

The core flow in axisymmetric steady compressible swirl flows with closed streamlines at high Reynolds numbers can be computed from equations in which the viscosity and the heat conductivity terms are omitted. Viscosity and heat conductivity, nevertheless, play a decisive role; one must postulate that their long time effects vanish. In a flow, free of viscosity and heat conductivity, there exist certain quantities which are constant along the streamlines, namely the moment of momentum of the particles with respect to the axis of symmetry, the entropy and the total energy (that is the constant in Bernoulli's equation). In general, these quantities are not the same for all streamlines. If these functions are not properly chosen, then certain expressions (computed from the inviscid flow field) which can be interpreted as the longtime effects of heat conductivity and viscosity, are different from zero. Examples computed on this basis are analyzed from a thermodynamic point of view. One can differentiate between a primary flow (swirl flow proper) with components perpendicular to the meridian planes and a secondary flow with components within the meridian planes. Heat conductivity and dissipation within the primary flow act as a heat input into the secondary flow. This effect vanishes for Prandtl number ½. Further heat inputs into the secondary flow come from the dissipation of the secondary flow and the heat conduction due to the deviation of the temperature distribution in the actual flow field from that of the primary flow. The in and outputs of mechanical work in the secondary flow and the work of the shear forces on the ring surfaces defined by the streamlines. A comparison of the contributions to the entropy balance with the corresponding heat in or outputs of the energy balance shows that the heat inputs into the secondary flow occur, in the average, at lower temperature than the heat outputs. One, therefore, needs an input of mechanical work (provided by the shear forces between the streamlines) to keep the process going. Physically speaking, one deals with a buoyancy effect. The particles move constantly from low pressures to high

Manuscript Received September 1979.

pressures and back but with slightly different entropies on the two legs of their cycle. This effect is more pronounced if the secondary motion is slow, for then the heat in and outputs during a cycle take place over longer times. One finds, indeed, that for Prandtl numbers larger than ½ the secondary flow cannot be arbitrarily slow. If one tries to compute a family of flow patterns in which the secondary flow becomes slower and slower, then there comes a point where the shear forces of the secondary flow can no longer provide the necessary mechanical work and then flow patterns of the simple type considered here become impossible. One comes to the following general conclusion: in a compressible medium the temperatures at which the heat in and outputs occur are extremely important. This holds, in particular, for experiments in which exothermic reactions occur.

THE ENERGY BALANCE IN AXISYMMETRIC COMPRESSIBLE STEADY SWIRL FLOWS WITH CLOSED STREAMLINES

K. G. Guderley

I. INTRODUCTION

There exists a number of ingenious devices in which Dr von Ohain has used swirling flows to perform difficult technical tasks; an example is the elimination of dust particles in high volume air flows. The basis of these inventions has been an intuitive understanding of the flow patterns in swirl chambers and of the means by which they can be modified in a desirable manner. Encouraged by these applications the author has carried out a theoretical analysis of certain aspects of swirl flows although in an idealized model. The results have been published in Ref. 1. The present article is an excerpt from this paper; it deals with general conclusions drawn from computed flow fields on the basis of thermodynamic considerations. These results are shown in a number of graphs; unfortunately, rather lengthy explanations are needed to provide an adequate background of the quantities represented there.

II. DESCRIPTION OF THE MODEL

In axisymmetric flows with swirl, we distinguish between the swirl flow proper, that is the flow with components normal to the meridian planes (in a system of cylindrical coordinates) and a secondary flow with components within the meridian planes. For the secondary flow one can draw paths of the particles with respect to the meridian planes; these paths will be called streamlines, to be parameterized by a stream function ψ. The stream function is defined in the familiar manner, so

that the equation of conservation of mass is automatically satisfied. In the flow fields considered here the streamlines are closed. There is one point within the flow field in which the velocity components in the meridian plane are zero; this is the center of the secondary motion. To this point we assign $\psi = 0$. The surfaces $\psi = \text{const}$ in 3 dimensional space are axisymmetric ring surfaces. Each particle stays permanently on one of these surfaces. All particles pertaining to the same surface have the same time history except for a time shift. All particles inside such a ring stay there. Ultimately we shall discuss the energy and entropy balance in swirl flows for volumes bounded by such surfaces.

In flows of this kind one can distinguish between a boundary layer in which viscosity and heat conductivity play an important role and a core flow in which the velocity and the temperature gradients are relatively small so that one can nearly disregard viscosity and heat conductivity terms. The analysis of Ref. 1 and that of the present article refer only to the core flow.

III. THE BASIS OF THE MATHEMATICAL APPROACH

The analysis is based on the following considerations. Consider an axisymmetric swirl flow without heat conductivity and viscosity in which the streamlines are not closed, for instance a swirling flow in an axisymmetric nozzle. For such flows a number of quantities are constant along the streamlines, namely the moment of momentum of the particles with respect to the axis of symmetry, the entropy and a quantity which might be called rest enthalpy; it is the constant which appears on the right hand side of Bernoulli's equation. For velocity zero it gives the enthalpy of the particles. Each of these quantities

may depend upon the stream function ψ. These three functions are given by data in the entrance cross section to the flow field. If the streamlines are closed, then there is no entrance cross section; one might gain the impression as if these quantities can be arbitrarily chosen. One must, however, remember that the particles are retained for all times in flows of this kind. The effects of viscosity and heat conductivity, no matter how small, can therefore accumulate. Accordingly, they are able to determine the flow field in the long time limit.

The three functions mentioned above are properly chosen if the balance equations for moment of momentum, energy and entropy are satisfied for the axisymmetric ring surfaces ψ = const mentioned above. One is thus led to the following algorithm. One tentatively chooses the above three functions and computes the flow field from equations in which viscosity and heat conductivity are disregarded. They reduce to a second order partial differential equation for ψ, with an inhomogeneous term that contains the x derivatives of these three functions. For the flow fields so obtained, one evaluates for all values of ψ from the viscosity and heat conduction terms so far neglected, the residuals in the balance equations for momentum, energy and entropy, that is the amount by which one fails to satisfy these equations. One thus has an algorithm which leads from three functions (moment of momentum of the particles, entropy and rest enthalpy) to three other functions, namely the residuals in the three balance equations. Now one must try to adjust the functions initially assumed in such a manner that the residuals vanish. (If the equations of the flow field with the viscosity and heat conductivity terms included, had

been solved, then the balance equations would be satisfied for any axisymmetric ring, not only for those given by ψ = const.)

If the coefficients of viscosity and heat conductivity are constants then the momentum balance are automatically satisfied if the swirl component of the motion is given by a potential vortex. One then deals only with two unknown functions (entropy and rest enthalpy) and one has to satisfy only two balance equations (energy and entropy). The examples are restricted to this case. The strength of the potential vortex is one of the input parameters of the problem. It is physically determined by conditions at the boundary of the swirl chamber. To establish the swirl strength in a specific case one needs an evaluation of the boundary layer in the swirl chamber. There is another parameter which must be fixed in some fashion; in an experiment one has some control over the speed of the secondary motion. (The control of the secondary motion is one essential feature in Dr von Ohain's devices). This means that the two functions (entropy and rest enthalpy) are not uniquely determined by the balance equations. Such an indeterminacy exists indeed, mathematically it manifests itself by the fact that at the center of the swirl (defined above as the point which the speed of the secondary motion is zero) the balance equations are linearly dependent. (This holds even if the coefficients of heat conductivity and viscosity are not constant). In other words, if two of the balance equations are satisifed at the center of the swirl, then the third one is also satisfied. This observation is quite important for the numerical procedure. One always obtains erratic results if one fails to take such a relation into account in a numerical scheme. For detailed formulae and a description of numerical experiences, see Ref. 1.

IV. THE BASIS OF THERMODYNAMIC EVALUATION

The streamline patterns obtained in this manner do not provide much physical insight, neither does the temperature distribution in the swirl chamber which is rather close to the temperature distribution in a potential vortex. Some deeper physical understanding is obtained by analyzing the entropy and energy balances for the rings ψ = const in some detail.

On their way within the swirl chamber the individual particles undergo periodic changes of state because of the presence of a secondary flow. It takes them from regions of high pressures to regions of low pressure and back. These changes can be regarded as a thermodynamic cycle. It is the strength of thermodynamic discussions that they are solely concerned with energies and temperatures while the detailed mechanisms (here the specific occurrences within the flow field) are unessential. In the absence of viscosity and heat conductivity the particles will retain their entropy. In the familiar temperature entropy diagram the particles will retain their entropy. The cycle is represented by a piece of a line of constant entropy traversed between the temperature limits experienced by the particle. Close to the center of swirl, for instance, the temperature variations will be very small. Viscosity and heat conductivity will cause small deviations from these lines. In the coming discussions we shall not try to trace these cycles, but distinguish between the energy and entropy inputs into a particle in the average over time from different sources and then try to make conclusions regarding their relative importance.

Thermodynamic considerations are based on the abstraction of quasi-equilibrium, no losses within the working medium are admitted.

All heat additions are assumed to come from outside reservoirs of appropriate temperatures and all work is performed by outside forces acting directly on the particles (in this case body forces). In accordance with this model one considers the terms containing viscosity and heat conductivity coefficients in the Navier Stokes equations and in the energy equations as the effects of body forces and of heat sources from outside reservoirs. In the following discussion we start with this model, but then carry out mathematical transformations which allow us to interpret the resulting expressions in terms of the original model, that is a gas with viscosity and heat conductivity. Let us examine these effects in detail.

The contribution of the body forces to the balance of moment of momentum for the particles within a ring with surface ψ = const requires an integration of the moment of the body forces over the interior of the ring. Because of the mathematical form of these terms in the equation of moment of momentum (that is in one of the Navier Stokes equations in cylindrical coordinates) it is possible to change the volume integral into a surface integral. The resulting expression is physically interpreted (for the model of a gas with viscosity and heat conductivity) as the moment of the shear forces at the surface ψ = const with respect to the axis of symmetry).

The energy balance in the thermodynamic model considers the work done by body forces, and heat inputs due to viscous dissipation of mechanical work and due to heat conductivity. Losses of mechanical work due to viscous dissipation do not appear. Now one formally divides the work done by body forces into a portion which is dissipated and a remainder. The volume integral over the remainder can be transformed into an integral over the surface ψ = const; in this form it can be interpreted as the work of the shear forces acting on this surface.

The term which expresses the heat input due to viscous dissipation in the energy balance is equal, except for the sign, to the loss of mechanical energy due to viscous dissipation. These two expressions cancel each other; nevertheless, they will be identified in the graphs.

The volume integral over the heat sources due to heat conduction can be transformed into an integral over the surface ψ = const and then interpreted as the heat inflow through this surface.

In the entropy balance one encounters only heat energies and the temperatures at which the heat is added to the particles. One volume integral in the entropy balance arises because of the heat input due to dissipation. The equation of energy balance for the individual particle defines the substitute heat source which replaces in the thermodynamic model the heat input into a particle by conduction. (It is the difference between heat in and outflow taken for the individual particle.) This heat input occurs at the temperature of the particle. On this basis one computes an entropy input due to the local substitute heat sources. A mathematical transformation of this term and a subsequent physical interpretation leads to the definition of two expressions, which may be called entropy sources due to heat conduction and flux of entropy through the surface. We illustrate the difference between these two terms by a simple example.

Consider a one-dimensional heat flow with heat conductivity coefficient $k(x)$ and a temperature distribution $T(x)$. The strength of the substitute heat sources due to conduction is then given by

$$d[k(x)(dT/dx)]/dx$$

The entropy input into the particle due to this heat source is

$$T^{-1}d[k(x)(dT/dx)]/dx$$

The integral of the heat sources over a slab extending from x = 0 to x = L is given by

$$\int_0^L \{d[k(x)(dT/dx)]/dx\}dx = k(x)(dT/dx)\Big|_0^L$$

The entropy input due to these heat sources into this slab is

$$\int_0^L T^{-1}\{d[k(x)(dT/dx)]/dx\}dx = T^{-1}k(x)(dT/dx)\Big|_0^L + \int_0^L k(x)T^{-2}[dT/dx]^2dx$$

The term on the left is the entropy input due to the local substitute heat sources. The first term on the right is interpreted as the inflow of entropy through the surfaces x = 0 and x = L, it corresponds to the inflow of heat in the energy equation; the second term defines the entropy sources due to heat conductivity. In the thermodynamic model the left hand side (the entropy input due to the substitute heat sources) must be considered. In a steady heat flow the left hand side of the last equation is zero while the terms of the right hand side, in particular the entropy sources due to conduction are not zero.

Accordingly we have

in the momentum balance equations

the moment with respect to the axis of symmetry of the shear forces acting on the surfaces ψ = const

in the energy balance equations

the mechanical work of the shear forces at the surfaces ψ = const

the loss of mechanical work due to dissipation,

the flux of heat energy through the surface ψ = const, and

the gain of heat energy due to dissipation.

in the entropy balance

entropy generated by the dissipation of mechanical work

entropy input pertaining to the local heat sources which replace the effect of heat conduction.

(The last contribution can be considered as the sum of two parts, the entropy inflow through the surface ψ = const and the entropy sources due to heat conduction in the interior).

In addition we differentiate between contributions due to the primary flow and due to the secondary flow.

In the examples the assumption has been made that the coefficients of viscosity and heat conductivity are constant. In such a flow the rest enthalpy, and the entropy (the right hand side of Bernoulli's equation) are the same for all streamlines.

This together with the velocity distribution which depends only upon the radius defines the temperature distribution which is to be ascribed to the swirl flow. The mechanical energies of the primary and of the secondary flow are easily separated because the velocity vectors are perpendicular to each other and because the dissipation terms are additive. We define as heat conduction of the primary flow the expression which is obtained from the temperature distribution just defined for the primary flow. The remainder of the heat conduction terms is ascribed to the secondary flow. In computing the entropies pertaining to these heat in or outputs we use the temperatures of the actual flow for the secondary flow as well as for the swirl flow.

The shear forces at a surface ψ const in a potential vortex have a braking effect at large radii and a driving effect at small radii. In the whole one has an input of mechanical work. It is completely dissipated in the interior. The temperature gradient pertaining to a potential vortex generates a heat flux. The computation shows that the heat

sources due to dissipation and the substitute heat sources due to heat conduction have the same dependence upon the radius and that the latter part is negative. The two effects cancel for Prandtl number 1/2; for larger Prandtl numbers the combined effect is a heat input.

In the secondary flow one distinguishes between a heat input due to secondary dissipation, a heat output due to the heat conduction of the secondary flow, an input of mechanical energy due to the shear forces of the boundary flow at the surfaces ψ = const and an output of mechanical energy due to secondary dissipation.

In the entropy balance one has the combined heat input due to dissipation and substitute heat sources of the primary flow, the entropy input due to secondary dissipation, and the entropy input due to the substitute heat sources for the secondary conduction.

After these preliminaries, we come to the discussion of energy balances. The contour of the swirl chamber in the meridian plane for which these computations have been carried out is a circle with radius 1/2 around the point x = 0, y = 1, Fig. 1. In all computations we have assumed constant coefficients of heat conductivity and viscosity and a Prandtl number 1. (Only the value of the Prandtl number, not the specific values of the coefficients of heat conductivity and viscosity, enters the computations.) The strength of the swirl is characterized by a quantity g_1 (constant in each example) which is proportional to the square of the moment of momentum of the particles in the primary flow. The value of g_1 is the same in Figs. 2 through 4, in Figs. 5 through 7 it is also constant but somewhat higher. The flow patterns differ by the speed of the secondary motion which is roughly characterized by the values of ψ_{max} shown in the legenda to the figures. The independent variable

in these figures is ψ/ψ_{max}. The value of ψ_{max} is reached at the contour of the swirl chamber. These curves give the energy balances for all values of ψ. Surfaces ψ = const can be regarded as the boundaries of swirl chambers which have a smaller non-circular cross section. Differentiating these curves with respect to ψ one obtains the energy balance for hollow rings bounded by surfaces ψ = const and ψ = const + $d\psi$; then one could say something about the energy balance of individual particles. The results are not accurate enough to allow for an unambiguous differentiation.

Curve 1 in these energy balances gives the heat input due to the primary flow (effect of heat conduction and dissipation of the primary flow combined). For the same value of the swirl, this heat input would be independent of ψ/ψ_{max}, if the streamlines retain their shapes while ψ_{max} varies. This contribution is indeed nearly independent of ψ_{max}. The contribution 3 is the input of heat due to secondary dissipation and at the same time, with the negative sign, the loss of mechanical energy due to dissipation. Finally, curve 4 gives the output of heat due to secondary heat conduction. One expects the contribution due to secondary dissipation to become smaller as the speed of the secondary motion is reduced. Nothing definite can be said about the work done by shear forces at surfaces ψ = const. The secondary dissipation depends, of course, upon the shape of the swirl chamber; the fact that it is relatively small need not be typical.

Figs. 8 shows the entropies together with the heat energies that occur in Fig. 5. Fig. 8a gives the heat input and the entropy input due to secondary dissipation, Fig. 8b the heat and entropy inputs of the primary flow, Fig. 8c the heat and entropy outputs due to secondary

conduction. The entropy contribution of these three graphs add up to zero. The same behavior is found in other cases not shown here. Particles on their paths from low to high pressures have on the average higher temperatures than those on the return section of the path.

The main heat input comes from the combined dissipation and heat conductivity of the swirl flow. This is the portion which is proportional to $2 - Pr^{-1}$. In the example shown in Figs. 8, the heat input due to secondary dissipation is relatively small. It will, of course, be larger if the speed of the secondary flow is taken larger. If the energy exchanges would take place at a constant temperature T_0, then the ratio between the values of the entropy and of the energy would be T_0^{-1}. Actually this ratio is not the same. The average temperatures of the heat inputs (Figures 8a and 8b, most pronounced in Fig. 8b) are lower than the average temperatures of the heat output (Fig. 8c). The same behavior is found for other flow fields (not shown here). An input of mechanical work into the secondary flow is, of course, needed to provide for the mechanical work lost by secondary dissipation, but in addition a considerable amount of additional mechanical work is required because the heat inputs occur at a lower average temperature than the heat outputs. (We mentioned before that the mechanical energy dissipated in the swirl flow is furnished entirely by mechanical work of the shear forces which maintain the swirl motion, this mechanical energy does not count in the energy balance and does not contribute to maintain the secondary flow). The mechanical energy needed to maintain the secondary motion is provided by the shear forces of the secondary motion at the surfaces of rings ψ = const.

The physical mechanism which is responsible for this requirement of an additional input of mechanical energy into the secondary motion is a buoyancy effect. The heat inputs occur primarily at low temperatures (and low pressures) and the heat output at high temperatures and high pressures.

While the particles move from low pressures to high pressures, their temperature is higher than the temperature which they experience on their way back. Because of these temperature differences, one needs forces in the direction of the secondary flow to maintain their motion. They are supplied to the individual particles by the difference of the shear forces at surfaces ψ = const and ψ = const + $d\psi$. This effect is more pronounced if the secondary motion is slow, for then the particles dwell longer in different temperature regions, and the deviation from the adiabatic temperature distribution become larger. The equations show indeed that the secondary flow cannot be arbitrarily slow except for Prandtl number 1/2.

One can draw a general conclusion. The secondary flow is sensitive because the energies involved and the shear forces that are supposed to provide for the necessary mechanical energy are small. A slight heating or cooling, resulting in unidirectional buoyancy, may have a profound effect. In the present setting this manifests itself as a dependence of the results on the Prandtl number. Heat sources within the flow field would have an effect similar to that of a change of the Prandtl number. If the heat is primarily added at low temperature then it impedes the secondary motion and may make secondary flow of the character considered here impossible.

This observation has, of course, experimental implications.

Ref 1.

Guderley, Karl Gottfried, Steady Compressible Swirl Flows with Closed Streamlines at High Reynolds Numbers, J. Fluid. Mech (1977) Vol. 82, Part 2, pp. 321-347.

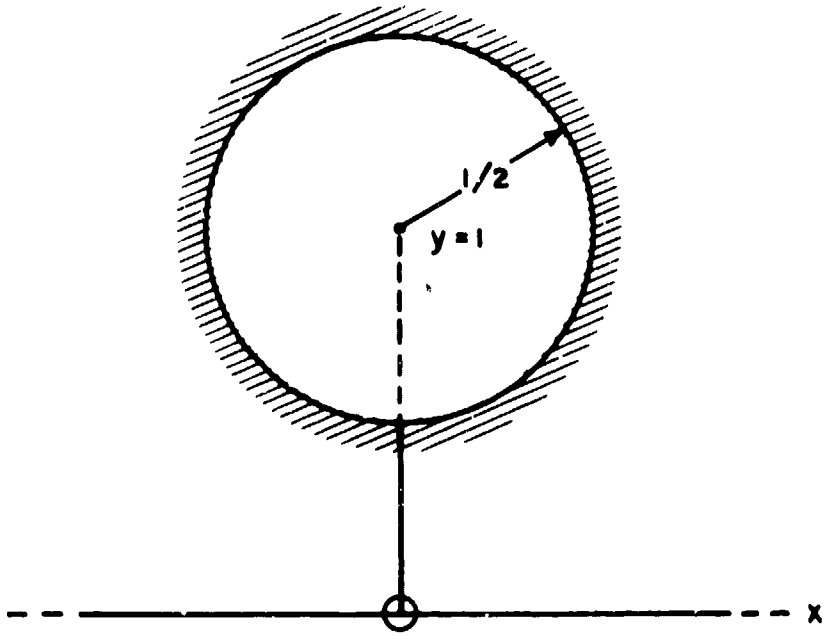

Figure 1. Cross-Section of a Swirl Chamber

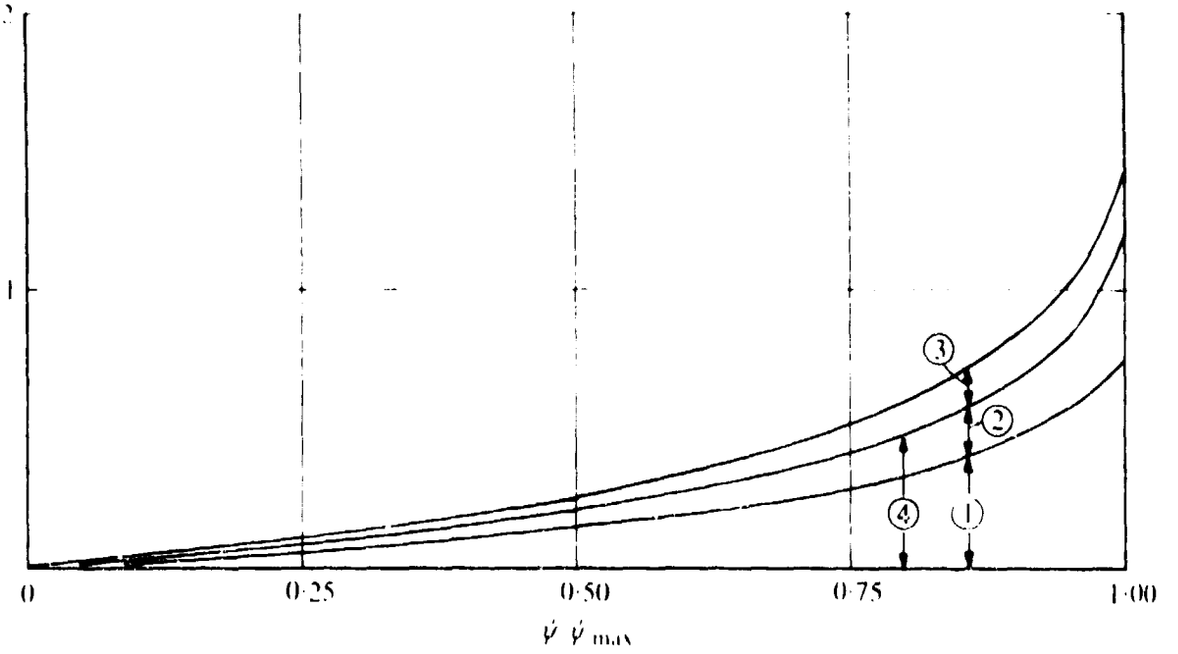

Figure 2. Energy Breakdown vs ψ (Pr=1, g_1=0.6, ψmax=0.070)

(See text for explanation of curves)

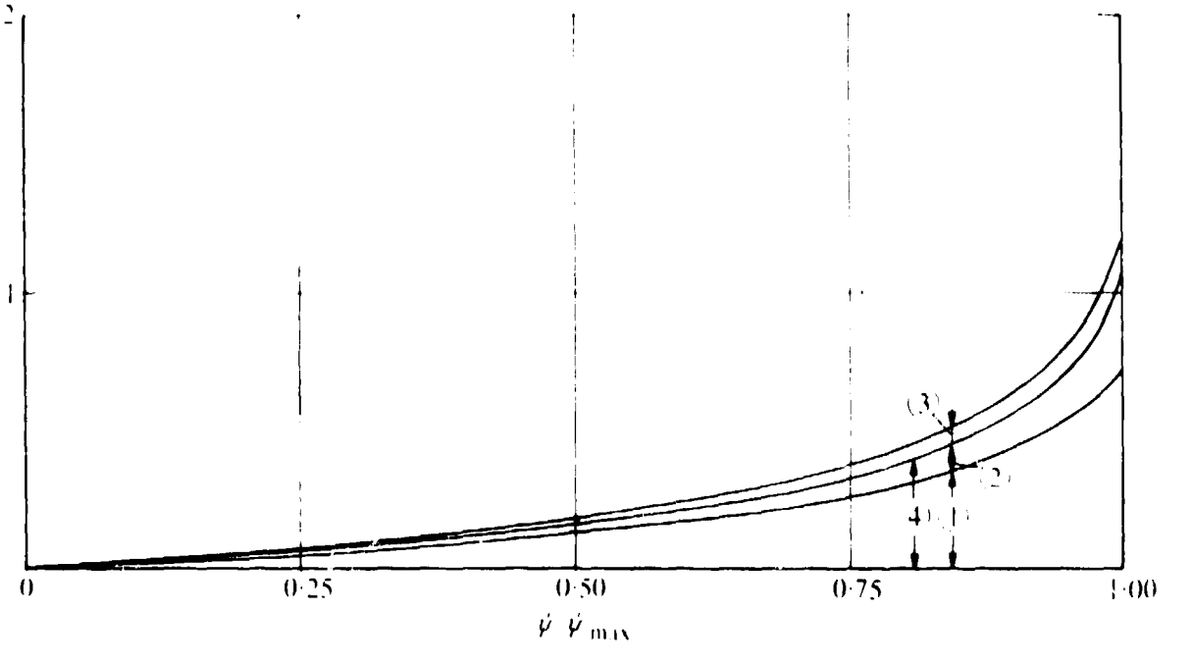

Figure 3. Energy Breakdown vs ψ (Pr=1, g_1=0.6, ψmax=0.046)

(See text for explanation of curves)

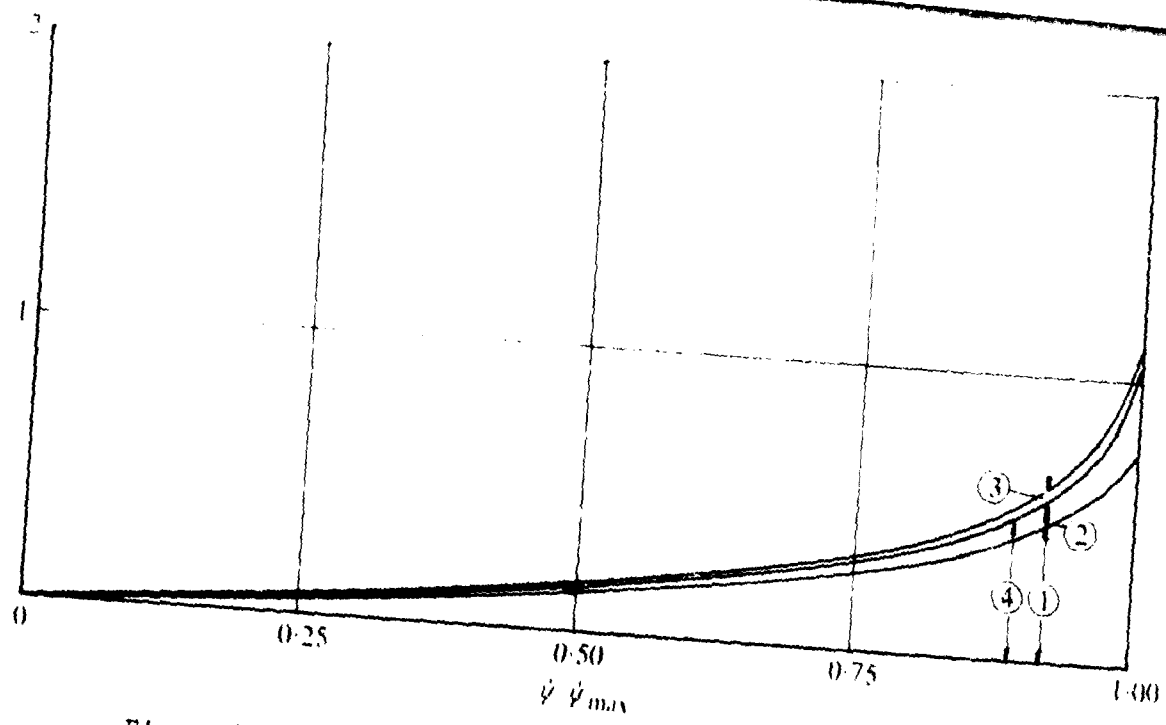

Figure 4. Energy Breakdown vs ψ (Pr=1, g_1=0.6, ψmax=0.029)
(See text for explanation of curves)

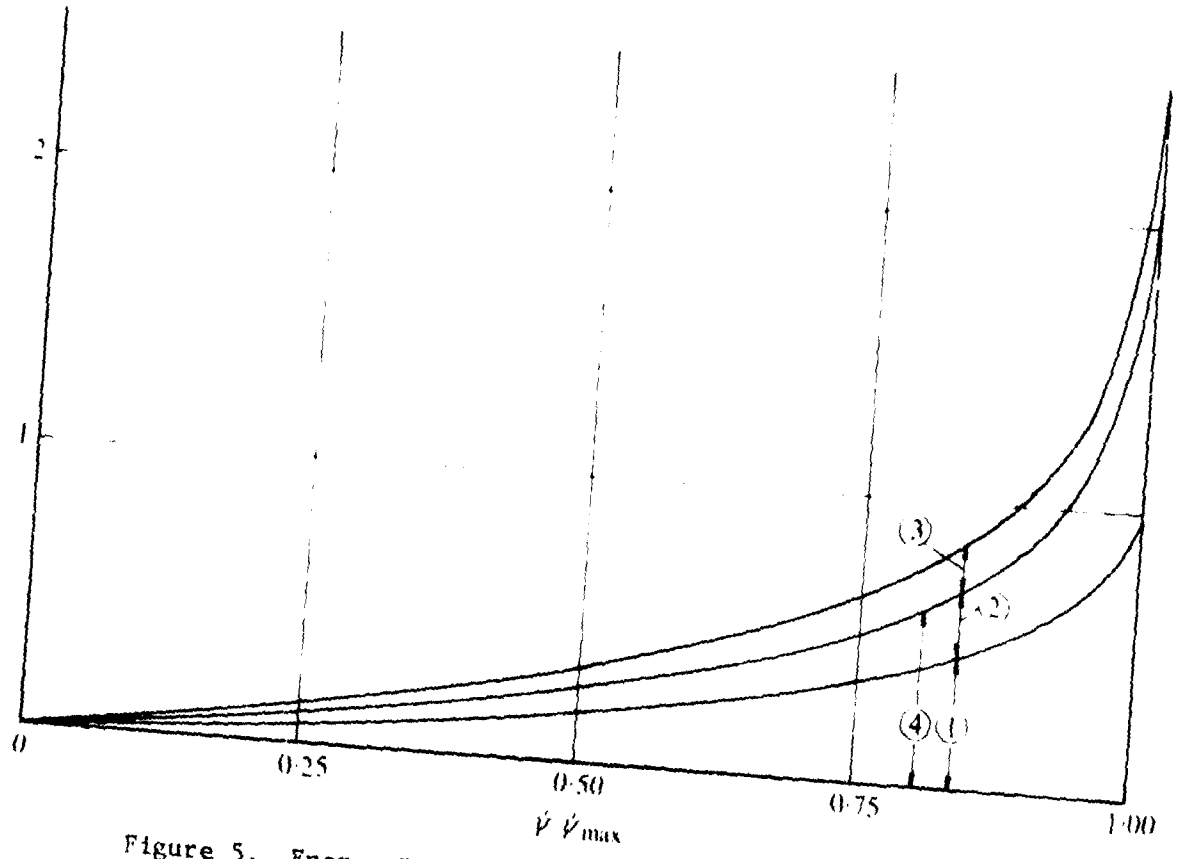

Figure 5. Energy Breakdown vs ψ (Pr=1, g_1=0.8, ψmax=0.070)
(See text for explanation of curves)

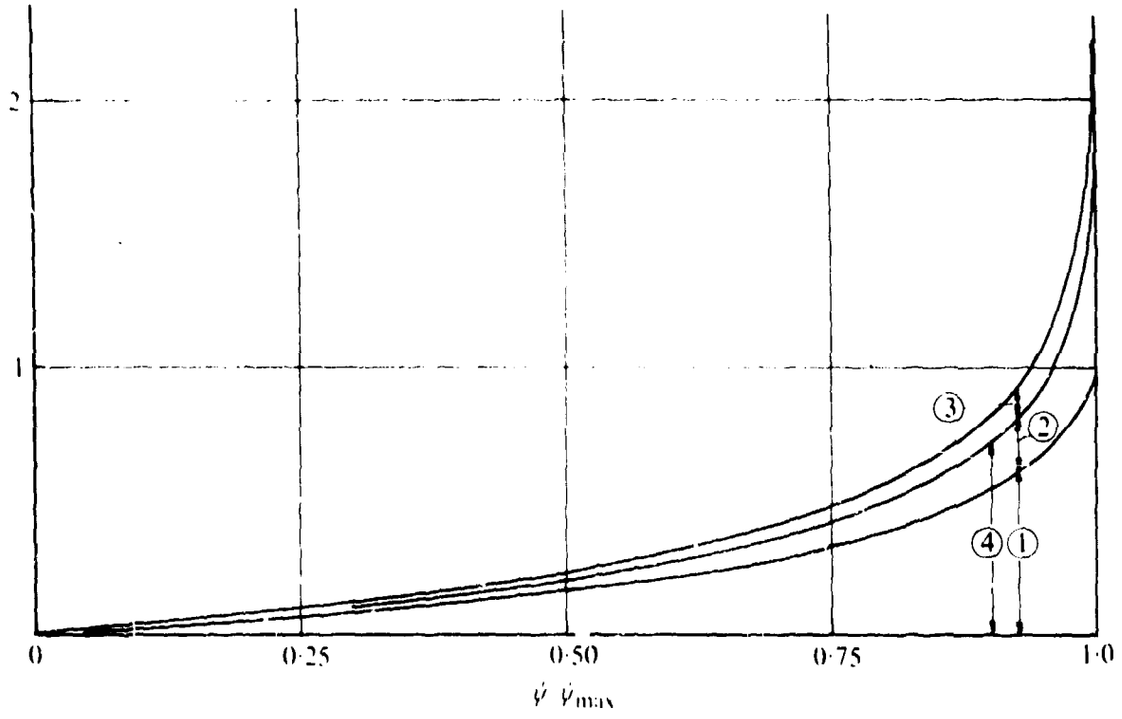

Figure 6. Energy Breakdown vs ψ (Pr=1, g_1=0.8, ψmax=0.046)

(See text for explanation of curves)

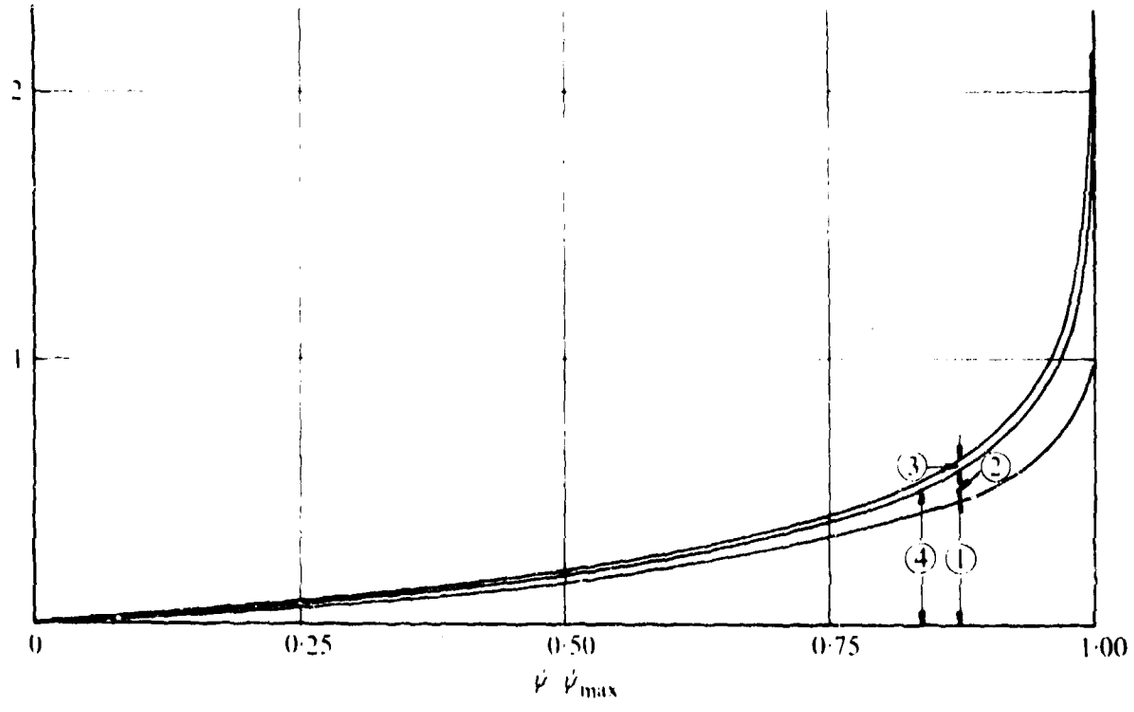

Figure 7. Energy Breakdown vs ψ (Pr=1, g_1=0.8, ψmax=0.029)

(See text for explanataion of curves)

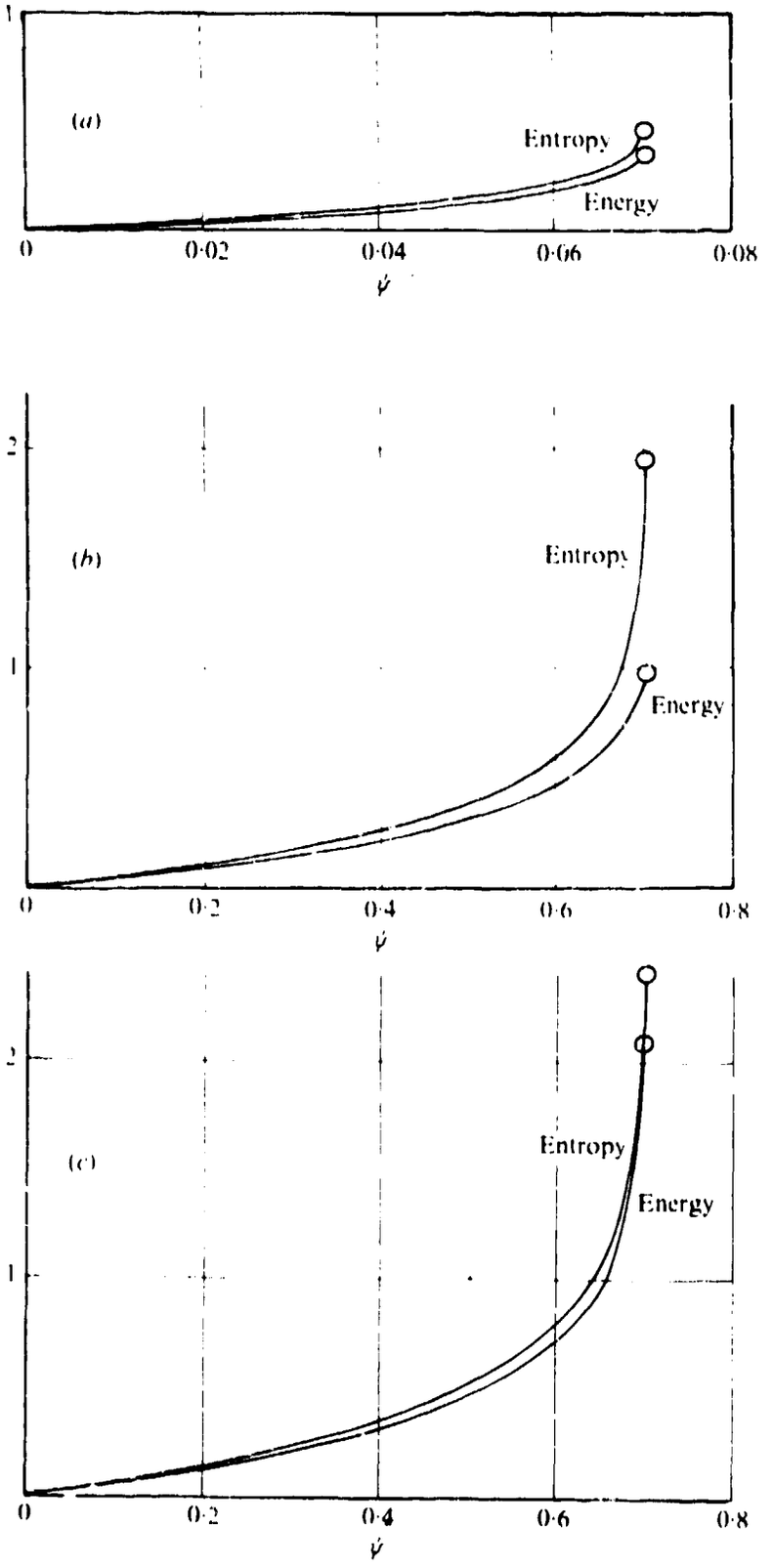

Figure 8. Entropies and Energies vs ψ for Case Shown in Figure 5

(See test for explanation of curves)

AD P000320

COMPOUND-COMPRESSIBLE NOZZLE FLOW

by

A. Bernstein and C. Hevenor
Pratt & Whitney Aircraft
East Hartford, Conn.

W. H. Heiser
General Electric Company
Cincinnati, Ohio

A one-dimensional theory based upon fundamental flow relationships is presented for analyzing the behavior of one or more gas streams flowing through a single nozzle. This compound-compressible flow theory shows that the behavior of each stream is influenced by the presence of the other streams. The theory also shows that the behavior of compound-compressible flow is predicted by determining how changing conditions at the nozzle exit plane affect conditions within the nozzle. It is found that, when choking of the compound-compressible flow nozzle occurs, an interesting phenomenon exists. The compound-compressible flow is shown to be choked at the nozzle throat, although the individual stream Mach numbers there are not equal to one. This phenomenon is verified by a wave analysis which shows that, when choking occurs, a pressure wave cannot be propagated upstream to the nozzle throat even though some of the individual streams have Mach numbers less than one. Algebraic methods based on this compound-compressible flow theory are used to demonstrate the usefulness of this approach in computing the behavior of compound-compressible flow nozzles. A comparison of the compound-compressible flow theory with three-dimensional computer calculations shows that the effects of streamline curvature on nozzle behavior can be disregarded for many practical nozzle configurations. Test results from a typical two-flow nozzle show excellent agreement with the predictions from the theory.

Copyright ASME. Reprinted with Permission.

A. BERNSTEIN
Analytical Engineer
Pratt & Whitney Aircraft
East Hartford, Conn.

W. H. HEISER
Assistant Professor
Department of Mechanical Engineering
Massachusetts Institute of Technology
Cambridge, Mass.

C. HEVENOR
Senior Analytic Engineer
Pratt & Whitney Aircraft
East Hartford, Conn.

COMPOUND-COMPRESSIBLE NOZZLE FLOW

Introduction

Modern propulsion engines often exhaust several different streams of gas side-by-side through a single nozzle, Fig. 1. These flows can exhibit sizeable compressiblity effects and they will be referred to here as compound-compressible nozzle flows. The purpose of this paper is to provide, for the first time, a simple method to predict the behavior and clarify the understanding of such flows.

A one-dimensional analysis similar to that used in single-stream compressible flow problems is applied here to compound-compressible flow problems. The great advantage of this type of approach is that it provides physical insight into the nature of the flow.

Mixing between the various streams is not considered in the development of the basic theory, but its effect on compound-compressible flow behavior will be discussed. It will be shown that mixing often has a negligible effect on the flow behavior.

The usefulness of the compound-compressible flow theory is demonstrated by comparing its predictions with both three-dimensional computer calculations and experimental results.

The basic approach used to develop the compound-compressible flow theory will be to determine how changing conditions at the nozzle exit plane change conditions within the nozzle. This will be seen to be the heart of the matter and all results obtained in this paper are presented in this light. Note should be taken of a pioneering contribution to compound-compressible nozzle flows made by Pearson, Holliday, and Smith [1].[4] Their results are consistent with the general conclusions arrived at in this paper.

Manuscript received by ASME Applied Mechanics Division, November 15, 1966 Paper No. 67 - APM-L

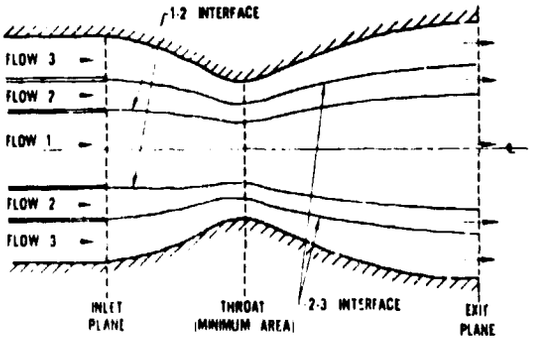

Fig. 1 Schematic drawing of axially symmetric compressible-nozzle flow

One-Dimensional Compound-Compressible Nozzle Flow Theory

The development of one-dimensional compound-compressible nozzle flow theory follows that of Shapiro [2] for single-stream flow. The most important alteration is that the fluid static pressure is chosen as the dependent parameter because it can vary only *along* the nozzle in one-dimensional flow, whereas all other fluid properties can also change from stream-to-stream *across* the nozzle.

This analysis is sufficiently general to include any arbitrary number of streams designated by the integer n. For example, at any position in the nozzle,

$$A = \sum_{i=1}^{n} A_i, \qquad \frac{dA}{dx} = \sum_{i=1}^{n} \frac{dA_i}{dx} \tag{1}$$

where A is the total flow area, A_i is the flow area of the ith stream, and x is the axial nozzle position coordinate. In single-stream one-dimensional theory, dA/dx is arbitrarily small and this carries over into the present case where all dA_i/dx are arbitrarily small. The transverse pressure gradients caused by streamline curvature can then be neglected and this leads to the conclusion that static pressure is only a function of axial position.

It is also assumed that the flow in each stream is steady, adiabatic, and isentropic and that each fluid is a perfect gas with constant thermodynamic properties. Note that these assumptions exclude mixing effects.

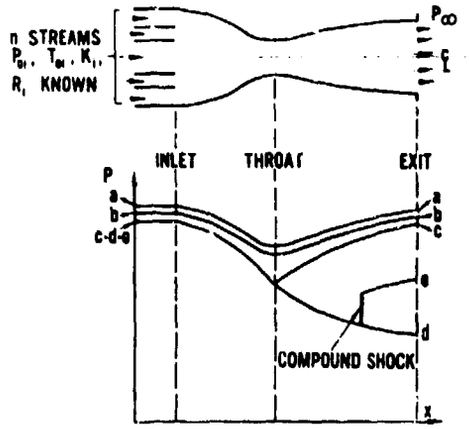

Fig. 2 Compound-compressible flow in a nozzle of fixed geometry

Each stream may then be separately treated as a single-stream one-dimensional flow (Shapiro [2], Table 8.2). Consequently,

$$\frac{dA_i}{dx} = \frac{A_i}{k_i}\left(\frac{1}{\mathbf{M}_i^2} - 1\right)\frac{d}{dx}(\ln p) \tag{2}$$

where k_i is the ratio of specific heats, $\mathbf{M}_i$ is the Mach number ($\mathbf{M}_i = V_i/\sqrt{k_i R_i T_i}$) for the ith stream, and p is the fluid static pressure. Equations (1) and (2) may be combined to yield

$$\frac{d}{dx}(\ln p) = \frac{\dfrac{dA}{dx}}{\displaystyle\sum_{i=1}^{n}\frac{A_i}{k_i}\left(\frac{1}{\mathbf{M}_i^2} - 1\right)} = \frac{1}{\beta}\frac{dA}{dx} \tag{3}$$

where

$$\beta = \sum_{i=1}^{n}\frac{A_i}{k_i}\left(\frac{1}{\mathbf{M}_i^2} - 1\right) \tag{4}$$

The term β, the compound-flow indicator, will subsequently be shown to be significant in determining the nature of the flow (i.e., whether it is *compound-subsonic* or *compound-supersonic*).

The behavior of compound-compressible flow in a nozzle of fixed geometry can be most profitably examined by regarding the inlet pressure as an independent variable, Fig. 2. If the stagnation pressures (p_{0_i}), the stagnation temperatures (T_{0_i}), and the gas properties are constant and known for each stream, the mass flows (w_i) are functions only of the local pressure and the local flow area:

$$w_i = \frac{A_i p_{0_i}}{\sqrt{T_{0_i}}}\left(\frac{p}{p_{0_i}}\right)^{\frac{1}{k_i}}\sqrt{\frac{2}{R_i}\left(\frac{k_i}{k_i - 1}\right)\left[1 - \left(\frac{p}{p_{0_i}}\right)^{\frac{k_i - 1}{k_i}}\right]} \tag{5}$$

Thus, for any given value of p at the inlet plane, where the A_i are known, equation (5) may be used to determine the corresponding values of w_i. With the w_i fixed by the inlet pressure, it can be seen from equation (5) that the local A_i are functions only of the local p and known quantities in the remainder of the nozzle. Since the local $\mathbf{M}_i$ are also functions only of the local p and known quantities, namely,

$$\mathbf{M}_i^2 = \frac{2}{k_i - 1}\left[\left(\frac{p_{0_i}}{p}\right)^{\frac{k_i - 1}{k_i}} - 1\right] \tag{6}$$

it follows directly that the local value of β, equation (4), is a function only of the inlet pressure, the local pressure, and known quantities. Therefore, equation (3) can be integrated in principle from inlet to exit for any chosen value of inlet pressure. Referring to Fig. 2, the consequences of the choice of inlet pressure can now be examined.

If the inlet pressure is sufficiently high (curves a and b), equation (6) will yield values of $\mathbf{M}_i^2$ small enough that β will be >0 everywhere in the nozzle and p will therefore change in the same direction as A throughout, equation (3). In particular, both p and A will have their smallest values at a geometric throat where A reaches its minimum. Note that the integration also shows what the back pressures must be to maintain these flows.

At the same time, the differentiation of β with respect to p yields

$$\frac{d\beta}{dp} = \sum_{i=1}^{n}\frac{A_i}{pk_i^2\mathbf{M}_i^4}\left[(1 - \mathbf{M}_i^2)^2 + 2\left(1 + \frac{k_i + 1}{2}\mathbf{M}_i^2\right)\right] > 0 \tag{7}$$

which shows that β always changes in the same direction as p. Therefore, for curves a and b, β will also change in the same direction as A and will also have its minimum value at the throat.

As the inlet pressure is decreased, the value of β at the throat will also decrease. In fact, when the inlet pressure is chosen to be sufficiently small, β reaches zero at the throat. When this occurs, equation (3) is indeterminant and no longer serves to determine the axial pressure gradient at the throat. Under this condition, application of L'Hospital's rule to equation (3) yields

$$\frac{d}{dx}(\ln p) = \pm\sqrt{\frac{\dfrac{d^2A}{dx^2}}{\displaystyle\sum_{i=1}^{n}\frac{A_i}{k_i^2\mathbf{M}_i^4}\left[(1 - \mathbf{M}_i^2)^2 + 2\left(1 + \frac{k_i + 1}{2}\mathbf{M}_i^2\right)\right]}} \tag{8}$$

The geometry of any throat is such that d^2A/dx^2 is always >0. Therefore, $d(\ln p)/dx$ will be either the positive or negative root of a real number.

Curve c represents the choice of the positive root while curve d represents the choice of the negative root. Comparison of curves c and d reveals a familiar single-stream compressible flow situation: The geometric throat is a saddle point for two isentropic solutions in the divergent section of the nozzle. No back pressure between curves c and d can correspond to an isentropic flow. It is anticipated that those back pressures which do not correspond to isentropic solutions, such as that of curve e, may be reached by means of *compound shocks* initiated at some point on curve d.

The behavior of the flow along curve c is similar to that of curves a and b; i.e., A, p, and β will reach their minimum values at the throat. Note that the positive root of equation (8) is chosen *only* when the back pressure corresponds exactly to that of curve c.

The implications of the choice of the negative root of equation (8) will now be considered in detail (curve d). Since equation (7) has shown that β always changes in the same direction as p, $d\beta/dx$ must also be negative at the throat. Accordingly, β must decrease from positive to negative as it passes through zero at the throat. Furthermore, with β negative entering the divergent section (where dA/dx is > 0), simultaneous examination of equations (3) and (7) shows that the local values of both p and β must continue to decrease through the divergent section. Note that the integration of equation (3) still shows what the back pressure must be to maintain this flow.

No isentropic solutions exist for *inlet* pressures corresponding to values less than that of curve d because β would reach zero upstream of the geometric throat. This would result in an infinite axial pressure gradient, equation (3).

Some interesting conclusions can be made by examining the influence of back pressure, p_n, on the inlet pressure. A back pressure greater than that of curve c will affect the pressure at the inlet plane and will thus influence the flow rates of the individual streams. Any back pressure less than that of curve c will affect neither the inlet pressure nor the flow rates. This condition will be referred to as *compound-choking*. Under such conditions, the nozzle geometric throat controls the behavior of the flow.

Also, since dp/dx is always <0 for curve d, Bernoulli's equation shows that a continuous acceleration of the flow takes place throughout the nozzle. Applying this to equation (3), it can be seen that, for continuous acceleration of the flow, $\beta > 0$ whenever $dA/dx < 0$ and $\beta < 0$ whenever $dA/dx > 0$. Thus, for continuous acceleration of the flow in a *single*-stream convergent-divergent nozzle, examination of β reveals that the flow must be subsonic in the convergent section, sonic at the throat, and supersonic in the divergent section, equation (4). In the following section, it will be shown that for compound-compressible flow an analogous situation exists: The flow must be compound-subsonic in the convergent section, compound sonic at the throat, and compound-supersonic in the divergent section. It will also be shown that these regimes are differentiated by the compound-flow indicator, β.

Compound Waves

The compound-choking phenomena just described can be explained by examining the effects of small pressure disturbances on the flow. A diagram of such a disturbance is shown in Fig. 3. It is consistent with one-dimensional theory to take the flow area as constant in wave calculations. If a weak plane pressure disturbance is imposed on the flow, Fig. 3(*a*), this disturbance cannot propagate at different absolute velocities in each stream without violating the condition that the static pressures at the stream interfaces be equal. Therefore, the wave must be continuous and must travel as a single compound wave, Fig. 3(*b*) Although the wave is not necessarily plane, the pressure rise across it cannot vary from stream to stream.

As indicated in Fig. 3(*b*), the absolute terminal velocity in the upstream direction of the compound wave is designated by α. It follows directly that: $\alpha > 0$ corresponds to *compound-subsonic* flow; $\alpha = 0$ corresponds to *compound-sonic* flow; $\alpha < 0$ corresponds to *compound-supersonic* flow.

An analytical expression for the compound wave velocity, α, can be derived by treating each stream separately as a flexible tube and conserving mass, momentum, and entropy across the compound wave in the frame of reference of the compound wave. It follows that

$$\frac{\Delta A_i}{A_i} = \frac{\Delta p_i}{k_i p_i}\left[\frac{1}{\left(\dfrac{\alpha}{\sqrt{k_i R_i T_i}} + M_i\right)^2} - 1\right] \tag{9}$$

where Δ signifies the change across the compound wave. Since the flow area is constant,

$$\sum_{i=1}^{n} \Delta A_i = \Delta A = 0 \tag{10}$$

across the wave. And since $p_i = p$ and $\Delta p_i = \Delta p$, equations (9) and (10) may be combined to yield the desired relation for the compound wave velocity α; namely,

$$\sum_{i=1}^{n} \frac{A_i}{k_i}\left[\frac{1}{\left(\dfrac{\alpha}{\sqrt{k_i R_i T_i}} + M_i\right)^2} - 1\right] = 0 \tag{11}$$

Equations (4) and (11) may be combined to yield

3a INITIAL PLANE PRESSURE DISTURBANCE

3b UPSTREAM MOVING COMPOUND WAVE IN TERMINAL STATE

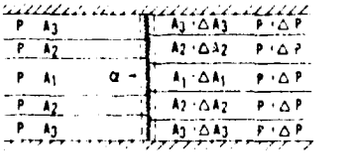

Fig. 3 Evolution of a one-dimensional compound wave

$$\beta = \sum_{i=1}^{n} \frac{A_i}{k_i}\left[\frac{1}{M_i^2} - \frac{1}{\left(\dfrac{\alpha}{\sqrt{k_i R_i T_i}} + M_i\right)^2}\right] \tag{12}$$

Examination of equation (12) shows that the compound wave velocity α, and the compound flow indicator β, must always have the same sign. Therefore $\beta > 0$ corresponds to compound-subsonic flow; $\beta = 0$ corresponds to compound-sonic flow; $\beta < 0$ corresponds to compound-supersonic flow.

Note that compound-choking can only occur at the nozzle minimum area for it is there only that β can equal zero. Note also that small-amplitude compound waves cannot move upstream in the compound-supersonic region. One would therefore expect that compound-shock waves could arise and cause the steady compound-compressible flow to be nonisentropic in the compound-supersonic region. By the same reasoning, compound-shock waves are not expected in the compound-subsonic region.

Several conclusions may be drawn from this analysis:

1 The concept of flow choking at Mach one is no longer valid in compound-flow analysis. Indeed, when compound flow is choked, the individual stream Mach numbers at the throat will *not* be equal to one (except for the unique case where the stagnation pressures of all the streams are equal and the Mach numbers of all the streams are unity). Rather, compound-choking is determined by the compound-flow indicator and can occur only when $\beta = 0$ at the minimum nozzle flow area.

2 Not every stream need have a Mach number <1 in order that the flow be compound-subsonic and not every stream need have a Mach number >1 in order that the flow be compound-supersonic. In fact, equation (4) shows that the various streams influence β in proportion to their flow areas, which agrees with intuitive reasoning.

3 The compound-flow regimes determined by β, compound-subsonic and compound-supersonic, are analogous to the subsonic and supersonic flow regimes encountered in single-stream nozzles. In fact, the usual *single*-stream results are obtained when $n = 1$ in the foregoing equations.

Computational Procedures for Compound-Compressible Nozzles

Despite the need for differential equations in drawing conclusions about one-dimensional compound-compressible flows, the solutions for the behavior of these flows will be seen to require only algebraic computations.

Although the equations in the preceding sections were derived for n flows, to illustrate the application of this analysis, only two-stream convergent-divergent nozzles will be considered in this section. This will not only result in the development of less involved equations but will also clarify the role of the geometric throat and the phenomenon of choking.

As has been shown, the behavior of compound-compressible flow is determined by the relationships of k_i, R_i, A_i, w_i, T_{0i}, p_{0i}, and p. Equations (1) and (5) can be combined to yield

$$\sum_{i=1}^{n} \frac{w_i \sqrt{T_{0i}}}{p_{0i}} \left(\frac{p_{0i}}{p}\right)^{\frac{1}{k_i}} \left\{ \frac{2}{R_i} \left(\frac{k_i}{k_i - 1}\right) \left[1 - \left(\frac{p}{p_{0i}}\right)^{\frac{k_i - 1}{k_i}} \right] \right\}^{-1/2} = \sum_{i=1}^{n} A_i = A \quad (13)$$

Using equation (13), the following expression may be written for two streams at any point in the nozzle:

$$\frac{w_2 \sqrt{T_{02}}}{w_1 \sqrt{T_{01}}} = \left\{ \frac{A}{A_1^*} \left[\left(\frac{2}{k_1 - 1}\right) \left(\frac{k_1 + 1}{2}\right)^{\frac{k_1+1}{k_1-1}} \right]^{1/2} - \left(\frac{p_{01}}{p}\right)^{\frac{1}{k_1}} \left[1 - \left(\frac{p}{p_{01}}\right)^{\frac{k_1-1}{k_1}} \right]^{1/2} \right\} \left\{ \frac{R_1 k_2}{R_2 k_1} \left(\frac{k_1 - 1}{k_2 - 1}\right) \times \left[1 - \left(\frac{p}{p_{02}}\right)^{\frac{k_2-1}{k_2}} \right] \right\}^{1/2} \left(\frac{p_{02}}{p_{01}}\right) \left(\frac{p}{p_{02}}\right)^{\frac{1}{k_2}} \quad (14)$$

where

$$A_1^* = \frac{w_1 \sqrt{T_{01}}}{p_{01}} \sqrt{\frac{R_1}{k_1} \left(\frac{k_1 + 1}{2}\right)^{\frac{k_1+1}{k_1-1}}} \quad (15)$$

These are the fundamental equations for solving two-stream compound-compressible flow problems.

When *unchoked* flow exists, it has been shown that the flow behavior is determined by the back pressure, Fig. 2, and $p_\infty = p_{exit}$. Thus, for unchoked flow, equation (14) may be applied at the exit plane. Typical solutions of equation (14) for unchoked flow are presented in nondimensional terms in Fig. 4 as the curved lines of different A_1^*/A_{exit}. Although these curves were generated for particular values of k, R, and temperature-corrected mass flow ratio ($w_2\sqrt{T_{02}}/w_1\sqrt{T_{01}}$), similar solutions can be generated for any other values of these parameters.

Under *choked* flow conditions, it has been shown that the flow behavior is determined by the nozzle geometric throat where $\beta = 0$. Equations (4) and (6) can be combined to yield the following equation for choked conditions:

$$\frac{w_2 \sqrt{T_{02}}}{w_1 \sqrt{T_{01}}} = \left(\frac{k_2}{k_1}\frac{p_{02}}{p_{01}}\right) \left\{ \frac{k_1 - 1}{2} \left[\left(\frac{p}{p_{01}}\right)^{\frac{1-k_1}{k_1}} - 1 \right]^{-1} - 1 \right\} \times \left(\frac{p}{p_{02}}\right)^{\frac{1}{k_2}} \sqrt{\frac{2}{R_2} \left(\frac{k_2}{k_2 - 1}\right) \left[1 - \left(\frac{p}{p_{02}}\right)^{\frac{k_2-1}{k_2}} \right]} \div \left\{ 1 - \frac{k_2 - 1}{2} \left[\left(\frac{p}{p_{02}}\right)^{\frac{1-k_2}{k_2}} - 1 \right]^{-1} \right\} \times \left(\frac{p}{p_{01}}\right)^{\frac{1}{k_1}} \sqrt{\frac{2}{R_1} \left(\frac{k_1}{k_1 - 1}\right) \left[1 - \left(\frac{p}{p_{01}}\right)^{\frac{k_1-1}{k_1}} \right]} \quad (16)$$

Equations (14) and (16) may be simultaneously solved, by trial-and-error, to determine the relationship between p_{02}/p_{01}, $w_2\sqrt{T_{02}}/w_1\sqrt{T_{01}}$, A_1^*/A_{throat} and p_{throat}/p_{01} at choking for any given gas properties. The relationship between p_{02}/p_{01}, $w_2\sqrt{T_{02}}/w_1\sqrt{T_{01}}$, and A_1^*/A_{throat} is shown in Fig. 5. It can be seen that, for any given value of $w_2\sqrt{T_{02}}/w_1\sqrt{T_{01}}$, there is a unique p_{02}/p_{01} corresponding to each A_1^*/A_{throat}. These values appear as horizontal lines in Fig. 4 because the back pressure does not affect the choked solution.

Referring to Fig. 4 for any given combination of A_1^*/A_{exit} and A_1^*/A_{throat} in a single nozzle, the *intersection* of the corresponding lines indicates the onset of choking (curve c in Fig. 2). For values of p_{02}/p_{01} smaller than that at the intersection, the flow behavior is given by the unchoked curve. For values of p_{02}/p_∞ greater than that at the intersection, the flow behavior is given by the choked straight line. *Therefore, the entire flow behavior of a compound-compressible nozzle can be described by a single line.* For example, the dashed line in Fig. 4 represents a nozzle with $A_1^*/A_{throat} = 0.431$ and $A_1^*/A_{exit} = 0.226$. (These are the actual dimensions of the test model described in the experimental section of this paper.)

The behavior of M_1 and M_2 at the throat for choked flow as a function of $w_2\sqrt{T_{02}}/w_1\sqrt{T_{01}}$ and fixed A_1^*/A_{throat} and gas properties is shown in Fig. 6. *Note that neither stream is sonic at the nozzle throat.*

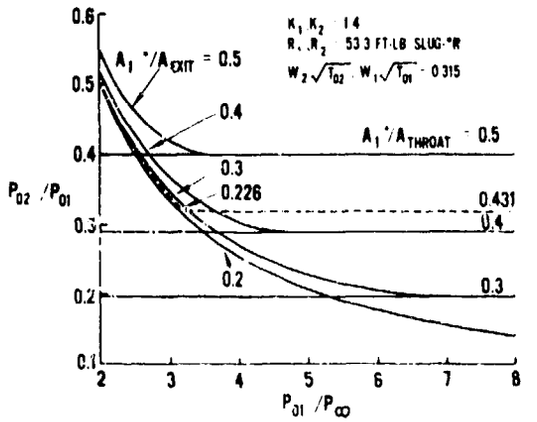

Fig. 4 Typical relationship of flow parameters in a convergent-divergent nozzle

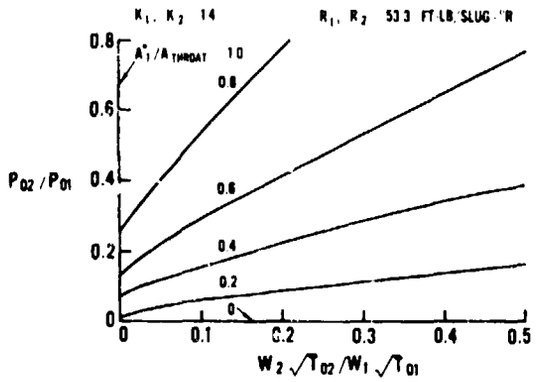

Fig. 5 Relationship of flow parameters during choked flow

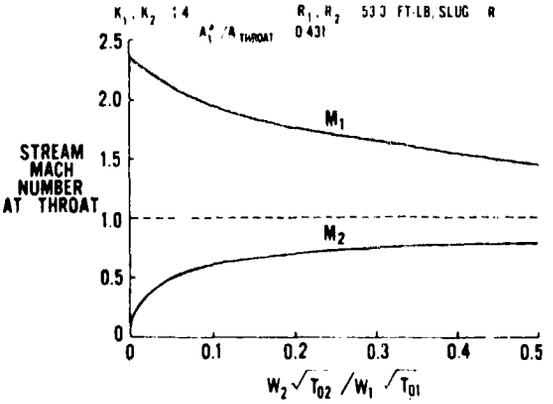

Fig. 6 Stream Mach numbers at the nozzle throat during choked flow

Additionally, it is important to note here that the solutions presented previously are independent of the individual flow areas at the inlet plane. In practice, however, it is possible for these areas, if not properly designed, to cause large three-dimensional effects at the inlet plane, due, for example, to independent choking of the primary stream. Nevertheless, it is still either the nozzle exit area or geometric throat, *not the inlet areas*, which will control the flow behavior. Thus, even if these three-dimensional effects cause stagnation pressure losses at the inlet plane, the theory still gives the correct solution provided that p_{01} and p_{02} are measured downstream of the loss. In any case, this situation can be avoided by designing the proper flow areas for the inlet plane. This can easily be done by solving equations (1) and (5) simultaneously at the inlet plane for the flow parameters corresponding to the one-dimensional solution.

The procedures outlined in this section are particularly suited to problems where $w_2\sqrt{T_{02}}/w_1\sqrt{T_{01}}$ is specified. However, the theory can be applied equally as well to generate solutions for any suitable set of given conditions. The methods presented here may also be extended to cases of more than two flows.

Three-Dimensional Two-Stream Nozzle Computer Calculations

One of the basic assumptions of the one-dimensional theory is that the effects of streamline curvature are small enough to be neglected. This can be an important restriction in the application of the theory to actual nozzles. Therefore, to demonstrate the effect of such curvatures, a three-dimensional two-stream nozzle solution will be compared with the one-dimensional theory. To do this, an axially symmetric two-flow nozzle computation was carried out. A brief description of the computation is given here to justify its use in evaluating the one-dimensional theory.

The basic idea behind this calculation can best be understood by recalling that the curves in Fig. 2 were obtained by an integration of equation (3) through the nozzle. Here a numerical integration includes three-dimensional effects.

Some important assumptions are made about the flow before this solution is applied; namely,

1 The system must be symmetrical with respect to its center line.

2 The two flows are isentropic and do not mix but are in contact along a slipline.

3 The static pressure is free to vary *along* the slipline but must be equal across it at every point.

4 The primary, or inner, stream must be everywhere supersonic while the secondary, or outer, stream is not restricted. This allows a method of characteristics to be used for the primary stream calculations.

For any one problem, the temperature-corrected mass flow ratio, the ratio of specific heats for each stream, the gas constant for each stream, the coordinates of the wall shape, and the primary stream inlet Mach number are considered to be specified.

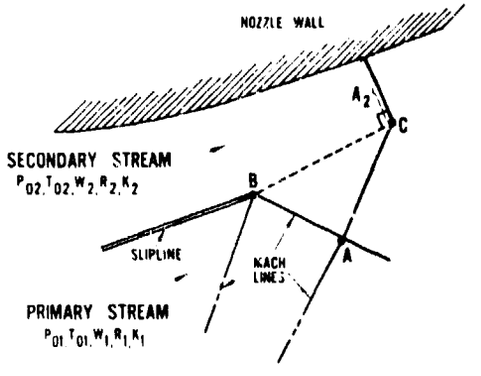

Fig. 7 Construction of a typical slipline point in three-dimensional flow

The flow field of the primary stream is constructed using standard numerical forms of the method of characteristics equations for axially symmetric flow. The secondary stream is calculated using one-dimensional, isentropic flow relations. The flow areas of the secondary stream are measured along a projection normal to the slipline, Fig. 7. The assumption that this flow is one-dimensional and has no streamline curvature effects is not a serious restriction. It should be noted that the secondary flow passage occupies only a small portion of the total radius at any section (relatively small mass flow rates and annular geometry). Therefore, the streamline curvature effects are small compared to those of the primary stream, where they have been accounted for.

The secondary and the primary streams meet along the slipline. The calculation of a succession of points along this slipline involves an iteration procedure incorporating the calculations of the flow properties of each stream simultaneously, Fig. 7. Point C illustrates a typical slipline point to be calculated. Point B, the previous slipline point, and point A, the previous point on Mach lines A-B and A-C, are known. The conditions of point C are that it be on the Mach line A-C and that the static pressure at C be the same in the primary and secondary streams. These conditions are satisfied through a trial-and-error solution involving the location of point C.

As was noted, the program is performing a numerical integration equivalent to the integration of equation (3). For any set of given conditions, the results can be presented in terms of the p_{02}/p_{01} required to drive the flow. A reduction in p_{02}/p_{01} corresponds to operation at a decreased back pressure p_a. The term p_a will correspondingly decrease until p_{02}/p_{01} reaches a minimum value. Any value below this minimum will cause the slipline iteration to converge on a secondary area ratio, $A_2/A_2^* < 1$, which is physically meaningless. This minimum value of p_{02}/p_{01} corresponds to choked flow. All values of p_{02}/p_{01} greater than the minimum value correspond to unchoked flow. In short, the three-dimensional solution closely parallels the one-dimensional solution, Fig. 4.

The three-dimensional computation for both choked and unchoked flows usually presents little difficulty, and the integration through the geometric throat is generally smooth. Difficulties may arise when the accelerating secondary stream approaches Mach 1. This is due to the usual mathematical sensitivities encountered in computing one-dimensional flow properties near Mach 1. However, the transition through this region can be made by special techniques.

This study was undertaken to find the effects of streamline curvature on the behavior of a compound nozzle. The first calculations were performed with geometry corresponding to the basic nozzle used for the experimental portion of this paper. The flow fields in these cases showed definite three-dimensional behavior, especially in the initial expansion region. However, the calculations showed *no important coalescing of Mach lines, so that the isentropic assumption was essentially valid.*

To further study three-dimensional effects, the nozzle geometry was modified. A series of nozzle shapes was generated by applying a scale factor to only the axial coordinates of the basic nozzle. The resultant series then consisted of nozzles which were identical one-dimensionally but had severe variation in the slopes of the contour. These geometries are shown in Fig. 8.

The results from this series of computations are presented in Fig. 9. Curves a and b demonstrate the compound-choked flow regime. The term p_{02}/p_{01} is plotted versus L_{throat}/D_{throat}, the length from the inlet to the throat divided by the diameter of the throat. Notice that for both curves the agreement with one-dimensional results is excellent for relatively large L_{throat}/D_{throat} ratios. For the smaller values of L_{throat}/D_{throat}, the three-dimensional effects influence p_a/p_{01}. This is not surprising since in this range the nozzle contour slopes are most severe. Also, the nozzle throat is close enough to the inlet to be in the influence in the initial expansion of the primary stream.

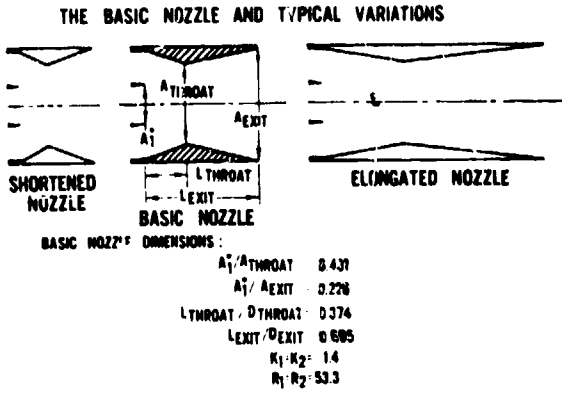

Fig. 8 Nozzles used in three-dimensional comparison

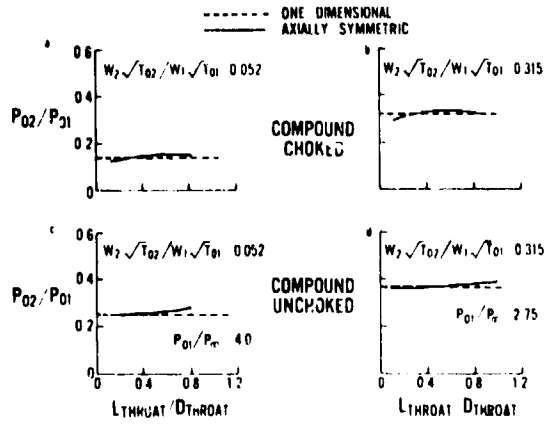

Fig. 9 Comparison of one-dimensional and three-dimensional results

Curves c and d demonstrate the compound-unchoked flow regime. Again, agreement with the one-dimensional results is excellent. The discrepancies for short nozzles are not so pronounced here since the exit conditions, and not the throat conditions, are dominant. Some departure from the one-dimensional line is seen for the longer nozzles. It is felt that this may be due to accumulating inaccuracies resulting from the finite difference techniques used. For long nozzles, these errors may become significant by the time the exit plane is reached.

The agreement between the one-dimensional and the axially symmetric solutions is excellent for the range of nozzle variation examined. Three-dimensional effects have little influence on the level of p_{02}/p_{01} for the nozzle geometries considered.

Experimental Results

Extensive test programs conducted on a wide variety of nozzle types and geometries have shown excellent agreement between the one-dimensional compound-flow theory and experimental results. These test programs have included convergent, cylindrical, and convergent-divergent nozzles with both two and three streams.

The success of the one-dimensional theory is not surprising. The previous section indicated that the behavior of compound flow nozzles is reasonably insensitive to three-dimensional effects. For nozzles with small wall frictional effects, and fairly undistorted inlet flow, only the effects of mixing can cause the one-dimensional model to be inaccurate when applied to real nozzles. It is reasonable to assume that, since the flow is turbulent, mixing is confined to a shear layer between adjacent streams which grows with axial position at an angle of less than 8 deg [3]. It is therefore clear that the shapes of the A_i^* and the nozzle length are the major factors which determine the degree of mixing. The tendency of the mixing will be to pump the low-velocity streams and

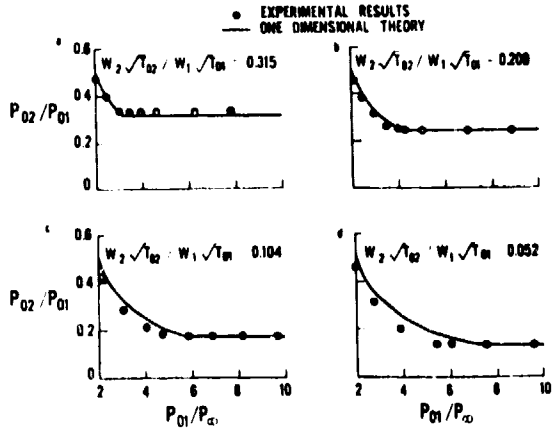

Fig. 10 Comparison of compound-compressible flow theory with experimental results

to retard the high-velocity streams. The extent of the influence of mixing depends primarily on the flow rates of each stream. The behavior of streams with proportionately low rates will be greatly affected by mixing while those with higher flow rates will experience only small effects. *Note, however, that in the important case of choked flow, mixing effects downstream of the nozzle throat can exert no influence whatsoever upon the behavior of the flow.* Thus, for many nozzle applications, mixing will influence only a small portion of the flow.

Because of the space limitations of this paper, a fully comprehensive comparison of one-dimensional theory with experimental data from a wide variety of compound-flow nozzle types and geometries is impractical. Accordingly, the basic nozzle previously discussed was selected for comparison. Being convergent-divergent, it is a representative two-stream nozzle in that it can display both the choked and unchoked regimes of compound flow.

Tests were run over a wide range of temperature-corrected mass flow ratios while varying p_{01}/p_∞ from approximately 2 to 10. This allowed the nozzle to exhibit both choked and unchoked behavior at each mass flow ratio. Fig. 10 is a comparison of experimental results with predictions based upon the one-dimensional compound-flow theory. The choked flow regime is the straight portion of the theoretical lines and, as expected, occurs at the higher p_{01}/p_∞. The unchoked flow regime is the curved portion of the lines which occurs at the lower primary nozzle stagnation pressure ratios.

It can be seen that the one-dimensional theory shows excellent agreement with the experimental data, particularly in the choked flow regime. Correlation with experimental data in the unchoked flow regime is somewhat less accurate. However, in view of the mixing effects previously discussed, this was to be expected. During choked flow, all mixing downstream of the nozzle throat can have no effect on the flow. Thus the effective mixing length for choked flow is merely the distance from the inlet plane to the throat. On the other hand, during unchoked flow, all mixing downstream of the nozzle throat will have a very definite effect on the flow behavior. With unchoked flow, then, the effective mixing length is the entire length of the nozzle.

As anticipated, we also observe that mixing has little effect at the higher mass flow ratios but exerts increasing influence as mass flow ratio decreases. Furthermore, the important effect of mixing is to pump the secondary flow and therefore reduce the required p_{02}/p_{01}.

It is noted that the model tested was not an ideally designed nozzle; i.e., the primary stream was independently choked and slightly underexpanded at the inlet plane. However, the model used in the experiments was operated sufficiently near to its isentropic design conditions that stagnation pressure losses in the supersonic stream were probably not important, and shock losses

are impossible in the subsonic secondary stream. This was indicated in the previous section, where the three-dimensional solution showed no significant coalescing of the primary stream Mach lines under conditions for which the tests were run. Although p_{01}/p_{02} is measured upstream of the inlet plane, these arguments justify our neglect of total pressure losses in all calculations.

Concluding Remarks

A new one-dimensional theory describing the behavior of compound-compressible nozzle flows has been developed and its implications have been examined from a number of viewpoints.

The theory yields simple algebraic methods for calculating the operation of compound-compressible nozzles. Comparison of the algebraic results with those of three-dimensional flow field computations indicates that the effects of streamline curvature are not important for many practical nozzle configurations. Comparison of the algebraic results with experimental data for flows with unimportant mixing effects shows that the theory can accurately predict the behavior of real devices.

A complete definition of the range of applicability of the simple theory requires a great deal of experimental experience. For example, little information is available about the rate of growth of the mixing zone between the high-velocity streams, and no information is available about the detailed nature of compound-shock waves. Furthermore, no predictions about the thrust or nozzle efficiency can be made when the flow is choked until the losses caused by a compound-shock wave are known. Consequently, it appears that the compound-compressible nozzle provides a number of interesting and important areas of research.

References

1 Pearson, H., Holliday, J. B., and Smith, S. F., "A Theory of the Cylindrical Ejector Supersonic Propelling Nozzle," *Journal of the Royal Aeronautical Society*, London, Section 62, 1958, p. 746.

2 Shapiro, A. H., *The Dynamics and Thermodynamics of Compressible Fluid Flow*, Ronald Press Co., New York, 1953.

3 Schlichting, H., *Boundary Layer Theory*, 4th ed., McGraw-Hill, New York, 1960, pp. 598–600.

COAXIAL DUMP COMBUSTOR INVESTIGATIONS

by

R. R. Craig, J. E. Drewry and F. D. Stull
Air Force Aero Propulsion Laboratory
Ramjet Technology Branch
Wright-Patterson AFB, Ohio

AD P003921

An experimental investigation was conducted involving coaxial dump combustors with two different types of flameholders (annular and Y) installed at the dump station in an attempt to correlate combustor performance with previous non-reacting flowfield results. Flameholder blockage, combustor length, exit area ratio, inlet temperature, and chamber pressure were varied for both wall injection and premixed fuel conditions. Lean blowout limits, combustion efficiency, combustor total pressure drop, and wall static pressure distributions were obtained from these runs using JP-4 fuel. In addition, a limited amount of surface heating patterns and combustion oscillation data were obtained.

This work was performed under AFAPL Work Unit No. 2308S101 in 1978.

COAXIAL DUMP COMBUSTOR INVESTIGATIONS

R. R. Craig, J. E. Drewry and F. D. Stull
Air Force Aero Propulsion Laboratory
Ramjet Technology Branch
Wright-Patterson AFB, Ohio

Abstract

An experimental investigation was conducted involving coaxial dump combustors with two different types of flameholders (annular and Y) installed at the dump station in an attempt to correlate combustor performance with previous non-reacting flowfield results. Flameholder blockage, combustor length, exit area ratio, inlet temperature, and chamber pressure were varied for both wall injection and premixed fuel conditions. Lean blowout limits, combustion efficiency, combustor total pressure drop, and wall static pressure distributions were obtained from these runs using JP-4 fuel. In addition, a limited amount of surface heating patterns and combustion oscillation data were obtained.

I. Introduction

Current volume limited ramjet missile designs employ dump combustors. In this engine system, the booster rocket is integrated into the ramjet combustor to conserve missile volume. Such combustors do not contain combustor liners or conventional flameholders within the combustion region and must depend to a large extent upon recirculation zones formed by the sudden enlargement area between the inlet duct and the combustor chamber.

Several previous studies[1-4] have been conducted at the Air Force Aero Propulsion Laboratory on coaxial dump combustors. Reference 1 dealt with the scaling of small dump combustors (2" to 5" D) with a baseline dump area ratio, A_2/A_3, of 0.25 and exhaust area ratio, A^*/A_3, of 0.50 using both JP-4 and Shelldyne fuel. This study showed that combustor length-to-diameter ratio, L/D, greater than 4.5 were required to obtain good combustion efficiency, η_c. Reference 2 considered the addition of flameholders to the inlet duct of the 5" D dump combustor and evaluated several basic flameholder configurations including the Y type. Increases of up to 30 counts in η_c were obtained when the best flameholder was added to the basic dump combustor with L/D = 3. Reference 3 extended the small scale combustor results, with and without flameholders, to a 12" D combustor and indicated that combustor performance with a flameholder does not appear to scale. The larger combustor achieved higher combustion efficiencies for equivalent flameholder blockage. Reference 4 presents basic detailed cold flowfield data and flow visualization results conducted in the Building 450 combustion research tunnel using a 1.84" D coaxial dump combustor with a dump area ratio of 0.42 and an exit area ratio of 0.42, including both Y type and annular flameholders. Gas concentration measurements of simulated fuel (argon)/air mixing were made in the combustor duct using a unique on-line, real time gas sampling system which helped formulate a cold flowfield model.

The objective of this current effort was to extend the previous combustion studies[1-3] to include the baseline geometry of the cold flow study[4] in an attempt to correlate combustor performance with non-reacting flowfield results. It was also desired to compare the symmetrical annular flameholder, which had looked promising in the cold flow study, to the basic Y type flameholder used in the previous combustion studies.

II. Experimental Procedure

Combustor Models

The combustor test hardware, as illustrated schematically in Fig. 1, was similar to the hardware used in previous test programs[1-3] except for actual size. It was fabricated from 6" ID stainless steel pipe and flanged at both ends. Additional length combustor sections were available which allowed for three combustor length variations of 6, 12, and 18 inches. A water cooled nozzle, 3 inches in length and with a throat diameter of 3.79 inches, was used to approximately match the $A^*/A_3 = 0.42$ ratio used in the previous cold flowfield tests.[4]

Fuel injection occurred normal to the air stream through 8 equally spaced .055" ID fixed-orifice wall injectors located 4 3/4 inches upstream of the inlet duct exit. These injectors were designed from previous fuel injection studies[5] to provide for fuel penetration of 16 percent of the inlet diameter by the time the fuel reached the dump plane at a fuel-to-air ratio of .06 and baseline pressure conditions. Another mode of fuel injection was employed in order to simulate a premixed fuel-to-air mixture. This was done by injecting fuel into the air stream approximately 5 feet upstream of the wall injectors by means of 8 radial fingers, each having 4 spray holes. Both sets of fuel injectors had their own fuel manifold system so that tests could be conducted consecutively by merely switching a toggle switch. The inlet duct, which was 8 feet long, was fabricated from 4" ID stainless steel pipe and flanged at both ends.

Flameholder Models

The Y type flameholder was the same design as employed in Ref. 3 and is shown in Fig. 2. Three webs, consisting of strip of stainless steel bent to form an angle of 60°, were mounted from the inlet duct wall and circumferentially distributed every 120°. The base of the flameholder was in the same plane as the sudden expansion. Flameholder blockage was varied by

changing the length of the V-gutter elements. The width of the flameholder web, which was 7/8 inch, was chosen so that the flameholder would be operating well within its DeZubay stability loop for all operating conditions.

The annular wedge flameholder was the same design as employed in Ref. 4 and is also shown in Fig. 2. The annular wedge was attached to the wall by four thin rods spaced 90° apart in order to try to preserve the coaxial symmetry, rather than trying to promote interaction between the flameholder and dump region. Flameholder blockage was varied by increasing the width of the annular wedge. Nominal blockages of 25 and 35 percent were tested for both types of flameholders.

Test Rig

The combustor hardware was mounted in the Room 18 combustor thrust rig designed for measuring absolute levels of thrust. The movable deck of the thrust stand is 14 feet in length and 4 feet wide. The deck is suspended from 4 flexures 15 inches long, 4 inches wide and .036 inch thick. Static calibration of the thrust stand load cell was accomplished by applying a force at the combustor centerline through a referenced load cell. Additional calibration was accomplished prior to each combustion test as described in a following section. High pressure air was supplied from the laboratory's compressors through twelve flex hoses (2" ID) to a J-85 combustor which was modified to be used as a vitiating heater burning ethylene. Makeup oxygen was added considerably upstream of the J-85. Air flow rates were measured with flange tap, square edge orifice plates, whereas turbine type flowmeters were used for measuring fuel and oxygen flow rates to the vitiating heater and fuel flow rates to the combustor. The nozzle of the combustor model was connected to the laboratory's exhauster system by means of a flexible rolling seal, so that a choked nozzle was maintained under all combustor operating pressures. The exhaust system was maintained at approximately 3 psia.

Data Acquisition

Data was collected by means of a Mod Comp II computer controlled data acquisition system sampling at a rate of 5000 channels per second. Because of the large memory of the computer, 64K words, the computer programs were written to collect and store the raw data on magnetic disc as well as computing and displaying, on a video screen, all required facility parameters. The programs also compute and display combustor temperature based on the thrust measurement, combustion efficiency, burner pressure loss and various other parameters as the test is being conducted. Each data point is the average of 45 separate scans of the data channels in order to average out any electrical noise in the data system. At the end of each fuel-to-air ratio traverse, selected data is listed on a Tektronix 4012 graphics display terminal. After a hard copy of this data has been made, plots of combustion efficiency versus fuel-to-air ratio and pressure loss versus stream thrust parameter are made on the graphics terminal. These are copied and the next series of test conditions established. At the end of the day, a standard computer printout is made of all the raw data and computed data.

The value of the computer system lies not only in its ability to collect and analyze large amounts of data, but also in its ability to compute rapidly certain critical parameters which tell the test engineer that all of the instrumentation is working properly. Before each test, the no air flow, pressure-area drags induced by the exhauster system are computed and compared with the thrust stand reading. If these values are within the larger of 2 lbs or 1/2%, airflow is begun. After air flow has been established, air temperature is computed from the thrust measurement and compared with the inlet air thermocouple reading. The same procedure is followed after the vitiating heater is ignited and the computed and measured temperatures must agree within ±2% before beginning the combustion tests.

Combustor Performance Calculations

The definition of combustion efficiency used throughout this paper is:

$$\eta_c = \frac{\Delta T_t}{\Delta T_{ti}}$$

where ΔT_t is the total temperature rise across the combustor as computed from the thrust measurement and ΔT_{ti} is the ideal total temperature rise for the measured fuel-to-air ratio as computed from equilibrium chemistry calculations. Since absolute thrust was measured, corrections for ambient pressure acting on the hardware and exhauster seal forces were made in order to obtain the sonic air specific stream thrust, S_a^*, see Ref. 3. A matrix of 240 values of S_a^* versus T_{t5} and P_{t5} was computed by means of equilibrium chemistry routines. These data were then input to a linear regression program to obtain a curve fit of S_a^* as a function of various combinations of T_{T5} and P_{T5}. These curve fits matched the input data within ±1% at all points. These curve fits were then used to determine T_{T5} from S_a^* and P_c.

Combustor total pressure ratios, P_{T5}/P_{T2}, are determined from measured static pressures, mass flows and thrust rather than from total pressure rakes. This method has been found to be more reliable and consistant than using total pressure probes. The combustor inlet total pressure, P_{T2}, is computed from the measured inlet static pressure, mass flow and total inlet temperature. The total pressure at the nozzle exit, P_{T5}, is computed from the throat area and the combustor total temperature as calculated from the measured thrust.

III. Discussion & Results

Baseline Combustor Tests

The 6" D baseline combustor was chosen so as to approximate the geometry of the cold flow combustor tested in the Building 450 combustor research tunnel. Table I shows a comparison

between the two combustors. Baseline test conditions were selected which approximated the "pressure scaling" criteria of PD = 200 used in the previous combustor studies.[3] Two different types of flameholders, each with blockages of 25 and 35 percent, were then added to the dump plane of the baseline combustor and tested. Inlet air temperature, T_{02}, was held constant at around 1000°R. Fuel-to-air ratios were selected to cover the range from .025 to .06. Both modes of fuel injection, from the wall and premixed, were tested under baseline conditions. Additional runs were made at T_{02} = 1300°R for each of the flameholder configurations with wall injection only. Changes from the baseline combustor L/D were made by using shorter combustor sections resulting in lower combustion efficiencies, thereby amplifying any difference in the effectiveness of the flameholders. A matrix of the tests conducted is shown in Table 2. Combustor performance results are shown in Figs. 3 thru 9. For purposes of reference, it should be noted that the value of fuel-to-air ratio, f/a, corresponding to an equivalence ratio of 1 is .0677.

The combustor performance data shown in Fig. 3 was obtained for the baseline test geometry without flameholders. The significant influence of combustor length and fuel injection mode on combustion efficiency is apparent from these results. It should be mentioned that, for the test conditions at L/D = 1 with wall fuel injection, the ramburner would not sustain combustion.

The results shown in Figs. 4 and 5 are the parametric performance data for the baseline test geometry with flameholders. In Fig. 4 combustion efficiency is given as a function of combustor L/D and fuel injection mode for tests with the Y type flameholders at inlet air total temperatures of 1000°R and 1300°R. Similar results which were obtained for the baseline test geometry with the annular wedge flameholders are shown in Fig. 5. The overall influence of the various flameholders on combustor performance relative to that without any flameholder is obvious when comparing the results of Figs. 4 and 5 to those in Fig. 3. In the case of the Y type flameholder, the highest combustion efficiency was always obtained at the lowest fuel-to-air ratio, with an almost linear decrease in η_c occurring with increased f/a. Ramburner operation at L/D = 1 was possible with the Y type flameholder installed. However, as can be seen in Fig. 4, the performance for this case was not very good.

The performance results obtained using the annular wedge flameholders were markedly different from those obtained with the Y type devices, particularly at L/D = 1. Ramburner combustion efficiency, as a function of f/a, did not follow the same consistent trend observed with the Y type flameholders. In the tests with the annular flameholders, the total temperature of the inlet air had a more significant influence on combustor performance than was apparent with the other test configurations. The best overall ramburner combustion efficiencies for all test configurations were obtained using the annular flameholders with L/D = 3 and T_{02} = 1300°R. It also should be noted that at L/D = 3, the variation of η_c with f/a was very slight over the full range of ramburner operation with the annular flameholders installed. At the shorter combustor lengths of 6 and 12 inches (L/D equal to 1 and 2, respectively), the performance pattern became more erratic in nature, as demonstrated in Fig. 5 by the sudden changes in combustion efficiency during the f/a excursion. Highly oscillatory combustion was observed during some periods of operation. This phenomena will be discussed further in a later section.

In Figs. 6-8, comparative plots of ramburner performance results for the various test configurations are shown for each combustor L/D at T_{02} = 1000°R and 1300°R. In terms of flameholder geometry, the observed performance is inconclusive. Under some test conditions the annular wedge appears superior, while under others it is obviously inferior.

Chamber Pressure And Exit Area Ratio

Combustor pressure was decreased from baseline conditions by decreasing the air mass flow through the combustor by 50 percent. These results are shown in Fig. 9 for the 0.25-Y and 0.25-AW flameholder combustors, resulting in measured chamber pressures of 15 to 16 psia and 14 to 15 psia respectively. Under these conditions, the baseline combustor without a flameholder could not sustain combustion. When air mass flow was again decreased by 50 percent, corresponding to PD = 50, none of the combustor configurations could sustain combustion. Figure 9 shows a significant decrease in η_c as chamber pressure is decreased for both types of flameholders. Previous results with a 12" D combustor showed small differences in combustion efficiency when chamber pressure was reduced from 16 to 10 psia, thereby indicating that it is not the absolute pressure level in the combustor that is the controlling parameter, but rather pressure times diameter (PD).

The effect of increasing nozzle throat diameter, D*, from 3.79 inches to 4.25 inches produced no appreciable change in performance for the 0.25-Y flameholder. However, in the case of the 0.25-AW flameholder, a significant increase in performance was measured with the larger D*. The reason for the sudden decrease in η_c at the highest value of f/a for this test condition is not presently clear.

Other Factors

In addition to the above parametric combustor tests, a few exploratory tests were conducted on other variations. In order to assure that hysteresis effects were not prevalent during a combustor run over a full fuel-to-air ratio excursion, two separate runs were conducted on the baseline configurations (no FH, 0.25-Y and 0.25-AW) with fuel-to-air ratio increasing in one run, and fuel-to-air ratio decreasing in the second run. Less than a 2 to 3 count change in combustion efficiency was noted for all test cases. Subsequently, for the rest of the test program only one run was conducted. It was

decided to use a decreasing fuel-to-air ratio in order to avoid a cold combustor wall temperature near the lean-blow out limits, where wall temperature effects were expected to be the greatest.

Likewise, a few variations in inlet diameter, D_2, were run with the baseline 0.25-Y flameholder combustor to observe the effects of dump area ratio. Performance was increased about 10 counts over most of the f/a range covered when the baseline A_2/A_3 was decreased from 0.44 to 0.35. Decreasing A_2/A_3 still further to 0.25 resulted in a slight combustion efficiency improvement, but only over the middle f/a range. This trend is in agreement with previous small scale combustor tests ($D_3 \leq 6"$), but is contrary to results obtained with larger scale combustor tests ($D_3 = 12"$). Apparently, the dump area ratio for optimum performance does not follow "PD scaling criteria."

The lean blow-out data was in general agreement with the previous combustor studies, occurring at $f/a \leq .015$ for the wall injection mode and at $f/a \sim .044$ for the premixed mode (slightly higher than $f/a \sim .035$ reported in Ref. 2). The addition of flameholders did not appear to change the lean blow-out limit, but did introduce considerably more scatter ($.040 \leq f/a \leq .048$) into the data for the premixed mode.

Combustor Pressure Losses

Combustor total pressure losses were not measured directly with a total pressure rake because of the difficulty in obtaining a representative mass averaged total pressure in a reacting combustor with unsteady flow and large recirculation zones. Only when the combustor is very long so that the flow has time to reattach itself to the wall and become established, can reasonable pressure measurements be made with a water-cooled pressure rake. Instead, combustor pressure recovery, P_{T5}/P_{T2}, was determined from measured inlet static pressure, mass flow, and thrust as described in Section II.

Figure 10 shows these results for the baseline combustors at 1300°R plotted against the heat addition parameter, $S_4^*/\sqrt{T_{02}}$, which is the sonic stream thrust divided by the square root of inlet total temperature. For a constant area combustor, pressure recovery will decrease as heat addition increases. However, for the dump combustor, pressure losses are a combination of aerodynamic losses, including the sudden expansion loss, plus heat addition losses. As heat addition increases, inlet Mach number decreases and the reduced aerodynamic losses overshadow the increased heat addition losses; hence, combustor pressure recovery increases. This is evident in Fig. 10 with the largest flameholder blockages (35%) having the steepest slope due to larger aerodynamic losses. For the baseline combustor without flameholder, the aerodynamic losses were only slightly greater than the heat addition losses, hence these losses tend to cancel each other and pressure recovery remains relatively constant over the range of fuel-to-air ratios tested. The data points on the far left hand side were obtained prior to combustion. Virtually no difference in pressure recovery was noted between the 25% blockage Y and annular flameholders. The 35% blockage annular flameholder showed a slightly greater pressure loss than did the 35% blockage Y flameholder.

Static Pressure Distributions

The baseline combustor (L/D = 3) contained wall static pressure taps every inch downstream of the dump plane. Data was recorded from each pressure transducer prior to a combustion run and during selected fuel-to-air ratios. A comparison of the baseline combustor with no flameholder and no combustion (f/a = 0) is made with similar cold flow test data from Ref. 4 and is shown in Fig. 11 as an axial static wall pressure distribution normalized by dump step height, h, where $h = (D_3-D_2)/2$. Although a slight difference in the absolute values are seen in the region near the dump, the characteristic shape of the curves are similar. This difference is attributed, in part, to the location where the inlet total pressure, P_{T2}, was measured in both experiments. The wall pressure plotted at x/D = 0 in the present tests was actually the inlet static pressure measured upstream of the wall fuel injectors and the flameholder. Also noted in this figure is the reattachment point, indicated by the dashed line L'/h, as determined from flow visualization techniques in the cold flow equipment.[4]

Figures 12 thru 14 show the axial static wall pressure distributions normalized by combustor diameter, D_3, for the baseline combustors at T_{02} = 1300°R for various fuel-to-air ratios, and are representative of the vast amount of static pressure data obtained. It is noted that without combustion (f/a = 0) the axial static wall pressure distributions characterize the type of flameholder employed and are very consistent and well defined. This is not true once combustion had occurred, as various patterns were observed. In some cases wall static pressure increased with distance downstream of the dump, and in other cases it decreased with length. In some cases the static pressure distribution was not appreciably affected by fuel-to-air ratio, and in others it was a strong function of fuel-to-air ratio. This is dramatically illustrated by the 25% annular flameholder in Fig. 14 where the only difference in test conditions was the inlet air temperature. The only general observation that could be made after looking at all of the wall static pressure data and the corresponding combustion efficiency curves was that very high combustion efficiencies tended to cause a decrease in wall static pressure with length, whereas poor combustion efficiencies tended to show an increase in wall static pressure with length. Likewise, when combustion efficiency was relatively constant over an entire f/a range, the wall static distribution tended not to show a large variation with f/a; however, this was not always true as exceptions were noted. Attempts to correlate a given axial wall static pressure to combustion efficiency were not too successful, as many apparent inconsistencies were noted. As an example, combustion efficiencies are tabulated in Table 3 corresponding to the fuel-to-air ratios shown in Figs. 12 thru 14.

From the above, it can be seen that caution must be exercised in attempting to define combustor performance from its static pressure distribution alone. This can have severe implications in attempting to design a ramjet control system based solely on a wall static pressure measurement, unless the combustor has been well characterized.

Surface Heating Patterns

Using bare wall stainless steel combustor models instead of water-cooled combustors allows one to obtain additional information in regards to what is happening within the combustor, and how the fuel injector/flameholder assembly is behaving. This is shown in Fig. 15 where photographs were taken of the hot combustor as viewed from the control room TV screen. Figure 15a shows the surface heating pattern for the 0.25-Y flameholder taken under the same test conditions as for the pressure distribution data previously shown in Fig. 13. Large circumferential temperature gradients are noted near the dump end of the combustor due to the unsymmetrical pattern of the Y flameholder. Surface temperature in the lightest regions, corresponding to wake regions from the flameholder struts, approached 1500°F as determined from other test programs in which thermocouples had been attached to the combustor wall. When uniform fuel injection was employed, the surface heating pattern became somewhat more uniform, although variations caused by the wake of the three flameholder struts could still be observed. One of the virtues in observing surface heating patterns is that it tells where to locate thermocouples in order to obtain the maximum amount of quantative heat transfer data with a limited number of thermocouples. This is especially valuable in relating to ramburner thermal protection investigations.

Figure 15b shows that a more uniform heating pattern is obtained with the 25% annular flameholder, although some circumferential variations are seen which correspond to the location of the four support struts which held the annular wedge in place.

Combustor Pressure Oscillations

During many of the combustion runs, an audible screech could be heard over a portion of the f/a range. A close coupled, high frequency response Kistler pressure transducer was attached to the front combustor flange to detect any unusually large pressure oscillations occurring. Output of the transducer was connected to a Tektronix oscilloscope to determine the amplitude of the pressure fluctuations and then to a fast Fourier transform spectral analyzer to determine the dominant frequencies. In general, two distinct types of oscillation were detected during the test series: (1) a low frequency oscillation on the order to 200 Hz with peak to peak amplitudes as high as 100% of the average chamber pressure, and (2) high frequency oscillations between 2500 and 5000Hz with peak to peak pressure fluctuations as much as 50 percent of the average chamber pressure. It was these latter frequencies which could be heard as combustor screech during some of the runs. Figure 16 shows examples of these types of oscillations detected while running the 25% annular flameholder under similar flow conditions at inlet air temperatures of 1000°R. Figure 16a is for the baseline (L/D = 3) combustor whereas Fig. 16b is for the short (L/D = 1) combustor. The change in combustor length alone was responsible for changing the pressure oscillations from the low frequencies to the high frequency screech. This may help to explain the peculiar nature of some of the combustion efficiency data noted earlier for the short combustor with the annular flameholder. Although the low frequency oscillations do not seem to have any significant effect on combustion efficiency, the high frequency oscillations can have a significant effect in increasing combustor efficiency by drastically altering the combustor flowfield. This effect was noted in a previous in-house combustor experiment in which high speed movies were taken of a 6 inch quartz dump combustor (A_2/A_3 = 0.25) in an attempt to observe the nature of the reacting flowfield. As the f/a was increased from .035 to .04 a drastic change in the entire flame pattern was observed and at the same time combustor screech was heard with subsequent breakage of the quartz chamber. Unfortunately, high frequency instrumentation was not used during that experiment, hence the combustor oscillations at that instant were not recorded. The high speed movies also illustrated the unsteadiness of the flame fronts both with and without high frequency combustor oscillations.

Some naive attempts were made to characterize the present oscillations as longitudinal, transverse, or radial waves based on the fundamental frequencies associated with a closed cylindrical vessel. These attempts were unsuccessful. For the low frequency instabilities, it was assumed that the sonic nozzle was one of the reflecting surfaces. The distance to the other reflecting surface was then computed assuming the measured frequency was the first harmonic. The required distance turned out to be midway in the inlet duct and thus incompatible with the requirements for a reflecting surface. The low frequency oscillations seem to be associated with the shedding of a ring vortex off the surface of the inlet duct at the dump station of the combustor. This frequency seemed to be independent of whether or not there was a flameholder in the inlet duct. In fact, using the Strouhal number of 0.21 for cylinders with a body diameter of 6 inches yields frequencies remarkably close to the measured values. However, in the absence of combustion, one would also expect to find some shedding frequency. Although the nonburning pressure oscillations were only 3 percent of the average chamber pressure, there was a measurable, predominant frequency which turned out to be 2 1/2 times the calculated shedding frequency.

The high frequency screech of the annular flameholder, at times, was also of the same frequency as predicted for vortex shedding off its base region. However, the oscillations can be just as easily identified as the first tangential, first radial, or second tangential modes of oscillation depending on what one assumes for the effective speed of sound for the chamber.

Correlation to Cold Flow Results

As previously mentioned, a comprehensive series of cold flow dump combustor tests was conducted prior to the present effort. A direct correlation of cold flow mixing results with then available ramburner performance data was made in Ref. 4. The ramburner test results now being reported provide a more extensive and consistent set of data with which to correlate. In Ref. 4 a comparison between centerline concentration of simulated injected fuel and ramburner combustion efficiency was given as a function of combustor L/D for various test configurations. It was shown that the cold flow mixing results did, in fact, correlate quite well in terms of overall combustor performance for mixing-limited configurations.

Using the same basis of comparison as given in Ref. 4, it is possible to make predictions of ramburner performance via cold flow mixing data for each of the configurations tested in this effort. These performance estimates, along with the actual measured combustor performance data, are given in Table 4. The ramburner performance results are those obtained at f/a ~ .045 which was being simulated in the cold flow tests. As can be seen in Table 4 some of the performance predictions agree quite well with observed performance, while in other cases the agreement is not so good. One trend is clearly obvious; namely, that better overall agreement is obtained at the higher inlet air total temperature of 1300°R than at the lower value of 1000°R. This would seem to indicate that improved vaporization of the liquid JP-4 was occurring at the higher total temperature, thus resulting in a better simulation with respect to the wall injection and mixing of a gaseous fuel with cold flow air.

The performance correlations given in Table 4 certainly do not tell the complete story. For that one must look at results over the entire range of f/a. The onset of highly oscillatory combustion at some point in a given f/a excursion, which results in large increases in η_c, is certainly not predictable on the basis of cold flow results.

IV. Conclusions

The performance characteristics of the two types of flameholders were very different, with the Y type flameholders showing consistent trends of decreasing combustion efficiency with increasing f/a. On the other hand, the annular flameholder showed less sensitivity to f/a and L/D but a much greater dependency upon inlet air temperature. This suggests that a more effective flameholder could be designed by combining features of both types of flameholders; i.e., replacing the thin support rods of the annular wedge with the V-gutter webs of the Y type so as to promote interaction between the annular wedge and the dump region.

Conducting premixed and wall injection tests consecutively can provide some insight into the sensitivity of fuel penetration, atomization and vaporization effects on combustor performance. Such tests help to define the potential gains to be made by fine tuning the fuel injector assembly with a given flameholder configuration.

The use of wall static pressure distributions as the sole basis for predicting overall combustor behavior is not felt to be sufficient without additional supporting data.

Surface heating patterns, obtained by using bare wall combustors, can be of value in developing ramburner thermal protection systems. The patterns may also be useful in locating reattachment points if, for combusting flows, the point of maximum heat transfer corresponds to the flow reattachment point.

Adequate high frequency pressure instrumentation is essential for detecting the occurrence of combustor oscillations which can affect combustor performance and durability. Combustor screech has profound effects on combustor performance, but can also produce very high local heating rates which can be detrimental to the combustor chamber thermal protection system. Low frequency oscillations appear to have little influence on combustor performance or heating patterns, but could impact inlet stability margins.

Detailed cold flow mixing results are useful in designing combustors. If the fuel-air distribution is not well mixed at the exit of the combustor, there is no chance that the combustor will perform well. The converse, however, is not true. Actual combustor performance is strongly dependent on many additional variables.

References

1. Stull, F. D., Craig, R. R., and Hojnacki, J. T., "Dump Combustor Parametric Investigations," ASME Fluid Mechanics of Combustion, Joint Fluids Engineering and CSME Conference, Montreal, Quebec, May 13-15, 1974.

2. Stull, F. D. and Craig, R. R., "Investigation of Dump Combustors with Flameholders," AIAA Paper 75-165, AIAA 13th Aerospace Sciences Meeting, Pasadena, California, January 20-22, 1975.

3. Craig, R. R., Buckley, P. L., and Stull, F. D., "Large Scale Low Pressure Dump Combustor Performance," AIAA Paper 75-1303, AIAA/SAE 11th Propulsion Conference, Anaheim, California, September 29 - October 1, 1975.

4. Drewry, J. E., "Fluid Dynamic Characterization of Sudden-Expansion Ramjet Combustor Flowfields," AIAA Journal, Vol. 16, April 1978, pp. 313-319.

5. Hojnacki, J. T., "Ramjet Engine Fuel Injection Studies," AFAPL-TR-72-76, August 1972.

Table 1 Comparison of test models

	Cold Flow Model	Baseline Combustor
D_2 (in)	2.50	4.00
D_3 (in)	3.84	6.00
D* (in)	2.50	3.79
L_C (in)	15.1	18.0
L_N (in)	1.5	3.0
h (in)	0.67	1.0
Injector Orifice Diameter (in)	0.035	0.055
Dist. from Inj. to Dump (in)	2.5	4.75
L_C/D_3	3.93	3.00
L_{C+N}/D_3	4.32	3.50
A_2/A_3	0.42	0.44
A^*/A_3	0.42	0.40
M_{inlet}	0.70	0.54

Table 3 Tabulation of combustion efficiency

No Flameholder T_{02} = 1300°R		0.25-Y 1300°R		0.25-AW 1000°R		0.25-AW 1300°R	
Fig 12		Fig 13		Fig 14a		Fig 14b	
f/a	η_c	f/a	η_c	f/a	η_c	f/a	η_c
.031	.687	.027	.883	.026	.712	.026	.773
.041	.717	.037	.863	.061	.724	.041	.883
.060	.663	.045	.814			.058	.901
		.059	.754				

Table 4 Baseline combustor correlation of performance data at f/a ≈ 0.045

		Cold Flow Mixing Predictions		Ramburner Performance	
Configuration	L/D	$\eta_c/\eta_{c_{max}}$	η_c	$\eta_{c_{1000}}$	$\eta_{c_{1300}}$
No FH	3	0.90	0.81	0.58	0.70
	2	0.50	0.45	0.48	0.60
	1	0.00	0.00	--	--
0.25-Y	3	0.95	0.85	0.75	0.80
	2	0.85	0.76	0.62	0.75
	1	0.30	0.27	0.25	0.39
0.25-AW	3	1.00	0.90	0.73	0.89
	2	0.98	0.88	0.75	0.90
	1	0.55	0.49	0.55	0.80

Table 2 Matrix of test points

Flameholder →		None		0.25-Y		0.25-AW		0.35-Y		0.35-AW		$\frac{A^*}{A_3}$	$\dot{W}_{air}$
L/D	T_{02} →	1000	1300	1000	1300	1000	1300	1000	1300	1000	1300		(lb/sec)
3	Wall Inj.	X	X	X	X	X	X	X	X	X	X		
	Premix	X		X		X		X		X			
2	Wall Inj.	X	X	X	X	X	X	X	X	X	X	0.40	3.2
	Premix	X		*		*		X		X			
1	Wall Inj.	*	*	X	X	X	X	X	X	X	X		
	Premix	X		X		X		X		X			
3	Wall Inj.	X	X	X	X	X	X					0.50	3.2
	Premix	X		X		X							
3	Wall Inj.	*		X		X						0.40	1.6
	Premix												

* Would not sustain combustion.

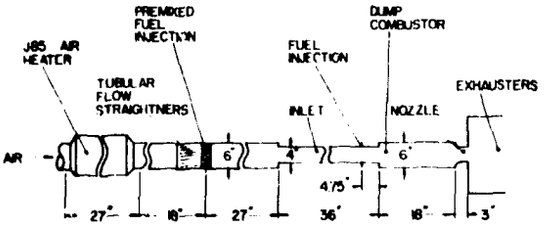

Fig. 1 Schematic illustration of AFAPL combustor thrust rig.

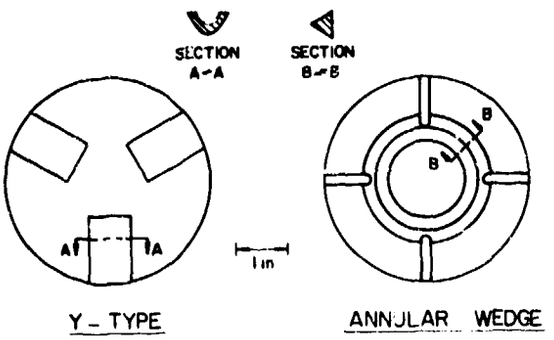

Fig. 2 Flameholder configurations.

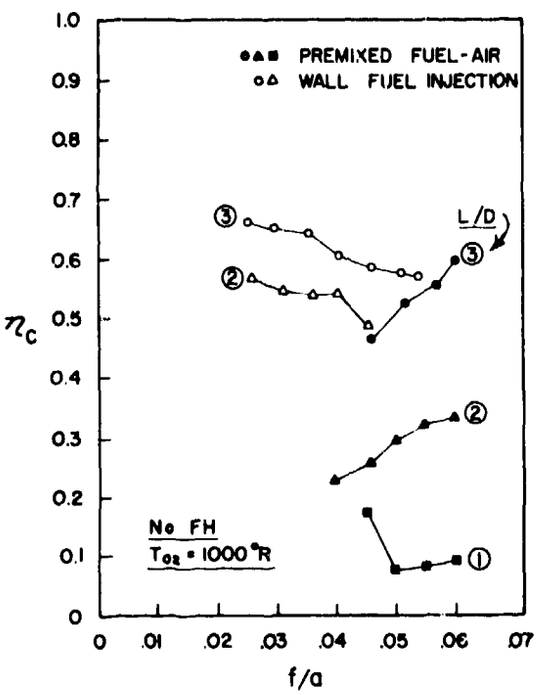

Fig. 3 Baseline combustor performance without flameholders.

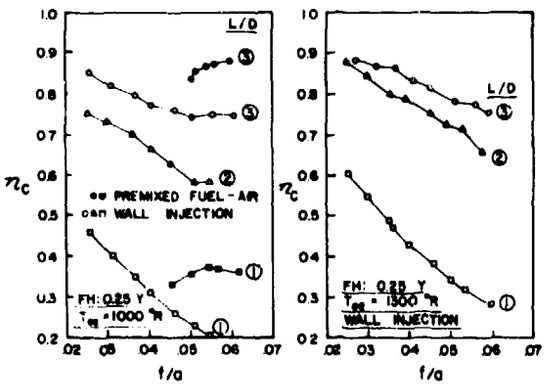

a. 25% blockage.

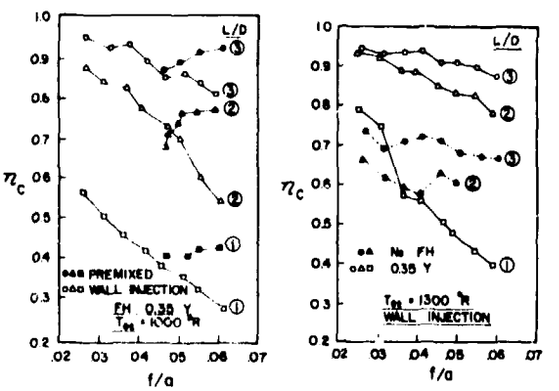

b. 35% blockage.

Fig. 4 Baseline combustor performance with Y type flameholders.

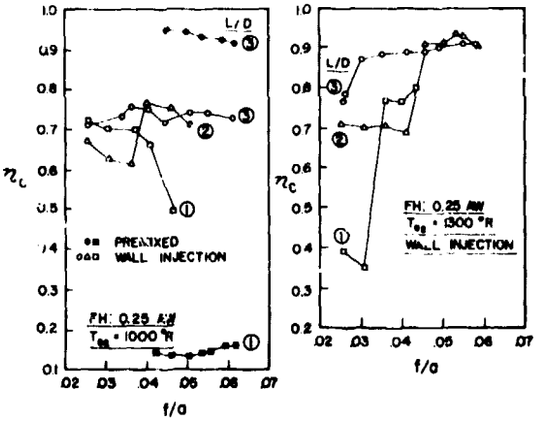

a. 25% blockage.

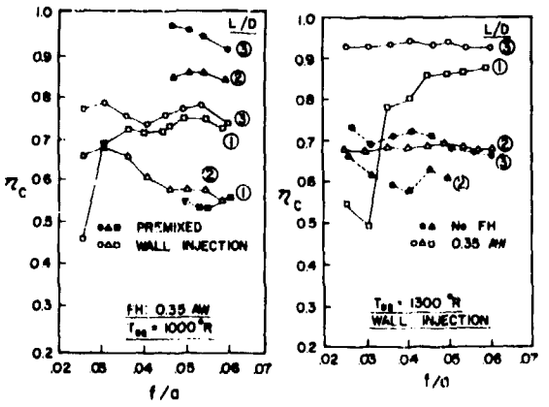

b. 35% blockage.

Fig. 5 Baseline combustor performance with annular wedge flameholders.

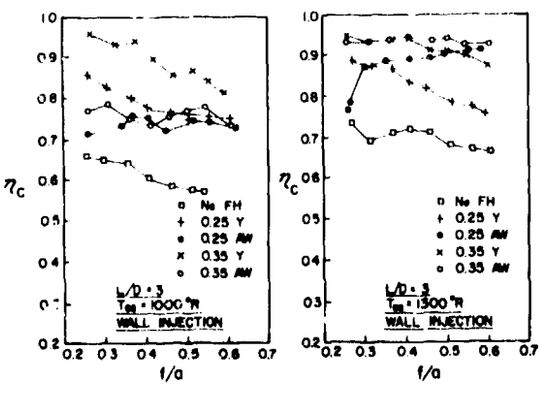

Fig. 6 Ramburner performance for various test configurations at L/D = 3.

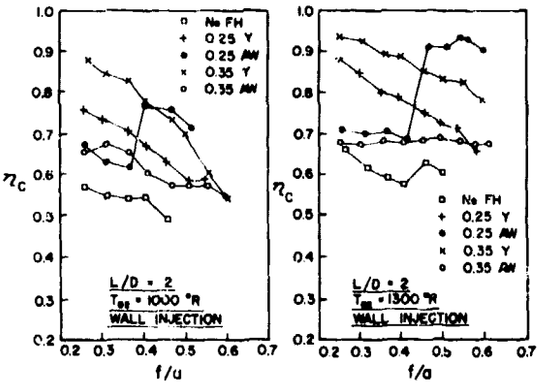

Fig. 7 Ramburner performance for various test configurations at L/D = 2.

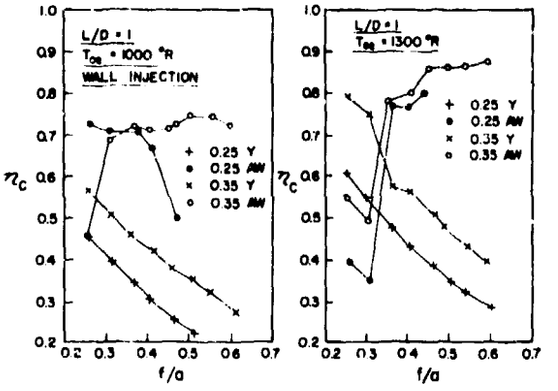

Fig. 8 Ramburner performance for various test configurations at L/D = 1.

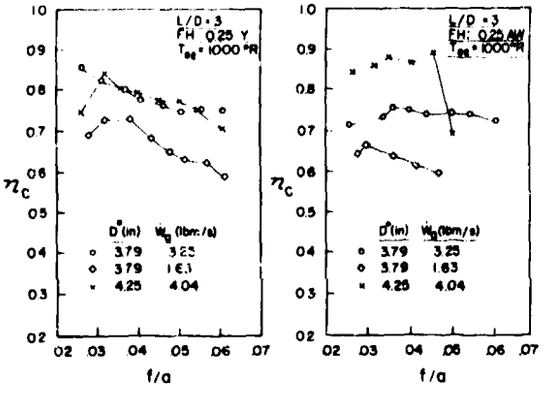

Fig. 9 Combustor performance for decreased $\dot{W}_A$ and increased D*.

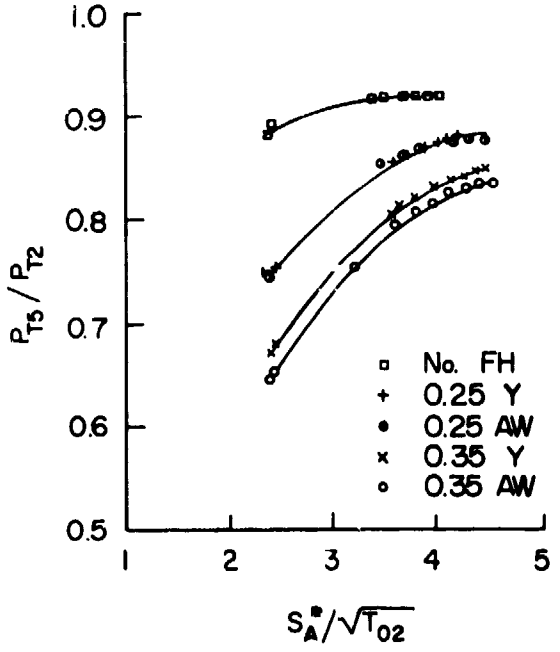

Fig. 10 Baseline combustor pressure loss.

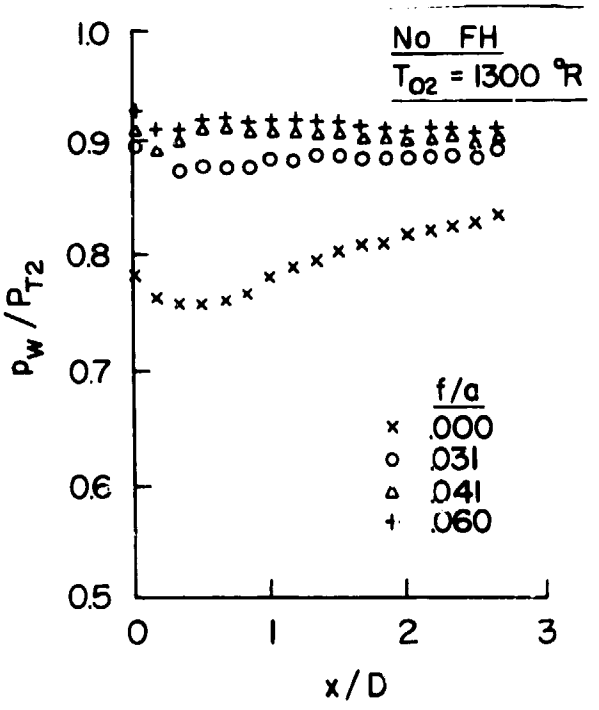

Fig. 12 Baseline combustor wall pressure distribution without flameholders.

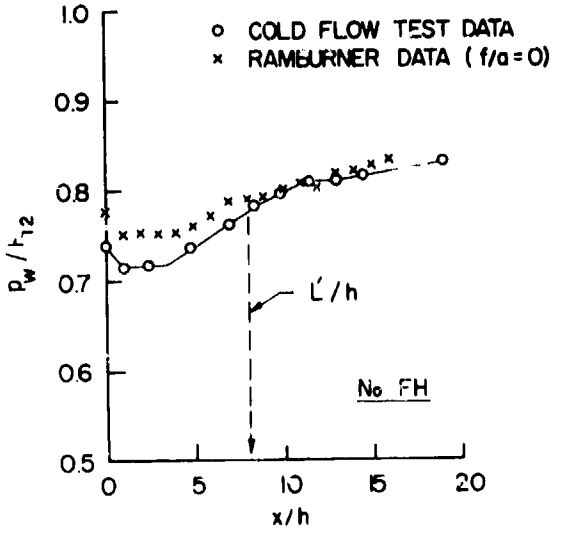

Fig. 11 Comparison of cold flow wall pressure distribution.

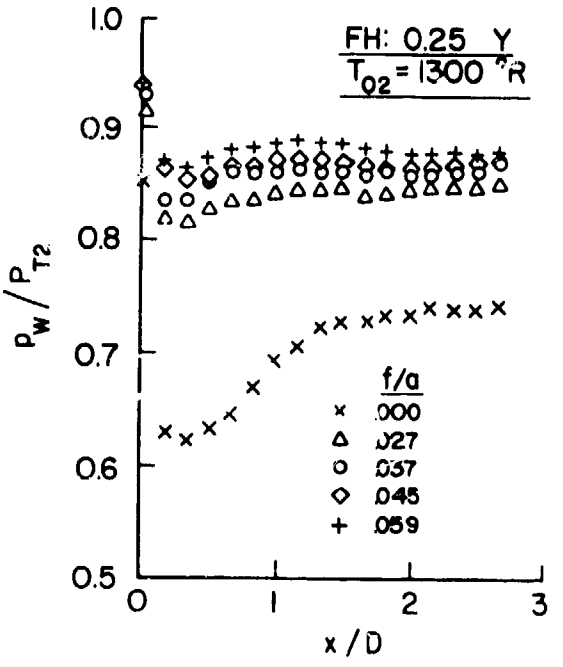

Fig. 13 Baseline combustor wall pressure distribution with Y type flameholders.

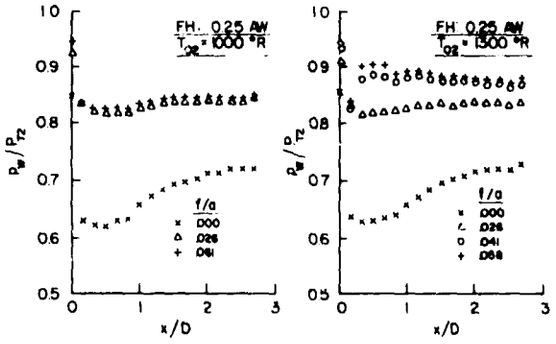

Fig. 14 Baseline combustor wall pressure distribution with annular wedge flameholders.

a. 0.25-Y flameholder.

b. 0.25-AW flameholder.

Fig. 15 Surface heating patterns for baseline combustor.

a. L/D = 3: 5 psi/cm and 2 millisec/cm

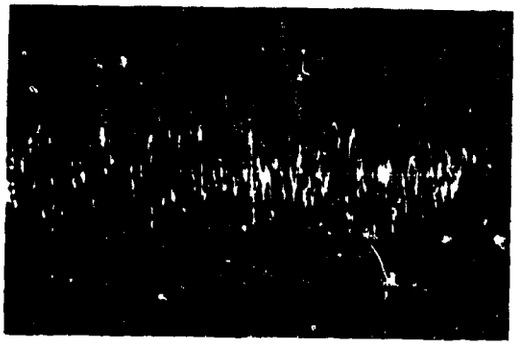

b. L/D = 1: 5 psi/cm and 1 millisec/cm

Fig. 16 Combustor pressure oscillations for 0.25-AW flameholder.

Pages 157 - 184 have been omitted

MILITARY AIRCRAFT NOISE

by

Paul A. Shahady
Air Force Aero Propulsion Laboratory
Wright-Patterson Air Force Base, OH

Opportunities to reduce military aircraft noise without inhibiting mission capability are considered. Emphasis is placed on the need for a comprehensive military aircraft noise abatement program involving compatible land use in the vicinity of military airports, operational constraints, and procedures to reduce noise impact and source noise reduction. The military to civil transfer of aircraft and engine technology is discussed together with the effect of increasing civil noise constraints on this evolutionary practice. Research and development activities to reduce military aircraft noise at the source are highlighted and plans to incorporate noise reduction technology early in the development cycle of military engines are outlined. Recommended noise goals for military aircraft are presented.

AD P000322

Copyright AIAA. Reprinted with Permission

Military Aircraft Noise

Paul A. Shahady*
Air Force Aero Propulsion Laboratory, Wright-Patterson Air Force Base, Ohio

Opportunities to reduce military aircraft noise without inhibiting mission capability are considered. Emphasis is placed on the need for a comprehensive military aircraft noise abatement program involving compatible land use in the vicinity of military airports, operational constraints, and procedures to reduce noise impact and source noise reduction. The military to civil transfer of aircraft and engine technology is discussed together with the effect of increasing civil noise constraints on this evolutionary practice. Research and development activities to reduce military aircraft noise at the source are highlighted and plans to incorporate noise reduction technology early in the development cycle of military engines are outlined. Recommended noise goals for military aircraft are presented.

Introduction

NOISE is not a new problem to the military services. They recognized many years ago that high noise levels were detrimental to personnel, contributed to structural failures, and degraded the general community environment. Comprehensive bioacoustic research efforts were conducted to assess the effect of high noise levels on personnel. As a result of these programs, allowable noise exposure limits were developed. Ear protection devices were issued to all personnel exposed to excessive noise, and hearing conservation programs were initiated throughout the military services. These early bioacoustic research efforts formed the basis for much of the current work on subjective response to aircraft noise.

With the advent of the jet engine, the problem of acoustically induced fatigue in aircraft structures became more predominant. In response to this problem, extensive in-house research facilities were established. Sonic fatigue and interior noise control techniques were developed and comprehensive standards were formulated. However, very little effort was directed toward the real culprit—the propulsion system, since at that time all engine noise reduction techniques were accompanied by intolerable performance and weight penalties.

The most elusive problem to face was community annoyance. To partially overcome this problem, the military services expended considerable manpower and funding to develop effective ground runup suppression equipment. This effort, together with a limited use of operational constraints and land use planning, represented the military's principal weapons against noise pollution. These efforts are now being expanded and, in addition, new efforts are being initiated to reduce aircraft propulsion system noise at the source. This paper emphasizes the community annoyance aspects of military aircraft noise and explores what opportunities exist to reduce the impact of military aircraft noise without inhibiting mission capability.

Military Aircraft Noise Control

The impact of noise emanating from military aircraft operations can be significantly reduced by a comprehensive noise abatement program involving compatible land use in the vicinity of military airports, operational constraints, and procedures, and source noise reduction, Fig. 1. Since a large majority of military aircraft are high performance aircraft not presently amenable to source noise reduction techniques, land use control is the single most important method to lessen the impact of military aircraft noise on communities adjacent to military flying installations.[1] The Department of Defense recognized this to be the case and recently published an environmental impact statement of the policy necessary to implement land use control in the vicinity of military airports.[2]

Operational constraints and procedures can be employed to reduce noise. However, military flight operations are somewhat unique and, therefore, noise abatement procedures which are applicable to civil aircraft operations may not be appropriate for military aircraft. The fact remains, however, that the potential for effective military aircraft noise abatement constraints and procedures does exist. Comprehensive studies should be conducted to fully evaluate this potential. This need was pointed out in a recently drafted Department of Defense Area Coordinating Paper on Environmental Quality.[3]

The potential for large source noise reductions for strategic and tactical military aircraft does not exist at the present time. These high performance aircraft cannot accept the performance degradations associated with current source noise reduction techniques. However, source noise reduction techniques can be successfully applied to selected military aircraft classes that operate in the civilian as well as the military domain, such as helicopters, transports, tankers, and patrol aircraft, without imposing excessive performance and weight penalties. The Department of Defense and other agencies of the Federal Government are conducting comprehensive research and development programs to develop source noise reduction techniques that can be applied to both military and civil aircraft.[4-6]

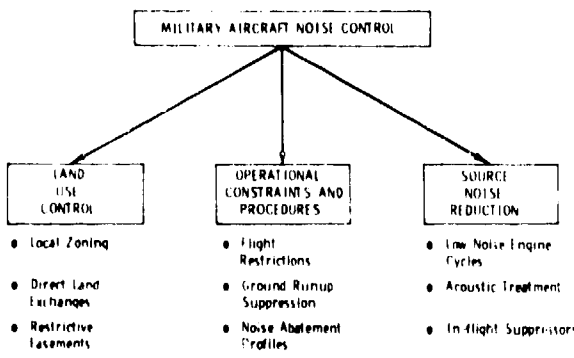

Fig. 1 Essential components for a comprehensive military aircraft noise abatement program.

Presented as Paper 73-1291 at the AIAA/SAE 9th Propulsion Conference, Las Vegas Nevada, November 5-7, 1973; submitted November 30, 1973; revision received November 14, 1974. The author sincerely appreciates the efforts of 1st Lt. G.D. Vest and the members of the Randolph Airport Environs Study Group whose publications were used extensively in the development of the land use planning sections of this paper.

Index categories: Aircraft Noise; Powerplant; Aircraft Powerplant Design and Installation; Airbreathing Propulsion, Subsonic and Supersonic.

* Aerospace Engineer.

Fig. 2 Representative sample of an airport environs compatibility land use plan.

Land Use Control

Military and civilian airfields attract activity in their immediate surroundings. New cities grow up near bases and existing cities grow outward toward the airfield. Since the military airfield structure has remained largely static the past fifteen years, this encroachment process has endangered the potential freedom of these bases to support flight operations. This trend can be combated by halting the encroachment process at existing bases or by constructing new bases at locations and with land procurement policies which would prohibit adjacent encroachment.[7] Given the anticipated limits of future military construction budgets, it seems very unlikely that the Department of Defense will be able to build many new military airfields. Therefore, the military services must strive to halt the encroachment caused by urbanization. In most cases this goal can be supported by the adjacent communities.

The incentive for an adjacent community to cooperate with the military services to establish compatible land use does have practical limitations. Large areas of land cannot be sterilized by unrealistic land use assumptions; this is contrary to laws which protect a property owner's right to profitable use.

Air Installation Compatible Use Zone (AICUZ)

The principal causes of concern relative to airbase encroachment are complaints against noise and fear of aircraft accidents. The military services have had procedures to evaluate noise and assess its effect on surrounding areas since the early 1960's.[8] Also, accident investigation and strong public information programs have been practiced to minimize the ill-effects of either noise or accident hazard. However, until recently, the Department of Defense did not have a policy that was designed to protect its operational capability from off-base intrusion. In May 1972, Headquarters, U. S. Air Force issued the draft of a Real Property Management Regulation (AFR 87-14) under the title, "Air Installation Compatible Use Zone' (AICUZ) Protection of Air Force Bases Against Urban Encroachment."[9] The concept established by this draft is designed to encourage compatible land use in nongovernment areas around military airbases. It does not require that the land remain open space, but that uses be compatible with the noise and occassional hazard which exist from aircraft operations. Three basic techniques are provided to insure compatible land uses: a) Encourage adoption of local zoning for compatible land use; b) Exchange excess or surplus Government land for land of equivalent value within the compatible use area; and c) Purchase restrictive easements or fee title.

Purchase of restrictive easements or fee title is considered a last resort method in view of the likelihood of budget restrictions. Land exchanges are limited by the availability of excess Government land. Therefore, it is clear that the principal technique of general use will be the adoption of local zoning.

Application of the AICUZ concept results in an airport environs land use compatibility plan which includes: 1) land areas upon which certain land uses could obstruct the airspace or otherwise be hazardous to aircraft operations, and 2) land areas which are exposed to the health and safety hazards of aircraft operations. The plan results from overlaying noise and accident zone maps and establishing compatible use districts from the overlays. The actual delineation of the accident zones for a given installation will, to a large degree, be the result of professional judgment by planners and aviation experts. The noise zones are generally formed by using four or five contour lines from NEF 30 to 50. The NEF prediction procedure utilizes an EPNdB source noise data base combined with a description of flight paths and their utilization to produce NEF contours using a sophisticated computer program. Overlays of the noise and accident zones produce a number of compatible use districts. This information serves as the basis for final districting decisions together with other land use determinants to form a comprehensive land use plan. Figure 2 shows a typical NEF and accident zone map.

In most cases it is not practical to simply overlay the Compatible Use Districts on a vicinity map and adopt a corresponding ordinance. These districts serve as the basis for final districting decisions together with other land use determinants to form the comprehensive land use plans. Land use planning experts point out that the airport environs compatibility use plan should not be considered an end in itself. It is only one of many inputs into a comprehensive environmental land use planning process. References 1 and 7 provide specific details concerning the land use planning process.

Operational Constraints and Procedures

Operational constraints and procedures for both flight and ground operations can reduce the impact of military aircraft noise on local communities. Operational constraints include such items as: a) Restricting hours of operation; b) Prescribing the number of operations permitted per unit of time; c) Limiting operations on weekends and holidays; d) Limiting areas in which operations may be performed; e) Prohibiting certain operations.

Operational procedures include such items as: a) Use of nonstandard techniques; e.g., high gliding, low power approaches, fast no flap approaches, etc.; b) Minimum power takeoffs, power reductions; c) Nonstandard departures and arrivals, d) Adjustment of flight patterns.

All of these constraints and procedures should be carefully reviewed to determine their applicability to the military aircraft noise problem. However, there are unique aspects of military aircraft operations that must be carefully assessed before adopting any operational constraints or procedures.

The training evolution of individual pilots and unit-

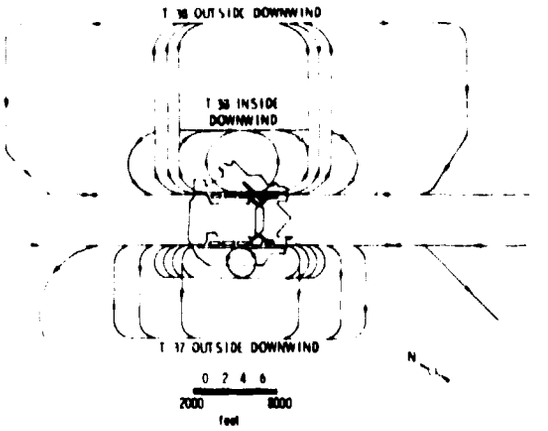

Fig. 3 Typical military aircraft flight patterns at a pilot training base.

requires the capability for flexible planning. The level of experience of assigned pilots, weather, target availability, hours of darkness, etc. require continuous adjustments in planning to achieve a proper readiness stature. Restrictions on the frequency or time of operations could be detrimental to the training process. Commanders must have the option, implemented wisely, to conduct the training they consider necessary to maintain readiness.

Aircraft traffic patterns must be evaluated in the light of mission requirements. Some adjustment may be made to alleviate noise; however, many of the apparent changes are not feasible. An example of the complexity of the problem is shown in Figure 3.

The figure shows five basic patterns used at military bases: straight out takeoff, straight in landing, overhead landing, closed pattern to the inside downwind, and closed pattern to the outside downwind. Similar patterns can be found at civil airports with National Guard or Reserve units; however most civil aviation patterns are essentially straight-in and straight-out. The complexity of the military patterns pose quite a problem to the development of effective military aircraft noise abatement procedures. Another significant point in establishing noise abatement procedures is that the current flight techniques developed for each aircraft are optimized for maximum performance in any particular mode of operation. These standard operating procedures are directly related to flight safety. Burdening pilots with a number of aircraft operating techniques for various air installations and aircraft operating conditions to reduce noise must be approached very carefully to avoid derogation of safety.

Source Noise Reduction

Extensive industry and Government efforts have been conducted over the past decade to reduce aircraft noise at the source. Some of the current noise abatement techniques that can be applied to reduce aircraft/engine noise include: a) New quieter engine designs with components and engine cycles selected for lower noise; b) Acoustically treated nacelles and ducts; c) Vehicle aerodynamics to allow for steeper ascent and descent, and reduction in time required for ascent/decent; d) In-flight suppressors to reduce jet noise.

However, because the performance, weight, and cost penalties involved, most military aircraft and engines do not include source noise reduction technology. Figures 4 and 5 show a comparison of the noise levels from selected military aircraft with the levels allowed by current Federal Aviation Regulation, Pt. 36 for subsonic commercial aircraft.

The data plotted in these figures were taken from a variety of sources. Noise levels for the F100, F4, KC135, B52, C5A, C135B, and the C141 were based on actual measurements conducted by the 6570th Aerospace Medical Research Lab. C9A and T43A levels were based on published FAA data on

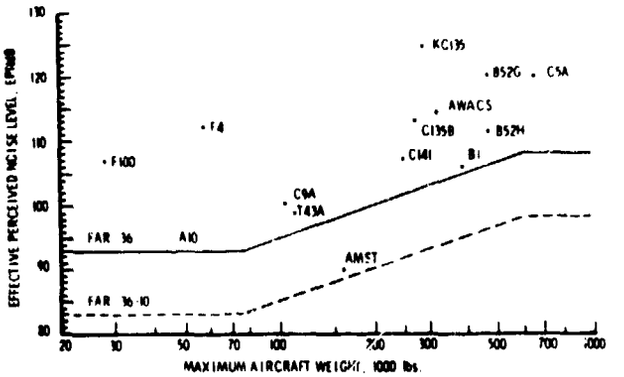

Fig. 4 Military aircraft noise at takeoff compared with the federal aviation administration's civil aircraft noise regulations (FAR PART 36).

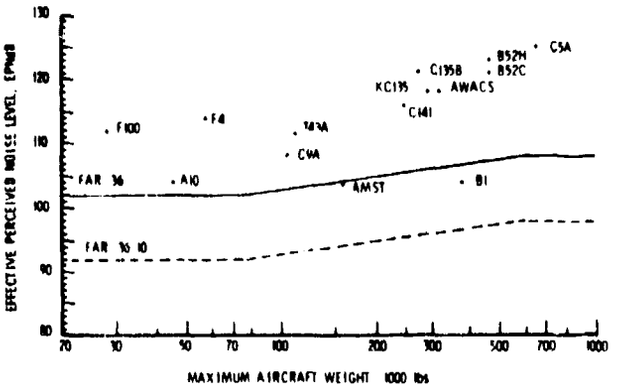

Fig. 5 Military aircraft noise at approach compared with the federal aviation administration's civil aircraft noise regulations FAR PART 36).

the DC9 and 737 aircraft, commercial versions of the C9A and T43A, respectively. The B1 and A10 data were predicted, based on aircraft/engine design and operational characteristics, and the AMST levels were obtained from Ref. 10. The major noise source for all of these aircraft is the propulsion system.

Military to Civil Technology Transfer

Figures 6 and 7 explore the commercial compatibility of some military aircraft with respect to FAR 36 requirements. The C9A, T43A, and C135B are all military versions of operational commercial aircraft (DC9, 737, and 707, respectively). By employing new nacelles with sound absorption material, these aircraft can be retrofitted to meet current FAR 36 noise requirements. The technology developed under the C5A program is compatible with current commercial noise constraints. The high bypass technology reduced the jet noise floor of the propulsion system and allowed the industry to concentrate on developing effective means to reduce fan inlet noise. By employing these noise reduction features in certain classes of future military aircraft, commercial compatibility with current and proposed FAA noise regulations can be assured.

Predicted noise characteristics for the Boeing version of USAF's Advanced Medium STOL Transport are shown. The General Electric CF6 engines powering this aircraft are identical to those used by the McDonnell Douglas DC10 wide bodied commercial transport. Many desirable noise reduction characteristics are incorporated into the propulsion system. In addition, the aircraft employs advanced vehicle aerodynamic techniques to allow for steeper ascent and descent. Therefore, the noise levels of the basic military configuration are sufficiently low to insure that commercial versions of the air-

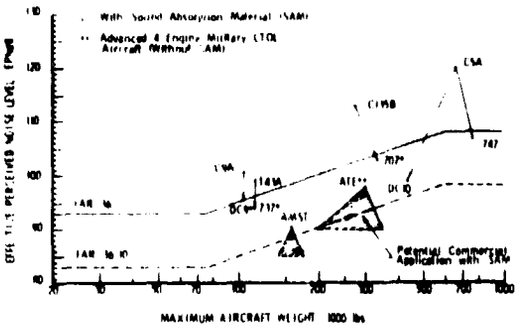

Fig. 6 Commercial compatibility of military transport aircraft with respect to current and proposed FAA noise regulations—Takeoff.

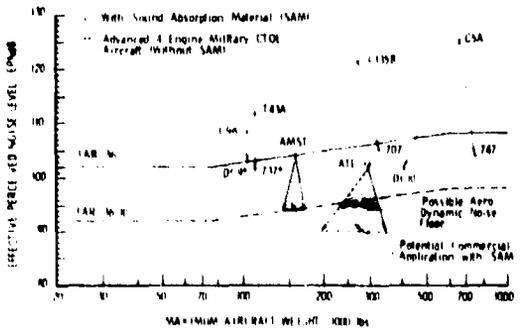

Fig. 7 Commercial compatibility of military transport aircraft with respect to current and proposed FAA noise regulations—approach.

craft, employing advanced acoustic treatment, will meet future FAA noise regulations.

The second example is a preliminary design four engine military transport/tanker. The aircraft employs advanced turbine engines in the 20,000 lb thrust class incorporating second generation noise reduction features based on advanced quiet engine technology development programs. Incorporation of noise reduction technology early in the development cycle of the engine and aircraft system insures that stringent commercial noise regulations of the future can be met by civil derivatives of this aircraft.

Current Research and Development

The Army, Navy, and Air Force are conducting a number of aircraft noise control research and development programs. Army efforts emphasize helicopter noise generation, propagation, and reduction. The Navy is concentrating on the development of new ground runup suppression techniques and assessments of the noise environments of aircraft carriers. The most extensive research and development efforts within the Department of Defense to control aircraft noise are being conducted by the Air Force. These efforts include the areas of bio and psycho acoustics, propulsion, and aircraft acoustics and aircraft noise measurement. Specific details concerning the Defense Department's aircraft noise research programs are presented in Refs. 11-13. Much of the technology developed under these programs is applicable to the solution of both military and civil noise problems. Therefore, the Department of Defense is conducting several noise research efforts jointly with other agencies of the Federal Government including the Department of Transportation (DOT), the National Aeronautics and Space Administration (NASA), and the Environmental Protection Agency (EPA). These joint programs include a DOT USAF program to investigate the fundamental mechanisms of supersonic jet exhaust noise, a NASA/Army cooperative effort to study helicopter noise generation characteristics, and an EPA USAF program to provide technical guidance relative to

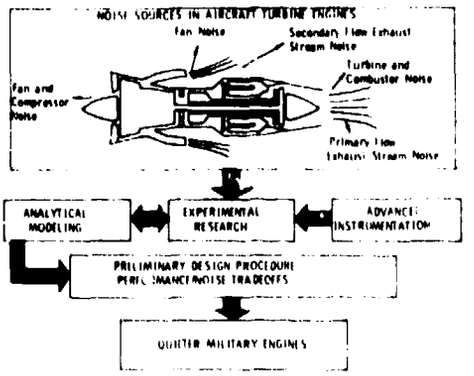

Fig. 8 Department of defense program to reduce propulsion system noise.

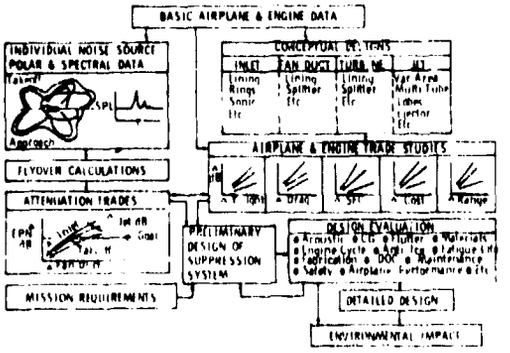

Fig. 9 Comprehensive procedure to assess noise/performance cost trades.

a wide variety of noise control activities. Figure 8 shows the structure of the Department of Defense's research program to reduce propulsion system noise.

The impact of source noise reduction techniques on system performance must be carefully and comprehensively assessed before any of these techniques can be applied to military aircraft. To achieve maximum noise reduction for minimum penalty, performance/noise/cost trade studies must be conducted early in the development of each new aircraft and engine system. These studies, coupled with expected technology advances, will aid in the practical application of noise control techniques to future military aircraft. Figure 9 indicates the complexity of a typical noise/performance/cost trade procedure.

Technology Implementation

The initiation of comprehensive research programs to develop noise reduction techniques is really only a first step. The technology developed under these programs must be incorporated into the hardware phases of the military engine development cycle. Figure 10 shows a typical aircraft engine development cycle from basic research to final production.

Most of the military's source noise reduction efforts have been limited to basic and exploratory research. Severe funding limitations have for the most part prevented the incorporation of noise control technology into the hardware phases of the military engine development cycle. The transition from the research to the development phases must be made to insure that available source noise reduction technology is properly implemented. This problem emphasized the need for a definitive Department of Defense policy on source noise abatement for military aircraft.

Recommended Noise Goals for Military Aircraft

Recently, the Department of Defense conducted an intra-agency study on environmental quality. One of the major ob-

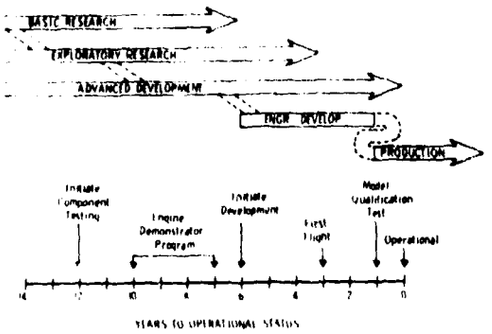

Fig. 10 Representative aircraft engine development cycle.

Table 1 Military aircraft noise goals

Strategic/tactical aircraft

Operational aircraft: Rely on land use planning, operational constraints/procedures, ground runup suppression

Future aircraft

1) Conduct noise/performance/cost trades early in the development cycle of each system

2) Implement noise reduction techniques only if they do not inhibit the military mission

3) Utilize land use planning, operational constraints/procedures, and ground runup suppression

Transport/other selected aircraft

Operational aircraft

1) Conduct source noise reduction community impact studies

2) Conduct noise retrofit/performance/cost trades

3) Where feasible, retrofit to meet FAR 36 based on tradeoff analyses

4) Utilize land use planning operational constraints/procedures, and ground runup suppression

Future aircraft

1) Conduct noise performance cost trades early in the development cycle of each system

2) Meet current FAR 36 noise requirements as a minimum

3) Employ state-of-the-art noise control technology to the greatest extent possible

4) Approach future commercial noise regulations to the greatest extent possible

5) Utilize and use planning operational constraints procedures and ground runup suppression

jectives of this study was to develop a coordinated long range plane for environmental quality research. The study included a discussion of the feasibility of developing source noise reduction goals for future military aircraft.

The Air Force Aero Propulsion Laboratory has formulated source noise reduction goals for current and future military aircraft and has recommended that these goals be adopted by the Air Force and the Department of Defense. The goals were developed under the premise that source noise reduction techniques can be applied to certain classes of military aircraft without inhibiting military missions. The goals address two separate classes of aircraft—strategic/tactical aircraft and transport other selected aircraft. Strategic and tactical aircraft include fighters, bombers, interceptors, tactical helicopters, etc. Transport and other selected aircraft include CTOL and STOL transports, tankers, navigator trainers, cargo aircraft, certain reconnaissance and long range patrol aircraft, etc. These goals are summarized in Table 1.

As a result of these recommendations, Air Force Headquarters modified Air Force Regulation 80-36 entitled "Civil Airworthiness Standards for U.S. Air Force Transport Aircraft." The modified regulation states that where military requirements permit, transport aircraft must be designed to comply with civil airworthiness standards including the FAA noise standard.

Summary

It is clear that the impact of noise from military aircraft operations can be significantly reduced by a comprehensive noise abatement program involving compatible land use in the vicinity of military airports, operational constraints and procedures, and source noise reduction. In the area of compatible land use, good community relations provide the key to success. The military services must work closely with local governments and community groups to provide protection for military flight operations within a framework of land use which the cities can afford. Operational constraints and procedures can be employed. However, specific research programs are required to develop realistic constraints and procedures and to evaluate their effect on mission performance and safety. Finally, source noise reduction is feasible for certain classes of military aircraft that operate in the civilian as well as the military domain. The techniques exist and have been demonstrated on operational commercial aircraft such as the DC10 and 747 and in technology programs such as the JT3D and JT8D and retrofit programs conducted by the FAA. The cost of such techniques, however, is relatively large. High performance aircraft (fighters, bombers, tactical helicopters, etc.), whose mission requirements are demanding, would incur significant penalties if they were subjected to current noise suppression techniques. Therefore, the Department of Defense is continuing to search for techniques that can be applied to high performance aircraft without adversely affecting their mission capabilities.

References

[1]"Military Aircraft and Airport Noise and Opportunities for Reduction Without Inhibition of Military Missions," EPA Aircraft/Airport Noise Rept. Study—Task Group 6, June 1973 (revised draft), Environmental Protection Agency, Washington, D.C.

[2]"DoD Impact Statement on Air Installation Compatible Use Zone," Dept. of Defense, Washington, D. C., March 1973.

[3]"Area Coordinating Paper on Environmental Quality," Dept. of Defense, Washington, D.C.

[4]Shahady, P. A., "Department of Defense Noise Research Programs—Source Noise Abatement Technology," Air Force Aero Propulsion Lab., March 1973, Wright-Patterson Air Force Base, Ohio.

[5]Roudebush, W. H. et al., "Aircraft Noise Reduction Technology," March 1973, NASA.

[6]Sperry, W. C., "Noise Source Abatement Technology and Cost Analysis Including Retrofiting (Draft)," EPA Aircraft/Airport Noise Rept. Study-Task Group 4, June 1973, Agency, Washington D.C., Environmental Protection Agency, Washington D.C.

[7]"Randolph Airport Environs Study," A Report to the Randolph Subregion Community Council, March 1973, Randolph AFB, Texas.

[8]"Land Use Planning with Respect to Aircraft Noise," Dept. of the Air Force, AFM 86-5; Dept. of the Army, TM 5-365; Dept. of the Navy, NAVDOCKS P-98, Washington, D.C., Oct. 1964.

[9]"Air Installation Compatible Use Zone (AICUZ)," Letter, Dept. of the Air Force (PRERD), May 1972 to Major Air Commands with Atch Draft AFR 87-14, "Air Installation Compatible Use Zone: (AICUZ) Protection of Air Force Base Against Urban Encroachment.

[10]Foody, J. J., "The Air Force/Boeing Advanced Medium STOL Transport Prototype," Air Transportation Meeting, Miami, Fla., April 1973.

[11]Schmitz, F. H., "Rotary Wing Acoustic Research," Ames Directorate, U.S. Army Air Mobility R&D Lab., Moffett Field, Calif., May 1973.

[12]Burns, R.P., "Noise Pollution Control in the U.S. Navy," May 1973, Naval Air Propulsion Test Center, Trenton, N.J.

[13]Shahady, P. A., "U. S. Air Force Noise Research," Presented to EPA Aircraft/Airport Noise Study—Task Group 4, May 1973, Environmental Protection Agency, Washington, D. C.

AD P000323

A NOTE ON ADAPTIVE WIND TUNNELS WITH IMPERFECT CONTROL

by

William R. Sears
Aerospace and Mechanical Engineering Department
University of Arizona
Tucson, Arizona

An earlier study of the convergence of the adaptive-wall wind-tunnel scheme for a sinusoidal model in a two-dimensional tunnel is extended to the case where ideal matching at the interface cannot be achieved. It is assumed that, in place of the desired sinusoidal correction, a correction including an extraneous harmonic always occurs. Two different assumptions are made regarding the fitting of this distorted sinusoid to the observed error signal. It is found that the iteration converges for the same range of relaxation constants as for the ideal case, but that unconfined flow is not achieved. For reasonable numerical values, the iteration nevertheless appears to make substantial improvement in a flow involving boundary interference.

Manuscript received March 1979. This research was sponsored by AFOSR under Grant 76-2954E.

Notations

a	coefficient in Equation 17 and Table I
A_n, a_n	coefficients defined in Equation 2, at n-th interation
a'_n	$a_n e^{2\beta\lambda h}$
$\mathbf{A}_n$	the column matrix $\begin{pmatrix} A_n \\ a_n \end{pmatrix}$
b	coefficient in Equation 17 and Table I
B_n, b_n	coefficients defined in Equation 2, at n-th iteration
C_n, c_n	coefficients defined in Equation 7, at n-th iteration
$f(x), f^{(n)}(x)$	wall-correction functions (Equation 1)
h	value of y at the tunnel interference
$\mathbf{I}$	the unit matrix
k	"relaxation coefficient" used in the iteration
K_n	the value, at the n-th iteration, of the constant in Equation 1
$\mathbf{K}$	modal matrix formed by the eigenvectors of $\mathbf{M}$
$\mathbf{K}^{-1}$	inverse of $\mathbf{K}$
ℓ_1, ℓ_2	eigenvalues of $\mathbf{M}$
$\mathbf{L}$	diagonal matrix $\begin{pmatrix} \ell_1 & 0 \\ 0 & \ell_2 \end{pmatrix}$
$\mathbf{M}$	the matrix $\begin{pmatrix} 1-\frac{a}{\lambda} & -\frac{b}{\lambda} \\ -\frac{\mu a}{3\lambda} & 1-\frac{\mu b}{3\lambda} \end{pmatrix}$
n	the number of iteration
V	stream speed
$w_1^{(i)}, w_2^{(i)}$	i-th modal coefficients (Equation 33)

β	Prandtl-Glauert factor $(1-V^2/a_\infty^2)^{\frac{1}{2}}$, where a_∞ is the speed of sound
$\delta^{(n)}u(x,h)$	the difference between $\phi_x^{(n)}(x,h)$ and $\Phi_x^{(n)}(x,h)$ (Equation 9)
$\Delta A_n, \Delta a_n, \Delta B_n, \Delta\Phi$	increments of A_n, a_n, B_n and Φ introduced at the n-th iteration
ε	model amplitude Equation 3. $\varepsilon\lambda << 1$
λ	model wave number; model wave length = $2\pi/\lambda$
μ	coefficient of the extraneous harmonic (Equation 1)
$\Phi^{(n)}(x,y)$	perturbation potential of flow in wind tunnel at n-th iteration
$\phi^{(n)}(x,y)$	perturbation potential of the (calculated) flow field outside the tunnel at n-th iteration

Introduction

The concept of the adaptive-wall wind tunnel has been presented in a number of papers.[1,2,3] Briefly, the proposal is to match, by successive iterations, the flow field within a wind tunnel in the presence of an arbitrary model and test configuration, to a computed exterior flow field that satisfies the required far-field boundary conditions.

Some studies of the convergence of this iterative process have been carried out. The most convincing of these studies are done by numerical simulation of the whole process.[3] There are also purely analytical studies, which are limited to rather simple classes of models and tunnels.[4,5] All of these studies, to date, assume ideal control conditions at the interface between interior and exterior regions. That is to say, at any n-th iteration, when an error function, say $\delta^{(n)}u(x)$, has been found, the operator is able to introduce a corresponding change, say $k\delta^{(n)}u(x)$, into the flow field at the interface. But in a real tunnel, such a correction function can only be achieved imperfectly because of nonzero size of control elements, finite number of control elements, limited number of instrument readings, etc.

We anticipate that these imperfections may have deleterious effects on the process of convergence to unconfined-flow conditions. This could (and should) be studied by numerical simulation. It is also interesting to restudy, analytically,

the simple cases previously studied by Lo and Kraft[4] and by Sears.[5] We consider first the simplest, which is the sinusoidal model in a two-dimensional tunnel. In the earlier studies it was assumed that a perfect sinusoidal correction $k\delta^{(n)}u(x)$ could be introduced, and convergence was found over a range of the "relaxation constant" k. We now want to assume, instead, that only a distorted sinusoid can be introduced at the interface.

Effect of an Extraneous Harmonic

Suppose, for example, that when a sinusoidal correction proportional to $\sin \lambda x$ is called for, where x is the streamwise coordinate, the response can be at best a periodic function of the correct wave-length but distorted by an extraneous higher harmonic, described by

$$f(x) = \text{constant} \times (\sin \lambda x + \mu \sin 3\lambda x) \qquad (1)$$

where μ is a constant not under control of the operator, but determined by the design of the tunnel.

As in our earlier analytic studies, we assume that the flow is adequately described by the linear, Prandtl-Glauert approximation. At the n-th iteration, then, the flow field will involve both the fundamental (λx) and the harmonic ($3\lambda x$): the perturbation potential will be of the form*

$$\phi^{(n)}(x,y) = (A_n e^{\beta\lambda y} + B_n e^{-\beta\lambda y})\cos\lambda x + (a_n e^{3\beta\lambda y} + b_n e^{-3\beta\lambda y})\cos 3\lambda x \qquad (2)$$

The boundary condition enforced by the sinusoidal model is

$$\phi_y(x,o) = V\varepsilon\lambda\cos\lambda x \qquad (3)$$

*See Table of Notation

which requires

$$A_n = B_n + \beta^{-1}\varepsilon V \tag{4}$$

and

$$a_n = b_n \tag{5}$$

At the interface y = h, the flow described by Equation 2 involves the perturbation component

$$\phi_y^{(n)}(x,h) = (A_n e^{\beta\lambda h} - B_n e^{-\beta\lambda h})\,\beta\lambda\cos\lambda x + a_n\,(e^{3\beta\lambda h} - e^{-3\beta\lambda h})\,3\beta\lambda\cos 3\lambda x \tag{6}$$

The iteration begins by adopting this expression as inner boundary condition for the exterior flow field; viz.,

$$\phi^{(n)}(x,y) = C_n e^{-\beta\lambda y}\cos\lambda x + c_n e^{-3\beta\lambda y}\cos 3\lambda x \tag{7}$$

becomes $-(A_n e^{\beta\lambda h} - B_n e^{-\beta\lambda h})e^{-\beta\lambda(y-h)}\cos\lambda x$

$$- a_n(e^{3\beta\lambda h} - e^{-3\beta\lambda h})e^{-3\beta\lambda(y-h)}\cos 3\lambda x \tag{8}$$

The "error signal" $\phi_x^{(n)}(x,h) - \Phi_x^{(n)}(x,h)$ is then found to be

$$\delta^{(n)}u(x,h) = \phi_x^{(n)}(x,h) - \Phi_x^{(n)}(x,h) = 2\lambda A_n e^{\beta\lambda h}\sin\lambda x + 6\lambda a_n e^{3\beta\lambda h}\sin 3\lambda x \tag{9}$$

We assume that the tunnel operator would like to introduce a correction proportional to this $\delta^{(n)}u(x,h)$, but is limited to functions of the form of f(x), Equation 1, where μ is determined by the equipment and is not under his control. We must also assume how he will choose the constant in Equation 1 in response to the error signal (9).

Two Assumptions Regarding Fitting

Let us investigate the convergence process under two different, rather arbitrarily chosen assumptions:

(a) "Single-Point" Fitting: Suppose there is only one measuring instrument in a half-cycle. The operator is then constrained to respond only to the value of $\delta^{(n)}u(x)$ at the value of x. For example, suppose the value at $\lambda x = \pi/2$ is the only datum available. From Equation 9,

$$\delta^{(n)}u(\pi/2\lambda,h) = 2\lambda A_n e^{\beta\lambda h} - 6\lambda a_n e^{3\beta\lambda h} \tag{10}$$

Putting the available correction $f^{(n)}(\pi/2\lambda)$ equal to this value, we have

$$(1-\mu)K_n = 2\lambda\,(A_n e^{\beta\lambda h} - 3a_n e^{3\beta\lambda h}) \tag{11}$$

and

$$f^{(n)}(x) = \frac{2\lambda}{1-\mu}\, e^{\beta\lambda h}(A_n - 3a_n e^{2\beta\lambda h})(\sin\lambda x + \mu \sin 3\lambda x) \tag{12}$$

We therefore manipulate the walls so as to introduce the u-increment $kf^{(n)}(x)$ to form the (n+1)th approximation.

(b) "Mean-Square" Fitting: Alternatively, suppose the wall configuration can be adjusted so as to minimize the difference between the ideal correction, Equation 9, and the available correction, Equation 1. This difference is

$$\delta^{(n)}u(x,h) - f^{(n)}(x) = (2\lambda A_n e^{\beta\lambda h} - K_n)\sin\lambda x + (6\lambda a_n e^{3\beta\lambda h} - \mu K_n)\sin 3\lambda x \tag{13}$$

To minimize this in the mean-square sense, we first calculate the square of expression (13) and integrate it over a half-cycle; the result is, except for a multiplicative constant,

$$(2\lambda A_n e^{\beta\lambda h} - K_n)^2 + (6\lambda a_n e^{3\beta\lambda h} - \mu K_n)^2 \qquad (14)$$

Putting the derivative of this expression with respect to K_n equal to zero, we find

$$\frac{K_n}{2\lambda e^{\beta\lambda h}} = \frac{A_n + 3a_n e^{2\beta\lambda h}\mu}{1+\mu^2} \qquad (15)$$

and

$$f^{(n)}(x) = \frac{2\lambda}{1+\mu^2} e^{\beta\lambda h} (A_n + 3a_n e^{2\lambda\beta h}\mu) \cdot(\sin\lambda x + \mu \sin 3\lambda x) \qquad (16)$$

In this case we manipulate the walls so as to introduce a u-increment equal to k times this function, to form the (n+1)th approximation.

Both of the hypotheses regarding fitting of the imperfect correction function have led to formulas of the form*

$$kf^{(n)}(x) = (aA_n e^{\beta\lambda h} + ba_n e^{3\beta\lambda h})(\sin\lambda x + \mu \sin 3\lambda x) \qquad (17)$$

The iterative process consists in introducing this perturbation at the interface, y = h; this contributes to the flow field a potential increment

$$\Delta\Phi(x,y) = (\Delta A_n e^{\beta\lambda h} + \Delta B_n e^{-\beta\lambda y})\cos\lambda x + (\Delta a_n e^{3\beta\lambda y} + \Delta b_n e^{-3\beta\lambda y})\cos 3\lambda x \qquad (18)$$

The boundary condition at the model, Equation 3, cannot be perturbed, and therefore requires

$$\Delta A_n = \Delta B_n \qquad \text{and} \qquad \Delta a_n = \Delta b_n \qquad (19)$$

---

*Values of a and b for the two fitting-assumptions appear in Table I, following

Equation 17 constitutes the boundary condition at y = h, and gives us

$$\Delta A_n = - \frac{a A_n e^{\beta\lambda h} + b a_n e^{3\beta\lambda h}}{\lambda (e^{\beta\lambda h} + e^{-\beta\lambda h})} \tag{20}$$

and

$$\Delta a_n = - \frac{\mu}{3\lambda} \frac{a A_n e^{\beta\lambda h} + b a_n e^{3\beta\lambda h}}{e^{3\beta\lambda h} + e^{-3\beta\lambda h}} \tag{21}$$

The perturbed flow field is described by the potential $\phi^{(n+1)}(x,y)$, which has the same form as Equation 2, but with A_n, B_n, a_n, b_n replaced by

$$\left.\begin{aligned} A_{n+1} &= A_n + \Delta A_n \\ B_{n+1} &= B_n + \Delta B_n = B_n + \Delta A_n \\ &= A_n - \beta^{-1}\varepsilon V + \Delta A_n = A_{n+1} - \beta^{-1}\varepsilon V \\ a_{n+1} &= b_{n+1} = a_n + \Delta a_n \end{aligned}\right\} \tag{22}$$

Convergence

Combining Equations 20-22, we have two simultaneous linear equations for A_{n+1} and a_{n+1} in terms of A_n and a_n. Before working out the convergence of these simple recurrence formulas, we propose to simplify them by observing that for cases of practical interest $\beta\lambda h$ is probably large enough so that the negative exponentials in 20 and 21 can be neglected; viz., $\beta\lambda h$ is π times the ratio of βh to the half-wave-length. Since the half-wave-lergth might be identified with "the model's chord length" and h is the tunnel half-height, it appears that $\beta\lambda h$ should be 1.0 or greater, for practical interest. If so, $e^{-\beta\lambda h}$ is small compared to $e^{\beta\lambda h}$, and $e^{-\beta\lambda h}$

even smaller compared to $e^{3\beta\lambda h}$. We therefore neglect these smaller terms and then find it convenient to define a new coefficient

$$a_n' \equiv a_n e^{-\beta\lambda h} \tag{23}$$

The recurrence formulas 20-22 then become

$$\left.\begin{aligned} A_{n+1} &= (1 - \tfrac{\epsilon}{\lambda})A_n - \tfrac{b}{\lambda}\, a_n' \\ a_{n+1} &= -\tfrac{\mu a}{3\lambda} A_n + (1 - \tfrac{\mu b}{3\lambda})a_n' \end{aligned}\right\} \tag{24}$$

In matrix notation,

$$\mathbb{A}_{n+1} = \mathbb{M}\,\mathbb{A}_n \tag{25}$$

where $\mathbb{A}_n$ denotes $\begin{pmatrix} A_n \\ a_n' \end{pmatrix}$ and $\mathbb{M}$ denotes the square matrix $\begin{pmatrix} 1-\frac{a}{\lambda} & -\frac{b}{\lambda} \\ -\frac{\mu a}{3\lambda} & 1-\frac{\mu b}{3\lambda} \end{pmatrix}$

Equation 25 can also be written as

$$\begin{aligned} \mathbb{A}_{n+1} &= \mathbb{M}^2\mathbb{A}_{n-1} = \mathbb{M}^3\mathbb{A}_{n-2} = \cdots \\ &= \mathbb{M}^n\mathbb{A}_1 \end{aligned} \tag{26}$$

The iterative procedure consists of starting with a wall configuration that produces a flow described by $\mathbb{A}_1$ and proceeding to $\mathbb{A}_2, \mathbb{A}_3$, etc. If the process converges, we arrive at a flow described by $\mathbb{A}_n (n \to \infty)$. This limit can be studied by applying matrix theory[6] to our little matrix $\mathbb{M}$.

We first find the eigen values of $\mathbb{M}$, viz., the roots ℓ_1, ℓ_2 of

$$|\ell\mathbb{I} - \mathbb{M}| = \begin{vmatrix} \ell - 1 + \frac{a}{\lambda} & \frac{b}{\lambda} \\ \frac{\mu a}{3\lambda} & \ell - 1 + \frac{\mu b}{3\lambda} \end{vmatrix} = 0 \tag{27}$$

These are easily found to be

$$\ell_1,\ \ell_2 = 1,\ 1 - \left(\frac{a}{\lambda} + \frac{\mu b}{3\lambda}\right) \tag{28}$$

so that the diagonal matrix of eigen values, say $\mathbb{L}$, is

$$\mathbb{L} = \begin{pmatrix} \ell_1 & 0 \\ 0 & \ell_2 \end{pmatrix} = \begin{pmatrix} 1 & 0 \\ 0 & 1-\left(\frac{a}{\lambda} + \frac{\mu b}{3\lambda}\right) \end{pmatrix} \tag{29}$$

Convergence requires $|\mathbb{L}| < 1$; viz.,

$$0 < \left(\frac{a}{\lambda} + \frac{\mu b}{3\lambda}\right) < 2 \tag{30}$$

This criterion is evaluated for our two fitting-assumptions in Table I.

Table I: Convergence Criteria

Fitting Assumption	a	b	$\frac{a}{\lambda} + \frac{\mu b}{3\lambda}$	Convergence Criterion
(a) Single-point	$\frac{2k\lambda}{1-\mu}$	$\frac{-6k\lambda}{1-\mu}$	$2k$	$0 < k < 1$
(b) Mean-square	$\frac{2k}{1+\mu^2}$	$\frac{6\mu k\lambda}{1+\mu^2}$	$2k$	$0 < k < 1$

We see that, for both kinds of fitting, the criterion for convergence of the iteration is the same as was found[5] for ideal wall-control, provided that the approximation $e^{-\beta\lambda h} << e^{\beta\lambda h}$ is made.

The Flow Field After Convergence

It is now interesting to determine what flow pattern is obtained in the limit. Is unconfined flow achieved in spite of imperfect wall-control?

The final flow is described by Equation 26 with $n \to \infty$. We require, therefore, the matrix $\mathbb{M}^n$ in this limit. An expression for $\mathbb{M}^n$ is given in matrix theory:

$$\mathbb{M}^n = \mathbb{K}\,\mathbb{L}^m\,\mathbb{K}^{-1} \tag{31}$$

where $\mathbb{L}$ is the diagonal matrix of $\mathbb{M}$'s eigenvalues (Equation 29), and $\mathbb{K}$ is the modal matrix formed by the eigenvectors, viz., the modes w_1/w_2 of the equation

$$(\ell_i\,\mathbb{I} - \mathbb{M})w^{(i)} = 0 \tag{32}$$

In our problem, taking ℓ_1, ℓ_2 from Equations 28 and 32 is

$$\left.\begin{aligned} \frac{a}{\lambda}\,w_1^{(1)} + \frac{b}{\lambda}\,w_2^{(1)} &= 0 \\ \frac{\mu a}{3\lambda}\,w_1^{(1)} + \frac{\mu b}{3\lambda}\,w_2^{(1)} &= 0 \end{aligned}\right\} \text{ and } \left.\begin{aligned} -\frac{\mu b}{3\lambda}\,w_1^{(2)} + \frac{b}{\lambda}\,w_2^{(2)} &= 0 \\ \frac{\mu a}{3\lambda}\,w_1^{(2)} - \frac{a}{\lambda}\,w_2^{(2)} &= 0 \end{aligned}\right\} \tag{33}$$

so that

$$\mathbb{K} = \begin{pmatrix} -b/a & 1 \\ 1 & \mu/3 \end{pmatrix} \text{ and } \mathbb{K}^{-1} = -\left(1 + \frac{\mu b}{3a}\right)^{-1} \begin{pmatrix} \mu/3 & -1 \\ -1 & -b/a \end{pmatrix} \tag{34}$$

The limiting value of $\mathbb{L}^m$ as $m \to \infty$, provided that criterion (30) is satisfied, is clearly

$$\mathbb{L}^m \to \begin{pmatrix} 1 & 0 \\ 0 & 0 \end{pmatrix} \text{ as } m \to \infty \tag{35}$$

The limiting value of $\mathbb{A}_{n+1}$ as $n \to \infty$ can now be calculated from Equations 26, 31, 34 and 35; it is

$$\mathbb{A}_\infty = \mathbb{K}\,\mathbb{L}^\infty\,\mathbb{K}^{-1}\,\mathbb{A}_1 = \begin{pmatrix} \frac{\mu b}{3a} & -\frac{b}{a} \\ -\frac{\mu}{3} & 1 \end{pmatrix} \left(1 + \frac{\mu b}{3a}\right)^{-1} \mathbb{A}_1 \tag{36}$$

where $\mathbb{A}_1$ describes the initial flow situation before the iteration is begun. Thus, $\mathbb{A}_\infty$ and the final flow depend on the initial flow; this is inevitable, since the amount of

the extraneous harmonic introduced must depend on how far the initial flow differs from unconfined flow.*

Let us now apply this result, Equation 36, to the two assumed fitting-assumptions. The results are given in Table II.

Table II: Final Flow

Fitting Assumption	A_∞	a'_∞
(a) Single-point	$\frac{-\mu A_1 + 3a'_1}{1-\mu}$	$\frac{-\frac{\mu}{3}A_1 + a'_1}{1-\mu}$
(b) Mean-square	$\frac{\mu^2 A_1 - 3\mu a'_1}{1+\mu^2}$	$\frac{-\frac{\mu}{3}A_1 + a'_1}{1+\mu^2}$

Since A_∞ is a measure of the residual error in the flow after convergence, it seems clear that for any given $|\mu| < 1$, mean-square fitting leads to a better approximation than single-point fitting at the midpoint of the half-cycle.

Numerical Example

In spite of the fact that the infinite sinusoidal case is an academic one, we think that a numerical example, albeit based on parameters chosen very arbitrarily, may have qualitative value in clarifying the effects of imperfect matching. For this purpose, let us choose the better of the two fitting-assumptions, viz., (b) above. Let us choose

*It might be pointed out that A_2 is identical with A_∞ if $k = 1/2$. This is called "one-step iteration" by Lo and Kraft.[4]

$\mu = 1/4$, which means that the tunnel walls can only reproduce a sine curve as a sort of square-wave.

Finally, as has already been pointed out, we have to select some initial conditions. It seems reasonable to say that the uncorrected wall configuration involves no third-harmonic component at all, viz., $a_1' = 0$; that is, the extraneous harmonic component is only brought into the flow by activation of the imperfect wall-control system.

Thus, our numerical example becomes the following:

Initial flow: $A_1 \neq 0$, $B_1 = -\beta\epsilon^{-1}V + A_1$, $a_1' = 0$

Wall control: $\mu = 1/4$, mean-square fitting

According to Table II, the converged flow is then described by

$$\left.\begin{aligned} A_\infty &= \frac{\mu^2 A_1}{1+\mu^2} = 0.059\ A_1 \\ a_\infty' &= -\frac{\mu}{3}\frac{A_1}{1+\mu^2} = -0.078\ A_1 \end{aligned}\right\} \qquad (37)$$

In Figure 1 are plotted curves of $\delta^{(1)}u(x,h)$ and $\delta^{(\infty)}u(x,h)$, viz., the initial and ultimate error signals, Equation 9, in this example. These functions are normalized in Figure 1 by dividing by $2\lambda e^{\beta\lambda h}A_1$, i.e.,

$$\frac{\delta^{(n)}u(x,h)}{2\lambda e^{\beta\lambda h}A_1} = \frac{A_n}{A_1}\ \sin\lambda x + 3\frac{a_n'}{A_1}\ \sin 3\lambda x \qquad (38)$$

For $n = 1$, a_n' is zero (see above); for $n = \infty$, A_n and a'_n are taken from Equations 37. The correction $f^{(1)}/2\lambda e^{\beta\lambda h}A_1$ is also plotted. (The function $f^{(\infty)}/2\lambda e^{\beta\lambda h}A_1$ reaches a maximum value of 0.0004 and cannot be shown on the scale of Figure 1).

The question arises: How large are the errors in flow at the model under these conditions, before and after correction? To cast some light on this, the error in $\phi_x^{(n)}(x,0)$ is plotted in Figure 2. Since the unconfined-flow value is $\lambda\beta^{-1}\varepsilon$ V sin λx, the error at the n-th iteration is

$$-2A_n \lambda \sin \lambda x - 6a_n \lambda \sin 3\lambda x \qquad (39)$$

To plot Figure 2, the conditions of our numerical example, above, have been chosen, and in addition, since the tunnel/model dimension ratio must be specified to evaluate a_∞, it has been assumed that $\beta\lambda h = 1$. Thus, $a_\infty = a'_\infty e^{-2\beta\lambda h} = -0.078 \times 0.1353\ A_1 = -0.01055\ A_1$.

In this example, since a_1 has been assumed to be zero--i.e., no extraneous harmonic in the uncorrected flow--the error at the model before correction is proportional to A_1. (With a solid wall at y = h, $A_1 = -\beta^{-1}\varepsilon V e^{-2\beta\lambda h} = -0.1353\ \beta^{-1}\varepsilon V$ in this example.) After iteration, the maximum error in $\phi_x(x,0)$ is reduced by a factor of 0.1813/2 = 0.09.

Conclusions

This preliminary, simplified investigation of the effects of imperfect wall control in an adaptable-wall wind tunnel suggests that (a) the iterative process can still converge, but (b) to an imperfect approximation to unconfined flow in which (c) the flow errors at the model may be substantially smaller than before iteration.

References

1. A. Ferri and P. Baronti, "A Method for Transonic Wind-Tunnel Corrections," AIAAJ, 2, 63-66 (1973).

2. W. R. Sears, "Self-Correcting Wind Tunnels," Aeronaut. J., 78, 80-89 (1974).

3. W. R. Sears, R. J. Vidal, J. C. Erickson Jr., and A. Ritter, "Interference-Free Wind-Tunnel Flows by Adaptive-Wall Technology," J. of Aircraft, Vol 14, No 11, 1042-1050 (November 1977).

4. C. F. Lo and E. M. Kraft, "Convergence of the Adaptive-Wall Wind Tunnel," AIAAJ, 16, 1, 67-72 (1978).

5. W. R. Sears, "A Note on Adaptive-Wall Wind Tunnels," ZAMP, 28, 915-927 (1977).

6. L. A. Pipes, "Matrix Methods for Engineering," Prentice-Hall (1963).

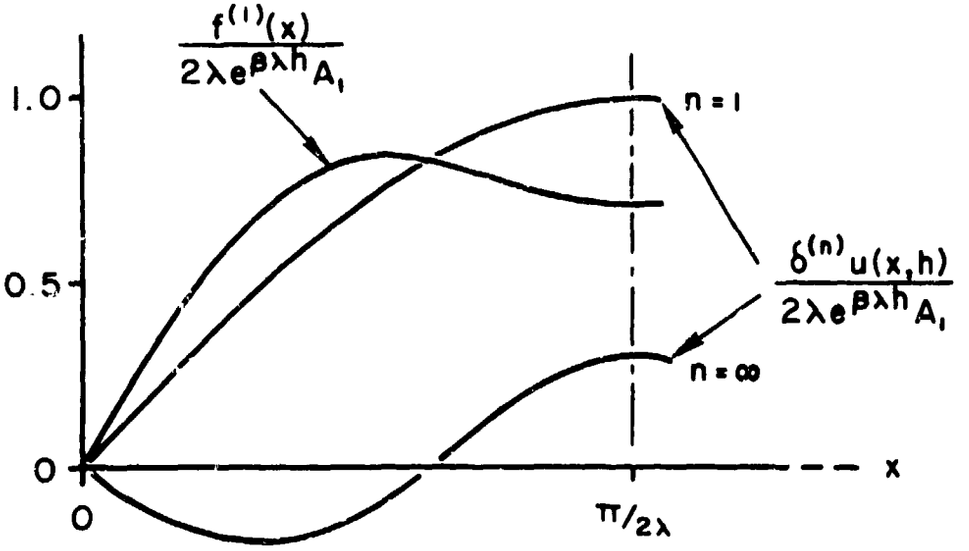

Figure 1. Error Signals $\delta^{(n)}u(x, h)$ and Correction Function $f^{(1)}(x)$

($a_1' = 0$, $\mu = 1/4$)

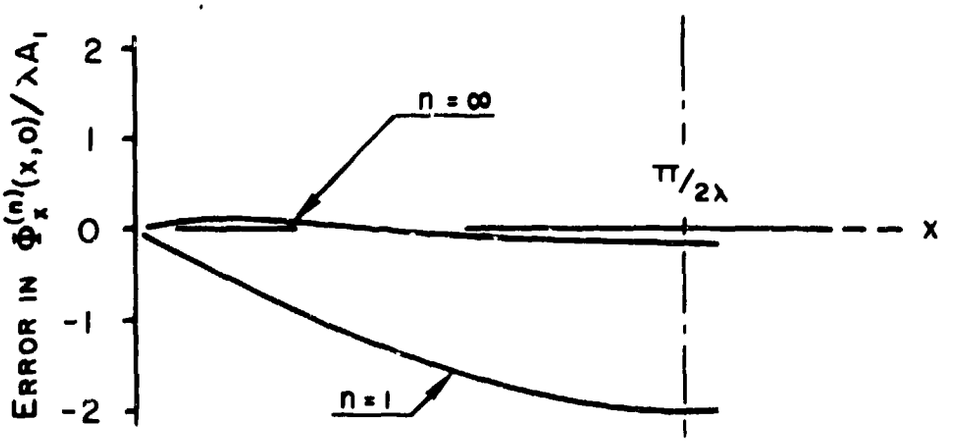

Figure 2. Relative Error in $\Phi_x^{(n)}$ at Model

($a_1' = 0$, $\mu = 1/4$, $\beta\lambda h = 1.0$)

AD P000324

THE NUMERICAL SOLUTION OF PRESSURE OSCILLATIONS IN AN OPEN CAVITY

by

W. L. Hankey and J. S. Shang
Air Force Flight Dynamics Laboratory
Wright-Patterson AFB, Ohio

Open cavities on aircraft exposed to high speed flow, such as bomb bays can give rise to intense self-induced pressure oscillations. The amplitude of these oscillations, under certain flight conditions, can cause structural damage. Substantial experimental and analytical efforts have investigated these pressure fluctuations, resulting in some understanding of the complex interaction of the external shear layer and cavity acoustical disturbances. However, no numerical computations have been obtained for the complete governing fluid mechanical equations. The purpose of this study is to obtain numerical solutions of the Navier-Stokes equations for an open cavity in order to provide a new tool for the analysis of this phenomenon.

Manuscript Received June 1979. This work performed under AFFDL Work Unit No. 2306N603.

NOMENCLATURE

a	=	speed of sound
A	=	coefficient in pressure perturbation equation
c	=	complex propagation speed
C_p	=	specific heat at constant pressure
D	=	cavity depth
e	=	specific internal energy
E, F	=	vector fluxes
f	=	frequency of wave
k	=	c_1/U_∞ propagation velocity ratio
L	=	cavity length
m	=	mode number
M	=	Mach number
n	=	node number
p	=	pressure
$\dot{q}$	=	heat transfer rate
R	=	gas constant
Re	=	Reynolds number
t	=	time
T	=	temperature
u, v	=	velocity components in Cartesian frame
U	=	vector of dependent variables
x, y	=	Cartesian coordinates
α	=	$2\pi\delta/\lambda$ dimensionless wave number
γ	=	ratio of specific heats
δ	=	shear layer thickness

λ	=	wave length
μ	=	viscosity (molecular and eddy)
ρ	=	density
σ	=	normal stress
τ	=	viscous shear stress
ϕ	=	amplitude of perturvation velocity
ω	=	$2\pi f$ frequency

Subscripts

∞	=	freestream condition
o	=	stagnation condition
w	=	wall condition
r	=	real part
i	=	imaginary part
1	=	forward traveling wave
2	=	rearward traveling wave

Superscripts

$'$	=	instantaneuos perturbation variable
-	=	vector

I. Background

As early as 1955, Krishnamurty[1] investigated flow induced pressure oscillations in open cavities. Other investigators[2,3,4,5,6,7,8,9] have conducted extensive research in an attempt to understand the physical mechanisms. Heller and Bliss[3] used a water table to simulate supersonic airflow over open cavities. They found that the inherently unstable shear layer fluctuates, causing periodic mass addition and expulsion from the cavity (Figure 1). When the rear reattachment point of the shear layer enters the cavity, a stagnation point is created; thus increasing the local cavity pressure. This mass addition creates a traveling pressure wave (as in a shock tube), which moves forward in the cavity (at supersonic speed relative to free stream), trailing an oblique shock in the free stream. When the traveling shock wave reflects from the forward bulkhead, a pressure doubling occurs in the cavity while disturbances in the external flow are not reflected, and thus a pressure jump across the shear layer deflects the shear layer. The reflected traveling shock wave in the cavity is now moving at subsonic speed relative to the free stream, hence, generates no oblique shock wave in the free stream. As the cavity traveling shock wave approaches the rear bulkhead, the shear layer bulges outward, and mass is ejected out of the cavity. The entire process then repeats itself in a periodic fashion.

Thus, sufficient experience from such extensive measurements exists so that a qualitative description of the flow process can be obtained. However, a quantitative prediction method does not exist which is the motivation for the present investigation.

To study self-induced pressure oscillations in an open cavity, an analytic study was first accomplished, followed by a numerical computation of the Navier-Stokes equations and a comparison with previous experimental investigations.

II. Analytical Study

Consider a system of traveling waves which produce the wave-diagram (x,t) shown in Figure 2. A resonant situation arises when a forcing function excites the shear layer in the frequency range where amplification is possible. The disturbances will grow until a limit cycle is reached due to viscous dissipation. A standing wave exists in the cavity when both the upstream and downstream traveling waves are synchronized. This wave pattern of Figure 2 may be approximated by considering forward and rearward traveling pressure waves of equal intensity but different propagation velocities and wave numbers.

$$p' = Ae^{i\alpha_1(x - c_1 t)} + Ae^{i\alpha_2(-x - c_2 t)} \tag{1}$$

The frequency of the pressure pulse can be determined directly from the wave diagram.

$$\frac{m}{f} = \frac{L}{c_1} + \frac{L}{c_2} \tag{2}$$

where m is the number of waves or mode number.

From observation of cavity oscillations the rearward traveling wave (α_2) is known to be an acoustical disturbance traveling at the speed of sound in the cavity.

$$c_2 = U_\infty \sqrt{1 + 0.2M_\infty^2}\; M_\infty^{-1}$$

The progagation speed of the forward traveling wave has been observed to be about half of the free stream value[6].

$$\frac{c_1}{U_\infty} \equiv k \sim 1/2 \tag{4}$$

The frequency can be evaulated by using these results.

$$f = \frac{mU_\infty}{L(M_o + k^{-1})} \qquad \text{Rossiter's Formula (Ref 4)} \tag{5}$$

This equation have been used successfully for determining cavity resonant frequencies but no satisfactory prediction method has been available for determining the disturbance intensity of the different modes.

The mode shape of these standing waves can also be deduced from the preceding equations. For a standing wave to occur both waves must possess the same frequency.

$$\omega = \alpha_1 c_1 = \alpha_2 c_2 = 2\pi f \tag{6}$$

Combining this result with equation 2 produces the following relationship:

$$\alpha_1 + \alpha_2 = \frac{2\pi m}{L} \tag{7}$$

The mode shape may be obtained by utilizing this information in the pressure equation (equation 1) and computing the rms value of pressure over a complete cycle.

$$\begin{aligned} p_{rms} &= A(1 + \cos\ (\alpha_1 + \alpha_2)x)^{\frac{1}{2}} \\ p_{rms} &= A\left|\cos \frac{m\pi x}{L}\right| \end{aligned} \tag{8}$$

These patterns have been documented in Ref 3. Nodes will occur when

$$\frac{m\pi x}{L} = n\frac{\pi}{2}; \qquad n = \text{odd}$$

Mode m	Nodes n		
	1	3	5
1	1/2	---	---
2	1/4	3/4	---
3	1/6	3/6	5/6

Table I Node Location for Various Modes

III. Stability Analysis

A necessary condition for resonance is that one of the waves must be unstable for the oscillation to persist, otherwise the disturbance will dissipate after an initial transient. Mathematically this means that the wave speed is complex, i.e., $c = c_r + ic_i$ with $c_i > 0$ unstable. The stability of the shear layer will now be examined.

Rayleigh[10], in 1880, showed for inviscid incompressible flow that velocity profiles with inflection points are unstable. Recently, Michalke[11] confirmed that a shear layer is unstable but only at low frequencies ($\lambda/\delta > 2\pi$ or $f\delta 4\pi/U_\infty < 1$). It was felt that more information about the stability of a compressible shear layer was needed, therefore, a linear stability analysis was undertaken[12]. The governing Euler equations were linearized by assuming small perturbations caused by small amplitude traveling waves. The resulting stability equation first derived by Lees and Lin[13], reduces to the Rayleigh equation for incompressible flow.

$$a^2[g^{-1}(U - c)\phi_y - g^{-1} U_y \phi]_y = \alpha^2(U - c)\phi \qquad (9)$$

where

$$v = \phi(y)e^{i\alpha(x - ct)} \tag{10}$$

$$g = a^2 - (U - c)^2 \tag{11}$$

The eigenvalues of this Rayleigh equation were then computed[12] for a shear layer with a hyperbolic tangent velocity profile.

$$\frac{U}{U_\infty} = 0.5\ (1 + \tanh \frac{y}{\delta}) \tag{12}$$

The propagation velocity (c_r) of the disturbances is shown in Figure 3.

$$\frac{c_r}{U_\infty} = k \tag{13}$$

This is the k value determined experimentally by Rossiter[6] and found to be in excellent agreement with his results.

$$.5 < k < .6$$

The amplification factors ($c_i > 0$) were found to be a function of wave number (α) and Mach number (Figure 4). Instability was observed only for wave numbers less than unity. This implies short cavities ($L < 2\pi\delta$) will not resonate. Note the Rayleigh instability vanishes above M = 2.5. This result confirms previous experimental and numerical results that separated flows are more stable at supersonic speeds than at subsonic.

It is possible to predict the relative intensity of the different modes occurring in an open cavity. Consider a cavity of L = 91.44 cm and $M_\infty = 0.85$, $U_\infty = 286.5$ mps

Hence,

$$\frac{c_r}{U_\infty} = k = .52 \quad \text{(from Fig 3)}$$

$$M = 0.79$$

$$f = 115\ \text{(Hz)} \quad \text{Rossiter's Eqn.}$$

These different mode frequencies are plotted in Figure 5 using results of Ref 12, and the second mode is observed to have the greatest amplification while modes four and above are found to be stable. A spectral analysis of a wind tunnel test (Ref 14) for an open cavity at these same conditions is also shown in Figure 5. Observe that only the first four modes are dominant and the relative amplitudes of these four modes are consistent with the analytic amplification factors.

The intensity of the pressure fluctuation will be proportional to the following:

$$p_{rms}\ (M) \sim q(e^{\alpha c_i} - 1) \tag{14}$$

Selecting the peak value of $e^{\alpha c_i}$ for each Mach number and multiplying by $q/P_o(M)$ the relative intensity as a function of Mach number may be deduced (Fig 6). The peak pressure value occurring in a series of wind tunnel tests at different Mach numbers can be expected to occur near Mach one. This is confirmed in Reference 3 and 14.

IV. Summary of Analytic Results

The analytic results based primarily upon stability theory provide us with the following conclusions.

a. Shear layers (with inflection points in the velocity profile) are unstable but only for low frequencies; $f\delta/U_\infty < 1/4\pi$.

b. Short cavities ($L < 2\pi\delta$) will not resonate.

c. No Rayleigh instability occurs above Mach number 2.5.

d. Peak amplification occurs at about half the cut-off frequency creating a situation where modes other than the fundamental can dominate.

e. Maximum pressure intensity of a shear layer oscillation will occur near Mach 1 (in a wind tunnel with constant p_o).

Linear stability theory is therefore useful in explaining the cause of the resonance and in estimating the relative intensity of the various modes including the influence of Mach number. However, the full non-linear equations are required to determine the absolute level of the pressure intensity. For that reason the numerical solution of the unsteady Navier-Stokes equations will be considered next.

V. Numerical Computation

With the completion of the simplified analytic approach (ie, inviscid, linear stability theory) a numerical solution of the exact equations was attempted to further improve the prediction capability. The analysis served to identify the primary mechanism involved in the oscillation and greatly assisted in the determination of the grid point distribution and step sizes required to resolve the flow features.

A case to compute was selected for which experimental data were available. The test conditions of Heller and Bliss[3] were selected to compare the numerical computations (Figure 7).

$M = 1.5$	$L = 91.44$ cm
$L/D = 2.25$	$D = 40.64$ cm
$Re = 1.28 \times 10^6/m$	$\delta_o = 2.54$ cm

The width of the cavity was 22.86 cm and found not to be a major factor in the overall phenomenon. For this reason, a two-dimensional computation appeared to be justified for the initial studies.

VI. Governing Equations

The time dependent explicit finite difference method originated by R. MacCormack[15] was selected to perform the numerical calculations. The two-dimensional Navier-Stokes equations follow:

$$\frac{\partial U}{\partial t} + \frac{\partial E}{\partial x} + \frac{\partial F}{\partial y} = 0 \tag{15}$$

$$U = \begin{vmatrix} \rho \\ \rho u \\ \rho v \\ \rho e \end{vmatrix} \quad ; \quad E = \begin{vmatrix} \rho \\ \rho u^2 - \sigma_{xx} \\ \rho uv - \tau_{xy} \\ \rho ue - \sigma_{xx} u - v\tau_{xy} - \dot{q}_x \end{vmatrix} \quad ;$$

(16)

$$F = \begin{vmatrix} \rho v \\ \rho uv - \tau_{xy} \\ \rho v^2 - \sigma_{yy} \\ \rho ve - v\sigma_{yy} - u\tau_{xy} - \dot{q}_y \end{vmatrix}$$

where

$$\sigma_{xx} = -p - 2/3\mu\nabla \cdot \bar{u} + 2\mu\, u_x$$

$$\tau_{xy} = \mu(u_y + v_x)$$

$$\sigma_{yy} = -p - 2/3\mu\nabla \cdot \bar{u} + 2\mu u_y$$

The turbulent closure of the present problem was achieved by implementing the Cebeci-Smith eddy viscosity model with relaxation modification[16]. The relaxation turbulence model was used in an attempt to describe the adjustment of the turbulence structure from an attached boundary layer to an oscillatory free shear layer. The relaxation length scale was assigned a value of 55 boundary layer thicknesses. Since there is no guidance to

assess the accuracy of the turbulence model relative to low frequency fluctuations, a parametric study seemed to be necessary. In the present analysis, several consecutive calculations with suppressed eddy viscosity were performed and the numerical results exhibited only a minor departure from the basic solution. Hence, the present eddy viscosity model was felt to be adequate. The computer program previously used by Shang[16,17] was modified to include the appropriate boundary conditions for this problem.

VII. Boundary Conditions

Four faces require attention in the specification of boundary conditions (Figure 7).

Wall and Cavity Surfaces:

On solid surfaces, the velocity components vanish, and the wall temperature must be prescribed. In addition, the pressure is derived from the respective compatibility conditions of the momentum equations.

$$u = 0 \qquad v = 0 \qquad T_w = T_o$$

$$\frac{\partial p}{\partial x} = \frac{\partial}{\partial x}\left[-2/3\mu\nabla \cdot \bar{u} + 2\mu u_x\right] - \frac{\partial}{\partial y}\left[\mu(u_y + v_x)\right] \tag{18}$$

$$\frac{\partial p}{\partial y} = \frac{\partial}{\partial y}\left[-2/3\mu\nabla \cdot \bar{u} + 2\mu u_y\right] - \frac{\partial}{\partial x}\left[\mu(u_y + v_x)\right]$$

Upstream Condition:

A supersonic free stream with a known boundary layer profile is given.

$$u = u\,(y) \qquad T = T_o - \frac{u^2}{2C_p} \tag{19}$$

$$v = 0 \qquad p = p_\infty$$

Downstream Condition:

A mild boundary condition is prescribed to avoid major reflections of disturbances.

$$\frac{\partial u}{\partial x} = 0 \qquad \frac{\partial T}{\partial x} = 0$$

$$\frac{\partial v}{\partial x} = 0 \qquad \frac{\partial p}{\partial x} = 0 \tag{20}$$

Upper Boundary:

A similar no-reflection condition is adopted.

$$\frac{\partial u}{\partial \zeta} = 0 \qquad \frac{\partial T}{\partial \zeta} = 0$$

$$\frac{\partial v}{\partial \zeta} = 0 \qquad \frac{\partial p}{\partial \zeta} = 0 \tag{21}$$

Where ζ is the outgoing characteristics on the upper boundary of the computational domain.

Initial Condition:

The upstream condition is imposed as the initial condition for the flow outside the cavity. Inside the cavity initially the flow is assumed to be static.

$$u = 0 \qquad v = 0 \qquad T = T_o \qquad p = p_\infty \tag{22}$$

VIII. Numerical Procedure

MacCormack's[15] alternating-direction-explicit numerical scheme was adopted for the present analysis. For this case pressure damping was required due to the transient multi-wave structure occurring in the flow

field. The current philosophy in computational fluid dynamics is to employ a body oriented coordinate system which turns out to be Cartesian in this case with non-uniform step size. For cases presented here, a grid of 78 x 52 was used to represent a field size of 182.9 cm x 91.44 cm enclosing a 91.44 cm x 40.64 cm cavity (see Figure 7). In order to achieve the desired temporal resolution, a time step corresponding to a Courant number of 0.2 was used. All calculations were performed on a CDC 6600 computer. The data processing rate was 0.0017 sec per grid point per time step. The central core memory required for the present problem is 205K octal.

Although dispersion, dissipation and phase errors are not negligible with the step sizes employed, previous numerical investigations of viscous interaction problems[15,16] using comparable step sizes have shown good agreement ($\pm$5%) with experimental data for the most significant features of the flow. In particular, periodic motions around a transonic airfoil have been studied by Levy[18] with a basic MacCormack's scheme. His results exhibited good agreement with experimental data not only in the pattern of a simple wave train but also in the predicted reduced frequency. Therefore, no additional modification other than a simple controlled spatial averaging was used to correct the possible dispersion error for the compound wave problem investigated.

IX. Discussion of Results

Time dependent numerical computations of supersonic flow over an open cavity were accomplished utilizing MacCormack's finite difference explicit method. The entire velocity field over the cavity is shown in

Figure 8. Since the problem is strictly a time dependent phenomenon, only a typical velocity distribution is presented here (t = 0.0062 sec) to reveal the basic features. The most obvious feature is that the flow field within the confined cavity is subsonic, except perhaps the region adjacent to the cavity opening. The experimental investigation[3] also recorded the identical observation. The orderly development of the shear layer above the cavity is also clearly exhibited. An attached turbulent boundary layer upstream of the cavity separates at the forward bulkhead to form a free shear layer over the cavity and finally reattaches downstream of the cavity. Due to the smaller magnitude of the velocity components within the cavity, the velocity distribution could not be shown with the same scale as that of the outer shear layer. A magnified velocity profile in the cavity is presented in Figure 9. All velocity distributions were drawn at a scale ten times greater than that in Figure 8. A recirculation flow configuration is demonstrated with the center of the recirculation located near the upper corner of the rear bulkhead. For clarity only every fourth velocity point in the streamwise direction was presented in both figures (Fig 8 and 9).

A quantitative comparison of the calculated mean velocity distribution with experiment is presented in Figure 10. The calculated velocity profile immediately upstream and downstream of the cavity compares very well with the experimental measurements. The upstream velocity profile is essentially independent of time as expected, and nearly duplicates the data. The downstream velocity profile indicates that the reattached shear layer thickens significantly over the cavity. The difference between data and calculation is a mere seven percent. The computed velocity profile downstream of the cavity exhibits an oscillatory behavior in the inner portion of the boundary layer which is confirmed by the experimental observation.

A comparison of the time-average surface pressure distribution in the cavity was performed. In Figure 11, one observes that the computed mean pressure, normalized by the free stagnation pressure, uniformly under predicts the experimental data[3] by about 10 percent. The maximum deviation between data and calculation occurs near the rear bulkhead were the pressure difference accross the cavity opening and cavity floor also reaches a maximum. Nevertheless, the calculated results indicate the identical trend to that of the experiment[3].

In Figure 12, a history of the static pressure at $x/L = 0.66$ and $y/L = 0.960$ is monitored ($y/L = 0.960$, $x/L = 0.33$, 0.50 and 0.66). Persistent oscillatory static pressures appeared within one characteristic time, t_{ch}. The characteristic time is defined as the period of time required for a fluid particle to traverse the length of the cavity at freestream speed. For the present problem t_{ch} has a value of 1.987×10^{-3} seconds. Since the pressure oscillation over the cavity is composed of several frequencies of different amplitude, a compound wave system develops. The present calculation was carried out only over a time span of about nine characteristic times ($t = 1.82 \times 10^{-2}$ secs). This result is compared with oscillogram data for the test results of Ref. 18 in Figure 12. In order to permit a qualitative comparison, computed results are repeated for several cycles. One can detect certain similarity between the data and the present result. In principle, the solid surface constraint and wave interference phenomenon of the present problem are inherently nonlinear. Therefore, caution must be exercised in discerning the discrete frequencies between the fundamental modes of oscillation. Other basic information such as the relative phase angle and the amplitude of each distinctive wave requires further spectral analysis.

A spectral analysis of this compound wave probably is the only reliable means for accurately obtaining mode frequency. However, this is impractical due to the large amount of computer time required to obtain solutions for a sufficiently long duration. Hence, an analysis was accomplished by assuming the waves to be commensurable. The spectral analysis reveals four distinctive discrete frequencies of 154 Hz, 308 Hz, 462 Hz, and 616 Hz recognized as the first, second, third and fourth mode respectively of the oscillatory pressure disturbance. The higher modes of oscillation decay rapidly as one may observe in Figure 13. Good agreement between the experimental measurement and present result is observed. Both exhibit a dominate second mode of the pressure oscillation. The level of pressure oscillation in db can be evaluated as

$$p(db) = 20 \log \frac{p_{rms}}{q_\infty} + 189$$

where q_∞ is the dynamic pressure (54 K pascal). The detected frequency for the second mode (308) compares well with the experimental data (300 Hz) and Rossiter's prediction[6] (328 Hz). The fluctuating pressure level between the data and present result is within about ten percent.

The compound wave pattern is best illustrated in Figure 14. The propagation of the wave train from the forward bulkhead is presented for a fixed time interval of 0.64×10^{-3} seconds. One observes the rearward traveling propagation wave has an unmodulated amplitude until interacting with reflected waves from the rear bulkhead. No repeatable wave front can be identified downstream of $x/L = 0.75$. Two pieces of important information have been determined from this graph, namely the rearward wave propagation speed and the amplitude of the pressure oscillation. The predicted wave speed has a value of 244.4 mps (or $k = .53$) and is in agreement

with the predicted value from Figure 3. The amplitude of the oscillating pressure also agrees well with data, (± 6.464 K pascal vs 7.182 K pascal; or 170 db) with the discrepancy about 10%.

In Figure 15 the sequence of density contours from the numerical computation is shown for a complete cycle of the periodic motion. The forward and rearward moving wave system originated from the instability of the free shear layer and the reflection at the rear bulkhead can be easily recognized in the cavity. The generation and movement of the external shock wave system also can be recognized. These compare favorably with the wave pattern shown in Figure 1 for the water table experiment.

X. Conclusions

The pressure oscillation for supersonic flow over an open cavity has been predicted by numerically solving the unsteady Navier-Stokes equations. Both the predicted frequency and magnitude of the unsteady pressure fluctuations were qualitatively confirmed through experiment. However, a spectral analysis of a numerical solution of longer duration is required for complete verification. This is the first time a complete viscous solution of the pressure oscillating cavity has been obtained and displays the outstanding capability inherent in the numerical methods of today.

References

1. Krishnamurty, K., "Acoustic Radiation from Two Dimensional Rectangular Cutouts in Aerodynamic Surfaces," NACA TN 3487, August 1955.

2. Heller, H., Holmes, G. and Covert, E., "Flow Induced Pressure Oscillations in Shallow Cavities," AFFDL-TR-70-104, WPAFB, Ohio, 1970.

3. Heller, H. and Bliss, D., Aerodynamically Induced Pressure Oscillations in Cavities: Physical Mechanisms and Suppression Concepts, AFFDL-TR-74-133, WPAFB, Ohio, 1974.

4. Clark, R. L., "Weapons Bay Turbulence Reduction Techniques," AFFDL-TM-75-147, WPAFB, Ohio, 1975.

5. Mainquist, R. S., "An Experimental Investigation into the Suppression of Flow-Induced Pressure Oscillations in Two Dimensional Open Cavities," AFIT Thesis, March 1978.

6. Rossiter, J. E., "Wind-Tunnel Experiment on the Flow Over Rectangular Cavities at Subsonic and Transonic Speeds, R & M No. 3428, British A.R.C., October 1964.

7. Spee, B. M., "Wind Tunnel Experiments on Unsteady Cavity Flow at High Subsonic Speeds," AGARD Conference Proc., No. 4, Separated Flow II, 1966.

8. Quinn, B., "Flow in the Orifice of a Resonant Cavity," AIAA Student Journal, 1963.

9. Borland, C. J., "Numerical Prediction of the Unsteady Flowfield in an Open Cavity," No. 77-673, AIAA 10th Fluid & Plasma Dynamics Conference, 1977.

10. Rayleigh, Lord, "On the Stability or Instability of Certain Fluid Motion," Scientific Papers, Vol. 1, pp. 474-484, 1880.

11. Michalke, A, "On the Inviscid Instability of the Hyperbolic-Tangent Velocity Profile," Journal Fluid Mechanics, Vol. 19, pp 543-556, August 1964.

12. Roscoe, D. and Hankey, W., "Stability of Compressible Shear Layers," (To be published as an AFFDL-TR, 1978).

13. Lees, L. and Lin, C.C., "Investigation of the Stability of the Laminar Boundary Layer in a Compressible Fluid," NACA TN 1115, Sep 1946.

14. Maurer, O., "Investigation and Reduction of Weapons Bay Pressure Oscillations Expected in the B-1 Aircraft," AFFDL-TM-74-101, WPAFB, Ohio, 1974.

15. MacCormack, R. W. and Baldwin, B. S., "A Numerical Method for Solving the Navier-Stokes Equations with Application to Shock Boundary Layer Interactions," AIAA Paper 75-1, Pasadena, California, 1975.

16. Shang, J. S. and Hankey, W. L., Jr., "Numerical Solutions for Supersonic Turbulent Flow over a Compression Ramp," AIAA J., Vol. 13, Oct 1975.

17. Shang, J. S. and Hankey, W. L., Jr., "Numerical Solution of the Navier-Stokes Equations for a Three-Dimensional Corner," AIAA J., Vol. 15, 1977, pp. 1575-1582.

18. Levy, L. L., Jr., "Experimental and Computational Steady and Unsteady Transonic Flows About a Thick Airfoil," AIAA J., Vol. 16, No. 6, June 1978, pp. 564-572.

Figure 1. Typical Pressure Oscillation Cycle (Ref. 3)

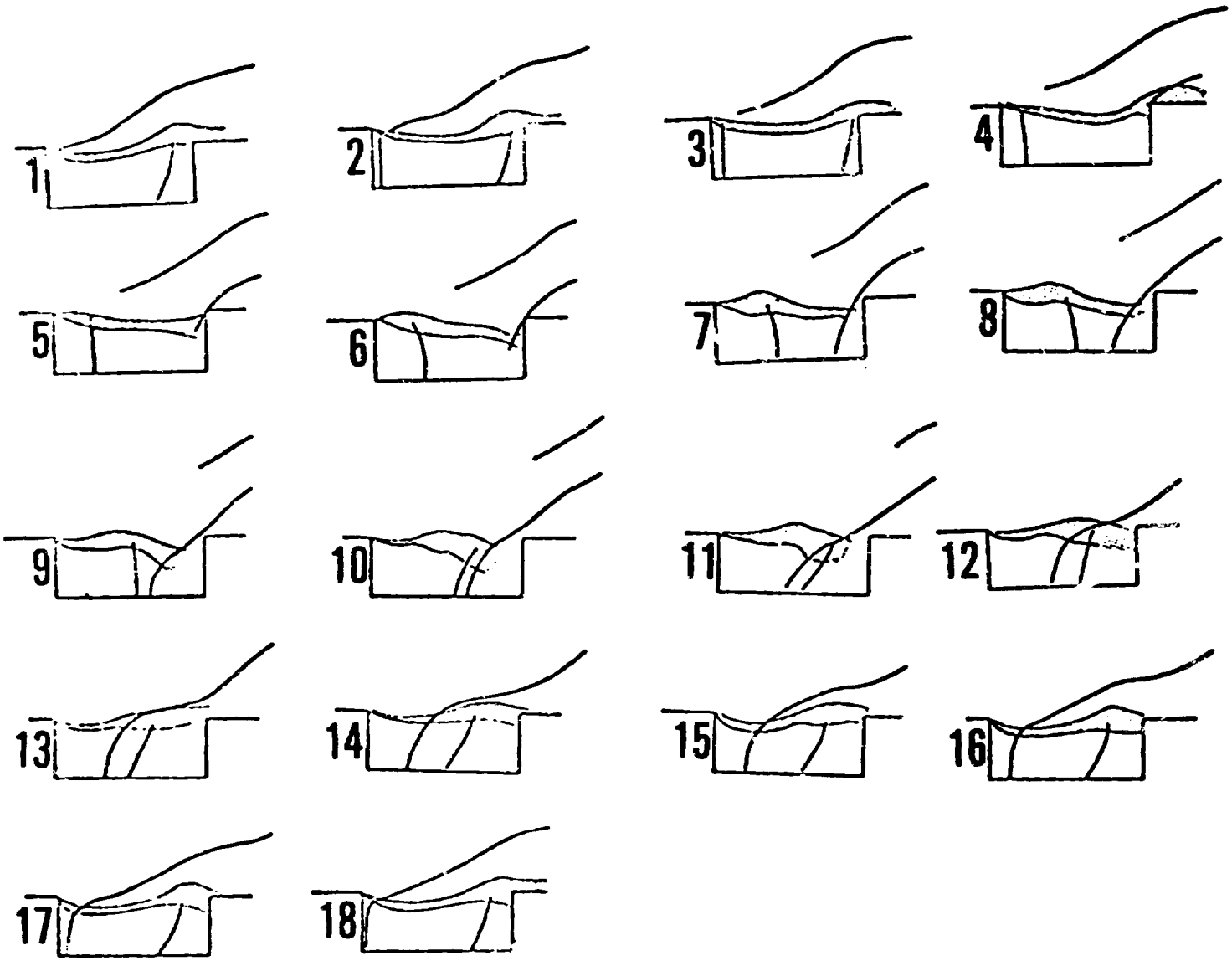

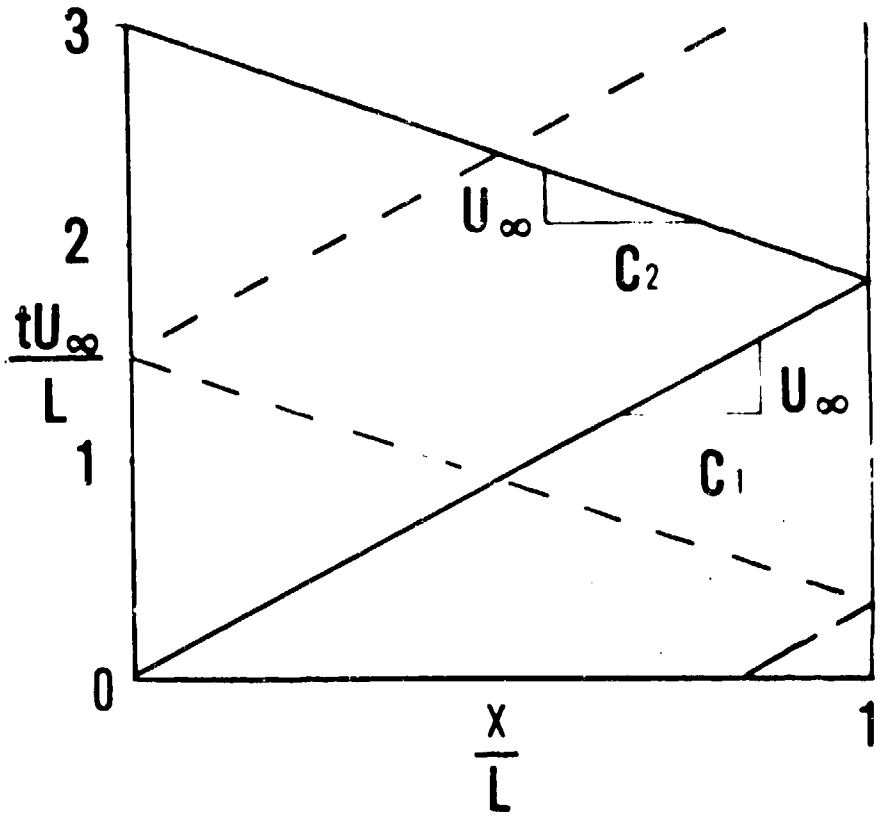

Figure 2. Wave Diagram

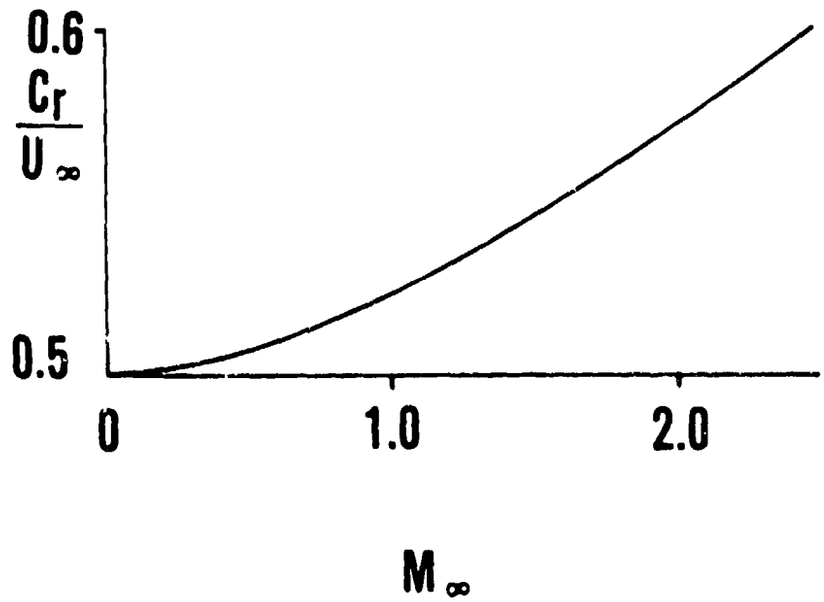

Figure 3. Propagation Velocity v.s. Mach Number of Traveling Waves in a Free Shear Layer (Ref. 12)

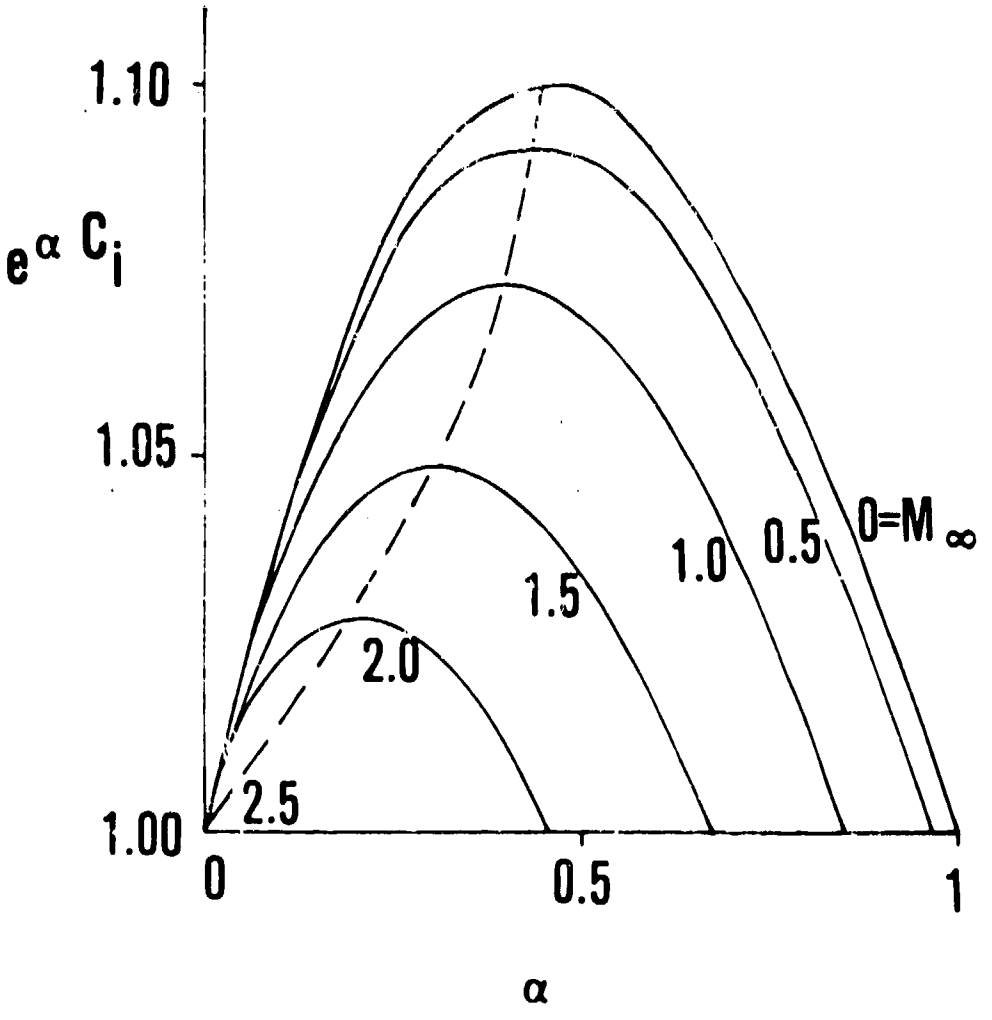

Figure 4. Amplification Factor v.s. Wave Number for Different Mach Number (Ref. 12)

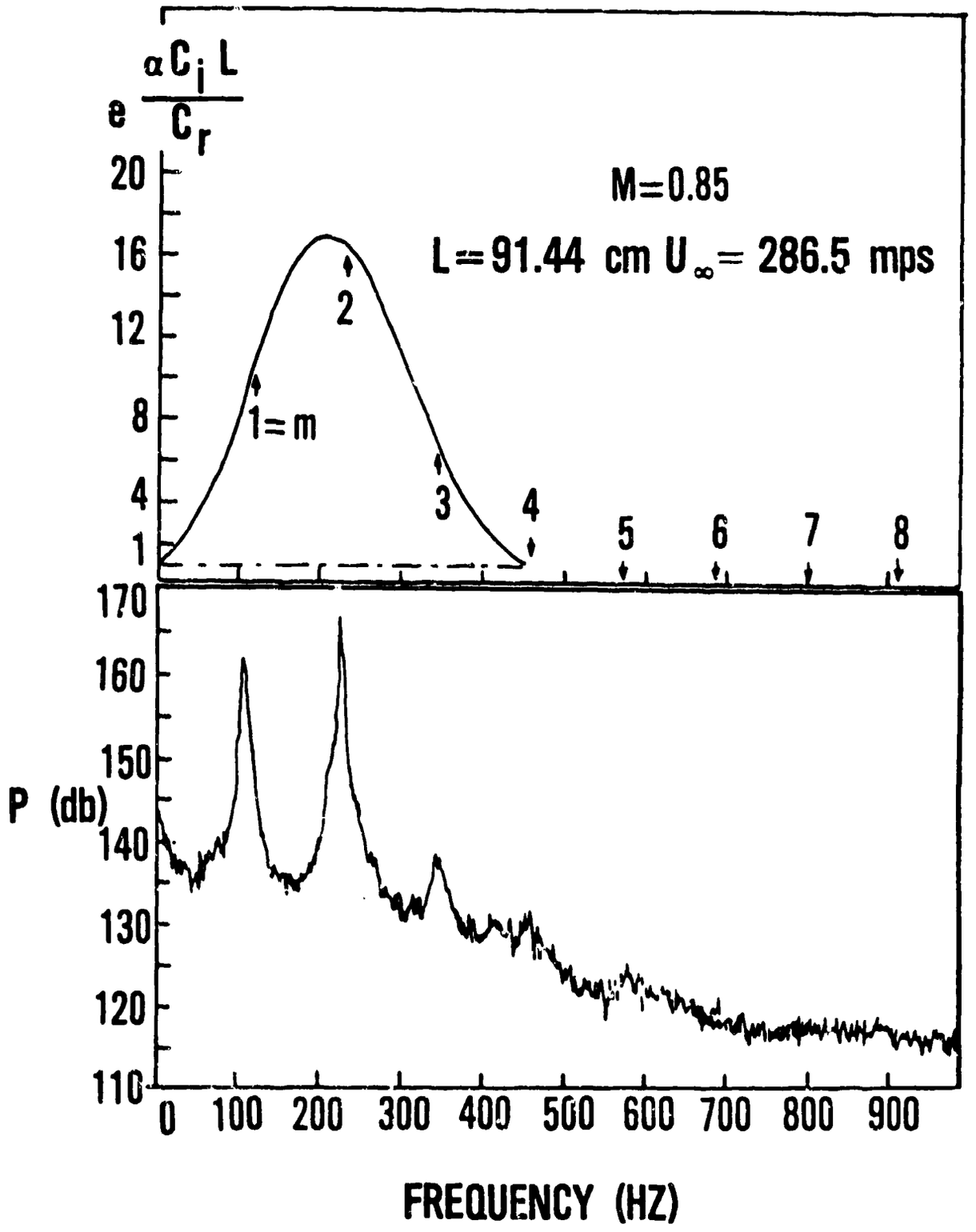

Figure 5. Comparison of Amplification for Different Frequencies with Experimental Data

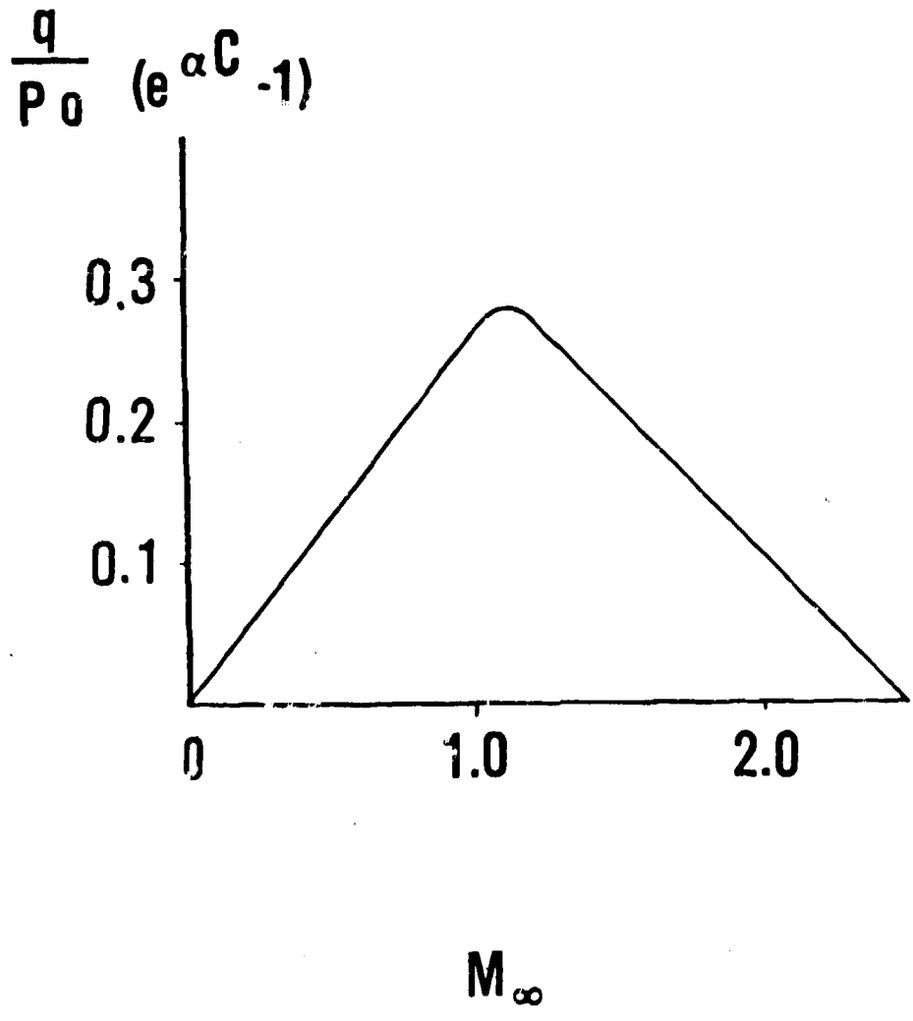

Figure 6. Relative Intensity of Disturbances for Different Mach Numbers

FIGURE 7. COMPUTATIONAL DOMAIN AND MESH POINT DISTURBATION FOR NUMERICAL INVESTIGATION

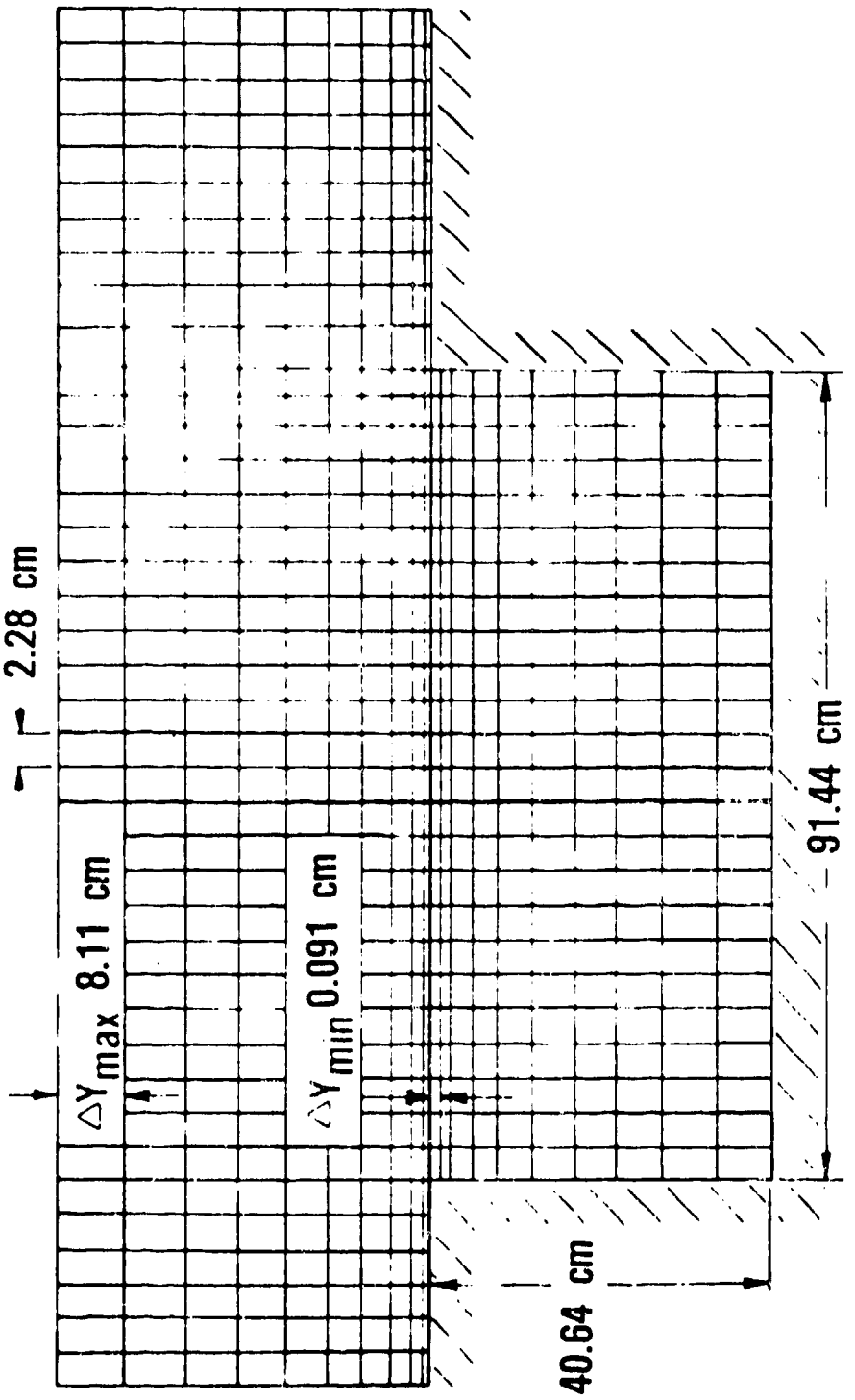

$M_\infty = 1.50$ $Re = 26 \times 10^6$ $L/D = 2.25$

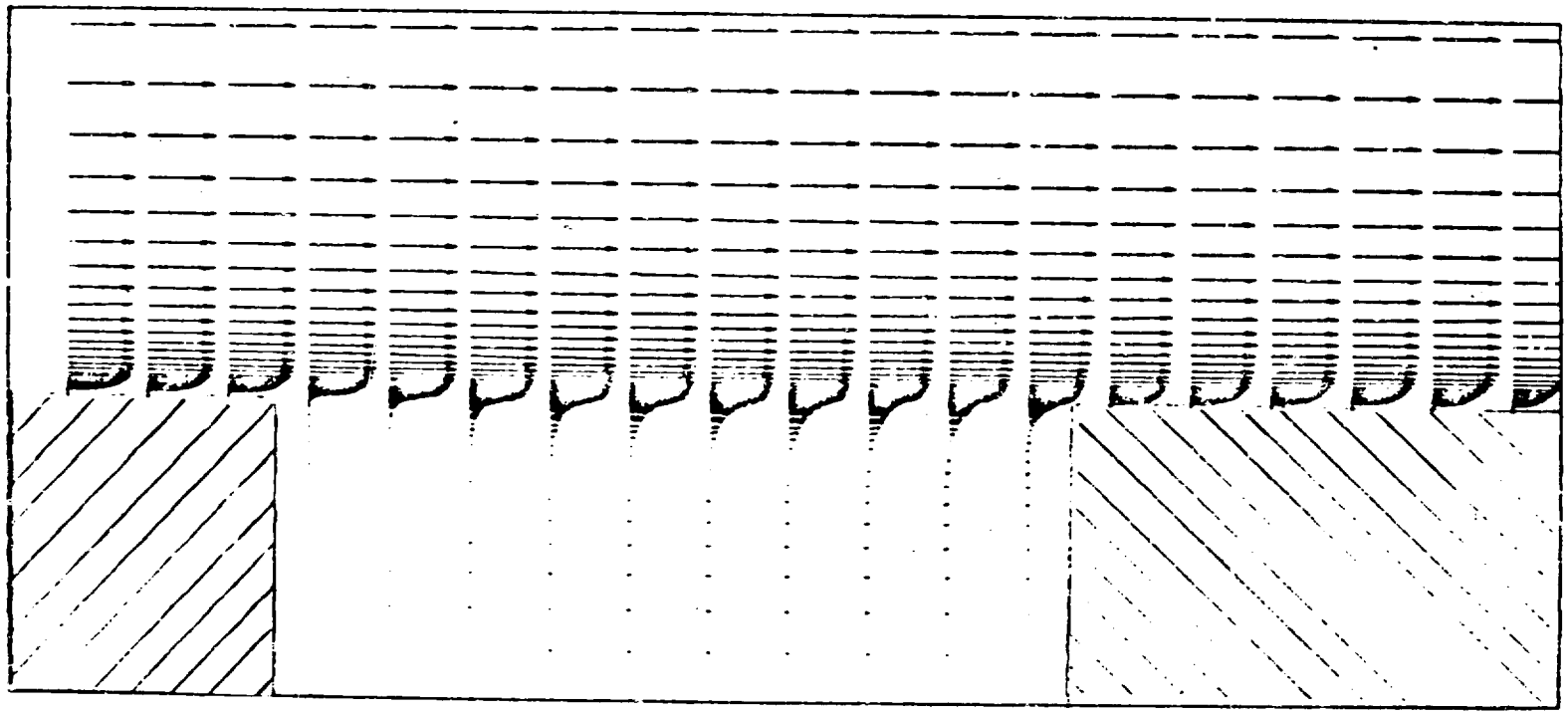

Figure 8. Velocity of the Entire Flow Field (t = 3tch)

$M_\infty = 1.50$ $Re = 2.6 \times 10^7$ $L/D = 2.25$

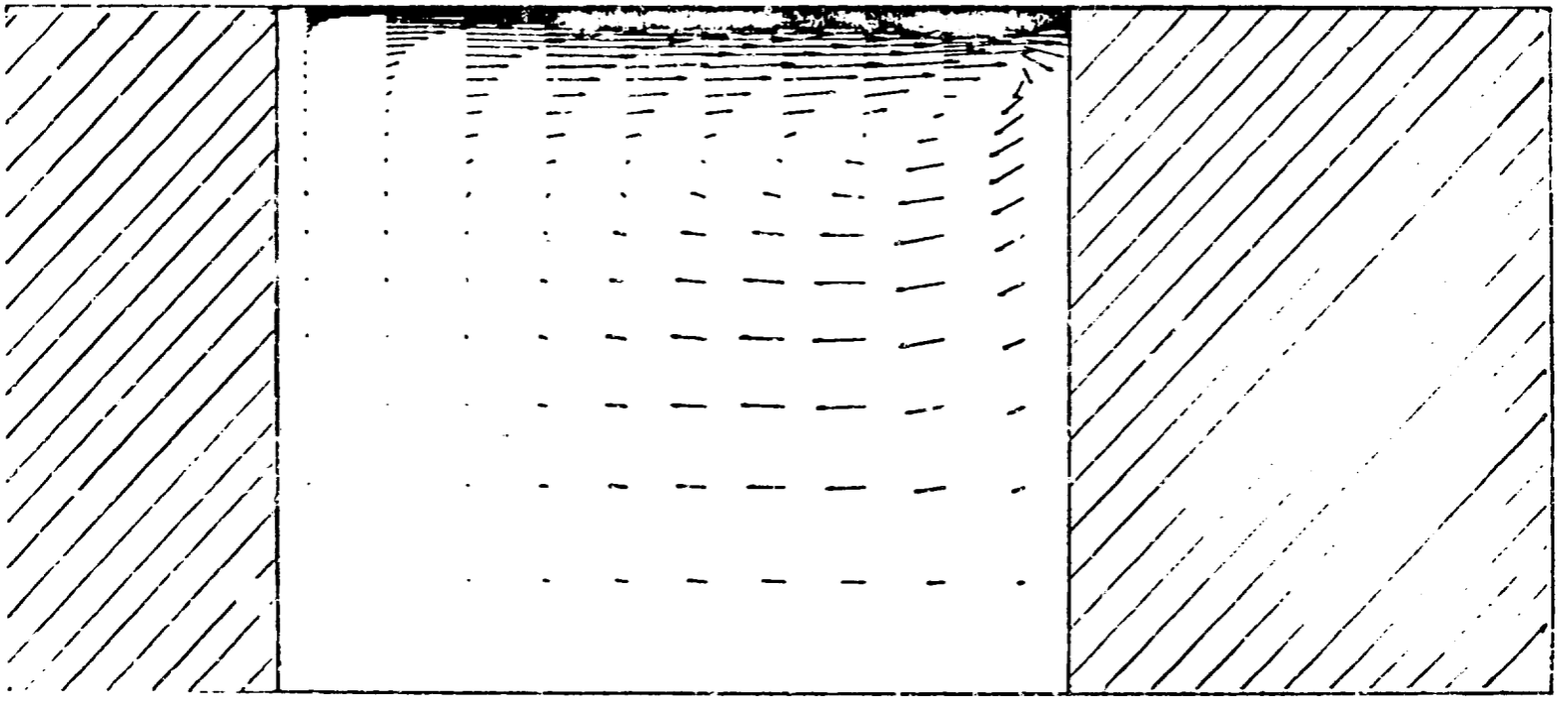

Figure 9. Velocity Profiles within the Cavity (t = tch)

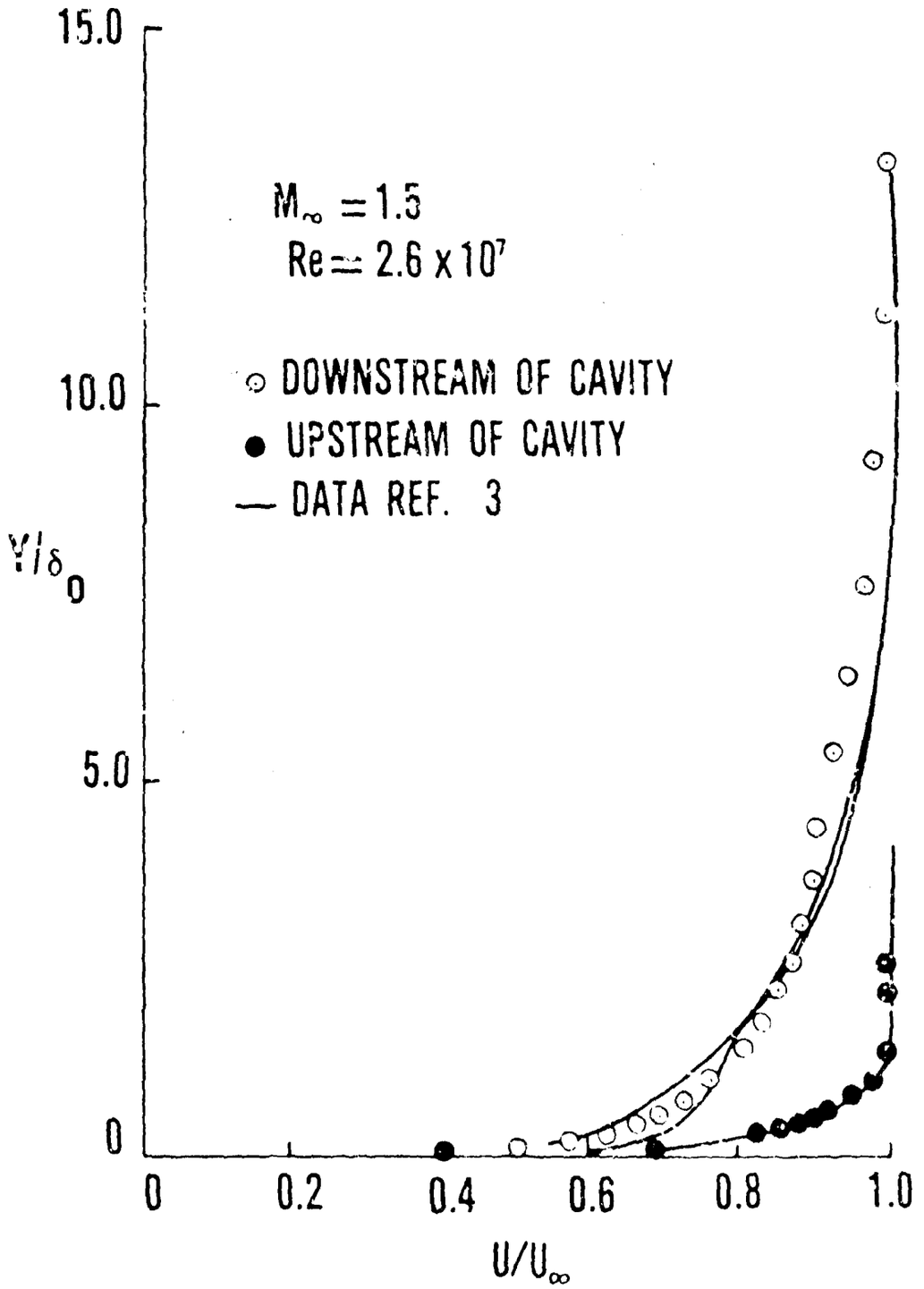

Figure 10. Comparison of Velocity Profiles

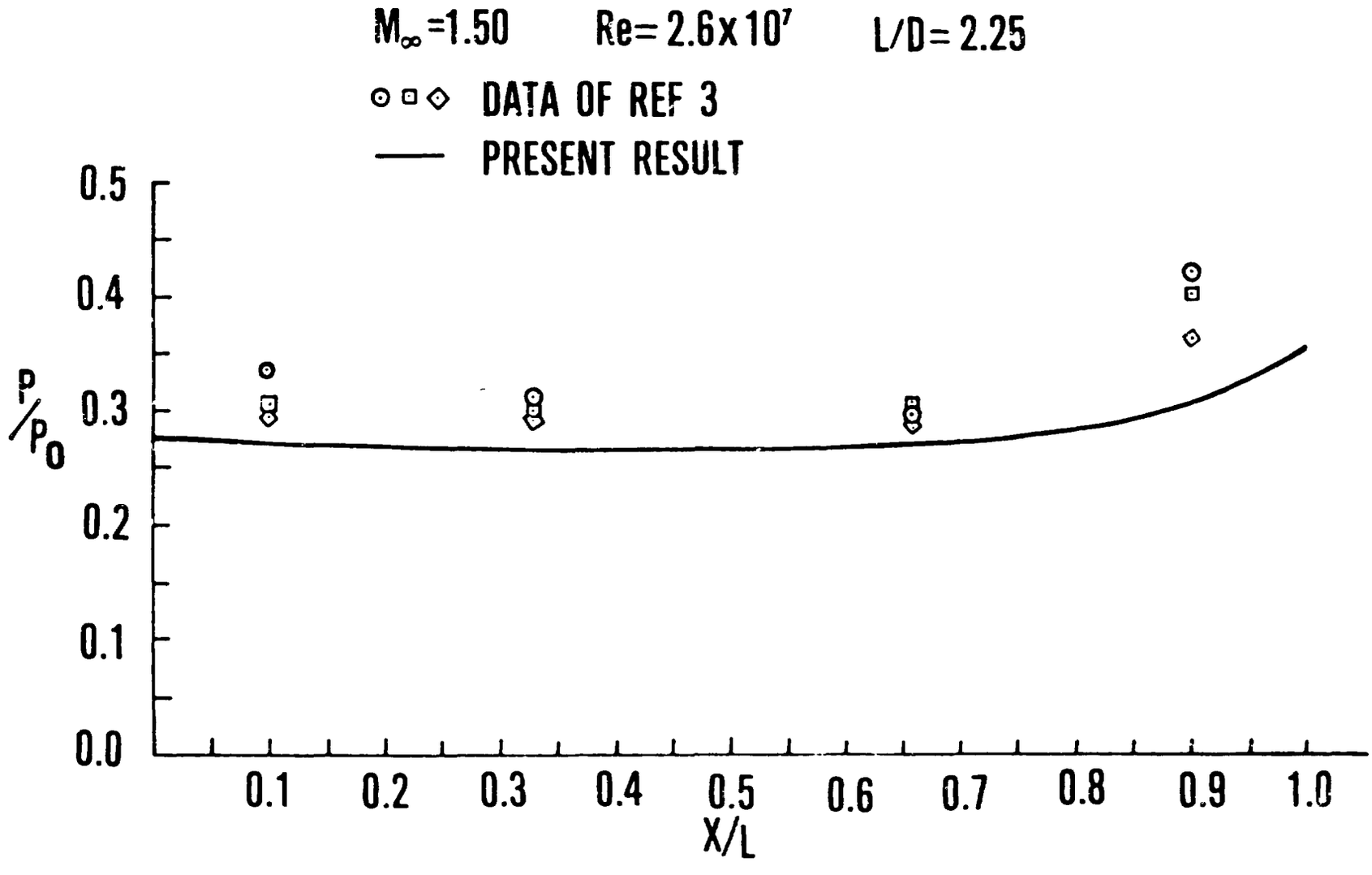

Figure 11. Comparison of Mean Static Pressure Over the Cavity

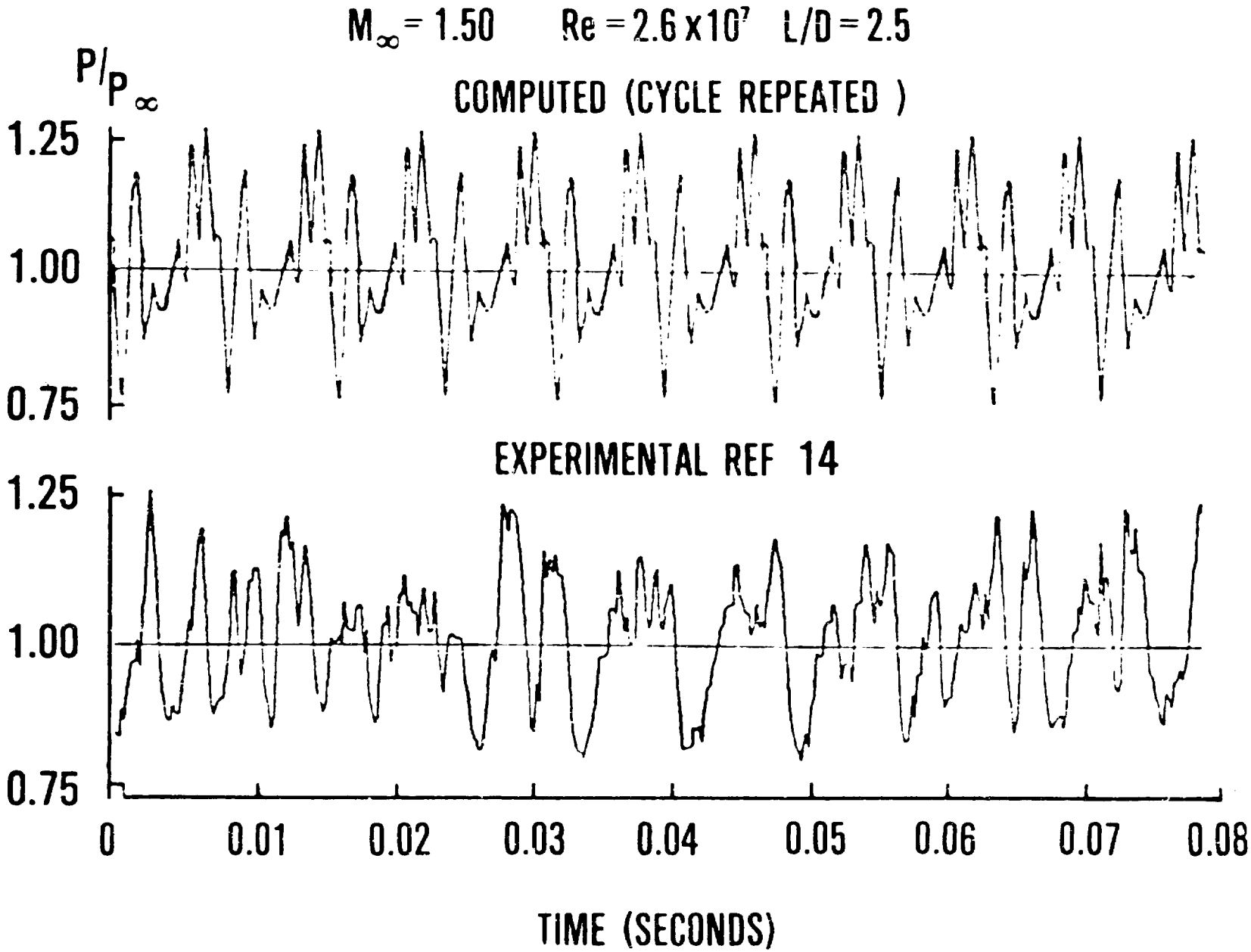

Figure 12. Pressure History in the Cavity

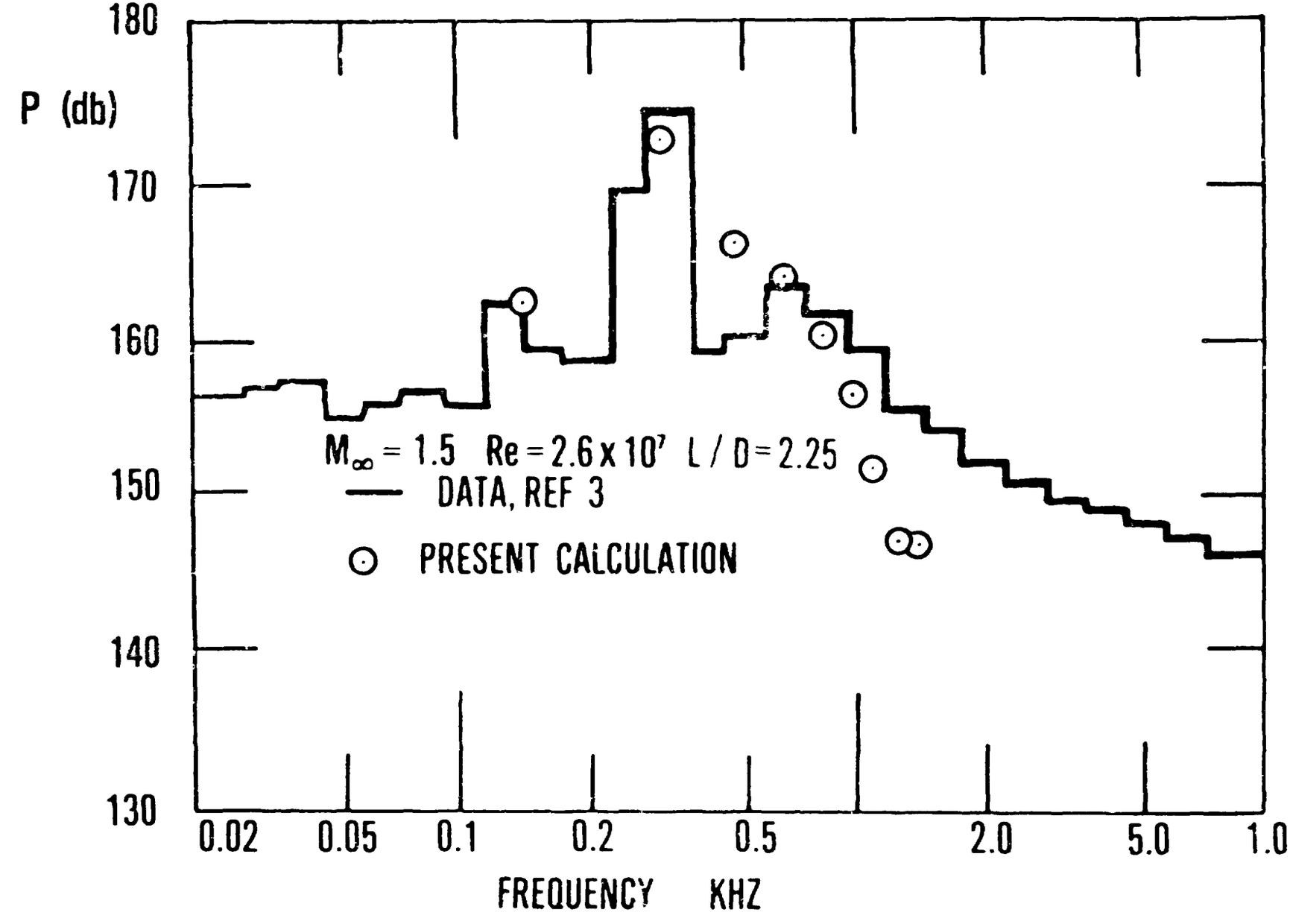

Figure 13. Comparison of Spectral Analysis Results

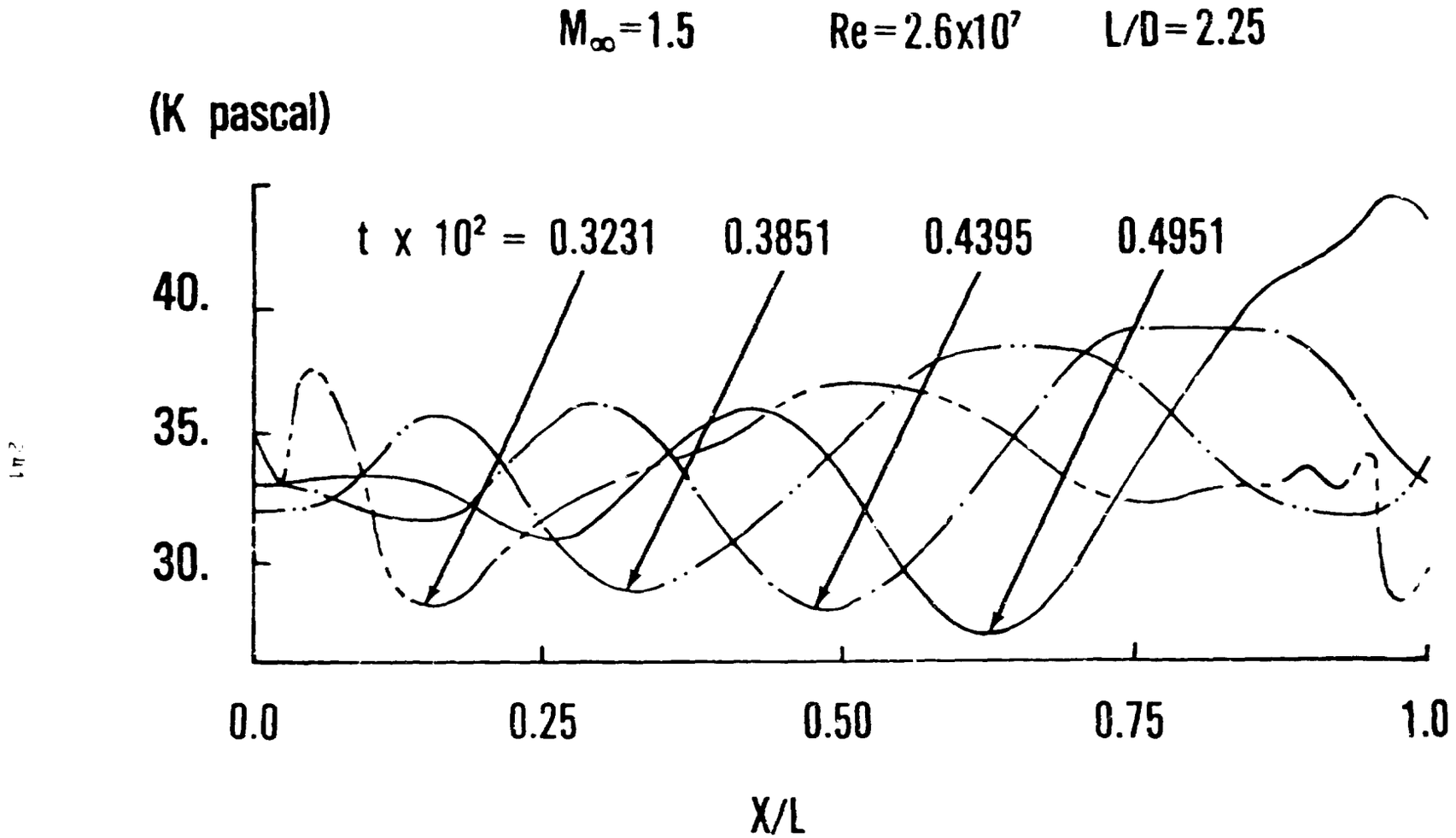

FIGURE 14. CAVITY WAVE PATTERN

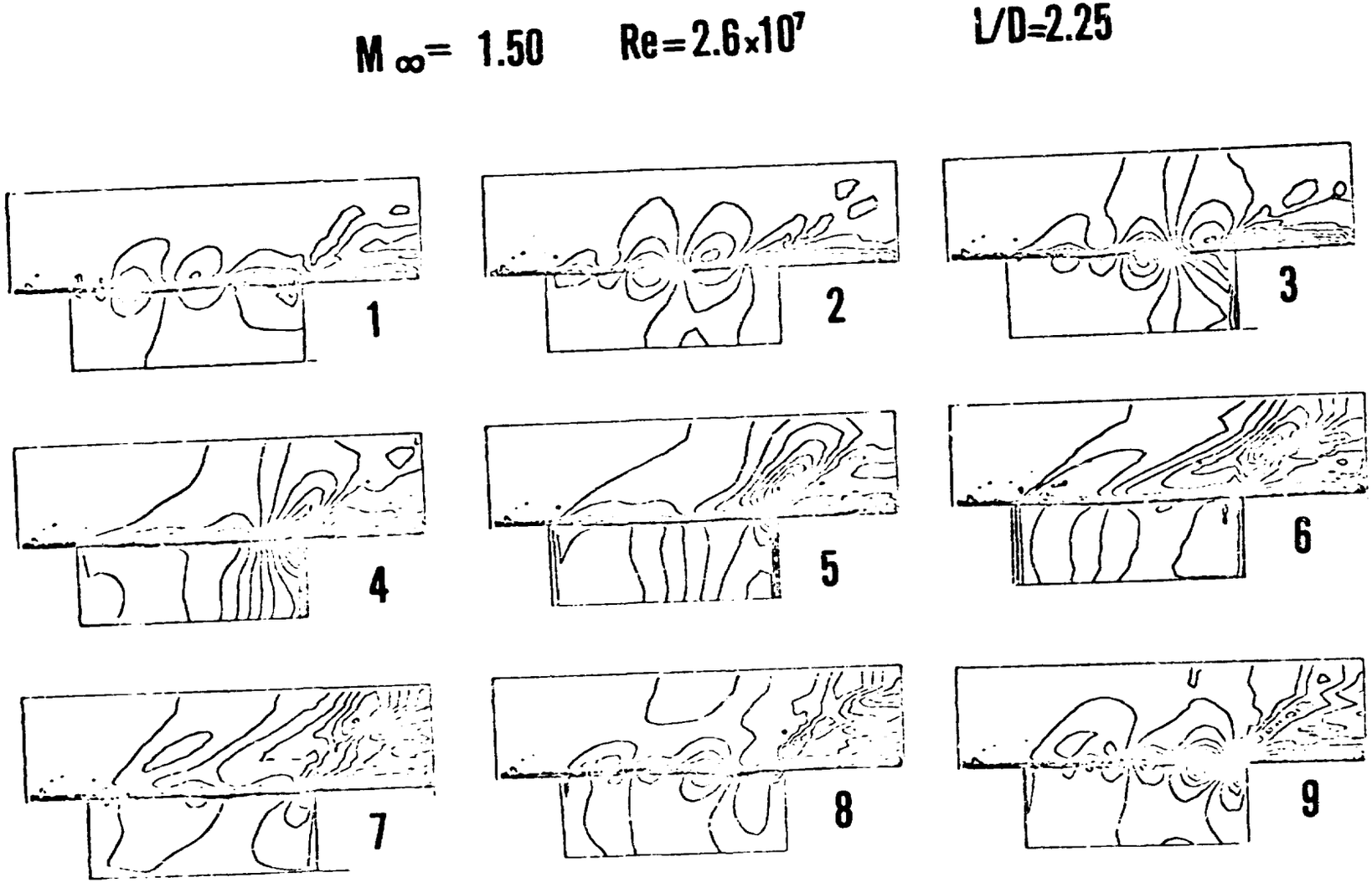

Figure 15. Sequence of Density Contour

BOUNDARY-LAYER TRANSITION ON BLUNT, SLENDER CONES AT HYPERSONIC MACH NUMBERS

by

Kenneth F. Stetson
Air Force Flight Dynamics Laboratory
Wright-Patterson Air Force Base, OH

AD P000325

New wind tunnel data has been obtained to investigate the effects of tip bluntness and angle of attack on boundary layer transition on slender cones. The rearward displacement of transition due to tip bluntness and the maximum displacement of transition are reasonably well understood and explainable primarily on the basis of a reduction in local Reynolds number due to pressure losses across the bow shock. The rapid forward movement of transition observed on the cone frustum is a mystery and will be studied further in future experiments. The observed rapid movement of transition from the sphere-cone tangency point to the subsonic region of the tip is compatible with stability analysis and has been observed by several experimentalists. The transition movements obtained on the sharp cone at angle of attack were compatible with both theory and other experiments. The movement of transition on blunt cones at angle of attack remains poorly understood. The present results appear reasonable; however, since many different trends have been observed in transition experiments and since there is little guidance available from stability analyses, additional confirmation of these transition trends are needed.

Manuscript received May 1979. This work was performed under AFFDL Work Unit No. 2307N423.

NOMENCLATURE

d	distance the model sting is off the tunnel centerline (in.)
h	local heat transfer coefficient (Btu/ft^2-sec^oR)
L	leeward side
M	Mach number
p	surface pressure (used in nondimensional ratio)
$\dot{q}$	heat transfer rate (used in nondimensional ratio)
R	Model nose or base radius (in.)
Re	Reynolds number
Re_θ	Reynolds number based upon conditions at the edge of the boundary layer and momentum thickness
Re_{xT}	transition Reynolds number based upon conditions at the edge of the boundary layer and surface distance from the sharp tip or stagnation point to the location of transition
X or S	surface distance (in.)
X_{sw}	swallowing distance (see Fig. 8) (in.)
X_T	distance from the sharp tip or stagnation point to the onset of transition (An exception is Fig. 1. Pate's predictions are based upon the end of transition) (in.)
X_{T_B} or $(X_T)_B$	distance to onset of transition on blunt configurations (in.)
X_{T_S} or $(X_T)_S$	distance to onset of transition on sharp configurations (in.)
W	windward
α	angle of attack (degrees)
θ_c	cone half angle (degrees)

SUBSCRIPTS

B	base or blunt
N	nose
ST	model stagnation point
∞	free stream

INTRODUCTION

Boundary layer transition is a problem that has plagued several generations of aerodynamicists. Although significant advances in stability theory and turbulence modeling have been made in recent years (e.g. Mack[1], Wilcox[2]), the technology in this area has lagged far behind most other aerodynamic areas. The development of the theory has been slow because of the extreme complexity of the problem and understanding through experimentation have been hampered by the difficulty of conducting a "good" experiment. The wind tunnel, which has been the major source of experimental aerodynamic data, has provided a vast amount of transition data; yet the majority of these data have produced empirical correlations which have not added a great deal to the general understanding of transition phenomena. In recent years it has been generally accepted that disturbances generated by the turbulent boundary layer on the nozzle wall of a supersonic or hypersonic wind tunnel can dominate wind tunnel transition results (e.g. Pate[3]) and that transition Reynolds numbers obtained in these wind tunnels can not be related directly to flight situations. In spite of this short-coming of wind tunnel transition testing, it may be possible to obtain valid transition trends from "noisy" wind tunnel experiments. Also, a very important potential of transition experiments in wind tunnels and other ground test facilities is the ability to identify what Morkovin refers to as a transition "by-pass"[4]. A by-pass is an occurrence of transition at a low Reynolds number which can not be identified with concepts from linear stability theory (that is, transition occurring at very low Reynolds numbers in a region where linear stability theory would not predict Tollmien-Schlichting waves to be amplified). The now well known blunt body

by-pass found on highly cooled surfaces was identified in the laboratory in 1957* ($Re_{\Theta_T} \simeq 250$) at a time when most boundary layer stability people were predicting the early copper heat sink ICBM's would maintain a laminar boundary layer throughout reentry. The present wind tunnel experiments have shown that the nosetip by-pass extends well beyond the nosetip and includes the forward portion of the cone frustum (reported also in Ref. 6).

The approach of this present investigation was to explore some of the hypersonic features of bluntness and angle of attack trends. Initially checks were made on the generality of the transition data obtained in the FDL Mach 6 wind tunnel to provide confidence that the transition trends obtained were not uniquely related to that facility. This involved a comparison of the new data with data obtained in other facilities and transition measured off the tunnel centerline to check the sensitivity of transition location to model position in the test rhombus.

The bluntness experiments extended previous work of Stetson and Rushton[7] on the effects of entropy layer swallowing by the boundary layer on boundary layer transitions and provided new, higher Mach number data, to demonstrate the effects of free stream Mach number on transition of slender, blunted cones. Angle of attack effects were investigated in detail to explore transition location sensitivity to small angles of attack and the resulting asymmetric transition patterns obtained.

---

* These results appeared in the unclassified literature in 1959 (Ref. 5).

EXPERIMENTAL APPARATUS AND PROCEDURES

The experiments were conducted in the FDL Mach 6 wind tunnel and the AEDC Tunnel F. The location of boundary layer transition was obtained from heat transfer measurements.

The Mach 6 tunnel is a blow-down facility operating at a reservoir temperature of 1100°R and a reservoir pressure range of 700 to 2100 psia, corresponding to a Reynolds number per foot range of 9.7×10^6 to 30.3×10^6. The test core of approximately 10 inches is produced by a contoured axisymmetric nozzle with a physical exit diameter of 12.3 inches.

A sketch of the nozzle and diffuser collector is shown in Fig 1. Additional details of the tunnel can be found in Ref. 8. The test model for the Mach 6 tunnel was a thin-skin (nominally 0.025 inches), 8-degree half angle cone containing two rays of thermocouples, located 180 degrees apart in the pitching plane. The base diameter of the model was 4 inches and the model had nosetips with the following bluntness ratios; R_N/R_B = 0, 0.02, 0.05, 0.10, 0.15, and 0.30. Nominal model surface finish was 15 microinches and the blunt nose tips were polished before each run. The model was cooled between runs so that the model surface temperature would always be the same at the start of each run (approximately 540°R). Heat transfer rates were calculated from the increase in the surface temperature of the model, during a time interval of one-half second, after the model arrived at the tunnel centerline. T_W/T_o was generally in the range of 0.52 to 0.58.

The AEDC Tunnel F is an arc-driven wind tunnel of the hotshot type and capable of providing Mach numbers from about 7 to 13 over a Reynolds number per foot range from 0.2×10^6 to 50×10^6. The test gas is nitrogen. This test was conducted with the 40-inch exit diameter contoured nozzle at a nominal free stream Mach number of 9. Because of the relatively short test

times the model wall temperature remained essentially invariant from the initial value of approximately 540 R, thus Tw/To = 0.20 to 0.38. Since the tunnel operates with a constant volume reservoir, the reservoir conditions decay with time. Timewise variations in Reynolds number permit acquisition of data at different Reynolds numbers for the same run. The test model for Tunnel F was a 48 inch, 7 degree half angle cone with eight nose bluntness ratios, R_N/R_B = 0, 0.01, 0.03, 0.05, 0.07, 0.10, 0.15, and 0.37. The model contained 75 coaxial surface thermocouples and 10 surface pressure gages. Nominal model surface finish was 30 microinches and the blunt nose tips were polished before each run. Additional details of Tunnel F and the model instrumentation can be found in Ref. 9.

CHECKS ON GENERALITY OF TRANSITION DATA

In order to utilize boundary layer transition trends obtained in a wind tunnel one has to assume these trends are not uniquely related to the facility being used. The FDL Mach 6 wind tunnel had not previously been used for transition investigations and tunnel freestream disturbance measurements had not been made for this tunnel, therefore, the basic question of nonuniqueness of transition data had to be explored. Based upon the results of previous investigators (e.g. Pate[3]) it was expected that aerodynamic noise, radiating from the turbulent boundary layers on the nozzle wall, would be the major tunnel factor influencing transition. That is, disturbances in the freestream of a wind tunnel have been identified as having three possible sources: (a) vorticity fluctuations (velocity fluctuations) (b) entropy fluctuations (temperature fluctuations) and (c) sound waves (pressure fluctuations). The vorticity and entropy fluctuations are essentially convected along streamlines and are traceable to conditions in the stilling chamber. Sound disturbances

can travel across streamlines and can originate in the stilling chamber and from the wall of the nozzle. For Mach numbers greater than 2.5 to 3, velocity and entropy fluctuations have been found to have a negligible effect on wind tunnel transition data. However, radiated sound, generated by the turbulent boundary layer on the wall of the nozzle, was found to be a major factor affecting transition in supersonic and hypersonic wind tunnels (Ref. 3 contains an excellent review of these developments).

In order to compare the influence of aerodynamic noise on transition in the Mach 6 tunnel with other wind tunnels sharp cone transition data was compared with the correlations of Pate[3]. Pate made an extensive study of the relationship between wind tunnel freestream disturbance and boundary layer transition and developed a method to predict boundary layer transition in wind tunnels; with Mach number, unit Reynolds number and tunnel size as parameters. Fig. 2 indicates Pate's predictions for the end of boundary layer transition on sharp cones in small size wind tunnels. The excellent agreement of these present transition data with the results of Pate indicated that boundary layer transition in the FDL tunnel is influenced by aerodynamic noise in a predictable manner, similar to the seventeen wind tunnels considered by Pate. Furthermore, since the occurrence of transition on a wind tunnel model is the result of the combined effect of all disturbance parameters, such as tunnel free stream disturbances, model surface roughness, model vibration, flow angularity, etc.; the fact that transition Reynolds numbers were found to be the same in several wind tunnels would infer a similarity in the influence of the combined effect of disturbance parameters on boundary layer transition. Although the disturbance parameters have not been investigated in detail in the Mach 6 wind tunnel utilized in this investigation, the similarity of transition results with other wind tunnels was believed to be an indication that the reported transition trends

were not unique to the facility being used (the possibility still exists that all wind tunnels have some general uniqueness of transition data). The AEDC Tunnel F was one of the tunnels considered in Pate's study and therefore has demonstrated a similarity with other tunnels.

A comparison of data from two other facilities provided a check on the trends of bluntness effects on transition. These results are shown in Fig. 3. In addition to these present data, wind tunnel results of Muir and Trujillo[10] and shock tunnel results of Stetson and Rushton[7] are included. The data presented in this manner illustrates the rearward displacement of transition in terms of the entropy layer swallowing. Additional discussions of this manner of presenting blunting data and related blunting characteristics will be included later. The central message to be obtained from this figure is the good agreement of data obtained from different facilities. All three facilities produced the same blunting features and trends, indicating the results were not unique to the facility being used.

Fig 4 compares transition location on the windward ray of a sharp cone with data from a shock tunnel[7], a Ludwieg tube[11], and another wind tunnel[12]. At this time the only guidance as to what the movement of transition with angle of attack should be is the direction of the movement. Both theory (e.g. Moore[13]) and experiment (e.g. Stetson and Rushton[7], Krogmann[11], DiCristina[12]) consistently indicated a rearward movement of the location of transition on the windward ray with angle of attack. The expected magnitude of this rearward displacement is uncertain. All of the facilities shown in Fig. 4 indicated a trend of rearward displacement with angle of attack, with variations in magnitude. These variations in magnitude do not necessarily indicate trends which are facility-peculiar. Angle of attack data from a single facility are often presented in

this nondimensionalized format with the implication that they represent a universal curve; however, it is believed that this point requires further substantiation before being accepted. That is, the influence of parameters such as Mach number, cone angle, surface roughness and wall temperature can not be identified and these effects may account for some of the observed variations.

BOUNDARY LAYER TRANSITION EXPERIMENTS OFF TUNNEL CENTERLINE

In regard to the study of transition trends in wind tunnels this author believes that angle of attack transition results may not have received enough scrutiny. Experimenters usually overlook or neglect the possibility that the results may be influenced by variations of parameters across the test section. When a model is pitched to an angle of attack the nosetip is displaced from the tunnel centerline and may be located in a different environment than the zero angle of attack model. Several effects may influence the location of transition. For axisymmetric nozzles (particularly in small wind tunnels where nozzle coordinate tolerances may be significant compared to the boundary layer thickness[14]) there may be some focusing of aerodynamic noise at the tunnel centerline, with some variations radially away from the centerline. Also, variations in pressure and flow angularity away from the centerline may influence the location of transition. Flow angularity was checked at several locations within the test rhombus of the Mach 6 wind tunnel and the maximum angularity found was $\pm$ 0.05 degrees[8]. Some variations in flow properties across the test section are typical in open-jet axisymmetric nozzles and Mach 6 tunnel calibrations found Mach numbers variations up to about 1.5% within the test rhombus. Fig. 5 is a sample of the Mach number distribution obtained for the Mach 6 tunnel at a station 2.5 inches from the nozzle exit. Variations in aerodynamic noise within the test rhombus of the Mach 6 wind tunnel have not been determined. It was not possible to assess the individual contributions of the above parameters regarding transition movement; however, the accumulative effect of all variations is the information needed to evaluate angle of attack transition trends obtained in this tunnel and these details could be obtained by conducting boundary layer transition experiments off the

tunnel centerline. A brief series of experiments were performed to assess this problem.

Data were obtained at two off-centerline stations; at 0.7 and 1.83 inches below the tunnel centerline. This was accomplished by inserting a collar on the injection strut to limit the travel of the model support system. The model could not be pitched in the off-centerline position. Data were obtained at $\alpha=4^{o}$ by utilizing a bent sting configuration. Fig 6 shows the locations of the model in the centerline and off-centerline positions. The tip of the sharp cone was one inch down-stream of the nozzle exit.

Fig 7 shows heat transfer coefficient plotted versus the surface distance along the model from the tip for the sharp cone at $\alpha=0^{o}$ for the two positions off the tunnel centerline. Transition on the tunnel centerline is shown for comparison as a solid curve. Transition occurred earlier on the bottom ray for both positions. For the top ray transition occurred at different locations for each position. At 1.83 inches from the centerline transition was at essentially the same location as found on the centerline, whereas at 0.7 inches transition was delayed.

The off-centerline results obtained with the sharp cone pitched to $\alpha=4^{o}$ are shown in Fig 8. The trend of early transition on the bottom ray (windward) persisted at $\alpha=4^{o}$. Unfortunately details of transition on the leeward side are not clear due to its forward location; however, the end of transition appeared to be unchanged at all three locations. Note from Fig 6 that when the model was in the 0.7 inch off-centerline location, the model tip was nearly on the centerline.

When the sharp tip was replaced with a spherically blunt tip whose radius was 10% of the base radius different transition trends were observed. These results are shown in Fig 9 with the model at $\alpha=4^{o}$. The onset of transition, for both positions off the centerline, although delayed slightly were not significantly different from the centerline locations. These data suggest that not only is the location of the model relative to the tunnel centerline and model attitude important, but also the model bluntness. Repeat runs were made for all of the data and the excellent repeatability demonstrated that the trends shown existed consistently.

Information regarding the changes in transition off the tunnel centerline could be obtained by observing the trends in the temperature versus time plots of the thermocouples while the model was being injected. Since the heat transfer rate is proportional to the slope of the T vs t curve a change in slope (in addition to the normal change resulting from increase in the surface temperature of the model) relates to a change in the heat transfer coefficient. Fig. 10 illustrates this point for the sharp cone at $\alpha=0^{o}$. The model enters the region of uniform flow at approximately two seconds and reaches the tunnel centerline at 3.45 seconds. Zero time relates to the start of the data acquisition system and not the start of model injection. The time of arrival at the tunnel centerline is recorded information. The thermocouples at S=4.0 and 4.5 inches (Fig. 10a) indicated a constant heat transfer coefficient throughout the injection phase and equal to that obtained at the tunnel centerline. Reference to Fig 7 confirms that at these stations the heat transfer coefficients did not vary with model position and were at a laminar level. The temperature history at 5.5 and 6.0 inches illustrates the case of a changing heat transfer coefficient. The slopes become smaller as the centerline is approached, with an increase in slope at the centerline. By looking at Fig 7 (for the top ray) it can be

seen that the heat transfer coefficients at these model locations decreased at the position nearest the centerline and then increased at the centerline. This sequence of events indicated, for this region on the model, the onset of transition when the model was well away from the centerline, a change to a laminar boundary layer as the model approached the centerline, and transition again when the model was on the tunnel centerline.

Fig 10b illustrates the case of a reduction in the heat transfer coefficient when the model reached the tunnel centerline. Again these results may be correlated with the data of Fig 7.

BLUNTNESS EFFECTS ($\alpha=0^{o}$)

Although the state of the boundary layer on a slender, blunted cone has been under study as an engineering problem for many years, the influence of nosetip bluntness on cone frustum transition remains an area which is poorly understood. The question of why nosetip blunting displaces the onset of transition rearward, and how much rearward displacement should be expected, has never been adequately resolved. From the results of early blunting investigations (e.g. Brinich[15], Moeckel[16]) it was concluded that the rearward displacement of transition was probably due to a reduction in local Reynolds number related to the pressure losses across the bow shock. Stetson and Rushton[7] also concluded that Reynolds number reduction due to blunting was the dominant effect. However, Softley's[17] results, which included a re-interpretation of the data of Stetson and Rushton, obtained local transition Reynolds number twice the sharp cone values. Such a conclusion would suggest that the rearward displacement of transition also involved significant changes in the growth of disturbances in a laminar boundary layer. It appears that both Reynolds number reduction and changes in the stability mechanisms of the laminar boundary layer are important for transition on a slender, blunted cone; each influencing transition in varying degrees, depending upon geometric and flow factors. On the basis of available information it is speculated that Reynolds number reduction is the dominant effect for the rearward displacement of transition and changes in boundary layer stability are the dominant effect in the reversal of this trend and the resulting forward movement of transition. Details of the

stability of the laminar boundary layer on a slender, blunted cone can not be answered from transition experiments such as these and must await the results of "microscopic" experiments.

Intuitively it could be predicted that the experimentally observed rearward displacement of transition on the frustum of a slender cone with increasing bluntness (at a given flow condition) must reach a maximum displacement and then be followed by a forward movement. This results from the fact that transition Reynolds numbers have been found to vary more than two orders of magnitude between the nosetip and the frustum. For example, transition experiments on blunt bodies, such as spherical configurations, have consistently found low transition Reynolds numbers; often less than 500,000 (based on surface distance) and 300 (based on momentum thickness) (e.g. Stetson[18], Anderson[19], Demetriades[20]). Based upon the Mach number independence principle it would be expected that transition in such flows would be essentially independent of free stream Mach number. However, on the frustum of a slender cone, where the entropy layer produced by the blunt tip has been essentially swallowed by the boundary layer, significantly larger transition Reynolds number have been observed, with the magnitude being Mach number dependent, (e.g. Berkowitz, Kyriss and Martellucci[21], Wright and Zoby[22] and Maddalon and Henderson[23]). Local Reynolds numbers, based on surface distance, exceeding 50×10^6 have been obtained. In order to understand and predict transition location on a slender, blunted cone knowledge of the local flow properties is required. One of the problems that currently exists is the inability to assess the uncertainty in local flow calculations and to "sort out" the variations found by using different

boundary layer codes. The results of Softley[17] illustrate this problem. Using the data of Ref 7 he arrived at conclusions different from those of the original investigation. These differences can be attributed directly to the different techniques used for obtaining local flow properties. Since it may be some time in the future before this problem is adequately resolved, caution should be exercised in drawing conclusions regarding slender, blunted cone transition which are based upon local Reynolds number calculations.

In the transition literature reference is often made to such expressions as "small bluntness" and "large bluntness" when discussing tip bluntness effects on boundary layer transition on the frustum of a cone. This can be misleading since these expressions should not be related only to the physical dimensions of the tip. A given tip size can be either "small" or "large", depending upon where transition occurs relative to the tip. An example is the case of a vehicle entering the earth's atmosphere. In order to relate frustum transition location with tip bluntness phenomena some reference to a quantity describing the bluntness effect, rather than a physical dimension such as nosetip radius, would seem a better choice. To provide such a relationship Stetson and Rushton[7] introduced the entropy swallowing length as a transition parameter. The swallowing distance is defined as the location on the cone frustum where the fluid which has gone through the strong portion of the bow shock has been swallowed by the boundary layer. The local Mach number and flow properties at the edge of the boundary layer at this location are nearly the same as would be obtained on the same cone with a sharp tip (see Fig 11). For this investigation the method of Rotta[24] was used to obtain swallowing distances. Rotta developed a method

to obtain certain boundary layer parameters as a function of a similarity parameter based upon swallowing distance, free stream Reynolds number and nose radius. The curves of Fig 12 are based upon Rotta's results. This method provided a simple and easy hand calculation technique which is convenient for handling a large amount of experimental data and maintaining a common reference base for comparing results.

Fig 13 presents local properties on an 8-degree half angle cone with a spherical nosetip radius of 0.04 inches in a $M_\infty = 5.9$ flow. X is the cone frustum distance, with X = 0 corresponding to the point of tangency between the tip and cone. These results were obtained with a recently developed boundary layer code[25] based upon integral solutions of the boundary layer equations. Also shown is the entropy layer swallowing length obtained for this situation by the method of Rotta. The calculated value of X_{sw} corresponds to a location on the cone where the boundary layer code indicated the local Mach number to be 0.97 M_{sharp}. Thus the hand calculated value of X_{sw} is considered to be compatible with these boundary layer code results. For a given cone half angle and free stream Mach number, the swallowing distance varies as $(Re_\infty/FT.)^{1/3}$ and $(R_N)^{4/3}$. Therefore as the nose radius of the cone is systematically increased the swallowing distance also increases. For moderate-to-large nosetip bluntness the entire model is then engulfed with low Mach number, low unit Reynolds number flow. Indicated on Fig 13 is the region of local flow properties where the maximum rearward displacement of transition location occurred. Thus maximum displacement of transition locations on the slender sphere cone was found to be associated with essentially blunt-body flow. Even with allowances for

possible variations of local properties by utilizing different boundary layer codes, it is believed that this blunt body conclusion should remain valid. This point will be discussed in more detail later. Fig 14 shows blunting results for four different Mach numbers. The M_∞ = 3.1 data was obtained by Rogers[26] in a conventional wind tunnel; the M_∞ = 5.5 data is shock tunnel results of Stetson and Rushton[7]; the M_∞ = 5.9 results are new data from the FDL wind tunnel; and the M_∞ = 9.3 data is new data from AEDC's arc driven Tunnel F facility. The transition lengths for the blunt cones $(X_T)_B$ were normalized by the transition length for the sharp cone $(X_T)_s$ [$(X_T)_s$ was different for each facility]. This provides a measure of the rearward displacement of transition on a cone when the sharp tip is replaced with a blunt tip. The abscissa is the transition distance normalized by the swallowing distance (X_{sw}). The swallowing distance for all of these data were based on the results of Rotta (Fig 12). The right side of the figure ($X_T/X_{sw} > 1$) corresponds to situations where transition occurs on a location on the cone where the entropy layer has been essentially swallowed and the conditions at the outer edge of the boundary layer are nearly the same as would be obtained if the cone had as sharp tip. The left side of the figure (X_T/X_{sw} small) corresponds to locations on the cone just downstream of the tip. The conclusions given below from this type of presentation are not very sensitive to X_{sw}. That is, if a different method of calculating X_{sw} were used which gave different values, the effect would be to shift the data to the right or left and not alter the basic conclusions. Data points shown with an arrow indicate conditions where the entire model had a laminar boundary layer. Transition would then occur at some unknown higher value. The main points to observe in Fig 14 are as follows:

a. The effect of tip blunting on cone frustum transition is very sensitive to freestream Mach number, with large Mach numbers producing large rearward displacement of transition. The reason for this sensitivity with freestream Mach number is believed to be primarily related to the Reynolds number reduction associated with pressure losses across the bow shock.

b. Small bluntness systematically moved the transition location rearward until the maximum displacement was obtained.

c. A blunting transition reversal occurred. That is, additional increases in nosetip radius, or freestream Reynolds number, reduced the value of X_T/X_{sw} and produced a forward movement of transition. This forward movement was very sensitive to both nose radius and Reynolds number. For example, for a given nose radius, a small increase in freestream unit Reynolds number could produce large forward movements of transition. In this situation it was often observed that portions of the cone frustum could be completely laminar while other areas of the model had early transition (this situation may have special significance for persons concerned with the effect of frustum transition on vehicle motion).

d. Maximum rearward displacement of transition occurred in situations where X_T/X_{sw} was small, indicating that the local Mach number was low and the flow was essentially of the blunt-body type (see Fig 13).

Fig 15 illustrates the forward movement of transition on a 7-degree half angle cone at a Mach number of about 9.1. At a free stream Reynolds number per foot of 5.4×10^6 the cone had a completely laminar boundary layer. A small increase in free stream Reynolds number caused transition to appear near the cone mid-point at a local Reynolds number of about

550,000. Further increases in freestream Reynolds number steadily moved the transition location to the sphere-cone tangency point, where the local transition Reynolds number was slightly over 300,000. This forward movement slowed as it progressed through the increasing favorable pressure gradient. These events occurred in a situation where the pressure gradient became increasingly more favorable, yet the transition Reynolds number decreased from 550,000 to nearly 300,000. Further increases in the freestream Reynolds number produced transition in the subsonic region of the tip, with a local transition Reynolds number of about 250,000. The local Reynolds number mentioned above were calculated by the finite difference boundary layer code developed by Adams[27] and co-workers. With the exception of the two largest Reynolds number conditions, all of the data of Fig 15 was obtained during a single run in Tunnel F. These variations in Reynolds number occurred during a 59 millisecond time period while the Mach number varied between 9.1 and 9.0 and the wall temperature remained essentially constant. All of the data shown were obtained along the same ray of the model. This situation, as in most boundary layer transition problems, reflects the result of several competing effects and any explanation of this cone frustum transition behavior at this time would be mostly speculative. The rapid movement of transition from the sphere-cone tangency point to the subsonic region of the tip is not a new observation. This transition pattern was first observed by Stetson[5] over twenty years ago and has been observed by several investigators since that time.

The recent analyses of Merkle[20], based upon linearized stability theory combined with nosetip roughness effects, provide an interesting comparison with this experimentally observed forward movement of transition. Merkle postulates two unstable regions on a sphere-cone, one associated with the

tip and the other with the cone frustum. He anticipated that transition on the frustum, due to the second unstable region, would occur at classical transition Reynolds numbers for cones in the appropriate Mach number regime. Merkle suggested that, with increasing freestream unit Reynolds number (such as a reentry vehicle descending), the transition location would move gradually forward on the frustum and would be generated by the second unstable region. During this time, the growth of disturbances on the nosetip would reach larger and larger amplitudes, but would not get sufficiently large to trigger transition. These disturbances in the boundary layer on the nosetip would grow for a time as they proceeded along the tip and then emerge from the unstable region associated with the tip and decay rapidly, thus being of no consequence in triggering transition. At some critical freestream unit Reynolds number, the peak amplitude of disturbances in the unstable region on the nosetip would surpass the level at which significant non-linear interactions begin, and transition would jump discontinuously from the frustum to the subsonic region of the nosetip.

Thus the rapid forward movement of transition on the cone frustrum at a freestream unit Reynolds number of 5.7×10^6, and the resulting low local Reynolds number for transition at this condition, does not seem to be compatible with the predictions of Merkle. It appears from these present results that the unstable region associated with the nosetip extends well beyond the tip and includes the forward portion of the cone frustum.

Fig 16 was prepared to illustrate the sensitivity of transition location to freestream Mach number. The local Mach number and Reynolds number on an 8-degree half angle cone with a 0.60 inch nose radius was calculated with the boundary layer code of Ref. 27. X is the cone frustum distance,

starting at the point of tangency of the tip and cone. Note that the local Mach number was low for both cases and relatively insensitive to freestream Mach number. As far as local Mach number is concerned the two flows were quite similar. The surface pressure distributions (not shown) differ somewhat, due to the fact that the region of overexpansion and subsequent recompression are Mach number dependent. Significant differences were found in the local Reynolds number. These differences are related to the fact that the total pressure losses across the bow shock increased with Mach number. The experimentally observed transition location for these two freestream Mach number situations are indicated and it can be seen that even though the transition locations differ considerably, the local Reynolds number for transition was essentially the same for both cases. These results indicated that the difference in transition location for the two cases shown can be accounted for by the Reynolds number reduction associated with the total pressure losses across the bow shock.

Fig 17 provides additional information to demonstrate the relationship between transition location and Reynolds number reduction. The trend of maximum transition displacement with free stream Mach number clearly follows the trend of Reynolds number reduction. These results, as well as those of previous figures, provide convincing evidence that the maximum rearward displacement of transition is strongly related to the Reynolds number reduction.

Fig 18 is shown partly to demonstrate the problem of calculating local Reynolds number and partly to illustrate the different flow situations found on a blunted, slender cone. The local Reynolds number for the present M_∞ = 5.9 data were obtained by using the unit Reynolds

number profile shown in Fig 13 and assuming that the relationship between Rotta's swallowing distance and this profile was the same for all of the data (for example; at 50% X_{sw}, $(Re/FT)_{Local}$ = 40% $(Re/FT)_{sharp\ cone}$). The results of Softley[17], with local transition Reynolds numbers of twice the sharp cone value, are shown for comparison. Since Softley's results had the entropy layer being swallowed much more rapidly than these present calculations, the local Reynolds numbers he calculated for transition were significantly larger in the small to medium bluntness regime. Since it is not possible to adequately assess at this time the accuracy of flow field calculations of this type, the "correct" trend for a local Reynolds number plot such as this is not known. The fact that the maximum Reynolds number shown for Softley's results coincide with the large increase in Re_{X_T} for these present data is believed to be fortuitous since the swallowing distances for the two sets of data are not compatible. The data on the left side of the figure, which should be relatively insensitive to the particular method used for calculating local Reynolds number since entropy layer swallowing plays a minor role, indicates frustum transition Reynolds number become small, of the same order as those found on nose tips, when transition occurs early on the cone frustum. It appears that for cases of small bluntness, local transition Reynolds number greater than those obtained on a sharp cone are possible; however, attaching a specific number seems to have little significance at this time. Martellucci[29] also calculated local Reynolds numbers for the data of Ref. 7, using a finite-difference boundary layer code, and obtained local transition Reynolds numbers, for the case of small bluntness, somewhat larger than the sharp cone values.

ANGLE OF ATTACK EFFECTS

Although transition trends on a sharp cone at angle of attack may defy one's intuition, there seems to be general agreement regarding the expected movement of transition. Theory and experiment both indicate a rearward movement of transition on the windward ray and a forward movement on the leeward ray. Moore's[13] results show that the boundary layer profiles assume a more stable shape on the windward side and a more unstable shape on the leeward side. Hot wire experiments of Kendall[30] at $M_\infty = 4.5$, which measured the boundary layer fluctuation spectra on the windward and leeward rays of a 4-degree half angle sharp cone, qualitatively confirm these theoretical predictions. References 10, 11, and 12 provide additional examples of confirmation of these trends.

Fig 19 presents results of local Reynolds number calculations for a sharp, 8-degree half angle cone at angle of attack. Also shown are the locations of transition obtained from these experiments. Comparison of the experimental transition locations with the calculated Reynolds numbers provide local transition Reynolds numbers. The local transition Reynolds number increased on the windward ray and decreased on the leeward ray as the angle of attack was increased.

Fig 20 illustrates the transition movement on the windward and leeward rays of an 8-degree half angle cone at $M_\infty = 5.9$. The transition distance (X_T) is normalized by the transition distance on the sharp cone at $\alpha = 0^\circ$ $\left[(X_{T_s})_{\alpha=0} \text{ varies with unit Reynolds number}\right]$. It was planned to test all of the blunt configurations at the same free stream unit Reynolds number; however, for the 15% blunt tip, transition moved off the end of the model at $\alpha = 2^\circ$. Therefore this configuration was tested at a slightly

larger Reynolds number. The sharp cone transition trends were consistent with expected results, as noted earlier. The blunt configurations; however, have trends which are somewhat different from those of Ref. 7. These differences relate to the windward ray at small angles of attack. Ref. 7 had the maximum rearward displacement at $\alpha = 0^{o}$ and a forward movement with angle of attack. The present data consistently had a rearward movement initially, as for the sharp cone, and then a forward movement at larger angles of attack. The reason for these differences is not known. Intuitively it would seem reasonable that the blunt cone boundary layer profiles might assume a more stable shape with angle of attack, analogous to the sharp cone, and therefore cause transition to move rearward on the windward ray. Transition would not continue to move rearward, as for the sharp cone, since the effect of bluntness diminishes with angle of attack. It would be expected that the curve would turn and approach the sharp cone curve. At some large angle of attack all of the curves should merge into a single curve. Variations of tunnel environment, as discussed earlier, may have a small influence on these data; nowever, it is not believed to be an effect capable of altering the major trends shown in Fig 20.

The data obtained with the 30% blunt nose tip is presented separately (Fig 21) due to the nature of the results. Initial experiments were conducted at $Re_{\infty}/Ft = 19.4 \times 10^{6}$, as were the other blunt configurations of Fig 20. The windward ray was completely laminar at all angles tested. (The all laminar condition is indicated with an arrow on the data point) Increasing the freestream unit Reynolds number produced a condition where the laminar boundary layer previously had been observed to be in a rather

delicate balance; one in which transition could be easily initiated (in Fig 14 this corresponds to situations where X_T/X_{sw} is in the range of 0.02 to 0.03 and is also illustrated in Fig 15 for the Tunnel F data). The $\alpha = 0^o$ data shown in Fig 21 is the same data shown in Fig 14. A small change in Reynolds number or repeated experiments at a given Reynolds number (open circles) produced a wide range in transition locations. A unit Reynolds number of 28 million was selected for the angle of attack tests in order to keep transition from moving off the model on the windward ray. The results are shown with the solid circles. The transition locations seemed to have two preferred locations - a large displacement and a short displacement. It can be seen from this figure that several transition trends are possible at this condition; that is, either a forward or rearward movement with angle of attack, and it was not possible to predict where transition would occur.

Ideally, to observe transition shape patterns, one would like to have a model completely saturated with heat transfer gages. Usually such a practice is not possible and compromises are necessary. For this series of experiments the model had two rays of thermocouples and circumferential patterns were obtained by rolling the model and making repeat runs. Test conditions could be duplicated very closely and the transition location, for a given situation, could be closely reproduced. Transition patterns were obtained by making a composite picture from the results of several runs. It is believed the results of this procedure provided a good representation of the pattern occurring during a single test. Figures 22 to 24 are samples of the transition asymmetries found at two degrees angle of attack and $M_\infty = 5.9$. $\phi = 0^o$ is the windward meridian and $\phi = 180^o$ is the leeward meridian. The shaded area represents the transition region

with "B" indicating the beginning of transition and "E" the end of transition. The beginning and end of transition at $\alpha = 0$ is shown for reference, along with calculated values of local Re_θ at $\alpha = 2^o$.

Fig 25 illustrates how the transition front moves with angle of attack. The data shown is for the 8-deg half angle cone with a 10% blunt tip. All data were obtained at $M_\infty = 5.9$ and a free stream Reynolds number of 19.4×10^6 per foot. Small angles of attack were found to produce large transition asymmetries.

Fig 26 illustrates how the transition front moves as a function of nosetip bluntness. Model and test conditions are the same as indicated in Fig 25. Large transition asymmetries were associated with all three nosetips and the transition front moved rearward with increased bluntness.

For utilization of experimental results and comparison with other data, data are often presented in a nondimensionalized format. Potter[31], for example, prepared a data base of wind tunnel angle of attack transition data in nondimensionalized form in order to correct ballistic range transition data for angle of attack effects. A problem he encountered was a scarity of angle of attack transition data. These present data add to the angle of attack data base; however it is still not possible to evaluate the generality of the results. The present results have the advantage of coming from one data source, whereas Potter's results represent a composite picture made up from several sources. Fig 27 presents the results found for the 8-deg half angle cone with a sharp tip, tested at $M_\infty = 5.9$ and $Re_\infty/Ft = 9.7 \times 10^6$. Potter's results are shown for comparison. Differences were found between the present results and those of Potter. The present results displayed a larger variation in transition location on the windward side of the model ($\phi = 0^o$ to 90^o) and less variation on the leeward side

(ϕ = 90° to 180°). Also, the forward movement of transition on the leeward side ceased at $\alpha/_{\theta c}$ = 0.25. The general trend of a rearward movement on the windward ray and a forward movement on the leeward ray with angle of attack was consistent with all data.

CONCLUSIONS

Following are the major conclusions obtained from this investigation:

1. Comparison of the present boundary layer transition data with data from other facilities and transition experiments off the tunnel centerline indicated the blunting and angle of attack trends obtained were general and not uniquely related to the facility used.

2. The rearward displacement of transition on the cone frustum due to tip bluntness was found to be quite sensitive to free stream Mach number as well as to bluntness. At $M_\infty = 9.3$ transition could be displaced rearward as much as nine times the transition length for a sharp cone.

3. Small bluntness systematically moved the transition location rearward until the maximum displacement was obtained.

4. A blunting transition reversal occurred. That is, additional increases in nosetip radius, or freestream Reynolds number, produced a forward movement of transition.

5. The forward movement of transition took place rapidly, with small changes in Reynolds number or nose radius. Asymmetric transition fronts at $\alpha = 0^o$ were common for this situation.

6. The maximum rearward displacement of transition occurred under situations of low local Mach number flow.

7. The trend of maximum transition displacement with freestream Mach number followed the trend of Reynolds number reduction. Reynolds number reduction is believed to be the dominant effect associated with the rearward displacement of transition.

8. Low transition Reynolds numbers, of the order found on the nosetip, extended onto the front portion of the cone frustum. It appears that the transition by-pass, associated with blunt bodies, includes the

forward portion of the cone frustum on a sphere-cone configuration.

9. Transition correlations based on local Reynolds number should be used cautiously, since it is not possible, at this time, to assess the accuracy of the Reynolds number calculations.

10. Transition locations were sensitive to small changes in angle of attack. Both the sharp and blunt tips produced a rearward movement of transition on the windward ray at small angles of attack.

11. The 30% blunt cone produced several transition trends and it was not possible to predict where transition would occur.

12. Large transition asymmetries were obtained at small angles of attack for both sharp and blunt tip configurations.

13. Some differences in angle of attack transition trends were observed when comparing the present data with other data.

References

1. Mack, L. M., "Transition and Laminar Instability," JPL publication 77-15, May 1977 (NASA-CP-153203).

2. Wilcox, D. C. and Traci, R. M., "A Complete Model of Turbulence," AIAA paper No. 75-351, San Diego, California, 1976.

3. Pate, S. R., "Dominance of Radiated Aerodynamic Noise on Boundary Layer Transition in Supersonic-Hypersonic Wind Tunnels, Theory and Application," AEDC-TR-77-107, March 1978.

4. Morkovin, M. V., "Instability, Transition to Turbulence and Predictability," AGARDograph No. 236 (May 1977).

5. Stetson, K. F., "Boundary Layer Transition on Blunt Bodies with Highly Cooled Boundary Layers," IAS Report No. 59-36 (Jan 1959).

6. Stetson, K. F., "Effect of Bluntness and Angle of Attack on Boundary Layer Transition on Cones and Biconic Configurations," AIAA preprint 79-0269 (Jan 1979).

7. Stetson, K. F. and Rushton, G. H., "Shock Tunnel Investigation of Boundary Layer Transition at M=5.5," AIAA Journal, Vol. 5, pp 899-906 (May 1967).

8. Fiore, A. W. and Law, C. H., "Aerodynamic Calibration of the Aerospace Research Laboratories M=6 High Reynolds Number Facility," ARL-TR-75-0028, Feb 1975.

9. Test Facilities Handbook (Tenth Edition), von Karman Gas Dynamics Facility, Vol. 3," Arnold Engineering Development Center, May 1974.

10. Muir, J. F. and Trujillo, A. A., "Effects of Nose Bluntness and Free Stream Unit Reynolds Number on Slender Cone Transition at Hypersonic Speeds," Proceeding of the Boundary Layer Transition Workshop, Vol III, 20 Dec 1971, Aerospace Report No. TOR-0172 (S2816) -5.

11. Krogmann, P. "An Experimental Study of Boundary Layer Transition on a Slender Cone at Mach 5, "AGARD Symposium on Laminar-Turbulent Transition, Technical University of Denmark, Copenhagen, Denmark, 2-4 May 1977.

12. DiCristina, V. "Three-Dimensional Laminar Boundary-Layer Transition on a Sharp 8^{o} Cone at Mach 10," AIAA Journal, Vol. 8, pp 852-856 (May 1970).

13. Moore, F. K., "Laminar Boundary Layer on a Circular Cone in Supersonic Flow at Small Angle of Attack," NACA TN 2521 (Oct 1951).

14. Anders, J. B., Stainback, P. C., and Beckwith, I. E., "A New Technique for Reducing Test Section Noise in Supersonic Wind Tunnels," AIAA Preprint No. 78-817 (April 1978).

15. Brinich, P. F., "Effect of Leading-Edge Geometry on Boundary-Layer Transition at Mach 3.1," NACA TN 3659 (March 1956).

16. Moeckel, W. E., "Some Effects of Bluntness on Boundary-Layer Transition and Heat Transfer at Supersonic Speeds," NACA Rept. 1312 (1957).

17. Softley, E. J., "Boundary Layer Transition on Hypersonic Blunt, Slender Cones," AIAA paper No. 69-705 (June 1969).

18. Stetson, K. F., "Boundary Layer Transition on Blunt Bodies with Highly Cooled Boundary Layers," J.A.S. Vol. 27, pp. 81-91 (Feb 1960).

19. Anderson, A.D., "Interim Report, Passive Nosetip Technology (PANT) Program, Vol, X, Appendix, Boundary Layer Transition on Nodetips with Rough Surfaces, SAMSO-TR-74-86 (Jan 1975).

20. Demetriades, A. "Nosetip Transition Experimentation Program, Final Report, Vol II," SAMSO-TR-75-120 (July 1977).

21. Berkowitz, A. M., Kyriss, C. L. and Martellucci, A., "Boundary Layer Transition Flight Test Observations," AIAA paper No. 77-125 (Jan 1977).

22. Wright, R. L., and Zoby, E. V., "Flight Boundary Layer Transition Measurements on a Slender Cone at Mach 20, AIAA paper No. 77-719 (June 1977).

23. Maddalon, D. V., and Henderson A., Jr., "Boundary Layer Transition at Hypersonic Mach Numbers," AIAA paper No. 67-130 (Jan 1967).

24. Rotta, N. R., "Effects of Nose Bluntness on the Boundary Layer Characteristics of Conical Bodies at Hypersonic Speeds," NYU-AA-66-66 (Nov 1966).

25. Hecht, A. M. and Nestler, D.E., "A Three-Dimensional Boundary Layer Computer Program for Sphere-Cone Type Reentry Vehicles, Vol. 1, Engineering Analysis and Code Description," AFFDL-TR-78-67 (June 1978).

26. Rogers, R. H., "Boundary Layer Development in Supersonic Shear Flow," Boundary Layer Research Meeting of the AGARD Fluid Dynamics Panel, London, England, AGARD Rept. 269 (April 25-29, 1960).

27. Adams, J. C., Jr., Martindale, W. R., Mayne, A. W., Jr., and Marchand, E. O., "Real Gas Scale Effects on Shuttle Orbiter Laminar Boundary Layer Parameters," Journal of Spacecraft and Rockets, Vol. 14, pp 273-279 (May 1977).

28. Merkle, C. L., "Stability and Transition in Boundary Layers on Reentry Vehicle Nosetips," AFOSR-TR-76-1107 (June 1976).

29. Martellucci, A., private communication.

30. Kendall, J. M., unpublished paper (1971).

31. Potter, J. L., "The Unit Reynolds Number Effect on Boundary Layer Transition," Dissertation submitted to Vanderbilt University (May 1974).

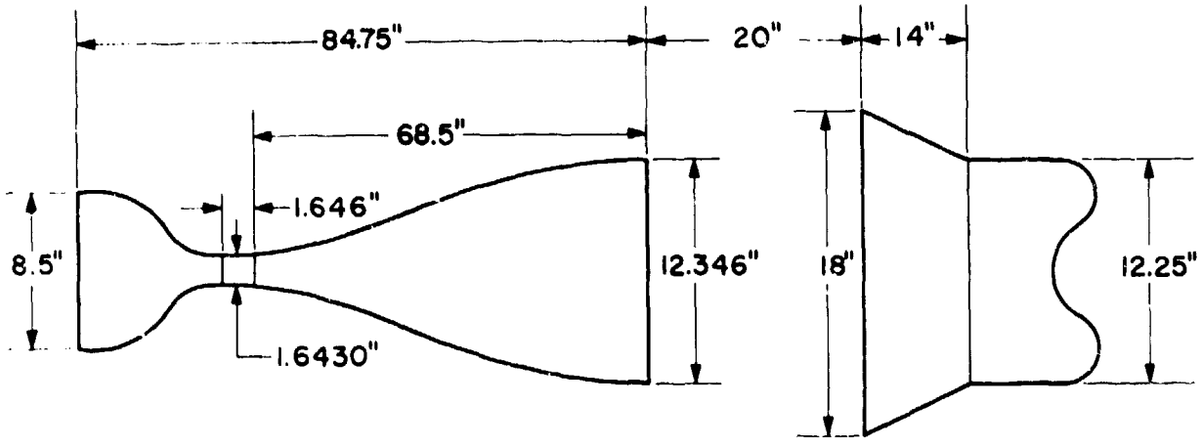

FIG. 1 M=6 WIND TUNNEL NOZZLE, JET AND COLLECTOR CONFIGURATION

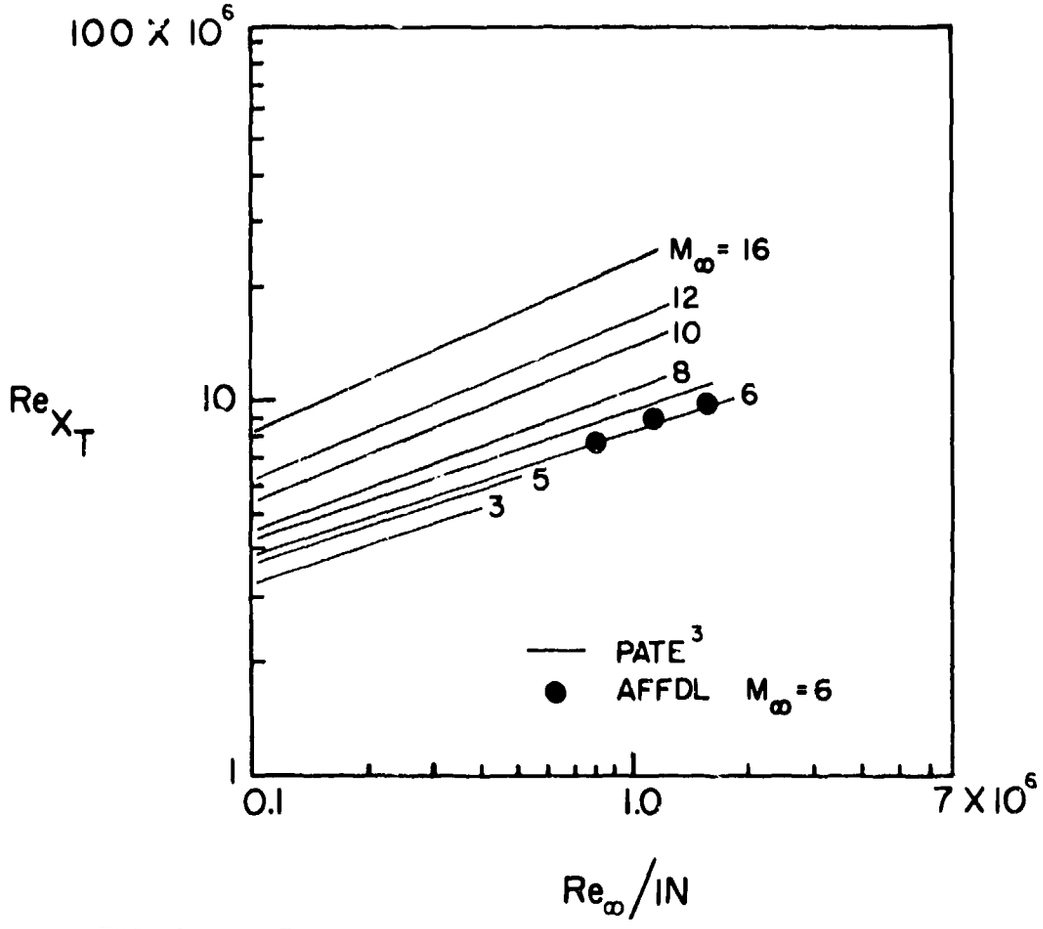

FIG. 2 EFFECT OF MACH NUMBER AND UNIT REYNOLDS NUMBER ON SHARP CONE TRANSITION FOR SMALL SIZE WIND TUNNELS (R_{e_x} IS THE END OF TRANSITION)

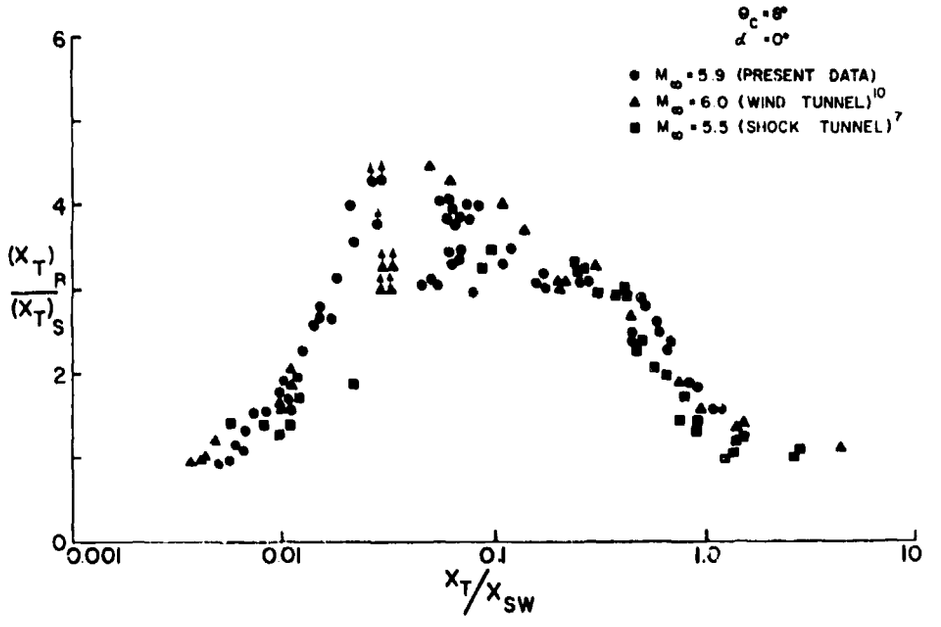

FIG. 3 A COMPARISON OF BLUNTNESS EFFECTS IN THREE FACILITIES

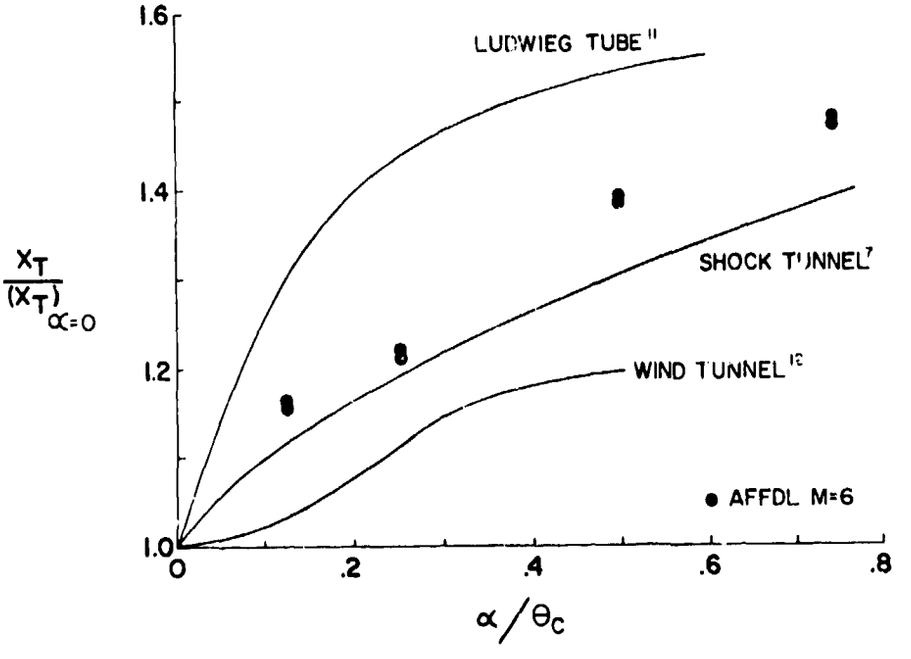

FIG. 4 A COMPARISON OF THE MOVEMENT OF TRANSITION ON THE WINDWARD RAY OF A SHARP CONE

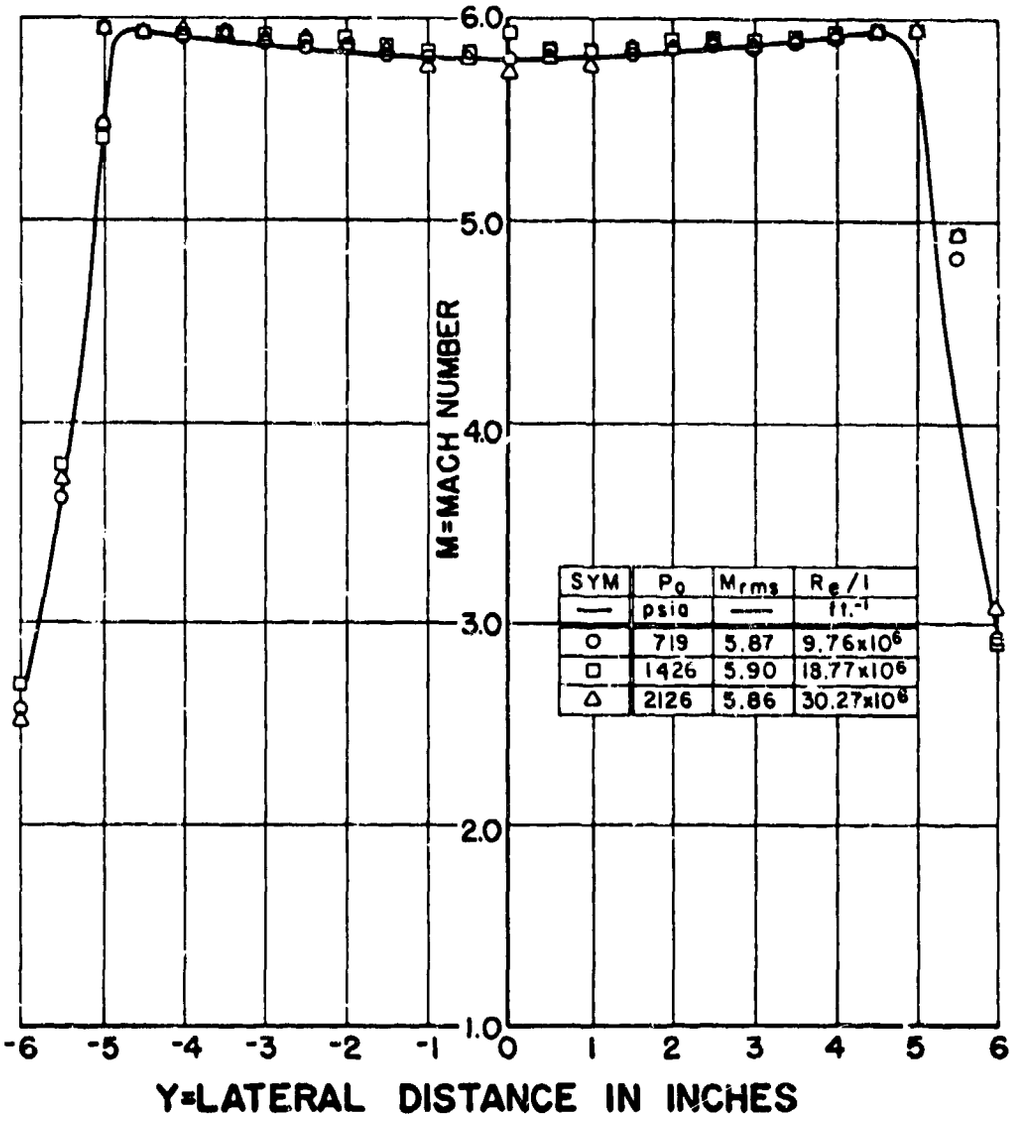

FIG. 5 LATERAL MACH NUMBER DISTRIBUTION AT X = 2.5 INCHES

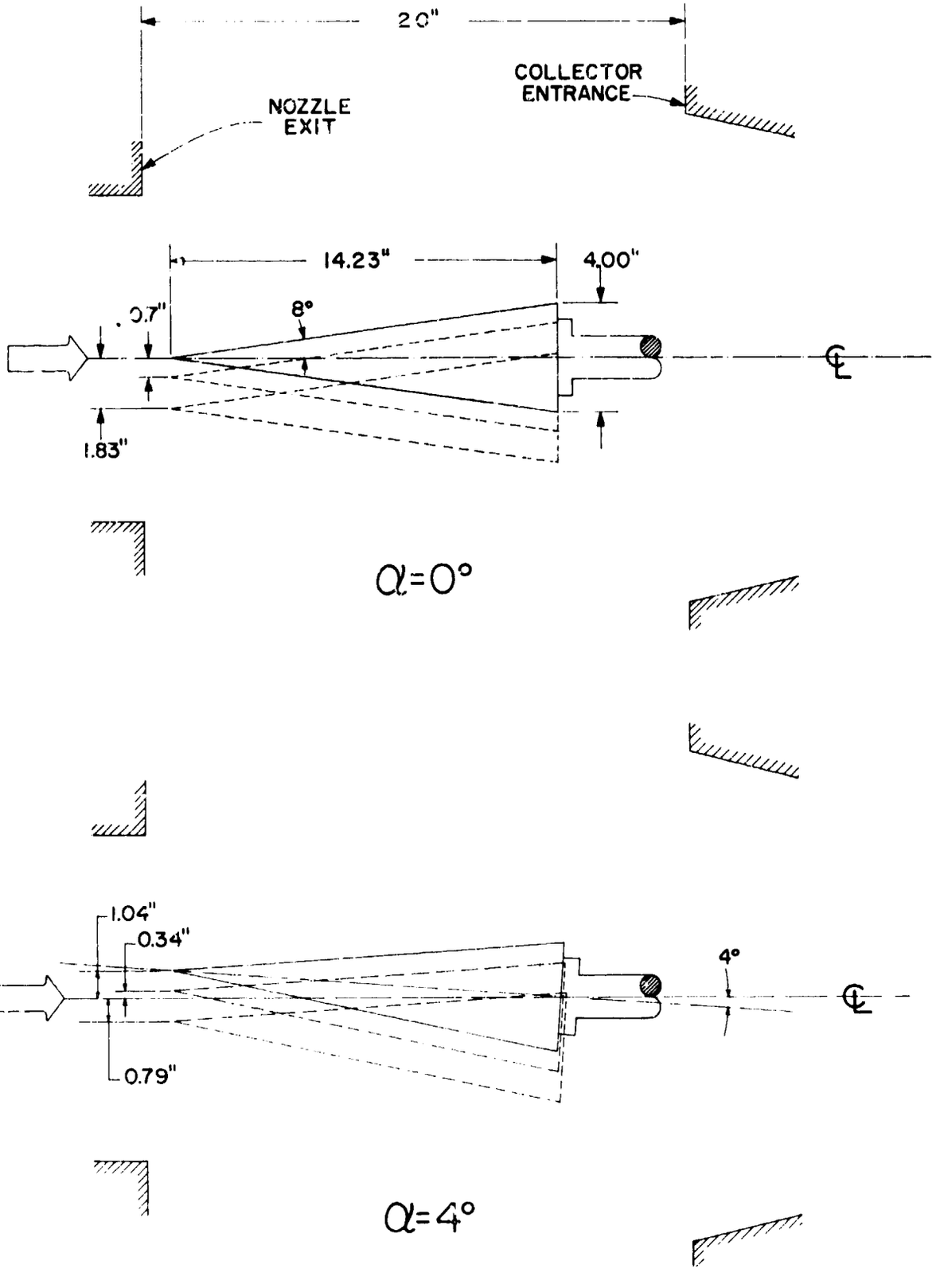

FIG. 6 SHARP CONE POSITIONS FOR $\alpha = 0°$ AND $\alpha = 4°$

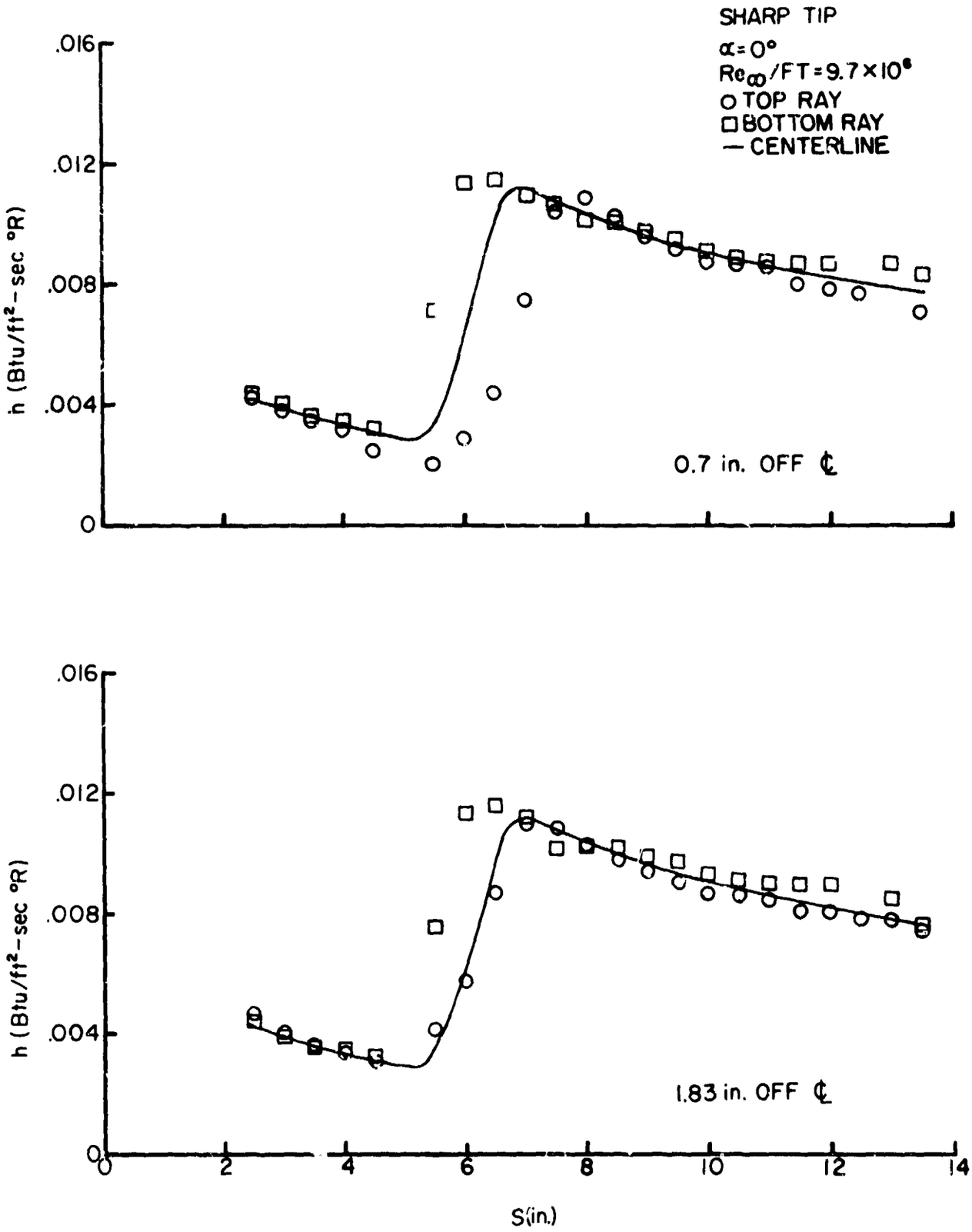

FIG. 7 TRANSITION LOCATION FOR DIFFERENT MODEL POSITIONS, SHARP TIP, $\alpha = 0°$ (RECOVERY FACTOR OF ONE)

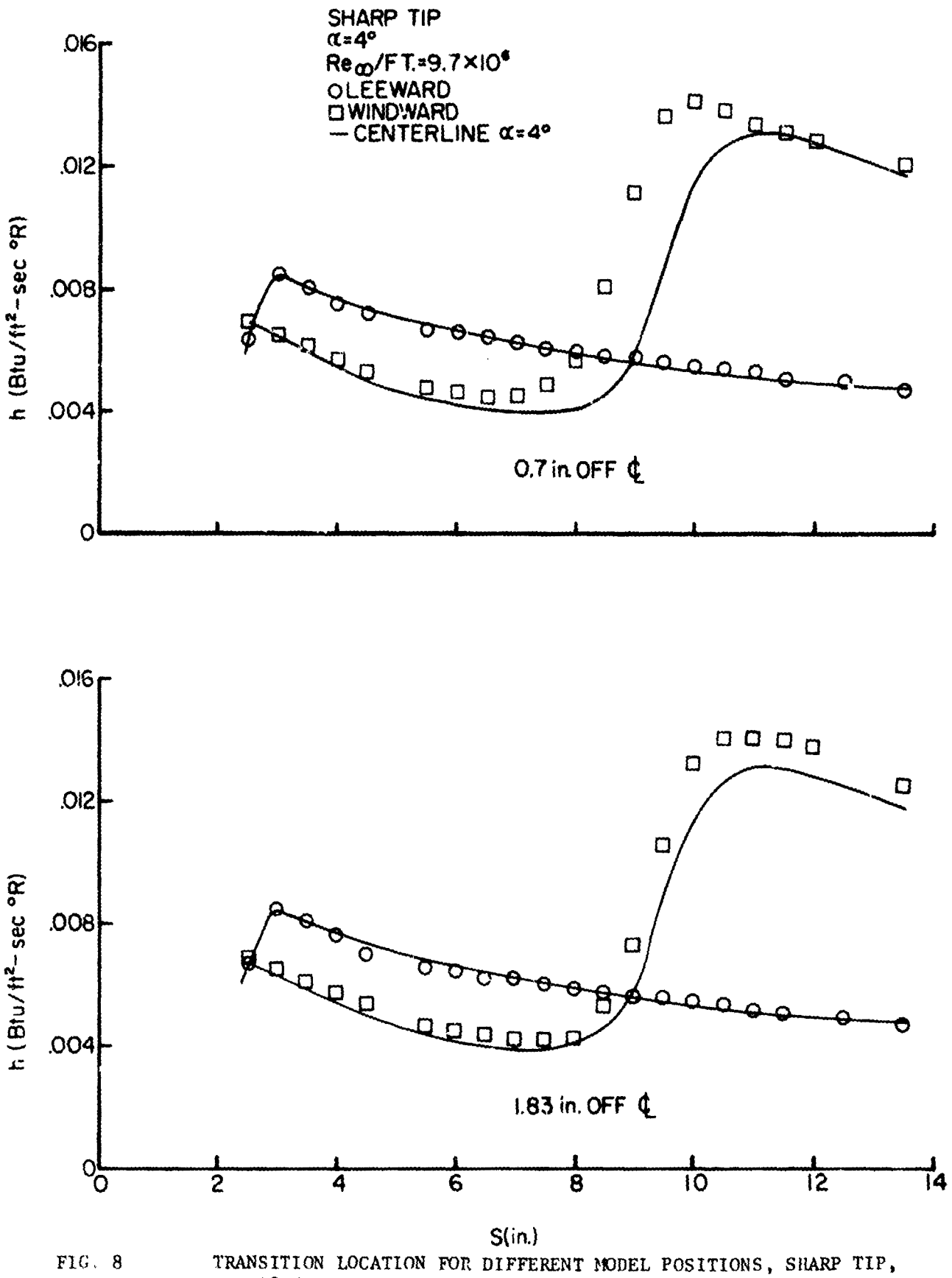

FIG. 8 TRANSITION LOCATION FOR DIFFERENT MODEL POSITIONS, SHARP TIP, $\alpha = 4°$ (RECOVERY FACTOR OF ONE)

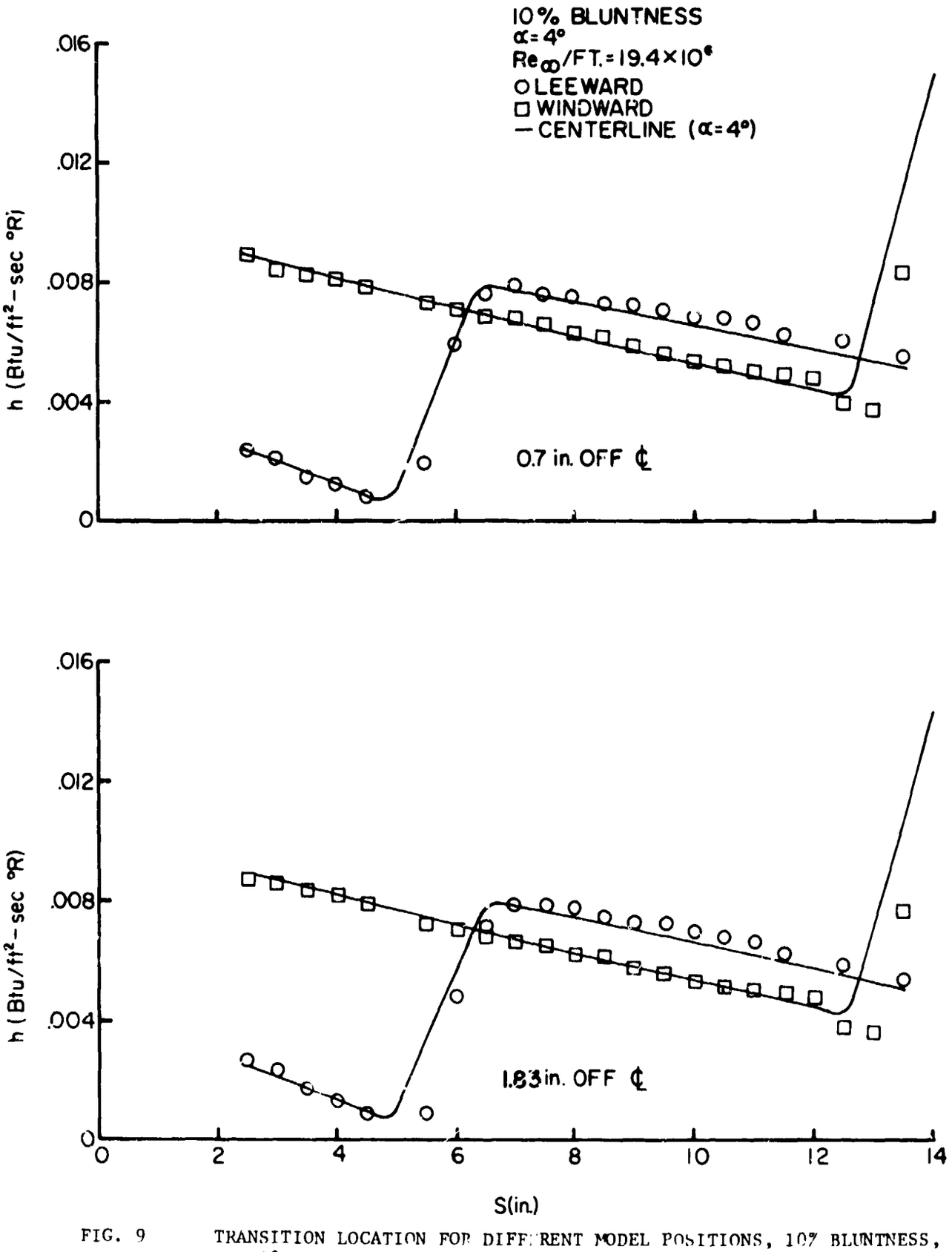

FIG. 9 TRANSITION LOCATION FOR DIFFERENT MODEL POSITIONS, 10% BLUNTNESS, $\alpha = 4°$ (RECOVERY FACTOR OF ONE)

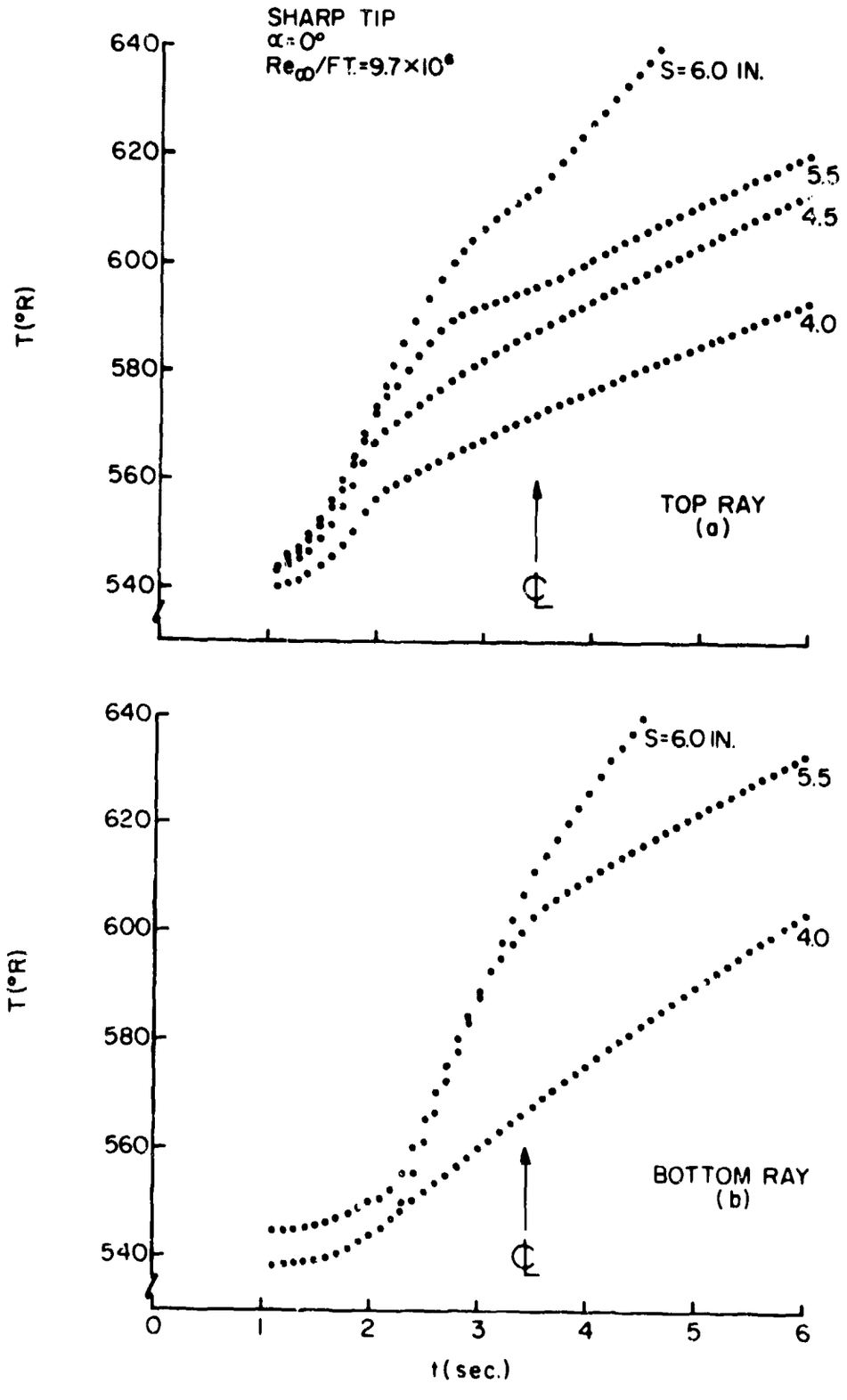

FIG. 10 SURFACE TEMPERATURE HISTORY FOR THE SHARP CONE AT $\alpha = 0°$

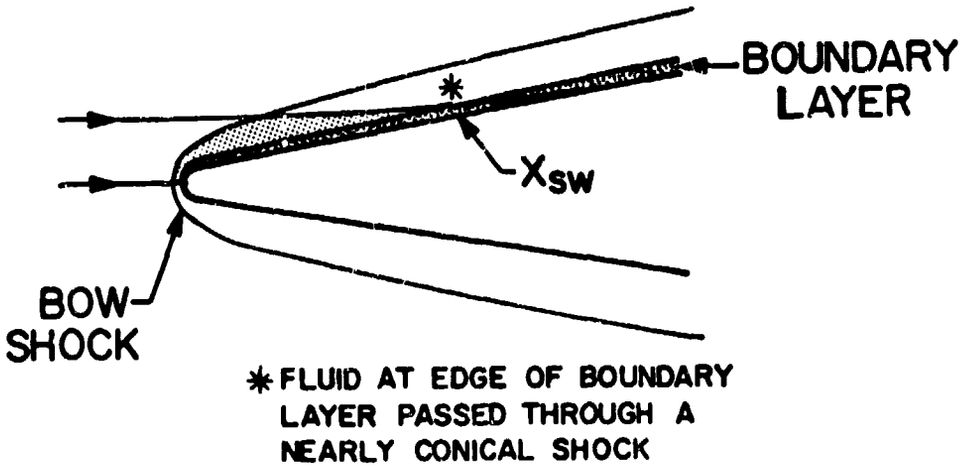

FIG. 11 A SCHEMATIC ILLUSTRATION OF FLOW OVER A SLENDER, BLUNT CONE

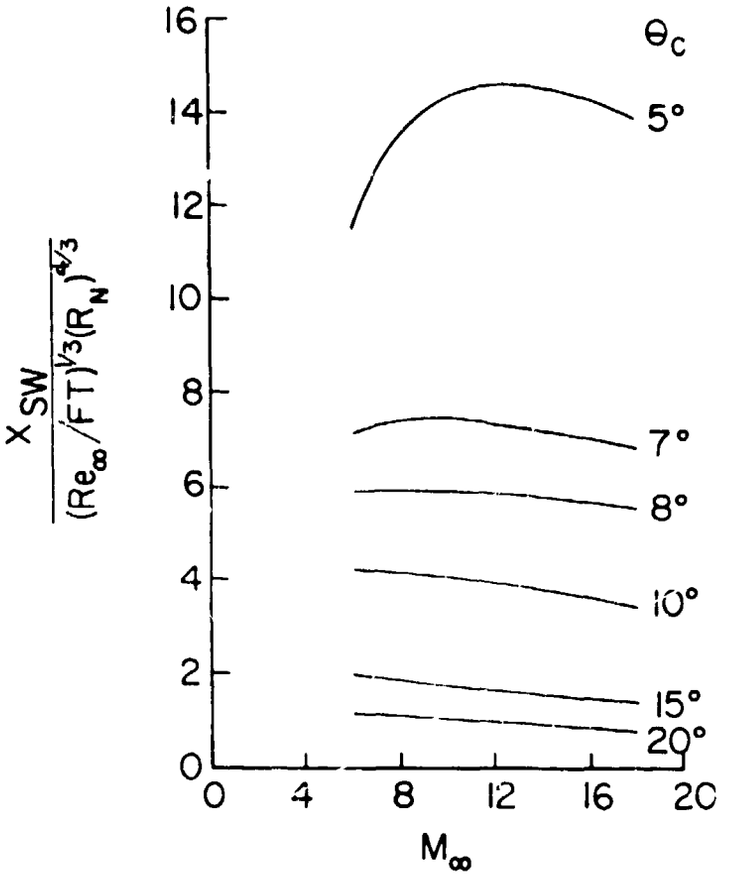

FIG. 12 ENTROPY LAYER SWALLOWING DISTANCE PARAMETER

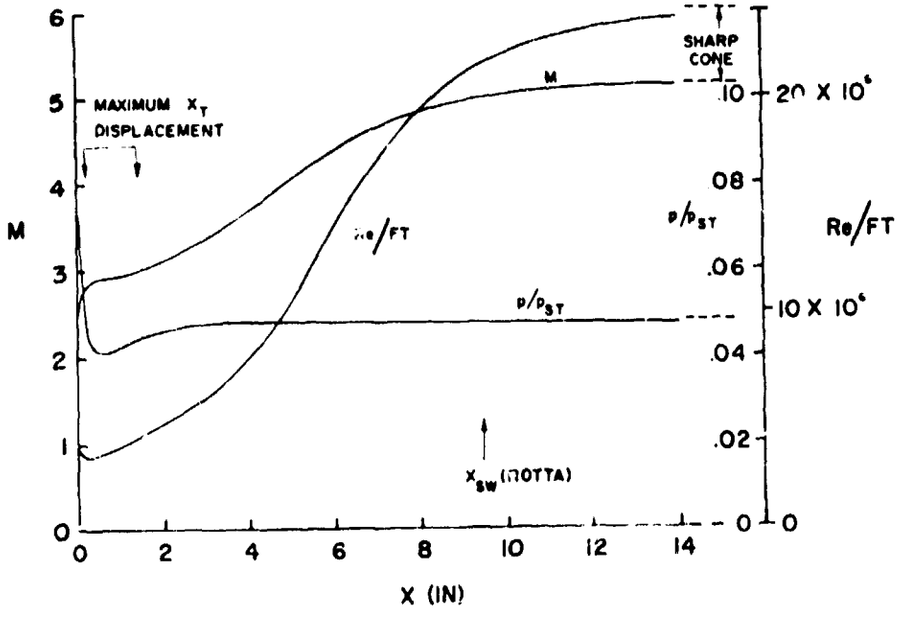

FIG. 13 CALCULATIONS OF LOCAL PROPERTIES ON AN 8-DEGREE HALF ANGLE CONE WITH 2% BLUNTNESS AT $M_\infty = 5.9$

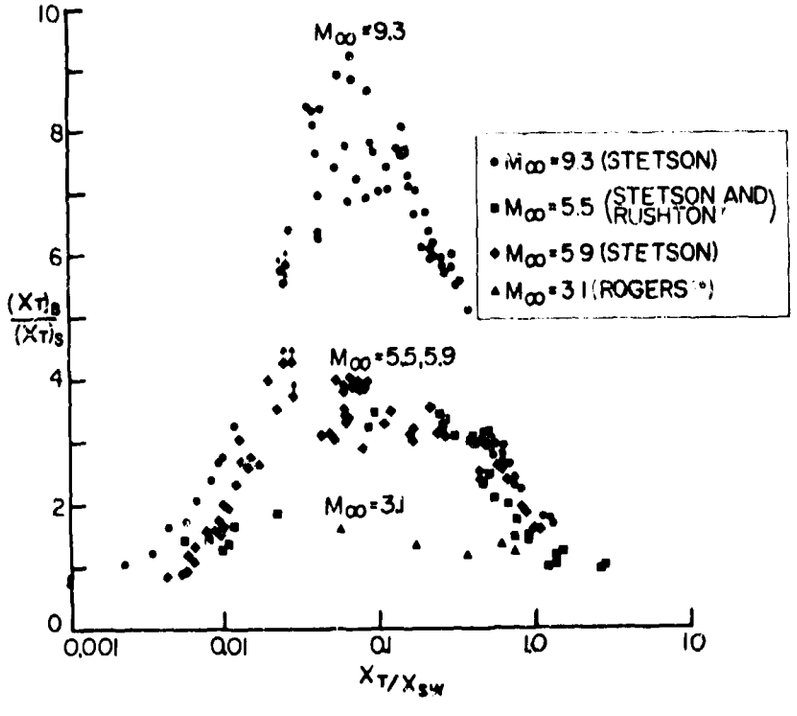

FIG. 14 EFFECT OF NOSE BLUNTNESS ON TRANSITION LOCATION

TRANSITION PROGRESSION TO NOSE TIP

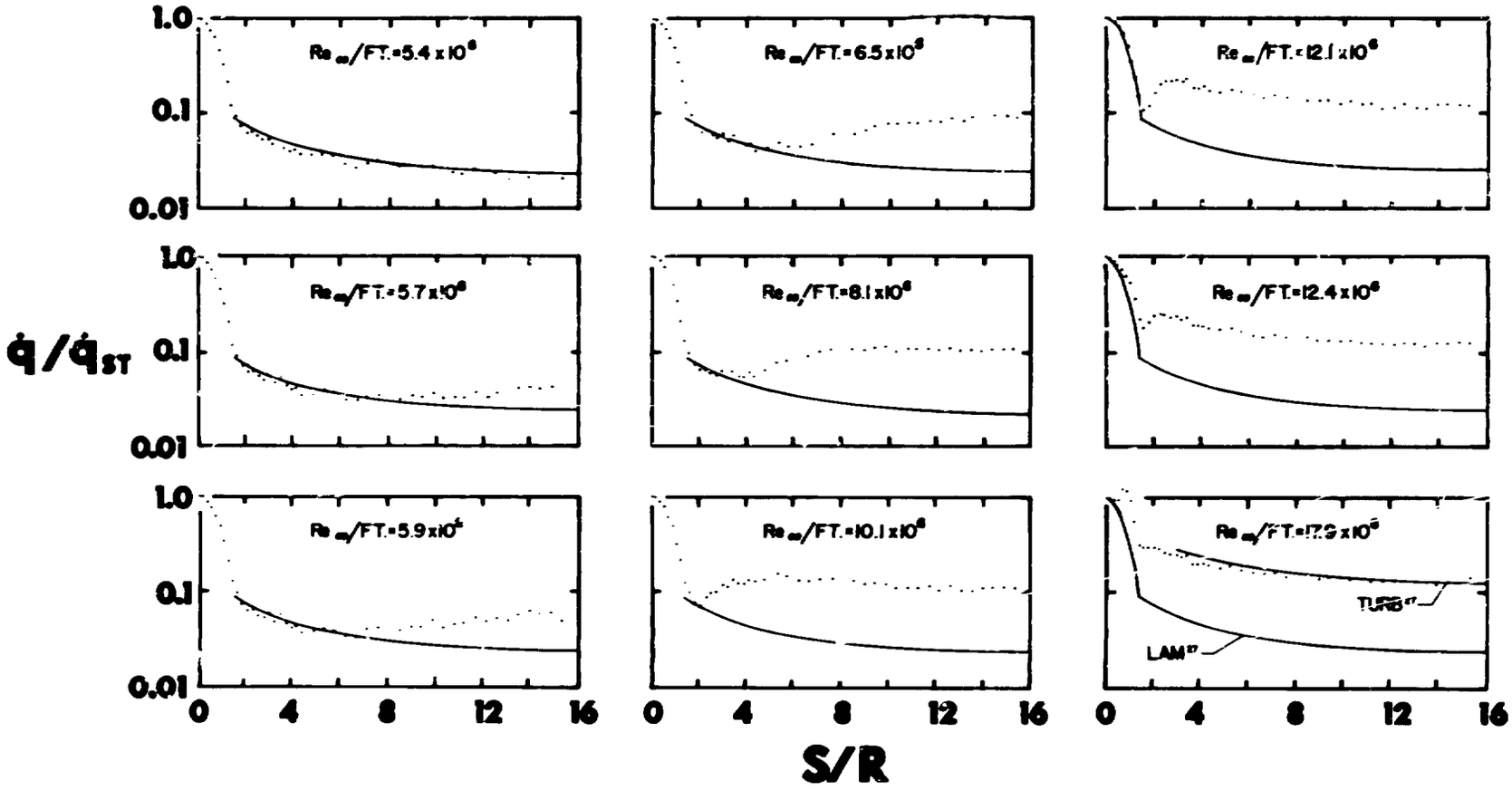

FIG. 15 TRANSITION MOVEMENT FROM CONE FRUSTUM TO NOSETIP ON A 7-DEGREE HALF ANGLE CONE AT $M_\infty = 9.1$

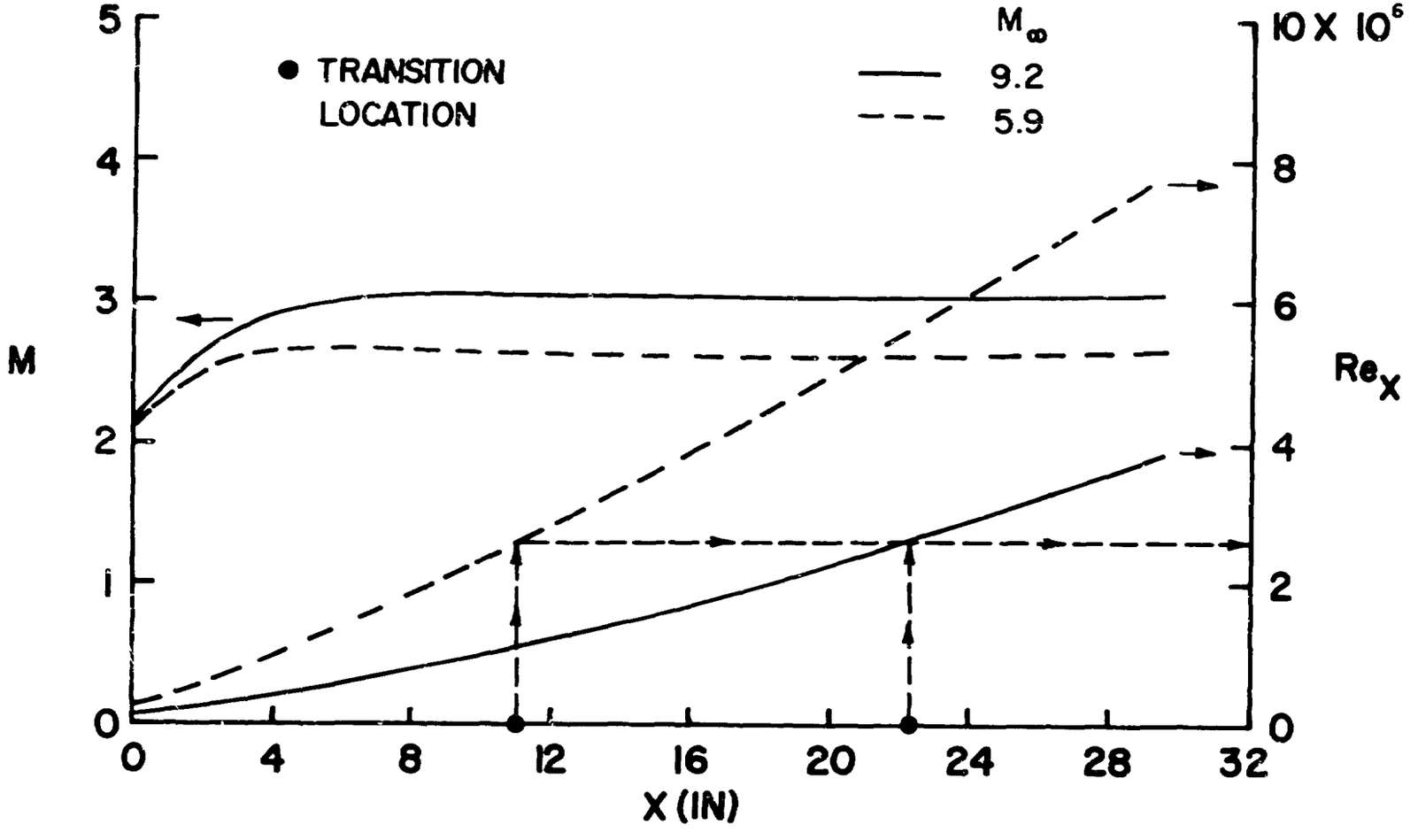

FIG. 16 TRANSITION LOCATION AND LOCAL MACH NUMBER AND REYNOLDS NUMBER ON AN 8-DEGREE HALF ANGLE CONE WITH A 0.60 INCH NOSE RADIUS AT M_∞ = 5.9 AND 9.2; Re_∞/FT. = 18.5 x 10^6 IN BOTH CASES

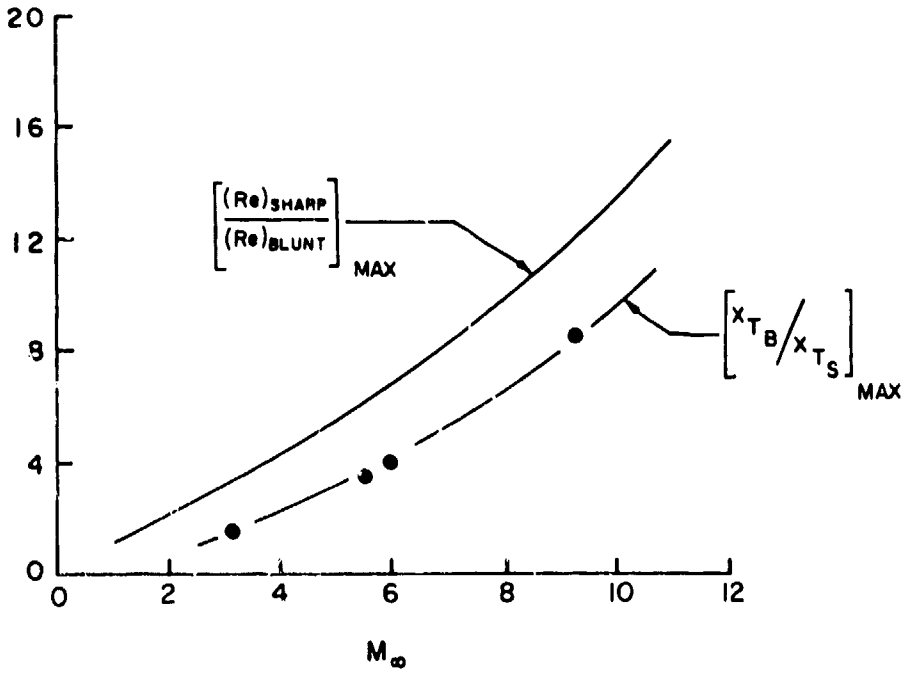

FIG. 17 TRANSITION DISPLACEMENT TREND WITH MACH NUMBER (DATA POINTS FROM FIG. 14)

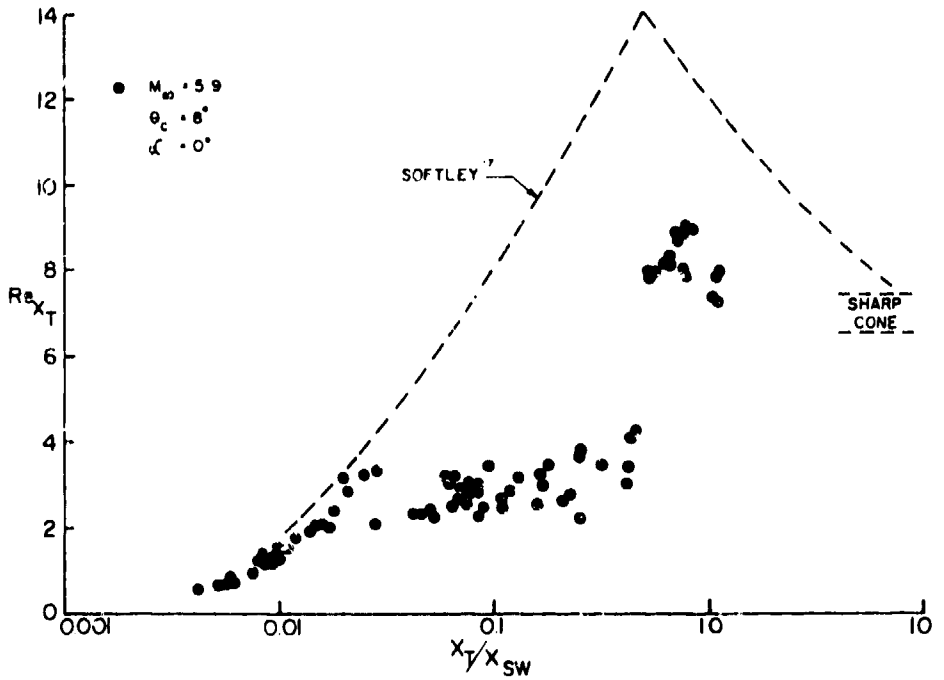

FIG. 18 LOCAL TRANSITION REYNOLDS NUMBER CALCULATIONS

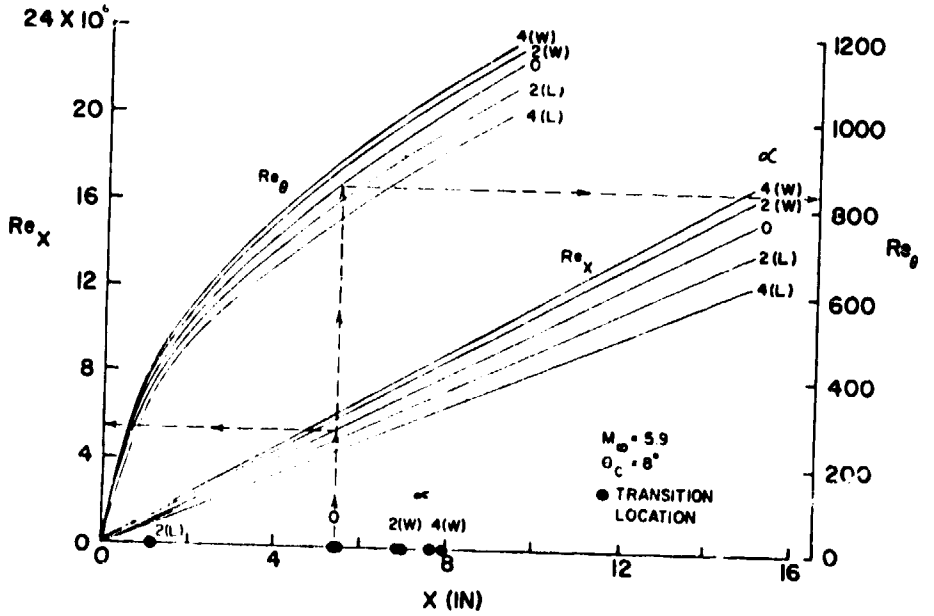

FIG. 19 LOCAL REYNOLDS NUMBER CALCULATIONS FOR A SHARP CONE AT ANGLE OF ATTACK

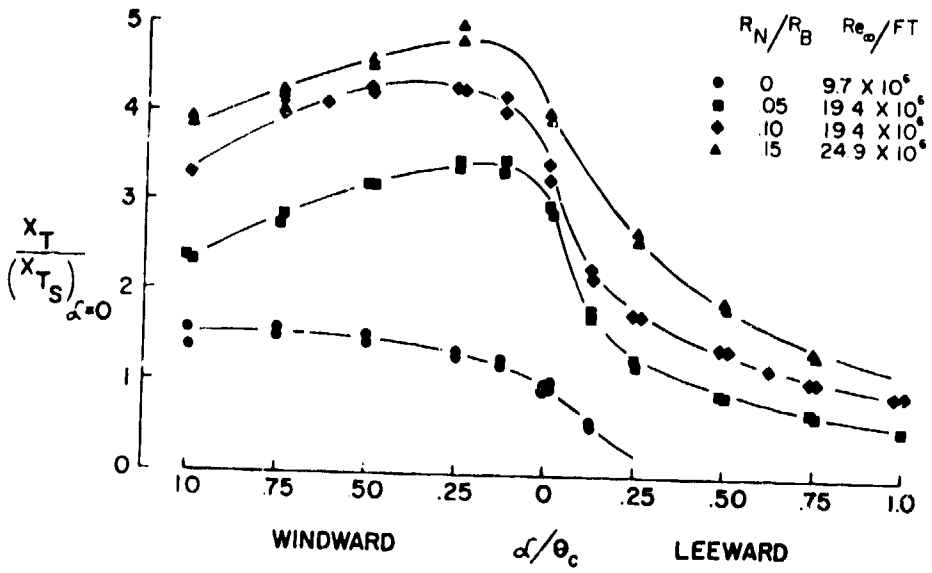

FIG. 20 TRANSITION MOVEMENT WITH ANGLE OF ATTACK FOR AN 8-DEGREE HALF ANGLE CONE AT $M_\infty = 5.9$

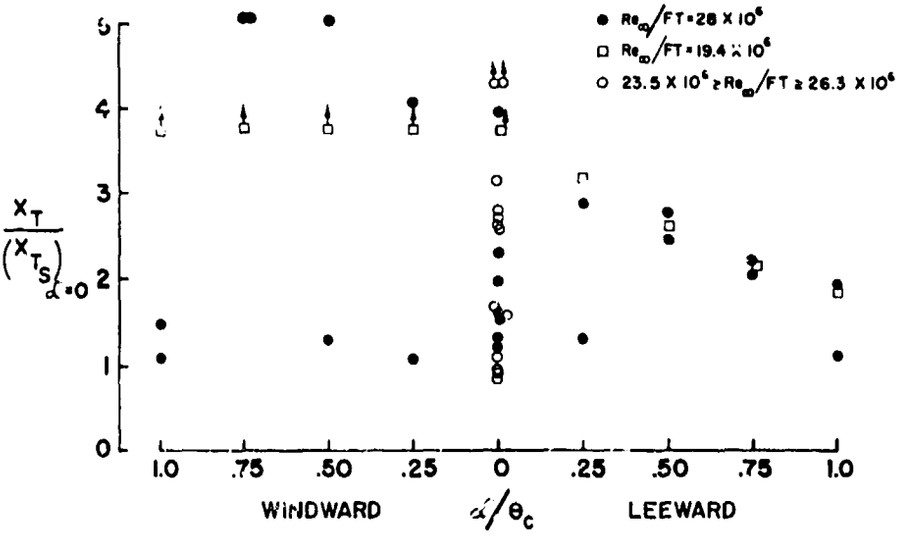

FIG. 21 TRANSITION MOVEMENT WITH ANGLE OF ATTACK FOR AN 8-DEGREE HALF ANGLE CONE WITH 30% BLUNTNESS AT $M_\infty = 5.9$

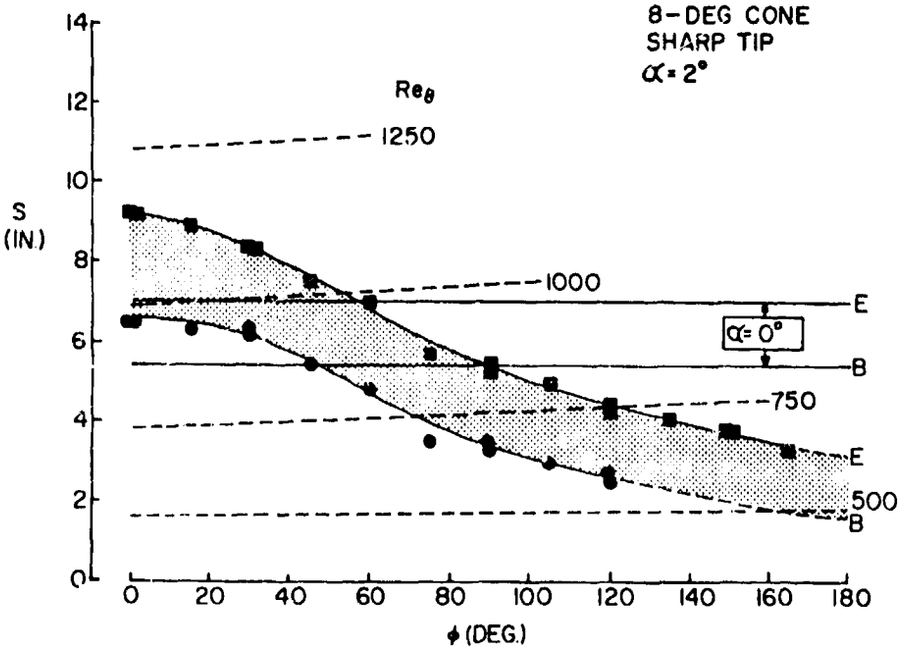

FIG. 22 TRANSITION PATTERN AT $\alpha = 2^\circ$, SHARP TIP

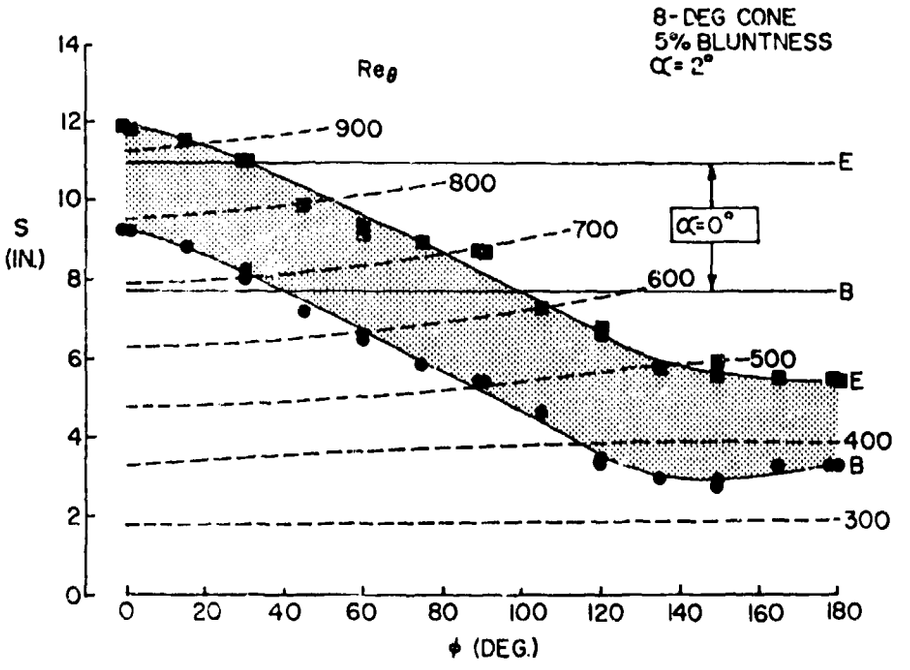

FIG. 23 TRANSITION PATTERN AT $\alpha = 2^{\circ}$, 5% BLUNTNESS

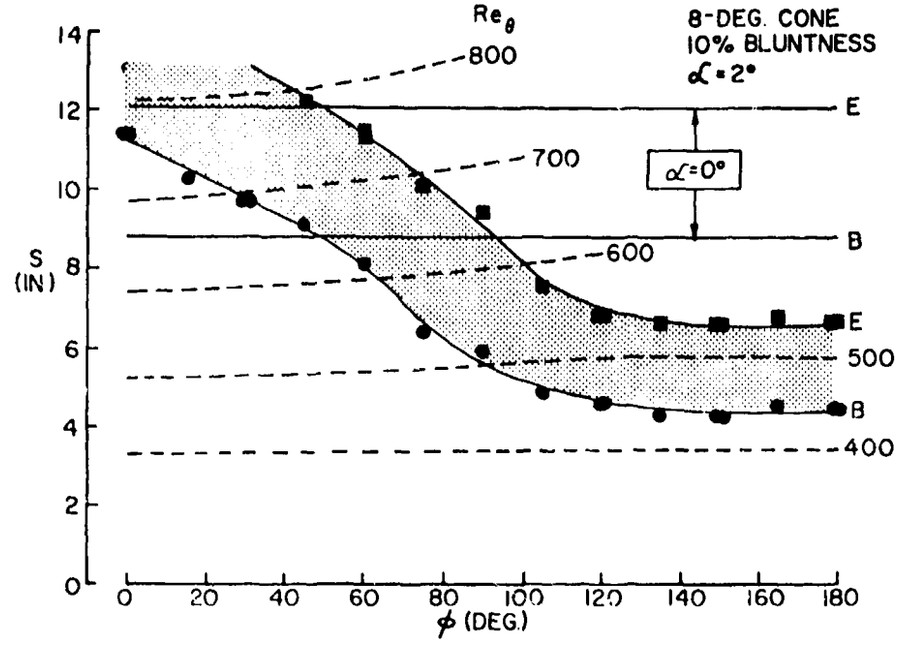

FIG. 24 TRANSITION PATTERN AT $\alpha = 2^{\circ}$, 10% BLUNTNESS

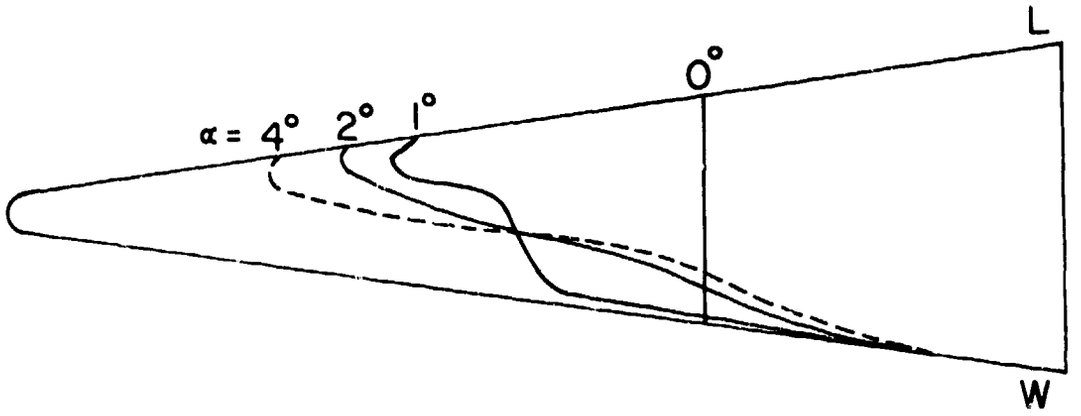

FIG. 25 TRANSITION PATTERN VS ANGLE OF ATTACK, 10% BLUNTNESS

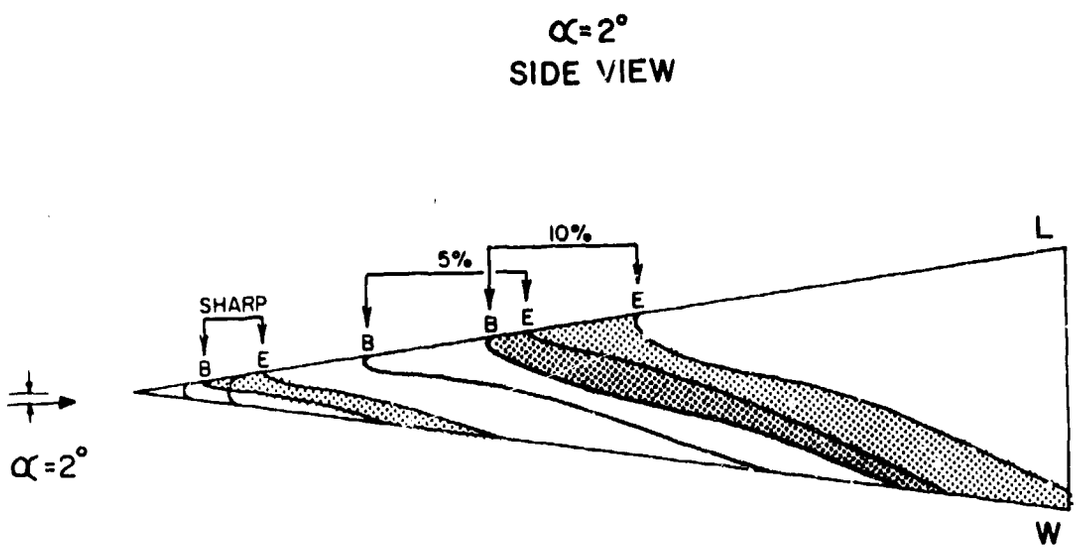

FIG. 26 TRANSITION PATTERN FOR DIFFERENT NOSETIPS, $\alpha = 2^{\circ}$

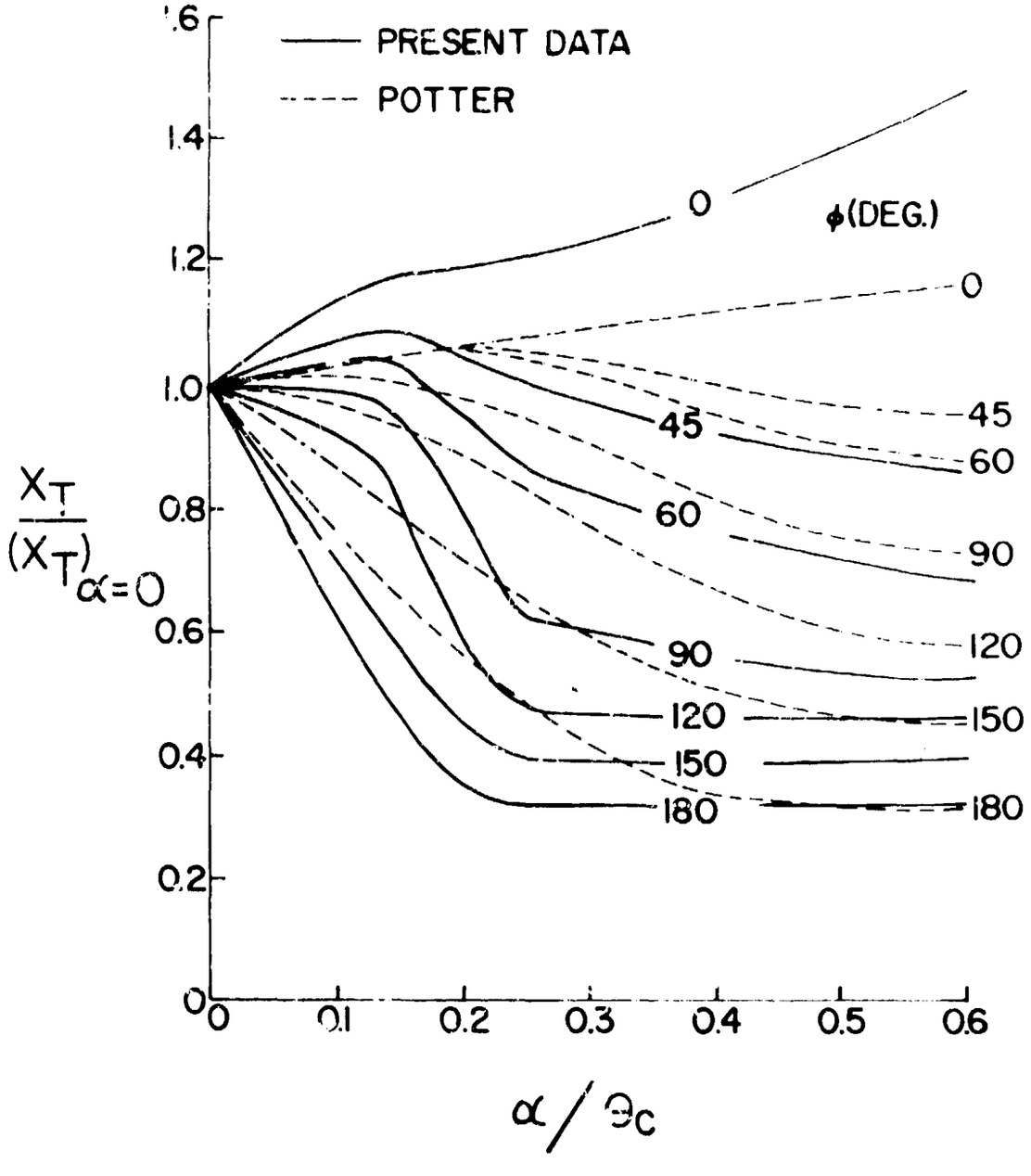

FIG. 27 TRANSITION ASYMMETRY DUE TO ANGLE OF ATTACK, SHARP TIP

AD P000326

A NOTE ON THE OSCILLATION OF CAVITIES COUPLED TO AERODYNAMIC FLOWS

by

Alexander H. Flax, President
Institute for Defense Analysis
Arlington, VA

The extensive recent literature on the oscillation of cavities interacting with aerodynamic flows has resulted in a bewildering array of models for frequency prediction, each of which may have theoretical or experimental bases for various of the physical processes being modeled to describe the overall system. Such models have generally been built on various representations of two physical phenomena and their interaction: the instability of vortex sheets between fluid layers of differing velocities and the acoustic resonance of cavities. Surprisingly, most of the models fit at least some set of experimental data amazingly well, especially in view of the complex interacting physical phenomena with which they deal. Almost all of the models can be rationalized within the phenomenological framework of a formula due to Rossiter. However, in this contex it seems that what this subject has evolved into is a methematical theory of integral wavelengths, much like the "old" quantum mechanics of Bohr, Sommerfeld and Wilson.

The overlapping and sometimes hidden assumptions in models for cavity oscillation often tend to obscure rather than clarify the mechanics of aerodynamically driven cavity oscillations. In this note, some relations between the physical pheonmena contemplated in various models are discussed, and some remarks made concerning the still largely unsolved problems of defining the aerodynamic and acoustic coupling and energy transfer mechanisms which could lead to methods for prediction of modal amplitude responses and conditions for the onset of self-excited oscillations.

Manuscript received in February 1979.

A Note on the Oscillation of Cavities Coupled to Aerodynamic Flows

Alexander H. Flax
Institute for Defense Analyses

Introduction

There is by now an extensive literature on the oscillation of cavities, and, more generally, duct and resonator systems, interacting with aerodynamic flows. Indeed interest in this subject in physics goes back to the eighteenth century when theoretical predictions of organ pipe frequencies were first set forth by Lagrange[1] (Ref. 1, Vol. 1, pp. xv-xvi). In the modern world of aerospace engineering, cavity oscillations are of importance in determining critical aerodynamic flow, noise and buffeting conditions as well as loads in landing gear wells, flap retraction recesses, bomb bays, boundary-layer bleeds, aft closure areas near jet and rocket nozzles and, in more complex form, in jet engine ducting systems.

The main focus of attention in the literature of the past twenty years,[2] as in earlier years, has been on two phenomena: the instability of vortex sheets formed between fluid layers of different velocities and the acoustic resonance of cavities. Interactions between these phenomena have been postulated in accordance with a variety of models, almost all of which surprisingly seem to lead to frequency prediction having reasonably good correlations with experimental results, give or take an empirical constant or two. Considering the wide range of complex physical processes involved in the overall phenomenon of cavity resonance, this is truly amazing. Such processes which play a part in cavity oscillation include instability of vortex sheets and vortex formation, turbulent mixing, shock wave motion, shock-boundary layer interaction, jet efflux and acoustic radiation into inhomogeneous flows. To complete the challenge, the investigator is called upon to deal with these problems for subsonic, transonic and supersonic flows.

Had it not been for the fact that apparently the frequency of aerodynamically induced oscillations is strongly determined by a very few dominating physical variables, the successes in correlating experimental data attained by minor variants of a simple phenomenological formula put forward by Rossiter[3] could not even be imagined. But, by the same token, the dominance of the few key variables over almost the entire range of the plentiful experimental data now available makes it exceedingly difficult to use these data in terms of

frequencies to discriminate between the merits of more detailed and ostensibly more rational models put forward by various authors. In fact, it appears that the subject of cavity oscillation has evolved into a mathematical theory of integral wavelengths, much like the "old" quantum mechanics of Bohr, Sommerfeld and Wilson, which gave many useful and insightful results concerning atomic structure, but which had to be replaced by more theoretically sound, complete and reliable theory before the subject could be considered to be scientifically in hand.

Thus, present methods for dealing with aerodynamically-induced cavity oscillations do not provide completely reliable and unequivocal means for predicting flow conditions under which large amplitude responses in self-excited modes may occur in cavities. To do this it appears that much more analytical (and closely related experimental) attention will have to be given to the mechanism of aerodynamic and acoustic coupling of cavities to external flows and to the energy transfers made possible by such coupling mechanisms.

This note is intended to illuminate the common and differing features of physical and mathematical models which have been proposed to analyze oscillations of cavities exposed to aerodynamic flows, and to illustrate the limitations of several of the more recent efforts to go much beyond what is implied in Rossiter's formula and its variants. A brief discussion will also be given of aerodynamic energy transfer and its role in inducing self-excited oscillations of cavities.

The subject matter covered in this note is limited to gases. Related phenomena occur in the flow of liquids with, however, additional features and complications introduced by the possibility of cavitation, "dead-water" regions, entrapped air or air surge capacities in flow systems and the relative incompressibility of liquids which tends to make structural distortions of pipe and cavity walls more likely to play a role in oscillations. For a general overview of the literature of flow related cavity oscillations, including phenomena in liquids, see Ref. 2.

The Principal Models

The types of resonant cavities which we shall deal with are illustrated in Fig. 1 [(a) to (e)]. 1(a) is the Helmholtz resonator which is classical in the acoustic literature and forms one of the basic physical models for studies of cavity resonance. The other classical physical model is the blown organ pipe which is similar to 1(b), the deep cavity.

A listing of the models which have been proposed for aerodynamically-induced cavity oscillations along with references to typical treatments of those models follows:

1) The cavity is an acoustic resonator, basically of the Helmholtz type, and responds to the acoustic noise spectrum of the air flow in the stream.[4,5]

2) Vortex shedding from the leading edge of the cavity essentially at a fixed Strouhal number (frequency times length divided by velocity) determines the frequency of cavity oscillation.[6,7]

3) The cavity provides a path for feedback upstream of downstream moving oscillatory disturbances either in the form of unstable vortex sheets or fully developed discrete vortices generated at the leading edge of the cavity. The sum of the transit times on both paths equals the period. In the primitive version, the disturbance convective velocity factor is an empirical constant.[3,8]

4) The frequencies for strong oscillatory amplitudes are determined by the coincidence of the feedback loop transit time frequency with an internal cavity resonance frequency (either Helmholtz or standing wave).[8,9]

5) The speeds with which disturbances are convected from the leading edge of the cavity is determined by the phase velocities of the unstable vortex sheet modes. By considering compressible flow near a wall, the upstream moving wave phase velocity can also be obtained. Thus, the two transit times required for an ostensibly more rational application of 2) are obtained.[10,11]

6) Instability of a Helmholtz resonator cavity occurs approximately at its resonator frequency whenever energy transfer from the external flow can be positive. No independent cyclic external flow phenomenon is involved.[12]

Feedback Transit-Time Models

The prototype of feedback transit-time models involving coupled oscillator airflow and acoustic phenomena appears to be Rayleigh's description (Ref. 1, Vol. II, pp. 310-412) of the action of such phenomena in a device called the "bird-call" in which "a stream of air issuing from a circular hole

in a thin plate impinges centrically upon a similar hole in a parallel plate held at a little distance." Rayleigh's qualitative explanation of the phenomenon is as follows: "When a symmetrical excrescence (in the jet) reaches the second plate, it is unable to pass the hole with freedom and the disturbance is thrown back, probably with the velocity of sound, to the first plate, where it gives rise to a further disturbance to grow in its turn during the progress of the jet."

This descriptive analysis was used by Powell[13] to formulate a quantitative model for the so-called edgetone which can be generated by a thin edge placed in the center of a jet stream. In this case, the unsymmetrical or sinuous jet instability is the pertinent phenomenon.

The same general line of reasoning has been used to explain a variety of phenomena involving self-sustaining oscillatory flows including wake-forming cylinders in tandem and cross-channel acoustic resonance in a duct caused by interaction with a periodic wake from an object in the duct.[14]

For the problem of a cavity interacting with an aerodynamic flow, Rossiter[3] devised a frequency formula for resonant or self-sustaining oscillators, based on transit-time concepts similar to those of Rayleigh, Powell and others. This formula has enjoyed wide general acceptance and success in correlating with experimental data. As many other authors have pointed out, however, Rossiter's phenomenological theory predicts fairly well what frequencies may occur in cavity oscillation, but not whether pronounced self-sustained oscillations will, in fact, occur.

To obtain Rossiter's formula, we postulate a periodic disturbance moving with the flow over a cavity with velocity $k_v u_o$ where u_o is the free stream velocity and k_v is a factor to account for the disturbance (which is often postulated to be a discrete vortex) being convected at a different velocity. Thus a disturbance wave crosses the length of the cavity denoted by L in time, $t_1 = L/k_v u_o$. An acoustic wave, usually assumed to be traveling inside the cavity, crosses the same distance in time $t_2 = L/a_c$, where a_c is the velocity of sound in the cavity. Thus the basic period of the phenomenon is

$$T = t_1 + t_2 = L/k_v u_o + L/a_c \tag{1}$$

Noting that the frequency, f, is equal to the reciprocal of the period, and noting that periodicity with multiplicity m may have the same effect in reinforcing oscillation as single periods, the frequency in terms of the Strouhal number fL/u_o is

$$\frac{fL}{u_o} = \frac{m - \alpha}{1/k_v + M\left(\frac{a_o}{a_c}\right)} \tag{2}$$

where m is the mode number referred to above and α is an empirical constant having the character of a phase to take account of the fact that the operative effect in a standing or traveling wave phenomenon may occur at a phase shifted from an integral multiple of π. (An example is the standing wave in an organ pipe open at one end--in this case the phase at the open end relative to the closed end is $\pi/2$.) Although it is generally acknowledged that k_v and α may vary with a number of variables, including Mach number, mode type, cavity geometry, Reynold's number, etc., no definitive systematic experimental investigations have been made and the values $k_v = 0.57$, $\alpha = 1/4$ have most commonly been used (e.g., by Heller and Bliss;[11] see Fig. 2 of this paper). The ratio of the velocity of sound inside the cavity to that in the free-stream flow, a_o/a_c, was not originally considered by Rossiter but was introduced by Heller and Bliss on the assumption that the cavity experiences very nearly the full stagnation temperature (recovery factor $\rightarrow 1.0$) which appears to be an acceptable approximation in most cases.

Analytical Estimates of Phase in Rossiter's Formula

Bilanin and Covert[10] have attempted to give a more rational determination of the phase in Rossiter's formula. They assume that the feedback is generated by a single point two-dimensional source disturbance at the cavity aperture trailing edge. They also examine the effects of approximating the satisfaction of the cavity wall boundary conditions by a two-fold infinity of image sources. They conclude, on the basis of further approximations limiting the source system to a finite number and curve fitting to a calculated set of points, that a straight line relation between $\omega L/a$ and phase exists for $L/D = \infty$ and that this is $\varphi = \omega L/a - \pi/4$, where L is cavity length D is cavity depth, ω is the circular frequency, and a is the velocity of sound.

It was also concluded that this relationship holds with sufficient accuracy from $L/D = \infty$ down to $L/D = 4$. Although this result was arrived at by curve fitting, it is basically a consequence of the analytical expression of the asymptotic formula for the potential of a cylindrical wave (Ref. 1, Vol. II, p. 307).

$$\varphi = -\left(\frac{\pi}{2kr}\right)^{\frac{1}{2}} \cos\left(\omega t - kr - \frac{\pi}{4}\right) \left\{ 1 - \frac{9}{128(kr)^2} + \ldots \right\} + \left(\frac{\pi}{2kr}\right)^{\frac{1}{2}} \sin\left(\omega t - kr - \frac{\pi}{4}\right) \left\{ \frac{1}{8kr} - \frac{3^2 5^2}{3!(8kr)^3} + \ldots \right\} \qquad (3)$$

where $k = \omega/a$, ω is the circular frequency, and a is the velocity of sound. For sufficiently large kr, only the cosine term remains.

The Bilanin and Covert assumption is that the pressure, which equals $-i\omega\varphi$, must be in phase with vortex sheet disturbances at the leading edge of the cavity. Since the pressure has a phase difference of $\pi/2$ from φ, we find that the phase of the acoustic pressure is equal to $kL + \pi/2$ which is their result. The downstream moving vortex sheet disturbance was characterized by a spatial frequency $K_r L$ and a phase φ which were determined by an analytical method to be discussed in the next section. The phase relation over the entire feedback loop is then given by

$$K_r L + \varphi + \pi + kL - \pi/4 = 2n\pi \tag{4}$$

n being an integer. Here the vortex sheet displacement η is assumed to be given by

$$\eta = e^{K_i x_1} e^{i(K_r x - \omega t + \varphi)} \tag{5}$$

where K_i is a spatial amplification factor, while K_r is the real wave number and φ is the phase representing the lag of vortex sheet displacement behind the forcing at the leading edge as noted above. The acoustic source at the trailing edge is assumed to be at its positive maximum when η is at its negative maximum (a phase difference of π relative to the maximum positive displacement). A formula akin to Rossiter's formula is obtained from Eq. (5) as

$$\frac{fL}{u_o} = \frac{n - 3/8 - \varphi/2\pi}{1/\kappa + M\left(\frac{a_o}{a_c}\right)} \tag{6}$$

where in effect $\kappa = \omega/K_r u_o$ and $\alpha = \varphi/2\pi + 3/8$.

Good agreement was found with experimental data from $L/D = 4$ to $L/D = 7$ mainly at Mach numbers of 1.5 and 2.0. From a theoretical standpoint, however, not only is the notion of a single source in free space as a representation of the back end of the cavity an extreme simplification, but also the representation by a two-dimensional source requires further study of ranges of validity especially when applied to cavities long in the streamwise direction.

In an attempt to include the effect of L/D on the equivalent source potential, Block[9] included the first image source reflected in the bottom of the cavity.

Again her results were obtained by fitting curves to a set of calculated points. However, using Eq. (3) to asymptotically represent both sources, we obtain for the additional phase shift, δ, relative to $kr - \pi/4$ in Eq. (3)

$$\tan \delta = \sin \frac{\omega L}{a}\left[\sqrt{1 + 4(D/L)^2} - 1\right] \div \left\{\sqrt{1 + 4(D/L)^2} + \cos \frac{\omega L}{a}\left[\sqrt{1 + 4(D/L)^2} - 1\right]\right\} \tag{7}$$

Block finds that her curve fits an additional phase shift equal to .514 $\omega L/a$.

When the arguments of the trigonometric function are small enough for sin x to be represented by x and cos x by unity in Eq. (7), the phase shifts given by Block and by Eq. (7) are as listed below at a nominal $\omega L/a = 1.0$ as

Table I

D/L	δ Eq. (7)	$\delta = .514(D/L)\frac{\omega L}{a}$
2.0	1.035	1.028
1.0	.495	.514
.5	.190	.257
.25	.05737	.1285

It should be noted in considering the limits of validity of these approximations that $\omega L/a = fL/u_o\left(\frac{M}{2\pi}\right)$

Block, following Bilanin and Covert, takes condition for the phases around the feedback loop to be

$$K_r L + \pi + \varphi + \beta + h = 2n\pi \tag{8}$$

where φ is as above the lag in displacement of the shear layer at the leading edge of the cavity behind the forcing mechanism there, while β is the difference in phase between the source and the shear layer displacement at the trailing edge, and h is the phase difference which Bilanin and Covert took to be $-\pi/4 + \omega L/a$. Block's curve fits lead to

$$h = -\pi/2 + \frac{\omega L}{a}(1 + .514\ D/L) \tag{9}$$

giving a difference of $\pi/4$ in the constant term from previous results affecting the $L/D = \infty$ case. However, β was taken equal to $-\pi/2$ and φ was taken to be zero, leading to

$$f L/u_c = \frac{n}{1/k_r + M\,(1 + .514/D/L)} \tag{10}$$

where as before n is an integer.

It is clear from the procedures described above that all attempts to rationalize the Rossiter formula through analytical phase computations for some or all stages of the feedback process are attended by arbitrary assumptions which can only be given validity by reference to experimental data. Block does present considerable experimental data which show a small but definite dependence of cavity resonant frequencies on L/D when governed by the modified Rossiter formula. The other thrust of this data, shown in Fig. 3, is to illustrate that resonance also occurs at points somewhat off the Rossiter predictions and on the curves corresponding to the organ pipe (depth) frequencies of the cavities when corrected for open-end effect by the empirical end correction formula of East.[8] However, it will be shown later that East's empirical formula ignores the effect of finite cavity width which, at least on theoretical grounds, may be the important end correction parameter for narrow slits with the long dimension transverse to the stream which were used in East's experiments.

A fundamental observation which Block made from her data, which has also been indicated by other data such as those of Quinn[6] and East,[8] is that the intersection of the frequency curves predicted by Rossiter's formula and the frequencies for internal resonance of the cavities seem to constitute a criterion for strong oscillatory response of cavities, especially those which have intermediate L/D ratios (e.g., 0.5 to 2.0).

Analytical Estimates of Transit Times in Rossiter's Formula

The two transit times in Rossiter's formula have been the subject of several analytical investigations. The simplest and earliest analysis bearing on this problem relates to the wave speed of disturbances on two-dimensional vortex sheets parallel to an infinite plane wall in incompressible flow (Ref. 1, Vol. II, p. 379; see also Ref. 6). For a vortex sheet formed by two streams of equal density with an outer stream of infinite extent and velocity V and an inner stream of velocity V′ bounded between the vortex sheet and a wall located at a distance D from the vortex sheet, the relation between complex frequency Ω and wave number k is given by

$$(\Omega + kV)^2 + (\Omega + kV')^2 \coth kD = 0 \tag{11}$$

for a surface disturbance of the form $\eta = c\,e^{i(\Omega t + kx)}$

This equation may also be considered a dispersion relationship for the speeds of waves of various wavelengths. In the cavity problem V' is usually taken to be zero. The solution is then

$$\Omega = \frac{kV \pm ik\sqrt{\coth kD}}{1 + \coth kD} \tag{12}$$

When D is infinite, this gives

$$\Omega = \frac{kV}{2} \pm \frac{ikV}{2} \tag{13}$$

Since the phase velocity of vortex sheet disturbance may be taken to be $c_R = \Omega_R/k$, we obtain the simple and important result

$$c_R = V/2 \tag{14}$$

If D is not infinite the corresponding result is

$$c_R = \frac{V}{1 + \coth kD} \tag{15}$$

Noting that $k = 2\pi/\lambda$, where λ is the wavelength, in Eq. (15) coth kD is significantly different from unity only for wavelengths less than about one-third the distance D. Since from the standpoint of the streamwise coupling process for a cavity of length L, wavelengths of interest tend to be of length L, this correction seems to be significant only for cavities of very low L/D, in which case the physical approximation of the cavity by an infinite plane wall is very doubtful.

For compressible flows, the problem of the vortex sheet parallel to a plane wall becomes much more complicated and simple closed form solutions of the dispersion equation cannot be obtained. There are, in addition, many modes of wave propagation and selection of the most critical modes is necessary. Belanin and Covert,[10] as has previously been noted, obtained numerical solutions to permit them to calculate phase angles for parts of the feedback process implied in the Rossiter formula. More recently, Heller and Bliss[11] extended the range of numerical solutions. They identified two propagation modes, one of which corresponded to a downstream moving wave whose important component was vortex sheet disturbance, and the other of which was an upstream moving wave whose principal character seemed to be acoustic in nature. By using these wave speeds to determine transit times to be used in the feedback transit time model, an analytical counterpart of the Rossiter formula was calculated. (We note, however, that this is still far from a complete analytical treatment of the cavity resonance problem, since the cavity walls other than the bottom are completely unaccounted for in the aerodynamic analysis.)

Figure 2 shows the results of the Heller and Bliss analytical model in comparison with experiment. Also shown is the Rossiter formula with k_v = .57 and α = 1/4. Where there is significant disagreement between the analytical model and the Rossiter formula, mainly at subsonic speeds, it is seen that the Rossiter formula gives closer agreement with experiment. Sharper examination of the results obtained by Heller and Bliss for wave speeds (plotted in Figs. 4 and 5) indicates that the area of agreement of their results with the Rossiter formula and with experiment generally corresponds to conditions ($\omega L/a > 0.5$, $L/D > 2$, $.6 < M < 2.5$) for which the downstream moving wave speed $\approx V/2$ and the upstream wave speed was close to the velocity of sound in the cavity. Thus, the confrontation of analysis with these experiments falls far short of providing a critical test of the theory vis-a-vis simpler theories and purely phenomenological constructs.

Finally, reference should be made to another line of investigation of vortex sheet stability which has been applied, particularly in the case of water flows, to study resonant flow conditions. Rayleigh (Ref. 1, Vol. II, pp. 392-400), found that, in contrast to the simple result of Eq. (12) which predicts wave amplification for all wavelengths, introducing a finite width for the vortex sheet had the effect of limiting the wavelengths of unstable disturbances to a much narrower range, roughly of the order of the vortex sheet thickness. More recent investigations, especially those of Drazin and Howard[15] and Michalke[16,17] have dealt with vorticity distributions roughly approximating jet and boundary layer profiles in incompressible flow. These can be applied to calculate wave speeds and wave amplifications which affect feedback cycle calculations.[18]

Cavity Aperture Impedance

Plumbee, Gibson and Lassiter[5] have emphasized the role of the coupling of cavity oscillations to the external air mass through the acoustic impedance of the air mass external to the aperture of the cavity. This, in the case of a still air external field, corresponds to the classical "end-correction" of an organ pipe or Helmholtz resonator in acoustics calculated over a century ago by Helmholtz and Rayleigh (Ref. 1, Vol. II, pp. 176-183). The idealized model for this coupling is the passage of a plane acoustic wave on an infinitely thin plate (usually only one-half the calculated effect is used since the flow inside the pipe or cavity near the end is hardly represented by the model); a separate inside end correction, which may be substantial for constricted pipes, cavities or resonators as in Fig. 1 (a), (d) and (e), has been given by Ingard[19] and applied to a specific resonator problem with aerodynamic flow coupling by Panton and Miller.[4] The internal end-effect problem for sufficiently constricted cavities seems to be very nearly the same as when the air external to the cavity is stationary in the usual acoustic case, and we shall not deal with it further here. The external end correction plays a central role in the theory of cavity oscillations of Plumbee et al and, as

will be shown, may also have significant secondary effects in the application of other analytical methods to the cavity oscillation problem.

Before going into the theoretical basis for calculating cavity aperture impedance, it would be well to give some of the major objections which can be made to the oversimplified approaches and linearizations employed. In the model of Plumbee et al, the presence of a non-uniform stream in the boundary layer immediately above the aperture is ignored as is the mixing of the external flow into the cavity; the possible unstable motions of the vortex sheets in the boundary layer are also not taken into account.

Further, the formation of a jet efflux from the aperture and its mixing with the free stream are not considered. Evidence for non-linearities in aperture impedance, probably associated with turbulence of the acoustic flow through the aperture (in the case when there is no mean aerodynamic flow outside), has been presented by Ingard.[19] The arguments for the consideration of aperture impedances based on overidealized linear acoustics and uniform external flow conditions must rest on the degree to which agreement with experimental data is achieved or improved by this means. The correlation with experimental data of Plumbee et al does indeed indicate a good correlation of calculated frequencies for maximum cavity response with experimental data for both subsonic and supersonic speeds. Some further confirmatory evidence as to the utility of the linearized impedance, as at least a gross measure of a significant effect, is also provided by the subsonic data of East[8] and Block.[9]

The linearized acoustic problem of passage of a plane wave through an aperture in an infinite thin plate requires the solution of the integral equation for acoustic velocity potential, φ,

$$\varphi = \frac{1}{2\pi}\iint_A \frac{\partial \varphi}{\partial n}\,\frac{e^{-ikR}}{R}\,d\sigma \qquad (16)$$

where $\partial\varphi/\partial n$ is the normal velocity through the aperture, $d\sigma$ is the element of area $k = \omega/a$, ω is the circular frequency, a is the velocity of sound, and

$$R = \sqrt{(x - \xi)^2 + (y - \eta)^2}$$

The motion is harmonic as varying as $e^{i\omega t}$. The pressure is given by $p = i\omega\varphi$ and is required to be constant over the aperture, while $\partial\varphi/\partial n$ is to be determined in the aperture, being, of course, required to be zero over the remainder of the plate. For the plane wave, the wavelength λ, is given by $\lambda = 2\pi/k$. Thus kR is $2\pi R/\lambda$ and, if the wavelength is large compared to the dimension of the aperture, Eq. (16) may be approximated by

$$\varphi = \frac{1}{2\pi}\left[\iint_A \frac{\partial \varphi}{\partial n}\,\frac{d\sigma}{R} - ik\iint d\sigma\right] \tag{17}$$

The second term represents a kind of dissipation in the form of wave energy transmitted through the aperture. However, we will not discuss the dissipative effect further here. The first term is of immediate interest since it represents the flow through the aperture in incompressible flow, which is physically a natural consequence of the assumption that the acoustic wavelength is large compared to the dimensions of the aperture. This term, as will be seen, leads to a reactive or "mass-like" impedance to flow through the aperture.

Helmholtz and Rayleigh (Ref. 1, Vol. II, pp. 176-180), recognizing that the problem in the long wavelength approximation merely requires solution of Laplace's equation for the aperture, related it to the problem of finding the static electric capacity of a thin conducting disc having the shape of the aperture. This problem can be solved exactly for discs of elliptical shape. The conductivity of the aperture, which is defined as the reciprocal of the specific reactive impedance, is found to be related to the electric capacity, M, by

$$c = \pi M \tag{18}$$

for unit density.

The reactive impedance is that of a plug of air having the area of the aperture, σ, and a virtual height, α, which constitutes an end correction for the depth of the aperture (or an appropriate equivalent length for constricted or tapered cavities). Thus the reactive impedance, Z, is given by $Z = i\omega\rho\sigma\alpha$ per unit area, and the specific impedance may be given by

$$z = i\rho\omega\alpha \tag{19}$$

In terms of conductivity, c, since

$$\alpha = \frac{\sigma}{c} \tag{20}$$

this leads to

$$z = i\rho\omega\left(\frac{\sigma}{c}\right) \tag{21}$$

Rayleigh shows that for elliptical apertures for an unrestricted air mass on one side

$$c = \frac{2\pi a}{F(e)} \tag{22}$$

where a is the semi-major axis of the ellipse and F(e) is the complete elliptic function of the first kind whose argument, e, is the eccentricity of the ellipse. If b is the semi-minor axis of the ellipse, $e = 1 - (b/a)^2$. The acoustic conductivity of the ellipse (one-sided free space) may also be represented as a series

$$c = 4\sqrt{\frac{\sigma}{\pi}}\left(1 + \frac{e^4}{64} + \frac{e^6}{64} + \ldots\right) \tag{23}$$

where the term outside the parenthesis is the conductivity of a circle of equal area. Up to an eccentricity of 0.5, the error incurred by neglecting the entire series in parenthesis is less than three per cent and thus the formula

$$c = 4\sqrt{\frac{\sigma}{\pi}} \tag{24}$$

is often recommended[19] as a good approximation for any compact not too elongated in shape. For elongated shapes F(e) may be approximated by

$$F(e) \approx \ell n\, 4/k' \tag{25}$$

where $k' = b/a = \sqrt{1 - e^2}$. This is good to within a few per cent when e is greater than .5.

Rayleigh also noted that the circle is the shape of aperture which gives minimum conductivity for a given area and that any addition to area will increase the conductivity. Thus, for example, the conductivity of any aperture is bounded by the conductivities of an inscribed and a circumscribed figure.

The concept of a constant end-correction independent of k fails when applied to the limit of a two-dimensional aperture as is evident from the logarithmic infinity exhibited by Eq. (25) when k' is made to approach zero. This is not a consequence of the approximations made in arriving at Eq. (25) but rather is fundamental and deep-seated, having its roots in the nature of the two-dimensional logarithmic potential. The problem has been discussed in detail by Rayleigh in connection with the notion of a two-dimensional organ pipe.[20] This difficulty of going to a two-dimensional limit in the end-correction has been overlooked by several investigators. It has even been suggested in the literature that the hydraulic radius can be used to relate the end-correction of a circle to that of a two-dimensional opening which, of course, is incorrect. Plumbee, Gibson and Lassiter[5] calculated aperture impedances numerically and their results include the pertinent three-dimensional effects, but perusal of either their formulation of the problem or their tables will not illuminate for the reader the existence of a difficulty in going to the two-dimensional limit. East, who used the impedance tables of Plumbee et al to calculate frequencies of maximum response,

also attempted to determine simple end-corrections for frequency, "following Lord Rayleigh's lead." However, he was forced into an empirical curve fitting process. His cavity apertures were all narrow (with the long dimension, w, transverse to the stream). In terms of the streamwise cavity dimension, b, and the cavity depth, d, his formula for the organ pipe frequency of the cavity was

$$\frac{fd}{a} = \frac{1}{4\{1 + .65\,(b/d)^{.75}\}} \tag{26}$$

where f is the frequency in Hertz and a is the velocity of sound.

East's cavities all had the same long dimensions (w = 18") transverse to the stream so such an empirical correlation without reference to w is possible. However, the resulting formula has no general validity for other geometries. Block[9] did use the formula to correlate other experimental data for apertures of different geometries, but to the extent that agreement with experiment was improved by this device, it must be regarded as fortuitious.

Using the conductivity of ellipses inscribed in East's narrow rectangles, the end-corrections for parameters corresponding to East's experimental data, all of which are at Mach numbers less than .2, have been calculated according to Eqs. (20), (22) and (25). The results are given in Fig. (6) and show good agreement with trends and fair approximation to the values of observed frequencies. Parenthetically, it should be noted that Wood's experimental data showed that oscillations occurred at practically constant values of Strouhal number based on cavity length, independent of cavity depth. Correspondingly, the values of the disturbance convection velocity factor k_v, varied from about 0.4 to 0.6.

Because exact solution of the electric capacity problem in closed form for aperture shapes other than ellipses has not been possible, and because when resonators have pipes or necks the outgoing flow is constrained in a way quite different from in flow through an infinite plate, a different approximation is often used to estimate open-end corrections for resonators. This approximation is based on the assumption that the conditions at the aperture may be represented by a rigid massless piston oscillating transverse to a plane wall. The impedance from the exterior air mass to the motion is calculated and then constitutes the end impedance of the open end of the resonator. Rayleigh (Ref. 1, Vol. II, pp. 162-169; 196-198) points out that, although the solution obtained for a circular piston of radius R is without restrictions as to the smallness of kR, "it is only when kR is small that the presence of the piston would not materially modify the question."

Plumbee, Gibson and Lassiter have calculated the piston impedance for rectangular shapes numerically, not only for a stationary air mass external to the cavity but also for both subsonic and supersonic flow. The questions raised concerning appropriate piston boundary conditions under conditions of external flow in relation to corresponding open-end boundary conditions have not been addressed by Plumbee et al and the cautions quoted from Rayleigh above have not been considered. However, in the pragmatic spirit which attends all analyses of aerodynamically coupled cavity oscillations, a vigorous approach to the problem again yielded an impressive degree of agreement with experiment.

Plumbee et al give as the expression for the force of a piston oscillating in time with transverse velocity $u_o e^{i\omega t}$ in a subsonic flow at Mach number, M

$$Z = \frac{i\rho\omega u_o}{2\pi} \int_0^{\ell_y} \int_0^{\ell_x} \int_0^{\ell_y} \int_0^{\ell_x} \frac{e}{D}^{-(ik/\beta^2)\,[-M(x'-x)+D]}\, dx\, dy\, dx'\, dy' \tag{27}$$

where $\beta^2 = 1-M^2$ and $D = \sqrt{(x'-x)^2 + \beta^2 (y'-y)^2}$. Here ℓ_y and ℓ_x are the dimensions of the rectangular aperture transverse to the stream and along the stream respectively.

It is interesting to note that this formulation admits a first-order term for small kD (as in Eq. (17)) which corresponds to a steady linearized subsonic flow and this in turn permits a standard Prandtl-Glauert-Goethert transformation so that, for small kD

$$Z(M, \ell_x, \ell_y) = \frac{1}{\sqrt{1 - M^2}}\; Z(0, \ell_x, \ell_y \sqrt{1 - M^2}) \tag{28}$$

For nearly square apertures using the approximation previously discussed in connection with Eqs. (23) and (24) that conductivity varies as the square root of area as does the end-correction (since $\alpha = \sigma/c$) we have the simple result for specific impedance (i.e., piston force divided by piston velocity and area)

$$z(M, \ell_x, \ell_y) = z(0, \ell_x, \ell_y)\,(1 - M^2)^{\frac{1}{4}} \tag{29}$$

The variation of the reactive part of z with Mach number for apertures of ℓ_y/ℓ_x ratios of 2.0 and 1.0 is shown in Fig. (7) for $k\ell_x = \omega\ell_x/a = 0.5$. At higher values of $k\ell_x$, the curves are no longer linear with $k\ell_x$ and the simple method of Mach number correction does not apply nor does the simple concept of an end-correction for an open cavity. It can be seen that the simple correction method applies reasonably well up to Mach numbers of about 0.6-0.7.

Finally, it is interesting to note the very slow variation with Mach number in properties of elongated apertures having their narrow dimension along the stream thus approximating the ordinary slender body and low aspect ratio wing theories in aerodynamics.

For such elongated cavities, the simple inscribed ellipse formula based on Eqs. (21), (22) and (25) gives good approximation to the reactive impedance as shown in Table II below. Also shown for comparison is the impedance at M = 0.80, which is seen not to differ greatly from the value at M = 0.

Table II

Aperture Reactive Impedances

M=0 and M=.8 ( )

	ℓ_y/ℓ_x = 0625		ℓ_y/ℓ_x = .125		ℓ_y/ℓ_x = 250	
$\omega\ell_x/a$	Eqs. (21), (22), (25)	Ref. 5	Eqs. (21), (22), (25)	Ref. 5	Eqs. (21), (22), (25)	Ref. 5
0.50	.0414	.0394(.0424)	.0689	.0655(.0712)	.11032	.1050(.1158)
1.00	.0827	.0777(.0773)	.1379	.1285(.1273)	.22064	.2048(.2010)
1.50	.1241	.1136(.1092)	.2068	.1869(.1775)	.33095	.2949(.2739)

Self-Excited Oscillations Induced by Ingestion of Boundary-Layer Air

Treanor and the author[12] analyzed and experimented with a ducted resonator similar to that in Fig. 1(e). Defining a variable F such that

$$F = \int_0^t q\, dt \tag{30}$$

where q is the oscillatory rate of volume flow into the duct, the equation of motion for the resonator was expressed as

$$\frac{\rho \ell_s \zeta_s}{A_s}\frac{d^2F}{dt^2} - \frac{\partial H_s}{\partial q}\frac{dF}{dt} + \frac{a^2 \rho F}{V} = 0 \tag{31}$$

where ρ is the air density, a is the velocity of sound, V is the resonator volume, ℓ_s is the duct length, A_s is the duct area and ζ_s is a factor to account for taper in duct area. ζ_s is given by

$$\zeta_s = \int_0^1 \frac{d(x/\ell_s)}{A/A_s} \tag{32}$$

$\partial H_s/\partial q$ is the rate of change of total head of air entering the duct with change of flow rate. As long as relatively smooth flow from the boundary layer into the inlet is occurring, this factor is positive (greater head at higher flow rates) and in Eq. (31) which is essentially that of a mechanical oscillator with a single degree of freedom, the $\partial H_s/\partial q$ term appears as a negative damping. In a physical system, there will, of course, be some positive damping to offset this, but under certain conditions self-excited oscillations may occur. In the experiments of Ref. (12), these were encountered but under conditions of oscillations around a steady flow into the inlet. A simple theoretical criterion, using measured positive damping for the resonator, gave reasonably good correlation of stable and unstable cases. The frequencies of instability were all very close to the classical Helmholtz resonator frequency of the system.

It would appear, however, that the same mechanism could come into play under some conditions of zero mean flow. The onset of instability proved quite sensitive to boundary layer conditions and injection of air into the boundary layer ahead of the inlet to make a more linear (laminar-like) velocity profile reduced $\partial H_s/\partial q$ and eliminated all instabilities.

For two-dimensional conditions, it is interesting to note that Lorentz in early investigations of the origin of turbulence expressed the energy growth in laminar steady streams of non-uniform velocity (with components U, V) due to perturbations (componerts u', v').[21]

With $E = \frac{1}{2}\rho(u'^2 + v'^2)$ constituting perturbation energy per unit volume

$$\frac{D}{Dt}\int\int E dV = \rho \int M dV - \mu \int\int N dV \tag{33}$$

where V is the volume, ρ is the density, μ is the viscosity and

$$M = -\left[u'^2 \frac{\partial U}{\partial x} + v'^2 \frac{\partial V}{\partial y} + u'v'\left(\frac{\partial U}{\partial y} + \frac{\partial V}{\partial x}\right)\right]$$

$$N = \frac{\partial v'}{\partial x} - \frac{\partial u'}{\partial y}$$

A similar process, perhaps expressible in terms of mixing length, must take place due to transfer of energy between layers of turbulent shear flows due to

perturbations of the mean flow. From a practical standpoint, there are several experimental indications that energy transfer to the cavity by the mixing of boundary layer air may be important, although as is usually the case, the experimental evidence is also possibly consistent with other explanations. First, Dunham[7] found that cavity oscillations could be entirely eliminated if a step of sufficient height were placed ahead of the cavity aperture. Frank and Carr[22] found in their efforts to find means of alleviating intense cavity oscillations that "the cavity configurations that had the greatest suppression of oscillations were those where the shear layer did not enter the cavity." And over a century ago, it was observed with organ pipes whose oscillation was maintained by a "sheet of wind" that "when...the external air tends to enter the pipe, it carries the jet with it more or less completely," and indicated that the organ pipe would not "speak" when the air jet was deflected so as not to enter it. (See Ref. 1, Vol. II, pp. 219-221.)

Conclusion

Our survey of the state of knowledge concerning the oscillations of cavities coupled to aerodynamic flows has disclosed a great variety of empirical, semi-empirical, heuristic, pragmatic and phenomenological methods of analysis, many of which depend on rather involved mathematical models of some aspects of the problem. Virtually all are limited in scope to prediction of the frequencies at which large amplitudes of cavity oscillation will be encountered, although in those theories which view cavity oscillation as simply a resonant response to a given forcing spectrum in the external flow, pressure amplitudes are also predictable. However, the notion that the external flow spectrum remains entirely independent of cavity response seems hardly credible for large cavities and certainly cannot account for all observed phenomena. Nevertheless, virtually all of the methods discussed have given results having some reasonable agreement with at least some experimental results and there seems to be little doubt that the various phenomena emphasized in the various methods play some role in the physics of cavity oscillations, the relative importance of the various phenomena being different for different resonator geometries and flow conditions.

What is needed are some new attempts at understanding at least approximately the detailed mechanisms of the coupling of the cavity to an external flow field and the resultant energy transfers which such coupling makes possible.

If one needs to be reminded of how difficult and intractible the problem of cavity resonance has been, it is only necessary to consult Rayleigh's discussion of the problem of explaining the sustained oscillation of organ pipes, which, like the cavities of interest in aeronautics and astronautics, are driven by a "sheet of wind" (Ref. 1, Vol. II, pp. 219-221). Then, too,

there were two or three different phenomenological explanations, overlapping in some ways yet quite different. As to the practical problems of controlling and suppressing undesirable cavity oscillations, as Rayleigh said, in relation to organ pipes, "in matters of this kind, practice is usually in advance of theory; and many generations of practical men have brought the organ pipe to a high degree of excellence." Nevertheless, in the complex and expensive technological ventures of the modern age, more is demanded of science and engineering than a contemplative viewing of practical progress by trial and error over several generations, and the cavity oscillation problem, because of its pervasive nature in so many areas of modern technology, certainly is one which should be made more amenable to rational analysis and design solutions.

REFERENCES

1. Rayleigh, Baron, The Theory of Sound, Dover Publications, New York, 1945.

2. Rockwell, D. and Naudascher, E., "Review of Self-Sustaining Oscillations of Flow Past Cavities," Trans. ASME, Journal of Fluid Engineering, Vol. 100, June 1978, pp. 152-165.

3. Rossiter, J. E., "Wind Tunnel Experiments on Flow over Rectangular Cavities at Subsonic and Transonic Speeds," British Aeronautical Research Council, R&M 3438, 1964.

4. Panton, R. L. and Miller, J. M., "Excitation of a Helmholtz Resonator by a Turbulent Boundary Layer," Journal of the Aeronautical Society of America, Vol. 58, No. 4, October 1975, pp. 800-806.

5. Plumbee, H. E., Gibson, J. S. and Lassiter, L. W., "A Theoretical and Experimental Investigation of the Acoustic Response of Cavities in an Aerodynamic Flow," Flight Dynamics Laboratory, Technical Report No. WADD-61-75, March 1962.

6. Quinn, B., "Flow in the Orifice of a Resonant Cavity," AIAA Student Journal, Vol. 1, 1963, pp. 1-5.

7. Dunham, W. H., "Flow-Induced Cavity Resonance in Viscous Compressible and Incompressible Fluids," Fourth Symposium on Naval Hydrodynamics," ONR, Washington, D. C., 1962, pp. 1057-1081.

8. East, L. F., "Aerodynamically Induced Resonance in Rectangular Cavities," Journal of Sound and Vibration, Vol. 3., No. 3, 1966, pp. 277-287.

9. Block, P. J. W., "Noise Response of Cavities of Varying Dimensions at Subsonic Speeds," NASA TN D8351, December 1976.

10. Bilanin, A. J. and Covert, E. E., "Estimation of Possible Excitation Frequencies for Shallow Rectangular Cavities," AIAA Journal, Vol. 11, No. 3, March 1973, pp. 347-351.

11. Heller, H. H. and Bliss, D. B., "Aerodynamically Induced Pressure Oscillations in Cavities--Physical Mechanisms and Suppression Concepts," Flight Dynamics Laboratory, Technical Report, No. AFDDL-TR-74-133, February 1975.

12. Treanor, C. E. and Flax, A. H., "The Effect of Boundary Layer Profile Airspeed and System Geometry on the Stability of Flow in Suction Systems, WADC Technical Report 55-318, July 1956.

13. Powell, A., "On the Edgetone," Journal of the Acoustical Society of America, Vol. 33, No. 4, April 1961, pp. 395-409.

14. Morse, P. M. and Ingard, K. U., Theoretical Acoustics, McGraw-Hill Book Co., New York, 1968, pp. 755-758.

15. Drazin, P. G. and Howard, L. N., "The Instability to Long Waves of Unbounded Parallel Inviscid Flow," Journal of Fluid Mechanics, Vol. 14, 1962, pp. 257-283.

16. Michalke, A., "On the Inviscid Instability of the Hyperbolic Tangent Velocity Profile," Journal of Fluid Mechanics, Vol. 19, 1964, pp. 543-556.

17. Michalke, A., "On Spatially Growing Disturbances in an Inviscid Shear Layer," Journal of Fluid Mechanics, Vol. 23, Part 3, 1965, pp. 521-544.

18. Rockwell, D., "Prediction of Oscillation Frequencies for Unstable Flow Past Cavities, Trans. ASME, Journal of Fluid Engineering, Vol. 99, 1977, pp. 294-300.

19. Ingard, U., "On the Theory and Design of Acoustic Resonators," Journal of the Acoustical Society of America, Vol. 25, No. 6, Nov. 1953, pp. 1037-1061.

20. Rayleigh, Lord, "On the Open Organ-Pipe Problem in Two Dimensions," Philosophical Magazine, Vol. VIII, 1904, pp. 481-487; Scientific Papers, Vol. V, Dover Publications, New York, 1964, pp. 206-211.

21. Schlichting, H., Boundary Layer Theory, McGraw Hill, New York, 1955, pp. 313-314.

22. Franke, M. E. and Carr, D. L., "Effect of Geometry on Open Cavity Flow-Induced Pressure Oscillations," Aeroacoustics: STOL Noise Airframe and Airfoil Noise, Vol. 45, Progress in Astronautics and Aeronautics, Eds., I. R. Schwartz, Nagamatsu, H. T., and Strahle, W. C., 1976.

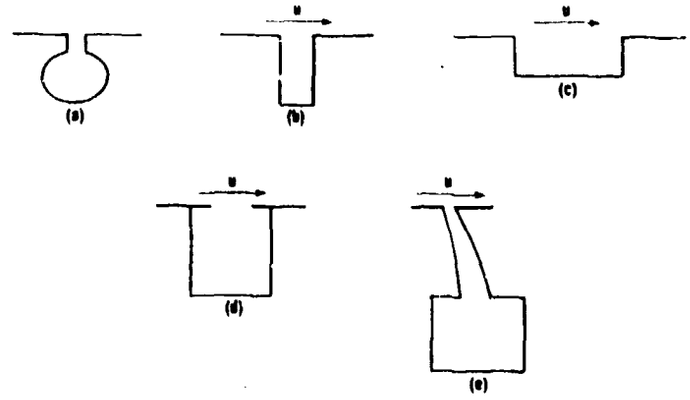

Figure 1. FORMS OF RESONANT CAVITIES
(a) CLASSICAL HELMHOLTZ RESONATOR, (b) DEEP CAVITY, (c) SHALLOW CAVITY, (d) CONSTRICTED CAVITY, (e) CAVITY WITH ENTRY DIFFUSER

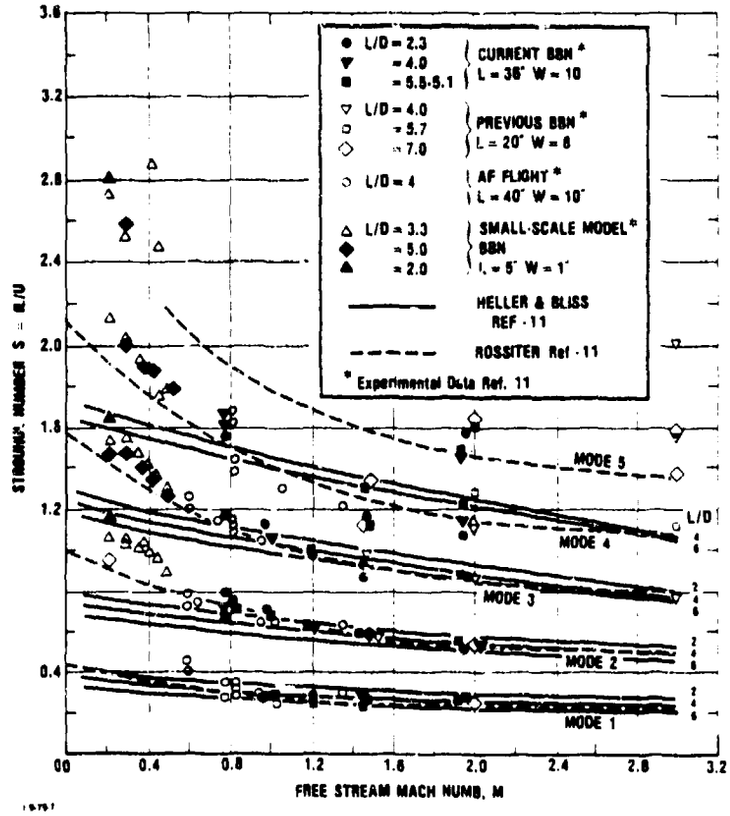

Figure 2. COMPARISON OF EXPERIMENTAL FREQUENCIES WITH ROSSITER'S FORMULA AND THE THEORY OF HELLER AND BLISS

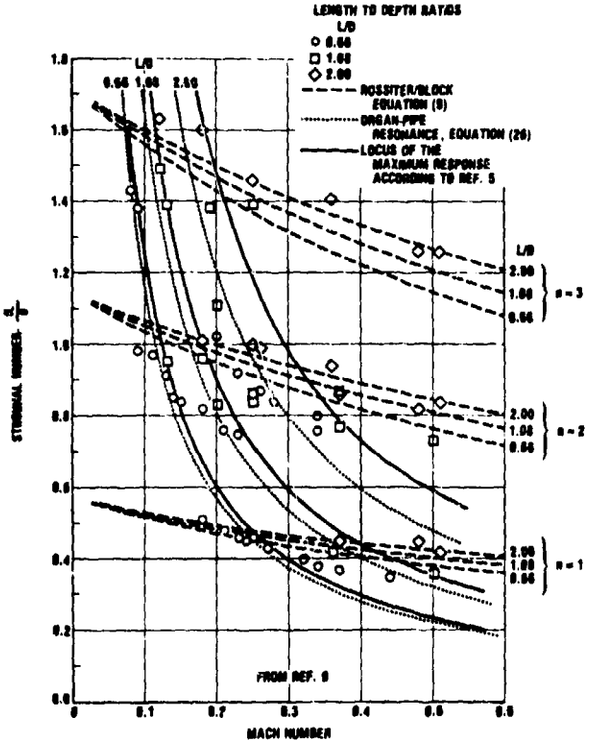

Figure 3 - COMPARISON OF BLOCK'S EXPERIMENTAL DATA (REF. 9) WITH ROSSITER/BLOCK FORMULA AND ORGAN-PIPE RESONANCE PREDICTIONS

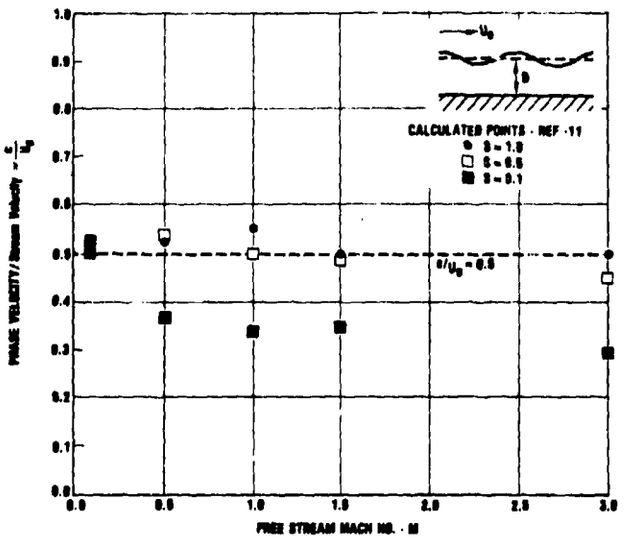

S - REDUCED FREQUENCY

$S = \frac{\omega\delta}{u_0}$

WHERE:

ω = FREQUENCY IN RADIANS/SECONDS

u_0 = VELOCITY OF SOUND IN STILL AIR AT STAGNATION CONDITIONS

δ = DISTANCE OF WALL FROM EDGE OF AIR MOVING AT VELOCITY u_0

Figure 4. RATIO OF REAL PART OF WAVE PHASE VELOCITY TO FREE STREAM VELOCITY (DOWNSTREAM MOVING WAVE)

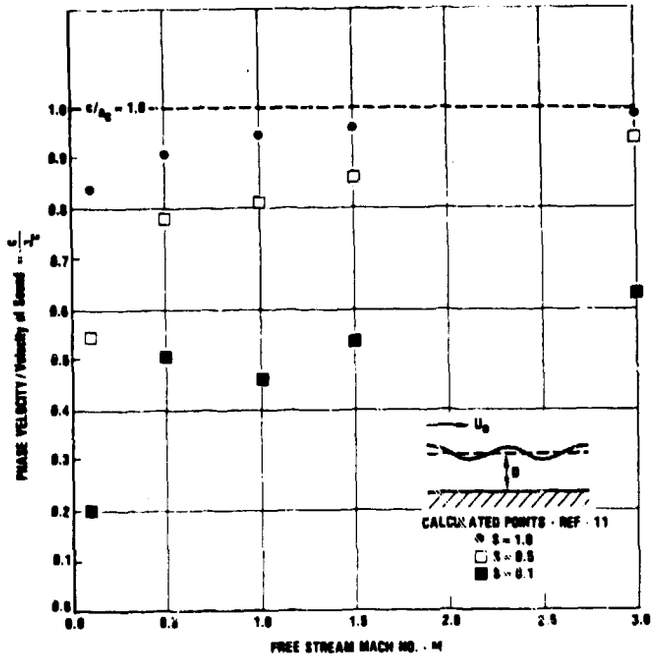

S - REDUCED FREQUENCY

$S = \frac{\omega \theta}{a_0}$

WHERE:

ω = FREQUENCY IN RADIANS/SECONDS

a_0 = VELOCITY OF SOUND IN STILL AIR AT STAGNATION CONDITIONS

θ = DISTANCE OF WALL FROM EDGE OF AIR MOVING AT VELOCITY U_0

Figure 5. RATIO OF REAL PART OF WAVE PHASE VELOCITY TO VELOCITY OF SOUND AT STAGNATION CONDITIONS (UPSTREAM MOVING WAVE)

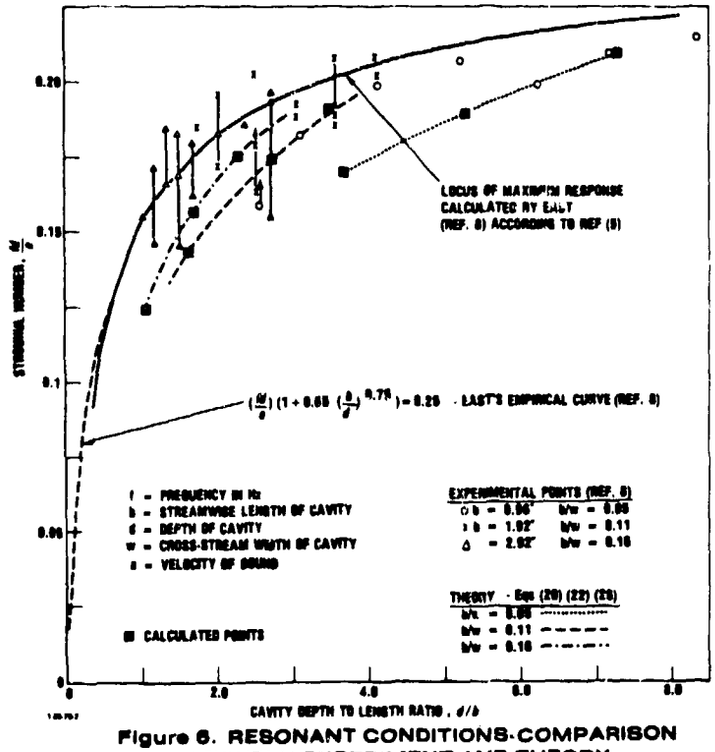

Figure 6. RESONANT CONDITIONS-COMPARISON BETWEEN EXPERIMENT AND THEORY

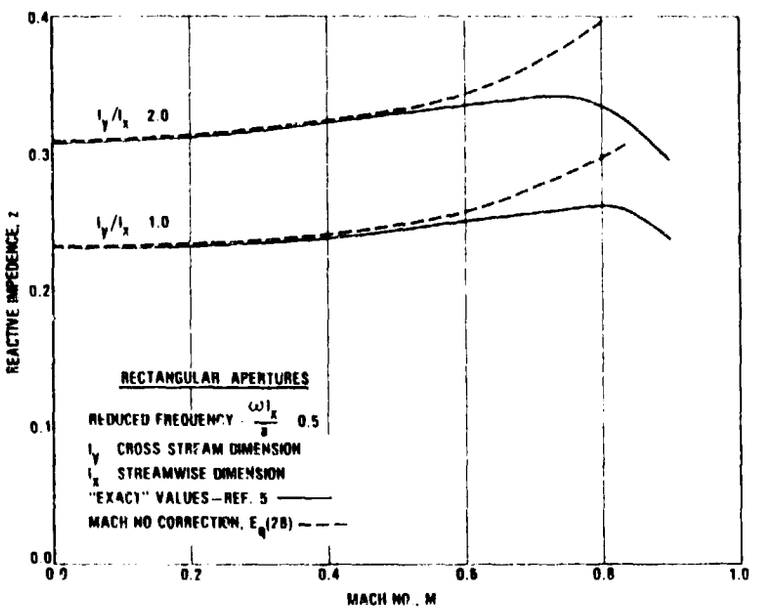

Figure 7. VARIATION OF REACTIVE IMPEDANCE WITH MACH NUMBER

AD P000327

ON THE STRUCTURE OF THREE-DIMENSIONAL SHOCK-INDUCED SEPARATED FLOW REGIONS

by

R. H. Korkegi, Director
Advisory Group for Aerospace Research and Development (AGARD)
Neuilly sur Seine, France

A study is made of existing experimental data on three-dimensional skewed shock-wave interactions with both laminar and turbulent boundary layers and recent results in which extensive regions of turbulent separation were obtained. Comparisons show that the structure of three-dimensional shock-wave/boundary-layer interactions is not fundamentally different for laminar or turbulent flow; it is primarily dependent on the extent of separation. A qualitative description is given for the flow structure from incipient to large extents of separation. For the latter, a secondary incipient condition arises within the primary separation vortex. For still larger extents of separation it is deduced that a secondary vortex arises adjacent to the surface and totally embedded in the primary separation vortex.

Copyright AIAA. Reprinted with Permission.

On the Structure of Three-Dimensional Shock-Induced Separated Flow Regions

R.H. Korkegi*
Air Force Aero Propulsion Laboratory, Wright-Patterson AFB, Ohio

A study is made of existing experimental data on three-dimemsional skewed shock-wave interactions with both laminar and turbulent boundary layers and recent results in which extensive regions of turbulent separation were obtained. Comparisons show that the structure of three-dimensional shock-wave/boundary-layer interactions is not fundamentally different for laminar or turbulent flow; it is primarily dependent on the extent of separation. A qualitative description is given for the flow structure from incipient to large extents of separation. For the latter, a secondary incipient condition arises within the primary separation vortex. For still larger extents of separation it is deduced that a secondary vortex arises adjacent to the surface and totally embedded in the primary separation vortex.

I. Introduction

IN recent years much progress has been made toward the understanding of three-dimensional shock-wave/boundary-layer interactions through studies on such models as blunt protuberances-fins, cylinders, etc.—mounted on flat plates (varying shock strength), and streamwise compression corners made up of sharp-edged intersecting wedges or of single wedges on flat plates (constant shock strength).[1,2]

Strong similarities have been noted between the characteristics of two- and three-dimensional shock induced regions of separation. In the case of blunt protuberances, several investigators have pointed to the strong resemblance of the flow structure in the plane of symmetry to that of two-dimensional interactions.[1] In the case of a streamwise compression corner, a more recent investigation[3] shows that spanwise pressure distributions and the extent of separation for both laminar and turbulent flow strongly resemble those for the respective two-dimensional cases. These observations have suggested that three-dimensional shock-wave/boundary-layer interactions could be viewed locally as equivalent to two-dimensional ones with strong crossflow and mass suction[1,3] (to account for the scavenging by vortices generated in the separated region in the the three-dimensional case).

Also identified recently is the effect of boundary-layer transition along a zone of three-dimensional shock interaction, whereby the extensive separation of a laminar boundary layer collapses through the transition region to the smaller one of a turbulent boundary layer.[4] It could, in fact, collapse entirely if the pressure rise were not sufficient to sustain turbulent separation. In both cases the excess vorticity is presumably carried downstream by the flow, eventually to dissipate.

Evidence of multiple vortices in regions of three-dimensional separation abounds for the interaction of the bow shock of a blunt protuberance with laminar or turbulent boundary layers.[5-7] For this configuration, one has locally the very strong interaction of a normal shock with the boundary layer in the plane of symmetry.

In the case of a streamwise compression corner, multiple vortices have been mainly found for shock interactions with laminar boundary layers for which regions of separation are invariable large.[8,9] Lack of evidence of multiple vortices for the turbulent case prompted two investigations[10,11] of sharp wedges mounted normal to planar surfaces in a supersonic stream, whereby the wedge angles were varied from low values (relatively weak shock strengths) to high values (strong shocks) which resulted in extensive turbulent separation and the appearance of more than one vortex.[11] It should be mentioned that some years ago McCabe[12] noted "a tendency towards a second separation in the dead air region" for large wedge incidences.

With the information presently available on three-dimensional shock-wave/boundary-layer interactions much is now known at least qualitatively about the physical aspects of the flow. It is the purpose of this paper to describe the structure of three-dimensional separated flow regions from incipient to extensive separation. Specifically discussed is separation due to a plane-skewed shock wave interacting with a boundary layer on a planar surface as a step in the understanding of the more general case of three-dimensional separation due to shocks whose strengths vary along lines of interaction.

II. Definition of Flow Model

The interaction flow model, shown in Fig. 1, represents a single axial compression corner (wedge on flat plate). The model could also be a double compression corner (axial intersection of two wedges) which has a more complex shock structure.[3] The common feature of these models is that in both cases a skewed shock interacts with the boundary layer on a planar surface. In the experimental data presented further on, no distinction is made between these two models. The

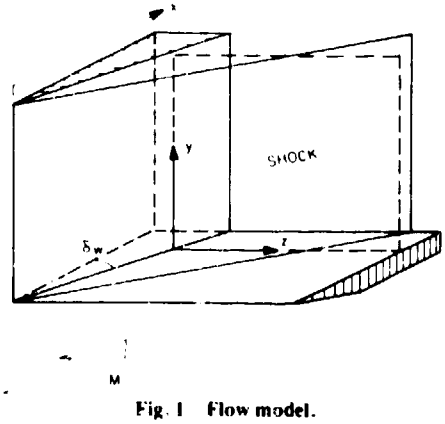

Fig. 1 Flow model.

Received June 30, 1975; revision received November 26, 1975. Presented as Paper 76-165 at the AIAA 14th Aerospace Sciences Meeting, Washington, D.C., January 26-28, 1976. This study was undertaken at the former Aerospace Research Laboratories.

Index categories: Jets, Wakes, and Viscid-Inviscid Flow Interactions; Shock Waves and Detonations; Supersonic and Hypersonic Flow.

*Senior Scientist, Ramjet Division. Associate Fellow AIAA

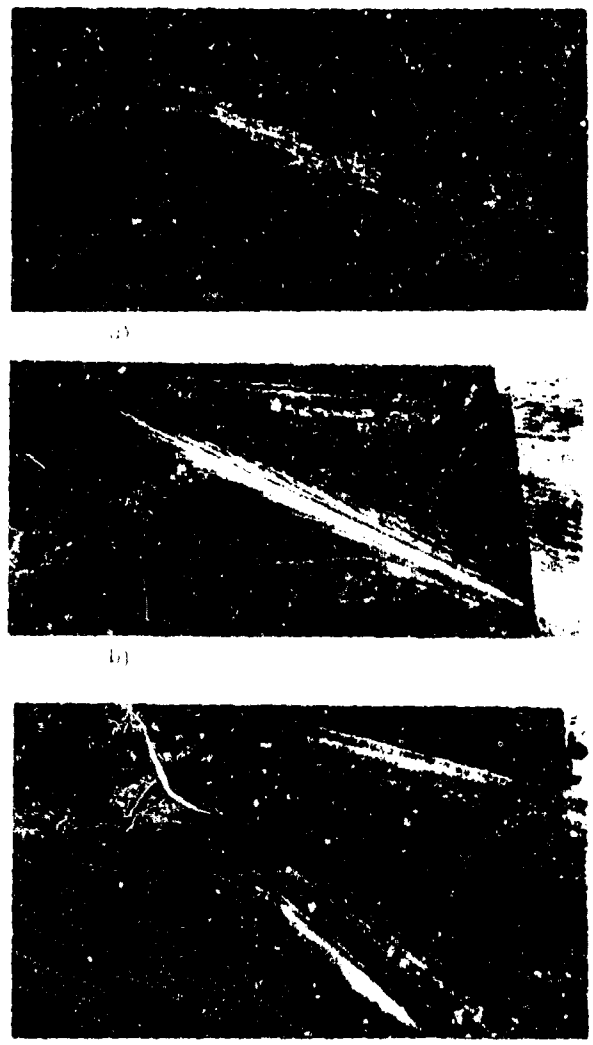

Fig. 2 Skewed shock interaction with a turbulent boundary layer at $M = 2.5$ (from Ref. 10). a) Unseparated $\delta_w = 6\frac{1}{2}°$; b) small separation $\delta_w = 10°$; c) extensive separation $\delta_w = 17°$.

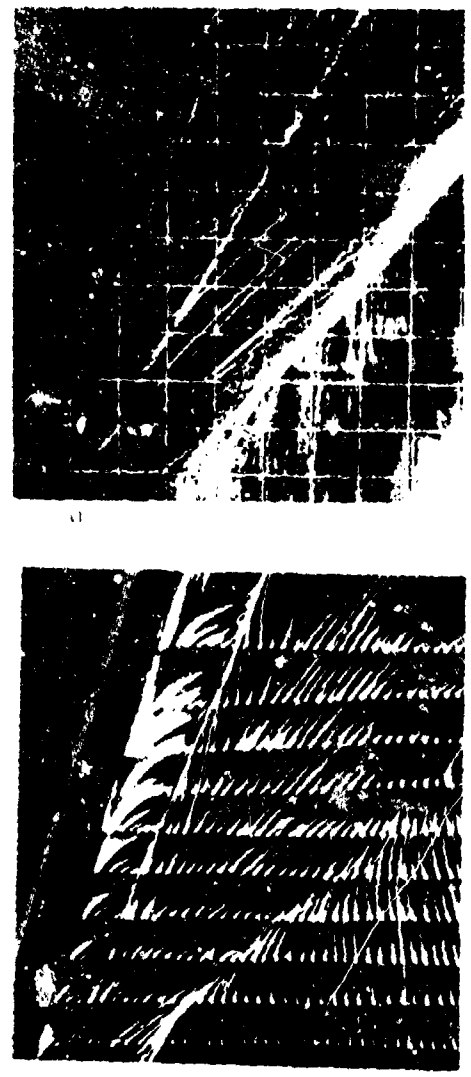

Fig. 3 Skewed shock interactions with secondary separation. a) Turbulent $\delta_w = 20°$, $M = 6$ (courtesy of C. H. Law[11]); b) laminar $\delta_w = 15°$, $M = 12.5$ (from Ref. 9).

coordinate system used in subsequent figures is also defined in Fig. 1.

The terms "separation" and "reattachment" for the three-dimensional case are used in a broader sense than in the two-dimensional case in which they are conventionally associated with a point (or line) at which the surface shear vanishes. In the three-dimensional case, separation is associated with a line or envelope of limiting streamlines.[1] From a physical, though perhaps less precise standpoint, separation may be viewed as a line along which the flow lifts off a continuous solid surface, and reattachment, a line of flow impingement onto a continuous solid surface. Only the component of surface shear normal to these lines vanishes; but the tangential component is finite except at singular points such as in the plane of symmetry of a continuous separation line. An extensive discussion of three-dimensional separation is given by Wang.[12]

III. Comparison of Laminar and Turbulent Interactions

All laminar data known to the author, for a skewed shock interaction, show extensive three-dimensional separation.[8,9,13] Recent experimental data for the turbulent case have extended skewed shock strengths (wedge angles) to large values,[10,11,14] thus generating sizeable regions of separation comparable with the laminar ones.

A. Surface Flow Patterns

Figure 2 shows a sequence of oil flow photographs from Ref. 10 for progressively larger wedge angles at Mach number 2.5 and Reynolds number based on chord length of 20×10^6 so that the boundary layer is turbulent over almost the entirety of the surface. The pattern is essentially conical as observed in other skewed shock interaction studies for either laminar or turbulent boundary layers.

In Fig. 2a the shock strength is insufficient to separate the flow as indicated by the oil lines (approximately surface shear lines) which are simply deflected by the shock wave. In Fig. 2b there is a small separated region as indicated by the oil accumulation line (approximate location of separation) and the less-well-defined inboard line along which the oil flow lines diverge (approximate location of reattachment). This separated region comprises a single vortex. In Fig. 2c the separated region is seen to be quite extensive and the oil flow lines exhibit a secondary inflection near the center of this region below which (lighter area) they again turn toward the oil accumulation line. This inflection is interpreted as the approach, with increasing shock strength, to a secondary separation within the primary vortex. The study of Ref. 10 does not quite extend that far.

For very strong skewed shock interactions with turbulent boundary layers, one does indeed obtain a second oil accumulation line indicative of secondary separation as shown in Fig. 3a (from the study of Ref. 11, courtesy of C.H. Law). The features of the oil flow pattern are virtually identical to those for the laminar case as illustrated in Fig. 3b taken from Ref. 9. In both Figs. 3a and 3b the reattachment line associated with the primary vortex is very near the corner formed by the vertical wedge and the plate as the Mach numbers in both cases are relatively high. The secondary reattachment line, just to the right of the secondary separation line for the laminar case of Fig. 3b, does not clearly appear in the turbulent case of Fig. 3a, most probably because of the effect of much higher shear rates for the latter, combined with a relatively large oil accumulation bubble.

B. Pressure Distributions

Further evidence of similarity between extensive turbulent and laminar separation due to a skewed shock interaction is given in Fig. 4 which shows a spanwise pressure distribution for each case. In each figure, going from right to left, the pressure rises from its undisturbed flow value just prior to separation (beginning of interaction), to a plateau beyond which it exhibits a dip and then a large pressure rise and overshoot associated with reattachment. The dip appears to be associated with the secondary separation. The overshoot is due to the high momentum of the reattaching flow after a long stretch of separation and mixing with the outer stream. It should be noted that a dip is also found, and is even more pronounced, in the plane of symmetry upstream of a blunt protuberance in supersonic flow,[6] for which case strong secondary vortices appear near the base of the protuberance.

C. Heat Transfer

Heat transfer rates, which are classically known to peak at reattachment following a region of separation in two-dimensional flow, exhibit two peaks in the case of laminar[8,13] and extensive turbulent separation[11,14] caused by skewed shock interaction. The two peaks are associated with the two reattachment lines as observed elsewhere[1,8] and shown in Fig. 5 for the laminar case. It should be noted that the turbulent case does not exhibit an initial drop in heat rates below the undisturbed flow value following primary separation, but rather, has an immediate rise above this value.[15] This observation is consistent with the similarity pointed out elsewhere[1,2] between crossflow in three-dimensional separation and streamwise flow in the two-dimensional case.

IV. Flow Structure

From these comparisons it seems quite clear that the characteristics of skewed shock-induced separated regions do not exhibit any basic difference between laminar and turbulent flow for comparable extents of separation. The shock intensities needed for extensive separation, however are clearly much larger for turbulent than for laminar flow, and the detail of the flow structure differs because of turbulent mixing in the one case and molecular mixing in the other. One can conjecture with a high degree of confidence that these similarities also prevail for two-dimensional flow separation.

From the evidence previously mentioned, it is now possible to define the structure of the separated flow region resulting from the interaction of a skewed shock wave with either a laminar or turbulent boundary layer since, basically, the two differ only in the intensity of the shock wave required to produce a certain extent of separation.

Figure 6 shows qualitatively a sequence of flow characteristics from unseparated flow to extensive separation on a planar surface caused by a wedge-induced shock wave of progressively increasing strength. The lines of interaction on the surface are essentially conical, as noted in virtually all experimental investigations of this axial corner configuration.

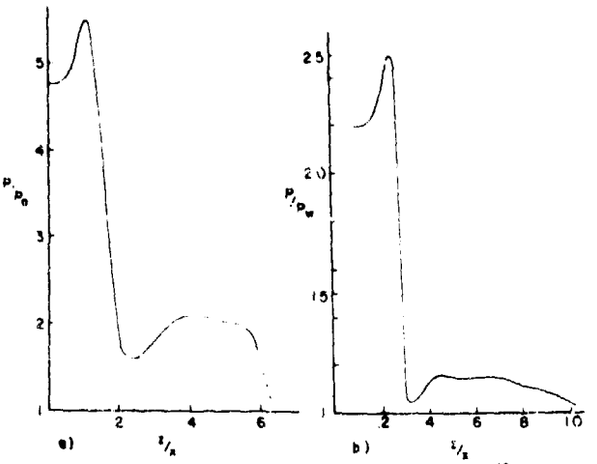

Fig. 4 Spanwise pressure distributions. a) Turbulent,[15] $M = 3.7$, $\delta_w = 20°$; b) laminar,[14] $M = 3.64$, $\delta_w = 12.2°$.

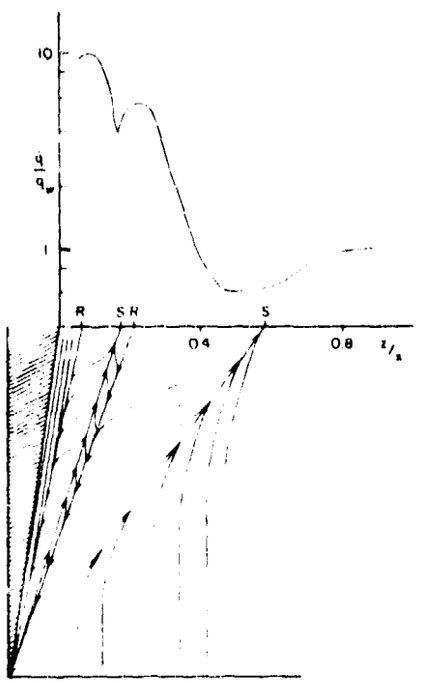

Fig. 5 Spanwise heat transfer for laminar flow, $M = 7.0$, $\delta_w = 10°$ (data from Ref. 8).

In Fig. 6a the wedge angle or shock strength is small and the boundary layer flow across the shock wave is fully attached, as indicated by the mild turning of the surface shear lines through a slight inflection before assuming their new direction parallel to the wedge face some distance downstream after the disturbed boundary layer has fully relaxed to its new condition. The symbol Sh indicates the location of the wedge-induced shock wave, and B, the beginning of interaction, or the line along which the boundary layer begins to respond to the pressure jump generated by the shock wave. As shown in Fig. 6a (2), τ_w, the component of surface shear normal to the lines of interaction generally decreases in absolute value, with a slight dip at the approximate shock location in traversing the region of interaction from right to left.

In Fig. 6b the wedge angle has been increased to the point where the boundary layer is on the verge of separating as indicated by the tangency of the surface shear lines at their point of inflection, to the approximate shock wave direction (indicated by I for incipient separation). At this point τ_w just equals zero.

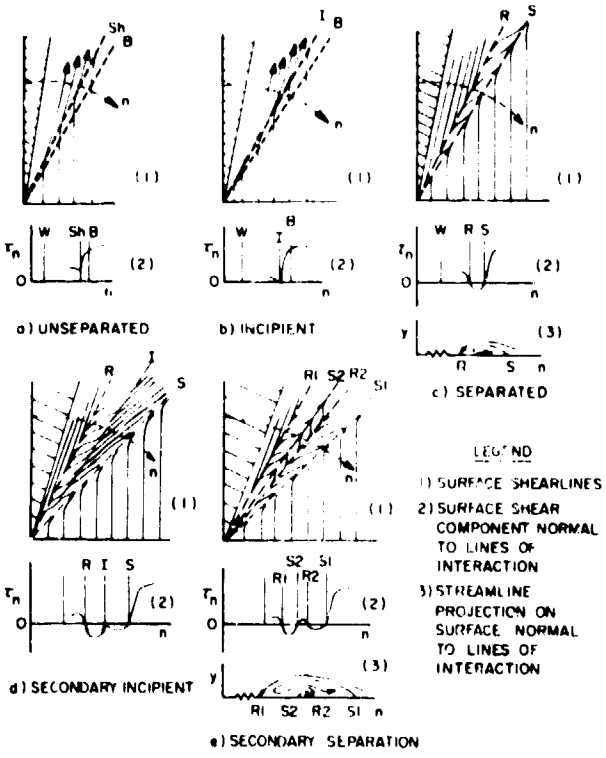

Fig. 6 Structure of three-dimensional shock-induced separation.

In Fig. 6c, for a still larger wedge angle, there is a small region of separation comprised of a counter clockwise vortex as viewed from upstream. The line along which surface shear lines converge is indicative of separation S, and the line along which they diverge, of reattachment R. τ_n undergoes a change in sign, going through zero at separation and again at reattachment. The streamline projection in the region of separation, sketched in Fig. 6c (3) shows that the separating and reattaching streamlines are not the same, but rather, that there is scavenging of the oncoming flow by the vortex. The two-dimensional equivalent would be mass injection in the separated region.

As the separated region grows in size due to a progressively stronger shock, the "reverse flow" itself is on the verge of separating, as indicated by the reversal of the surface shear lines to tangency with the line I in Fig. 6d (1). This condition can be viewed as a secondary incipient separation of the flow along which line τ_n is zero as well as at the original separation and reattachment lines, shown in Fig. 6d (2). Note that the doubledip of the shear has also been found for extensive regions of separation in two-dimensional flow.[16]

With further increase in shock strength a secondary separation region develops within the primary one as shown in Fig. 6e. S1 and R1 are respectively the primary separation and reattachment lines, and S2 and R2 the secondary ones. The surface shear component τ_n undergoes three reversals in sign as shown in Fig. 6e(2). The flow structure is deduced to consist of a secondary vortex embedded in the primary one as shown in Fig. 6e (3). The secondary vortex scavenges flow from the primary vortex, as does the primary vortex from the oncoming boundary layer. Justification for this model stems from the fact that the secondary incipient condition and secondary separation occur gradually near the middle of the primary vortex and not as a departure in either separation or reattachment conditions of the vortex. Furthermore, the inner heat peak (see Fig. 5), associated with reattachment of the primary vortex, is clearly larger than the outer one which is associated with reattachment of the secondary vortex.

V. Conclusions

With reference to previous investigations of the interaction of a skewed shock with a boundary layer, the following observations were made: 1) For the laminar three-dimensional case, as for the two-dimensional case, a small shock-induced pressure rise causes extensive separation; 2) For the turbulent three-dimensional case, a pressure rise greater than 1.5 is required to induce separation, and a considerably greater pressure rise is necessary to produce extensive separation; 3) In a transverse plane, three-dimensional separation is similar to two-dimensional separation with mass transfer.

From the present study, the following conclusions arise: 1) The structure of the three-dimensional interaction is not fundamentally different for laminar or turbulent flow; it is primarily dependent on the extent of separation; 2) For large extents of separation due to a skewed shock interaction, a secondary incipient condition arises within the primary separation region following which a secondary separation arises for still larger extents of separation. It is deduced that the latter flow structure takes the form of a secondary surface vortex embedded in the primary one, the secondary vortex scavenges flow from the primary vortex which, in turn, scavenges flow from the oncoming boundary layer.

References

[1]Korkegi, R.H., "Survey of Viscous Interactions Associated with High Mach Number Flight," *AIAA Journal*, Vol. 9 May 1971, pp. 771-784.

[2]Ryan, B.M., "Summary of the Aerothermodynamic Interference Literature," TN 4061-160, April 1969, Naval Weapons Center, China Lake, Calif.

[3]West, J.E. and Korkegi, R.H., "Supersonic Interaction in the Corner of Intersecting Wedges at High Reynolds Numbers," *AIAA Journal*, Vol. 10, May 1972, pp. 652-656.

[4]Korkegi, R.H., "Effect of Transition on Three-Dimensional Shock Wave Boundary-Layer Interaction," *AIAA Journal*, Vol. 10, March 1972, pp. 361-363.

[5]Winkelmann, A.E., "Experimental Investigations of a Fin Protuberance Partially Immersed in a Turbulent Boundary Layer at Mach 5," NOLTR 72-33, Jan. 1972, Naval Ordnance Lab., White Oak, Silver Spring, Md.

[6]Young, F.L., Kaufman, L.G. II, and Korkegi, R.H., "Experimental Investigation of Interactions between Blunt Fin Shock Waves and Adjacent Boundary Layers at Mach Numbers 3 and 5," ARL 68-0214, Dec. 1968, Aerospace Research Labs., Wright-Patterson Air Force Base, Ohio.

[7]Sedney, R. and Kitchens, C.W., Jr., "The Structure of Three-Dimensional Separated Flows in Obstacle, Boundary-Layer Interaction," AGARD Conference Proceedings No. 168, 1975, pp. 37-1, 37-15.

[8]Watson, R.D. and Weinstein, L.M., "A Study of Hypersonic Corner Flow Interactions," *AIAA Journal*, Vol. 9, July 1971, pp. 1280-1286.

[9]Cooper, J.R. and Hankey, W.L., Jr., "Flow Field Measurements on an Axisymmetric Axial Corner at $M_\infty = 12.5$," *AIAA Journal*, Vol. 12, Oct. 1974, pp. 1383-1387.

[10]Freeman, L.M. and Korkegi, R.H., "Experiments on the Interaction with a Turbulent Boundary Layer of A Skewed Shock Wave of Variable Strength at Mach 2.5," ARL TR 75-0182, June 1975, Aerospace Research Labs., Wright-Patterson Air Force Base, Ohio.

[11]Law, C.H., "Three-Dimensional Shock Wave-Turbulent Boundary Layer Interactions at Mach 6," ARL TR 75-0191, June 1975, Aerospace Research Labs. Wright-Patterson Air Force Base, Ohio.

[12]McCabe, A., "The Three-Dimensional Interaction of a shock Wave with a Turbulent Boundary Layer," *The Aeronautical Quarterly*, Vol. 17, Aug. 1966, pp. 231-252.

[13]Wang, K.C., "Separation Patterns of Boundary Layer Over an Inclined Body of Revolution", *AIAA Journal*, Vol. 10, Aug. 1972, pp. 1044-1050.

[14]Charwat, A.F. and Redekopp, L.G., "Supersonic Interference Flow Along the Corner of Intersecting Wedges," *AIAA Journal*, Vol. 5, March 1967, pp. 480-488.

[15]Newmann, R.D. and Token, K.H., "Prediction of Surface Phenomena Induced by Three-Dimensional Interactions on Planar Turbulent Boundary Layers," Paper 74-058, Oct. 1974, International Astronautical Federation XXV Congress, Amsterdam, Netherlands.

[16]Shang, J.S. and Hankey, W.L., Jr., "Numerical Solution of the Navier Stokes Equations for Supersonic Turbulent Flow over a Compression Ramp," AIAA Paper 75-3, 1975.

AD P000328

COMPUTATIONAL FLUID DYNAMICS-AN ENGINEERING TOOL?

by

John D. Anderson, Jr.
Professor and Chairman
Department of Aerospace Engineering
University of Maryland

Computational fluid dynamics in general, and time-dependent finite-difference techniques in particular, are examined from the point of view of direct engineering applications. Examples are given of the supersonic blunt body problem and gasdynamic laser calculations, where such techniques are clearly engineering tools. In addition, Navier-Stokes calculations of chemical laser flows are discussed as an example of a near-engineering tool. Finally, new and exciting calculations of the flowfield in a reciprocating internal combustion engine are offered as a promising future engineering application of computational fluid dynamics.

Copyright ASME (1976). Reprinted with Permission.

Reprinted from Numerical/Laboratory Computer Methods in Fluid Mechanics, ASME, December 1976.

COMPUTATIONAL FLUID DYNAMICS—AN ENGINEERING TOOL?

John D. Anderson, Jr.
Professor and Chairman
Department of Aerospace Engineering
University of Maryland
College Park, Maryland

ABSTRACT

Computational fluid dynamics in general, and time-dependent finite-difference techniques in particular, are examined from the point of view of direct engineering applications. Examples are given of the supersonic blunt body problem and gasdynamic laser calculations, where such techniques are clearly engineering tools. In addition, Navier-Stokes calculations of chemical laser flows are discussed as an example of a near-engineering tool. Finally, new and exciting calculations of the flowfield in a reciprocating internal combustion engine are offered as a promising future engineering application of computational fluid dynamics.

I. INTRODUCTION

The corner-stone of theoretical fluid dynamics is a set of conservation equations which describe the physics of fluid motion; these equations speak words, such as: (1) mass is conserved; (2) F = ma (Newton's 2nd law), and (3) energy is conserved. These equations also describe the variations of fluid pressure, temperature, density, velocity, etc. throughout space and time. In their most general form, they are partial differential equations, and consequently are difficult to solve. Indeed, no general analytical solution to these equations has been found, nor is it likely to be found in the foreseeable future. Sometimes the governing equations are neat and compact, such as for inviscid flows [1] (flows without friction, thermal conduction or diffusion); for other problems the fully viscous equations -- the Navier-Stokes equations -- are required, and are long and horrendous [2]. For the two centuries since Bernoulli and Euler first formulated some of these equations in St. Petersburg, Russia, in the 1730's [3], fluid dynamicists have been laboring to obtain analytical solutions for certain restricted and/or simplified problems.

In contrast, the modern engineer of today is operating in a new third dimension in fluid dynamics -- computational fluid dynamics, which readily complements the previous dimensions of pure experiment and pure theory. Computational fluid dynamics, in principle, allows the practical solution of the exact governing equations for a myriad of applied engineering problems,

and it is this aspect which is the subject of the present paper.

What is computational fluid dynamics? It is the art of replacing the governing partial differential equations with numbers, and advancing these numbers in space and/or time to obtain a final numerical description of the complete flowfield of interest. The end-product of computational fluid dynamics is indeed a collection of numbers, in contrast to a closed-form analytical solution. However, in the long run, the objective of any engineering analysis, using closed-form analysis or otherwise, is a quantitative description of the problem, i.e., numbers.

Perhaps the first major example of computational fluid dynamics was the work of Kopal [4], who in 1947 compiled massive table of the supersonic flow over sharp cones by numerically solving the governing differential equation (the Taylor-Maccoll equations [5]). These solutions were carried out on a primitive digital computer at MIT. However, the first generation of computational fluid-dynamic solutions appeared during the 1950's and early 1960's, spurred by the simultaneous advent of efficient, high-speed computers and the need to solve the high velocity, high temperature re-entry body problem. High temperatures necessitated the inclusion of vibrational energies and chemical reactions in flow problems, sometimes equilibrium and othertimes nonequilibrium. Such physical phenomena generally cannot be solved analytically, even for the simplest flow geometry. Therefore, numerical solutions of the governing equations on a high-speed digital computer were an absolute necessity. Examples of these first generation computations are the pioneering work of Fay and Riddell [6] and Blottner [7] for boundary layers, and Hall et al [8] for inviscid flows. Even though it was not fashionable at the time to describe such high temperature gasdynamic calculations as "computational fluid dynamics", they nevertheless represented the first generation of the discipline.

The second generation of computational fluid-dynamic solutions, those which today are generally descriptive of the discipline, involve the application of the conservation equations to applied fluid-dynamic problems which are in themselves so complicated (without the presence of chemical reactions, etc.) that a computer must be utilized. Examples of such inherently difficult problems are mixed subsonic-supersonic flows, such as the supersonic blunt body problem, and viscous flows which are not amenable to the boundary layer approximation, such as separated and recirculating flows. For the latter case, the full Navier-Stokes equations are required for an exact solution. In these cases, the time-dependent technique, introduced in a practical fashion in the mid-1960's, has created a revolution in flowfield calculations. Time-dependent calculations have now become engineering tools for some problems, and are nearly so for others. The time-dependent technique is the major subject addressed in the present paper.

This paper is not a survey of computational fluid dynamics; Refs. [9] and [10] nicely serve such a purpose. Moreover, the powerful application of steady-state finite-difference solutions to practical problems, such as supersonic flowfield calculations about the space-shuttle [11], are not considered here. Rather, some specific applications of the time-dependent technique to problems of engineering interest, drawn from past and current work of the author, are discussed. In particular, examples of time-dependent calculations are given for: (1) supersonic blunt bodies, (2) gasdynamic lasers, (3) chemical lasers, and (4) internal combustion engines. The latter item -- the calculation of flowfields in reciprocating IC engines -- is a new and very promising application in a field of extreme contemporary importance. In each case the question is posed: Is computational fluid dynamics an engineering tool? Hopefully, after reading this paper, the reader will answer: "yes, but ---".

II. PHILOSOPHY OF THE TIME-DEPENDENT TECHNIQUE

The idea of the time-dependent technique is best presented in the context of an example. Consider the flowfield about a blunt body moving at supersonic speed, as shown in Figure 1. There is a detached curved bow shock in front of the body, and the flow between the body and the shock has mixed

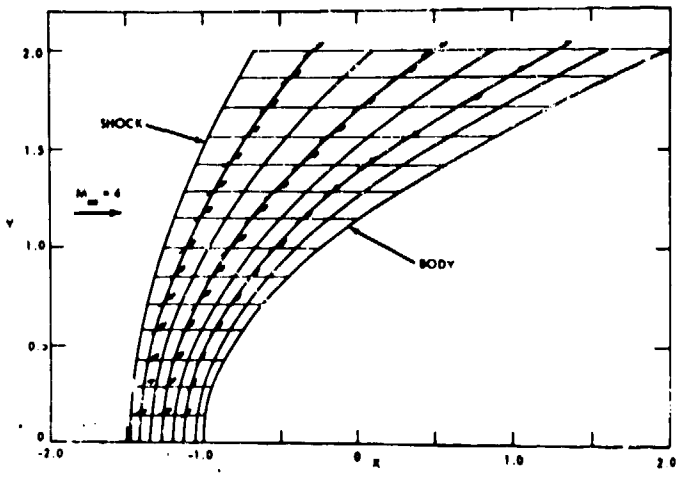

Fig. 1. Model of blunt body flowfield and grid system. Arrows show final steady-state velocity field for a parabolic cylinder at Mach 4.

regions of subsonic and supersonic flow. Imagine that the flowfield is divided into a number of grid points, as shown. Now guess (or otherwise arbitrarily specify) the values of the flowfield variables (pressure, density, velocity, etc), as well as the shock wave shape and detachment distance. (Unless you are a wizard, the guessed flowfield will not be the correct one). Consider these guessed values to be initial conditions at time $t = 0$. Then, at each grid point, calculate new values of the flowfield variables at time $t = \Delta t$, where Δt is a fixed time increment, chosen to satisfy certain stability criteria. Specifically, if $\rho(t)$ is the density at time t at a given grid point, the value $\rho(t+\Delta t)$ can be obtained from a Taylor series expansion:

$$\rho(t+\Delta t) = \rho(t) + \left(\frac{\partial \rho}{\partial t}\right)_t \Delta t + \left(\frac{\partial^2 \rho}{\partial t^2}\right)_t \frac{\Delta t^2}{2} + \ldots \qquad (1)$$

In eq. (1), (t) is known. The derivatives, $\left(\frac{\partial \rho}{\partial t}\right)_t$ and $\left(\frac{\partial^2 \rho}{\partial t^2}\right)$ are obtained from the continuity equation (in cylindrical coordinates):

$$\frac{\partial \rho}{\partial t} = -\frac{\partial (\rho u)}{\partial x} + \frac{\partial}{\partial y}(\rho v) + K\frac{\rho v}{y} \qquad (2)$$

In eq. (2), all the spatial derivatives on the right-hand side are known numbers -- they are given by central finite-differences

$$\frac{\partial u}{\partial x} = \frac{u(x+\Delta x) - u(x-\Delta x)}{2\Delta x} \qquad (3)$$

etc., using the known flowfield values at time t. Thus, a number for $\frac{\partial \rho}{\partial t}$

is obtained from eq. (2), which gives the value of the second term in eq. (1). The value of $\frac{\partial^2 \rho}{\partial t}$ can be obtained by differentiating eq. (2) alternately with respect to x and t. In this fashion, the application of eq. (1) at each grid point allows the advancement of the flowfield variables at each grid point to time (t+Δt). This entire process is repeated for a number of time steps, during which the shock wave will move, as shown in Figure 2, and the flowfield variables will change, as shown in Figure 3 for the stagnation point

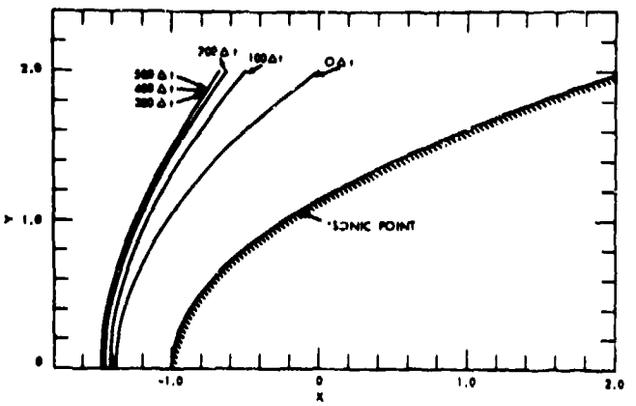

Fig. 2. Time-dependent shock wave motion, parabolic cylinder, Mach 4.

pressure. Note, however, that at large values of time (after many time steps), the variables do not change very much, and the shock wave becomes almost stationary. I.e., at large values of time, the flowfield approaches asymptotically the proper steady-state values. This steady-state is the desired result -- the transient calculations are just a means to the end. Also, numerically, this technique has 2nd order accuracy.

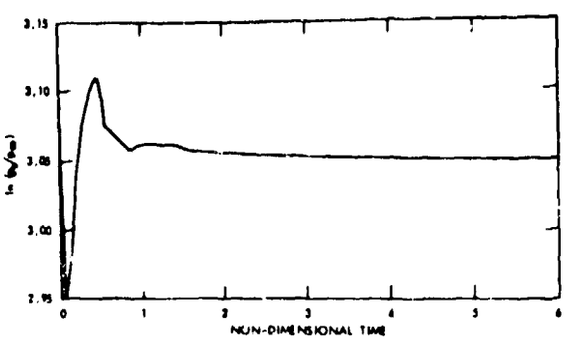

Fig. 3. Time-variation of stagnation point pressure, parabolic cylinder, Mach 4.

What does the time-dependent technique do for you? In the present example, the steady flowfield about the blunt body has a region that is subsonic (described by elliptic equations) and another region that is supersonic (described by hyperbolic equations). This mixed nature of the flow makes a consistent steady-state solution extremely difficult. In contrast, the unsteady flow is completely hyperbolic with respect to time -- for both the subsonic and supersonic regions. Thus, an initial value problem is well-

posed, and the complete flowfield is obtained numerically in a relatively painless manner.

The application described above was first developed on a practical basis by Moretti and Abbett [12] in 1966. It was subsequently extended by Anderson et al [13-15], among others. Time-dependent calculations of blunt body flowfields have now become standard engineering tools for industry and government.

More recent time-dependent calculations employ a modified philosophy, after that of MacCormack [16]. Here, eq. (1) is replaced by a two-term series

$$\rho(t+\Delta t) = \rho(t) + \left(\frac{\partial \rho}{\partial t}\right)_{ave} \Delta t \qquad (4)$$

where $\left(\frac{\partial \rho}{\partial t}\right)_{ave}$ is an average between t and $(t+\Delta t)$. This average is obtained by first "predicting" the value of $\rho(t+\Delta t)$ using forward spatial differences in eq. (2), and then using the predicted values to "correct" $\rho(t+\Delta t)$ by utilizing rearward differences in eq. (2). This "predictor-corrector" approach is also of 2nd order accuracy, and has the advantage of negating the tedious calculation of $\frac{\partial^2 \rho}{\partial t^2}$, hence saving computer time. The MacCormack approach appears to be the best available finite-difference technique in use today, and it is still being improved [17]. Indeed, for viscous flow solutions, it has been very recently revolutionized [18], with orders of magnitude reduction in computer time.

The value of Δt in eqs. (1) and (4) is obtained from the Courant-Fredericks-Levy (CFL) stability criterion [19], namely

$$\Delta t \leq \text{Minimum of } \left(\frac{\Delta x}{u+a}, \frac{\Delta y}{v+a}\right) \qquad (5)$$

Physically, this means that Δt must be less than, or at best equal to, the time necessary for a sound wave to propagate from one grid point to another.

Clearly, the time-dependent philosophy is a straightforward method of calculating rather complex flowfields. We have already seen an example where it has become an engineering tool -- the blunt body problem. Other examples of time-dependent engineering tools are given below.

III. GASDYNAMIC LASERS

Gasdynamic lasers are essentially supersonic wind tunnels in which a nonequilibrium expansion through the nozzle creates a laser medium. If mirrors are placed on both sides of the test section, a powerful laser beam can be extracted. The physics and technology associated with such lasers are described in a recent book[20].

The heart of a conventional gasdynamic laser is a vibrational nonequilibrium expansion of CO_2, N_2 and H_2O or He. In turn, time-dependent calculations have been advantageously applied to nonequilibrium nozzle flows in Ref. 21, and have subsequently been used to calculate gasdynamic laser performance[22,23] The nature of time-dependent nonequilibrium flow solutions is illustrated in Fig. 4, which illustrates the variation of the combined vibrational energy of N_2 and the ν_3 mode of CO_2 through a simple wedge nozzle, $e_{vib_{II}}$. The dotted line represents the guessed initial distribution of $e_{vib_{II}}$, the solid lines are transient values during the approach to the steady-state, and the solid circles are the final steady-state results at large time. The advantage of applying the time-dependent technique to such nozzle flows, where nonequili-

brium prevails both upstream and downstream of the nozzle throat, is that no saddle-point singularity is encountered in the throat region. Purely steady-state techniques encounter such a singularity in attempting to integrate through the throat region, and require special mathematical methods to overcome the difficulty. In contrast, the time-dependent technique completely circumvents the problem[21].

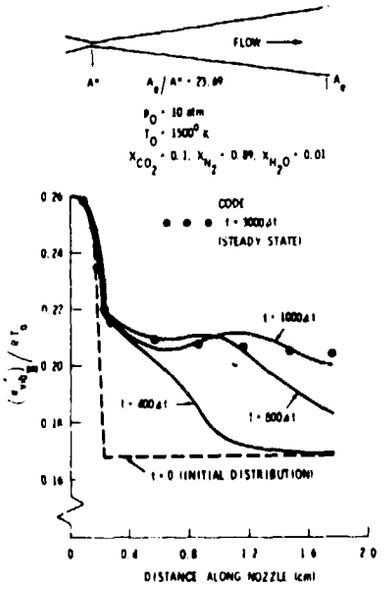

Fig. 4. Time-variation of vibrational energy of N_2 and CO_2 (ν_3) through a gasdynamic laser nozzle.

Time-dependent calculations of gasdynamic laser perforamnce lead to accurate results, as illustrated in Fig. 5. Here, the small-signal laser gain, a direct measure of the population inversion in the laser gas[20], is plotted as a function of distance through a wedge supersonic nozzle and a constant area section downstream. The solid line is a theoretical prediction from the time-dependent method, and the open circles are experimental data obtained in the 3-megawatt arc-tunnel at the Naval Ordnance Laboratory (now the Naval Surface Weapons Center). Clearly, good agreement between theory and experiment is obtained.

Such time-dependent calculations of gasdynamic laser performance are now a fairly standard engineering tool, and are available from a proven computer code[24]. This engineering tool has been recently used to study various fuel combinations for combustion-driven gasdynamic lasers[25]. Also, the time-dependent program[24], or variants of it, have been used extensively by NASA Ames[26] and Rolls-Royce[27], among others, for calculation of laser performance.

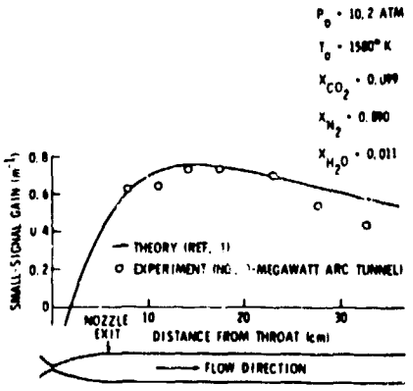

Fig. 5. Comparison of theoretical gain obtained from a time-dependent calculation with experimental data from the Naval Ordnance Laboratory. P_o=10.2 atm, T_o=1580°K, X_{CO_2}=0.099, X_{N_2}=0.89, X_{H_2O}=0.011.

IV. CHEMICAL LASERS

In a chemical laser, the active medium is created as the direct product of a chemical reaction[28]. In the HF supersonic diffusion laser, the chemical reaction and resulting laser action occur in the mixing region of two supersonic streams of Flourine and Hydrogen, as sketched in Fig. 6.

Time-dependent calculations of this chemical laser flow have been made by Kochari et al[29-30], solving the complete two-dimensional Navier-Stokes equations with detailed multicomponent diffusion and finite-rate chemical kinetics. These calculations are the most detailed representation of chemical laser flows to date.

Details of the equations and numerical analysis are given in Refs. 29-30. Even though the Navier-Stokes equations are utilized, the basic time-dependent philosophy is the same as outlined in Section II above. For example, consider a point at x/h = 10 and y/h = 0.375

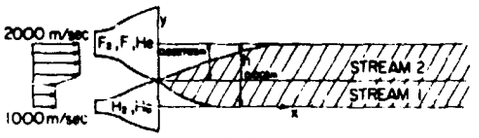

fig 1
NOZZLE CONFIGURATION

	STREAM 1	STREAM 2
P n/m²	500	500
T °K	150	150
ρ Kg/m³	1.2862X10⁻³	2.4514X10⁻³
ρ_{H_2} Kg/m³	—	7.3128X10⁻⁴
ρ_{He} Kg/m³	3.2328X10⁻⁴	—
ρ_F Kg/m³	—	2.4376X10⁻³
ρ_{H_2} Kg/m³	—	—
ρ_{He} Kg/m³	9.6288X10⁻⁴	1.4764X10⁻³

INITIAL CONDITIONS
$A_k = 0$ for k = 6, 7, ···· 14

Fig. 6. Schematic of the supersonic mixing flowfield for an HF diffusion chemical laser, with the flowfield conditions given for the subsequent two figures. After Ref. 30.

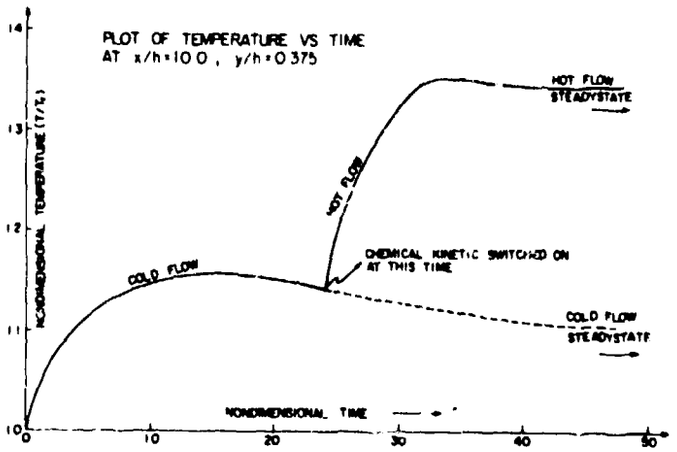

Fig. 7. Time-variation of the gas static temperature at the end of the duct; comparison between cold flow (no kinetics) and hot flow (kinetics switched on). After Ref. 30.

at the end of the computational region shown in Fig. 6. The time variation of T at this point is shown in Fig 7. During the first part of the transient variation, the chemical kinetics are "switched off" to allow the purely fluid dynamic phenomena to approach a "cold flow" solution. The temperature increase is due simply to viscous dissipation. Then, the chemical kinetics are switched on, and are fully coupled with the fluid dynamics. The subsequent temperatur

increase is due primarily to chemical reactions. Note that the final steady-state is approached at large times; again, this steady-state is the desired result, and the time-dependent approach is just a means to that end. The steady-state profiles of several vibrational level populations of the product HF are illustrated in Fig. 8. Note that among several of the levels, designated by v, a population inversion exists; i.e., $\rho_{v+1} > \rho_v$. It is this population inversion that makes a laser work[20]

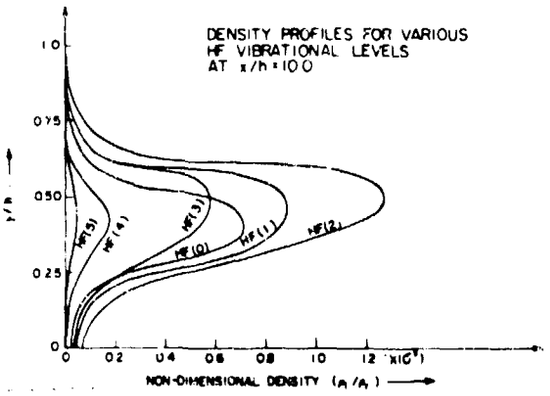

Fig. 8. Steady-state density distributions of various HF vibrational levels at the end of the duct. After Ref. 30.

Many different calculations of chemical laser properties exist[28]. However, the present time-dependent calculations using the Navier-Stokes equations introduce the most recent generation of analyses. They have the distinct and unique advantage of being able to treat recirculating and separated flows. They have the disadvantage, however, of consuming large amounts of computer time -- the results shown in Figs. 7 and 8 required 30 minutes on a UNIVAC 1108. Hence, such an approach is not yet useful for a myriad of parametric studies. Rather, its application is in the detailed investigation of several well-selected design points. For these reasons, time-dependent solutions of the Navier-Stokes equations for chemical laser flows have to be considered as "near-engineering" tools at present.

V. INTERNAL COMBUSTION ENGINES

In all of the above examples, the steady state solutions have been the desired end-product. However, keep in mind that the time-dependent technique is a finite-difference solution to the physically proper governing equations for unsteady flow -- hence, the transient variations are real phenomena, starting from the assumed initial conditions. Therefore, the time-dependent technique is a natural for application to real transient problems of interest.

In this vein, a recent and very promising application of the time-dependent technique has been made by Griffin et al[31] and Diwakar et al[32] to the flowfield inside a reciprocating internal combustion engine. These calculations have impact on the design of high efficiency, low emission IC engines, and represent a direct transfer of aerospace-oriented analysis to a problem of energy conservation.

In particular, consider the idealized model of a piston-cylinder geometry as shown in Fig. 9. The flowfield between the top of the cylinder and the piston face is computed as a function of position and time as the piston moves through a conventional four-stroke cycle with the intake and exhaust valves

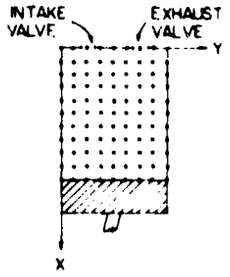

Fig. 9. Geometric model and computational grid for IC engine calculations.

opening and closing appropriately. Even though the cylinder geometry is axi-symmetric, the off-set location of the valves leads to an inherently three-dimensional flow. The main problem is to numerically solve the complete three-dimensional Navier-Stokes equations including multi-component diffusion and finite-rate chemical reactions (for H-C-O-N chemistry), and obtain a complete solution for the velocity, pressure, temperature and chemical composition of the flowfield throughout the four-stroke cycle. The effects of turbulence, the ignition process, fuel droplet breakup, and proper coupling with the intake and exhaust manifolds should also be taken into account. At present, this total problem is a horrendous task, and its exact numerical solution will most likely be an evolutionary process over a long period.

Some first steps in this evolution have been taken by Griffin, Anderson and Diwakar[31-32]. In this work, the piston-cylinder arrangement in Fig. 9 is assumed to be two-dimensional, i.e., an "infinite aspect-ratio" engine. It is found that such 2-D solutions save computer expense, while at the same time providing valuable information on the qualitative and semi-quantitative aspects of the real flow problem. Also, in these analyses, combustion is not considered in detail; rather, it is artificially simulated by increasing the temperature at the beginning of the power stroke. In Ref. 31, the complete compressible Navier-Stokes equations are solved, whereas in Ref. 32 compressible inviscid solutions to the same problem are sought. Considerable details concerning the equations, the boundary conditions, and the numerical analysis can be found in Refs. 31 and 32, so no further elaboration will be given here.

Figs. 10-13 give some sample results from the Navier-Stokes solutions of Griffin et al[31]. Velocity distributions for the intake, compression, power and exhaust strokes are shown respectively. The speed of the engine is 600 RPM (idling). It should be noted that the Navier-Stokes solutions labor under a severe restriction, namely that the unit cell Reynolds number (the Reynolds number based on distance between successive grid points) must not be larger than approximately unity. Otherwise, accuracy and even stability is compromised. This is a natural problem encountered in all Navier-Stokes solutions[9]. As a result, the flowfields shown in Figures 10-13 are for low Reynolds number -- a thimble-size engine at low intake air density. The results are therefore dominated by viscous effects.

To circumvent this difficulty, purely inviscid solutions are obtained by Diwakar et al[32]. A sample of these results are shown in Fig. 14 for the inviscid flow during the intake stroke of a conventional size engine operating at atmosphere conditions. Comparison with the highly viscous case shows the inviscid flow to be dominated by circulation patterns and standing waves. Even more striking differences are observed on the compression and power strokes; such results are described in detail in Ref. 32.

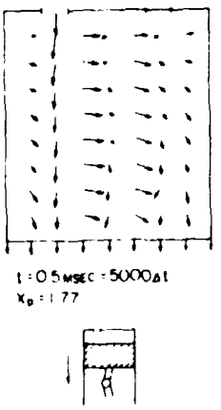

Fig. 10. Velocity distribution at a given instant during the intake stroke. Navier-Stokes calculations after Ref. 31.

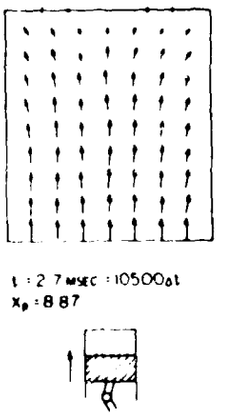

Fig. 11. Velocity distribution at a given instant during the compression stroke. Navier-Stokes calculations after Ref. 31.

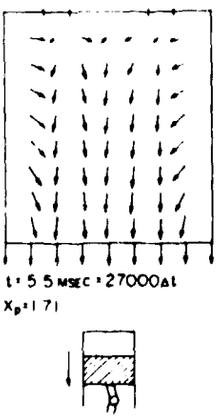

Fig. 12. Velocity distribution at a given instant during the power stroke. Navier-Stokes calculations after Ref. 31.

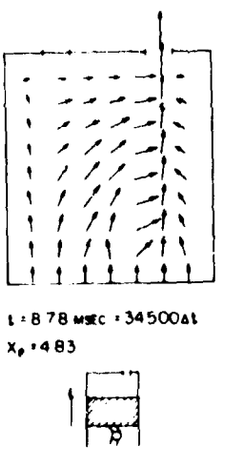

Fig. 13. Velocity distribution at a given instant during the exhaust stroke. Navier-Stokes calculations after Ref. 31.

However, the purpose of this present section is to emphasize that an interesting and complex flowfield does exist inside the cylinder of a reciprocating IC engine, and that this flowfield must have some impact on the combustion processes. This work is just beginning, and future results will be forthcoming. Also, a second purpose is to emphasize that the time-dependent finite-difference technique highlighted in this paper finds a natural application in such IC engine flowfield solutions. Finally, the present calculations are an example of a numerical solution that is not yet an engineering tool, but which has promise of becoming a very powerful one in the future.

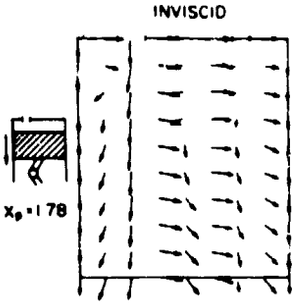

Fig. 14. Velocity distribution at a given instant during the intake stroke. Inviscid calculations after Ref. 32.

VI. CONCLUSIONS

Time-dependent finite-difference solutions constitute a large bulk of modern computational fluid dynamics; indeed, they have been developed to the stage of "engineering tools" for some applications, and "near-engineering tools" for others, as noted in the present paper. They have been used to obtain steady-state flowfields as asymptotic results at large values of time. Moreover, such time-dependent techniques are natural methods for computing transient flows of interest. The example of the reciprocating internal combustion engine is a case in point. Such IC engine calculations should encourage a marriage between computational fluid dynamics and future advanced engine developments.

Therefore, a contemporary answer to the question posed in the title of this paper is "yes" in some cases, and "no" in other cases. However, computational fluid dynamics is still an infant in comparison to other forms of engineering investigation; it has every indication of growing to be a giant during the last quarter of this century. It is well-worth keeping abreast of its future development.

REFERENCES

1 Karamcheti, K., Principles of Ideal-Fluid Aerodynamics, John Wiley, New York, 1966.

2 Schlichting, H., Boundary-Layer Theory, 6th Edition, McGraw-Hill, New York, 1968.

3 Bernoulli, Daniel, Hydrodynamics, Translated from the Latin by Thomas Carmody and Helmut Kolius, Dover Publications, 1968.

4 Kopal, Z., Tables of Supersonic Flow Around Cones, Dept. of Electrical Engineering, Center of Analysis, Massachusetts Institute of Technology, Cambridge, 1947.

5 Taylor, G.I. and Maccoll, J.W., "The Air Pressure on a Cone Moving at High Speed," Proceedings of the Royal Society (A), Vol. 139, 1933, p. 278.

6 Fay, J.A. and Riddell, F.R., "Theory of Stagnation Point Heat Transfer in Dissociated Air," Journal of the Aeronautical Sciences, Vol. 25, No. 2, Feb. 1958, p. 73.

7 Blottner, F.G., "Chemical Nonequilibrium Boundary Layer," AIAA Journal, Feb. 1964, pp. 232-239.

8 Hall, J.G., Eschenroeder, A.Q. and Marrone, P.V., "Blunt-Nose Inviscid Airflows with Coupled Nonequilibrium Processes," Journal of the Aerospace Sciences, Vol. 29, No. 9, Sept. 1962, pp. 1038-1051.

9 Roache, P.J., Computational Fluid Dynamics, Hermosa Publishers, 1972.

10 Taylor, T.D., "Numerical Methods for Predicting Subsonic, Transonic and Supersonic Flow," AGARDograph No. 187, Jan. 1974.

11 Kutler, P., Reinhardt, W.A. and Warming, R.F., "Multishocked, Three-Dimensional Supersonic Flowfields with Real Gas Effects," AIAA Journal, Vol. 11, No. 5, May 1973, pp. 657-664.

12 Moretti, G. and Abbett, M., "A Time-Dependent Computational Method for Blunt Body Flows," AIAA Journal, Vol. 4, No. 12, Dec. 1966, pp. 2136-2141.

13 Anderson, J.D., Jr., Albacete, L.M. and Winkelmann, A.E., "On Hypersonic Blunt Body Flowfields Obtained With a Time-Dependent Technique," NOLTR 68-129, Naval Ordnance Laboratory, White Oak, Maryland, Aug. 1968.

14 Anderson, J.D., Jr., Albacete, L.M. and Winkelmann, A.E., "Applications of the Time-Dependent Technique for the Computation of Compressible Flows," Proceedings of the 8th Navy Symposium on Aeroballistics, Vol. 2, May 1968, pp. 239-266.

15 Anderson, J.D., Jr., Albacete, L.M. and Winkelmann, A.E., "Comment on Shock-Wave Shapes around Spherical and Cylindrical Nosed Bodies," Journal of Spacecraft and Rockets, Vol. 5, No. 10, Oct. 1968, pp. 1247-1248.

16 MacCormack, R.W., "The Effect of Viscosity in Hypervelocity Impact Cratering," AIAA Paper No. 69-354.

17 MacCormack, R.W. and Paullay, A.J., "Computational Efficiency Achieved by Time-Splitting of Finite-Difference Operators," AIAA Paper No. 72-154, 1972.

18 MacCormack, R.W., "Numerical Solutions of the Compressible Navier-Stokes Equations with Shocks and Separation," Presented as part of the seminar sequence: Computational Fluid Dynamics, held at the Dept. of Aerospace Engineering, University of Maryland, College Park, Md., March, 29, 1976.

19 Courant, R., Friedrichs, K.O., and Lewy, H., "Ueber die Differenzengleichungen der Mathematischen Physik," Math. Ann., Vol. 100, 1928, p. 32.

20 Anderson, J.D., Jr., Gasdynamic Lasers: An Introduction, Academic Press, New York, 1976.

21 Anderson, J.D., Jr., "A Time-Dependent Analysis for Vibrational and Chemical Nonequilibrium Nozzle Flows," AIAA Journal, Vol. 8, No. 3, March 1970, pp. 545-550.

22 Anderson, J.D., Jr., "Time-Dependent Analysis of Population Inversions in an Expanding Gas," The Physics of Fluids, Vol. 13, No. 8, Aug. 1970, pp. 1983-1989.

23 Anderson, J.D., Jr., Humphrey, R.L., Vamos, J.S., Plummer, M.J. and Jensen, R.E., "Population Inversions in an Expanding Gas: Theory and Experiment," The Physics of Fluids, Vol. 14, No. 12, Dec. 1971, pp. 2620-2624.

24 Glowacki, W.J. and Anderson, J.D., Jr., "A Computer Program for CO_2-N_2-H_2O Gasdynamic Laser Gain and Maximum Available Power," NOLTR 71-210, Naval Ordnance Laboratory, White Oak, Md., Oct. 1971.

25 Anderson, J.D., Jr., "Gasdynamic Lasers: Review and Extension," Acta Astronautica, Vol. 2, No. 11-12, Nov.-Dec. 1975, pp. 911-927.

26 Lee, G., Gowen, F.E., and Hagen, J.R., "Gain and Power of CO_2 Gasdynamic Lasers, AIAA Journal, Vol. 10, No. 1, January 1972, pp. 65-71.

27 Hill, R.J., Jewell, N.T., Jones, A.T. and Price, R.B., "Air Breathing Gasdynamic Lasers," AIAA Paper No. 76-206, 1976.

28 Warren, W.R., "Chemical Lasers," Astronautics and Aeronautics, Vol. 13, No. 4, April 1975, pp. 36-49.

29 Kothari, A.P. and Anderson, J.D., Jr., "Navier-Stokes Solutions for Chemical Laser Flows: Cold Flows," AIAA Journal, Vol. 14, No. 5, May 1976, pp. 702-703; also, AFOSR-TR-75-1447 (AE 75-6), Dept. of Aerospace Engineering, Univ. of Md., June 1975.

30 Kothari, A.P., Anderson, J.D., Jr. and Jones, E., "Navier-Stokes Solutions for Chemical Laser Flows," submitted to the AIAA Journal, May 1976.

31 Griffin, M.D., Anderson, J.D., Jr., and Diwakar, R., "Navier-Stokes Solutions of the Flowfield in an Internal Combustion Engine," AIAA Paper No. 76-403, July 1976.

32 Diwakar, R., Anderson, J.D., Jr., and Griffin, M.D., "Inviscid Solutions of the Flowfield in an Internal Combustion Engine," submitted to the AIAA Journal, May 1976.

AD P000329

CONSTANT PARAMETER TWO COMPONENT CHANNEL FLOWS

Kenneth R. Cramer
Thermomechanics Branch
Air Force Wright Aeronautical Laboratories

ABSTRACT

Johnson and Von Ohain proposed the RHEA concept for accelerating air to velocities significantly greater than that produced by expanding heated air from a reservoir The RHEA process employs a low molecular weight gas to accelerate a dense particle cloud to very high velocities which is then separated and introduced into an expanded air stream which is then further accelerated by the drag of the particle cloud. The air is cleansed prior to its entry into the wind tunnel test section.

This paper examines constant parameter, two component channel flows as a basis for designing the air acceleration section. Results demonstrate that a constant static air temperature channel would be a useful choice for producing high Mach number, high recovery pressure flows for testing reentry missile nose tips.

The work was performed in 1966 in the Air Force Aerospace Research Laboratories.

CONSTANT PARAMETER TWO COMPONENT CHANNEL FLOWS

Kenneth R. Cramer

I. INTRODUCTION

The Intermediate Re-Entry Heating Energies Analyzer (RHEA)[1] system, Figure 1, for simulating re-entry flow conditions in wind tunnels employs a two component flow to attain significant augmentation of the air velocity while avoiding the dissociation that would occur in equivalent conventional high temperature facilities. Solid particles are accelerated to high velocities by the drag forces of hydrogen jets having velocities substantially higher than can be achieved with air. Momentum and energy are transferred from the separated particle cloud to the tunnel air in the mixing region. Finally, the particle cloud is separated from the tunnel air prior to its entry into the test section.

Momentum and energy balances between the inlet and exit of the mixing region can provide the exit air conditions. However, solution of the differential equations for the flow system is required to provide the channel area scheduling and channel length. This paper presents numerical solutions for the case of no confining walls and for selected constant parameter channels.

II. ANALYSIS

The transfer of energy and momentum from the particle cloud to the tunnel air will be analyzed as a steady, one dimensional, two component flow with a sudden and uniform injection of the high speed particle cloud. The following are the equations[2] for this system that includes the dissipation of the particle cloud kinetic energy by the relative motion, radiation from the particle cloud, and heat conduction between the particle and air clouds. Also, the temperature was assumed to be uniform in the small particles.

CONTINUITY $$\frac{d(\rho_g A v_g)}{dx} = \frac{d\dot{m}_g}{dx} = 0 \qquad \text{(air cloud)} \qquad (1)$$

$$\frac{d(\rho_p A v_p)}{dx} = \frac{d\dot{m}_p}{dx} = 0 \qquad \text{(particle cloud)} \qquad (2)$$

MOMENTUM $$u_p \frac{du_p}{dx} = \frac{u_g - u_p}{\tau_v} \qquad \text{(particles)} \qquad (3)$$

$$\frac{du_g}{dx} + \left(\frac{\dot{m}_p}{m_g}\right) K_m \frac{du_p}{dx} = -\frac{A}{m_g}\frac{dp}{dx} \qquad \text{(mixture)} \qquad (4)$$

ENERGY $$u_p \frac{dc_p T_p}{dx} = \frac{c_p}{\tau_T}(T_g - T_p) + \frac{(u_g - u_p)^2}{\tau_v} + \frac{\sigma \varepsilon A_p}{m_p}(T_w^4 - T_p^4) \qquad \text{(particles)} \qquad (5)$$

$$\frac{d(u_g^2 + c_g T_g)}{dx} + \left(\frac{\dot{m}_p}{m_g}\right)\frac{d(u_p^2 + c_p T_p)}{dx} =$$

$$\left(\frac{\dot{m}_p}{m_g}\right)\frac{(u_g - u_p)^2}{\tau_v u_p} + \left(\frac{\dot{m}_p}{m_g}\right)\left(\frac{\sigma \varepsilon A_p}{m_p}\right)\left(\frac{T_w^4 - T_p^4}{u_p}\right) \qquad \text{(mixture)} \qquad (6)$$

CLOUD DENSITIES $$\frac{\rho_g}{\rho_g} = 1-\phi \;,\; \frac{\rho_p}{\rho_p} = \phi \qquad (7)$$

STATE $$P = \bar{\rho}_g \bar{R} \bar{T}_g \qquad (8)$$

STOKES RELATIONS $$\tau_v = \frac{\bar{\rho}_p d_p^2}{18\mu} \;,\; \tau_T = \frac{c_p \bar{\rho}_p d_p}{3 k_g} \qquad (9)$$

INITIAL CONDITIONS $X=0$: $U_g = U_{g_1}$, $T_g = T_{g_1}$, $U_p = U_{p_1}$, $T_p = T_{p_1}$, & $P = P_1$ (10)

FINAL CONDITIONS $X \rightarrow U_{g_1} \tau_{v_1}$: $U_g \rightarrow U_{g_2} \leftrightarrow U_{p_2}$ (11)

$$T_g \rightarrow T_{g_2} \leftrightarrow T_{p_2}$$

$$P \rightarrow P_2$$

Even though the anticipated conditions at the exit of the mixing section are stated, the analytical problem was solved as an initial value problem. Also, the equations contain the cloud interaction parameter K_m and Soo[2] recommends that it be chosen as approximated in Figure 2. However, the following representation was chosen to simplify the solution of the equations.

$$K_m = U_{p_2}/U_p \quad \text{and} \quad X=0: \; K_m = U_{p_2}/U_{p_1} \;,\; X \rightarrow \infty : \; K_m \rightarrow 1 \qquad (12)$$

The consequences of this assumption will be revealed thru the examination of numercial results for a range of particle spacings. This representation requires an estimate of U_{p_2} and the following relation was obtained by evaluating the integral of the non-dissipative, mixture energy equation at the inlet and exit stations

$$U_{p2} = \left[\frac{1 + \left(\frac{\dot{m}_p}{\dot{m}_g}\right) U_{p1}^2}{1 + \left(\frac{\dot{m}_p}{\dot{m}_g}\right)}\right]^{1/2} \qquad (13)$$

SOLUTIONS

A. The system of equations was solved first for a range of the various parameters without confining walls and Figure 3 presents the results for the following initial conditions:

$$U_{p_1} = 17650 \text{ ft/sec}, \; T_{p_1} = 20°R, \text{ Hafnia: } Cp = 0.11 \text{ Btu}/\#_m{}^\circ R \;, \; \bar{\rho}p = 606 \; \#_m/ft^3,$$

$$\frac{\dot{m}_p}{\dot{m}_g} = 7.36, \; Ug_1 = 7730 \text{ ft/sec}, \; M_1 = 41, \; Tg_1 = 14.8°R, \; \bar{\rho}g = 0.515 \times 10^{-6} \; \#_m/ft^3$$

$$Pg_1 = 0.000409 \; \#/ft^2 \; \& \; Ug_1 \tau v_1 = 16.4 \text{ ft} \qquad (14)$$

The air velocity, total temperature, and particle temperature increase as the particle velocity and air density decrease thru the mixing section. The initial difference between the particle and air velocities heats the particles which radiate and conduct to the air and this heating drives the inlet air Mach No towards one until the air velocity decreases the slip velocity, static air temperature, static pressure and density. The Mach number then increases thru the remaining portion of the mixing section. Since no walls were imposed and the component mass flows were constant, the particle stream dialates and the air stream contracts. The approximately 6 percent reduction in particle velocity limits the variation of K_m which produces a strong interaction between the clouds that is not warranted by the wide particle spacing and the initial slip velocity (9920 ft/sec) according to the Figure 2 model. The initial Re_{slip} (s/d)=-136. However, eventually the slip velocity decreases to near zero and then the strong interaction will occur and the qualitative features of the flow system will be produced but over a much

greater length. The computed velocity relaxation length was 16.4 ft. Note that U_{p2}/U_{p1} computed with Equation (12) was 0.938 which is approached. The most important result of this calculation, for reentry missile nose tip testing, is that the nose tip recovery pressure produced is 1.88 lbs/ft^2 which is far below the desired 423,360 lbs/ft^2 (200 atm). Since the results show that the total pressure increases in the mixing section, after an initial decrease, the low value was produced by excessive expansion of the air prior to its entry into the mixing section (M=41). Consequently, all of the constant parameter channel solutions were based on an inlet M_1=1.41.

Since the adequancy of the K_m assumption was questioned, calculations were made for a range of particle spacings, actually mass flow rates, see Figure 4. The results are shown in Figure 5 and demonstrate that most quantities computed for Figure 3 are not very different from the asymptotic values for the higher particle mass flows. Thus, the general features were demonstrated even with the strong coupling assumption. The plotted mixing section length decreases rapidly with increased particle mass flows. The lengths are incorrect even for the higher particle mass flows. A more realistic, or experimentally determined, K_m assumption is required for valid length estimates.

B. Classical constant parameter channel flow solutions have been useful for selecting near optimum designs for various devices. Thus, selected parameters were held constant for the initial design of a RHEA mixing section and the system of differential equations solved for each case. The initial values for all cases were:

U_{p_1} = 17,655 ft/sec, T_{p_1} = 3580°R, d_p = 20μ, C_p = 0.11 BTU/#$_m$°R

$\ddot{\rho}_p$ = 606 #$_m$/ft^3, $\frac{\dot{m}_p}{\dot{m}_g}$ = 4.08, s/d = 30, M_1 = 1.41,

U_{g_1} = 4125 ft/sec, T_{g_1} = 3580°R, $T_{g_{t_1}}$ = 5000°R, P_{g_1} = 89,000 #/ft^2, (15)

P_{g_t} = 288,000 #/ft^2, $\bar{\rho}_{g_1}$ = 0.467 $\#_m$/ft^3, and $U_{g_1}\tau_{v_1}$ = 0.86 ft

Note that the results for the constant area channel were obtained for s/d=20 and m_p/m_g= 7.36.

RESULTS

(1) Constant Channel Area, Figure 6.

Since the mass flow ratio was held constant also, the air and particle velocities drop rapidly while the pressure and temperature increase rapidly and the channel becomes subsonic along its entire length. Such a channel is not practical in a wind tunnel application since it produces extremely high air pressures and temperatures.

(2) Constant Static Air Pressure, Figure 7.

The rapid increase in static air temperature reduces the Mach number to subsonic values near the entrance region and, as the heating rate diminishes, it returns to supersonic values in the remainder of the channel. A real channel may not flow in this manner and the problem can be avoided by increasing the entry Mach number to maintain supersonic flow thru the channel. Also, the area ratio increases rapidly and then decreases to maintain a constant static pressure as the static air temperature rises. Thus, a practical channel would terminate before the exit area becomes less than the throat area that produced the inlet air flow. This channel is a candidate for the wind tunnel application in which the cleansed air would be further accelerated to provide a high test section Mach number. Unfortunately, the static air temperature would be increased by a factor of eight thru the mixing channel.

(3) Constant Static Air Temperature, Figure 8.

The air velocity, Mach number, particle temperature, and total air temperature increase thru the entire channel as the particle velocity and static air density decrease. Again, the area ratio increases and then decreases and the channel must be terminated. Note, that the static air pressure and particle temperature increase moderately. Both are assets in a practical design.

(4) Constant Static Air Density, Figure 9.

The static air temperature rise reduces the Mach number thru the channel but remains supersonic. The area ratio is reduced to values lower than the area ratio that produced the inlet air flow. The channel could be shortened to avoid the starting problem, but only modest air velocity increases would be produced in very short channels.

(5) Constant Air Cloud Density, Figure 10.

This channel suffers from the same deficiencies as the previous channel in addition to a subsonic portion and is not practical for the RHEA system.

C. The constant static air temperature and static pressure cases are the best choices for the RHEA design. However, the constant static air temperature case is superior and the following calculation demonstrates how the channel could be employed in a wind tunnel design after the particles are magically separated:

Design Test Section Conditions:

M=6 and Nose Tip Recovery Pressure = 150-200 atm.

Truncated Channel Exit Conditions:

$M=5.16$, $A/A_1=0.905$, $T_{gt}/T_{gt1}=4.55$, $p_{gt}/p_{gt1}=60.42$, $u_g/u_{g1}=3.68$ and $q/q_1=4.09$

Expansion Conditions:

$M_{inlet}=5.16$, $M_{outlet}=6.0$, $q/p_{t,M=5.16}=0.02929$ and $q/p_{t,M=6.0}=0.1596$.

Calculation

$$P_{rec} = 1.84\left(\frac{q_{6.0}}{q_{5.13}}\right)\left(\frac{q_{5.13}}{q_{1.41}}\right)\left(\frac{q_{1.41}}{P_{res}}\right)P_{res} \sim \left(\frac{P_{t2}}{P_{t2}}\right)_{\substack{M=6\\N.S.}} \times \left(\frac{P_{t2}}{P_{t1}}\right)_{CHAN.} \times P_{res} \qquad (16)$$

$$= 1.84\,\frac{0.01596}{0.02929} \times 4.09 \times 0.4312 \times \frac{2000}{14.7} = 240.6\ \text{atm} \sim 0.02965 \times 60.42 \times \frac{2000}{14.7} = 243.7$$

Since a 150-200 atm range for the recovery pressure was the goal, then a larger expansion would produce a Mach number range of 6.27 - 6.71.

III. CONCLUSIONS

The two component flow of the RHEA air acceleration section was examined to select the most appropriate channel geometry. First, the unbounded one-dimensional system of equations was solved to exhibit the general features of the flow and to examine the role of the parameter that couples the particle and air clouds. Results demonstrate that the assumed form of the coupling parameter produced too strong of an interaction and the resulting channel length estimates were incorrect. However, the behavior of the flow system was adequately demonstrated. The second effort examined the flow system for channels in which chosen parameters were held constant as a basis for selecting a near optimum channel design. The constant static air temperature and the constant static pressure channels were found to be the best choices on the basis of practicality and conditions produced. The constant static air temperature channel was the best choice and specific exit conditions were chosen for calculating wind tunnel test section conditions of interest for testing reentry missile nose tips.

RHEA type acceleration channels can be designed optimumly with the two component flow equations if an improved cloud interaction parameter is included to improve channel length estimates.

FOOTNOTE: There is an abstract physical similarity between this paper and S. H. Hasinger's "Highlights of an Ejector Analysis". The RHEA acceleration section is an ejector.

IV. REFERENCES

1. Johnson, E. G. and Von Ohain, H. J. P., "Generation of Ultra High Total Enthalpy Gases Through Multi-Component Flow Techniques", AIAA 10th Aerospace Sciences Meeting Paper 72-167 or ARL 72-1000, available as NTIS No. N72-26247 also ARL 72-1250, ARL 73-0065, and ARL TR 74-0018.

2. Soo, S. L., "Fluid Dynamics of Multiphase Systems", Blaisdell Publishing Company, Waltham, Massachusetts.

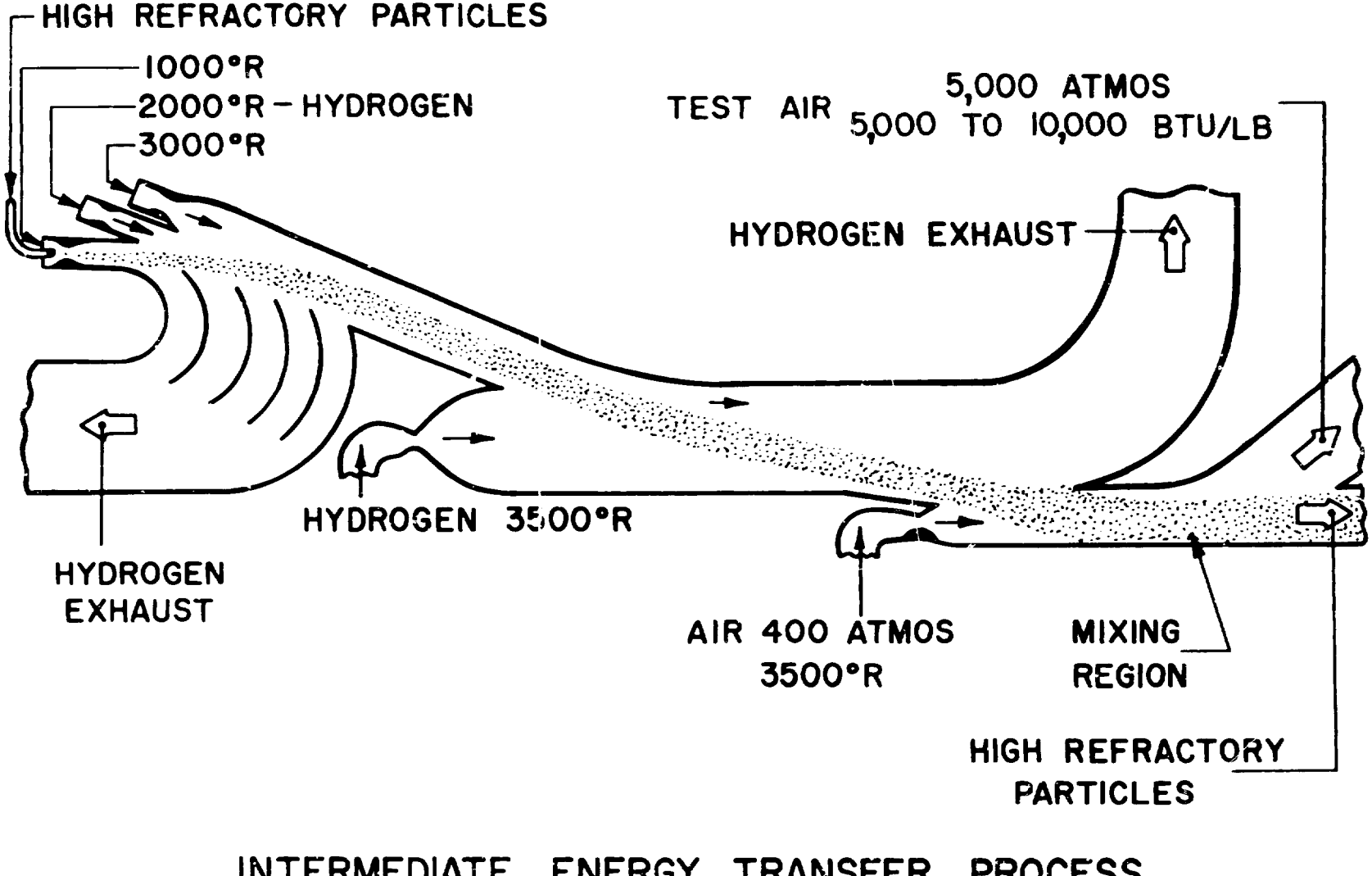

INTERMEDIATE ENERGY TRANSFER PROCESS

FIG. 1

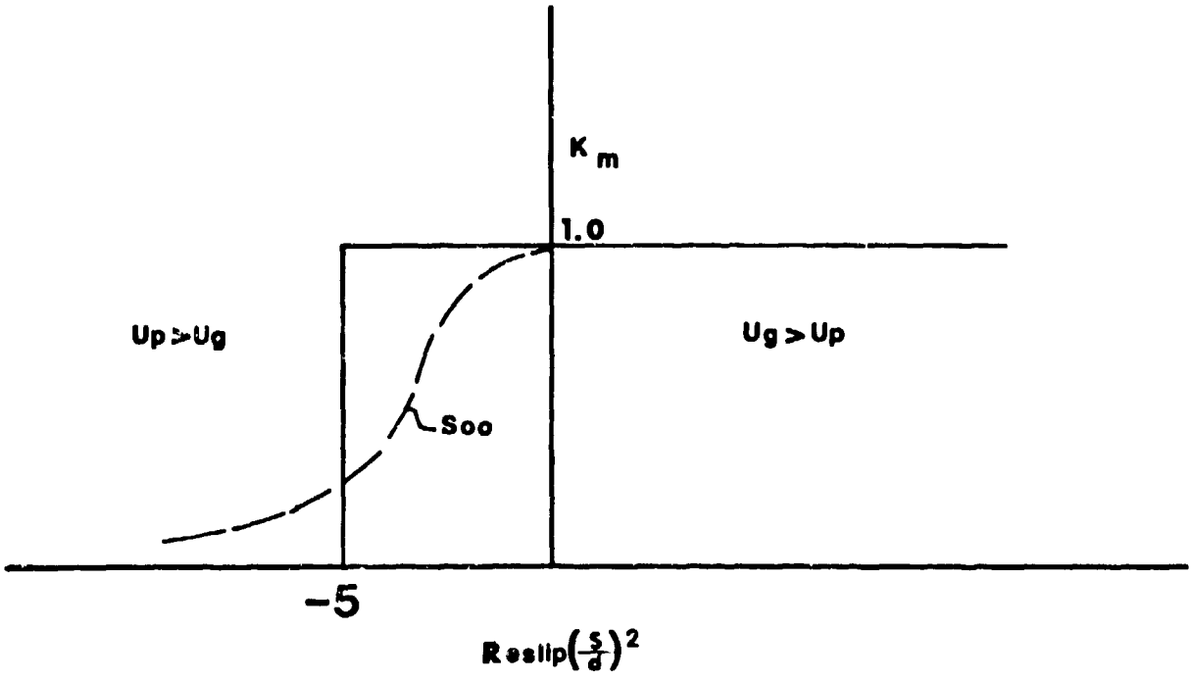

PARTICLE CLOUD INTERACTION PARAMETER

FIGURE 2

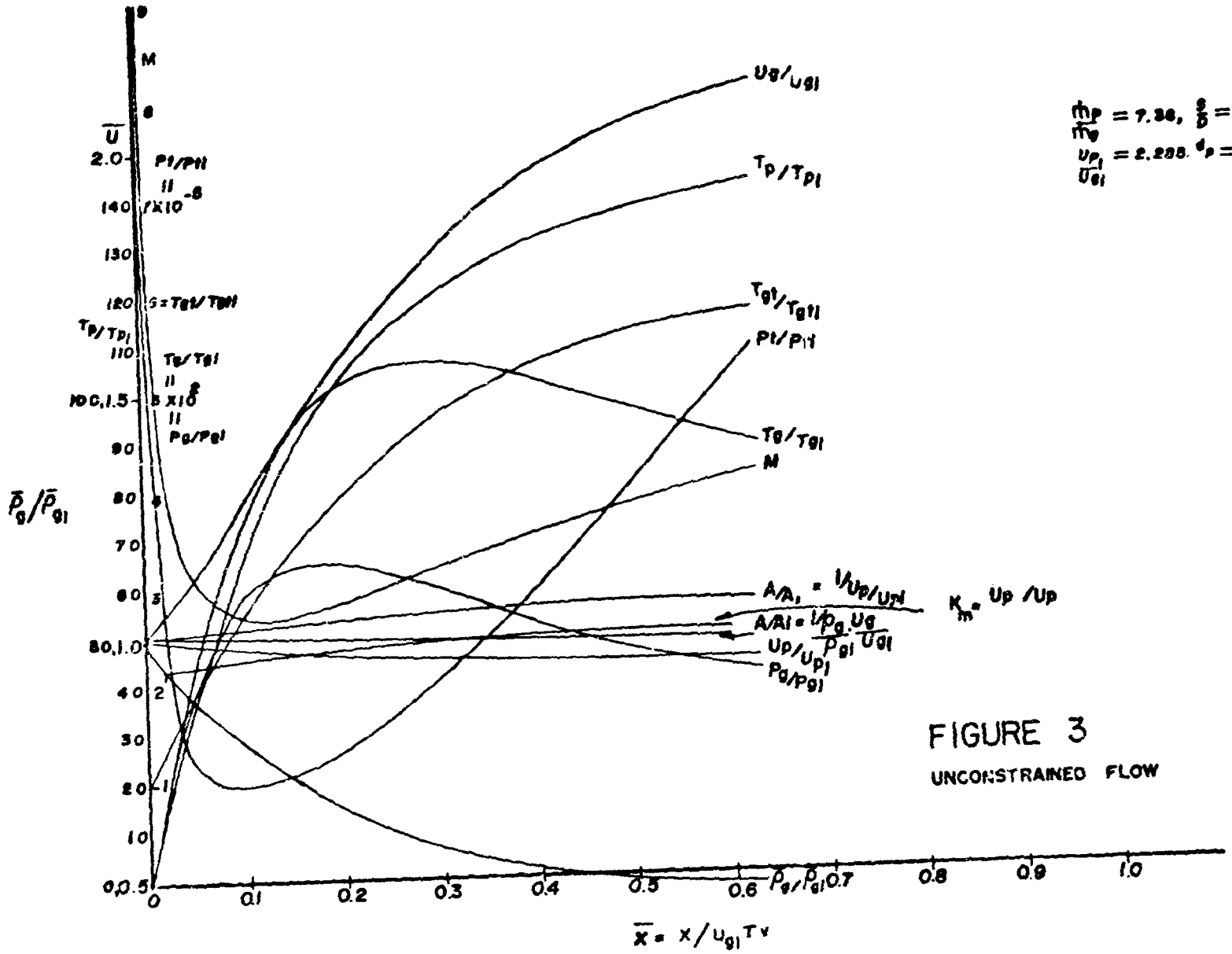

$\frac{m_p}{m_g} = 7.36, \frac{s}{D} = 20$

$\frac{U_{p1}}{U_{g1}} = 2.235. \ d_p = 20\mu$

FIGURE 3

UNCONSTRAINED FLOW

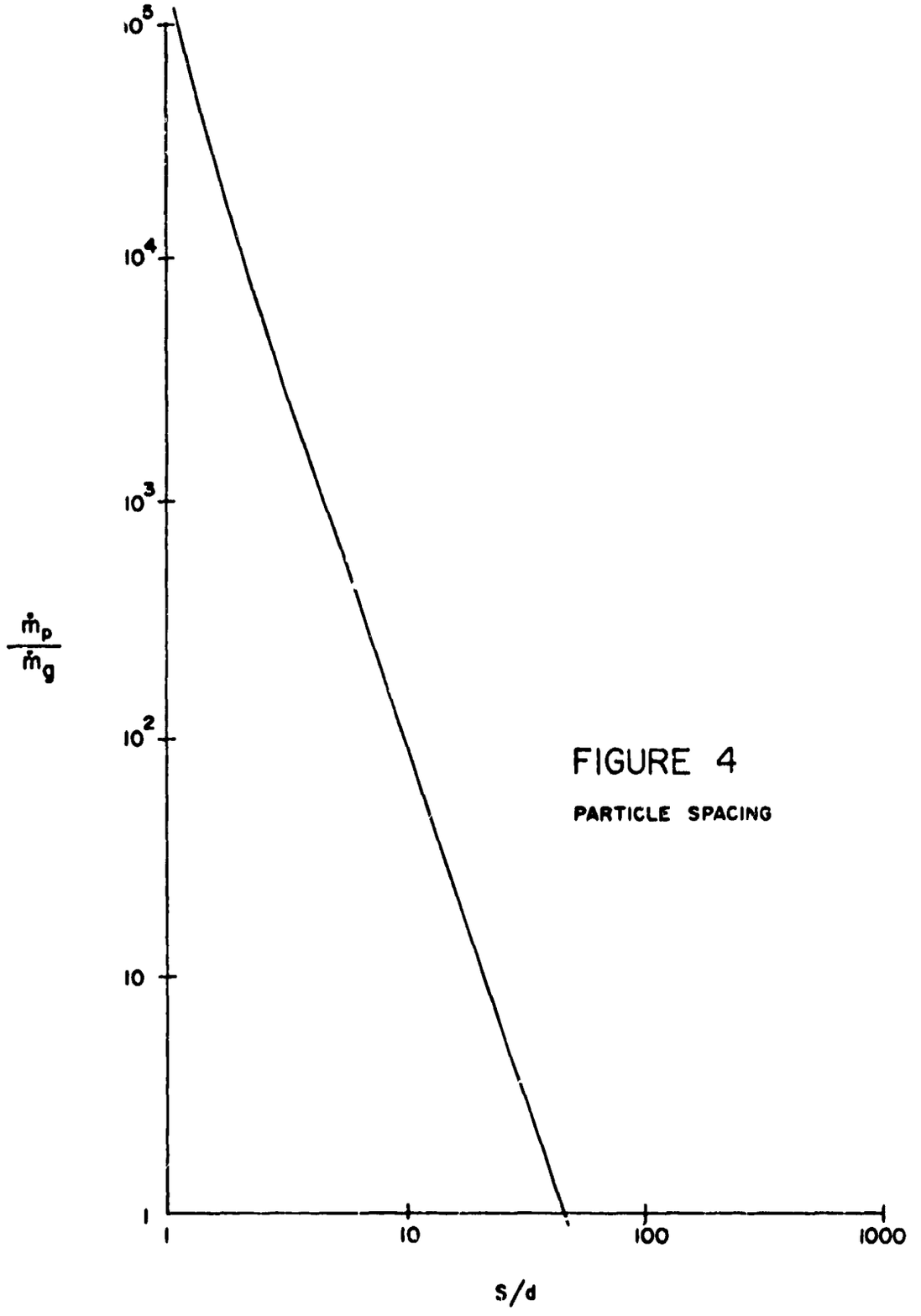

FIGURE 4

PARTICLE SPACING

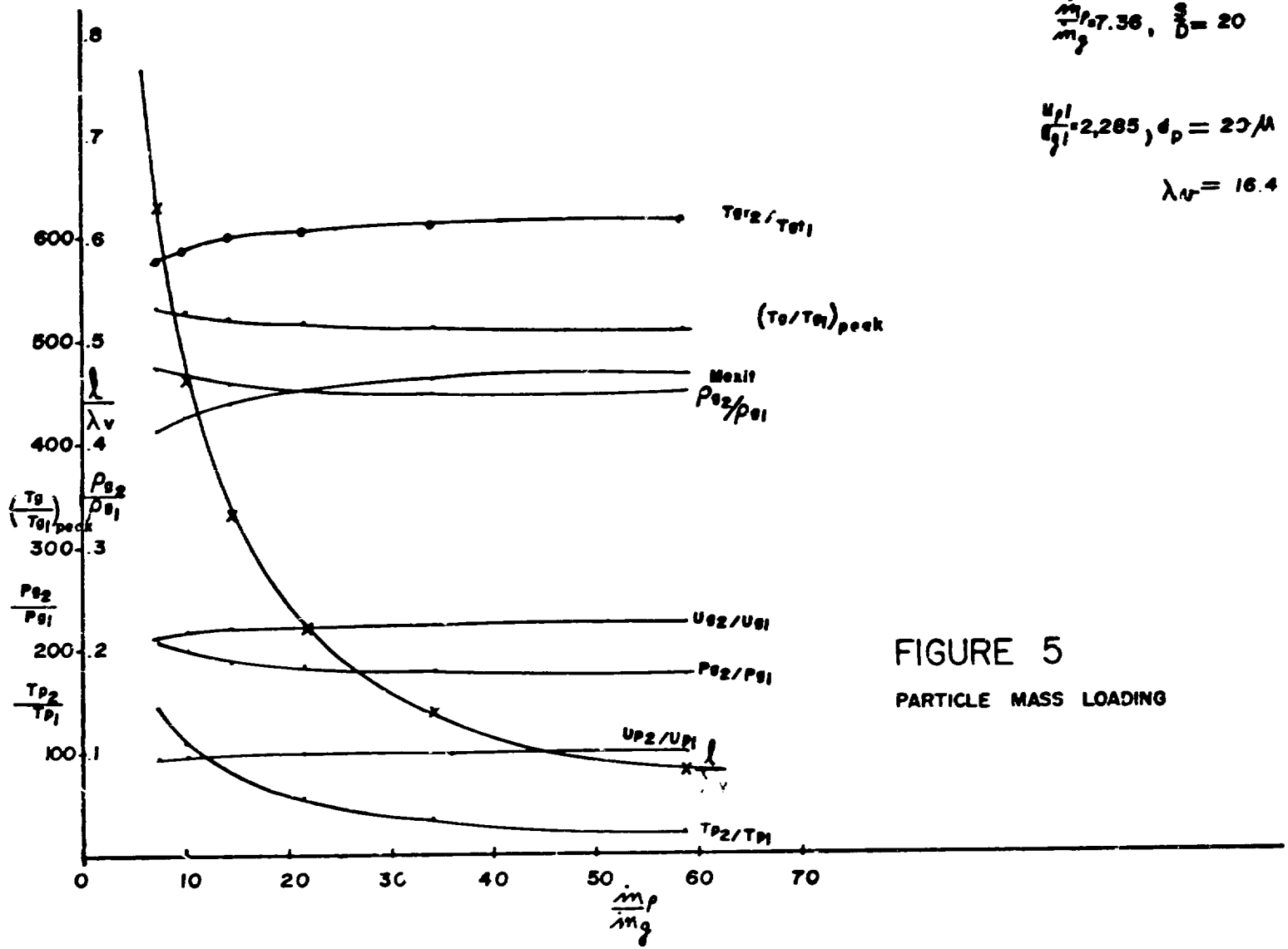

FIGURE 5

PARTICLE MASS LOADING

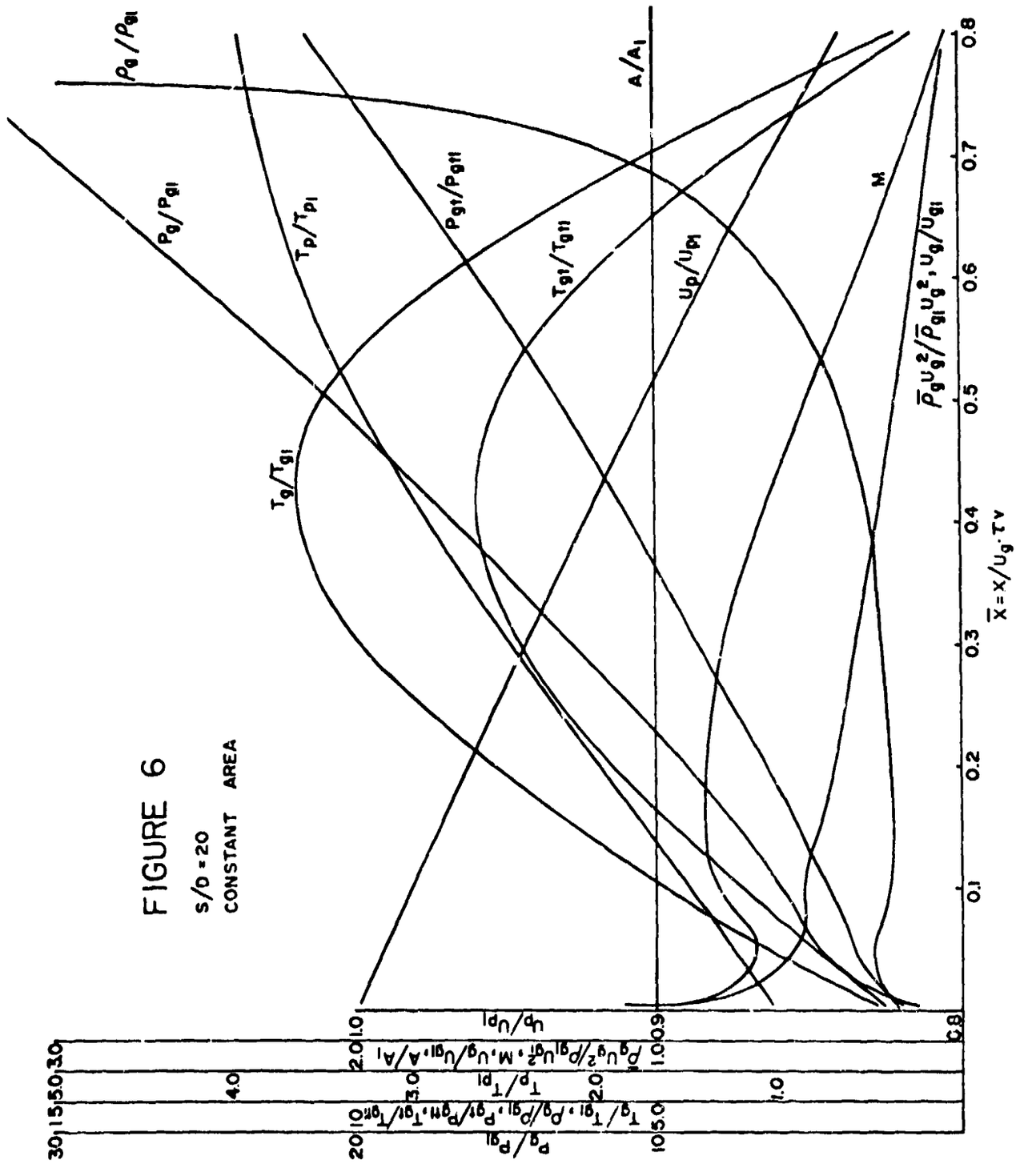
FIGURE 6
S/D = 20
CONSTANT AREA
ρ_g/ρ_{g1}
P_g/P_{g1}
T_p/T_{p1}
P_{gt}/P_{gt1}
T_{gt}/T_{gt1}
A/A_1
U_p/U_{p1}
M
T_g/T_{g1}
$\bar{\rho}_g U_g^2/\bar{\rho}_{g1} U_g^2, U_g/U_{g1}$
$\bar{X} = X/U_g \cdot \tau_v$
U_b/U_{p1}
$\rho_g U_g^2/\rho_{g1} U_{gt}^2, M, U_g/U_{g1}, A/A_1$
T_p/T_{p1}
$T_g/T_{g1}, \rho_g/\rho_{g1}, P_{gt}/P_{gt1}, T_{gt}/T_{gt1}$
P_g/P_{g1}

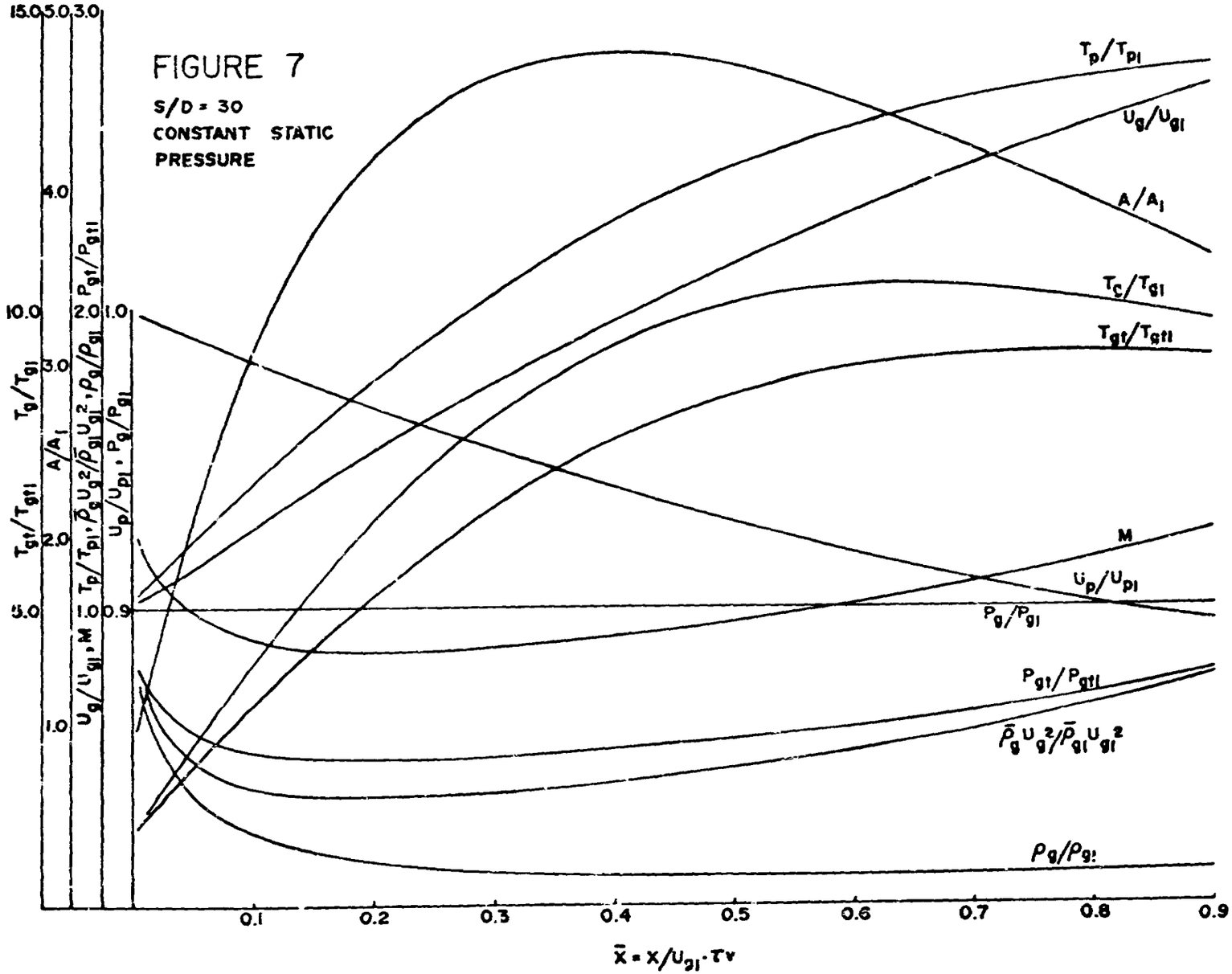
FIGURE 7
S/D = 30
CONSTANT STATIC PRESSURE
T_p/T_{pl}
U_g/U_{gl}
A/A_l
T_c/T_{gl}
T_{gt}/T_{gtl}
M
U_p/U_{pl}
P_g/P_{gl}
P_{gt}/P_{gtl}
$\bar{\rho}_g U_g^2/\bar{\rho}_{gl} U_{gl}^2$
ρ_g/ρ_{gl}
T_g/T_{gl}
T_{gt}/T_{gtl}
A/A_l
U_g/U_{gl}, M
T_p/T_{pl}, $\bar{\rho}_g U_g^2/\bar{\rho}_{gl} U_{gl}^2$, ρ_g/ρ_{gl}
P_{gt}/P_{gtl}
U_p/U_{pl}, P_g/P_{gl}
15.0 5.0 3.0
10.0 4.0 2.0 1.0
5.0 3.0 1.0 0.9
2.0
1.0
0.1 0.2 0.3 0.4 0.5 0.6 0.7 0.8 0.9
$\bar{x} = x/U_{gl} \cdot \tau v$

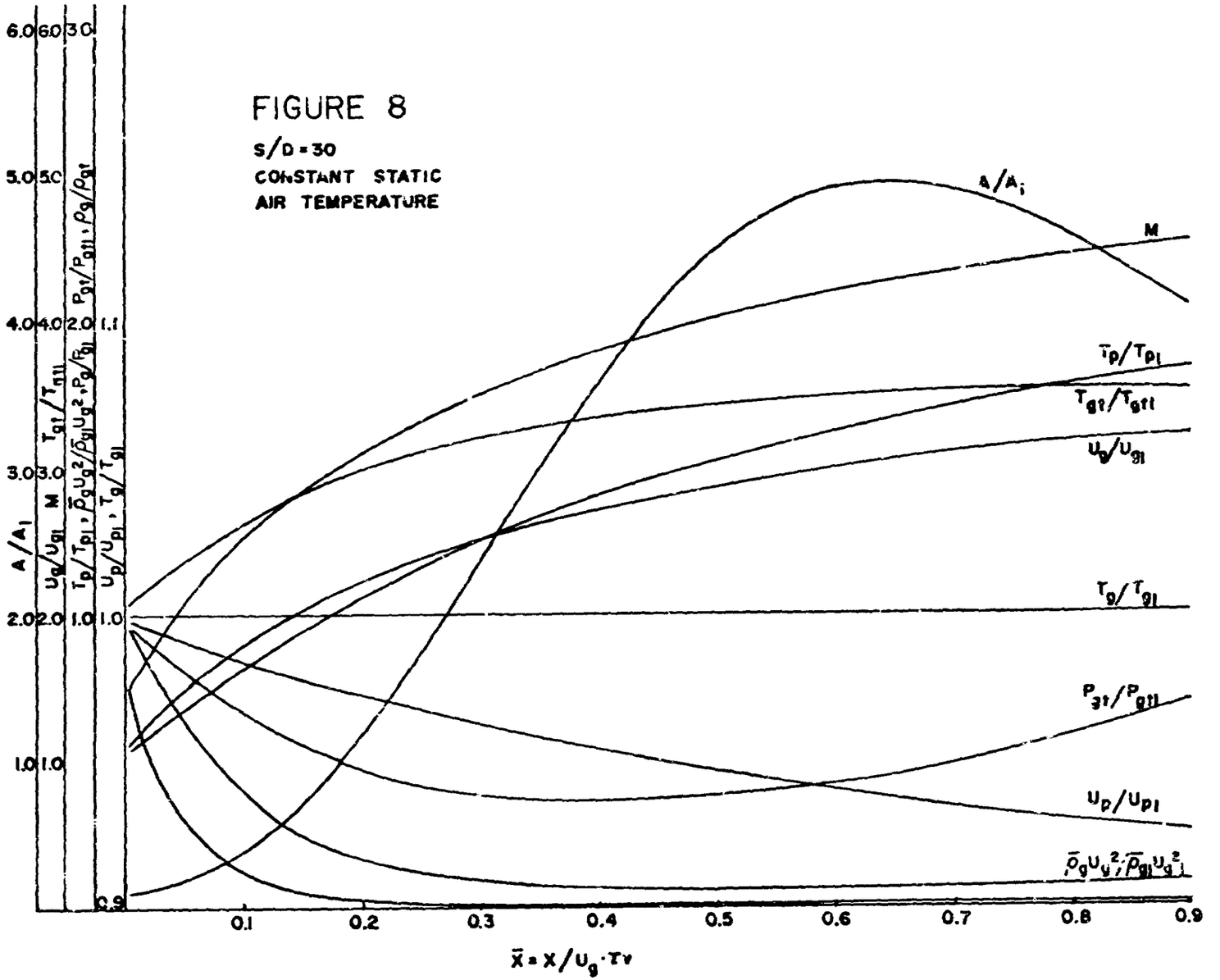
FIGURE 8
S/D = 30
CONSTANT STATIC
AIR TEMPERATURE
A/A_i
M
T̄p/Tp1
Tg1/Tg11
Ug/Ug1
Tg/Tg1
Pg1/Pg11
Up/Up1
ρ̄gUg²/ρ̄g1Ug1²
A/A1
Ug/Ug1 M Tg1/Tg11
T̄p/Tp1, ρ̄gUg²/ρ̄g1Ug1², Pg1/Pg11, ρg/ρg1
Up/Up1, Tg/Tg1
6.0 6.0 3.0
5.0 5.0
4.0 4.0 2.0 1.1
3.0 3.0
2.0 2.0 1.0 1.0
1.0 1.0
0.9
0.1 0.2 0.3 0.4 0.5 0.6 0.7 0.8 0.9
X̄ = X/Ug·τv

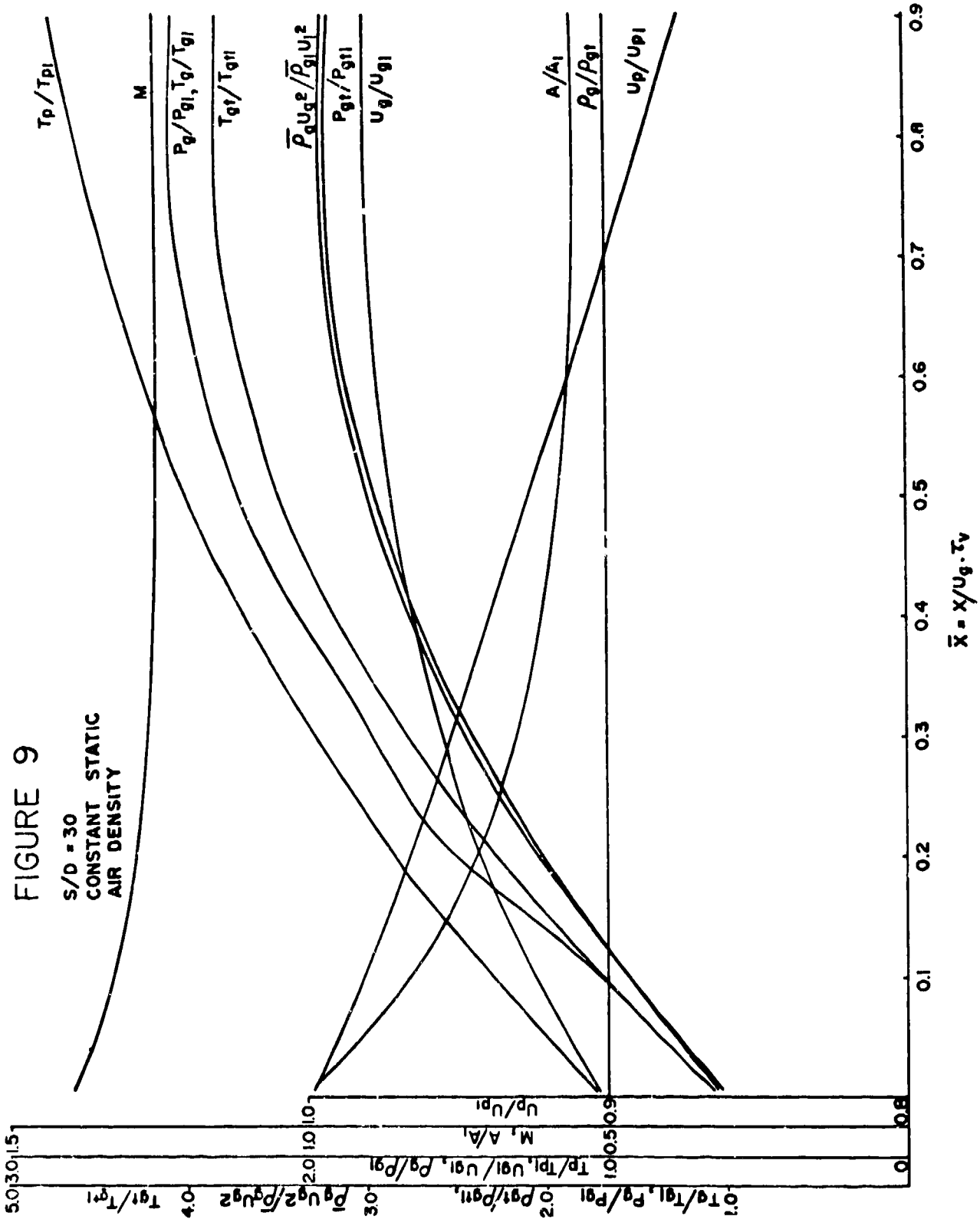
FIGURE 9
S/D = 30
CONSTANT STATIC AIR DENSITY
T_p/T_{pl}
M
$P_g/P_{gl}, T_g/T_{gl}$
T_{gt}/T_{gtl}
$\overline{\rho}_g U_g^2/\overline{\rho}_{gl} U_{gl}^2$
P_{gt}/P_{gtl}
U_g/U_{gl}
A/A_1
ρ_g/ρ_{gt}
U_p/U_{pl}
T_g/T_{gl}, P_g/P_{gl}, U_g/U_{gl}, ρ_g/ρ_{gl}
T_p/T_{pl}, U_p/U_{pl}, M, A/A_1
$\rho_g U_g^2/\rho_{gl} U_{gl}^2$
T_{gt}/T_{gtl}
$\bar{x} = x/U_g \cdot \tau_v$

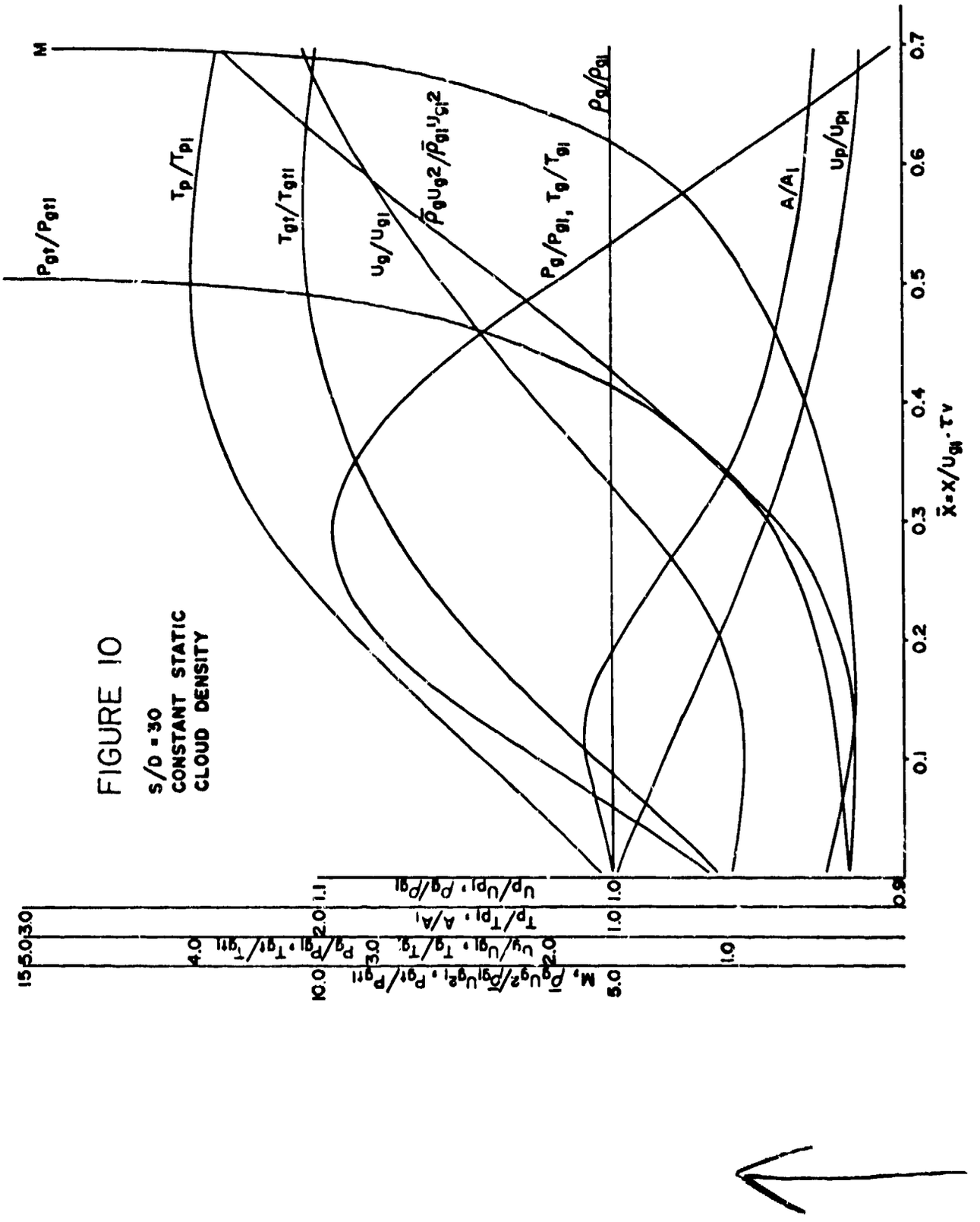

FIGURE 10

s/D = 30
CONSTANT STATIC
CLOUD DENSITY

AD P000330

THE USE OF VORTEX GENERATORS AS INEXPENSIVE COMPRESSOR CASING TREATMENT

by

C. Herbert Law, Arthur J. Wennerstrom, and William A. Buzzell
Turbine Engine Division, Air Force Aero Propulsion Lab
Wright-Patterson Air Force Base, OH

This paper describes an inexpensive form of casing treatment which was found to increase both efficiency and stall margin in an axial compressor stage and which could be easily and cheaply retrofitted to existing engines. The method consists of placement of a row of vortex generators on the outer casing of an axial compressor, upstream of the rotor. Design techniques are described. An experimental investigation is also described in which vortex generator tip treatment was applied to a single stage axial compressor. Gains in compressor efficiency and stall margin were observed.

This work was performed under AFAPL Work Unit No. 23075127

THE USE OF VORTEX GENERATORS AS INEXPENSIVE COMPRESSOR CASING TREATMENT*

C. HERBERT LAW, ARTHUR J. WENNERSTROM, AND WILLIAM A. BUZZELL

Turbine Engine Div., Air Force Aero Propulsion Lab,
Wright-Patterson AFB

The in-house program of research in axial compressor technology, first at the Aerospace Research Laboratories and subsequently at the Air Force Aero Propulsion Laboratory, is one of many which has benefitted from the continuing interest, advice and support of Hans von Ohain. This small contribution is offered as a token of the authors' fond recollections of many fruitful discussions held with Hans during this association.

Several techniques have been devised to improve the performance of axial flow compressors with respect to increasing stall margin and relaxing tip clearances. These techniques generally involve some form of casing treatment near the rotor tip for the purpose of delaying rotor tip stall or reducing the detrimental secondary flow effects resulting from excessive tip clearance. Most forms of casing tip treatment which are now in common use employ casing inserts fabricated of honeycomb or with circumferential grooves or slots. These forms of casing tip treatment are typically expensive to manufacture, sometimes require appreciable depth in the casing, and are difficult to retrofit to existing engines.

The mechanism through which most forms of casing treatment benefit performance is not well understood. However, it is evident that in some ways casing treatment acts to delay flow separation on the outer casing and possibly also on the tip sections of the adjacent airfoils. This can result in an improvement in performance at a given tip clearance or the ability to maintain a given performance at increased clearance. In instances where stall is initiated at the tip, an improvement in stall margin is often obtained.

* Presented at the Aerospace Engineering and Manufacturing Meeting of the Society of Automotive Engineers, San Diego CA, Dec 76

The type of casing tip treatment described in this paper consists of a row of vortex generators on the outer casing of an axial compressor, upstream of the rotor, for the purpose of energizing the fluid boundary layer on the outer casing adjacent to the rotor tips. The use of vortex generators is viewed as an alternate and less expensive form of casing tip treatment than other forms in common use. This form of tip treatment is also easier to r .rofit to existing engines. The following sections of this paper discuss the design, principles of operation and application of vortex generators to axial flow compressors. Experimental results are presented which demonstrate the effectiveness of vortex generators in one axial compressor configuration.

PART I - VORTEX GENERATOR DESIGN CONCEPTS

Several factors govern the choice of vortex generator configuration. First, should the design produce co-rotating or counter-rotating vortices? Successful examples of both types exist for non-turbomachine applications. To succeed in beneficially influencing the casing boundary layer, it is obviously vital that the vortices remain on the casing. We have assumed that the mass of fluid in a vortex will behave according to the gyroscopic laws of motion. The reaction of a gyroscope to a force tending to tilt the axis of rotation is motion perpendicular both to the force and to the axis as illustrated in Fig. 1. If it is assumed that the circumferential pressure gradient from blade-to-blade within the rotor is equivalent to the applied force, then the direction of rotation of all vortices should be chosen such that the reaction of the vortex is toward the casing. This logic results in the vortex generators being staggered in the same direction as the downstream rotor blades, producing co-rotating vortices rotating in a direction opposite to that of rotor rotation.

The second most important consideration concerns vortex generator height. Reference (1) provides some useful empirical guidance concerning vortex generator design. Vortex generator height (h) is the length dimension with which all other length dimensions have been non-dimensionalized. One approach has been to make h equal to or slightly greater than the local boundary-layer displacement thickness. In the turbomachine, other considerations may be more important. For example, Reference (1) indicates that the vortices from

a well designed co-rotating configuration will remain effective up to a downstream distance of 80h to 100h. Furthermore, the vortices will not become fully effective until reaching a downstream distance of 10h to 30h. Consequently, since the vortices should remain effective at least across the full depth of the rotor, a minimum height can be arrived at by considering the rotor tip to lie between 30h and 80h measured from the plane of the vortex generators.

Several other judgements affecting vortex generator height were made on an intuitive basis. For example, it was felt that h should be at least twice the rotor tip running clearance so that the vortices would be large enough and energetic enough to mix low momentum tip leakage flow which would have a thickness closely related to the clearance. Also, since the spacing between vortex generators should lie between 4h and 8h (Reference (1)), the number of vortices desired per blade passage affects h. It was felt that a multiplicity of vortices per blade spacing would be most likely to influence the casing boundary layer beneficially while minimizing adverse effects on the main stream. Less than four vortices per blade spacing was judged undesirable; four or more were considered acceptable. Finally, manufacturing and operational considerations cannot be neglected. Ease and cost of manufacturing and mechanical integrity require that the minimum number (and maximum size) of vortex generators be chosen within the aerodynamically acceptable range of sizes.

Several other design criteria were also taken from Reference (1). Specifically, a good value for vortex generator chord length appears to be 4h. An effective setting angle for co-rotating designs is about 20 degrees from the flow direction for simple uncambered vanes. Also h should be not less than four times the vane thickness so that the vane behaves aerodynamically more like an airfoil than a blunt object.

The only known published investigation of vortex generators mounted in a compressor casing, upstream of a rotor, was documented in Reference 5. The tests were unsuccessful, in our opinion, because counter-rotating vortices, not co-rotating, were produced and the vortex generators were spaced too closely, only 2.7h apart rather than the minimum of 4h recommended. The counter-rotating vortices reacted oppositely under the influence of the rotor pressure gradient

and the close spacing tended to promote rapid dissipation of each vortex by its neighbors with resultant poor penetration downstream.

PART II - EXPERIMENTAL TEST PROCEDURE

A vortex generator configuration was designed, built and tested in a single stage, high pressure ratio, supersonic axial flow compressor. The design and test of the compressor without vortex generators are described in References (2) and (3). This compressor was designed for an overall stage total pressure ratio of 3.06 to 1 at an isentropic efficiency of 81.5 percent. Design tip speed was 1600 ft/sec at standard inlet conditions, and the inlet hub/tip radius ratio was 0.75. No inlet guide vanes were used and the rotor design incorporated a "splitter vane" between each of the principal rotor airfoils. The splitter vane consisted of an airfoil located circumferentially mid-way in the downstream half of each rotor blade passage and extending full span.

The compressor tested was designed for diffusion levels beyond the range of past experience in both rotor and stator. This choice was deliberate in order to provide a suitable test bed for the evaluation of boundary layer control devices applicable to a compressor and to obtain data at values of diffusion factor above 0.5. The performance of the original design without splitter vanes in the rotor, reported in Reference (4), was extremely poor. The results obtained after the addition of splitter vanes, reported in Reference (3), represented a major improvement in both rotor and stage performance. No boundary layer control devices were installed in either of these baseline compressor configurations.

The test facility used was of the open-loop variety. A cross-section of the research compressor is shown in Fig. 2. The rotor was of integral construction, the blades and disc being machined from a single forging of titanium. The stator blades were individually inserted but were machined integrally with platforms at hub and tip. The rotor tip clearance was nominally about 0.025 inch at design conditions or about 0.8 percent of rotor tip chord.

The compressor research vehicle had a total of 133 sensors measuring aerodynamic parameters at various points throughout the stage and additional measurements were made throughout the facility. Compressor stage aerodynamic measurements consisted of total pressure and temperature at the stator leading edges and downstream of the stators. Static pressure measurements were made along the inner and outer flow path, on the suction and pressure surfaces of one pair of stator blades, and over the rotor tip. Test facility measurements consisted of rotor speed, facility mass flow rate, compressor inlet pressure, temperature and relative humidity. The experimental data were acquired on magnetic tape for later reduction. The performance of the rotor and stator blade elements was calculated and expressed in terms of the conventional parameters. The aerodynamic analysis of the data was accomplished in a manner analogous to the design using the geometry of the stage and the experimental measurements as inputs. The system of equations is solved in finite difference form by the streamline curvature method which includes a full treatment of the axisymmetric equations of motion of an inviscid fluid, including blade-force terms, and the assumption of a thermally-perfect gas as the working fluid. Wake and boundary layer blockages are determined such that experimental casing static pressures are matched by the calculated values. Computing stations may be located within the blade-rows, as well as at the blade edges and in the duct regions of the compressor. Computing stations need not be radial and may be curvilinear, defined by a series of points.

PART III - BASELINE COMPRESSOR PERFORMANCE AND VORTEX GENERATOR MODIFICATIONS

The mass-averaged performance of the rotor and of the completed compressor stage without vortex generators is tabulated in Table 1 and plotted in Fig. 3. At 100 percent design corrected speed, corrected flow was approximately 12 percent low, rotor efficiency was 5 points low, stage efficiency was 1/ points low, rotor total pressure ratio peaked at 3.36 versus a design value of 3.35, and stage total pressure ratio peaked at 2.71 versus 3.06, respectively. The compressor was throttled to stall at each corrected speed shown on the map. The data point nearest

stall was taken at a throttle opening approximately 0.5 percent further open than the setting which precipated stall. This change in throttle area is equivalent to about 0.9 percent of the annulus area at the rotor inlet.

The geometry and critical dimensions of the casing vortex generators tested are shown in Fig. 4. A total of 144 vortex generators were equally spaced on the compressor casing at a setting angle of 20° to the flow direction. The generators were individually fabricated from 0.25 inch wide, 0.010 inch thick nichrome ribbon and inserted through slots in four 0.5 inch wide, 0.040 inch thick strips of stainless steel. Each of the four metal strips covered a quarter of the casing inner circumference. Each vortex generator was spot welded on the back side of the pre-curved strips: these strips were then flush-mounted in the outer casing 1.69 inches upstream of the rotor leading edge plane.

With vortex generators installed, a complete performance map was obtained. The mass-averaged performance of the rotor and of the complete compressor stage with vortex generators (configuration 3) is tabulated in Table 2 and compared with the maximum efficiency points for the original configuration (configuration 2). Compared with the baseline build rotor performance at design speed, maximum flow increased from 88 percent design flow to 90 percent design flow, maximum rotor total pressure ratio increased from 3.36 to 3.42, and maximum rotor isentropic efficiency increased from 84.7 percent to 86.1 percent. Stage performance increased by comparable amounts and similar improvements were observed over the entire speed range, as indicated in Table 2.

PART IV - DISCUSSION OF RESULTS AND RECOMMENDATIONS

This investigation of the applicability of vortex generators for casing tip treatment demonstrated the anticipated gain in rotor efficiency and improvement in stall margin through increased overall pressure ratio. The profile losses associated with the addition of the vortex generators were outweighed by the benefits derived with a total effect of improved efficiency. No changes were made to tip clearance during this investigation.

Among other parameters, the aerodynamic analysis of the test data produced distributions of diffusion factor and total pressure loss coefficient through the compressor flow path. For design purposes,

the total pressure loss coefficient was assumed to be the sum of the shock losses and diffusion losses (which include secondary flow losses). The addition of vortex generators produced increases in flow and overall pressure ratio which allow the rotor to operate at higher levels of diffusion. The improved efficiency resulted from reduced losses principally associated with reduced diffusion losses. Since the diffusion levels were higher with vortex generators than without, it is presumed that the reduction in diffusion losses was associated with reduced secondary flow losses. The distributions of diffusion factor and diffusion loss parameter across the annulus at the rotor trailing edge at the design speed, peak efficiency operating point are shown in Fig. 5, with and without vortex generators. Definitions for diffusion factor, total pressure loss coefficient and diffusion loss parameter are the customary ones and can be found in Reference 6.

The reduced diffusion losses and increased efficiency were distributed uniformly across the entire annulus. The effects of the vortex generators were not confined to the rotor tip region. The compressor configuration investigated was characterized by strong shock waves and high levels of diffusion. The strong secondary flows undoubtly present in this design enhanced rapid mixing of the energized casing boundary layer flow and provided a means by which the effects of the vortex generators were effectively distributed across the entire annulus. This mixing would presumably be more rapid for low aspect ratio stages, such as the compressor configuration investigated.

For the axial compressor configuration investigated, it was encouraging to find that the addition of vortex generators actually improved the overall efficiency, over and above the inherent profile losses which the vortex generators introduced. It is conceivable that tip clearance might be relaxed using vortex generators with less loss in overall performance. This suspicion has yet to be verified, but experiments are currently being conducted to investigate the interaction of casing vortex generators and varying tip clearance on a low hub/tip ratio transonic compressor stage. Preliminary results using vortex generators on this compressor with a tight tip clearance have been completed. This compressor incorporated a rotor with a much lower inlet hub to tip ratio and higher aspect ratio that the High Pressure Ratio rotor. This rotor was transonic, but the tip relative Mach

number was nearly the same as for the HPR rotor. The transonic rotor was not as highly loaded as the HPR rotor and the pressure ratio was lower.

The use of vortex generators on the transonic compressor with design tip clearance (0.3 percent of tip cord) produced an increase in overall efficiency across the entire speed range. At design speed, the stage efficiency increased about 1.0 percent with little change in pressure ratio or flow. The baseline compressor pumped design flow, slightly higher than design pressure ratio, had very high efficiency and did not have an unusually adverse tip condition. The addition of vortex generators again demonstrated their ability to increase the overall efficiency, more than offsetting their own profile losses. Future tests will be conducted to investigate the effects of increased tip clearance with and without vortex generators. Hopefully, the addition of vortex generators will produce sufficient gains to maintain the baseline build performance at increased clearance.

The design of the vortex generators used on the transonic compressor followed the guides outlined earlier. However, the manufacturing process was modified with respect to the manner in which the slots in the stainless steel strips were machined. The original (HPR Compressor) slots were Electrical-Discharge-Machined (EDM) whereas the latter (transonic compressor) slots were punched. The latter technique was found to be acceptable and much cheaper.

PART V - CONCLUSIONS

The use of vortex generators as casing tip treatment has been demonstrated to be effective in producing increased efficiency and stall margin in some axial compressor applications. Compared to typical forms of tip treatment in use today, the use of vortex generators does not require as elaborate modifications to the casing and could be easily and cheaply retrofitted to existing engines. The method consisted of placement of a row of vortex generators on the outer casing of an axial compressor, upstream of the rotor, for the purpose of energizing the fluid boundary layer on the outer casing adjacent to the rotor tips. The aerodynamic effect of energizing the casing boundary layer adjacent to the compressor rotor was to improve the efficiency of the flow across the entire annulus and to delay stall at the rotor tip. Performance

increases would be expected to be greater for low aspect ratio stages which are highly loaded. The presence of casing wall boundary layer separation, rotor flow separation, and strong secondary flow effects contribute to rapid mixing of the energized casing boundary layer flow across the annulus. While the gains in performance using vortex generators have only been demonstrated on axial compressors the potential exists for similar improvements in the performance of centrifugal compressors. Centrifugal compressors are typically highly loaded low aspect ratio configurations in which secondary flow effects are substantial.

REFERENCES

1. G.V. Lachmann (Editor), "Boundary Layer and Flow Control", Vol. II, pp 1281-1286, Pergamon Press, New York 1961

2. A.J. Wennerstrom and G.R. Frost, "Design of a Rotor Incorporating Splitter Vanes for a High Pressure Ratio Supersonic Axial Compressor Stage." Aerospace Research Laboratories, Wright-Patterson AFB, Ohio. ARL-TR-74-0110, AD786025, August 1974

3. A.J. Wennerstrom, W.A. Buzzell, and R.D. DeRose, "Test of a Supersonic Axial Compressor Stage Incorporating Splitter Vanes in the Rotor." Aerospace Research Laboratories, Wright-Patterson AFB OH ARL-TR-75-0165, Jun 75

4. 4. A.J. Wennerstrom, G.R. Frost, and R.D. DeRose, "Test of an Axial Compressor Stage Designed for a Total Pressure of Three to One." Aerospace Research Laboratories, Wright-Patterson AFB OH. ARL-TR-74-001, AD778844, Jan 74

5. K.G. Harley, J. Harris, and E.A. Burdsall, "High-Loading Low-Speed Fan Study, III. Data and Performance Slotted Blades and Vanes, Rotor Tip Treatment." NASA-Lewis Research Center, Cleveland, OH NASA CR-2895. Jul 71

6. I.A. Johnsen and R.O. Bullock, "Aerodynamic Design of Axial-Flow Compressors." NASA-Lewis Research Center, Cleveland, OH. NASA SP-36, 1965, pp 201-205

Table 1 - Performance of Supersonic Compressor Without Vortex Generators

PERCENT DESIGN RPM	CONF. NO.	FLOW (LB/SEC)	ROTOR PRES. RATIO	ROTOR EFF	STAGE PRES. RATIO	STAGE EFF
40	2	11.85	1.231	.933	1.184	.754
40	2	11.22	1.239	.919	1.215	.834
40	2	10.22	1.250	.907	1.233	.849
40	2	9.40	1.255	.876	1.238	.823
40	2	8.91	1.254	.860	1.234	.797
40	2	8.62	1.255	.855	1.234	.790
60	2	15.59	1.633	.910	1.540	.795
60	2	15.64	1.630	.911	1.491	.735
60	2	15.60	1.629	.910	1.440	.668
60	2	15.01	1.640	.901	1.569	.816
60	2	14.57	1.639	.880	1.577	.806
60	2	13.87	1.637	.862	1.573	.787
80	2	19.96	2.277	.879	1.964	.706
80	2	19.87	2.278	.875	1.962	.701
80	2	19.73	2.279	.875	2.008	.727
80	2	19.69	2.275	.874	2.052	.753
90	2	21.90	2.695	.846	2.286	.689
90	2	21.80	2.695	.846	2.308	.698
90	2	21.75	2.697	.845	2.324	.703
90	2	21.83	2.696	.847	2.258	.678
100	2	25.56	3.352	.844	2.699	.671
100	2	25.63	3.344	.843	2.708	.674
100	2	25.76	3.353	.847	2.645	.657
100	2	26.04	3.362	.846	2.682	.665

Table 2 - Comparison of Performance at Maximum Efficiency Points With (3) and Without (2) Vortex Generators

PERCENT DESIGN RPM	CONF. NO.	FLOW (LB/SEC)	ROTOR PRES. RATIO	ROTOR EFF	STAGE PRES. RATIO	STAGE EFF
40	2	10.22	1.250	.907	1.233	.849
40	3	10.27	1.252	.909	1.231	.859
60	2	15.01	1.640	.901	1.569	.816
60	3	15.28	1.637	.917	1.566	.830
80	2	19.69	2.275	.874	2.052	.753
80	3	19.90	2.285	.887	2.080	.776
90	2	21.75	2.697	.845	2.324	.703
90	3	22.19	2.718	.864	2.335	.717
100	2	25.63	3.344	.843	2.708	.674
100	3	25.86	3.418	.859	2.806	.700

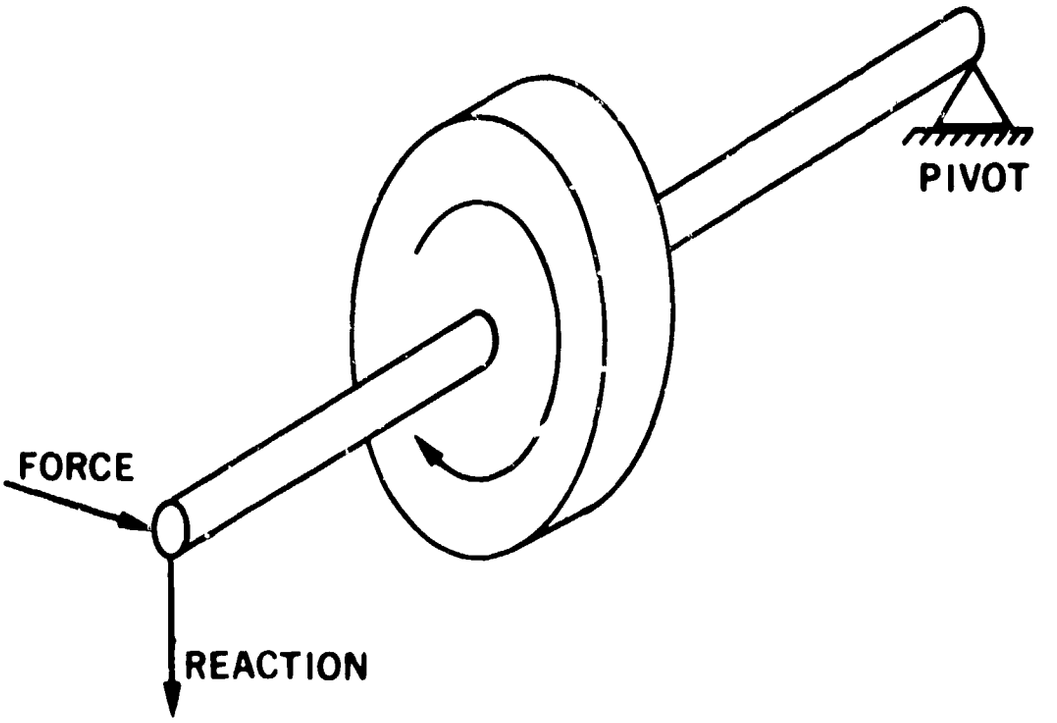

Fig. 1 - Reaction of a gyroscope to a force

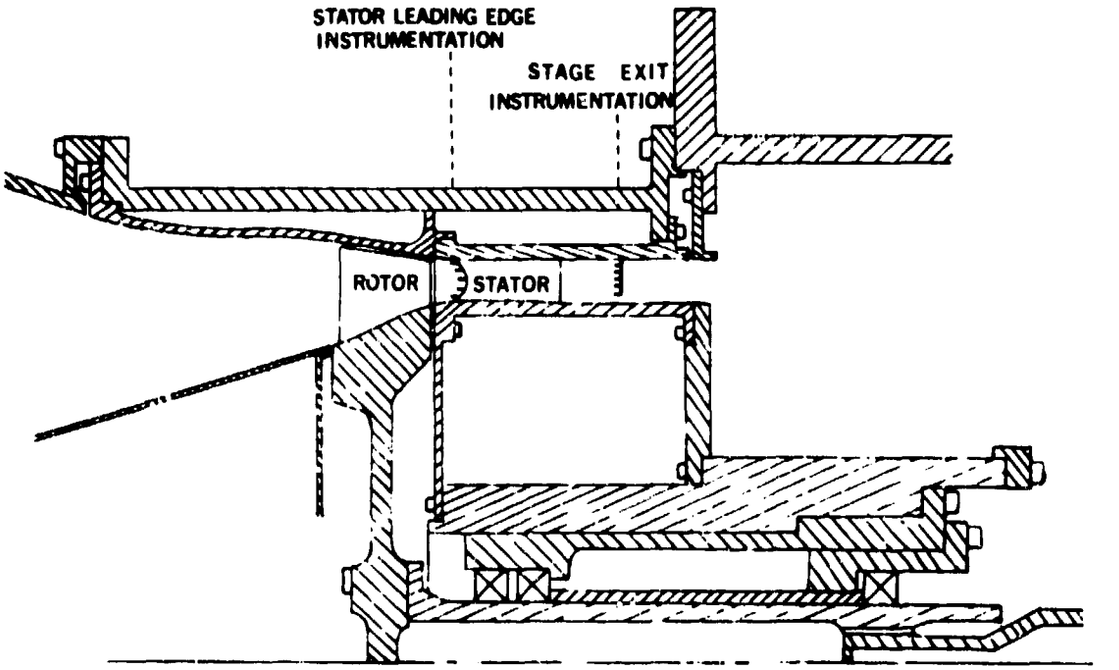

Fig. 2 - Cross section of supersonic research compressor

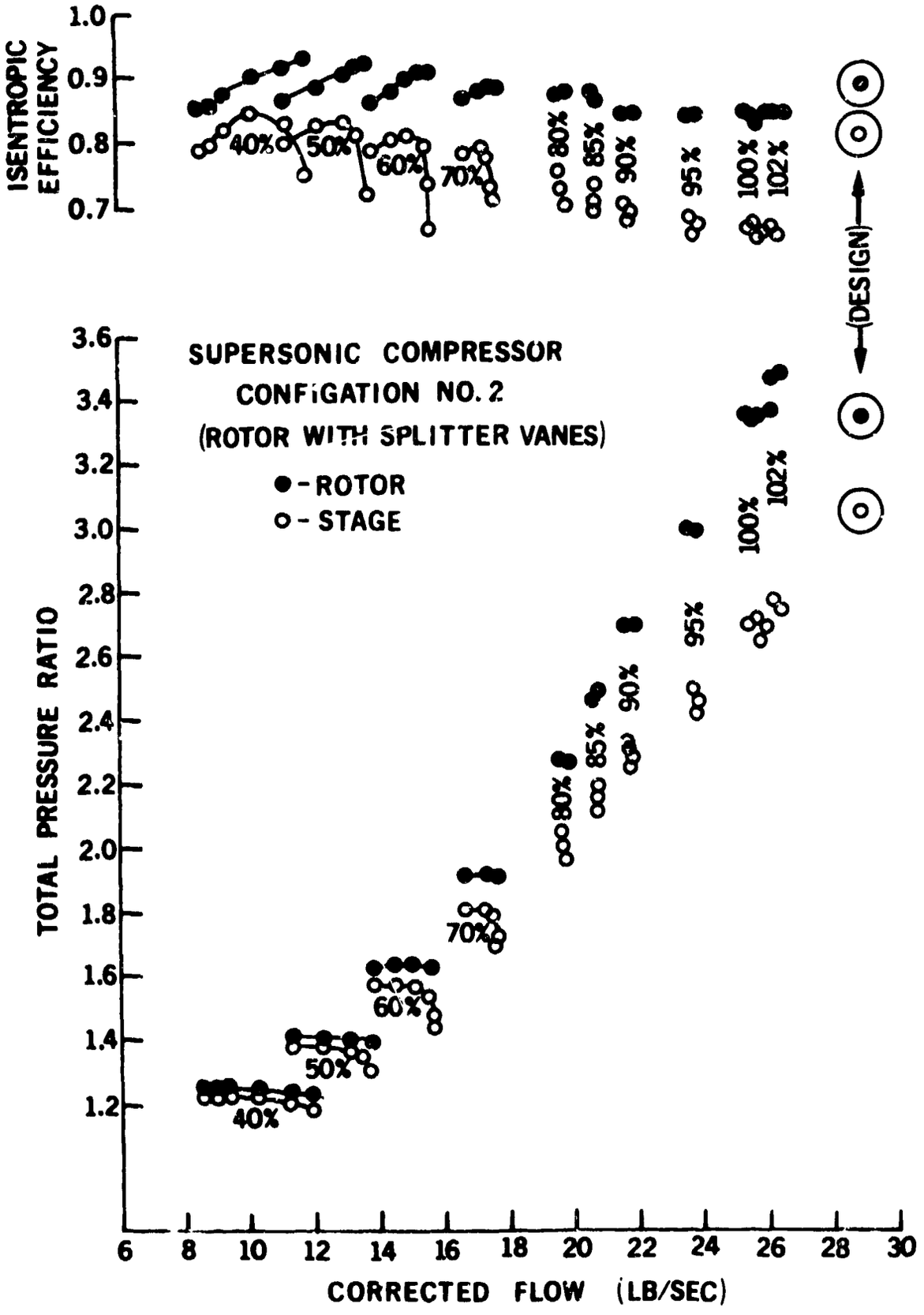

Fig. 3 - Performance map of supersonic compressor without vortex generators

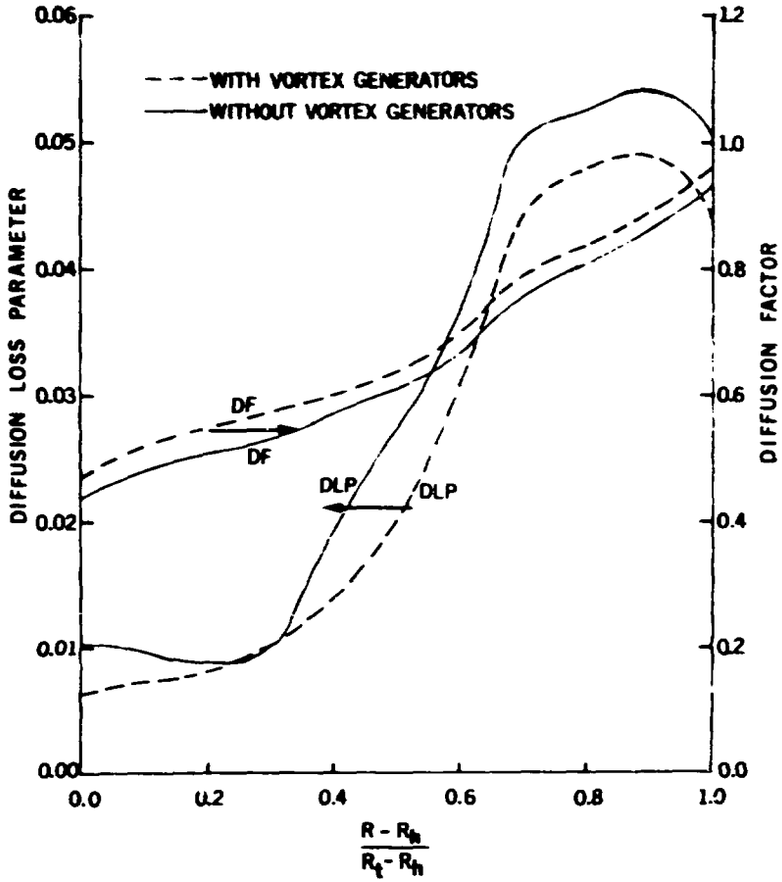

Fig. 5 - Distributions of diffusion factor and diffusion loss across the annulus at the rotor trailing edge for the supersonic compressor with and without vortex generators

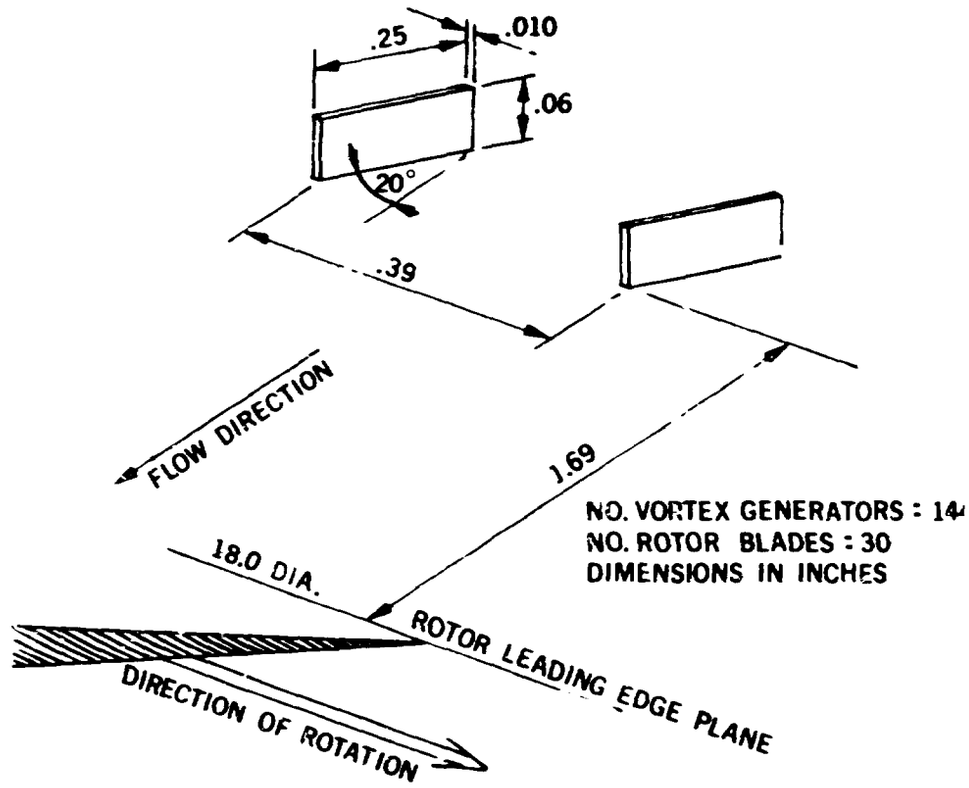

Fig. 4 - Geometry of casing vortex generators

AD P000331

DEGRADATION OF A LASER BEAM BY A TURBULENT JET

by

G. F. Cudahy, J. T. Van Kuren, H. E. Wright
Air Force Flight Dynamics Laboratory
Wright-Patterson Air Force Base, OH

A laser beam traversing turbulence undergoes an intensity reduction which is correlated with the statistical behavior of refractive index perturbations. The analytical relation predicts degradation as a function of beam diameter, path length, wave number and wave structure function. Refractive index perturbations are approximated via the equations of state, using temperature and velocity perturbations. An experiment was conducted in which visible wavelength lasers traversed a well documented two-dimensional jet. Temperature perturbations vary from 0.25 to 1.89 ^{o}K and velocity fluctuations range from 9.2 to 30.8 m/sec. Measured central spot intensities are as low as 18% of the undisturbed beam, depending on jet Mach number, beam position relative to the jet exit and wavelength. The average difference between theory and experiment is two percent in terms of far field intensity.

Manuscript received June 1981.
Portions of this work were reported earlier in the AFIT Ph.D. Thesis of Col. Cudahy.

DEGRADATION OF A LASER BEAM BY A TURBULENT JET

G. F. Cudahy*
Director Fighter/Attack System Program Office
Aeronautical Systems Division

J. T. Van Kuren†
Air Force Wright Aeronautical Laboratories
Flight Dynamics Laboratory

H. E. Wright‡
Department of Aeronautics and Astronautics
Air Force Institute of Technology

A laser beam traversing turbulence undergoes an intensity reduction which is correlated with the statistical behavior of refractive index perturbations. The analytical relation predicts degradation as a function of beam diameter, path length, wave number, and wave structure function. Refractive index perturbations are approximated via the equations of state, using temperature and velocity perturbations. An experiment was conducted in which visible wavelength lasers traversed a well-documented, two-dimensional jet. Temperature perturbations vary from 0.25 to 1.89 K, and velocity fluctuations range from 9.2 to 30.8 m/s. Measured central spot intensities are as low as 18% of the undisturbed beam, depending on jet Mach number, beam position relative to the jet exit, and wavelength. The average difference between theory and experiment is 2% in terms of far-field intensity.

Nomenclature

B = correlation function

C = constant

F = focal length of far-field forming lens

---

* Colonel, USAF.
† Aerospace Engineer.
‡ Professor.

I = laser beam intensity

J_o = Bessel function of the first kind of order zero

k = wave number of the laser beam

L = beam path length through turbulence

L_o = turbulence outer scale or integral scale

m = correction constant in temperature correlation

N = refractive index perturbations

P = pressure

R = input beam radius

r = optical radius in the near field

S = optical radius at which the Gaussian input beam is truncated

s = optical radius in the far field

T = modulation transfer function (MTF)

U = velocity

x = coordinate in the direction of the jet

y = coordinate in the direction of the laser beam

z = coordinate normal to beam and jet

λ = wavelength

ρ = density

θ = temperature

Subscripts

d = relative to input beam diameter

i = finite-difference index

lens = far-field forming lens

m,q = variable indices

n = index of refraction

o = turbulence or unperturbed value; or relative to initial jet size

p = pressure

u = velocity

θ = temperature

θ_s = measured value

τ = turbulence refractive index

1,2 = time indices

I. Introduction

Over the years joint research projects of the former Aerospace Research Laboratory and the Air Force Institute of Technology and in more recent years between the Air Force Aero-Propulsion Laboratory (currently AFWAL/P) and the Institute of Technology concerning the diagnostics of flow fields has received excellent guidance under the leadership of Dr. Hans von Ohain. The activity has included schlieren, shadowgraph, Moire, laser velocimeter, and holographic systems. These systems all utilize collimated light sources as part of the diagnostic system while the last two use a collimated coherent light beam. This paper deals with one aspect of this work, namely the interaction between the light beam and a shear flow field.

The effect that the turbulent flow field of a high subsonic Mach number, two-dimensional jet shear layer produces on a coherent light beam has not been quantified. The refractive index perturbations cause a decrease in the central spot intensity of the beam in the far field because the total energy is spread over a larger area than in the unperturbated case. Furthermore, the long-time average at the mean location of the central spot is decreased by beam wandering. Numerous theoretical and experimental efforts have been presented concerning the propagation of laser beams through natural atmospheric turbulence; however, in the atmosphere, the absolute intensities of the velocity, temperature, and pressure perturbations are relatively low, the beam path lengths are usually

long, and the turbulence scales are quite large compared to beam diameter[1-6]. Recently, lasers have been used for wind tunnel diagnostics and in certain applications involving propagation out of aircraft, in which case the beams must pass through boundary layers and free shear layers where the turbulence scales are the same order as the beam size.

The present study was an attempt to provide a controlled, well-documented turbulence field and to correlate the degradation of the far-field central spot intensity formed by a collimated coherent light beam traversing the high-intensity turbulence of a shear layer. In addition, an attempt was made to measure the spreading of the energy over a larger area in the far field (termed broadening) and the motion of the beam in the far field (called wandering).

A two-dimensional jet with a well-designed stilling chamber and subsonic nozzle was fabricated. This setup also provided double shear layers for added sensitivity. The uniform velocity coreflow could be varied with Mach numbers ranging from 0.4 to 0.8 to emphasize the compressible regime. To determine if wavelength and beam size relative to turbulence scale were important, two laser frequencies were used and three beam sizes were used at each frequency. The beam traversed the turbulent jet successively at 25, 50, and 75 nozzle widths downstream from the nozzle exit.

II. Theoretical Considerations

The purpose of this study is to determine the far-field central spot reduction in intensity caused by the turbulence-induced refractive index perturbations through which the laser-generated Gaussian plane wave propagates. For homogeneous, isotropic turbulence, the transformation of the laser beam from the area of turbulence perturbations to the observation point in the far field can be described by:

$$I(S) = C \int_{\theta}^{S} T_{lens}(r)T_{\tau}(r)T_{d}(r)J_{o}(\frac{2\pi Sr}{F\lambda})rdr \qquad (1)$$

The far-field forming lens MTF reduces to approximate unity if the lens diameter is larger than the truncated beam diameter, and the far field is observed in the focal plane of the lens. Equation (1) is a Hankel transformation which derives from a Fourier transformation when the function to be transformed has circular symmetry.

The cylindrical coordinates r and s are perpendicular to the y axis, which lies on the center of the laser beam and is positive in the direction of the beam propagation. The x axis has its origin on the center of the beam and is positive in the direction of the airflow exhausting from the nozzle. The z axis is normal to the beam and the jet.

A correlation function is defined as:

$$B_{mq}(r,y) \equiv \langle m(\bar{r}_1,\bar{y}_1)q(\bar{r}_2,\bar{y}_2)\rangle \qquad (2)$$

and is the statistical measure of the interdependence of the variables being correlated.

Owens[7] shows that the refractive index for dry air and 5328 Å light is:

$$N \simeq 1 + (79.0 \times 10^{-6})(P/\theta) \qquad (3)$$

where P is the pressure in millibars and θ is the temperature in Kelvin.

Elimination of the steady-state portion of Equation (3) and dropping of the second-order terms yields

$$n = (79.0 \times 10^{-6})(\frac{P}{\bar{\theta}} - \frac{P\bar{\theta}}{\bar{\theta}^2}) \qquad (4)$$

For homogeneous, isotropic turbulence, the refractive index correlation function can now be described in terms of the turbulence pressure and temperature perturbations.

$$B_n(r) = (79.0 \times 10^{-6})^2 \left[\frac{B_p(r)}{\bar{\theta}^2} + \frac{\bar{P}^2}{\bar{\theta}^4} B_\theta(r) \right] \tag{5}$$

As a result of heuristic arguments, it is assumed that

$$\frac{2\bar{P}}{\bar{\theta}^3} B_{p\theta}(r) << \frac{B_p(r)}{\bar{\theta}^2} + \frac{\bar{P}^2}{\bar{\theta}^4} B_\theta(r) \tag{6}$$

and that $B_p(r)$ and $B_\theta(r)$ are of the same order.

The assumed relationship between pressure perturbations and velocity perturbations, based on results of several authors[8], is

$$B_p(r) = (\rho^2/2) B_u(r)^2 \tag{7}$$

The ability to measure accurately the high-frequency temperature perturbations also proves to be difficult. Analysis show the mild dependence of the frequency response of a thin finite length unheated wire upon mean velocity. It also shows that the frequency response of a typical wire probe is insufficient to measure the small-size eddies expected in the type of flow used in this investigation. A method was developed to correct the temperature correlation function, which is obtained with a temperature sensor of inadequate frequency response. The correction is based on two concepts. The first is that the normalized temperature and velocity correlation functions at the same point in space in the same homogeneous flow field are almost identical[9,6].

The second concept is that the correlation function at large r has complete dependence upon the flow field eddies with wavelengths larger than r[9]. Using the two concepts, a correction to the measured correlation function was developed

$$B_\theta(r) = m B_{\theta s}(0) \hat{B}_u(r) \tag{8}$$

Now, the final form of the turbulence MTF, which was used in this study, can be presented.

$$T_\tau = \exp\left[-4k^2 L \int_0^\infty [B_n(y) - B_n(\sqrt{r^2 + y^2})]dy\right] \tag{9}$$

Substitution of Eqs. (5) and (7) into Eq. (9) yields, for smoothly varying turbulence characteristics in the direction of beam propagation, where N layers of homogeneous turbulence are assumed,

$$T_\tau = \exp\left[-4k^2(79 \times 10^{-6})^2 \sum_{i=1}^{N}\left[\frac{\Delta L_i}{\bar{\theta}_i^4}\int_0^\infty \left(\frac{\rho_i^2 \bar{\theta}_i^2}{2}\left[B_{ui}^2(y) - B_{ui}^2(\sqrt{r^2 + y^2})\right] + \bar{P}_i^2\left[B_{\theta i}(y) - B_{\theta i}(\sqrt{r^2 + y^2})\right]\right)dy\right]\right] \tag{10}$$

In order to find the modulation transfer function of the unperturbed beam intensity, the unperturbed beam amplitude is transformed into the observation plane, that is, the far field. The unperturbed beams prior to the turbulence field are Gaussian plane waves, whose amplitude is symmetrical about the y axis. The input beam modulation transfer function T_D has been shown in Ref. 8.

The modulation transfer functions for the turbulence-induced refractive index perturbations, as determined by Eq. (10), is a statistical quantity, in that the time of measurement of the velocity and temperature perturbations is large as compared to the time scale of the turbulence, $L_0/\bar{U}$[10]. The far-field intensity, as determined by Eq. (1), when using these statistical quantities for the turbulence MTF is, therefore, an average intensity. If the perturbed intensity is normalized by the unperturbed central spot intensity, and the lens and beam amplitude MTFs are substituted into Eq. (1),

$$\frac{I(s)}{I_0(0)} = \hat{I}(s)$$

$$= \left[\int_0^S e^{-r^2/2R^2}\, T_\tau J_0\left(\frac{2\pi rs}{F\lambda}\right) rdr\right] \Big/ \left[\int_0^S e^{-r^2/2R^2}\, rdr\right] \tag{11}$$

If, as in this investigation, the far-field central spot intensity is the variable of interest, Eq. (11) becomes $\hat{I}(0)$.

III. Experiments

Laser Beam Generation

The lasers used were the Spectra Physics Model 124A with Model 255 Exciter, which is a 15 mW He-Ne laser with a 6328 Å output, and a Spectra Physics Model 285 Exciter, which is a He-Cd laser with a 4416 Å output. The beam-

Table 1 Test Conditions

Mach number	0.4	0.6	0.8
Test station, cm	25	50	75
Wavelength, Å		6328	4416
Beam size, 2R (mm)	50.0	26.0	12.3

forming telescope attached to the output port of each laser was a Spectra Physics Model 336 collimating lens utilizing Spectra Physics Model 332 spatial filters. The expanding lenses and spatial filters were chosen to yield approximate Gaussian beams of diameters shown in Table 1.

Far-Field Measurements

Figure 1 shows the physical layout of the far-field forming and detection equipment. The far field was formed in the focal plane of a lens which was

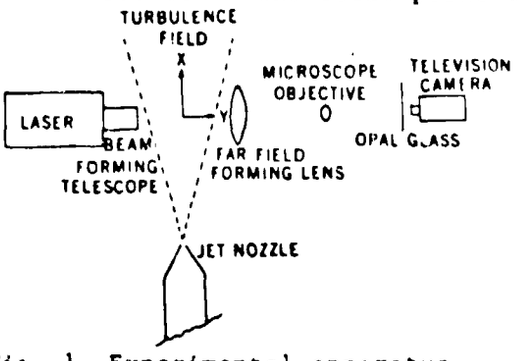

Fig. 1 Experimental apparatus.

considerably larger than the largest laser beam tested. The far field was observed by means of a microscope objective projecting the far-field image onto an opal glass and the output of the camera was viewed on an oscilloscope. A digital counter was used to provide external synchronization to the oscilloscope, such that the amplitude of any desired horizontal line or groups of horizontal lines may be viewed. These amplitudes were recorded with a polaroid camera.

The recording of the perturbed beam's far field spot in a very short time, in order to separate degradation due to beam broadening from that due to beam wandering, was one of the goals of the experiment. If the videcon could be single-line scanned, the laser beam integration time on the target could be greatly reduced, thus reducing the persistence of the image of the laser beam on the target. This would then increase the frequency response of the laser beam measuring capability. The silicon target videcon could be single-line scanned without significantly degrading the videcon output; thus, the silicon target videcon was chosen to be the laser beam far-field spot detection device.

Several prerequisites were imposed on the turbulent refractive index field to be generated. The turbulence had to be classical, precisely duplicatable from test to test, fairly uniform across the laser beam, vary smoothly in the direction of laser beam propagation, and have no physical surfaces in the immediate vicinity of the turbulent field through which the beam would have to propagate. This led to the choice of a free jet issuing into quiescent room air. The free jet is well documented analytically and experimentally[9,11].

Free Jet Nozzle

The constraint of uniformity across the laser beam in planes perpendicular to the direction of propagation is most closely satisfied by a plane free jet.

A 1 x 10 cm knife-edge nozzle was chosen to provide an approximation to a plane free jet. The nozzle was symmetrically convergent to the exit, except that the last 1 cm of the nozzle inside face is parallel to the x direction. The transitions from the convergent sections to the exit faces were well rounded. At 25, 50, and 75 nozzle widths downstream from the nozzle exit, the laser beam turbulent field path lengths are approximately 10, 20, and 30 cm, respectively, and, at these locations, the turbulence field is fully developed.

The desire to trace the turbulent field origin to the shear layer caused by the free jet issuing into quiescent laboratory air dictated laminar flow in the nozzle exhause plane. Also, most free jet theories assume that the nozzle exit velocity is uniform. Therefore, the nozzle exit velocity design specifications required a turbulence intensity of less than 1% and a uniform mean velocity across the entire exhaust plane.

Two basic requirements for the turbulence measuring equipment were established - one was to determine whether the turbulence was well defined and repeatable, and the other was to obtain the turbulence information required to fulfill the demands of this experiment.

The primary instrumentation for the turbulence measurements was a Thermo-Systems, Inc., (TSI) anemometer system using fine wire sensors and associated equipment.

TSI Model 1050 anemometers were used to process signals from the fine wire sensors during calibration and data collection. For velocity measurements, both mean and perturbations, the anemometers were operated in the constant temperature mode with their electrical circuits optimized for maximum frequency response. The sensors were operated at a temperature several hundred degrees above the flow mean temperature in order to achieve maximum sensitivity to velocity perturbations. For temperature perturbation measure-

ments, only one sensor and one anemometer were used and the anemometer was operated in the constant-current mode with a very small sensing current flowing in the wire sensor; thus, the sensor temperature followed the temperature of the fluid.

Sensors 4μ in diameter were selected, since they were readily available and gave acceptable frequency response for velocity measurements. However, they did not give a completely acceptable frequency response for measuring temperature perturbations.

Using the constant temperature anemometry system, including single-wire sensor and linearizer with proper coefficients, the jet nozzle exit flow was examined at the three exit velocities selected for this study in order to determine uniformity of the velocity, time variance of velocity, turbulence intensity, and velocity measured vs calculated from total conditions. The exit velocity was very nearly constant across the nozzle exit plane. The boundary layer was less than 0.2 mm thick. The turbulence intensity was less than 0.3%; that is, the rms turbulence velocity was less than 0.3% of the mean flow velocity for all exit velocities examined. The 0.3% value was established as the measuring system limitation due to electronic noise.

Next, the jet flow and turbulence field were examined using the constant temperature anemometry system. The jet was symmetrical in the vertical and horizontal directions about the x axis. The maximum mean velocity occurred along the x axis. The spread of the jet calculated by taking $\bar{U}_{loc}/\bar{U}_{cen} = 1/2$ shows a half-angle of 5.0 deg, as compared to predicted values of 6.5 deg for a plane jet and 5.0 deg for a round jet.

Figure 2 shows the nondimensionalized mean velocities at 25, 50, and 75 jet nozzle widths downstream from the nozzle exit. Here $Y_{1/2}$ is the point at each test station where $U_{loc} = 1/2\ U_{cen}$ and is used to nondimensionalize the

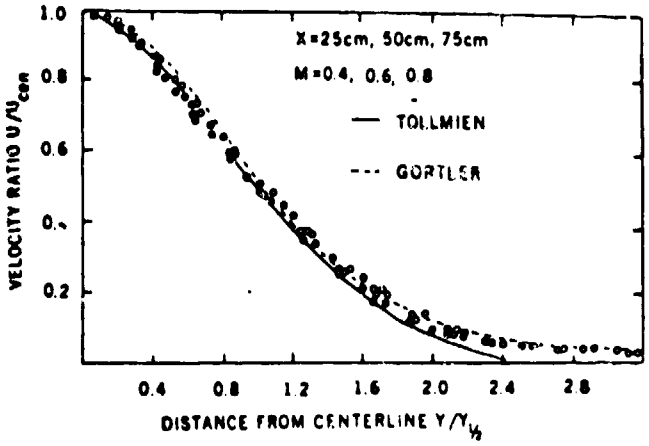

Fig. 2 Velocity similarity.

measurement distance from the x axis in the y direction, and U_{cen} is the velocity on the centerline and is the nondimensionalizing parameter. Figure 2 shows that the flow mean velocities were similar and agreed closely with the theoretical values of Gortler and Tollmien.

The nondimensionalized turbulence intensity profiles for all three test planes and test velocities are shown in Fig. 3. The turbulence intensities

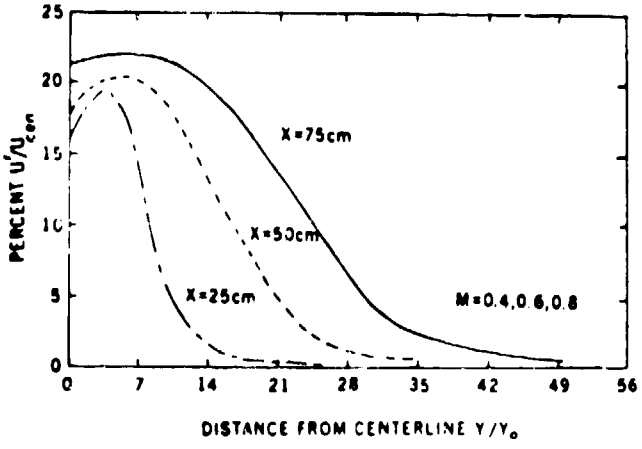

Fig. 3 Turbulence intensity profiles.

were similar in each test plane, and the point of maximum intensity spreads at half angle of approximately 3 deg in the direction of the jet flow. Additional information about the flowfield generated by the nozzle used in this experiment can be obtained from Ref. 11.

Initially, the Spectra Physics Model 336 collimating lens, together with the Spectra Physics Model 332 spatial filters, was adjusted to give a symmetrical beam with maximum central spot intensity as measured by a Spectra Physics 401C power meter. The power meter was equipped with a small aperture and was scanned across the beam close to the exit of the collimating lens to insure symmetry and also to determine the points at which the central spot intensity value was reduced by exp (-2). The beam diameter was defined as the distance between two diagonally opposed points at which the maximum intensity was reduced by exp (-2).

IV. Results

Turbulence Characteristics Used to Predict Laser Beam Degradation

The refractive index perturbations, which have the major effect on the laser beam degradation of this investigation, were caused by turbulence-induced density variations in the active medium through which the laser beam propagates. These density variations were not amenable to direct measurement; thus, the equation of state was used to determine turbulent density variations via other readily measurable turbulence quantities. It was determined that velocity and temperature perturbations could be transformed into density and, subsequently, refractive index perturbations. Since the frequency response of the temperature measuring device was insufficient for the temperature field to be measured, a method was developed to correct the temperature measurements obtained with this device.

The measurement and recording of instantaneous turbulent flow field characteristics for the entire flow field area of interest for a given experimental configuration of investigation were not possible. Statistical characterization of the turbulent flow field was, therefore, resorted to, and the prediction of the laser beam degradation was then necessarily limited to average degradation.

The turbulence parameters used to predict the laser beam degradation were the spatial temperature correlation function, spatial velocity correlation function, and the path length of turbulence field thickness associated with each correlation function. The correlation functions actually measured were temporal correlation functions. These functions and Taylor's hypothesis were used to approximate the spatial correlation functions.

Figure 4 shows an example of temperature correlation functions. The time scale equals 33.3 μs. Notice that correlation is imperfect at short time

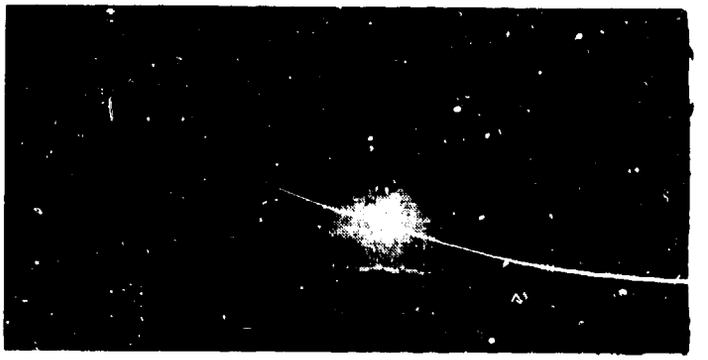

Fig. 4 Temperature correlation function at Mach 0.4, 25 cm station, y = 1.5 cm.

scales. As discussed earlier, the frequency response of the constant current anemometer system, used to measure the temperature perturbations of the turbulent field of this study, was insufficient for many of the flow conditions experienced.

Table 2 lists the rms velocity perturbations, rms measured temperature perturbations, temperature correction factors, corrected rms temperature perturbations, thickness of turbulence field each of these measurements represents, and mean velocity of the flow field for each of these measurements. The Mach number and downstream test station of each set of parameters is also given.

Predicted vs Measured Unperturbed Laser Beam Far-Field Spot Profiles

In order to compare the unperturbed beam intensity profile actually detected

Table 2 Turbulence Parameters

Location Test station	y, cm	Mach no.	u, m/s	θ_{rr}, K	$\sqrt{m}$	θ, K	Δl, cm	U, m/s
25	0	0.8	24.0	1.23	1.4	1.72	0.5	156.0
25	0.5	0.8	26.4	1.31	1.4	1.83	1.0	147.0
25	1.0	0.8	29.0	1.35	1.4	1.89	1.0	133.0
25	1.5	0.8	30.8	1.29	1.4	1.81	1.0	114.0
25	2.0	0.8	30.4	1.23	1.3	1.60	1.5	91.8
25	3.0	0.8	25.6	1.09	1.1	1.20	2.0	54.0
25	4.0	0.8	17.6	0.87	1.15	1.00	2.0	27.0
25	5.0	0.8	8.0	0.44	1.1	0.48	2.0	12.4
50	0	0.8	18.4	0.88	1.3	1.15	1.0	112.0
50	1.0	0.8	19.6	0.93	1.4	1.31	2.0	107.0
50	2.0	0.8	21.0	0.91	1.2	1.10	2.0	92.6
50	3.0	0.8	22.2	0.83	1.1	0.92	2.0	77.8
50	4.0	0.8	21.4	0.72	1.1	0.79	2.0	63.4
50	5.0	0.8	19.6	0.62	1.05	0.65	2.0	51.2
50	6.0	0.8	17.4	0.53	1.05	0.55	3.0	38.6
50	8.0	0.8	11.4	0.36	1.0	0.36	4.0	19.4
50	10.0	0.8	5.8	0.26	1.0	0.26	4.0	16.1
75	0	0.8	16.6	0.61	1.0	0.61	2.0	87.6
75	2.0	0.8	17.8	0.62	1.0	0.62	4.0	78.9
75	4.0	0.8	18.4	0.57	1.0	0.57	4.0	65.0
75	6.0	0.8	17.4	0.48	1.0	0.48	4.0	50.8
75	8.0	0.8	15.2	0.38	1.0	0.38	4.0	36.0
75	10.0	0.8	12.7	0.29	1.0	0.29	6.0	25.6
25	0	0.6	19.6	0.77	1.46	1.12	0.5	119.0
25	0.5	0.6	21.0	0.81	1.09	1.0	1.0	112.0
25	1.0	0.6	23.0	0.82	1.3	1.06	1.0	99.4
25	1.5	0.6	23.6	0.79	1.3	1.02	1.0	85.8
25	2.0	0.6	23.0	0.72	1.1	0.79	1.5	70.8
25	3.0	0.6	20.0	0.62	1.05	0.65	2.0	43.1
25	4.0	0.6	13.6	0.26	1.1	0.29	2.0	21.6
25	5.0	0.6	6.8	0.17	1.0	0.17	2.0	8.6
50	0	0.6	15.4	0.54	1.05	0.56	1.0	84.4
50	1.0	0.6	16.6	0.56	1.05	0.58	2.0	81.8
50	2.0	0.6	17.6	0.56	1.0	0.56	2.0	73.2
50	3.0	0.6	17.2	0.50	1.0	0.50	2.0	61.8
50	4.0	0.6	16.4	0.44	1.05	0.46	2.0	50.1
50	5.0	0.6	15.6	0.37	1.0	0.37	2.0	39.4
50	6.0	0.6	13.7	0.31	1.0	0.31	3.0	29.2
50	8.0	0.6	9.5	0.21	1.0	0.21	5.0	16.4
75	0	0.6	12.8	0.38	1.05	0.40	2.0	61.6
75	2.0	0.6	13.4	0.39	1.0	0.39	4.0	56.4
75	4.0	0.6	13.6	0.34	1.0	0.34	4.0	47.6
75	6.0	0.6	12.8	0.28	1.0	0.28	6.0	36.4
75	10.0	0.6	9.5	0.17	1.0	0.17	10.0	17.8
25	0	0.4	13.8	0.43	1.1	0.47	0.5	81.6
25	0.5	0.4	15.2	0.43	1.2	0.51	1.0	76.6
25	1.0	0.4	15.8	0.43	1.2	0.51	1.0	68.4
25	1.5	0.4	16.2	0.41	1.2	0.49	1.0	58.2
25	2.0	0.4	15.8	0.38	1.05	0.4	1.5	48.0
25	3.0	0.4	13.0	0.31	1.05	0.33	2.0	29.6
25	4.0	0.4	9.6	0.23	1.1	0.25	2.0	16.5
25	5.0	0.4	5.0	0.17	1.0	0.17	2.0	7.3
50	0	0.4	11.0	0.29	1.1	0.32	1.0	60.6
50	1.0	0.4	11.8	0.30	1.1	0.33	2.0	57.5
50	2.0	0.4	12.4	0.30	1.0	0.30	3.0	49.6
50	4.0	0.4	11.6	0.23	1.0	0.23	4.0	35.1
50	6.0	0.4	9.4	0.23	1.0	0.23	6.0	21.4
75	0	0.4	9.2	0.25	1.0	0.25	2.0	41.1
75	2.0	0.4	9.6	0.24	1.0	0.24	4.0	39.2
75	4.0	0.4	8.8	0.23	1.1	0.25	4.0	31.8
75	6.0	0.4	8.8	0.20	1.05	0.21	6.0	26.4
75	10.0	0.4	6.3	0.16	1.0	0.16	10.0	13.6

with that which would be analytically predicted, Eq. (11) was numerically integrated with T_τ set equal to unity. This yielded the far-field spot in the focal plane of the far-field forming lens. Figures 5a and 5b show the traces of the test beam spots as projected on the opal glass, measured by the TV camera, and portrayed on the oscilloscope. Figures 6a and 6b show the analytically predicted beam spots. As can be seen from the plots, the predicted and measured beam spots were similar for four of the six test beams.

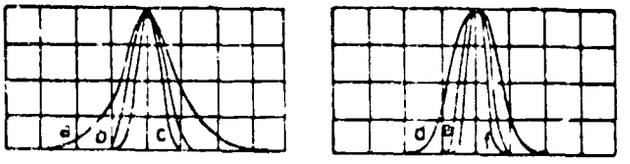

Fig. 5 Measured beam images. 6328 Å: a) 11 mm beam; b) 26.8 mm beam; c) 50 mm beam; 4416 Å: d) 12.3 mm beam; e) 26 mm beam; f) 50 mm beam.

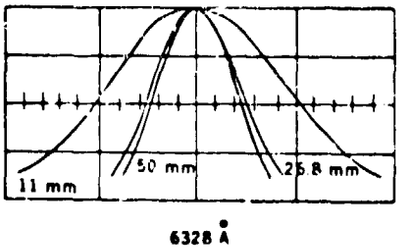

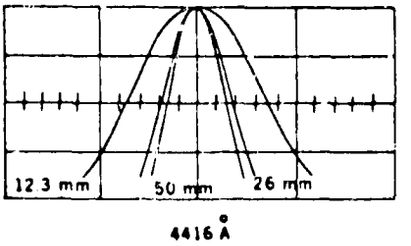

Fig. 6 Calculated beam images.

Solution of the Laser Beam Degradation Equations

Equation (11), in combination with Eq. (10), is not amenable to exact solution; thus, numerical techniques were resorted to in an endeavor to solve these equations. Simpson's rule was used to integrate numerically the equations

with "Δr" of 0.125 mm. In order to utilize conveniently the temperature and velocity correlation functions in the numerical integrations, the correlation functions were digitized using a least-squares fit subroutine. The results of the numerical integration of this equation are shown in Table 3. Solutions were obtained for measured input laser beam diameters.

Table 3 Measured and Calculated Laser Beam Degraded Intensities

λ, Å	Laser beam size, mm	Mach no.	Test station, cm	Measured intensity, %	Calculated intensity, % Eq. (10)	λ, Å	Laser beam size, mm	Mach no.	Test station, cm	Measured intensity, %	Calculated intensity, % Eq. (10)
6328	50.0	0.4	25	93	92.8	4416	26.0	0.6	50	81	74.2
6328	26.8	0.4	25	94	93.6	4416	12.3	0.6	50	89	86.6
6328	11.0	0.4	25	98	96.9	4416	21.0	0.6	50	81	77.1
4416	50.0	0.4	25	90	85.8	4416	10.8	0.6	50	89	88.7
4416	26.0	0.4	25	92	87.6	6328	50.0	0.8	50	60	60.7
4416	12.3	0.4	25	97	92.9	6328	26.8	0.8	50	68	65.6
4416	21.0	0.4	25	92	88.8	6328	11.0	0.8	50	85	83.9
4416	10.8	0.4	25	97	93.9	4416	50.0	0.8	50	41	38.2
6328	50.0	0.6	25	70	72.8	4416	26.0	0.8	50	51	45.2
6328	26.8	0.6	25	76	75.8	4416	12.3	0.8	50	72	67.3
6328	11.0	0.6	25	86	87.7	4416	21.0	0.8	50	51	50.0
4416	50.0	0.6	25	56	53.1	4416	10.8	0.8	50	72	71.5
4416	26.0	0.6	25	63	58.1	6328	50.0	0.4	75	97	96.9
4416	12.3	0.6	25	79	74.2	6328	26.8	0.4	75	98	97.4
4416	21.0	0.6	25	63	61.6	6328	11.0	0.4	75	100	99.0
4416	10.8	0.6	25	79	77.3	4416	50.0	0.4	75	98	93.8
6328	50.0	0.8	25	34	40.6	4416	26.0	0.4	75	97	94.9
6328	26.8	0.8	25	45	46.0	4416	12.3	0.4	75	99	97.7
6328	11.0	0.8	25	67	69.1	4416	21.0	0.4	75	97	95.6
4416	50.0	0.8	25	18	18.6	4416	10.8	0.4	75	99	98.1
4416	26.0	0.8	25	25	24.2	6328	50.0	0.6	75	91	90.6
4416	12.3	0.8	25	48	45.4	6328	26.8	0.6	75	92	92.0
4416	21.0	0.8	25	25	28.4	6328	11.0	0.6	75	98	96.9
4416	10.8	0.8	25	48	50.4	4416	50.0	0.6	75	83	81.8
6328	50.0	0.4	50	96	95.3	4416	26.0	0.6	75	87	84.8
6328	26.8	0.4	50	97	96.0	4416	12.3	0.6	75	94	92.7
6328	11.0	0.4	50	98	98.4	4416	21.0	0.6	75	87	86.7
4416	50.0	0.4	50	94	90.7	4416	10.8	0.6	75	94	93.9
4416	26.0	0.4	50	95	92.1	6328	26.8	0.8	75	80	78.6
4416	12.3	0.4	50	98	96.2	6328	50.0	0.8	75	74	75.0
4416	21.0	0.4	50	95	93.0	6328	11.0	0.8	75	90	91.1
4416	10.8	0.4	50	98	96.8	4416	50.0	0.8	75	57	56.6
6328	50.0	0.6	50	83	83.6	4416	26.0	0.8	75	65	62.7
6328	26.8	0.6	50	86	86.0	4416	12.3	0.8	75	81	80.4
6328	11.0	0.6	50	95	94.1	4416	21.0	0.8	75	65	66.9
4416	50.0	0.6	50	78	69.8	4416	10.8	0.8	75	81	83.3

Predicted vs Measured Turbulent Refractive Index-Induced Laser Beam Degradations

Examples of the degraded far-field laser beam spots, as recorded on the oscilloscope, are shown in Fig. 7. These photographs show the long-term average degraded laser beam spots, as measured by the TV camera in the regular scan mode.

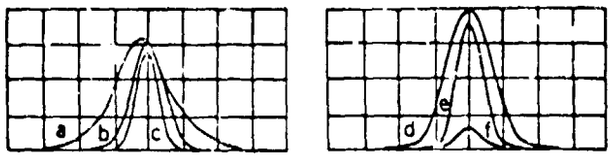

Fig. 7 Degraded beam images. 6328 Å: a) 11 mm, Mach 0.8, 50 cm station; b) 26.8 mm, Mach 0.6, 25 cm station; c) 50 mm, Mach 0.6, 25 cm station; 4416 Å: d) 12.3 mm, Mach 0.4, 50 cm station; e) 26 mm, Mach 0.6, 75 cm station; f) 50 mm, Mach 0.8, 25 cm station.

Since these examples show little motion of the far-field spot, it is apparent that any motion which contributes to the overall degradation, occurs at a frequency equal to or higher than the reciprocal of the integration time of the TV camera system. This frequency of motion will be discussed further when the results of the far-field measurements using the TV camera in the single-line scan mode are presented. Figure 8 shows the percentage of the detected long-term average central spot intensities at the 25 cm station for all laser beams and Mach numbers. Table 3 lists these same data along with the solution of Eq. (11) using Eq. (10) for T_τ. Figure 9 shows in graphical form the detected far-field spot intensities versus those predicted by the solution of Eq. (11) using Eq. (10) for T_τ with input beam diameters that would yield the far-field spot diameters measured.

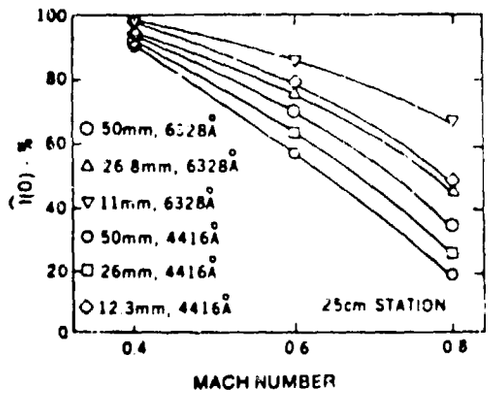

Fig. 8 Average degraded intensities.

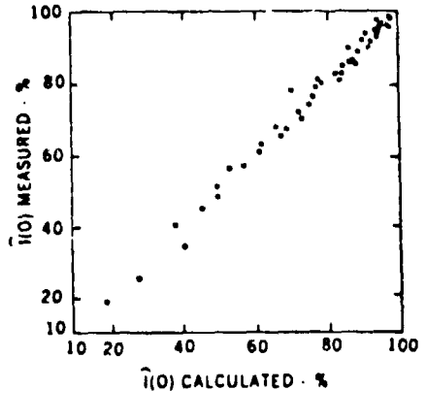

Fig. 9 Measured vs calculated intensities.

Laser Beam Far-Field Spot Broadening and Wandering

With the TV camera in the single-line scan mode, the detection system was able to detect motions with a frequency up to 3000 Hz. Examples were made of several measurements of the beam spots with the TV camera in the single-line scan mode and with several detected spots superimposed. The maximum intensity recorded was taken as the intensity remaining after degradation by broadening alone. The percentage of this maximum, which yields the long-term average intensity, was taken as the intensity remaining after degradation by beam motion (or wandering) alone. Table 4 lists these percentages for all test conditions.

V. Summary and Conclusions

This investigation correlated the degradation of the far-field central spot intensity formed by a collimated coherent light beam traversing high-intensity turbulence with the statistical behavior of the turbulence-generated refractive index perturbations causing the degradation. Since refractive index perturbations could not be measured readily, a method to approximate these perturbations, via the equation of state, using velocity and temperature perturbations was autocorrelated. The turbulence quantities measured were path

Table 4 Laser Beam Wandering vs Broadening

		λ(Å), beam size, mm					
		6328			4416		
		50.0	26.8	11.0	50.0	26.0	12.3
25 cm test station							
0.4 Mach	/	99	99	100	100	100	99
	/	93	94	98	90	92	97
	%	94	95	98	90	92	98
0.6 Mach	/	80	91	95	77	83	92
	/	70	76	86	56	63	79
	%	88	84	91	73	76	86
0.8 Mach	/	55	65	75	28	40	65
	/	34	45	67	18	25	48
	%	62	69	90	64	63	74
50 cm test station							
0.4 Mach	/	99	99	99	100	100	100
	/	96	97	98	94	95	98
	%	97	98	99	94	95	98
0.6 Mach	/	92	96	98	95	95	98
	/	83	86	95	78	81	89
	%	90	90	97	82	85	91
0.8 Mach	/	80	86	94	70	82	90
	/	60	68	85	41	51	72
	%	75	79	90	59	62	80
75 cm test station							
0.4 Mach	/	100	100	100	100	100	100
	/	97	98	100	98	97	99
	%	97	98	100	98	97	99
0.6 Mach	/	100	99	99	100	100	100
	/	91	92	98	83	87	94
	%	91	93	99	83	87	94
0.8 Mach	/	90	91	95	96	96	96
	/	74	80	90	57	65	81
	%	82	85	95	59	68	84

length, velocity correlation function, and temperature correlation function. The path length had a minimum at the 25 cm test station of about 10 cm and a maximum of about 30 cm at the 75 cm test station. The rms velocity perturbations had a maximum of 30.8 m/s at the 25 cm test station at 0.8 Mach and an on-axis minimum of 9.2 m/s at the 75 cm test station at 0.4 Mach. The corrected temperature perturbations had a maximum of 1.89 K and minimum of 0.25 K at the preceding respective test stations and nozzle exit flow conditions.

The actual far-field central spot intensities were measured. The 4416 Å, 50 mm beam traversing the 25 cm test station when the nozzle exit velocity was 0.8 Mach, had an intensity of 18% of the reference intensity. At the 75 cm

test station, with 0.4 Mach nozzle exit velocity, the 6328 Å, 11.0 mm laser beam had a far-field central spot intensity of 100% of the reference intensity.

The results of the experimentally measured central spot degraded intensities were compared with those that were analytically predicted using experimentally determined turbulence characteristics (Fig. 9). For the same laser beams traversing statistically identical flowfields, the greatest difference between experimentally measured and analytically predicted degraded far-field, central spot intensities was 8.2%. The average difference between the experimentally and analytically determined intensities for all test conditions was less than 2%. These results support the approximations used to arrive at the analytical expressions which predict the laser beam far-field central spot intensity degradation caused by turbulent flow fields and yield confidence in the ability to accurately predict those degradations using readily measurable turbulent flow field statistical parameters.

VI. References

1. Hufnagle, R. E. and Stanley, N. R., "Modulation Transfer Function Associated with Image Transmission Through Turbulent Media," Journal of the Optical Society of America, Vol. 54, No. 1, 1964.

2. Lutomirski, R. F., Huschke, R. E., Meecham, W. C., and Yura, H. T., "Degradation of Laser Systems by Atmospheric Turbulence," R-1171-ARPA/RC, The Rand Corp., June 1973.

3. Lutomirski, R. F., Shapiro, A. R., and Yura, H. T., "Experiments on Turbulence Effects in Laser Propagation," WN-7063-ARPA, The Rand Corp., September 1970.

4. Lutomirski, R. F. and Yura, H. T., "Wave Structure Function and Mutual Coherence Function of an Optical Wave in a Turbulent Atmosphere," Journal of the Optical Society of America, Vol. 61, 1971, p. 482.

5. Sutton, G. W., "Effect of Turbulent Fluctuations in an Optically Active Fluid Medium," AIAA Journal, Vol. 7, September 1969, p. 1751.

6. Tatarski, V. I., Wave Propagation in Turbulent Medium, McGraw-Hill Book Co., New York, N.Y., 1961.

7. Owens, J. C., "Optical Refractive Index of Air: Dependence on Pressure, Temperature and Composition," Applied Optics, Vol. 6, January 1967, p. 51.

8. Cudahy, G. F., "An Investigation of the Degradation of a Laser Beam by High Intensity Turbulence," Ph.D. Thesis, Air Force Institute of Technology, 1976.

9. Corrsin, S. and Uberoi, M. S., "Spectra and Diffusion in a Round Turbulent Jet," NACA Report 1040, U.S. Government Printing Office, 1951.

10. Hinze, J. O., Turbulence, McGraw-Hill Book Co., Inc., New York, N.Y., 1959.

11. Shepard, W. K., "Turbulence Measurements in Plane Free Jet at High Subsonic Velocities," GAE/AE/74D-24, Air Force Institute of Technology, Air University, Wright-Patterson AFB, Ohio, 1974.

AD P000332

ON THE LARGE SCALE STRUCTURE OF TURBULENCE IN BOUNDARY LAYER AND SHEAR FLOWS

by

M. A. Badri Narayanan
Indian Institute of Science
Bangalore, India

The basic understanding of the physics of turbulence has undergone many radical changes in the last few years. Turbulent fluctuations which were considered to be purely random in nature is no more accepted to behave in that fashion but made up of somewhat coherent and orderly structures mixed with noise like random disturbances. The major difficulty experienced in the experimental investigations is the identification of these coherent structures from the overall signal. New methods are being developed to identify them. These orderly motions are large in scale and seem to play an important role in the dynamics of the mixing and the transport processes which are the essential features of turbulence. In this paper the properties of the large scale fluctuations in boundary layers as well as in shear flows are discussed.

Manuscript Received July 1980.

LARGE SCALE COHERENT STRUCTURES IN TURBULENT SHEAR FLOWS

Introduction:

Turbulent flows are more often encountered in nature than laminar flows. The physics of laminar flows is reasonably well formulated while that of turbulence is yet to be fully understood. Many engineering fields such as aeronautics, turbomachinery, fluid transportation in ducts, chemical processing and combustion, frequently require solutions to turbulent flows. Analytical approach to many of these problems being difficult, empirical relations are resorted to. Organized experimental data is available only for simple flows and very often, investigations with scale models are required when dealing with complicated flow situations.

Early research activities on turbulence up to the fifties were mainly concerned with time dependent quantities such as mean velocities, wall shear stress and mixing rates. Concepts like eddy viscosity and mixing length were used to model turbulent shear stress so that the basic equations could be solved analytically in a laminar like fashion. However, it was felt that a fresh relook was required into the nature of turbulent fluctuations to progress further in this field.

In the early sixties, intensive studies were initiated to examine the time dependent patterns in the flow, using flow visualization methods which were later supplemented by hot wire techniques. These investigations revealed the existence of many interesting and significant features of the flows hitherto unknown, such as the large scale coherent structures, the bursting phenomenon, the nature of the Reynolds stress. This article aims to present these recent trends and views on turbulence for scientists and engineers who are concerned with turbulent flows but are not familiar

with the exciting basic research activities in the field.

General:

All turbulent flows are governed by the well-known Navier-Stokes equations which are formulated on the basis of the equilibrium of forces. A solution of these equations should yield all the properties of the flows. However, our present day mathematical techniques are inadequate to handle these highly non-linear partial differential equations. In the absence of a complete solution, attempts are being made to understand the behaviour of the fluctuations and to formulate some laws governing them, using experimental results and observations. Quasi-analytical solutions of Navier-Stokes equations are also being attempted using models for shear stress. Modern computers are a great boon for this type of analysis. Large number of models have been employed and many useful results obtained for a variety of flows. However, to achieve the final goal the modeling needs further improvements.

Turbulent flows contain a large number of eddies of differnet sizes and they generate velocity fluctuations in a random fashion. Such randomness is observed in the magnitude, phase and frequency of these time dependent motions and hence a statistical approach is resorted to, to define them. The eddies are responsible for the transportation of mass and momentum on a macro scale across the flow field. Depending on the flow conditions, the eddies get deformed and larger ones get broken down into smaller ones in a cascade shower till they become unidentifiable and dissipate into heat. This situation introduces a large variety of velocity and length scales into the problem.

The energy content in the eddies is represented by the energy density - wave number spectra in a general way (Fig 1). Wave number is defined as $\frac{2\pi n}{U}$ where n is the frequency of the velocity fluctuations and U is

the velocity. For all turbulent shear flows, the turbulent kinetic energy is found to be concentrated in the low wave number region of the spectra, which represents large scale eddies (Ref 1). Since the spectral curve forms the basis of many analyses, detailed studies have been made on the nature of the spectrum, searching for similarities. While some success has been achieved in the small scale fluctuations, the shape of the spectrum is not unique for large scale motions and appreciable differences exist from flow to flow. The similarity in the small scale fluctuations (large wave numbers) has been examined extensively but it remained as an academic exercise as far as engineers are concerned. In the last two decades serious attempts are being made to investigate the behaviour of the large scale fluctuations in a variety of ways, since without an understanding of their dynamics further progress remains stalled.

Even though turbulence was accepted to be a random phenomenon for many years, there were doubts in the minds of many investigators about the true nature of the randomness, because of the existence of organized motions in shear flows. Examples of this are, the vortices formed behind circular cylinders, the wavy structure of the flows in the outer region of a jet or a wake or a boundary layer, consisting of alternating rotational and irrotational motions. These structures are of large scales which represent the low wave number region of the spectra where the energy is maximum. Based on these observations one is tempted to conjucture that these large scale motions are not truly random and that they could also be considered, on account of their energy content, to contain the primary mechanism for the extraction of energy from the mean flow, to be later converted to turbulent fluctuations.

In a flow where the production of turbulence and its dissipation are in equilibrium, there exists a continuous process in which the large scale fluctuations break down into smaller and smaller eddies. In such a situation, the large ordered motions as well as the small scale structures which are random would get mixed together, the existence of the former being inconspicuous. Hence, to study the orderly motions, they have to be identified from the rest of the fluctuations. If the existence of the orderly large scale motions is established to be a general feature of all turbulent flows, the analysis of turbulence has to be approached in an entirely different manner from the methods adopted previously to solve the problem as a random process. The information available on the large scale coherent structures as observed in different shear flows is discussed in the following paragraphs.

Turbulent Boundary Layers

The instantaneous behaviour of the velocity fluctuations in a turbulent boundary layer is being studied in great detail for the past two decades. One of the main features of a boundary layer flow is its ability to maintain turbulence continuously, unlike grid and free shear flows and it is conjuctured that the surface on which the boundary layer is formed might be responsible for this behaviour. The exact mechanism of the process remains still unknown. Some well recognizable time dependent flow patterns were first observed by Kline and his co-workers at Stanford University (Ref 2) in the wall region of a turbulent boundary layer and these events are now generally known as "bursts". A low speed water channel was employed in their investigations using micro hydrogen bubbles as tracers for instantaneous flow visualization. Bursts were found to be

localized three dimensional patterns associated with large velocity gradients around them. The intensity of the Reynolds stress was found to be large during the bursting period. It was then concluded that the bursting phenomenon is primarily responsible for the production of turbulence in a boundary layer. Since the bursts were observable only near the wall, the production was considered to be wall oriented. A few years later, similar flow visualization studies were repeated but in a pipe flow at the University of Ohio by Brodkey and his group (Ref 3). Instead of hydrogen bubbles a birefrengent liquid was used to identify the events. Many stages of bursting were observed, the main ones being the ejection of the slow moving fluid away from the wall in the form of jets and an inrush of the outer fluid towards the wall. All the experiments were conducted at very low speeds and also at low Reynolds numbers just above the critical value for transition. Flow visualization becomes difficult if the velocities are high.

Further investigations were made by the author on the bursting phenomenon in boundary layers at the Indian Institute of Science, Bangalore, (Ref 4 & 5) and also at the University of Southern California with Laufer (Ref 6) in wind tunnel boundary layers at high Reynolds numbers, using hot wire techniques. Turbulent signals at the wall region were found to be intermittent for low free stream velocities from which bursts could be identified to some extent; however, as the velocity was increased, the burst signals became obscure. Several methods were employed to extract the burst signals and the most successful one is the selective filtering technique. The period of the bursts were obtained by this method and also from the auto correlation of the hot wire signals. This period (T) which

is the average time between two consecutive bursts was found to scale with the free stream velocity (U) and the boundary layer thickness (δ). In all the experiments UT/δ was nearly constant with a value around 5.0 even though the Reynolds number of the flow was varied by a factor of 10. Recent experiments conducted by the author (Ref 7) at NASA, Ames Research Center, at high Reynolds numbers also confirm the above trend. The bursting period obtained earlier by the Stanford group agreed with the above result. In addition, it was also noticed that by using the selective filtering technique intermittency of the signals could be identified not only at the wall but also in all the regions in the boundary layer. For a given boundary layer, the period (T) remained constant irrespective of the distance from the wall. The above result raised the doubt whether the burst in the wall region is the primary agency for the production of turbulence as envisaged earlier or is it the complete boundary layer involved in the process in an integrated manner. On examining all the results, then available, it was speculated by the author that the boundary layer might consist of large scale cyclic motions spanning the entire width and convected along the flow (Fig 2). The bursts near the wall, the ejection and the inrush processes and the wavy interface in the outer part of the boundary layer could be just various manifestations of this large scale structure. It was also suggested that this near cyclic motion could be responsible for the production of turbulence by extracting energy from the mean flow. The existence of the large scale motions were later confirmed experimentally by the detailed measurements of the flow at the University of Adelaide by Brown and Thomas (Ref 8).

The dynamics of the large scale coherent structure is still subject to speculation. One possibility is that the outer flow which has higher velocity and momentum, imparts motion to the cyclic structure periodically. When this flow reaches the wall, it is seen as an inrush. Temporarily, the original onward mean flow in the wall region gets retarded on account of this inrush, resulting in accumulation of mass and is followed by a pressure rise. As a consequence of this, the excess mass is ejected outwards which appears as a jet shooting out away from the wall. This motion forms the other half of the cyclic process. The time delay between the retardation of the flow near the wall and the ejection of the accumulated mass determines the periodicity of the large scale structures. Bursting process includes all the events occuring near the wall region in a single cycle. Hence, the bursts as well as the large scale coherent structures have the same cyclic period.

During the bursting process, the flow in the wall region manifests into different forms. The flow patterns near the wall is of considerable importance, since wall shear as well as the turbulent stress are influenced by them. Experiments with hot wire ladders have revealed that the instantaneous velocity profiles close to the wall vary with time during a bursting cycle and contain inflexion points which are dynamically unstable (Ref 9). Landahl (Ref 10) has proposed a burst regeneration mechanism whereby a large velocity defect in the shear flow may trigger new breakdown thus continuously producing turbulence. The exact nature of the flow patterns is still not very clear even though many flow visualization experiments have been performed by several investigators. Some kind of horse-shoe vortex type pattern has been observed by some, the scale of the vortices being small compared to the large scale structures. The

possibility that the pattern might depend on the Reynolds number cannot be ruled out (Ref 11).

Recent investigations on the instantaneous structure of the turbulent shear stress have revealed many interesting features of the mixing process, entirely different from the views held earlier. It was previously assumed that the turbulent shear stress, especially the u'v' component is mainly associated with the large scale motions. Reynolds stress was always measured as a time averaged quantity and most of the present day stress models are developed on this basis. With the use of modern electronic circuits it has become possible to obtain continuous signals of the stress and an examination of the u'v' trace indicates (Fig 2) that the stress occurs intermittently (Ref 12) and not continuously. This stress is active only for short periods spaced at intervals corresponding to the time scale of the large fluctuations.

The overall picture of the mixing process emerging from the above observations could be viewed in the following manner. Transport of mass as well as of momentum on a macro scale is due to the large scale cyclic motions spanning the entire width of the boundary layer. However, homogeneous mixing of a fine scale is confined only to a small region along the contour of the large coherent structure.

Free Shear Flows

The structure of turbulence in jets and in mixing layers has been studied in great detail for many years and in the last decade attention is focussed towards large coherent structures in these cases (Ref 13). The flows in the outer edge of a jet and the free stream edge of a boundary layer resemble each other in many respects. Alternating wavy motions

containing rotational and irrotational fluctuations could be observed and they form part of the coherent cyclic structure. Hot wire signals of the turbulent shear stress fluctuations clearly indicate that the stress is active only during certain periods, the duration between the periods being approximately equal to the time scale of the large coherent motions (Ref 14). Similar behaviour had been already observed in boundary layer flows.

Experiments conducted on jet noise with different jet configurations including aircraft jet exhausts have also revealed the existence of the coherent structures in the spectral distribution of noise (Ref 15). In all the measurements the intensity of noise was found to reach a maximum around a Strouhal's number of 0.30, the Strouhal's number defined as $St = \eta D/U$ where U & D are the velocity and the diameter of the jet at the exit and η is the frequency to which the output of the microphone is tuned.

Another interesting feature of the large scale structure in free shear flows is the pairing process, when the period of the structure gets doubled. This phenomenon could be easily observed in a round jet by examining the hot wire traces at different locations down-stream of the exit (Ref 14). Very close to the orifice, near sinusoidal fluctuations of a single frequency can be noticed. As the wire is slowly shifted down-stream, the intensity gets modulated, the frequency remaining the same. At a particular distance alternate fluctuations slowly disappear and the frequency gets reduced to half the original value. The pairing process is now complete (Fig 3). The physics of the phenomenon is not yet well understood. One of the plausible explanations is the merger of two sets of vortex trains in a synchronised fashion, one set formed inside the core of the jet and the other outside in the entrainment region. It has been conjuctined (Ref 16) that on account of the interaction between two vortices during pairing, pressure fluctuations

are produced which acts as the primary source for the radiation of noise. Experiments indicate that the frequency of the fluctuations at the end of pairing is the same as the frequency of the radiated noise at its maximum intensity (Ref 14). Both correspond to a Strouhal's number of 0.3.

Large scale organized structures have also been observed in two dimensional mixing shear layers and extensive investigations have been carried out on this topic by Roshko and his group (Ref 17) at the California Institute of Technology. In their experiments two different gases were allowed to mix and the complete mixing process was visualized using shadowgraph technique. Short duration photographs revealed many interesting features of the flow pattern. The eddies formed near the origin were small to start with but grew rapidly as the flow moved down-stream. Two dimensionality was maintained by the organized motions for large distances. Pairing of nearby vortices were also observed. A sketch of the flow pattern is shown in Fig 4. In the experiments the boundary of the coherent structures could be clearly seen. These structures were vortex like with a tendency to rotate as a whole. Mixing seems to be confined to the contour of the large scale motions similar to jet and boundary layer flows.

General Comments

All turbulent shear flows including boundary layers contain large scale coherent structures. They are vortex like and are convected along the flow. Some periodicity and orderliness are exhibited by these motions and hence their behaviour is far from being random. In low speed flows these motions could be observed with some clarity whereas at higher velocities, their existence is masked with other random fluctuations which are of smaller scales. Special techniques have to be employed to isolate them.

The coherent structures play an important role in the dynamics of turbulence. They are large scale eddies spanning the entire width of the shear layer and are initially set into motion by the mean flow, most probably by the flow in the outer region in a boundary layer and in the inner region of a jet, where the momentum is maximum. During this process the energy in the mean flow is transferred into turbulent kinetic energy but in an orderly manner with a frequency equal to the time scale of the large structure. Later, these motions break down into smaller eddies and then disintegrate into fine structures before getting dissipated into heat. Since the coherent structures span the entire width of the shear flow, mass as well as momentum are transported by them all across the layer on a macro scale. However, fine scale homogeneous mixing is confined to narrow regions along the contour of these large eddies. The above trend is suggested by the intermittent nature of the turbulent shear stress fluctuations. This new concept of mixing has bearing on many practical applications. For example, in combustion problems where the fuel and the oxidiser are to be mixed thoroughly (i.e. fine scale mixing) for spontaneous ignition, the burning of the fuel will take place only along the periphery of the large eddies. The passage of many large scale motions will be required for complete combustion. Similarly, many reaction problems in chemical industries will be governed by the above process. On the other hand if momentum has to be transported, the strength of the large scale structure has to be enhanced. A typical example is the ejector where the induced mass flow depends on the overall momentum transfer. Since the large scale coherent motions play an important role, any alteration to this structure would have appreciable effect on the overall characteristics of the flow in general. Periodic suction or tangential blowing

in a shear flow, synchronised with the large scale motions might have engineering applications.

For the shear flows so far investigated for large scale motions, the Strouhal's number is nearly constant having a value of about 0.25, if appropriate velocity and length scales are taken into account. The results are tabulated below:

(a) Boundary layer (two dimensional) - $St = \frac{n\delta}{U} \simeq 0.20$

(b) Wake (two dimensional) - $St = \frac{n\delta_w}{U} \simeq 0.25$

(c) Channel flow (two dimensional) - $St = \frac{nD}{U} \simeq 0.25$

(d) Vortex street (two dimensional) - $St = \frac{nD_c}{U} \simeq 0.24$

(e) Jet (asisymmetric) - $St = \frac{nD_J}{U} \simeq 0.16$

St - Strouhal's number; δ - boundary layer thickness

δ_w - Half width of the Wake; D - Half width of the channel

D_c - Diameter of the circular cylinder;

D_j - Half width of the jet at the exit.

U - Maximum velocity of the particular flow.

The existence of the large scale coherent motions and their significance to turbulence having been established, the next phase of the investigation is to formulate laws governing them. Though the large scale structures are far from random, their patterns are irregular except in special cases. Hence, one should look only for average properties. The relation between the size of the large eddies and the magnitude of the velocities contained in them is of primary interest. If similarity exists

in the energy wave number spectra, the above formulation would have been somewhat simpler but it is found that the spectral curves in the low wave number region vary appreciably from flow to flow (Fig 1). Even otherwise the spectrum being based on Fourier components of the fluctuations and containing no information regarding the phase relations, it is difficult to separate the structure of the coherent motions from other random contaminations. Hence, for a study of the properties of the large scale motions an entirely different approach is needed. This calls for new ideas.

With the help of the modern high power computers attempts are being made to simulate the large eddy structures directly from the Navier-Stokes equations (Ref 18 & 19). In this approach the Navier-Stokes equations are not solved in their entirety and the computations are simplified by using models for small scale structures. The results obtained so far are very encouraging. It is however too early to assess the applicability of this approach for engineering purposes.

Recently, the author attempted to identify the large scale motions directly from the hot wire traces, on the assumption that a large scale eddy and the zero crossings are related (Fig 2). The hot wire trace of longitudinal velocity fluctuations in a boundary was examined. Very small crossings of doubtful nature were neglected and only the primary ones were considered. It was observed in this study that the average duration between two consecutive zero crossings was the same as the burst period (Ref 20). The rate of the zero crossings remained almost constant across the boundary layer. The above result established, though not conclusively, that the primary zero crossings are the signature of the large eddies when they cross the mean value.

Some analyses were made on the period of the zero crossings which represents the time scale of the large eddy, and the amplitude of the velocity fluctuations. These investigations were also extended to two dimensional jet flows. As a preliminary measure the velocity scale was represented by the maximum value of the fluctuations in between two zero crossings. A wide range of experiments were conducted and in all of them some unique relations were observed (Ref 21). The author is of the opinion that further investigations in this direction might yield fruitful results.

References

1. Hinze, J.O. — Turbulence, McGraw-Hill Book Company (1975)

2. Kline, S.J. et.al. — The Structure of Turbulent Boundary Layers. J. Fluid, Mech. Vol. 30, P 741 (1967)

3. Corino, E.R. and Brodkey, R.E. — A Visual Investigation of the Wall Region in Turbulent Flow., J. Fluid, Mech. 37, 1 (1969)

4. Badri Narayanan et.al. — Bursts in Turbulent Shear Flows. Proceedings of the Fourth Australasian Conference on Hydraulics and Fluid Mechanics (1971)

5. Rao, K.N. et.al. — The Bursting Phenomenon in a Turbulent Boundary Layer. J. Fluid, Mech. Vol. 48 P 33 (1971)

6. Laufer, J. and Badri Narayanan, M.A. — Mean Period of the Turbulent Production Mechanism in a Boundary Layer. The Physics of Fluids, Vol. 14, P 182 (1971)

7. Badri Narayanan, M.A. and Marvin, G.J. — On the Period of the Coherent Structure in Boundary Layers at Large Reynolds Numbers. NASA Technical Memorandum 78477 (1978)

8. Brown, G. L. and Thomas, A.S.W. — Large Structure in a Turbulent Boundary Layer. The Physics of Fluids, Vol. 20, No. 10, P S 243 (1977)

9. Blackwelder, R. and Kaplan, R.E. — The Intermittent Structure of the Wall Region of a Turbulent Boundary Layer. Paper presented at the 13th International Congress of Theoretical & Applied Mechanics, Moscow (1972)

10. Landahl, M.T. — Wave Breakdown and Turbulence. SIAM J. Appl. Math. Vol. 28, No. 4, P 735 (1975)

11. Head, N.R. and Bandyopadhyay, P. — Combined Flow Visualization and Hot-Wire Measurements in Turbulent Boundary Layers. Proceedings on the workshop on coherent structure of turbulent boundary layers. Edited by C.R. Smith and D.E. Abbott, Lehigh University (1978)

12. Willmarth, W.W. and Lu, S.S. — Structure of the Reynolds stress and the occurrence of bursts in the turbulent boundary layer. Advances in Geophysics, Academic Press, Vol. 18-A, P 287 (1974)

13. Crowe, S.C. and Chamgagne, F.M. — Orderly Structure in Jet Turbulence. J. Fluid, Mech. Vol. 48, P 547 (1971)

14. Badri Narayanan, M.A. and Kuehn, D.M. — Experiments on the Large-Scale Structure of Turbulence in the Near-Jet Region. NASA Technical Memorandum 78567 (1979)

15. Fuchs, H.V. — Space Correlation of the Fluctuating Pressure in Subsonic Turbulent Jets. Journal of Sound and Vibration, 2 (1), P 77 (1972)

16. Laufer, J. et.al. — On the Generation of Jet Noise. AGARD Conference Proceedings. CP No. 131 - Noise Mechanisms (1974)

17. Roshko, A. — Structure of Turbulent Shear Flows: A New Look. AIAA Journal, Vol. 14, No. 10 (1976)

18. Ferziger Joel, H. — Large Eddy Numerical Simulations of Turbulent Flows., AIAA Journal, Vol. 15, No. 9 (1977)

19. Rubesin, N.W. — The Role of Coherent Structure in Turbulent Boundary Layer Analysis. Proceedings on the workshop on coherent structure of turbulent boundary layer. Lehigh University (1978)

20. Badri Narayanan, M.A. et.al. — Experiments on Fine Structure of Turbulence. J. Fluid, Mech., Vol. 80, 2, P 237 (1977)

21. Badri Narayanan, M.A. — Universal Trends observed in the Maxima of the Longitudinal Velocity Fluctuations and Zero crossings in Turbulent Flows. AIAA Journal, Vol. 17, No. 5, P 527 (1979)

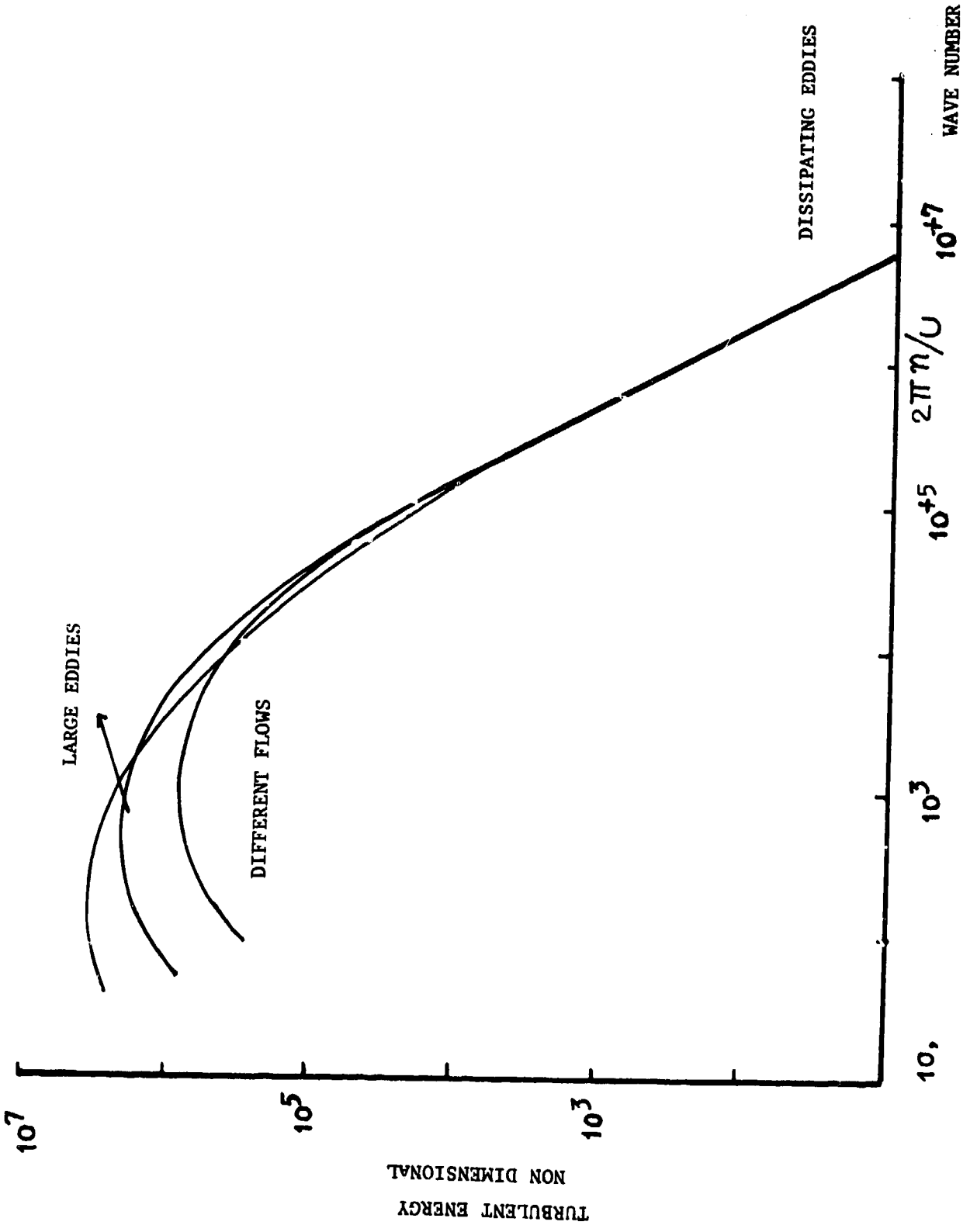

FIG. 1. TURBULENT ENERGY SPECTRA

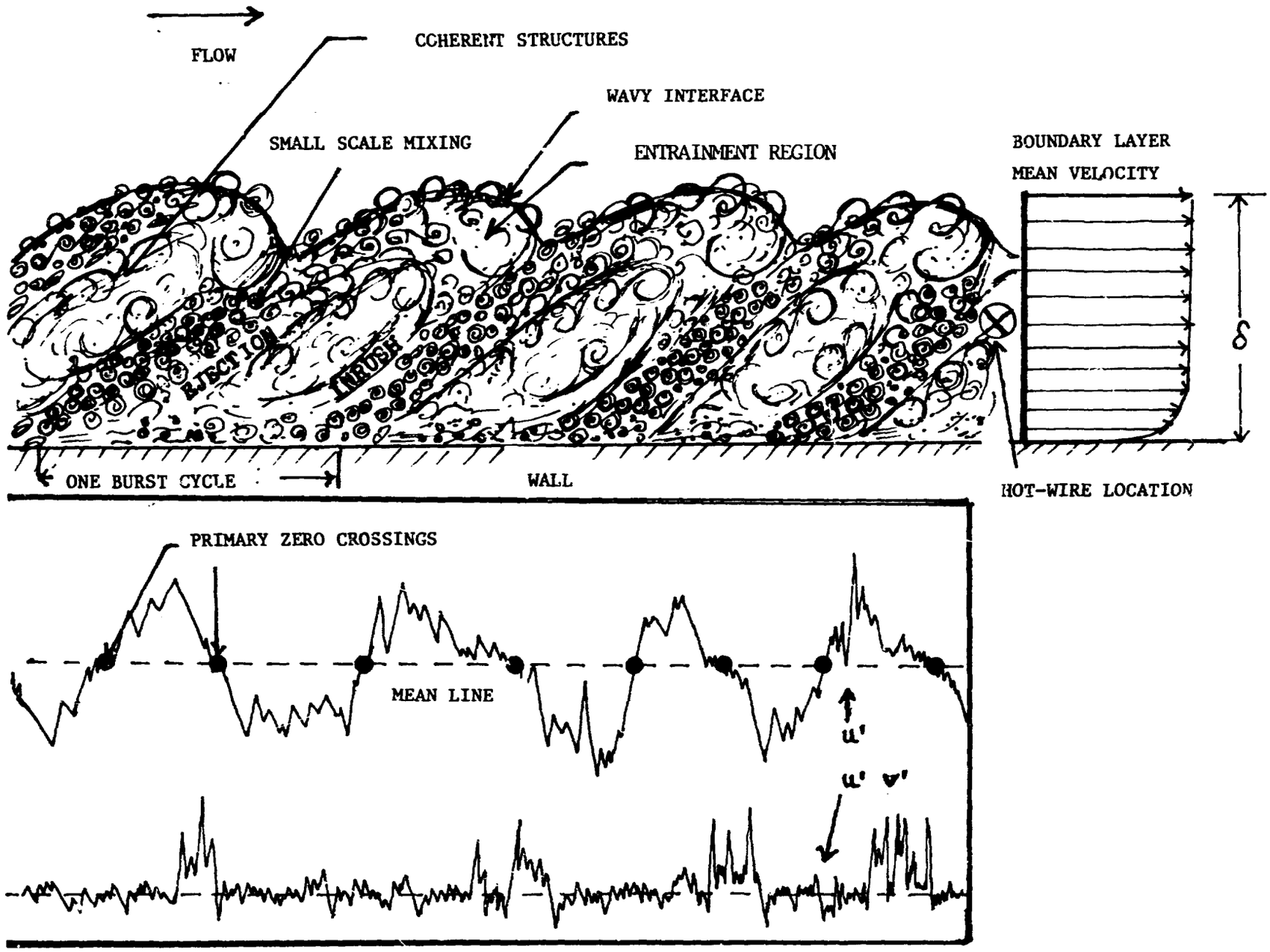

FIG. 2. LARGE SCALE MOTIONS IN BOUNDARY LAYERS

NOTE: ONLY CROSS SECTION OF RING
VORTICLES ARE SHOWN HERE

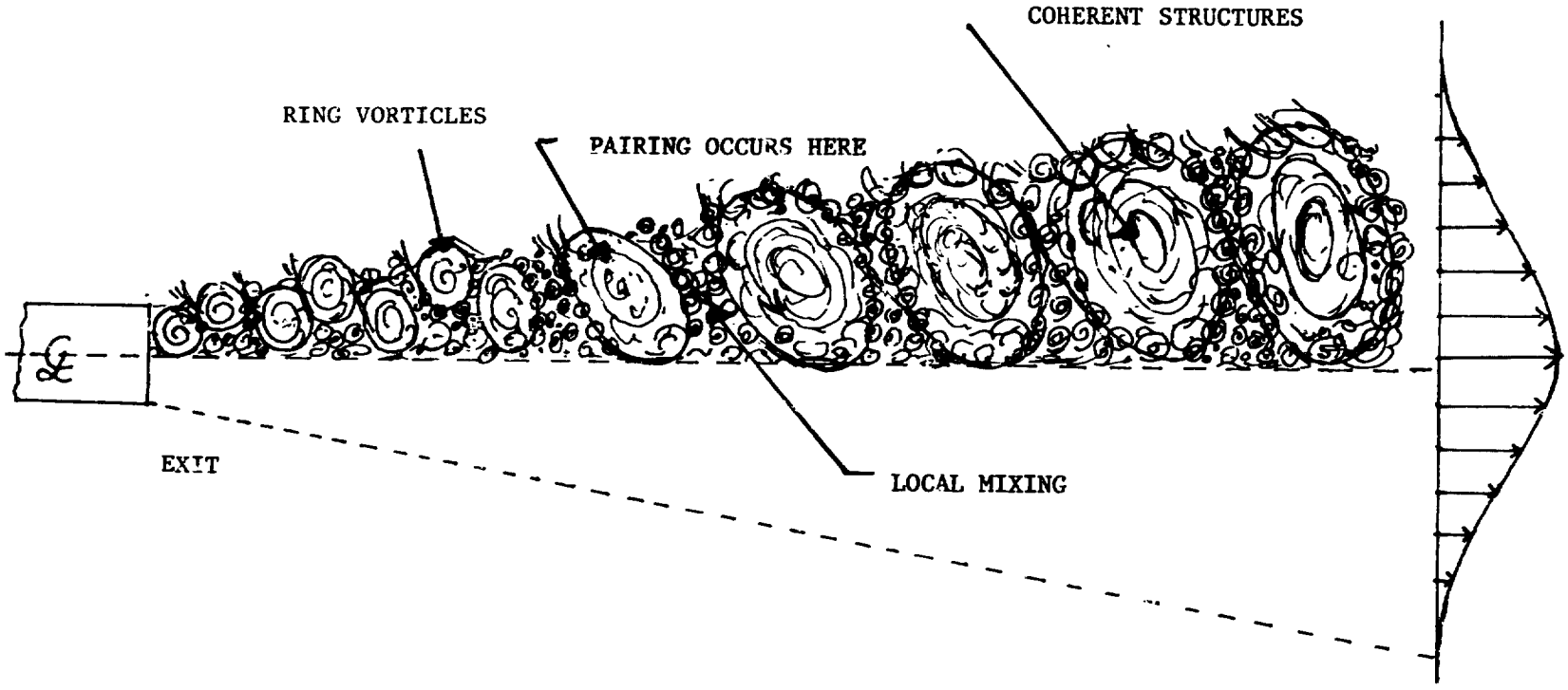

FIG. 3. COHERENT STRUCTURES IN TURBULENT JET

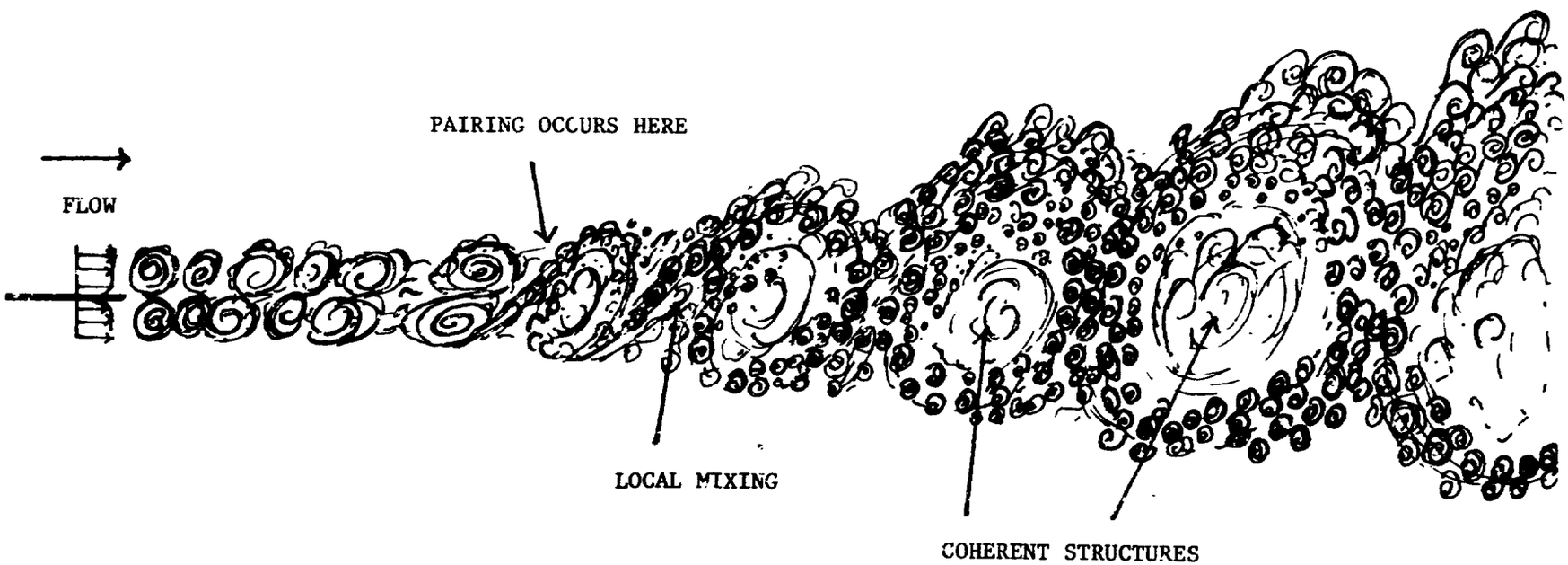

FIG. 4. COHERENT STRUCTURES IN MIXING LAYER

AD P000333

IMPROVED ANALYTICAL AND NUMERICAL TECHNIQUES FOR CALCULATING EXPLOSIONS AND IMPLOSIONS

by

John W. Goresh* and Henry E. Fettis**

Theoretical investigations in connection with the hypervelocity launcher research efforts carried on at the Fluid Dynamics Facilities Research Laboratory have required a detailed study of strong explosions and implosions.

For some time, it has been known that the system of partial differential equations defining pressure, density, and particle velocity can be converted to a system of ordinary differential equations by means of a similarity transformation. In the case of an exploding blast wave, the similarity transformation can be explicitly determined by consideration of the principle of energy conservation. The resulting system of equations which ultimately contains only one parameter, namely the adiabatic constant, γ, can then be integrated numerically, using the known relations at the shock front as initial conditions. Alternatively, known analytic solutions are available, but these have not been used extensively since they are implicit and do not allow the direct determination of the desired physical quantities (pressure, density, and velocity) at a given point. On the other hand, the numerical approach is time-consuming and also results in inaccuracies in the vicinity of the center. As a means of circumventing the above difficulties, the exact analytical solutions have been cast into a form which permits an iterative determination of all of the physical quantities directly as functions of position.

The implosion problem is complicated by the fact that the similarity variable is not uniquely determined, but is different for each value of γ. The equations in this case possess a singular point and the similarity variable must be so chosen that the resulting solutions are continuous in

* Deceased, formerly of AFARL, WPAFB
** Mountain View, CA

Manuscript Received March 1980 Based on Work Performed in the Air Force Aerospace Research Laboratories During 1965-66.

this vicinity. Since no complete analytic solution is known for this problem, the only recourse is to numerical integration. However, since the system now contains two parameters, a trial and error technique has been used to find the proper exponent in the similarity transformation. If this exponent is not correctly chosen, and the equations are integrated starting at the shock, the resulting solutions will diverge. Such an approach is clearly, numerically untractable. As an alternative, the equations can be transformed in such a way that the singular point and the trajectories which pass continuously through it are clearly defined. This permits the unknown exponent to be systematically determined, using the known shock conditions and the method of false position. These procedures have resulted in a more extensive and accurate tabulation of these important physical quantities than has heretofore been practical. Typical calculated values are presented in graphical form for both problems.

NOMENCLATURE

A	separation constant (see Eq 7)
a	speed of sound
E	total energy of gas per unit mass
f	similarity variable representing pressure
I	total heat of gas
p	pressure
Po	pressure of undisturbed flow
r	radial distance
R	shock radius
t	time
U	shock velocity
$\bar{u}$	radial velocity
γ	ratio of specific heats
δ	exponent in the similarity transformation
η	non-dimensional radius $(\frac{r}{R})$
ν	spatial index (see following Eq 3)
ρ	density
ρ_0	density of the undisturbed flow
$\phi(\eta)$	similarity variable representing velocity
$\psi(\eta)$	similarity variable representing density

I. INTRODUCTION

Hypervelocity research facilities require extensive numerical data relating to pressure, velocity, and density in both exploding and imploding blast waves. In the ideal case of a strong point-source explosion or a strong implosion, the partial differential equations determining the above quantities can be reduced to a system of ordinary differential equations by means of similarity transformation and can be non-dimensionalized in such a way that only one parameter is involved; namely, the adiabatic constant, γ. This is done by introducing a new independent variable, η, defined by the ratio $\frac{r}{R}$, where R is the radius of the shock wave.

The similarity transformation involves an exponent, δ, which for the explosion case can be determined uniquely by the requirement of the conservation of energy. However, in the implosion case, the exponent cannot be determined in such a simple manner. The differential equations contain singular points in the region where the solution is required and the exponent, which is different for each value of γ, must be chosen in such a way that no infinite derivatives occur in this region.

Solutions which describe the flow fields in terms of pressures, velocities, and densities induced behind the shock wave as well as the variation of the pressure exponent, δ, with the adiabatic constant γ, have been determined for

the implosion case. The results are presented in graphical and tabular form in the Appendix. An additional quantity of physical interest is the energy ratio, $\lambda(\eta)$, which is defined as the ratio of kinetic to thermal energy at varying stages of the implosion.

II. THEROETICAL CONSIDERATIONS

If we assume one-dimensional, perfect, and inviscid gas conditions, the equations of state/continuity, and motion are the following:

$$\left(\frac{\partial}{\partial t} + \bar{u}\frac{\partial}{\partial r}\right) p\rho^{-\gamma} = 0 \tag{1}$$

$$\frac{\partial \rho}{\partial t} + \frac{\partial}{\partial r}(\rho \bar{u}) + \frac{(\nu-1)\rho\bar{u}}{r} = 0 \tag{2}$$

$$\frac{\partial \bar{u}}{\partial t} + \bar{u}\frac{\partial \bar{u}}{\partial r} + \frac{1}{\rho}\frac{\partial p}{\partial r} = 0 \tag{3}$$

where γ is the adiabatic constant, r is a spatial coordinate, and the value of ν depends on the coordinate system:

$\nu = 3$ spherical

$\nu = 2$ cylindrical coordinates

$\nu = 1$ planar coordinates

From Eqs (1), (2), and (3), by certain algebraic manipulations, we can also derive the so-called energy equation

$$r^{\nu-1}\frac{\partial E}{\partial t} + \frac{\partial}{\partial r}\left[r^{\nu-1}\bar{u}I\right] = 0 \tag{4}$$

where

$$E = \frac{1}{2}\rho\bar{u}^2 + \frac{1}{\gamma-1}p \tag{5}$$

and

$$I = \frac{1}{2}\rho\bar{u}^2 + \frac{\gamma}{\gamma-1}p \tag{6}$$

Two additional assumptions are now made. They are: (1) the profiles of the physical quantities behind the shock front are self-similar and (2) the resulting blast wave is strong.

Because of the first assumption, Eqs (1), (2), and (3) can be reduced to a system of ordinary differential equations by introducing a new independent variable, n, defined by $\frac{r}{R(t)}$, where R(t) is the radius of the shock wave forming the outer edge of the disturbance. It is found that

$$\frac{dR}{dt} = AR^{-\frac{\delta}{2}} \tag{7}$$

where A is an arbitrary constant and the exponent δ is as yet unspecified. The system of partial differential equations is now (after introducing appropriate non-dimensional variables) transformed into the following system of ordinary differential equations:

$$f' + \gamma\psi(\phi-n)\phi' = \frac{\delta}{2}\gamma\psi\phi \tag{8}$$

$$\phi' + (\phi-n)\frac{\psi'}{\psi} = -(\nu-1)\frac{\phi}{n} \tag{9}$$

$$(\phi-n)f'-\gamma(\phi-n)f\frac{\psi'}{\psi} = \delta f \tag{10}$$

where

$$\frac{p}{p_o} = \frac{A^2}{a^2} R^{-\delta} f(n) \tag{11}$$

$$\frac{\rho}{\rho_o} = \psi(n) \tag{12}$$

$$u = AR^{-\frac{\delta}{2}} \phi(n) \tag{13}$$

and

$a^2 = \frac{\gamma p_o}{\rho_o}$ is the speed of sound, while the energy equation in terms of the new variables, becomes

$$\eta^{\nu-\delta} \frac{d}{d\eta} \left[\eta^{\delta} F(\eta)\right] = \frac{d}{d\eta}\left[\eta^{\nu-1} G(\eta)\right] \tag{14}$$

with

$$F(\eta) = \frac{1}{2} \psi\phi^2 + \frac{1}{\gamma(\gamma-1)} f \tag{15}$$

and

$$G(\eta) = \phi \left[\frac{1}{2} \psi\phi^2 + \frac{1}{\gamma-1} f\right] \tag{16}$$

Eqs (8) through (10) must be solved subject to the Rankine-Hugoniot conditions at the shock front, $\eta=1$. By assuming a strong shock, these conditions may be put in the following form consistent with the similarity assumption:

$$f(1) = \frac{2\gamma}{\gamma+1} \tag{17}$$

$$\psi(1) = \frac{\gamma+1}{\gamma-1} \tag{18}$$

$$\phi(1) = \frac{2}{\gamma+1} \tag{19}$$

From Eq (14), it is clear that, in the explosion problem, δ must have the value ν in order to meet the requirement of energy conservation. In the implosion problem this is not the case, and the correct value of δ must be determined by

other considerations. Specifically, it must be determined in such a way that no infinite derivatives occur in the region of physical interest which in the present problem corresponds to the range $1 \leq \eta < \infty$. This requirement can only be met if, in any of the expressions for the derivatives, either the denominator does not vanish or both the numerator and denominator vanish simultaneously. The latter condition determines a "singular point" at which the derivatives are finite but must be determined by a limiting process. The treatment of this problem is simplified if two new variables

$$u = \frac{f}{\eta^2 \psi} \tag{20}$$

and $y = \frac{\phi}{\eta}$ are introduced. (21)

Substituting Eqs (20) and (21) into (8), (9), and (10), and solving explicitly for f', ψ', and ϕ', we obtain the following:

$$\eta \frac{f'}{f} = \frac{(y-1)[\delta-(\nu-1)\gamma y] - \frac{\delta\gamma y}{2}}{(y-1)^2-u} = \frac{P(y)}{(y-1)^2-u} \tag{22}$$

$$\gamma\eta \frac{\psi'}{\psi} = \frac{\frac{\delta u}{(y-1)} - \gamma(\nu-1)y(y-1) - \frac{\gamma\delta y}{2}}{(y-1)^2-u} = \frac{P(y)}{(y-1)^2-u} - \frac{\delta}{y-1} \tag{23}$$

$$\phi' = \frac{(\nu-1)uy - \frac{\delta}{\gamma} u + \frac{\delta}{2} y(y-1)}{(y-1)^2-u} = \frac{-uP(y)}{\gamma(y-1)[(y-1)^2-u]} + \frac{\delta}{2} \frac{y}{y-1} \tag{24}$$

where

$$P(y) = (y-1)[\delta-(\nu-1)\gamma y] - \frac{\delta\gamma}{2} y$$

The conditions that the numerator and the denominator in each of the above equations vanish simultaneously will only be satisfied if $y = y_1$ is a root of the quadratic equation

$$P(y) = \gamma y^2(1-\nu) + y\left[\delta + \nu\gamma - \gamma - \frac{\delta\gamma}{2}\right] - \delta = 0 \qquad (25)$$

and if

$$u_1 = (y_1 - 1)^2 \qquad (26)$$

Equations (25) and (26) define two singular points corresponding to the two roots of (25).

In general, the solution of the system of differential equations which satisfies the shock conditions will not pass through such a point unless the proper value of "δ" has been used. On the other hand, the trajectories which pass through a singular point and which, clearly, are the only physically acceptable ones will not, in general, meet the specified shock conditions.

The analysis can be simplified if Eqs (22) and (23) are replaced by a single equation with u and y as variables. This is done by noting that

$$\eta \frac{u'}{u} = \eta\left(\frac{f'}{f} - \frac{\psi'}{\psi}\right) - 2 \qquad (27)$$

and

$$\eta y' = \phi' - y$$

Whence

$$\frac{1}{u}\frac{du}{dy} = \frac{(\gamma-1)P(y)(y-1) + [\delta - 2\gamma(y-1)][(y-1)^2 - u]}{-uP(y) + \gamma y\left[\frac{\delta}{2} - y + 1\right][(y-1)^2 - u]} \qquad (28)$$

It is seen that any point (u_1, y_1) as determined by Eqs (25) and (26) will also be a singular point of Eq (28). The procedure to be followed is described in the next paragraph.

A value of δ is assumed and a singular point is located from Eqs (25) and (26). Since both the numerator and the denominator of Eq (28) vanish at this point, the expression for $\frac{du}{dy}$ in Eq (28) is indeterminate but can be found by applying L'Hospital's rule to the right side. The result is the following quadratic equation

$$\gamma y_1\left[\frac{\delta}{2} - y_1 + 1\right]\beta^2 - \left\{2\gamma y_1(y_1-1)\left[\frac{\delta}{2} - y_1 + 1\right] + u_1\left[\delta + 2\gamma(1-y_1)\right] - u_1P'\right\}\beta - (\gamma-1)(1-y_1)u_1P' - 2u_1(1-y_1)\left[\delta + 2\gamma(1-y_1)\right] = 0 \tag{29}$$

where β is the value of $\frac{du}{dy}$ at the singular point. Since u is known to be an increasing function of y, only a positive root of Eq (29) is admissible. Once the initial value of $\frac{du}{dy}$ has been found, Eq (28) can be integrated numerically until the point

$$y = \frac{2}{\gamma+1} \tag{30}$$

corresponding to the shock front conditions is reached. Had the right value of δ been chosen, u would then have had the value

$$u(1) = \frac{f(1)}{\psi(1)} = \frac{2\gamma(\gamma-1)}{(\gamma+1)^2} \tag{31}$$

In general, this will not be the case but, after several values of δ are tried, it is a simple matter to locate the correct one by the method of false position.

For want of a better trial value of δ, the following upper bound found by equating to zero the discriminant of Eq (25) can be used as a starting point:

$$\delta_{max} = \frac{2(\nu-1)\gamma}{(\sqrt{2} + \sqrt{\gamma})^2} \tag{32}$$

Of the two possible singular points determined by Eq (25), only one will yield a solution which meets the shock requirements. The incorrect point can be identified by the fact that the value of u(1) will tend further from the value given by Eq (31) as δ is decreased from its initial value, Eq (32). (Experience has indicated that the smaller of the two roots should always be used.)

Having found the correct value of δ, we can now obtain f, ψ, and ϕ directly as functions of η by numerically integrating eqs (8), (9), and (10); and finally, the energy ratio, λ, defined by

$$\lambda = \frac{\frac{1}{\gamma(\gamma-1)}\int_1^\eta f\eta^2 d\eta}{\frac{1}{2}\int_1^\eta \psi\phi^2\eta^2 d\eta} \tag{33}$$

can be determined by quadrature.

DISCUSSION

The formulations presented in this paper constitute the first numerically tractable ones for the calculation of incoming blast waves. The formulations can be converted into a completely self-contained computational routine which permits all the physical quantities to be computed directly without recourse to trial and error methods.

Shock and combustion wave dynamics in gases can be applied to produce gases of extremely high pressures and enthalpies. Gases in this state can be used to study problems in magnetogasdynamics and plasma physics. One direct application of these results is found in the preliminary design and use of hypervelocity launchers. In particular, it is seen that the above described gas can be used to produce, in hypervelocity launchers, theoretical gun velocities of aerodynamic models up to 50,000 ft/sec and more. A facility has been built at UTIAS which substantiates many of the calculated results given in this paper. An understanding of the phenomena at the core of the earth, where temperatures and pressures are in the same order of magnitude as those validating the intense blast wave theory, can be gained by applying these results.

TABLE I

I. Values of the Similarity Exponents δ for Various γ's

$\nu = 3$

γ	This Report	Flagg[2]	Butler[1]	Guderly[3]	Welsh[9]	Stanyukovich[6]
	0.6415130	0.6416	0.641513			0.8
1.2	0.7887215	0.7887	0.788728	0.792		
1.4	0.8810576	0.8810				
1.6	0.9053854	0.9053	0.905385			
$\frac{5}{3}$	0.9474459	0.9475				
1.8	0.9982936	1.000				
2.0	1.0387500	1.039				
2.2	1.0717973	1.072				
2.4	1.0993327	1.099				
2.6	1.1226397	1.123				
2.8	1.1426252	1.143			1.14262	1.1
3.0	1.1599511	1.159				
3.2	1.1751135	1.166				
3.4	1.1884919	1.188				
3.6	1.2003819	1.199				
3.8	1.2110174	1.211				
4.0	1.3996883					3.0

$\nu = 2$

	0.3224406		0.322441			
1.2	0.3942828		0.394589			
1.4	0.4399181					
1.6	0.4521075		0.452108			
$\frac{5}{3}$	0.4734110					
1.8	0.4996489					
2.0	0.5209979					
2.2	0.5388152					
2.4	0.5539632					
2.6	0.5670279					
2.8	0.5784273					
3.0	0.5884699					
3.2	0.5973901					
3.4	0.6053698					
3.6	0.6125524					
3.8	0.6190534					
4.0	0.7508497					
∞						

ACKNOWLEDGMENT

The authors wish to express their sincere appreciation to Mr. James C. Caslin of the Applied Mathematics Research Laboratory, Aerospace Research Laboratories, for his work in programming and carrying out the numerical calculations on the IBM 1620 and 7094.

BIBLIOGRAPHY

1. Butler, D. S., Converging Spherical and Cylindrical Shocks, Armament Research Establishment, Report 54/54, Fort Halstead, Kent, December 1954.

2. Flagg, R. F., The Application of Implosion Wave Dynamics to a Hypervelocity Launcher, ARL Report 67-0220, December 1967.

3. Guderley, G., "Strong Spherical and Cylindrical Shock Waves in the Neighborhood of the Center of the Sphere of the Axis of a Cylinder," Report of the Institute for Gasdynamics of the Herman Goring Aviation Research Institutem Braunschweig (Luftfahrtforschung, Vol. 19, No. 9, pp. 302-312, October 1942.)

4. Stanyukovich, "Unsteady Motion of a Continuous Media," Pergamon Press, 1960.

5. Welsh, R. L., Imploding Shocks and Detonations, Report No. AS-66-1, College of Engineering, University of California, Berkeley, January 1966.

Appendix A

DETAILS OF COMPUTATIONAL PROCEDURE FOR THE IMPLOSION CASE

Integration of the appropriate differential equations was accomplished by a combination of the Runge-Kutta and Adams-Moulton methods. In order to determine the parameter δ, Eq (32) was integrated numerically, starting at a singular point as determined by Eqs (29) and (30) and continued until y attained the value corresponding to the shock as given by Eq (34). The resulting value obtained for u was then compared with the value given by Eq (35). If the two did not agree, a new value of δ was tried. This process was continued until the computed value of u agreed with that of Eq (35). A relatively coarse interval of integration was used at first in order to obtain a reasonably accurate value of δ. The integration was then repeated, using continuously smaller intervals until two successive values of δ were obtained which agreed to within a specified tolerance.

For each value of γ, the starting value of δ was determined by means of Eq (36). This value was then decreased by constant increments until two successive δ's yielded value of u above and below the one specified by the shock conditions. At this point, the method of false position was employed to locate δ more precisely.

Having found a reasonably accurate value of δ, the original system of differential Eqs (8), (9), and (10) could then be

integrated numerically, using the known initial conditions at the shock front. The computational results could be partially checked by making use of the following analytic relation obtained by eliminating $(\phi-\eta)$ between Eqs (9) and (10), writing the resulting expression as an exact differential and integrating. The result is

$$(\eta-\phi)\eta^{\nu-1} f^{\frac{\nu}{\delta}} \psi^{\left(1-\frac{\nu\gamma}{\delta}\right)} = C \qquad \text{(A-1)}$$

where C is given by the shock conditions. When the computed value of the left side failed to agree with the more exact value determined by the initial conditions, the interval of integration was automatically cut until satisfactory agreement was obtained. In carrying out the integration of systems (8), (9), and (10), it was found to be more satisfactory to use $\frac{1}{\eta}$ as the independent variable.

Appendix B

THE IMPLOSION PROBLEM FOR $\gamma \to \infty$

The behavior of the solutions for large γ can be better understood by examining the limiting form of the Eq (28) as γ approaches infinity. We introduce a new independent variable

$$\zeta = \gamma y. \tag{B-1}$$

Substituting into Eq (28), and letting $\gamma \to \infty$, we obtain the limiting form of the differential equation for large γ:

$$\frac{1}{u}\frac{du}{d\zeta} = \frac{\delta - \left[2 - \frac{\delta}{2}\right]\zeta + 2(1-u)}{\left[\frac{\delta}{2} + 1\right]\zeta + u(\delta - 3\zeta)} \tag{B-2}$$

The limiting form of the shock condition becomes $u = 2$ when $\xi = 2$,

while the singular point of Eq (B-2) occurs when

$$\zeta = \frac{\delta}{2 - \frac{\delta}{2}}$$

$$u = 1 \tag{B-4}$$

The value, β, of $\frac{du}{d\xi}$ at the singular point, obtained by applying L'Hospital's Rule to the right side of Eq (B-2) is found by calculating the positive root of the equation

$$\delta\left[\frac{\delta}{2} + 1\right]\beta^2 - \frac{\delta}{2}\left[\gamma - 1 - \frac{\delta}{2}\right]\beta - \left[\gamma - 1 - \frac{\delta}{2}\right]^2 = 0 \tag{B-5}$$

Now that the initial conditions and the initial slope are known, Eq (B-2) can be integrated numerically. At the point $\zeta=2$, u should equal 2 if the right value of δ had been used. As before, the correct value of δ can be located by the method of false position. The resulting values of δ as determined by the above method are found to be

$$\delta_\infty = 0.75084978 \ldots\ldots, \quad \nu=2$$

$$\delta_\infty = 1.399688 \ldots\ldots, \quad \nu=3$$

The latter differs appreciably from the value $\delta_\infty = 3$ as given by Stanyukovich.

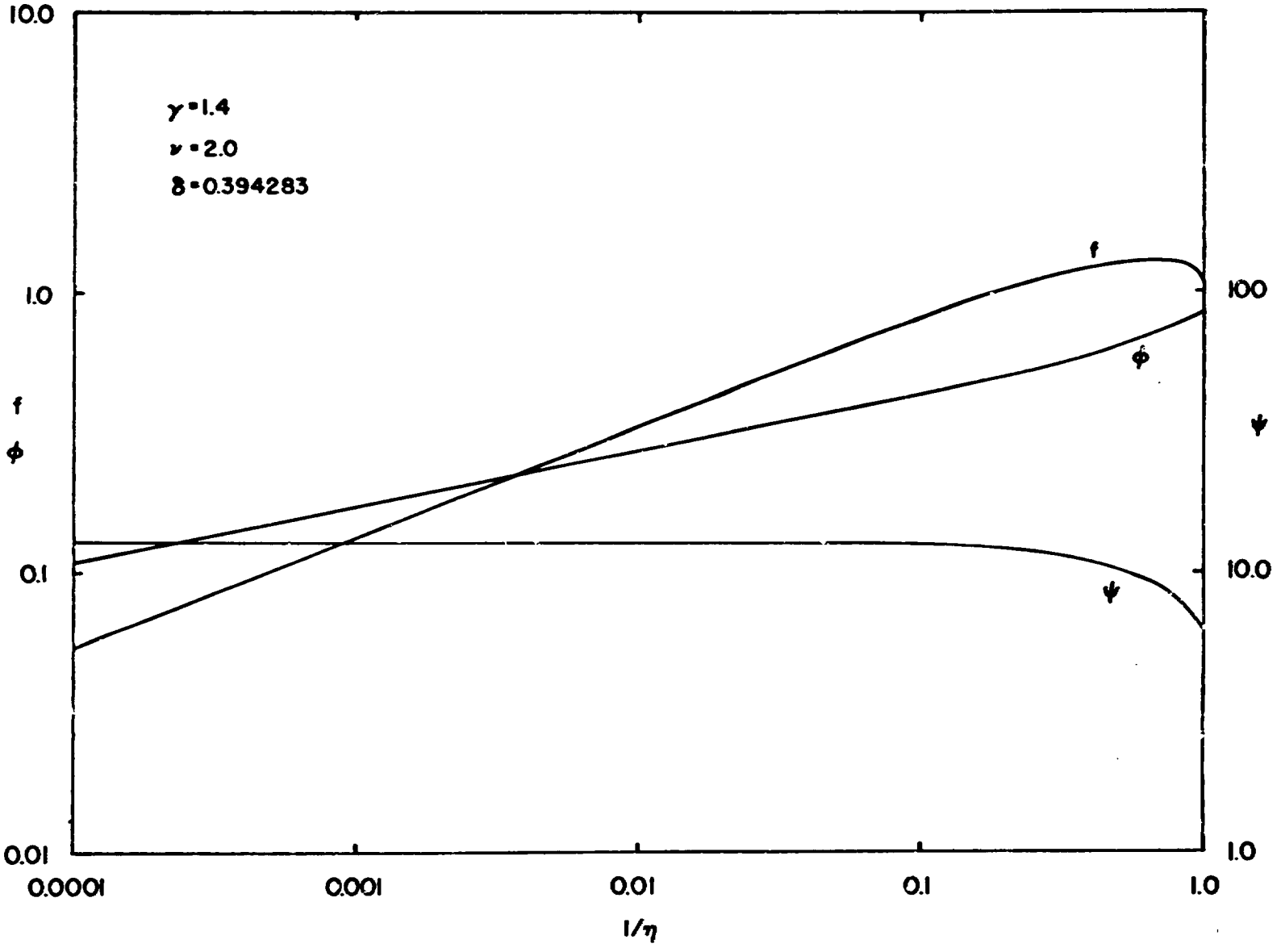

FIG. 1 THE SIMILARITY VARIABLES FOR PRESSURE, VELOCITY AND DENSITY AS FUNCTION OF $1/\eta$.

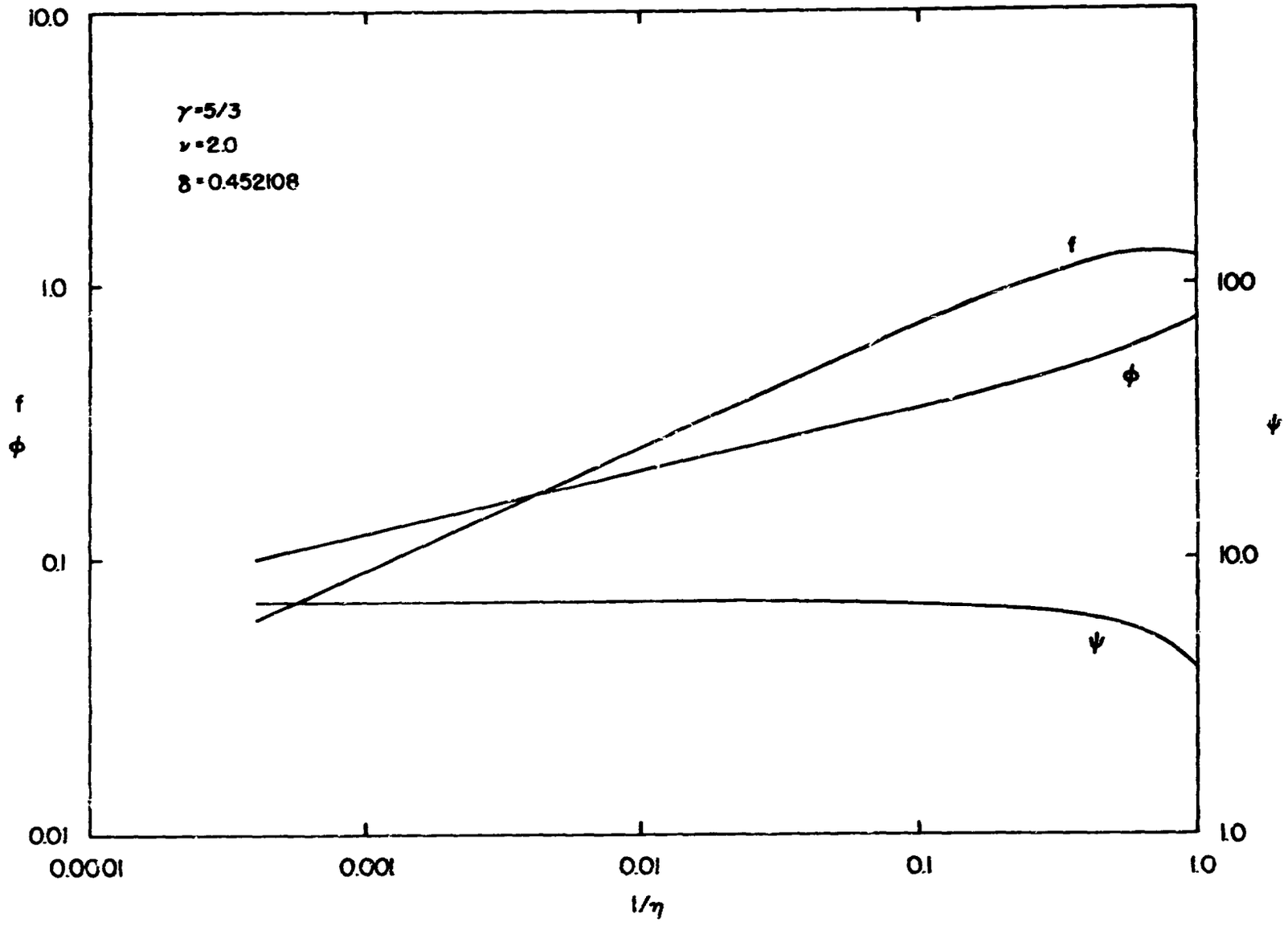

FIG. 2 THE SIMILARITY VARIABLES FOR PRESSURE, VELOCITY AND DENSITY AS FUNCTION OF $1/\eta$.

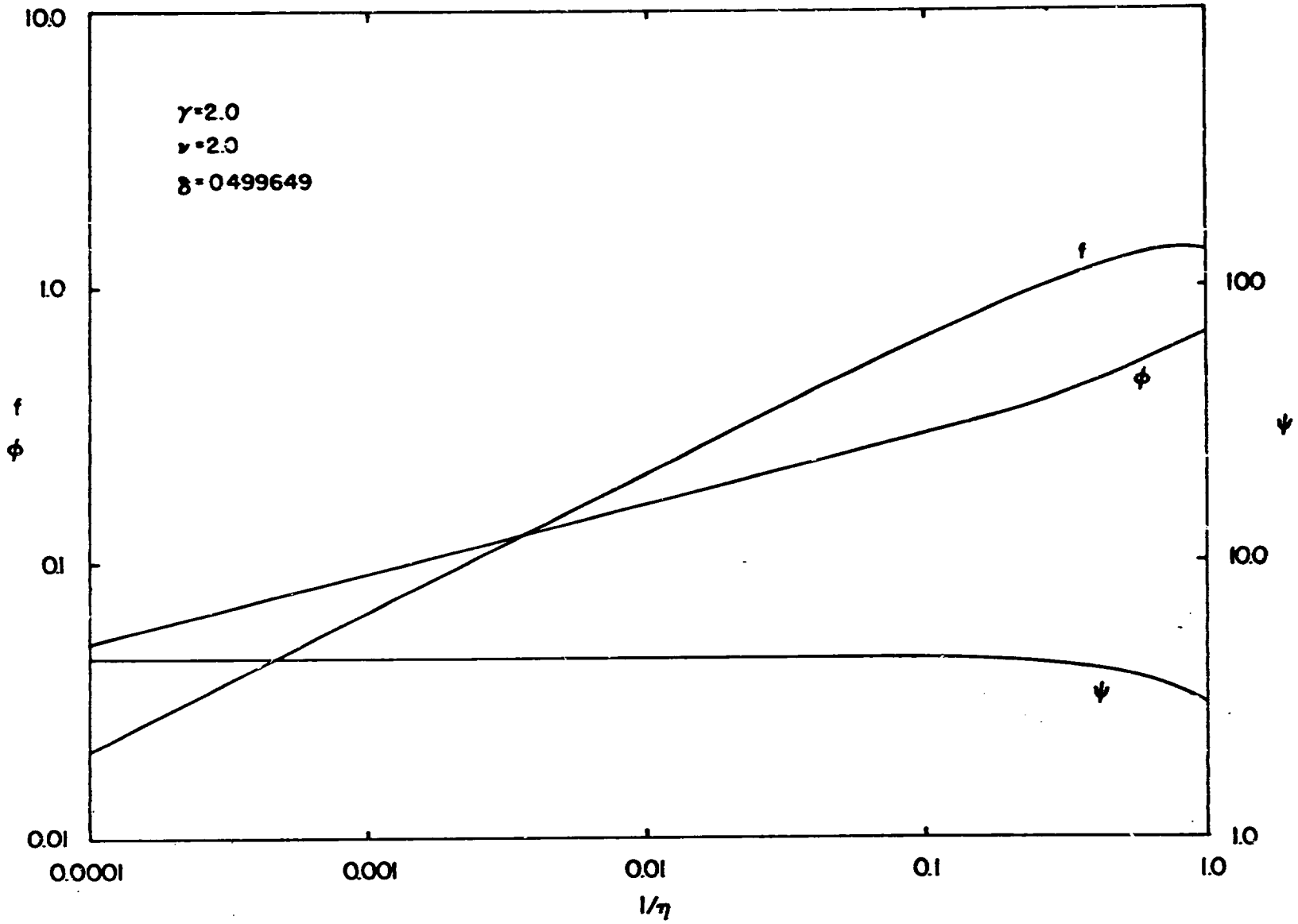

FIG. 3 THE SIMILARITY VARIABLES FOR PRESSURE, VELOCITY AND DENSITY AS FUNCTION OF $1/\eta$.

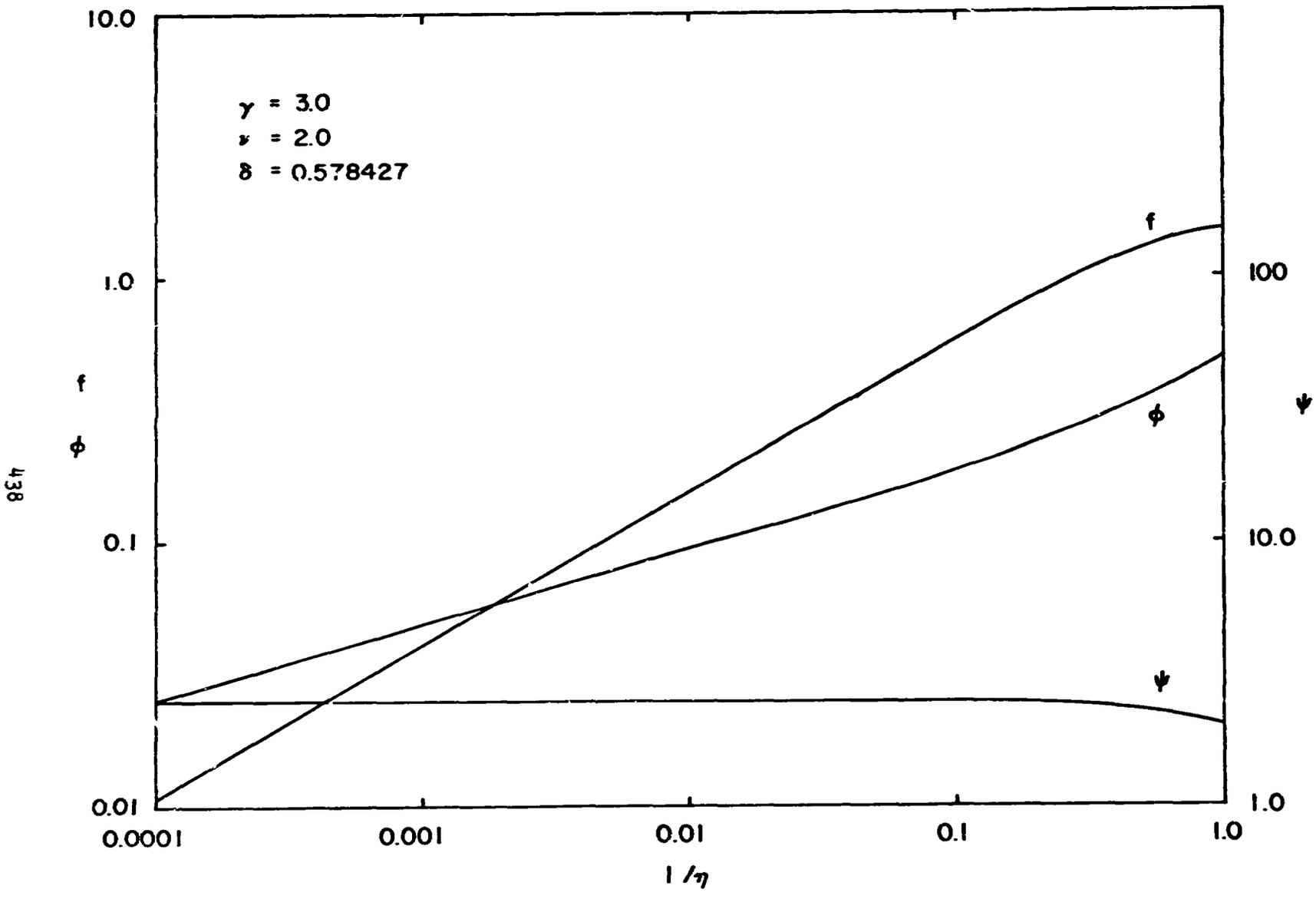

FIG. 4 THE SIMILARITY VARIABLES FOR PRESSURE, VELOCITY AND DENSITY AS FUNCTION OF $1/\eta$.

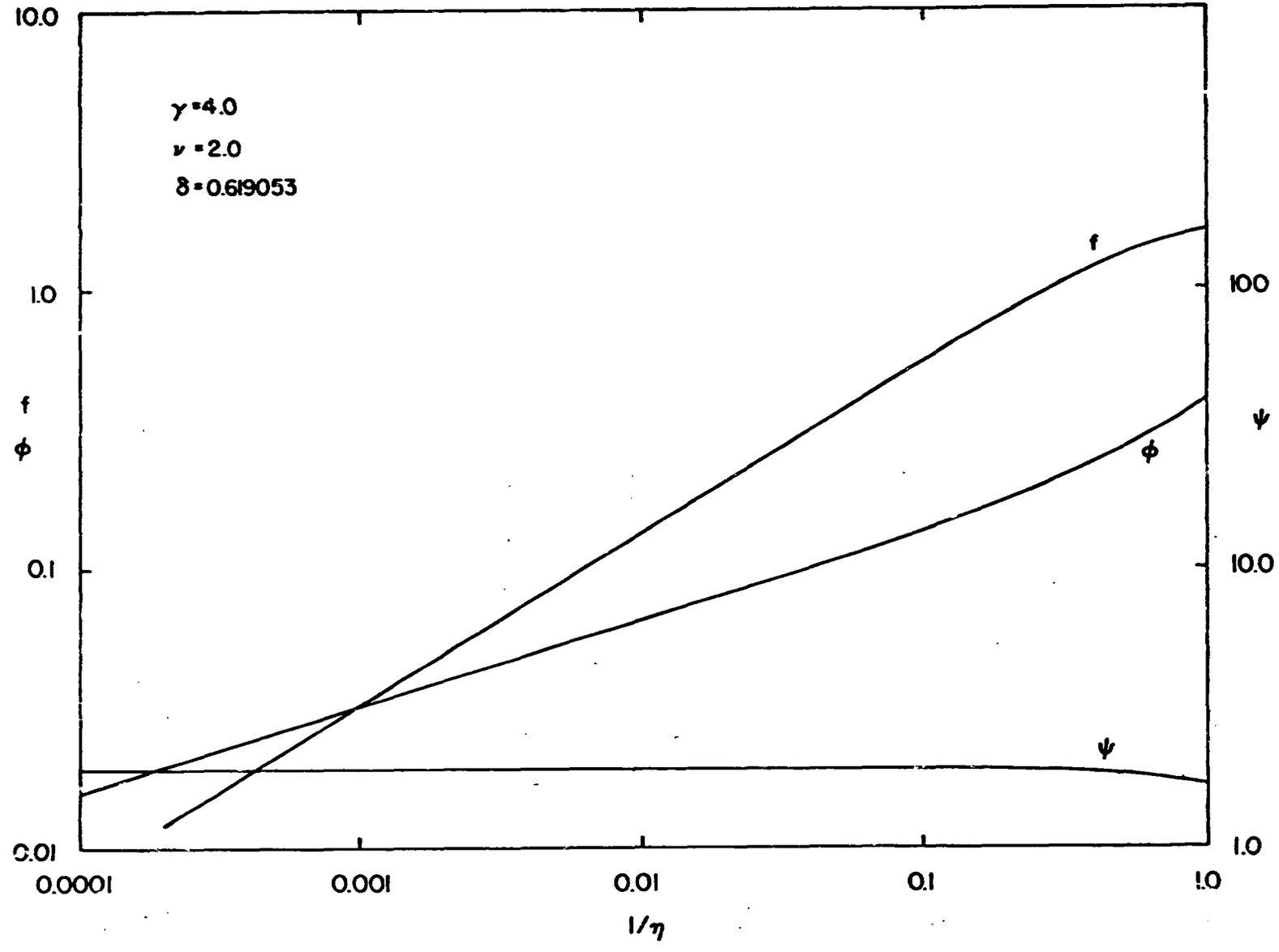

FIG. 5 THE SIMILARITY VARIABLES FOR PRESSURE, VELOCITY AND DENSITY AS FUNCTION OF $1/\eta$.

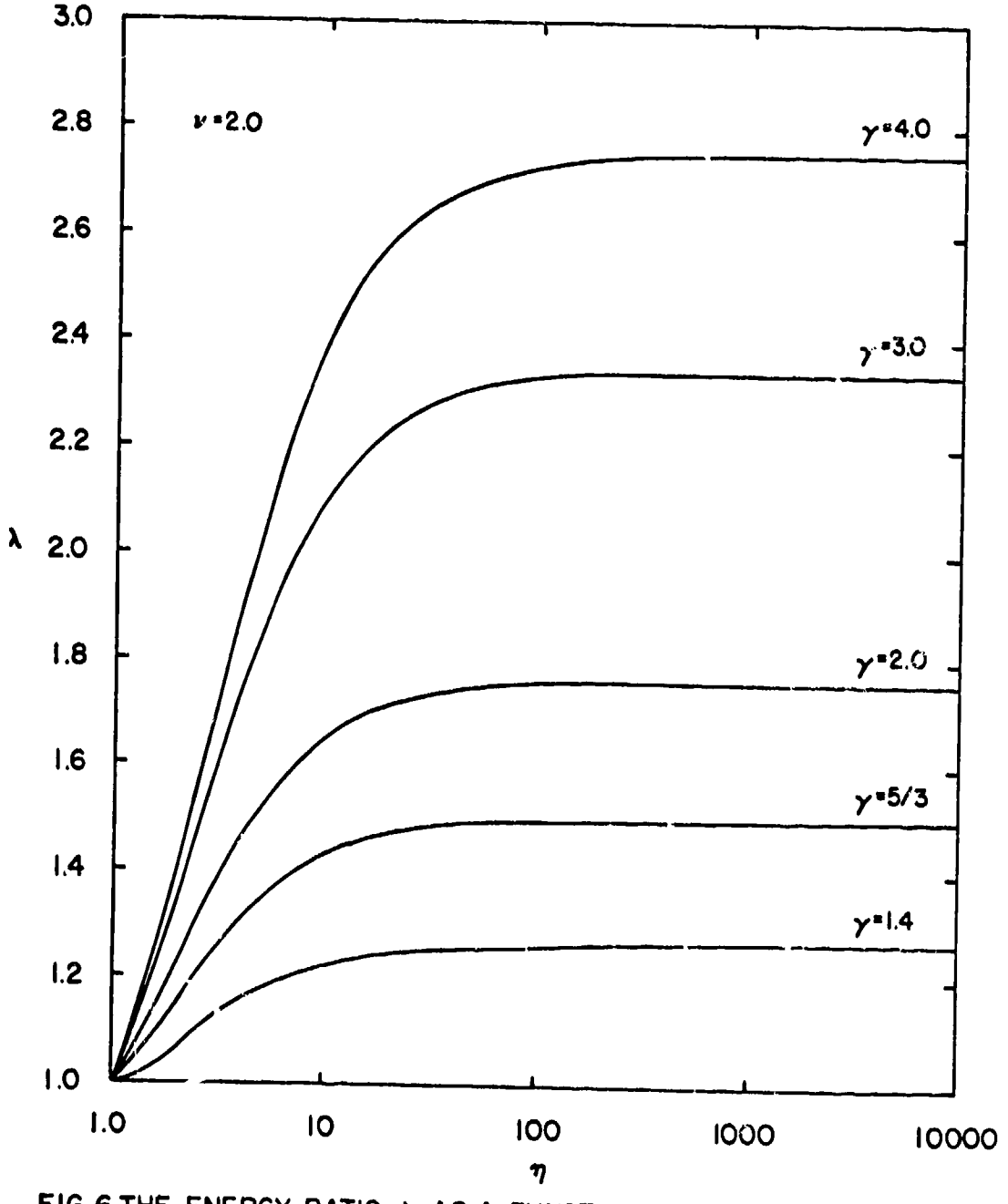

FIG. 6 THE ENERGY RATIO, λ, AS A FUNCTION OF THE NON-DIMENSIONAL DISTANCE PARAMETER, η, FOR VARIOUS VALUES OF THE ADIABATIC CONSTANT γ.

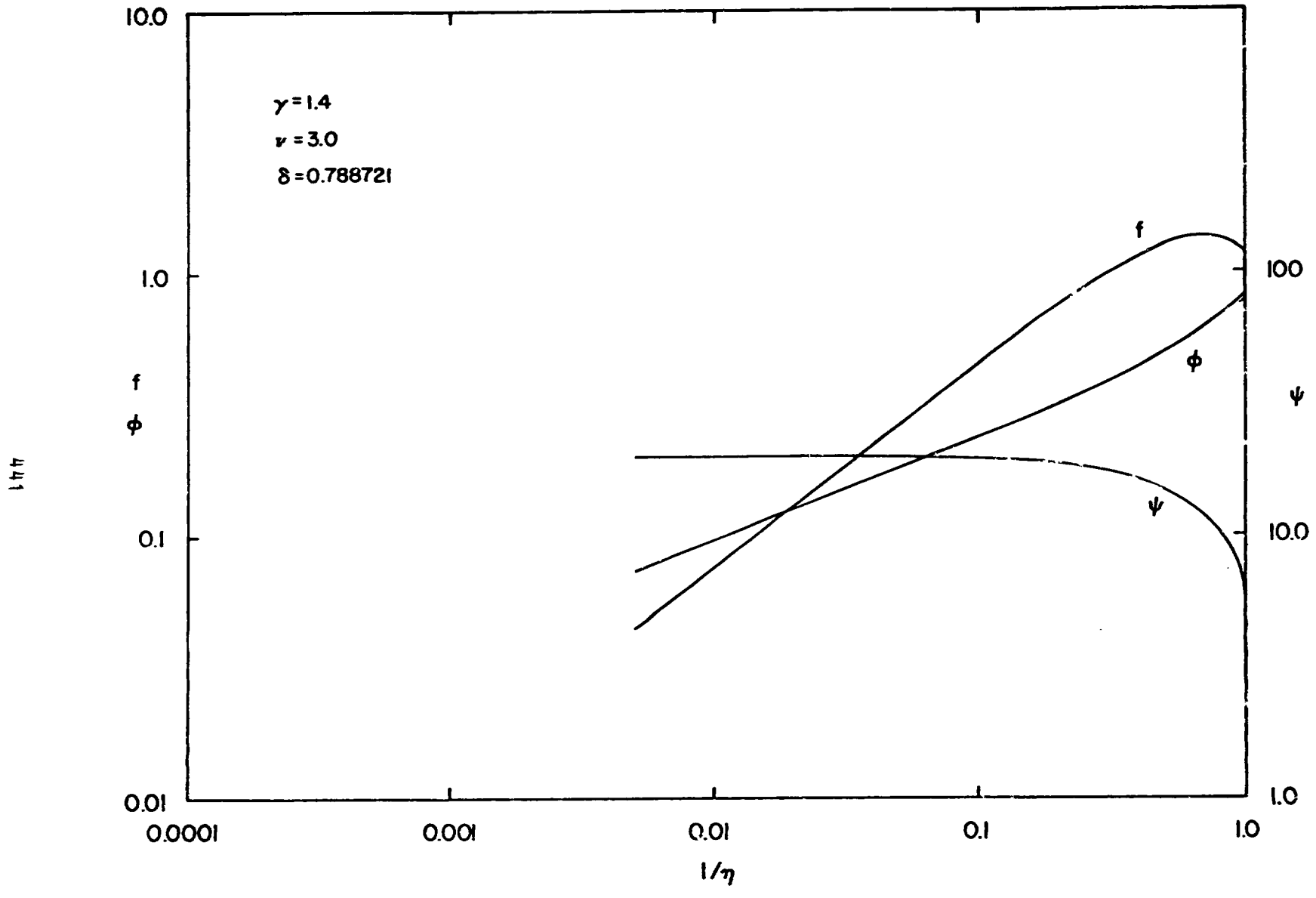

FIG. 7 THE SIMILARITY VARIABLES FOR PRESSURE, VELOCITY AND DENSITY AS FUNCTION OF $1/\eta$.

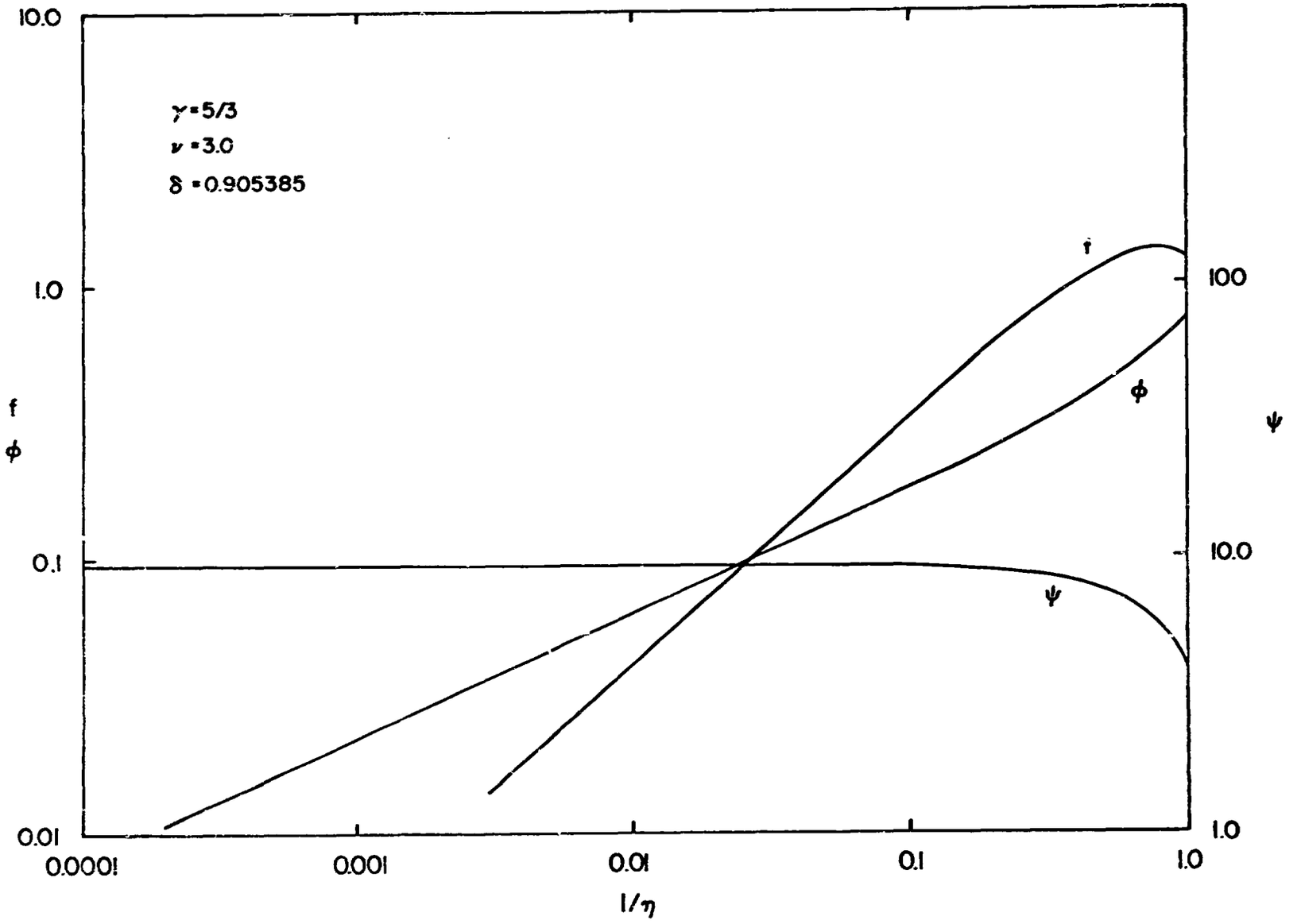

FIG. 8 THE SIMILARITY VARIABLES FOR PRESSURE, VELOCITY AND DENSITY AS FUNCTION OF $1/\eta$.

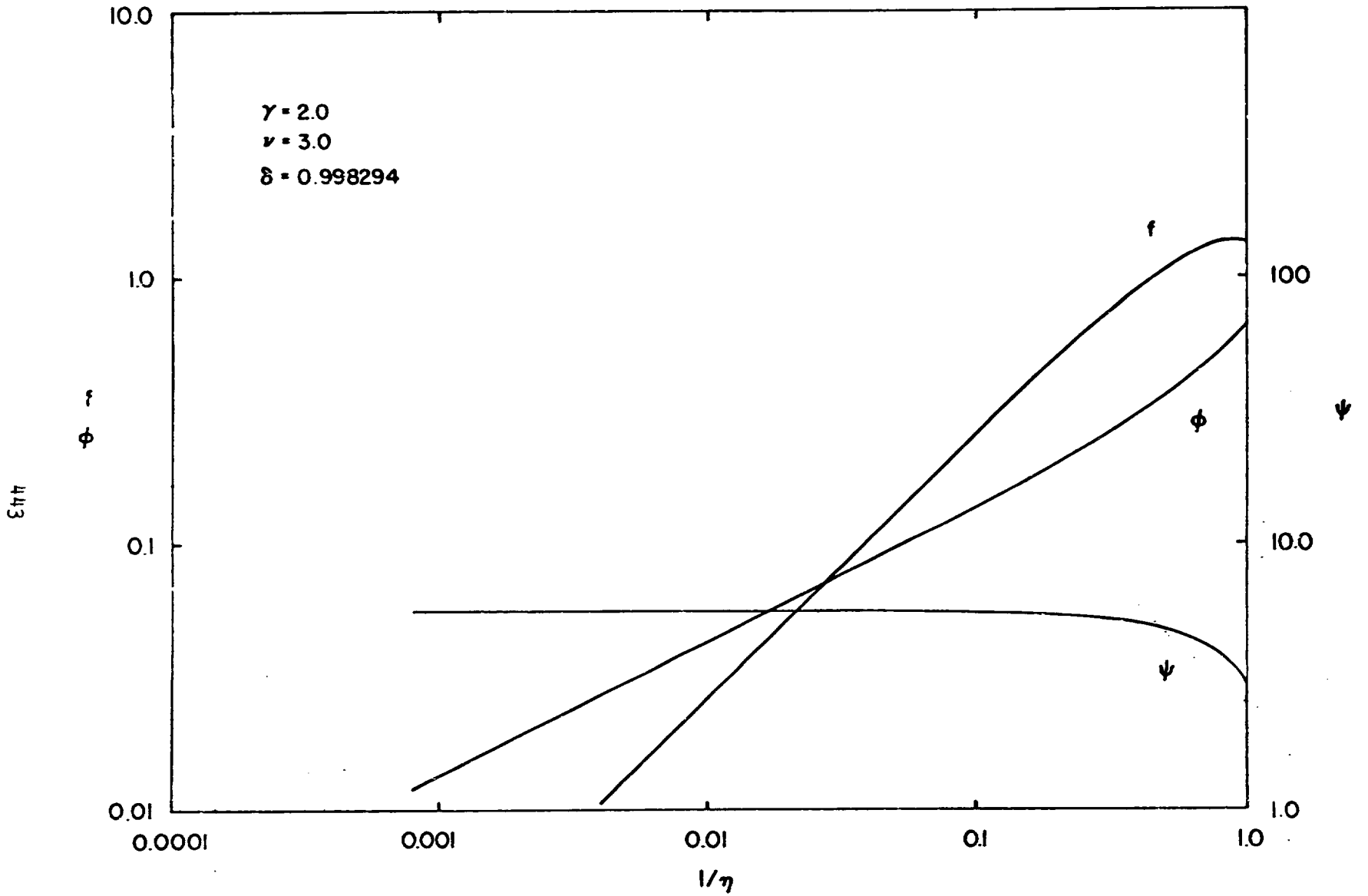

FIG. 9 THE SIMILARITY VARIABLES FOR PRESSURE, VELOCITY AND DENSITY AS FUNCTION OF $1/\eta$.

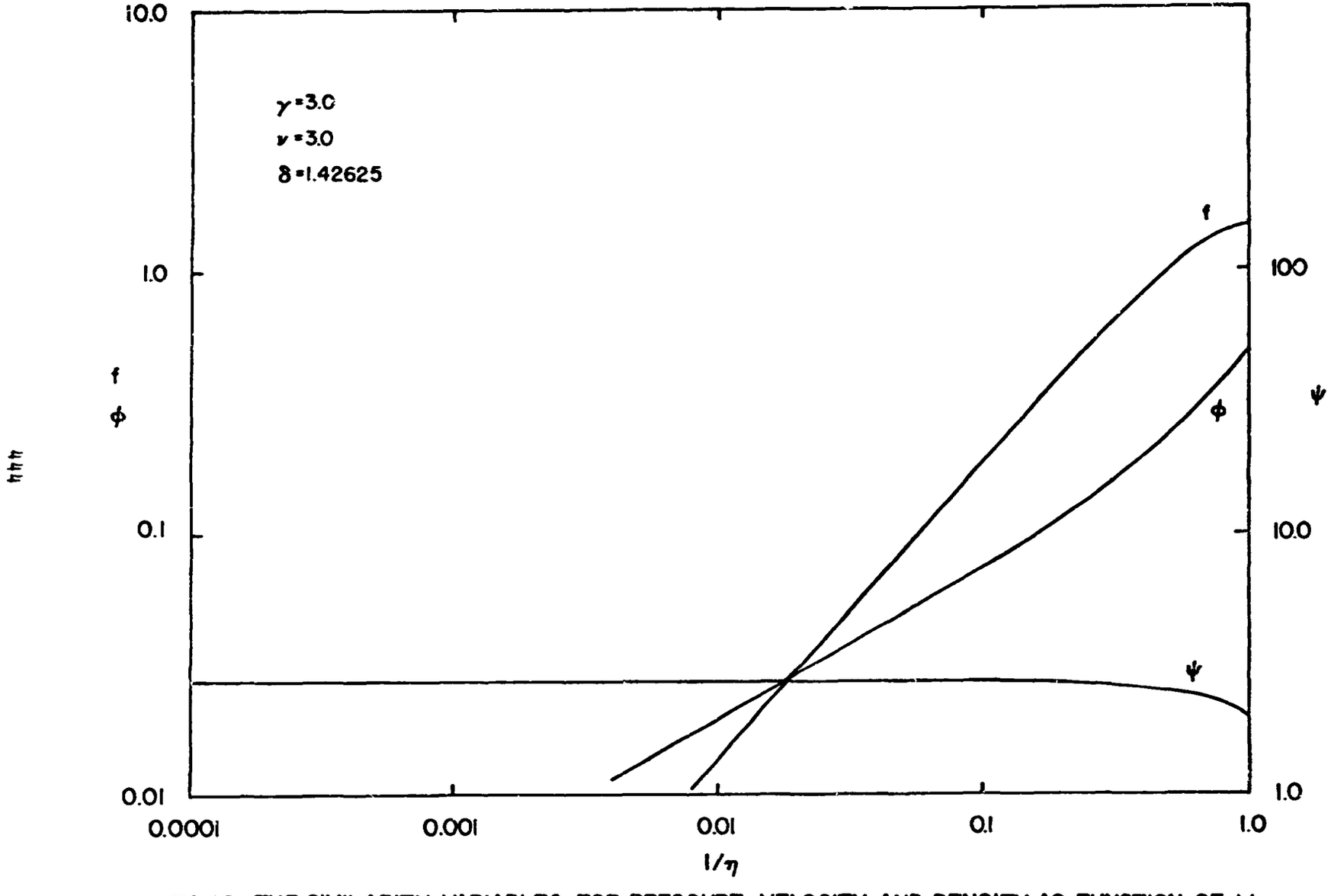

FIG. 10 THE SIMILARITY VARIABLES FOR PRESSURE, VELOCITY AND DENSITY AS FUNCTION OF $1/\eta$.

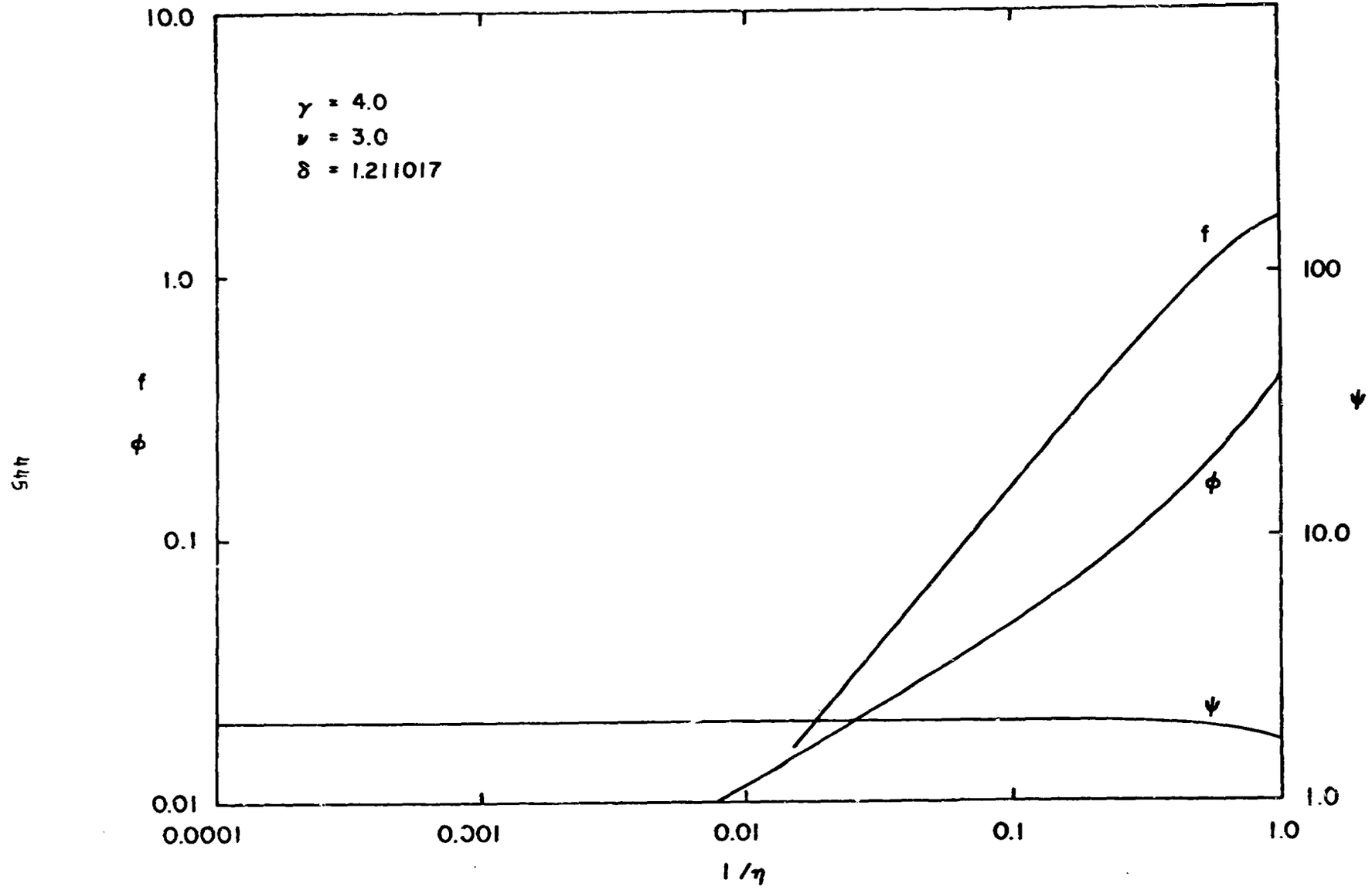

FIG. 11 THE SIMILARITY VARIABLES FOR PRESSURE, VELOCITY AND DENSITY AS FUNCTION OF $1/\eta$.

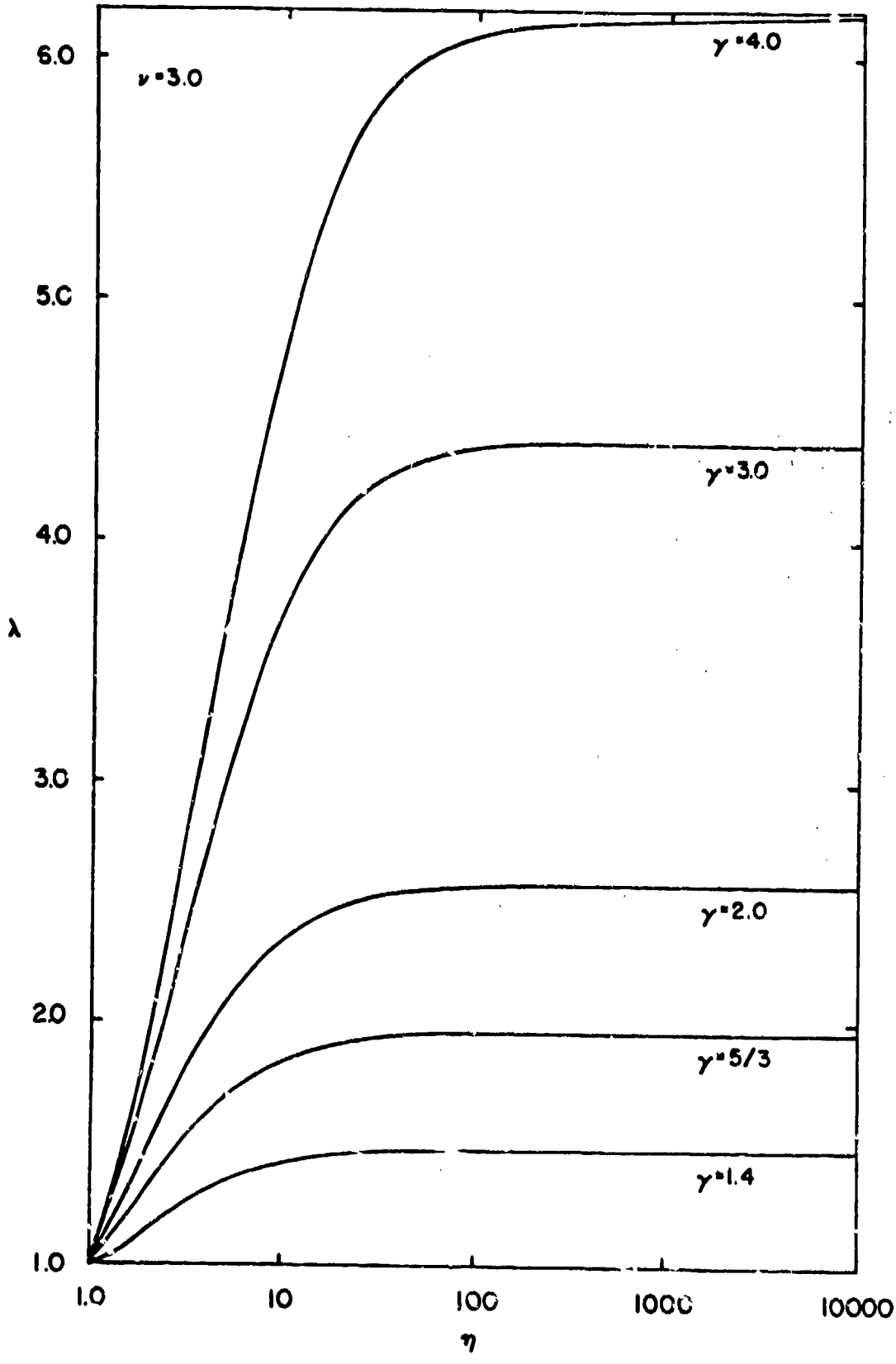

FIG. 12 THE ENERGY RATIO, λ, AS A FUNCTION OF THE NON-DIMENSIONAL DISTANCE PARAMETER, η, FOR VARIOUS VALUES OF THE ADIABATIC CONSTANT γ.

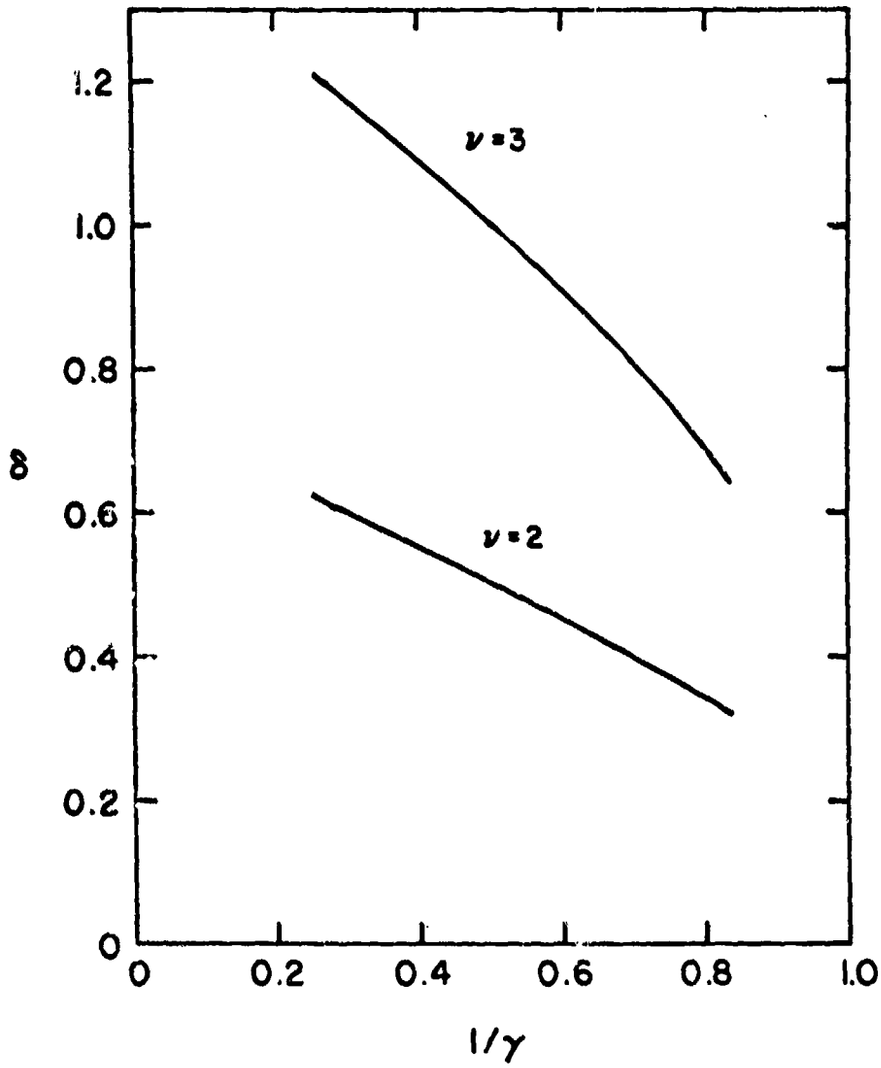

FIG. 13 THE VARIATION OF THE PRESSURE EXPONENT δ VERSUS $1/\gamma$ FOR SPHERICAL AND CYLINDRICAL IMPLOSIONS.

AD P000334

ON SYNGE'S CRITERION FOR THE STABILITY OF PLANE COUETTE FLOW

by

K. F. Lee and Knox Millsaps
Department of Engineering Sciences
University of Florida

A simple proof for the conjectured hydrodynamical stability of plane Couette flows against perturbations of all frequencies and of infinitesmal amplitude is one of the classically formulated problems in theoretical fluid dynamics, and its solution has eluded everyone including many of the most powerful mathematical analysts of modern times. J. L. Synge made one of the most appealing approaches to the solution by giving a simple criterion for the lower bound of the minimally critical Reynolds Number. Synge's criterion was thought to be relatively weak although the limit of applicability has not been reported, and this investigation examines exactly the weakness by determining the extremum in terms of the maximum Reynolds Number, Rm, for stability. It is shown that $R_m = 4$ is the maximum using Synge's criterion which is unfortunetely less than $R_m = 44.3$ using a much more complicated analysis due to Orr. The importance of these results is enhanced somewhat if the eventual proof, assuming the truth of the conjecture, follows von Mises' formulation in which stability for a small finite range from zero is required as a starting point in the subsequent analysis.

Manuscript Received January 1979.

INTRODUCTION

One of the classical methods for examining the transition of a viscous flow from the laminar to the turbulent state is due to Sommerfeld and Orr and consists of the mathematical superposition $\psi + \psi'$ of a perturbation in the stream function

$$\psi' = f(y^*)\exp[\sigma t + i\lambda x]$$

where f and σ are generally complex, λ is real and non-negative, and x, y^* and t are the physical coordinates, upon a viscous flow described by the Navier-Stokes equation for plane motion

$$D\Delta\psi = \nu\Delta\Delta\psi$$

where ν is the kinematic viscosity, ψ is the stream function, Δ is the Laplacian, and D is the substantive derivative. Of course, one then attempts the solution of the linearized bounary value problem for $f(y^*)$. All references to the original works will be omitted since they can be found in the classic work, C. C. Lin, The Theory of Hydrodynamic Stability, Cambridge, 1955.

At first glance everyone would think that the easiest analysis would occur for the mathematically simplest flow between two planes, $y^* = \pm h$, moving at velocities $-U_o$ and U_o in the x-direction, the so-called plane Couette flow for which $\psi = -\frac{U_o y^{*2}}{2h}$; unfortunately, for this simple idea, history has shown that the answer transcends the analytical abilities of many of the most celebrated researchers in fluid mechanics --- Heisenberg, L. Hopf, von Kármán, Landau, H. A. Lorentz, von Mises, F. Noether, Orr, Prandtl, Rayleigh, Schlichting, Sommerfeld, Squire, Synge, G. I. Taylor, T. Y. Thomas, Tollmien, and,

more recently, Morawetz, Press, and Wasow. Of these, L. Hopf undertook quite early the straightforward approach and delineated a real difficulty; von Mises made a brilliantly powerful, yet unsuccessful, attack; Prandtl and T. Y. Thomas used truly novel methods; and Orr gave the "best" result after an exceedingly complicated and painstaking analysis. Of all, Synge presented the most appealing analysis because of its simplicity, and, although he called his result, "very weak", no one ever looked far enough into its weakness to see if it might not be stretched to include Orr's result. This paper investigates its strength.

Incidentally, on one hand, nearly all of the investigations indicate that plane Couette flow is stable for all infinitesimal disturbances at all Reynolds numbers --- an almost incredible result from the physical viewpoint. On the other hand, fifty years ago nearly all mathematical physicists thought that plane Poiseuille flow was stable, but L. H. Thomas by direct numerical methods displayed the minimum critical Reynolds number for that flow and settled that problem once and for all time although the historian would concede that considerable doubts had been raised by the time of the computations of Thomas.

I. SYNGE'S CRITERION

If L denotes $\frac{d^2}{dy^2} - \lambda^2$, where $y = \frac{y^*}{h}$, then the boundary value problem for f(y) can be put into the following form:

A fourth order ordinary differential equation

(1.1) $$LLf = \sigma Lf + i\lambda RyLf$$

with the boundary conditions

(1.2) $$f(\pm 1) = f'(\pm 1) = 0$$

where R is the Reynolds number, $R = \frac{U_o h}{\nu}$

If one denotes a complex conjugate by a bar and differentiation with respect to y by a prime and if one multiplies Eq.(1.1) by $\bar{f}\,dy$ and integrates from -1 to +1, one will obtain

(1.3) $$\sigma(I_1^2 + \lambda^2 I_o^2) = -i\lambda RQ - (I_2^2 + 2\lambda I_1^2 + \lambda^4 I_o^2)$$

where

$$I_o^2 = \int_{-1}^{+1} f\bar{f}\,dy,\quad I_1^2 = \int_{-1}^{+1} f'\bar{f}'\,dy,\quad I_2^2 = \int_{-1}^{+1} f''\bar{f}''\,dy,$$

and

$$Q = \int_{-1}^{+1} (f'\bar{f} + yf'\bar{f}' + \lambda^2 f''\bar{f}'')dy$$

Of course, Eq.(1.2) has been used in the integrations by parts, and one observes that a definite difficulty is contained in the integral $\int_{-1}^{+1} f'\bar{f}\,dy$ in Q.

Now, if the complex conjugate of Eq.(1.3) is added to itself, it follows that

$$\sigma_1(I_1^2 + \lambda^2 I_o^2) = -\frac{1}{2}\lambda R(Q - \bar{Q}) - (I_2^2 + 2\lambda^2 I_1^2 + \lambda^4 I_o^2)$$

where

$$\sigma = \sigma_1 + i\sigma_2$$

Upon noting that $|Q - \bar{Q}| < 2I_o I_1$ from Schwarz's inequality and, after integrating by parts, it then follows that

(1.4) $$\sigma_1(I_1^2 + \lambda^2 I_o^2) < \lambda R I_o I_1 - (I_2^2 + 2\lambda^2 I_1^2 + \lambda^4 I_o^2)$$

Now, it is obvious that

$$(1.5)\qquad \int_{-1}^{+1} (f + \alpha y f' + \beta f'')(\bar{f} + \alpha y \bar{f}' + \beta \bar{f}'')dy > 0$$

where α and β are real, and it follows that

$$(1.6)\qquad \beta^2 I_2^2 > I_1^2(\alpha\beta - \alpha^2 + 2\beta) + I_o^2(\alpha - 1)$$

after noting $\int_{-1}^{+1} y^2 f'\bar{f}'\, dy < I_1^2$. The combination of Eq.(1.4) times β^2 and Eq.(1.6) gives

$$\sigma_1\beta^2(I_1^2 + \lambda^2 I_o^2) < \beta^2\lambda R I_o I_1 - I_1^2(2\lambda^2\beta^2 + \alpha\beta - \alpha^2 + 2\beta) - I_o^2(\lambda^4\beta^2 + \alpha - 1);$$

therefore, $\sigma_1 < 0$ (the condition for stability) whenever

$$(1.7)\qquad R^2 < \frac{4.2\lambda^2\beta^2 + \alpha\beta - \alpha^2 + 2\beta)(\lambda^4\beta^2 + \alpha - 1)}{\lambda^2\beta^4}$$

provided that $2\lambda^2\beta^2 + \alpha\beta - \alpha + 2\beta > 0$ and $\lambda^4\beta^2 + \alpha - 1 > 0$.

The three cases that were considered by Synge are

(1) $\alpha = \beta = 1$ which gave $R^2 < 8\lambda^2(\lambda^2 + 1)$ and which yielded $R_c = 0$ at $\lambda_c = 0$ --- a none too satisfactory result,

(2) $\alpha = \beta = 2$ which gave $R^2 < \frac{(2\lambda^2 + 1)}{\lambda^2}(4\lambda^4 + 1)$ and which yielded $R_c = 2.6873$ at $\lambda_c = .57328$ and

(3) $\alpha = \beta = \frac{1}{\lambda}$ which gave $R^2 < 8(1 - \lambda^2 + \lambda^3 + \lambda^4)$ and which yielded $R_c = 2.7258$ at $\lambda_c = .42539$.

Using an entirely different and more elaborate method Orr was able to show $R_c = 44.3$, and, quite naturally, it would be interesting to know if Synge's simple and elegant considerations could be expanded to include or to improve upon Orr's result by carefully selecting α and β.

II. THE UPPER BOUND FOR SYNGE'S CRITERION

Upon selecting α and β, one can determine the values of λ for which the right hand side of Eq.(1.7) reaches its minima, and the maximum of these minima would constitute the upper bound for Synge's criterion.

If one introduces a notation

$$(2.1) \qquad F(\alpha,\beta,\lambda) = \frac{4(2\lambda^2\beta^2 + \alpha\beta - \alpha^2 + 2\beta)(\lambda^4\beta^2 + \alpha - 1)}{\lambda^2\beta^4}$$

then the problem becomes a determination of $F_{max,\ min}$. This mini-max solution is found by solving simultaneously the following equations:

$$(2.2) \quad \frac{\partial F}{\partial \alpha} = [(\beta - 2\alpha)(\lambda^4\beta^2 + \alpha - 1) + (2\lambda^2\beta^2 + \alpha\beta - \alpha^2 + 2\beta)][4/\lambda^2\beta^4] = 0$$

$$(2.3) \quad \frac{\partial F}{\partial \beta} = [\beta(4\lambda^2\beta + \alpha + 2)(\lambda^4\beta^2 + \alpha - 1) + 2\lambda^4\beta^2(2\lambda^2\beta^2 + \alpha\beta - \alpha^2 + 2\beta)$$
$$-4(2\lambda^2\beta^2 + \alpha\beta - \alpha^2 + 2\beta)(\lambda^4\beta^2 + \alpha - 1)][4/\lambda^2\beta^5] = 0$$

$$(2.4) \quad \frac{\partial F}{\partial \lambda} = [2\lambda^2\beta^2(\lambda^4\beta^2 + \alpha - 1) + 2\lambda^4\beta^2(2\lambda^2\beta^2 + \alpha\beta - \alpha^2 + 2\beta)$$
$$- (2\lambda^2 + \alpha\beta - \alpha^2 + 2\beta)(\lambda^4\beta^2 + \alpha - 1)][8/\lambda^3\beta^4] = 0$$

One can verify by direct substitution that $\alpha = 4/3$, $\beta = 2/3$ and $\lambda = \sqrt{2}/2$ are solutions of these equations. One then obtains

$$(2.5) \qquad F_{max,min} = F\left[\frac{4}{3}, \frac{2}{3}, \frac{\sqrt{2}}{2}\right] = 16.$$

or

$$(2.6) \qquad R_c = 4$$

An extensive computer search indicates that this solution is global. Two tables of five-place values for $F(\alpha,\beta,\lambda)$ are given to show its behavior near its saddle point.

TABLE I: Values of $F(1.3333,\beta,\lambda)$ near $\beta = .6667$ and $\lambda = .7071$

β/λ	0.6671	0.6771	0.6871	0.6971	0.7071	0.7171	0.7271	0.7371	0.7471	0.7571
0.6067	3.9267	3.9234	3.9216	3.9214	3.9225	3.9251	3.9290	3.9343	3.9410	3.9490
0.6167	3.9563	3.9522	3.9497	3.9486	3.9491	3.9511	3.9544	3.9592	3.9654	3.9729
0.6267	3.9786	3.9738	3.9707	3.9692	3.9692	3.9706	3.9736	3.9780	3.9838	3.9910
0.6367	3.9946	3.9894	3.9859	3.9839	3.9835	3.9847	3.9873	3.9915	3.9970	4.0040
0.6467	4.0052	3.9997	3.9959	3.9937	3.9930	3.9940	3.9964	4.0004	4.0058	4.0127
0.6567	4.0112	4.0055	4.0015	3.9991	3.9983	3.9992	4.0015	4.0054	4.0108	4.0176
0.6667	4.0132	4.0074	4.0032	4.0008	4.0000	4.0008	4.0032	4.0070	4.0125	4.0193
0.6767	4.0117	4.0058	4.0017	3.9993	3.9985	3.9993	4.0017	4.0057	4.0112	4.0182
0.6867	4.0072	4.0014	3.9973	3.9949	3.9943	3.9952	3.9977	4.0018	4.0075	4.0146
0.6967	4.0000	3.9944	3.9904	3.9882	3.9876	3.9887	3.9914	3.9957	4.0016	4.0089
0.7067	3.9907	3.9851	3.9814	3.9793	3.9790	3.9803	3.9832	3.9877	3.9937	4.0013

TABLE II: Values of $F(\alpha,.6667,\lambda)$ near $\alpha = 1.3333$ and $\lambda = .7071$

α/λ	0.6671	0.6771	0.6871	0.6971	0.7071	0.7171	0.7271	0.7371	0.7471	0.7571
1.2733	3.9656	3.9606	3.9574	3.9560	3.9563	3.9583	3.9619	3.9671	3.9738	3.9821
1.2833	3.9802	3.9749	3.9714	3.9696	3.9696	3.9712	3.9744	3.9793	3.9857	3.9936
1.2933	3.9921	3.9866	3.9828	3.9808	3.9805	3.9818	3.9847	3.9893	3.9954	4.0030
1.3033	4.0014	3.9957	3.9917	3.9895	3.9890	3.9901	3.9928	3.9971	4.0029	4.0103
1.3133	4.0080	4.0022	3.9981	3.9958	3.9951	3.9960	3.9986	4.0027	4.0083	4.0154
1.3233	4.0120	4.0061	4.0020	3.9995	3.9988	3.9996	4.0020	4.0060	4.0115	4.0185
1.3333	4.0132	4.0074	4.0032	4.0008	4.0000	4.0008	4.0032	4.0070	4.0125	4.0193
1.3433	4.0117	4.0059	4.0019	3.9995	3.9988	3.9996	4.0019	4.0058	4.0112	4.0180
1.3533	4.0073	4.0018	3.9979	3.9957	3.9950	3.9959	3.9983	4.0023	4.0077	4.0145
1.3633	4.0002	3.9949	3.9912	3.9892	3.9887	3.9898	3.9923	3.9964	4.0019	4.0088
1.3733	3.9902	3.9852	3.9818	3.9801	3.9798	3.9811	3.9838	3.9881	3.9937	4.0007

Unfortunately, $R_c = 4$ is far below Orr's value of 44.3. Nevertheless, the idea of Synge that uses inequalities that are obtained by integrating the fundamental equations after multiplying by various quantities and by algebraically manipulating the integrated equations might produce a simple proof for the stability of plane Couette flow if someone were clever enough. The parting comment by Synge in his address before the 1938 Semi-Centenial Meeting of the American Mathematical Society is as valid today as the day he first wrote it. "The outstanding challenge to mathematicians in the field of hydrodynamic stability (is) --- a simple proof, not involving elaborate computations, that plane Couette motion is stable under all circumstances." In these days of large scale digital computers a small improvement on the challenge might be the presentation of an elaborate computation showing that plane Couette flow is not stable if in fact it is unstable, or the requirement for simplicity might have to be abandoned if the stability of plane Couette flow is ever to be decided.

ACKNOWLEDGEMENT

The authors are grateful for the substantial help that they received from two of our colleagues, John S. Letcher, Jr. and Karl Pohlhausen.

AD P000335

MIXING OF COMPRESSIBLE FLOWS WITH APPLICATION TO EJECTOR THRUSTERS

by

Morton Alperin and Jiunn-Jenq Wu
Flight Dynamics Research Corporation
Van Nuys, California

Mixing of two streams of compressible fluid having arbitrary properties at the start of mixing results in one of two possible states upon conclusion of the mixing process. These two final states can be differentiated by the fact that the Mach Number of the fully mixed flows are related in the same manner as are the Mach Numbers across a normal shock wave. One of these states is always representative of a subsonic flow and the other a supersonic flow.

Since both solutions represent flows which satisfy the laws of mass flow and energy conservation and the momentum theorum in a channel of uniform cross-section, the physical possibility of achieving these end end states must be corroborated by examination of the process in terms of the Second Law of Thermodynamics. Therefore the total entropy change of the flows from the initial to the final state have been determined. It is shown that both solutions correspond to flows which have a positive entropy change in certain ranges of the initial conditions while in other ranges the solution corresponding to a supersonic end state may violate the Second Law of Thermodynamics

Applications of these solutions to the flow through an ejector provide a means for design optimization which results in high thrust autmentating capability at any given flight speed.

Manuscript Received March 1979.

Mixing of Compressible Flows With Application to Ejector Thrusters

by

Morton Alperin and Jiunn-Jenq Wu
Flight Dynamics Research Corporation
Van Nuys, California

During his years of association with the U.S. Air Force, Dr. Hans von Ohain has been an inspiration to those, within and outside of government service, who were interested in the pursuit of new concepts. His encouragement of the efforts to develop efficient ejectors has been of particular stimulus to the evolution of the present state-of-the-art, and in particular to the development of the jet-diffuser ejector, and it is with mixed emotions of pleasure and sorrow that we observe his retirement from official duties in the U.S. Government. Our pleasure derives from the fact that in retirement von Ohain will be free to devote whatever time he wishes to the pursuit of matters of interest to himself, and we sincerely hope this will include further effort towards the goal of improved ejectors. Our sorrow of course is related to the loss of sincere, informative advice and encouragement, from someone as well informed as von Ohain.

The preparation of this volume of original papers by those scientific personnel who had the pleasure of knowing von Ohain during his years of involvement in research associated with aircraft propulsion, is an appropriate means for recognition of his contributions to this science, and we are pleased to have been included in this group. To participate in what we believe to be a well deserved honor for Hans von Ohain, we have prepared a brief exposition of our most recent work related to ejector technology, illustrating the role of mixing upon the performance and optimization of ejectors, and including a recent discovery of a means for the design of translating as well as stationary ejectors whose injected, energized gas may be of high velocity and high temperature. The following brief analysis of the ideal ejector processes should stimulate new areas of research which have a high potential for improvement of the overall efficiency of existing thrusters by their use in combination with ejectors.

The analysis which follows, describes initially the mixing process by itself, and then relates the characteristics of the mixed gases to the performance of ejectors, described in terms of the ratio of the change of momentum flux (net thrust) to the net thrust of the gas generator operating as an ideal free jet.

List of Symbols

a	primary jet thickness or area
M	Mach number
$\dot{m}$	mass flow rate
n	(= $(\gamma - 1)/\gamma$)
P_o	stagnation pressure
p	pressure
R	gas constant
r	entrainment ratio
S	entropy
s	specific entropy
T	temperature
T_o	stagnation temperature
U	secondary or mixed flow velocity
V	primary or injected flow velocity
X	duct width
α	inlet area ratio (= X_2/a_1)
γ	ratio of specific heats
δ	outlet area ratio (= X_3/X_2)
ΔS	entropy production due to mixing
ρ	mass density
ϕ	thrust augmentation

Subscripts

c	choking
i	secondary (induced) flow
p	primary flow
r	reference
$1,2,3$	ejector stations
∞	ambient conditions

Theoretical Considerations

The injection of two uniform flows of compressible fluid into a duct results in processes of kinetic and thermal mixing. If the duct is of sufficient length and if skin friction is neglected, the mixing process will continue until the resulting flow is uniform in all of its properties. Assuming that the fluids have arbitrary properties at the start of mixing and that they satisfy the perfect gas law throughout the mixing process, the laws of mass flow and energy conservation and the momentum theorem can be written for the process in a duct of constant cross-section in terms of the notation and station designation described on Figure 1.

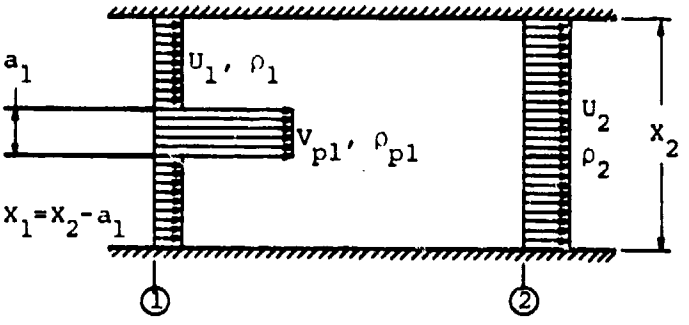

Figure 1. Schematic diagram of mixing duct

Mass Flow Conservation.

$$\rho_1 X_1 U_1 + \rho_{p1} a_1 V_{p1} = \rho_2 X_2 U_2 \tag{1}$$

Energy Conservation.

$$\dot{m}_p T_{op} + \dot{m}_i T_{o1} = (\dot{m}_p + \dot{m}_i) T_{o2} \tag{2}$$

Momentum Theorem, assuming pressure is uniform at Station 1.

$$p_1 X_2 + \rho_1 X_1 U_1^2 + \rho_{p1} a_1 V_{p1}^2 = p_2 X_2 + \rho_2 X_2 U_2^2 \tag{3}$$

Using the perfect gas law

$$P_k = \rho_k R T_k \qquad k = 1, 2, pl \tag{4}$$

and expressing the densities, velocities and static temperatures in terms of Mach numbers, the Mach number at Station 2 (M_2) can be expressed in terms of conditions at Station 1, by rearrangement of Equations 1, 2 and 3. The resulting relationship is

$$A(\gamma M_2^2)^2 + B(\gamma M_2^2) + 1 = 0 \tag{5}$$

where

$$A = 1 - J^2(\gamma - 1)/2 \tag{6}$$

$$B = 2 - \gamma J^2 \tag{7}$$

and

$$J = \frac{\sqrt{\frac{T_{pl}}{T_{op}}}\left(\frac{\alpha}{\gamma M_{pl}} + M_{pl}\right) + rM_1\sqrt{\frac{T_1}{T_{op}}}}{\sqrt{\left[1 + r\left(\frac{T_{ol}}{T_{op}}\right)\right](1 + r)}} \tag{8}$$

$$r = \frac{\dot{m}_i}{\dot{m}_p} = \frac{\rho_1}{\rho_{pl}}\frac{X_1}{a_1}\frac{U_1}{V_{pl}} = (\alpha - 1)\frac{M_1}{M_{pl}}\sqrt{\frac{T_{pl}}{T_1}} \tag{9}$$

$$\frac{T_{ol}}{T_1} = 1 + \frac{\gamma - 1}{2} M_1^2 \tag{10}$$

$$\frac{T_{op}}{T_{pl}} = 1 + \frac{\gamma - 1}{2} M_{pl}^2 \tag{11}$$

and therefore

$$M_2 = \sqrt{\frac{-B \pm \sqrt{B^2 - 4A}}{2\gamma A}} \tag{12}$$

Thus for any given set of flow properties (M_1, M_{pl} or P_{op}/P_{ol}, T_{op}/T_{ol}) at the start of mixing, there are two possible flows after completion of the mixing process.

Examination of these flow properties indicates that the two solutions to Equation 5 are related by the expression,

$$M_{2(-)}^2 = \frac{(\gamma - 1)M_{2(+)}^2 + 2}{2\gamma M_{2(+)}^2 - (\gamma - 1)} \tag{13}$$

which is the relationship between Mach numbers across a normal shock wave.

Thus the two solutions represent flows which at the completion of mixing, may be either subsonic or supersonic. Depending upon the initial properties of the unmixed flows at Station 1, either or both solutions may represent realistically achievable flows or in some cases may represent a state which is not realistically achievable from the given initial conditions but which is consistent with the four laws represented by Equations 1, 2, 3 and 4. To determine the validity of solutions, it is essential to investigate the entropy production in the light of the Second Law of Thermodynamics.

At Station 1, the entropy of each flow with respect to an arbitrary reference value can be expressed as

$$S_1 - S_r = \dot{m}_p(s_{p1} - s_r) + \dot{m}_i(s_1 - s_r) \tag{14}$$

$$= \dot{m}_p R\left[\left(\frac{1}{n}\right)\ell n\left(\frac{T_{p1}}{T_r}\right) + \left(\frac{r}{n}\right)\ell n\left(\frac{T_1}{T_r}\right) - (1 + r)\ell n\left(\frac{p_1}{p_r}\right)\right] \tag{15}$$

and

$$S_2 - S_r = \dot{m}_p R\left[\left(\frac{1}{n}\right)\ell n\left(\frac{T_2}{T_r}\right) - \ell n\left(\frac{p_2}{p_r}\right)\right](1 + r) \tag{16}$$

and the change of total entropy is

$$\Delta S = S_2 - S_1 = \dot{m}_p R\left[\left(\frac{1}{n}\right)\ell n\left(\frac{T_2}{T_{p1}}\right) + \left(\frac{r}{n}\right)\ell n\left(\frac{T_2}{T_1}\right) - (1 + r)\ell n\left(\frac{p_2}{p_1}\right)\right] \tag{17}$$

and only those flows in which $\Delta S \geq 0$ are considered realistic.

Therefore all solutions to the equations of mass flow and energy conservation and the momentum theorem which do not satisfy this condition are discarded as being physically unrealistic.

Other important fluid mechanical characteristics and limitations imposed by the prescribed laws are divulged from a detailed examination of the solutions.

Obviously the quadratic equation (5) has no real solution when $B^2 < 4A$, and has a single solution when $B^2 = 4A$. It can be shown that when $B^2 = 4A$, $M_2 = 1$, which can be considered as the choking limit. When $B^2 > 4A$ the two solutions obtained from the quadratic equation (5) represent flows at the conclusion of the mixing process which, in one case is supersonic and in the other case is subsonic and the two solutions become identical when $M_2 = 1.0$, i. e. when $B^2 = 4A$. Thus at this condition ($M_2 = 1.0$), the flow is choked and the condition for the choking limit is

$$B^2 = 4A \tag{18}$$

Solution of this equation yields a value for $J = J_c$ which is

$$J_c = \frac{1}{\gamma}\sqrt{2(\gamma + 1)} \qquad (=1.565 \text{ for } \gamma = 1.4) \tag{19}$$

and therefore from Equation 8, using the choking value of $J(= J_c)$, it can be shown that

$$\left(\frac{T_{op}}{T_{o1}}\right)_c = K\sqrt{\left(\frac{T_{op}}{T_{o1}}\right)_c} - 1 \tag{20}$$

or

$$\left(\frac{T_{op}}{T_{o1}}\right)_c = \left(\frac{K}{2} \pm \sqrt{\frac{K^2}{4} - 1}\right)^2 \tag{21}$$

where

$$K = \frac{\frac{1}{J_c^2}\left[\frac{\alpha}{\gamma M_{p1}} + M_{p1} + (\alpha - 1)\frac{M_1^2}{M_{p1}}\right]^2 - (\alpha - 1)^2\left(\frac{M_1}{M_{p1}}\right)^2\left(\frac{T_{o1}}{T_1}\right) - \frac{T_{op}}{T_{p1}}}{(\alpha - 1)\frac{M_1}{M_{p1}}\sqrt{\left(\frac{T_{o1}}{T_1}\right)\left(\frac{T_{op}}{T_{p1}}\right)}} \tag{22}$$

The two values of T_{op}/T_{o1} represented by Equation 21 can be shown, for $\alpha \neq 1$, to be inversely related or

$$\left(\frac{T_{op}}{T_{o1}}\right)_{c(+)} = \left(\frac{T_{o1}}{T_{op}}\right)_{c(-)} \qquad (23)$$

where in this case the + and - signs refer to the positive and negative signs in the solutions to Equation 21.

The relationship indicated by Equation 23 illustrates the fact that if M_1, M_{p1} and α are held fixed, choking will occur at a given ratio of the larger to the smaller stagnation enthalpy, regardless of which of the two flows contains the larger stagnation enthalpy.

To illustrate the relationship among the various flow parameters, the choking limits and the regions in which the solutions represent flows which violate the Second Law of Thermodynamics, the Mach No. at Station 2 (M_2) and the entropy change across the mixing process are calculated as functions of the stagnation temperature ratio (T_{op}/T_{o1}), for various initial conditions. For convenience in comparison between theory and experiment, the illustrations presented on Figures 2 and 3 were prepared for a fixed ratio of stagnation pressures ($P_{op}/P_{o1} = 3$) instead of a fixed value of M_{p1}. Thus M_{p1} is a function of M_1 only and remains fixed when M_1 is constant. The dependence of M_{p1} upon M_1 for the stagnation pressure ratio of 3 is shown in Table I and the relationship is given by Eq. 24.

TABLE I

M_1	0.4	0.6	0.8	1.0	1.2	1.4	1.6	1.8	2.0
M_{p1}	1.44	1.53	1.65	1.79	1.95	2.13	2.31	2.51	2.71

$$M_{p1} = \sqrt{\frac{2}{\gamma-1}\left[\left(\frac{P_{op}}{P_{o1}}\right)^{\frac{\gamma-1}{\gamma}}\left(1 + \frac{\gamma-1}{2} M_1^2\right) - 1\right]} \qquad (24)$$

Figure 2 illustrates the relationship among M_2, $\Delta S/\dot{m}_p R$ and T_{op}/T_{c1} for a fixed value of P_{op}/P_{o1} in the range where M_{p1} is greater than 1.0, and M_1 varies parametrically over a subsonic range. Figure 3 illustrates the relationship among the same parameters when the Mach No. (M_1) is supersonic. The mixed flows are observed to choke at values of T_{op}/T_{o1} which are close to zero and again at large values of T_{op}/T_{o1} as indicated by Equation 23. At intermediate values of T_{op}/T_{o1}, M_2 is subsonic when the negative sign of Equation 12 is utilized and supersonic when the positive sign is used, regardless of whether the secondary flow at Station 1 is subsonic or supersonic.

The entropy changes across the mixing process are illustrated on Fig. 2 for M_1 = 0.4 and 0.6 only, since for M_1 = 0.8 and 1.0, the entropy production is very close to the curve for the negative solution with M_1 = 0.4, within the appropriate range of T_{op}/T_{o1}. Thus the entropy change can be observed to remain positive over the entire range of values of T_{op}/T_{o1} when the negative solution is utilized, and to become negative in certain ranges of T_{op}/T_{o1} and M_1 when the positive solution is utilized. Those regions where the entropy change is negative represent flows which violate the Second Law of Thermodynamics (shown in dotted lines) and are to be avoided in the use of the analysis for prediction of flow properties or experiment design.

In the case where both M_1 and M_{p1} are supersonic (Figure 3), the resulting Mach No. (M_2) has dependencies upon T_{op}/T_{o1} which are similar to that shown on Figure 2 where M_1 is subsonic, but as illustrated, the entropy change does not become negative for either solution in the range of parameters utilized. This is an indication that perhaps the positive solution to Equation 12 represents a more natural flow when initial conditions are supersonic and that in this case the negative solution represents a flow corresponding to the positive solution after a normal shock wave at Station 2, as indicated by Eq. 13.

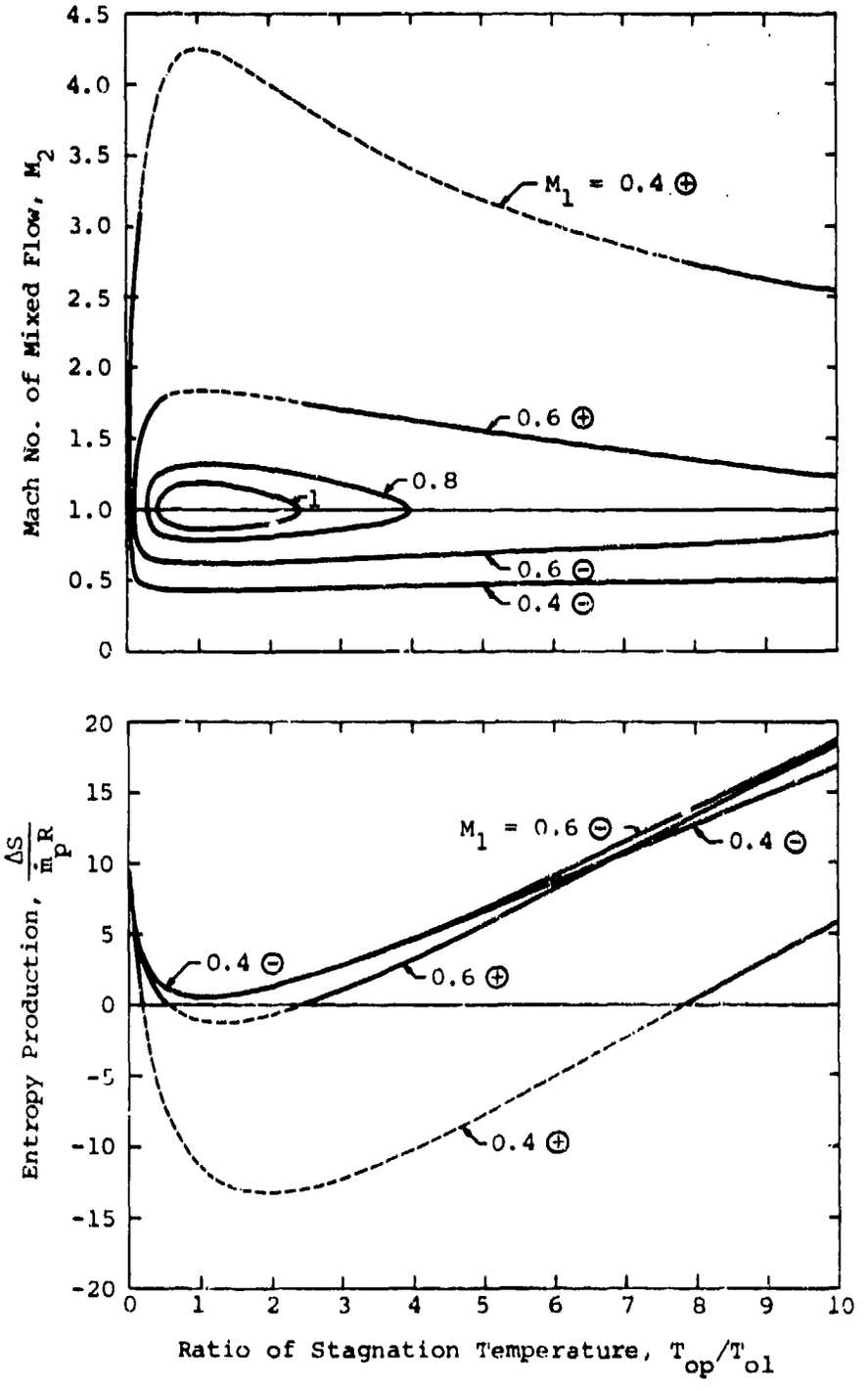

P_{op}/P_{o1} = 3; α = 20

Figure 2

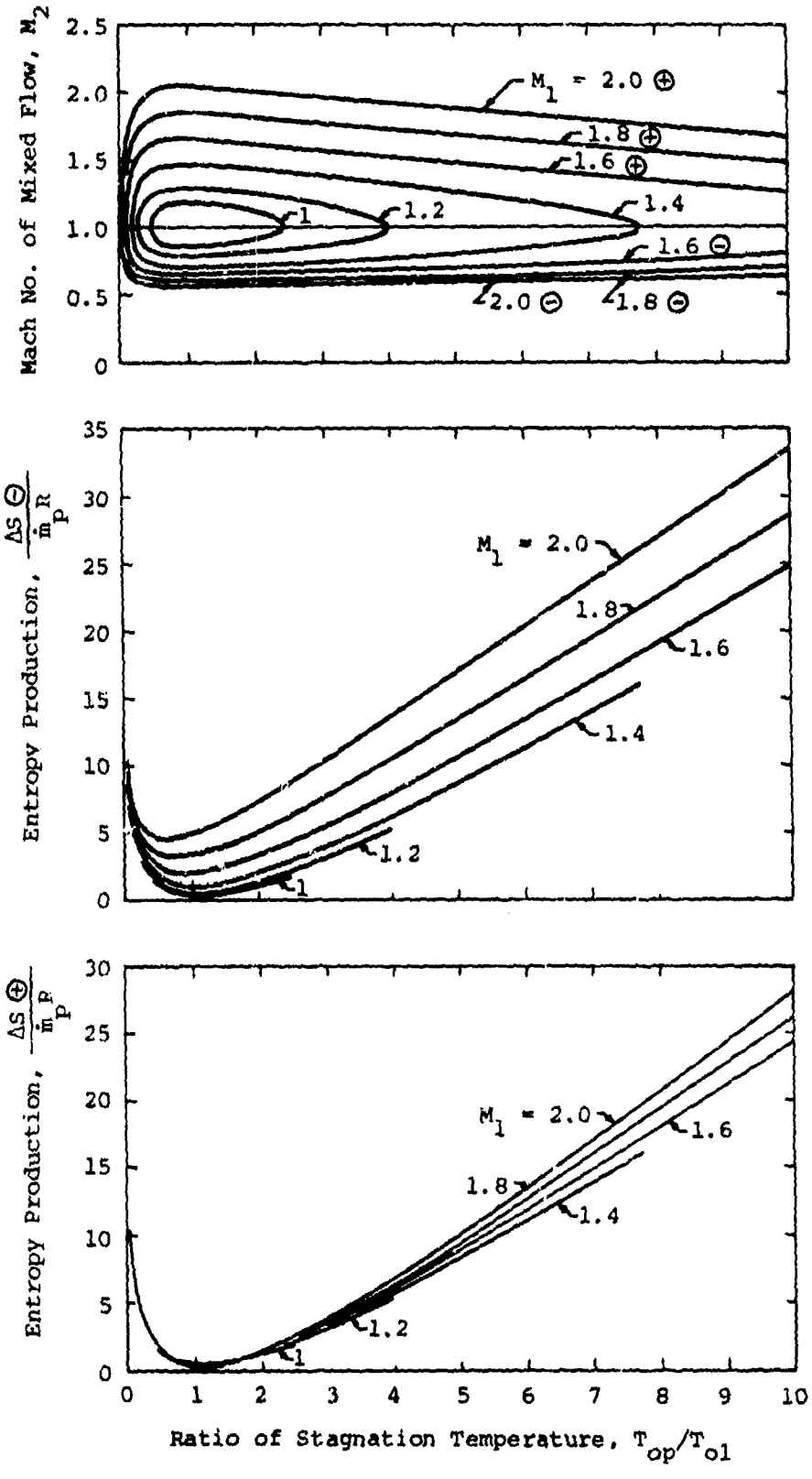

$P_{op}/P_{o1} = 3; \quad \alpha = 20$

Figure 3

Ejectors

The mixing process described above is fundamental to the operation of ejectors, which are duct arrangements designed geometrically to accept free-stream fluid, mix this fluid with an energized stream and to discharge the mixture to the environment in a manner which produces the largest possible momentum increment from the processes involved. Theoretical treatments of the processes of ingestion, mixing and discharge, including the possible ingestion of boundary layer fluid from vehicle surfaces upstream of the ejector's inlet, the influence of incomplete thermal and kinetic mixing, the influence of all losses due to skin friction and flow separation, shock waves, and the limitation due to choking, are presented in Reference 1. It is of interest here however to relate the performance of ideal ejectors to the mixing process to illustrate the limiting performance of these devices as thrust augmenters assuming complete thermal and kinetic mixing and ideal fluid flow. A schematic representation of an ejector illustrating its section designations, is presented on Figure 4.

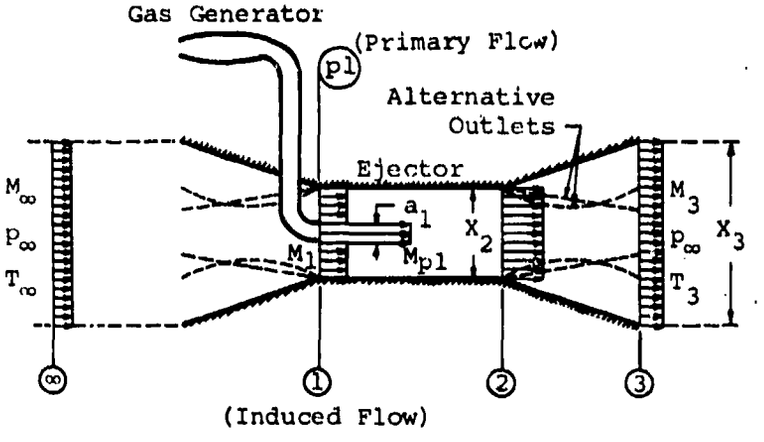

Figure 4. Schematic representation of an ejector

The ejector is assumed to ingest fluid from a given free-stream Mach No. (M_∞) without loss between the free-stream and Station 1. After complete mixing, the resulting uniform flow at Station 2 is exhausted through a perfect diffuser or nozzle whichever is required to return to ambient pressure at Station 3.

Assuming the primary fluid injected through the inner core (Station P1) to be energized, and the secondary fluid at the outer region (Station 1) to be the ingested free-stream fluid, the ejector performance (ϕ) is described by the ratio of the momentum increment between the free-stream and Station 3, to the momentum of the primary mass flow exhausted isentropically to ambient pressure. Thus for an air breathing propulsive system,

$$\phi = \frac{(\dot{m}_p + \dot{m}_i)(U_3 - U_\infty)}{\dot{m}_p (V_{p\infty} - U_\infty)} = (1 + r) \frac{M_3 \sqrt{T_3} - M_\infty \sqrt{T_\infty}}{M_{p\infty} \sqrt{T_{p\infty}} - M_\infty \sqrt{T_\infty}} \tag{25}$$

and since

$$P_{o3} = P_{02} \text{ and } T_{o3} = T_{o2} \tag{26}$$

$$P_{o\infty} = P_{o1} \text{ and } T_{o\infty} = T_{o1} \tag{27}$$

$$(P_{op}/p_\infty)^n = T_{op}/T_{p\infty} = 1 + \frac{\gamma - 1}{2} M_{p\infty}^2 \tag{28}$$

when the ingestion and injection into and the discharge from the ejector are isentropic, the thrust or momentum augmentation (ϕ) can be evaluated for any given values of M_∞, M_1, P_{op}/p_∞, T_{op}/T_∞, and $X_2/a_1 (= \alpha)$, using Equations 6-12 to evaluate conditions at Station 2.

The two solutions (Equation 12), describe distinct types of ejectors requiring nine different configurations to achieve ingestion from and discharge to free-stream or ambient conditions. These configurations are combinations of three types of inlets (convergent, divergent and De Laval Nozzles) and the same three types of outlets, and are described in Reference 1, but for purposes of this discussion, only the fluid mechanical properties of the flows and the thrust augmentation achievable under ideal conditions will be described.

Stationary Ejectors ($M_\infty = 0$)

Using the above method, the ideal thrust augmentation for an ejector at rest with respect to the undisturbed medium was evaluated under each solution to Eq. 5 over a range of stagnation temperature ratios and for various values of M_1 as a parameter. For comparison purposes, the value of the stagnation pressure ratio (P_{op}/P_{o1}) was assumed to have the same value as that used for the preparation of Figures 2 and 3. The curves representing subsonic mixing ($M_1 < 1$) and those representing supersonic mixing ($M_1 > 1$) are presented separately on Figures 5 and 6 to avoid the confusion of superposition.

As can be observed by comparison of Figures 2 and 5 for subsonic mixing and Figures 3 and 6 for supersonic mixing, the evaluation of thrust augmentation terminates when $M_2 = 1.0$ (choking) at both choking limits ($T_{op}/T_{o1} > 1$ and $T_{op}/T_{o1} < 1$). In addition the curves are shown in dotted lines when the entropy change across the mixing process becomes negative.

Data presented on Figures 5 and 6 illustrate the importance of a proper selection of M_1 for the design of a stationary ejector. For example designs using the negative solution to Equation 5 provide a maximum performance when M_1 is close to 1.0. Under the conditions selected for the preparation of these figures, the optimal value of M_1 is about 1.06. However this optimal value will vary depending upon the choice of stagnation pressure ratio and upon the selection of the geometric parameter which is held fixed during the calculation. In this example α ($= X_2/a_1$) was held fixed for ease of comparison with the mixing problem, although it is more realistic to evaluate ejector performance while α_∞ ($=X_2/a_\infty$) is held fixed, if the comparison of the ejector size is to be made to a given free jet whose exit area is a_∞. In this mixing problem, where α is held constant, α_∞ increases rapidly with increasing values of M_1. This results in a supersonic M_1 for optimal performance under the negative solution. In practical ejector design analyses, α_∞ is held constant for purposes of comparison with a given free jet and optimal performance under the negative solution usually occurs at a subsonic value of M_1. The rapid increase in the entropy production for high supersonic values of M_1 (Figure 3) nullifies the benefit derived from the mixing process and degrades the ejector performance under the negative solution, as clearly indicated on Figure 6.

Using the positive solution to Equation 5 with subsonic mixing, it essential to design the stationary ejector with a value of M_1 which is as small as possible without violation of the Second Law of Thermodynamics. This is observable on Fig. 5, where the thrust augmentation is shown to increase rapidly with decreasing values of M_1. With supersonic mixing (Figure 6) the dependence of thrust augmentation on the stagnation temperature ratio (T_{op}/T_{o1}) is very critical and its maximum value increases with increasing values of M_1, as illustrated. The fact that the maximum thrust augmentation increases with increasing values of M_1, does not have practical importance, since the increase in thrust augmentation is primarily due to the increase in α_∞ (or ejector size compared to the free jet area) when M_1 is increased and α is held fixed.

As shown on Figure 5, ejectors operating at stationary conditions with subsonic secondary flow at Station 1 require high temperature injected gas for optimal performance if designed under the positive solution, and relatively low temperature injected gas if designed under the negative solution. Further, as shown on Figure 6, stationary ejectors (or ejectors operating at subsonic speeds) with supersonic secondary flow at Station 1, require relatively low temperatures for optimal performance under both the positive and negative solutions to the flow equations.

Although all ejectors designed to date have utilized the negative solution, it appears desirable to design stationary ejectors under the positive solution with subsonic mixing when maximum thrust augmentation is desired. Furtner studies of the influence of P_{op}, ejector size and losses, are essential prior to the selection of optimal design configurations.

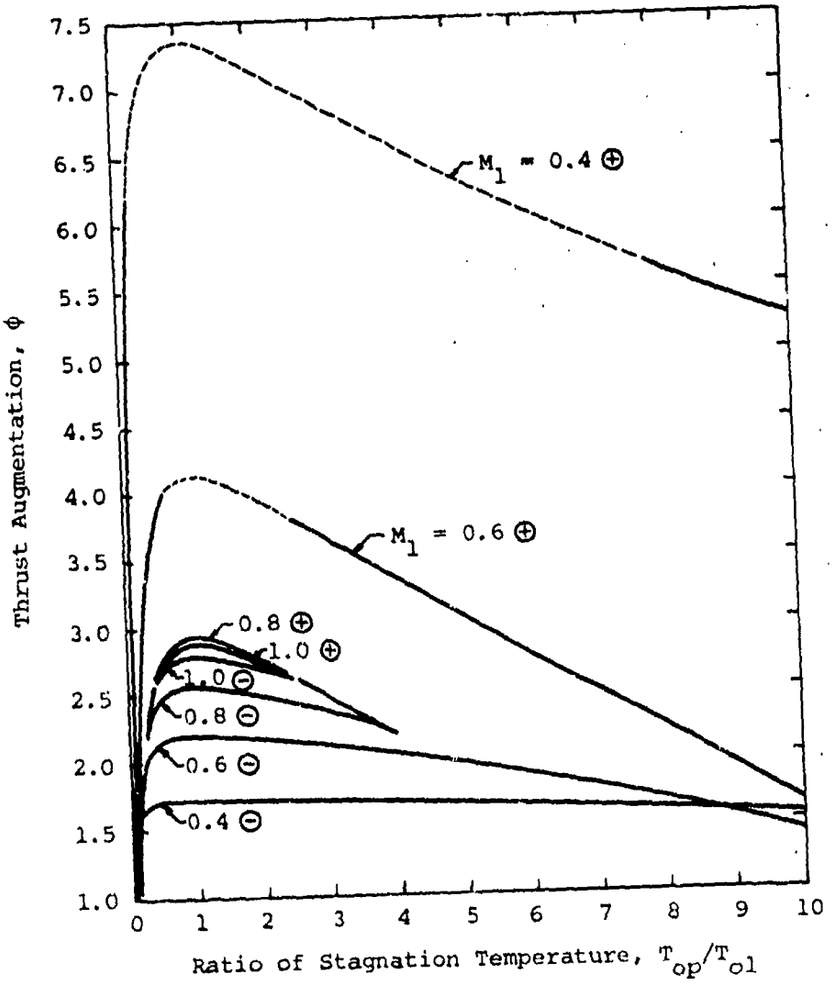

$P_{op}/P_{o1} = 3$; $\alpha = 20$; $M_\infty = 0$

Figure 5

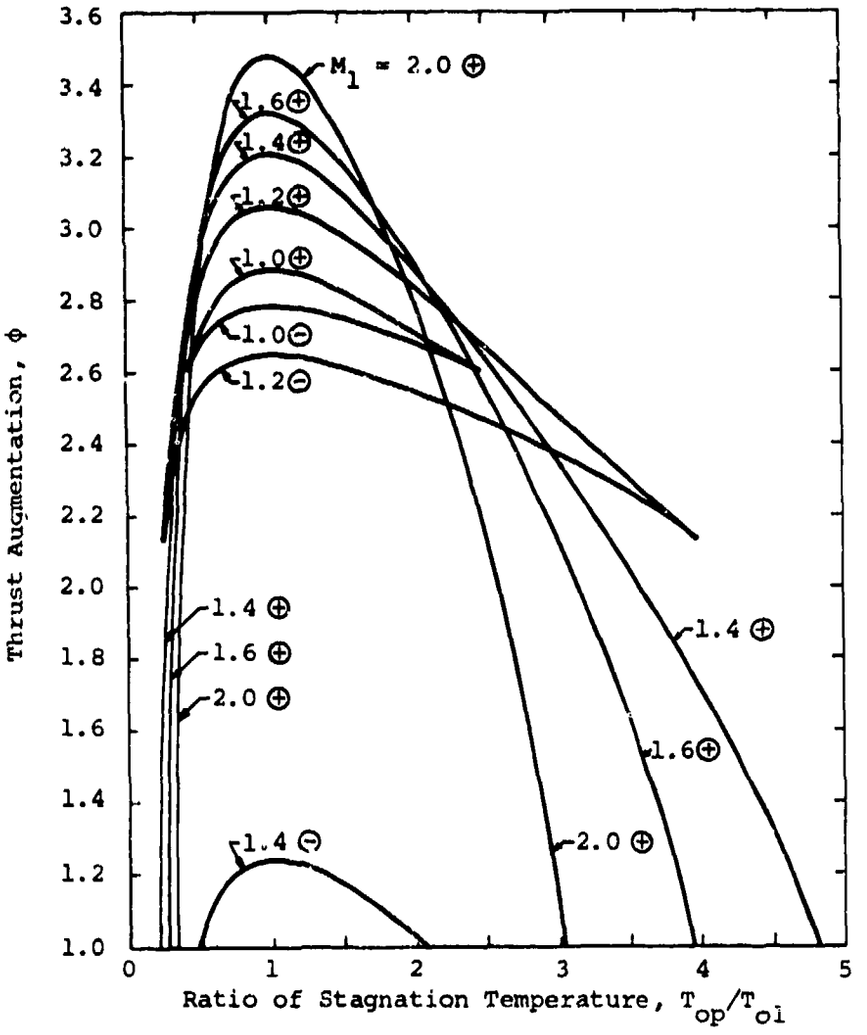

$P_{op}/P_{o1} = 3; \quad \alpha = 20; \quad M_\infty = 0$

Figure 6

Ejectors in High Speed Flight

Ejectors designed to accept the discharge from one of the existing types of gas generators, if properly designed, can provide large increases of net thrust (gross thrust minus ram drag) even during high speed motion in the thrust direction. The previous example illustrated the thrust augmenting capability of a stationary ejector, as a function of the characteristics of the injected gas. At high translational speeds however, the thrust augmentation of an ejector varies with the temperature of its injected gas in a very different manner from that of the stationary ejector. For example as shown on Figures 7 and 8, the thrust augmentation achievable by an ejector translating in its thrust direction at a Mach No. of 2, increases with increasing stagnation temperature of its injected gas. As shown, this characteristic is of a similar nature under both the negative and positive solutions to the flow equations, over most of the range of values of the Mach No. of the secondary flow at Station 1. Regions of the stagnation temperature ratio which cannot be utilized due to violation of the Second Law of Thermodynamics are shown in dashed lines on Figure 7.

A comparison of the stationary and high speed ejector performance indicates similarities and differences in their optimization, as follows:

1. High temperatures are always desirable when the ejector is designed under the positive solution with subsonic secondary flow at Station 1.

2. With supersonic secondary flow at Station 1, stationary (or low speed) ejectors designed under either solution require low temperature injected gas for optimal performance, whereas high temperature injected gas is most desirable for high speed ejectors, as shown by a comparison of Figures 6 and 8.

3. With subsonic secondary flow at Station 1, the conventional negative solution requires low temperature injected gas for stationary applications, as shown on Figure 5, but as shown on Figure 7, high temperatures are required for optimal ejector performance at a flight Mach No. of 2.

Although not shown, it has been observed that in general, ejectors designed under the negative solution for operation at intermediate flight speeds, display high performance with two distinct types of injected gas characteristics. These ejectors require either high temperature and low pressure (ramjet type) injected gas, or low temperature and moderate pressure (fanjet type) injected gas.

The use of turbojet exhaust as the energy supply to an ejector is intermediate to these optimal characteristics of the injected gas, but can also provide excellent ejector performance, if properly designed, as will be shown in the following example.

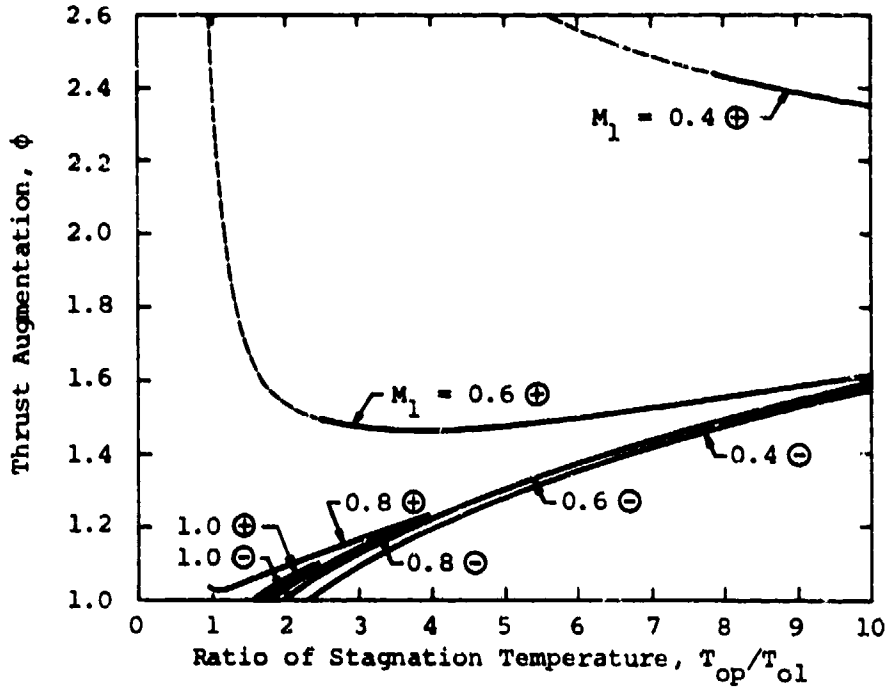

P_{op}/P_{o1} = 3; α = 20; M_∞ = 2

Figure 7

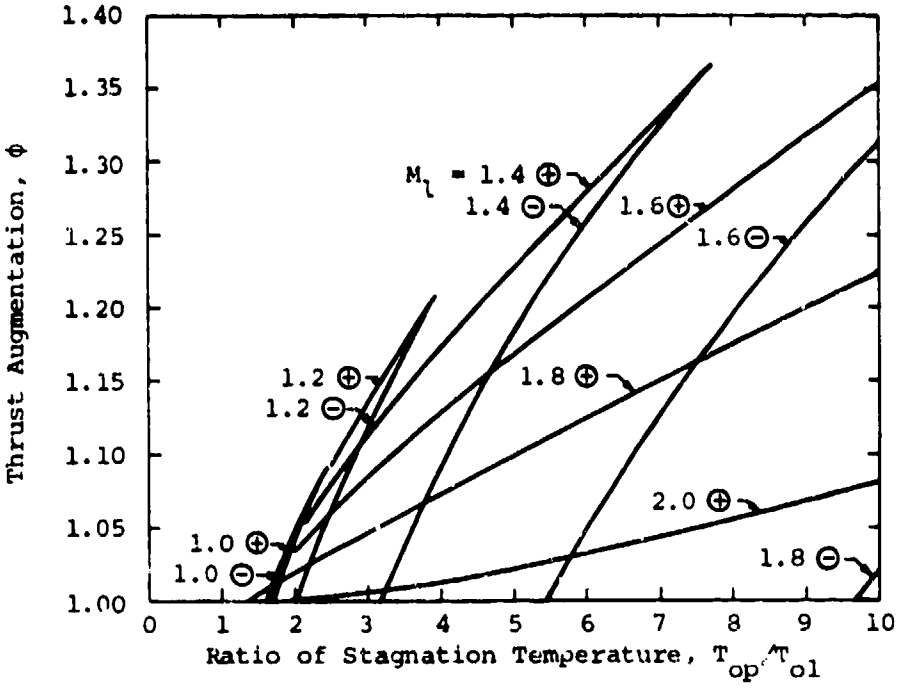

P_{op}/P_{o1} = 3; α = 20; M_∞ = 2

Figure 8

Specific Example

The existence of an optimal value of the Mach No. at Station 1, can be observed by a study of Figures 7 and 8, but its precise value is best determined by a calculation of the variation of the thrust augmentation with M_1 at a given set of flight conditions and injected gas characteristics. The results of this type of calculation are presented, for a typical case in which the ejector is assumed to be thrusting while being energized by the effluent gas from a typical turbojet with afterburner.

Flight Conditions
Mach No. (M_∞) = 2.0
Altitude = 40,000 ft. above sea level
ambient pressure = 2.72 psia
ambient temperature = 392 $^\circ$R

Exhaust or injected gas characteristics
stagnation pressure = 50 psig
stagnation temperature = 4000 $^\circ$R

The influence of the ejector's geometry (or M_1) upon its performance when its throat area (X_2) is 20 times the jet area (a_∞) required to discharge the mass flow from the turbojet to ambient pressure and whose flight conditions and injected gas characteristics are described above, is presented on Figure 9. In this example the value of α is not held constant as was done in the calculation for Figures 7 and 8. Instead, to be more realistic the value of α_∞ ($=X_2/a_\infty$) is held constant as described above, to provide direct size comparison with a given gas generator which is discharging its exhaust to ambient pressure. As indicated clearly on Figure 9, where the negative solution is dashed and the positive solution is in solid curves, ejectors designed under either solution can be optimized to function advantageously at this high speed.

The ideal thrust augmentation achievable with designs corresponding to the positive solution of Equation 12 is again shown to be considerably larger than that achievable by ejectors designed under the negative solution, except in the immediate vicinity of the choking points, where both solutions coincide.

The area ratio (δ) required for isentropic exhaust to ambient pressure is also illustrated on Figure 9. Although these curves indicate similar area ratios for both solutions, it must be recognized that under the stated conditions, the exhaust flow from the ejector is supersonic. Thus under the positive solution where $M_2 > 1.0$, the exhaust duct between Stations 2 and 3, will be either convergent or divergent and not convergent-divergent. However under the negative solution, M_2 is subsonic and the exhaust duct must therefore be convergent-divergent (De Laval type). This difference may result in geometric and aerodynamic conditions which are favorable to the positive solution.

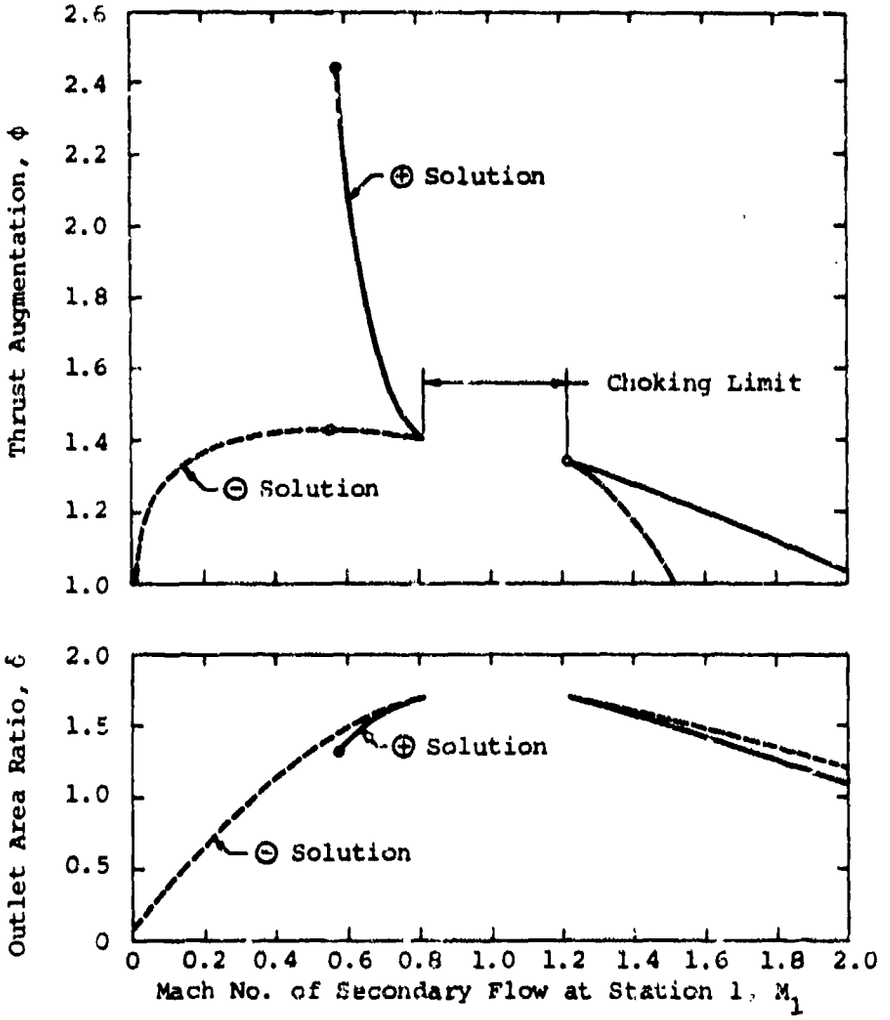

M_∞ = 2 @ 40,000 feet, p_∞ = 2.72 psia, T_∞ = 392°R

P_{op} = 50 psig; T_{op} = 4,000°R; α_∞ = 20

Figure 9

Conclusions

The concepts of ejector design optimization for both the positive and negative solutions of the equations governing the flow through an ideal ejector provide a means for achieving high ideal thrust augmentation while in translational motion in the thrust direction, even at supersonic speeds, and for V/STOL applications. Popular beliefs that ejectors must be relegated to low speed flight or stationary conditions and that they must be energized by cold gas, are shown to be unfounded, and since the discussion presented in this paper establishes the basic requirements for design of high performance ejectors over the entire practical flight and propulsion spectrum, it is the sincere hope of the authors that additional technical support from other branches of fluid mechanics and thermodynamics will be brought to bear on some of the important problems facing the practical development of these devices.

References

1. Alperin, M., Wu, J.J. "High Speed Ejectors" Flight Dynamics Research Corp., Air Force Flight Dynamics Laboratory, AFFDL-TR-79-3048, May 1979.

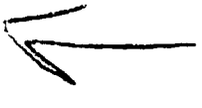

AD P000350

HIGHLIGHTS OF AN EJECTOR ANALYSIS

by

Siegfried Hasinger
Air Force Flight Dynamics Laboratory
Wright-Patterson Air Force Base, OH

Ejectors are fluid energy transfer devices which rely on direct fluid momentum exchange in a mixing process. This direct exchange is responsible for the mechanical simplicity of ejector devices. This simplicity is, however, not shared by the analysis of these devices. The great number of variables which are of interest for ejector operations lead to considerable functional complexities. In addition the influence of some of the variables on the ejector performance can be extremely sensitive. These conditions make an intuitive estimate of ejector performances in many cases impossible. The direct momentum exchange process allows, however, the establishment of a very reliable fluid dynamic picture as a basis for the anlaysis. Details of the mixing process do not enter the analysis and mixing can be treated as a completely independent problem. The simplifying assumption of one-dimensional flow has an inherent validity for the fluid momentum considerations. By overcoming the functional difficulties of the analysis very realistic performance predictions can be made for a great variety of operating conditions including those which provide optimum ejector layouts.

Manuscript received in April 1979. This work was performed in AFFDL in 1978 Under Work Unit No. 23070426.

HIGHLIGHTS OF AN EJECTOR ANALYSIS

Siegfried Hasinger
Air Force Flight Dynamics Laboratory
Wright-Patterson Air Force Base

I. INTRODUCTION

A comprehensive ejector analysis must deal with an extremely wide range of ejector conditions involving a large number of variables. The result is a high complexity of the analysis. These analytical difficulties arise, however, not from the ejector physics, at least not for the steady flow ejector contemplated here. A simple force equation adequately describes the basic ejector mechanism. The difficulties are rather caused by the necessity to deal with a large number of equations describing the thermodynamic and fluid-dynamic states of the ejector process. If these algebraic difficulties can be overcome without undue simplifications, very realistic performance predictions can be made and certain unifying principles for the wide operating range of ejectors can be established.

The following considerations are a condensation and also to some degree an extension of ejector investigations reported in References 1 to 3. The basic aim of these investigations was the optimization of the ejector pump. However, the analysis has been also applied to thrust augmentation.

II. THE EJECTOR EQUATION

In the following the essential steps leading to the solution of the ejector equation are given. They should provide an idea about the algebraic complexities of the analysis and serve as a basis for subsequent discussions on the generalized presentation of ejector operations.

The ejector equation applicable to an ejector system as shown in Figure 1 is commonly written in terms of forces in the following way:

$$m_p v_p + m_s v_s = (m_p + m_s) v_{Ex\text{-}m} + F_w + F_p + F_f \qquad (1)$$

where (1) the m·v type expressions represent the fluid impulse forces,

(2) F_w are the fluid pressure forces acting on the wall in flow direction,

(3) F_p are the fluid pressure forces in the fluid medium in flow direction,

(4) F_f are the wall friction forces.

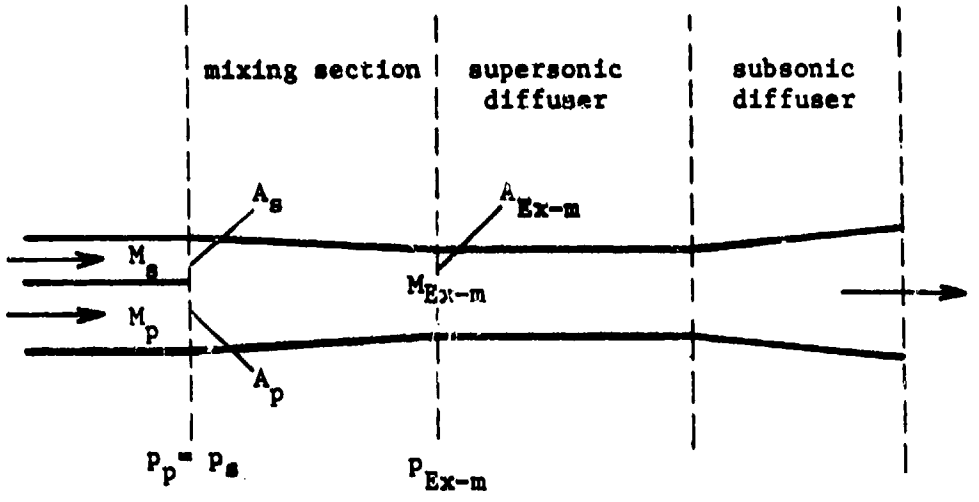

M	Mach number	Indices:	p	refers to primary flow
p	static pressure		s	" " secondary flow
A	flow cross section		Ex-m	" " mixing section exit

Figure 1. Ejector Flow Scheme

A basic assumption for this equation is that the mixing is completed at the mixing section exit. Equation 1 can be further developed with the following substitutions (for notations see Figure 1; a detailed derivation of all equations can be found in Reference 1)

$$v \cdot m = A \cdot p \cdot \gamma \cdot M^2 \tag{2}$$

$$F_w + F_c = t(A_p + A_s) p_s \cdot \tau \left(\frac{p_{Ex-m}}{p_s} - 1 \right) \tag{3}$$

where

$$t = \frac{A_{Ex-m}}{A_p + A_s} \tag{4}$$

$$\tau = \frac{i}{2t} + 1 - \frac{i}{2} \qquad \text{(for definition of i see Eq. 37 of Ref. 1)} \tag{5}$$

The factor i characterizes the shape of the pressure distribution in the mixing section. It can be determined analytically only for special cases.

In general it must be estimated. It has been introduced to facilitate the integration of the wall pressure forces. It is the only algebraic simplification used in the analysis. The factor i becomes only essential for high pressure ratio ejectors which require a substantial mixing section area reduction. However, even in this case, experience shows that the shape of the pressure distribution along the mixing section has a kind of standard character which allows to consider i as a constant.

The wall friction forces can be expressed in terms of the pipe friction coefficient c_f in the following way

$$F_f = \left[\frac{c_f L}{2D}\right]_m \cdot p_{Ex\text{-}m} \cdot \gamma_{Ex} \cdot M^2_{Ex\text{-}m} \cdot A_{Ex\text{-}m} \tag{6}$$

(L/D is a defined length to diameter ratio of the mixing section)

With these substitutions Equation 1 becomes

$$\frac{\gamma_p M_p^2}{t\left(1+\frac{A_s}{A_p}\right)} + \frac{\gamma_s M_s^2}{t\left(1+\frac{A_p}{A_s}\right)} + \tau = \frac{p_{Ex\text{-}m}}{p_s}\left[\gamma_{Ex} M^2_{Ex\text{-}m}\left(\left[\frac{c_f L}{2D}\right]_m + 1\right) + \tau\right] = B_m \tag{7}$$

With ejector geometry and inlet flow conditions given, this equation has two unknowns, $M_{Ex\text{-}m}$ and $p_{Ex\text{-}m}/p_s$. Mass and energy conservation provide a second equation to eliminate the pressure ratio as an unknown in Equation 7. The result is the final ejector equation

$$\frac{M_{Ex\text{-}m}\left(1+\frac{\gamma_{Ex}-1}{2} M^2_{Ex\text{-}m}\right)^{\frac{1}{2}}}{\gamma_{Ex} M^2_{Ex\text{-}m} C_m + \tau} = E = \frac{M_s\left(\frac{m_p}{m_s}+1\right)}{B_m t\left(\frac{A_p}{A_s}+1\right)} \sqrt{\frac{\left(1+\frac{m_p R_p}{m_s R_s}\right)\left(\frac{c_{p\text{-}p}\, m_p (T_p)_0}{c_{p\text{-}s}\, m_s (T_s)_0}+1\right)(T_s)_0}{\left(1+\frac{m_p \gamma_p}{m_s \gamma_s}\right)\left(\frac{c_{p\text{-}p}\, m_p}{c_{p\text{-}s}\, m_s}+1\right) T_s}} \tag{8}$$

where T abs. temperature
R gas constant
γ ratio of spec. heats
c_p spec. heat at const. pressure

$$\frac{m_p}{m_s} = \frac{A_p}{A_s}\frac{M_p}{M_s}\sqrt{\frac{\gamma_p R_s (T_s)_0 \left[2+(\gamma_p-1)M_p^2\right]}{\gamma_s R_p (T_p)_0 \left[2+(\gamma_s-1)M_s^2\right]}} \tag{9}$$

$$\gamma_{Ex} = \frac{\gamma_s}{\left(1+\frac{m_p}{m_s}\right)}\left(1+\frac{m_p}{m_s}\frac{\gamma_p}{\gamma_s}\right) \tag{10}$$

The solution of Equation 8 is

$$M^2_{Ex\text{-}m} = \frac{1-\left[\pm\sqrt{1-\frac{\alpha_m \tau^2}{c_m}\left(2\frac{c_m}{\tau}+\frac{1}{\gamma_{Ex}}-1\right)}+\alpha_m \tau\right]}{c_m \alpha_m \gamma_{Ex} - \gamma_{Ex} + 1} \tag{11}$$

where

$$\alpha_m = 2\gamma_{Ex} E^2 c_m \tag{12}$$

$$c_m = 1 + \left[\frac{c_f L}{2D}\right]_m \tag{13}$$

This equation gives the solution for the general case of an ejector with a tapered mixing section operated with heterogeneous gases. Its evaluation which is otherwise straight forward requires with the associated equations a calculator program with several hundred steps for only one performance point. The negative sign before the root in Equation 11 yields the supersonic flow solution for the mixing process. For determining the performance characteristic given in Figure 2, where the inlet flow conditions must be found for a given ejector performance, the equations must be solved by iteration (see Reference 3).

Equation 8 has a particular significance for a generalized interpretation of ejector operations. This will be shown in Section V.

III. RELIABILITY OF THE ANALYSIS

The basic reliability of the analysis was checked in experiments with a constant area mixing section ejector (t = 1). The ejector arrangement provided particularly well defined flow conditions. The factor i becomes irrelevant in this case since no wall pressure forces appear. The mixing section was made long enough to assure complete mixing in all cases. The ejector had no subsonic diffuser. From a static pressure survey along the mixing section the peak pressure achieved in the process was determined and used to calculate the ejector performance. The wall friction factor was determined directly from the pressure drop in the mixing section under single flow conditions. Figure 2 shows the good agreement between experiment and analysis over a wide range of ejector operations. A round as well as a square mixing section were tested and no significant differences in performance were found. The evaluation of the test results revealed that the exact determination of the mixing section cross section area was the most decisive factor for obtaining agreement between analysis and experiment, suggesting that in a reversed fashion the diameter of a mixing section could be determined from the required performance with considerable accuracy (within a few per mil).

All pressure ratios shown in Figure 2 were obtained with a Mach number 2.7 nozzle, i.e. the performances were obtained with an underexpanded nozzle.

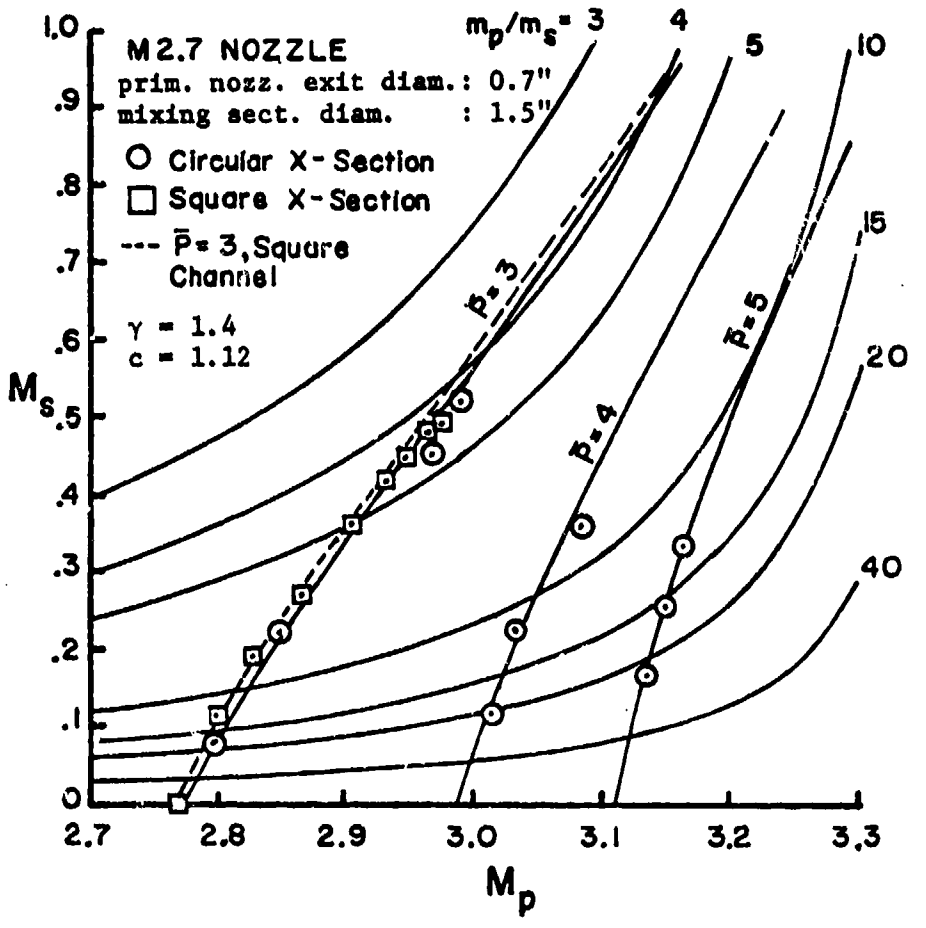

Figure 2 Comparison of Analytical and Experimental Performance of an Ejector with Constant Area Mixing Section and no Subsonic Diffuser. $\bar{P}$ = total exit/total second. inlet pressure; m_p/m_s = primary/secondary mass flow. (Mixing is subsonic which is superior to supersonic mixing in case of constant area mixing).

The analysis accounts for these conditions by simply applying momentum conservation to the flow expansion outside the primary nozzle (see Reference 2). The undiminished good agreement of the analysis with the tests in the off-design nozzle region proves again that simple force considerations for dealing with the flow in an ejector are adequate for realistic predictions. Reference 3 shows other examples of good agreement between analysis and experiments, in this case for an optimized ejector featuring a tapered mixing section and operated with heterogeneous gases.

IV. SPECIAL CASES OF THE EJECTOR EQUATION

In general the mixing section area of an ejector must be reduced toward the exit to obtain best performance. For high pressure ratio ejectors a typical mixing section "taper" is around $t = 0.7$ (see Reference 3). The taper becomes insignificant ($t \to 1.0$) for low pressure ratio ejectors such as used for common thrust augmentation. This is for practical purposes the case of constant area mixing for which the value of τ in Equations 7, 8, and 11 becomes unity and the factor i is irrelevant as already pointed out before.

Another special case of the ejector equation is constant pressure mixing. In this case the pressure ratio occurring in Equation 7 becomes unity and τ can be canceled out. In Equations 8 and 11 the value of τ becomes zero. Constant pressure mixing has no special significance as an ejector design goal. However, as we will see in Section V, it represents an important operational state for accomplishing supersonic mixing.

The ejector equations have also a useful application outside the mixing process. For primary and secondary Mach number being equal, the equations apply to subsonic or supersonic flow with wall friction in a tapered duct. In this form the equations are particularly useful to calculate the performance of the "pseudo shock" diffuser of an ejector with the inclusion of wall friction. For zero wall friction and a constant area duct the results of the ejector equations are identical to those of the common normal shock relations.

The application of the ejector equations to single flow conditions can be extended to flow expansion in a nozzle in the presence of wall friction. In this case the necessary τ -value is found from isentropic expansion conditions and inserted in the ejector equations for calculating the flow in the nozzle with wall friction. The implied assumption is, however, that τ is not significantly affected by wall friction. Reference 4 explores in more detail this kind of application of the ejector equations.

V. THE FLOW DENSITY PARAMETER

Equation 8, which contains only dimensionless magnitudes, allows a generalized interpretation of ejector operations. The right side of this equation is strictly given by the ejector geometry and the inlet flow conditions. It results in a number, denoted here as "E", which uniquely characterizes a certain state of ejector operation. This number had been originally called "flow density parameter" since it can be interpreted (see Reference 3) as the exit flow density over the inlet momentum density made dimensionless by the stagnation speed of sound of the mixed operating media. Since it is uniquely given by the ejector layout including the inlet flow conditions, it is useful to consider it simply as a number characterizing a given ejector operational state. With E standing for its right side, Equation 8 becomes a reduced ejector equation.

The left side of Equation 8 contains only the mixing section conditions as given by τ and c and the exit flow conditions. A graphic presentation of

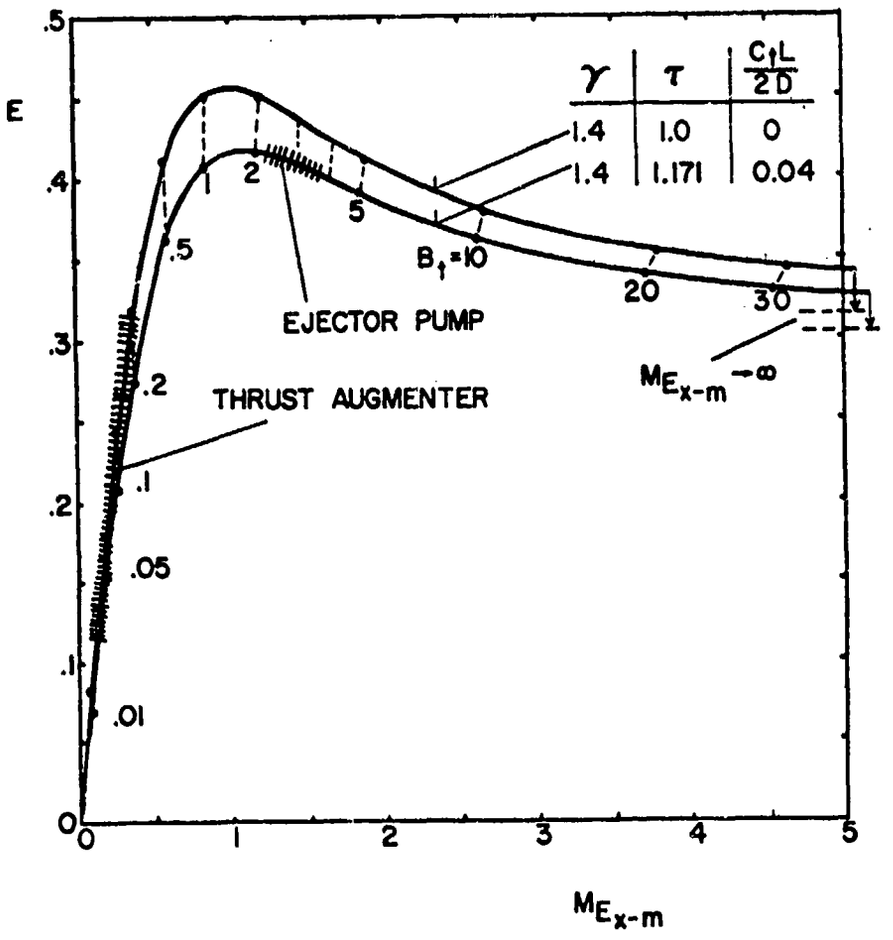

Figure 3. Typical E-Curves of the "Reduced" Ejector Equation

this reduced ejector equation, as given in Figure 3, demonstrates its properties. The three magnitudes, γ_{Ex}, τ and c enter as parameters in this presentation. These three parameters have, compared with the exit Mach number M_{Ex-m}, a minor influence on the shape of the "E-curve" and are in general constants of a given ejector problem.

Figure 3 shows two examples of E-curves. The top curve is for $\tau = 1$ and $c = 1$ representing a straight frictionless tube as mixing section. The lower curve represents the experimental ejector described in Reference 2. and is characterized by $\tau = 1.171$ and $c = 1.04$ ($\gamma_{Ex} = 1.4$). Both curves are representative for opposite extremes of ejector operations. The top curve is typical for thrust augmentation, i. e., very low pressure ratio ejectors, while the lower curve is typical for high pressure ratio ejectors operating with supersonic mixing, i. e., supersonic exit Mach-number. There is little difference in the general character of these two curves. However, as will be discussed below, there is a significant difference in the location of each operating regime on the pertinent E-curve.

For the general properties of an E-curve it is apparent that for very low E-values no supersonic exit Mach number is possible. For higher E-values a subsonic and supersonic solution appears. Above a certain E-value no solution is possible, i. e., the mixing section becomes choked.

Typical operating regimes of ejectors can be located on their respective E-curves. As shown in Reference 2, a supersonic exit Mach number is a prerequisit for an optimized high pressure ratio ejector pump, i. e., it operates on the supersonic branch of its E-curve. As will be discussed further below, its actual operation is restricted to almost a single point of the supersonic branch. First, it is of interest to explore the circumstances under which transition from subsonic to supersonic mixing occurs. It is obvious that very high supersonic exit Mach numbers would require suction at the ejector exit. However, there is a minimum E-value where a supersonic exit Mach number can be produced without a pressure drop during mixing. This is the case of constant pressure mixing. At this condition the inlet impulse forces are able to push the supersonic shock system out of the mixing section into the supersonic diffuser.

The point of transition to supersonic mixing can be identified on an E-curve with the help of Equation 7. For constant pressure mixing the pressure ratio p_{Ex-m}/p_s in this equation becomes unity and drops out. Writing for the left side

$$\frac{\gamma_p M_p^2}{t\left(1+\frac{A_s}{A_p}\right)} + \frac{\gamma_s M_s^2}{t\left(1+\frac{A_p}{A_s}\right)} = B_t \qquad (14)$$

Equation 7 becomes

$$B_t = c_m \gamma_{Ex} M_{Ex-m}^2 \qquad (15)$$

This relation allows one to assign to any point of the E-curves in Figure 3 a B_t-value as an indicator that constant pressure mixing is possible. It becomes obvious for both curves in Figure 3 that B_t must have at least a value of about 2 before supersonic mixing becomes possible. For constant pressure mixing to really occur, the second condition must be fulfilled that E has the value indicated by the B_t-point in Figure 3. The magnitudeswhich determine B_t in Equation 14 cannot be chosen arbitrarily, since they enter also Equation 8 which determines E. The general trend is that with increasing ejector pressure ratio the point, where the right combination of B_t and E occurs, moves to higher exit Mach numbers.

The investigations of Reference 3 have shown that for the optimized ejector with supersonic mixing the pressure during mixing invariably rises. This means that the point of optimum operation on the E-curve lies at a higher E-value (or lower B_t-value) than that at which transition to supersonic mixing occurs. In particular it was found that optimum operation

always occurs as near to the highest E-value as possible (see Reference 3). This coincides with practical experience which requires that the ejector is first "started", i. e., is brought to supersonic mixing, with a high primary pressure, which can then be reduced to reach the optimum operating point. This point is then also just short of the condition where the flow breaks down again to subsonic exit flow.

Ejectors with B_t-values below about unity, which do not allow transition to supersonic mixing, may be classified as low pressure ratio ejectors. Experience shows that for this class of ejectors the pressure during mixing also rises under optimum operating conditions. This general trend of a pressure rise during mixing is not an inherent feature of the optimized ejector. A pressure drop during mixing minimizes the mixing losses and a pressure rise minimizes the pressure recovery losses in the diffuser. In balancing these conflicting requirements, the magnitude of common wall and diffuser losses makes a pressure rise during mixing necessary. In the cae of the supersonic diffuser, which is in general limited to normal shock recovery, the pressure rise must apparently be as high as maintaining of supersonic mixing allows.

For the low pressure ratio ejector a pressure rise during mixing means that optimized operation takes place again at a lower B_t-value than applicable to constant pressure mixing. However, since the operation takes place on the subsonic branch of the E-curve, the associated E-value is also lower.

For the lower end of the subsonic regime of the E-curve, say below E = 0.3, it follows from Equation 8 that

$$M_{Ex\text{-}m} \approx E$$

If we also assume that m_p/m_s and consequently $A_p/A_s \ll 1$, as it applies to thrust augmentation, Equation 8 indicates also that

$$M_s \approx M_{Ex\text{-}m}$$

As shown in Reference 1, secondary Mach numbers for common thrust augmentation fall into the range of about 0.1 to 0.3. Thus the typical range for thrust augmentation on the E-curve is correspondingly between about E = 0.1 and 0.3.

VI. CONCLUSION

The nature of the energy transfer taking place between the two operating media of an ejector allows ejector performance predictions without the knowledge of the details of the mixing process. The present analysis provides no data on the length of the mixing section. So far only practical experience can provide information on the mixing length. The application of multiple primary nozzles provides a convenient means to adjust the mixing length within a wide range. For certain ejector applications such as thrust augmentation a mixing length as short as possible is of extreme importance. For such cases the mixing process becomes a special subject of investigation requiring analytic exploration.

Generalized ejector considerations based on the here developed flow density parameter provide a useful picture for classifying ejector operations, but it can only give general trends for designing ejectors. To provide readily useable design data for optimized ejectors of any kind, the full implication of the present ejector analysis is necessary as shown in References 1 and 3.

REFERENCES

1. Hasinger, S., "Performance Characteristics of Ejector Devices", Aerospace Research Laboratories, Technical Report ARL TR-75-0205, Wright-Patterson AFB, Ohio, June 1975.

2. Hasinger, S. and Fretter, E., "Comparison of Experiment and Analysis for a High Primary Mach Number Ejector", Air Force Flight Dynamics Laboratory, Technical Report AFFDL-TR-38, Wright-Patterson AFB, Ohio, May 1977.

3. Hasinger, S., "Ejector Optimization", Air Force Flight Dynamics Laboratory, Technical Report AFFDL-TR-78-23, Wright-Patterson AFB, Ohio, June 1978.

4. Hasinger, S., "Design of a Radial Outflow Expansion and Diffusion System", Air Force Flight Dynamics Laboratory, to be published.

ADVANCES IN EJECTOR TECHNOLOGY - A TRIBUTE TO HANS VON OHAIN'S VISION

by

K. S. Nagaraja
Air Force Flight Dynamics Laboratory
Wright-Patterson Air Force Base, OH

A review of the advances in the ejector technology area accomplished in the Air Force cannot overstate the contributions made by Hans von Ohain. Hans von Ohain's extraordinary perceptions are clearly evident in many innovative technological programs that he brought into existence during his extremely colourful and extraordinarily fruitful career at the Aerospace Research Laboratories, WPAFB.

A brief review of the significant accomplishments made at ARL in the basic understanding of the aerothermo fluid dynamic characteristics of ejectors is given. The studies of AFFDL which further enhanced the state-of-the-art of the ejectors for V/STOL applications are also indicated. The spectrum of activities in the Air Force not only gave a great deal of insight into the characteristics of the ejector flows, but also resulted in the development of compact ejectors that are relevant for aircraft application. The saga of ejector investigations is continuing and it is within the realm of possibility that ejector systems will be successfully applied for a variety of aircraft operations in the coming years.

This work was performed in 1979 in AFFDL under Work Unit No. 24041056.

AD P000337

ADVANCES IN EJECTOR TECHNOLOGY - A TRIBUTE TO HANS VON OHAIN'S VISION

K. J. Nagaraja

Air Force Wright Aeronautical Laboratories
Flight Dynamics Laboratory
Wright-Patterson Air Force Base, Ohio

Hans Von Ohain has made many significant contributions in the aeropropulsion area. His invention of the first turbojet engine is well known. The impact of that invention is all too well illustrated by the enormous commercial and military aircraft development that has happened since that time when the first jet powered aircraft was successfully flown in Germany in August 1939. Since the time of his arrival in the United States, Hans Von Ohain has contributed significantly to other technology programs. The development of ejector technology in the Air Force illustrates vividly Hans' farsightedness and leadership. Hans' magnetic personality, very striking characteristics of humility and humanity and absolute devotion to science and technology as well as to the well-being of his co-workers make him a unique person. I express my deep affection and high regard to what Hans Von Ohain means to me by dedicating this article to him.

A great deal of fundamental investigations and applied research has been performed in the area of ejectors as jet pumps over a period of several decades. However, it is only recently that ejectors are recognized as thrust augmentors since the early work of Von Karman (Ref. 1). Subsequently, U. S. Air Force undertook a project of developing the ejector technology for thrust augmentation purposes. A great deal of fundamental and applied work (see the References section) was performed in the course of the last fifteen to twenty years, and a considerable amount of the results has been published.

Initially, a systematic fundamental study was undertaken at the Aerospace Research Laboratories (ARL) at WPAFB under the direction of Hans Von Ohain. Subsequently, an applied study was initiated in the early 1970's at the Air Force Flight Dynamics Laboratory, and the specific task of completing the design of an ejector thrust augmented V/STOL aircraft was completed.

The basic studies at ARL conducted over a period of about ten years yielded several significant results (Ref. 2-14). Extensive in-house studies at ARL and several contracted studies provided considerable information on ejector characteristics and on the design aspects of practical ejector for aircraft applications.

Following are some of the significant and fundamental developments in thrust augmenting ejectors that resulted from ARL's studies (Ref. 6).

1. Development of hypermixing nozzles for mixing enhancement was achieved. This provided a basis for designing a more compact ejector (Refs. 4, 5, 7-10).

2. Demonstration that mixing and diffusion of flows could be done simultaneously with performance advantage was accomplished. Previously, it was believed that performance advantage would result if diffusion is preceded by the accomplishment of complete mixing.

3. An incompressible ejector analysis which will parametrically evaluate an ejector performance was performed (Ref. 5).

4. Thrust augmentation of the order of two in an ejector of inlet area ratio 23 was successfully achieved experimentally (Ref. 8).

5. Good thrust augmentation for V/STOL purposes was also realized by using full-scale multichannel ejectors (Ref. 12). Bypass air from a turbofan engine was diverted by suitable valving into the ejectors installed in a wing. Test data confirmed that an aircraft-installed ejector would perform satisfactorily.

6. It was demonstrated that diffusion normal to the plane of the velocity profile always leads to improved mixing in contrast to diffusion in the plane of the velocity profile (Refs. 7, 13).

7. An ejector-wing model (6 ft model) was designed, fabricated and tested (under an ARL sponsored study which was performed by the Bell Aerospace Company in a wind tunnel (Ref. 14). The tests showed that the resulting favorable supercirculation effects due to the ejector flow would enable transitioning from hover to cruise condition even when the lift due to the thrust component is drastically reduced. This supercirculation effect resulting from an ejector wing in flight points out the inherent shortcoming of an ejector incorporated in the fuselage of an aircraft (as was done in the case of the Hummingbird).

8. Further compactness of the ejector was realized by the utilization of a device that combines efficient boundary-layer energization with a configured diffusion device, that is, trapped vortex cavity (Ref. 15). This work was performed under contract by the Advanced Technology Center, Inc. of the Vought Corporation, Dallas, Texas.

A few of ARL's publications and others which describe the fundamental ejector developments are indicated in the bibliography which also includes the reports resulting from other AF projects on thrust augmenting ejectors.

Air Force Flight Dynamics Laboratory of WPAFB undertook some exploratory study in the ejector area in the late 1960's. A more systematic design study of a V/STOL demonstrator aircraft was initiated in the early 1970's.

Initial exploratory studies supported under AFFDL contract led to the development of the so-called Jet Flap Diffuser Ejector (JFDE). Although jet flap diffuser concept had been proposed earlier in France, no systematic effort was undertaken then to develop an effective configuration. Hans Von Ohain's suggestion regarding the orientation of the primary jet injection relative to the inlet geometry proved successful, and the subsequent tests performed on the jet diffuser ejector at the Flight Dynamics Research Corporation in California showed that relatively high thrust augmentation could be realized in a compact ejector.

In support of the design study of a V/STOL demonstrator vehicle trailing-edge ejectors on wings were fabricated and tested (Refs. 16, 17). One of the wind-tunnel models (Ref. 16) was fabricated and tested in the 7- by 10-ft low speed tunnel at NASA-Ames. This wind-tunnel model was a constant chord two-dimensional 30-in. span and 44.5-in. chord (with the flaps up) model. The tests assessed the lift off and low speed transition phases of flight. The results of the tests showed that in an aircraft configuration, with sufficient BLC provided, a trailing-edge ejector system could provide predicted levels of thrust augmentation. Some insight was also gained about optimal flap settings for transitioning the aircraft from hover to cruise condition.

Preliminary design of an ejector thrust augmented aircraft required a theoretical methodology which could evaluate the performance of the ejectors subject to a wide range of variation in the thermodynamic parameters of the injected and entrained fluids. A compressible ejector flow analysis was developed by assuming that the primary and the secondary streams mixed in a constant area duct (Ref. 18). The schematic of the single-stage ejector is shown in Figure 1. The analysis was performed in steps as shown below:

1. Pressures were prescribed incrementally at station 1, and the other flow quantities were determined from the thermo fluid dynamic relations.

With choked primary flow, the static pressure of the secondary flow was allowed to take on values less than the primary static pressure. The computations were cut off just before the secondary Mach number reached unity.

The analysis was extended to include the ejector flight velocities in the performance calculations. While in flight, the static pressure at station 1 was allowed to take on values greater than the ambient air static pressure, but less than the ambient stagnation pressure. It was noted in some instances from the results that the ejector performance reached optimum levels whenever the entrained

air was compressed as it entered the injection station 1. This characteristic requires some further examination.

2. The momentum balance equation in the constant area mixing duct also included the total ejector flow losses evaluated empirically from the test results of ARL.

The velocity of the mixed flow at station 2 was provided by a quadratic equation - one solution corresponding to mixed subsonic flow, and the other corresponding to mixed supersonic flow. Only the subsonic solution was considered, and the supersonic solution was ignored.

3. Diffuser flow was evaluated isentropically. However, any diffuser loss that arises has been accounted for empirically in the momentum equation.

4. Considerations to the thermodynamic constraints (i.e., no entropy decrement as the flow moves forward) were given in the computations.

Typical results of the calculations are shown in Figure 2. It is worth noting that the net thrust augmentation reaches a peak value around 2 for the diffuser area ratio and then begins to drop. This indicates that the flow in the diffuser is separating from the walls. Further, the net thrust augmentation decreases as the primary air stagnation temperature is increased. In fact, the performance degradation with increasing primary stagnation temperature was consistently demonstrated by the computed data for all cases of inlet area ratio, temperature conditions and pressure ratio. It should, however, be noted that experiments have also shown that the effect of temperature is minimal on an incompletely mixed flow (Ref. 12). Regarding the pressure ratio effect on the ejector performance, the situation is quite complicated. The pressure ratio effect seems to depend on the inlet area ratio, the primary stagnation temperature and the static pressure at the injection plane (i.e., the diffuser area ratio).

The effect of ejector forward velocity on the thrust augmentation ratio is quite conceivable. As the forward velocity increases, the net thrust augmentation

decreases due to ram drag. The results shown in Figure 3 illustrate typically the ejector performance in flight. However, as will be shown later, an ejector with a different operating thermodynamic condition in the shroud would provide a different performance characteristic (Ref. 20). This will be discussed subsequently in some detail.

The sensitivity of ejector performance to inlet conditions is illustrated in Figure 4. In fact, an operating ejector in an aircraft may well require a variable inlet geometry for yielding optimal performance. Inlet design is a significant factor in optimal ejector designs, for it is the effect of the pressure forces acting on the inlet that determines the thrust magnitude. However, the performance may become sensitive to other ejector components also, for example, at higher forward velocities. Sensitivity of the ejector components as well as of the ejector itself will have to be carefully evaluated, especially when the ejector is installed in an airplane.

It is worth making reference to the performance calculation of a two-stage ejector. A schematic of a two-stage ejector being considered is shown in Figure 5. The performance calculations are illustrated in Figure 6. It is seen that with smaller inlet area ratios in the two staging process, augmentations which correspond to those of high inlet area ratios in single-stage ejector can be achieved. The potential usefulness of staging may also be realized if a staged ejector becomes necessary due to the packaging problems in an airframe.

Based on the data obtained from the analysis, preliminary design study of a V/STOL demonstrator vehicle was conducted (Ref. 21). An RPV vehicle having a canard wing arrangement with a trailing-edge ejector, balanced by a forward fuselage ejector was designed (Figure 7). The injection area ratio of the ejectors was an optimum 13.5 which was designed to produce a thrust augmentation ratio of 1.66 or a VTOL gross weight of 896 lb. The design configuration was

powered by the Williams F107-WR-100 engine which in turn fed the fuselage and wing trailing-edge ejectors. At the maximum VTOL weight, the vehicle was designed with fuel capacity of 205 lb, and with full control capability. Further, it had hover acceleration margin of 1.02, radius of 100 n. mi. and loiter time of 100 min. Internal ducting characteristics were evaluated based on the pressure losses due to the internal aerodynamics (Ref. 22). A digital computer program for calculating the internal gas ducting system weight of the ejector thrust augmented vehicle was developed for the vehicle sizing determination (Ref. 23). This program is capable of generating a large and consistent amount of trade-off data for achieving an optimum vehicle.

Aside from the design studies performed at AFFDL, some theoretical studies on augmentors and augmentor wings were also performed. Particularly, Hasinger's investigations (Refs. 24-27) were noteworthy. Although the objective of the investigations is to design a jet pump which would yield the lowest possible primary plenum pressure to achieve a given pressure ratio (of the ejector exhaust stagnation pressure to the secondary stagnation pressure) at a given mass flow ratio (of the primary mass flux to the entrained mass flux), the analysis which deals with both subsonic as well as supersonic mixed flow cases is capable of yielding information that will be relevant to thrust augmenting ejector designs as well. The analysis also indicates the inlet flow conditions which determine whether the mixed flow is coming subsonically or supersonically at the exit of the mixing duct.

High lift characteristics of an ejector-flapped wing was theoretically evaluated by Woolard (Ref. 28) for a two-dimensional wing section with a point sink located aft of the wing chord for simulating the ejector intake flow. The work also treated the matching problem of the airfoil external flow with the ejector internal flow and derived the overall ejector-flapped wing section aerodynamic performance. Comparisons of the lift characteristics of an ejector-flapped wing

with those of a jet augmented flapped wing show the superior performance of the former at low forward speeds. Significant items in the analytical approach and evaluation of the results are presented in the author's paper presented elsewhere, (Ref. 30).

A three-dimensional calculation method for determining the aerodynamic characteristics of arbitrary ejector-jet-flapped wings was developed under AFFDL contract by the McDonald-Douglas Aircraft Company. The computer program which is user oriented is capable of generating the aerodynamic coefficients including the ground effect of arbitrary wing-ejector configurations. The analysis program is based on the linear theory, and compressible ejector flow program is coupled with the wing aerodynamic program of Douglas.

A trailing-edge ejector installed on a wing was fabricated and tested in the AFFDL subsonic tunnel whose test section measures one square meter (Ref. 29). The wing-tunnel model was provided with an upper door at the inlet which in cruise flight condition would fold down as the ejector flaps would fold up to provide the conventional cruise wing. The upper door which captured the external flow and directed the flow into the ejector shroud was designed to be set at different angles relative to the wing plane. It was possible also to set the ejector flaps at desired angles. The semispan wing ejector model was one fourth the scale of the wing ejector designed for the AFFDL V/STOL demonstrator vehicle. Lift, drag, and pitching-moment data were taken over a range of upper door setting angles, the ejector flap angles and at several angles of attack as the wind-tunnel airspeed was varied from 20 to 60 ft/sec. The test result showed, for example, that the wing stall angle was substantially larger compared to the unpowered (or the unaugmented) case. Flow visualization tests were also performed utilizing helium bubbles. These tests showed the separated flow region on the exterior side of the aft flap of the ejector for certain configuration positions. The tests demonstrated again the favorable lift characteristics that would result in the ejector augmented case.

Recent theoretical calculations of ejector performance have shown that under certain conditions, it appears to be possible to achieve relatively high thrust augmentation values in forward flight (Ref. 20). Based on the results obtained from a simple, incompressible evaluation of the ejector performance (Fig. 8), it became clear that proper aerothermodynamic matching of the ejector flows (also including the ejector geometric characteristics) would play a significant role in optimal ejector designs. An effort on a more systematic evaluation of ejector performance was undertaken under AFFDL contract by the Flight Dynamics Research Corporation, Van Nuys, California. The investigations utilized one-dimensional compressible flow equations much the same way as was done in Reference 18, and these equations, without accounting for ejector losses, were solved by incrementally assigning values to the inlet flow Mach number M_1 of the entrained stream at the injection plane. In reference 18, the solution process was explicitly started by assigning values incrementally to the static pressure at the injection plane.

Loss effects were not analytically accounted for in the initial studies primarily because all the realistic losses could be estimated only after the geometric and other related flow parameters were fixed based on the objectives of the specific ejector mission roles. However, the analysis that would account for the incomplete mixing effects as well as the skin-friction effects was performed in a general sense.

The calculations in Reference 20 were performed by imposing the thermodynamic constraint that the entropy did not decrease as the flow progressed in the ejector toward the exit. This ensured that only physically acceptable solutions were utilized in the ejector performance calculations. The present investigations considered mixed supersonic flow conditions also, unlike those reported in Reference 18. The ejector performance was evaluated based on both the first solution (corresponding to the subsonic mixed flow) and the second solution (corresponding to the supersonic mixed flow).

The results of the calculations are shown in Figures 9-16. The results shown in Figure 9 pertain to the same ejector as indicated in Figure 10. The plus and minus signs in parentheses indicate that the results correspond to supersonic and subsonic mixed flows respectively at the end of the mixing duct. Propulsive efficiency, if defined in the classical manner where the reference jet energy is purely mechanical, can exceed one in certain thermodynamic situations because the thermal energy of the primary jet can also contribute along with the jet kinetic energy to the useful work produced by the system. However, if the reference jet energy is the total jet energy (including mechanical and thermal components), then the propulsive efficiency will be less than unity.

The data in the Figures 9-16 indicate that ejectors, based on the so-called second solution, exhibit a great deal of potential usefulness as thrust augmentors. It is necessary to pursue further the design aspects of such practical ejectors. A great deal of parametric analysis as well as design optimization studies will be required before new ejector configurations can be defined. However, the possibility of deriving new ejector concepts for thrust augmentation purposes is clearly indicated by the recent Air Force studies.

NOTE:
(i) Figure 8 was taken from a communication sent to AFFDL by FDRC in 1976.

(ii) Progress Reports as well as the final report submitted by FDRC and published as AFFDL-TR-79-3048 contributed to Figures 9-16.

References

1. Von Karman, T., "Theoretical Remarks on Thrust Augmentation", Reissner Anniversary Volume, Contributions to Applied Mechanics, 1949.

2. Fancher, R. B., A Compact Thrust Augmenting Ejector Experiment, ARL-70-0137 (AD 713634), Aug 1970.

3. Fancher, R. B., Low-Area Ratio Thrust Augmenting Ejectors, J. Aircraft, Vol. 9, Mar 1972 (Also AIAA Paper 71-576, Jun 1971).

4. Eastlake, C. N., The Macroscopic Characteristics of Some Subsonic Nozzles and the Three-Dimensional Jets They Produce, AFL 71-0058, Mar 1971.

5. Quinn, Brian, Compact Ejector Thrust Augmentation, J. Aircraft, Vol. 10, No. 8, Aug 1973.

6. Quinn, Brian, Recent Developments in Large Area Ratio Thrust Augmentors, AIAA Paper 72-1174, Nov 1972.

7. Viets, Hermann, Thrust Augmenting Ejectors, ARL 75-0024, Jun 1975.

8. Quinn, Brian, Experiments with Hypermixing Nozzles in an Area Ratio 23 Ejector, ARL 72-0084, Jun 1972.

9. Quinn, Brian, Wind Tunnel Investigations of the Forces Acting on an Ejector in Flight, ARL 70-0141, Jul 1970.

10. Bevilaqua, P. M., An Evaluation of Hypermixing for V/STOL Aircraft Augmentors, AIAA Paper 73-654, Jul 1973.

11. Bevilaqua, P. M., An Analytic Description of Hypermixing and Test of an Improved Nozzle, AIAA Paper 74-1190, Oct 1974.

12. Campbell, David R., and Quinn, Brian, Full Scale Tests of an Augmentor VTOL Concept, AIAA Paper 73-1185, Nov 1973.

13. Viets, Hermann, and Quinn, Brian, Concurrent Mixing and Diffusion in Three-Dimensions, AIAA Paper 75-873, Jun 1975.

14. Ryan, P. E., and Breidenstein, R. M., Wind Tunnel Test Data Report for a Powered 1/5 Scale ARL/Bell V/STOL Aircraft Model, Bell Aerospace Company Report No. 2353-921002, Jun 1969.

15. Haight, Charles H., and O'Donnell, R. M., Experimental Mating of Trapped Vortex Diffusers with Large Area Ratio Thrust Augmentors, ARL 74-0115, Sep 1974.

16. Brown, Squire L., and Murphy, Ronald D., Design and Test of Ejector Thrust Augmentation Configurations, AGARD CPP-143, Apr 1974.

17. Clark, Rodney L., Ejector Blown Lift/Cruise Flap Wind Tunnel Investigation, AFFDL-TR-73-132, Nov 1973.

18. Nagaraja, K. S., Hammond, David L., and Graetch, J. E., One-Dimensional Compressible Ejector Flows, AIAA Paper 73-1184, Nov 1973.

19. Quinn, Brian, Ejector Performance at High Temperatures and Pressures, J. Aircraft, Vol. 13, No. 12, Dec 1976, pp 948-954.

20. Alperin, Morton, and Wu, Jiunn-Jeng, High Speed Ejectors, AFFDL-TR-3048, May 1979

21. Byrnes, J. M., Murphy, R. D., Ball, R. F., Nagaraja, K. S., Hammond, D. L., Langleben, E. A., and English, R. B., V/STOL Demonstrator Vehicle for Thrust Augmentation Technology, AIAA Paper 74-995, Aug 1974.

22. Ball, Raymond F., Internal Ducting Design Methodology for Applications to V/STOL Systems, AFFDL-TM-74-183-PTB, 1974.

23. Langleben, Edward A., Digital Computer Program for Computing Total Internal Gas Ducting System Weights for an Ejector Thrust Augmented Vehicle, AFFDL-TM-74-181-PTB, 1974.

24. Hasinger, Siegfried H., Simplified Lay-Out of Supersonic, Heterogeneous Ejectors, ARL 73-0149, Nov 1973.

25. Hasinger, Siegfried H., Performance Characteristics of Ejector Devices, ARL TR-75-0205, Jun 1975.

26. Hasinger, Siegfried H., and Fretter, Earnest F., Comparison of Experiment and Analysis for a High Primary Mach Number Ejector, AFFDL-TR-77-38, May 1977.

27. Hasinger, Siegfried H., Ejector Optimization, AFFDL-TR-78-we, Jun 1978.

28. Woolard, Henry W., Thin-Airfoil Theory of an Ejector - Flapped Wing Section, J. Aircraft, Vol. 12, Jan 1975 (Also AIAA Paper 74-187).

29. Nagaraja, K. S., and Clark, G. W., A Wind Tunnel Study of the Effect of Free Stream Capture Area on the Aerodynamic Forces of a Thrust Augmenting Ejector-Wing, (To be published).

30. Work Shop on Thrust Augmenting Ejectors, co-sponsored by NASA-Ames Research Center, Naval Air Development Center and the Air Force Flight Dynamics Laboratory, 28-29 Jun 1978, NASA CP-2093 (Sep 79), Edited by A. E. Lopez, D. G. Koenig, K. A. Green and K. S. Nagaraja.

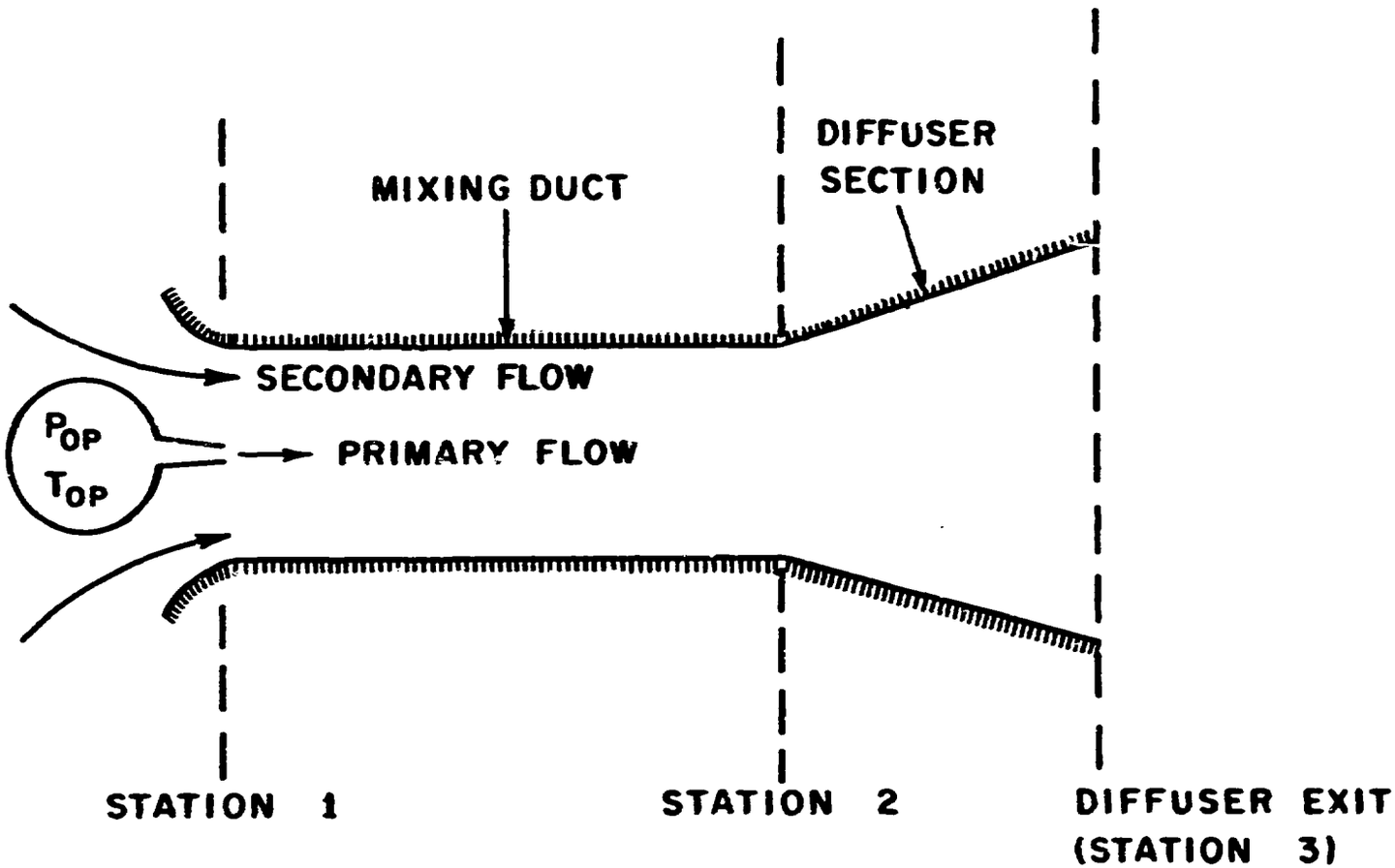

Figure 1.- Schematic of a single-stage ejector.

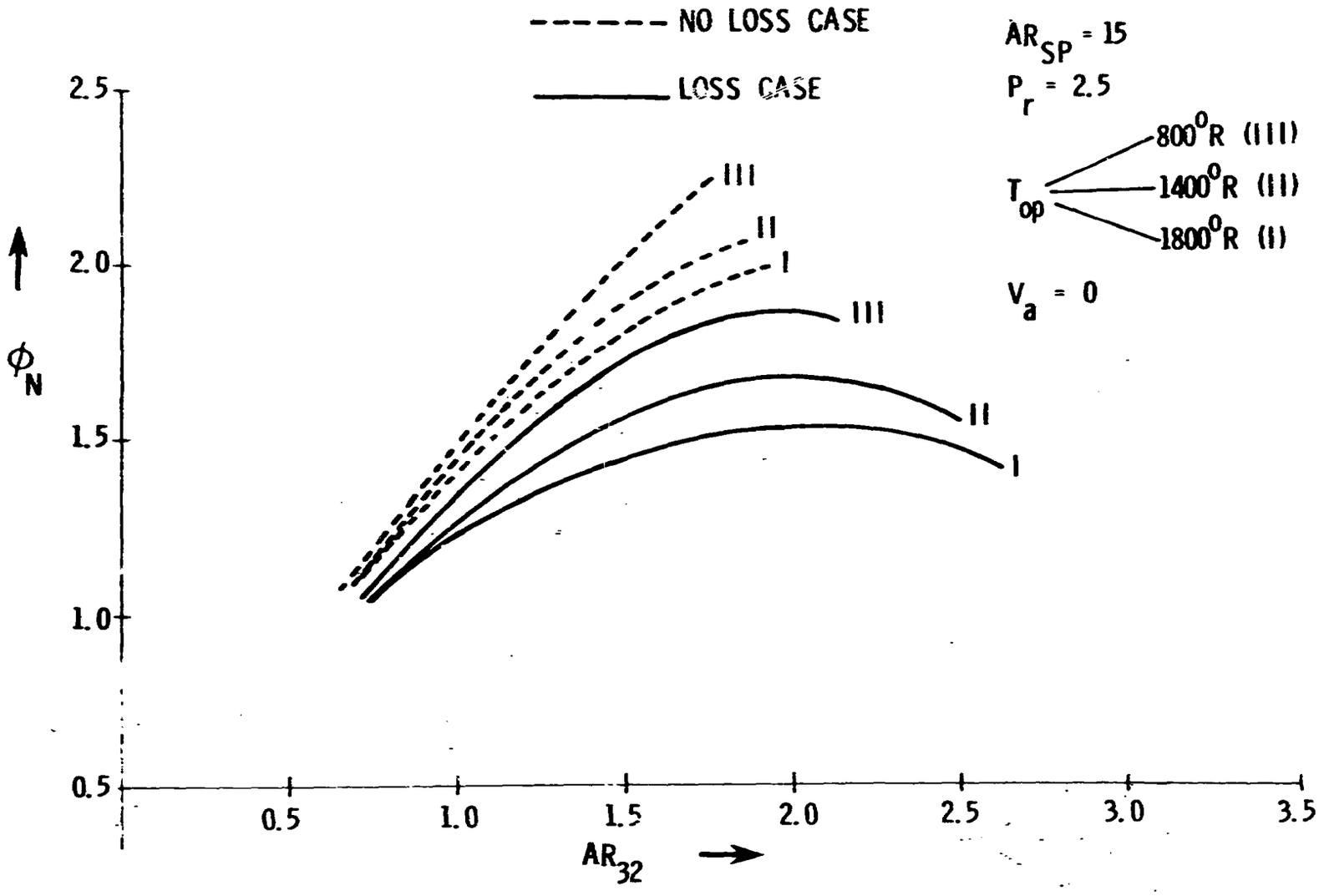

Figure 2.- Thrust augmentation ratio vs diffuser area ratio.

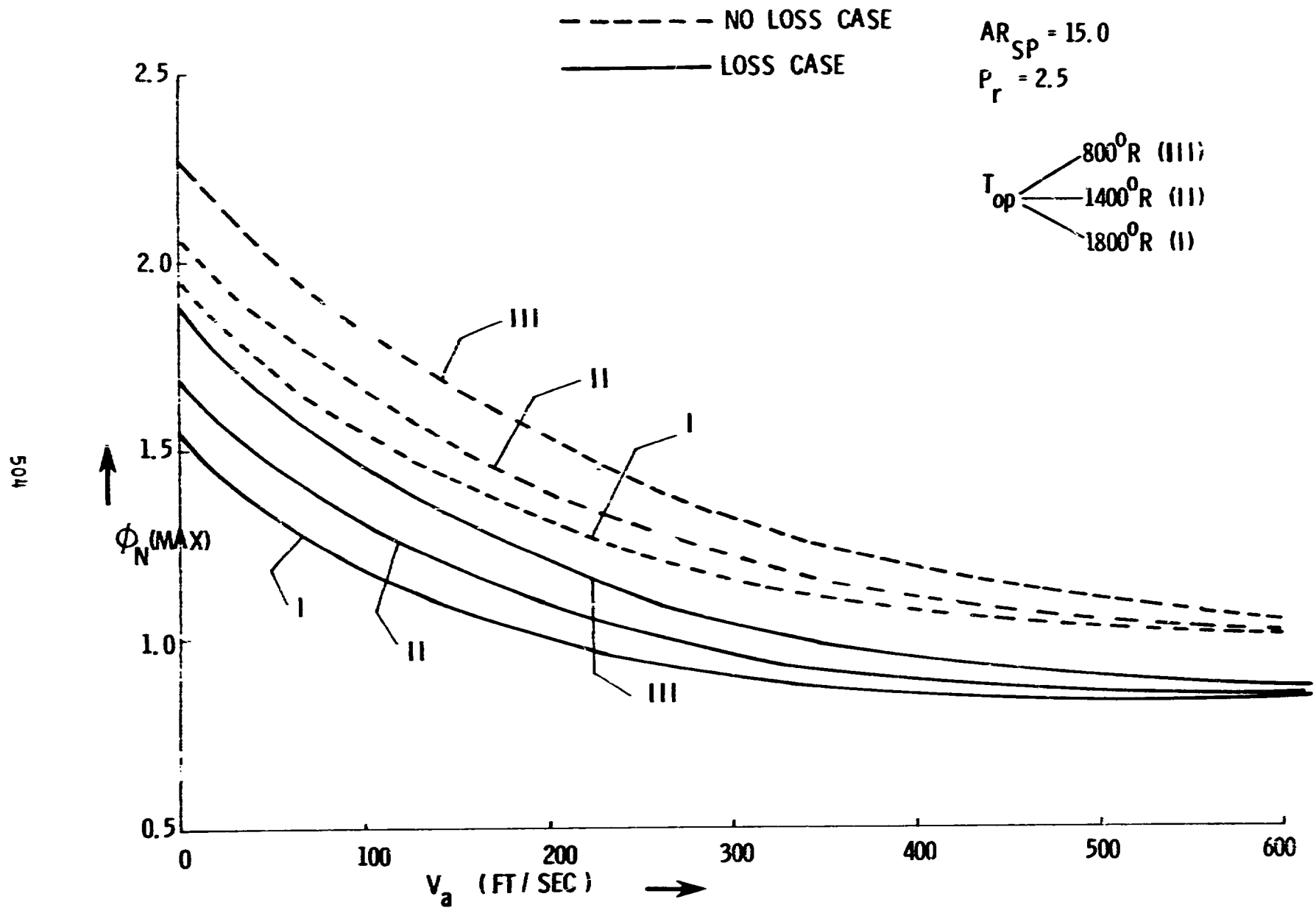

504

Figure 3.- Distribution of ϕ_N(max) vs V_a(forward velocity).

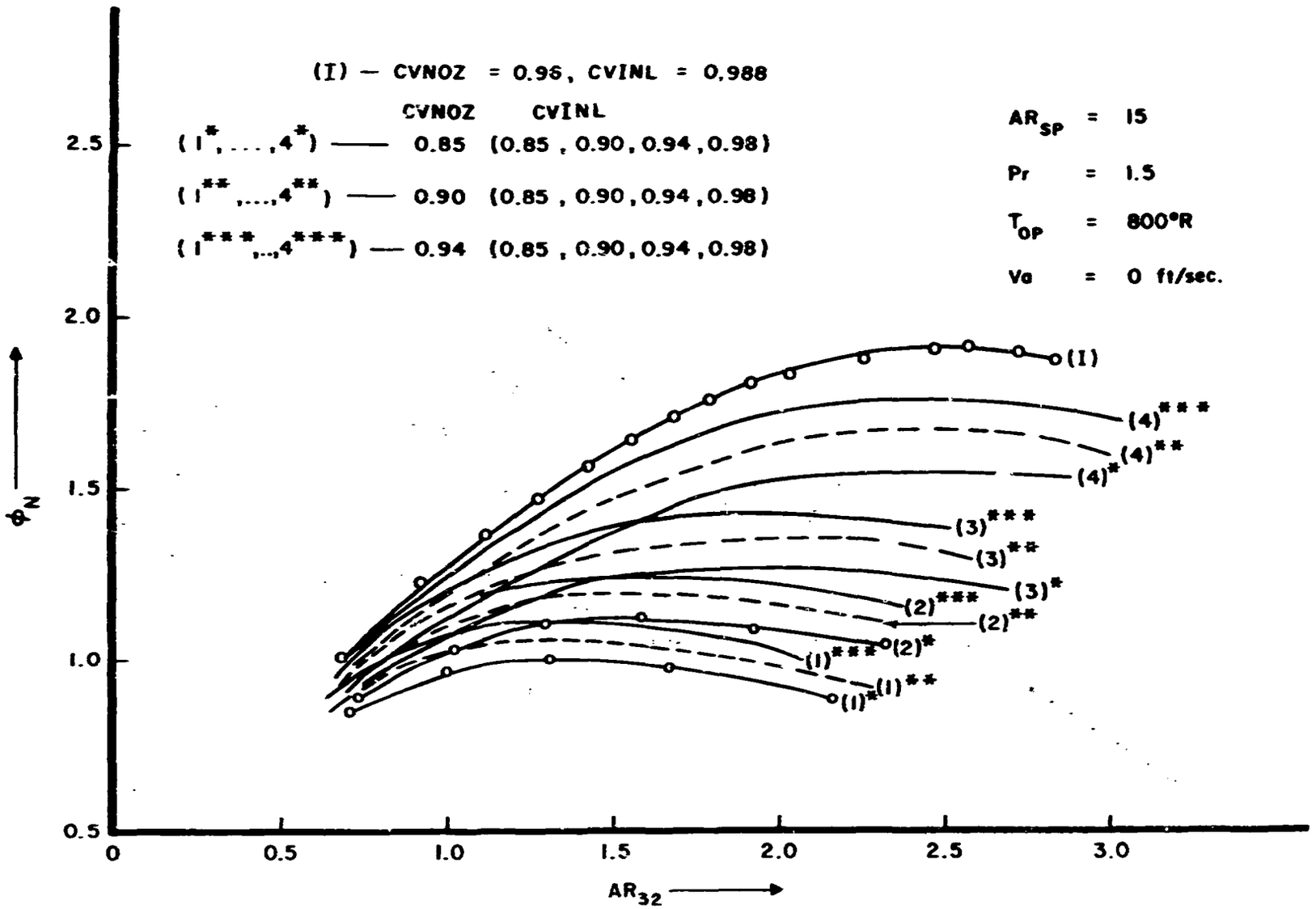

Figure 4.- Thrust augmentation characteristics for several nozzle and inlet losses.

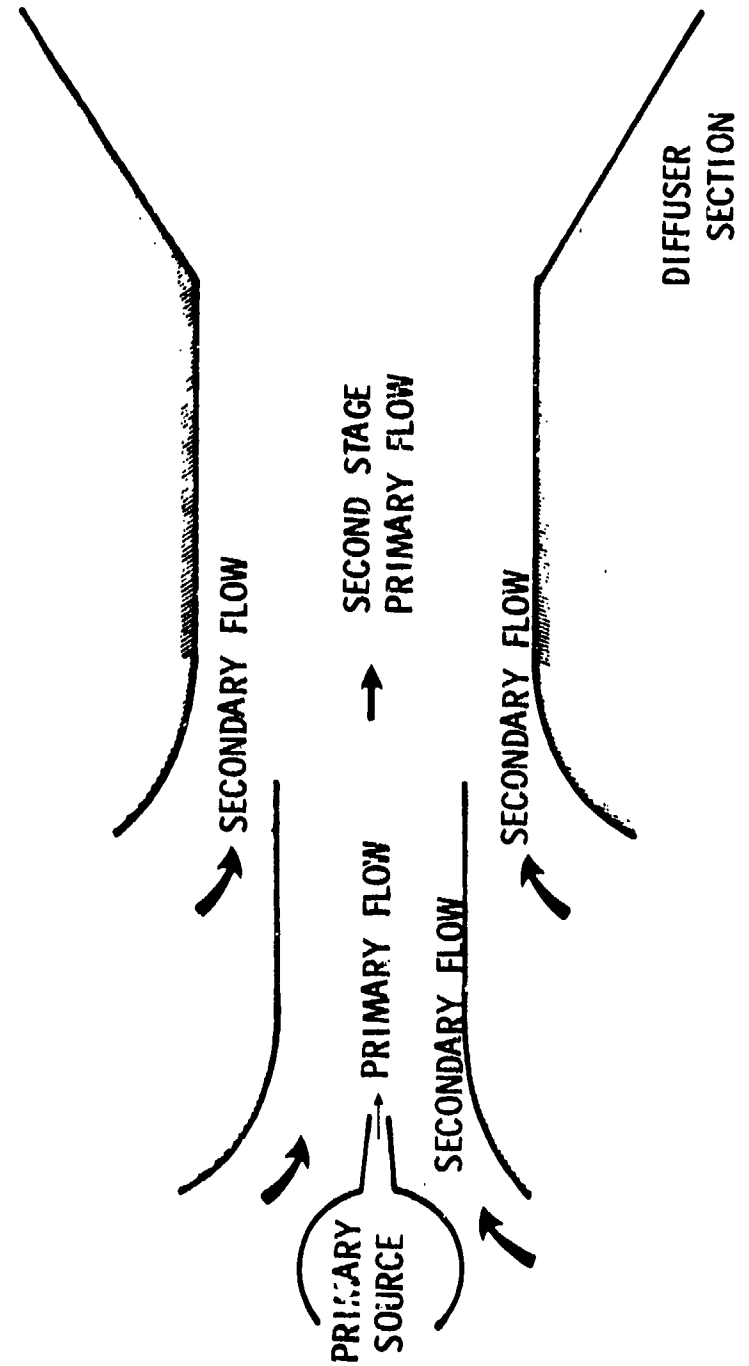

Figure 5.- Schematic of a two-stage ejector.

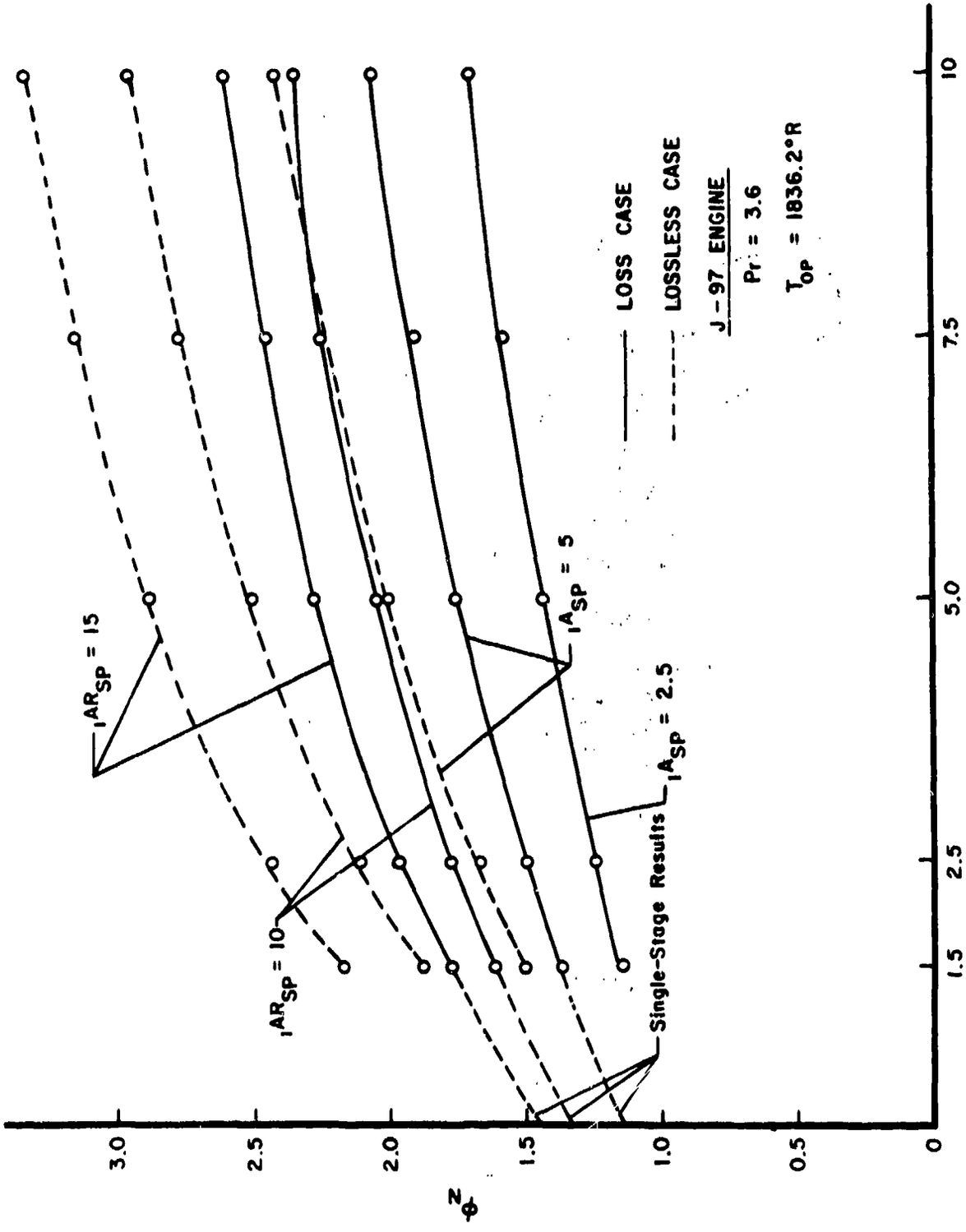

Figure 6.- Thrust augmentations in two-stage ejector flows.

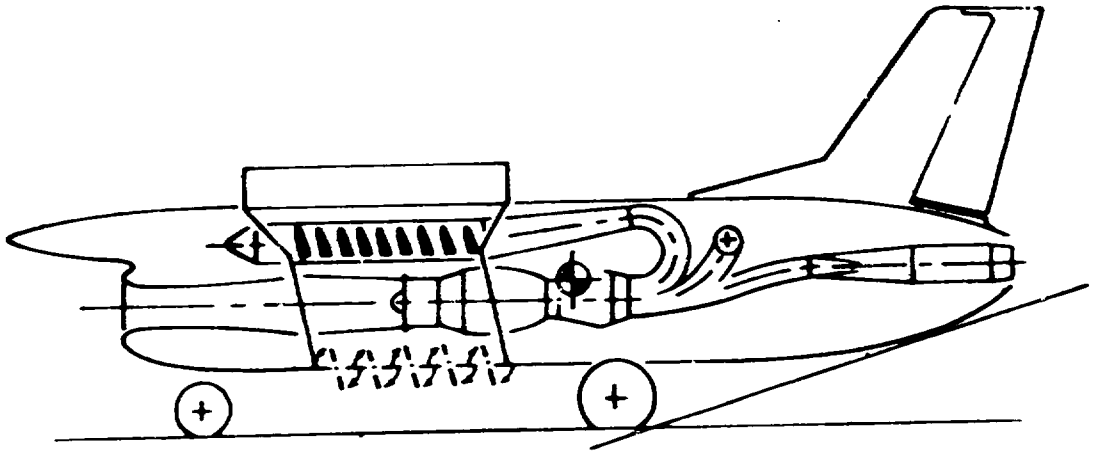

F107-WR-100 DEMO ENGINE

- 600 LBT CLASS

121 LB WEIGHT

GAS DUCTING SYSTEM

6.25% PRESSURE LOSS

210 LB WEIGHT

EJECTOR STATIC PERFORMANCE

OPTIMUM IAR = 13.5

OPTIMUM Φ = 1.66

Figure 7.- Propulsion system.

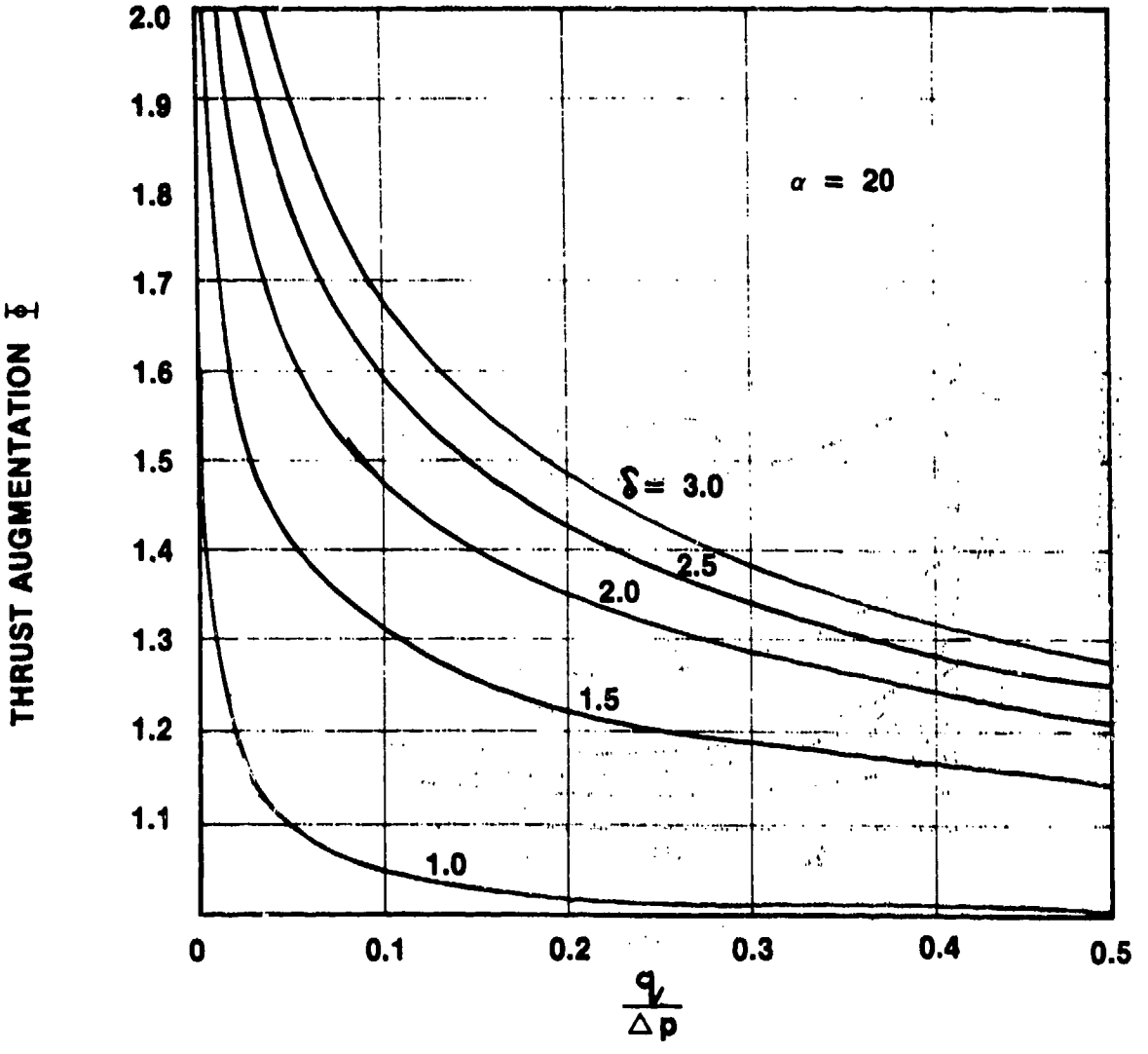

q · DYNAMIC PRESSURE

Δp · INCREMENTAL STAGNATION PRESSURE = $P_{op} - P_\infty$

α · INLET AREA RATIO

δ · DIFFUSER AREA RATIO

Figure 8.- Variation of thrust augmentation with $q/\Delta p$.

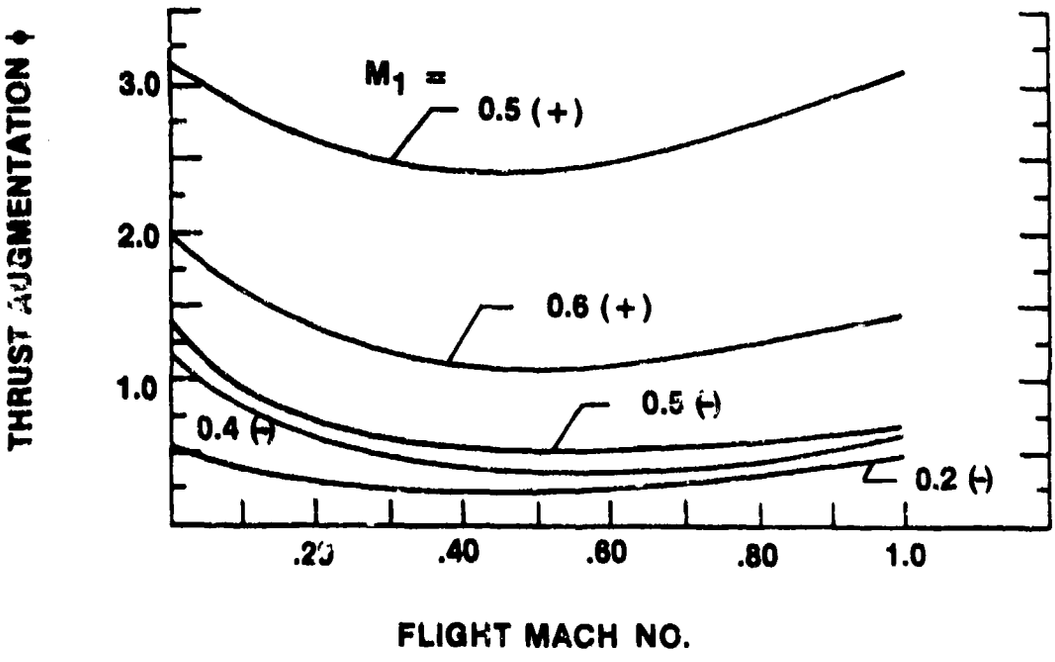

Figure 9.- Variation of thrust augmentation flight Mach number.

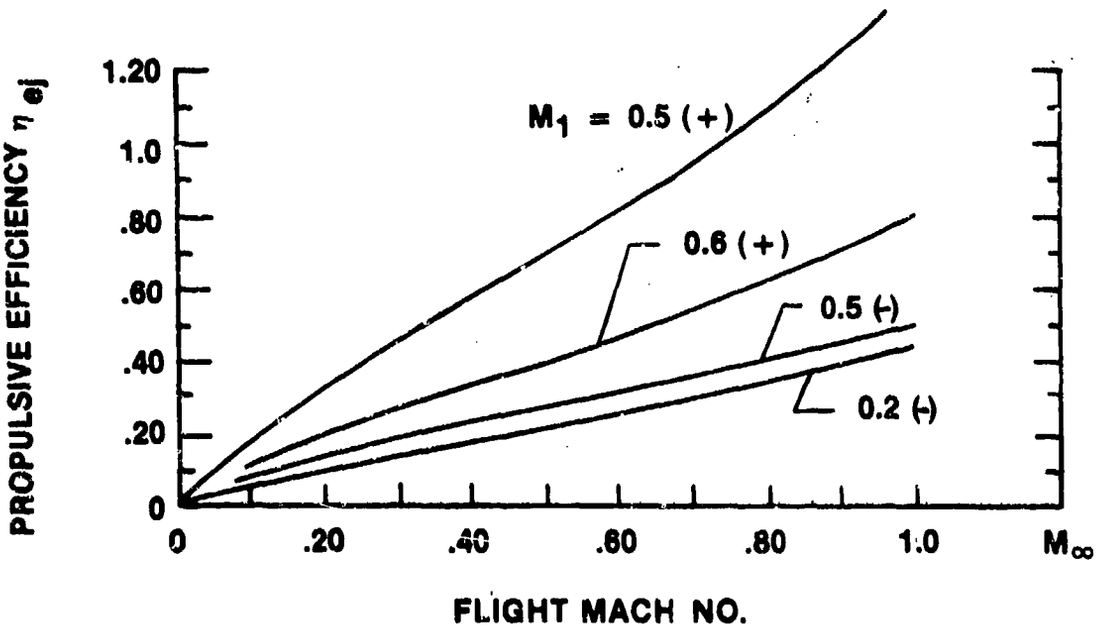

Figure 10.- Solid diffuser ejector performance; $\alpha_\infty = 20$, $\Delta T/T_\infty = 5.0$, $\Delta P/p_\infty = 3.0$, $C_{di} = C_F = C_\mu = 0$.

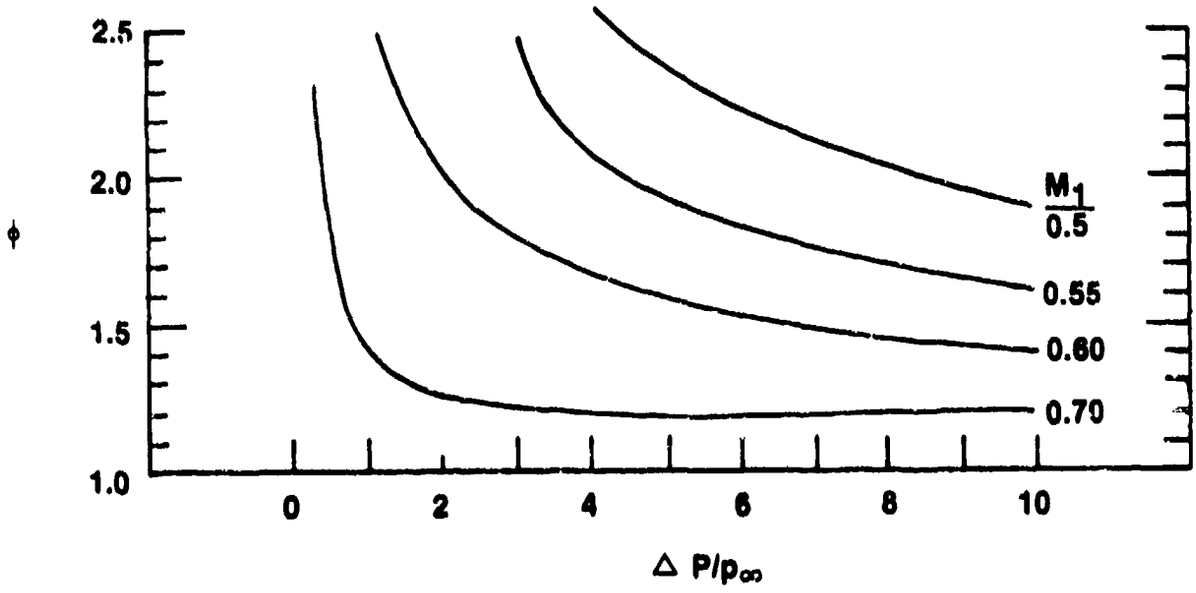

Figure 11.- Ideal high-speed ejector; $M_\infty = 0.5$, $\alpha_\infty = 20$, $\Delta T/T_\infty = 3.0$; second solution.

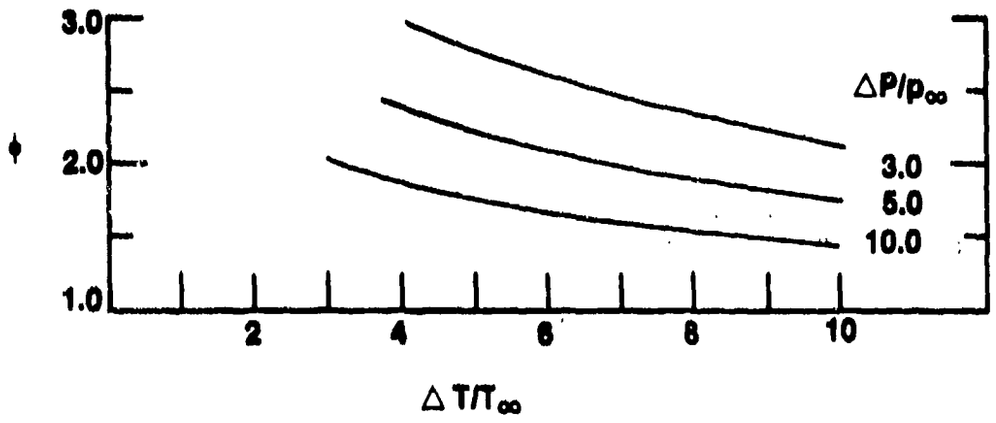

Figure 12.- Ideal high-speed ejector; $M_\infty = 0.8$, $\alpha_\infty = 20$, $M_1 = 0.5$; second solution.

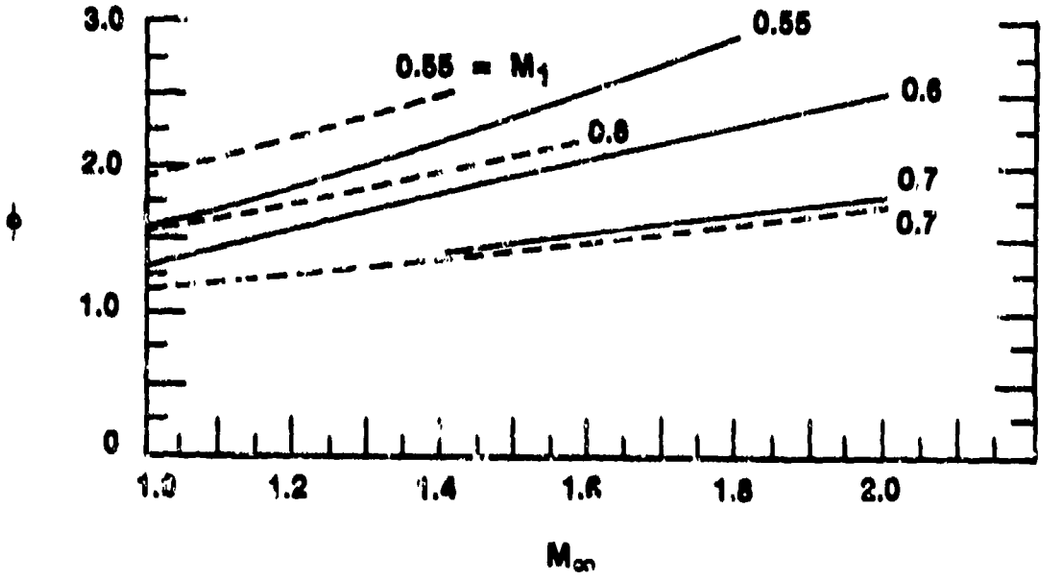

Figure 13.- Supersonic ejector performance; $\alpha_\infty = 20$, $P/p_{t_\infty} = 5.0$, $\frac{\Delta T}{T_\infty} = \begin{cases} \text{——} & 10.0 \\ \text{----} & 5.0 \end{cases}$; second solution.

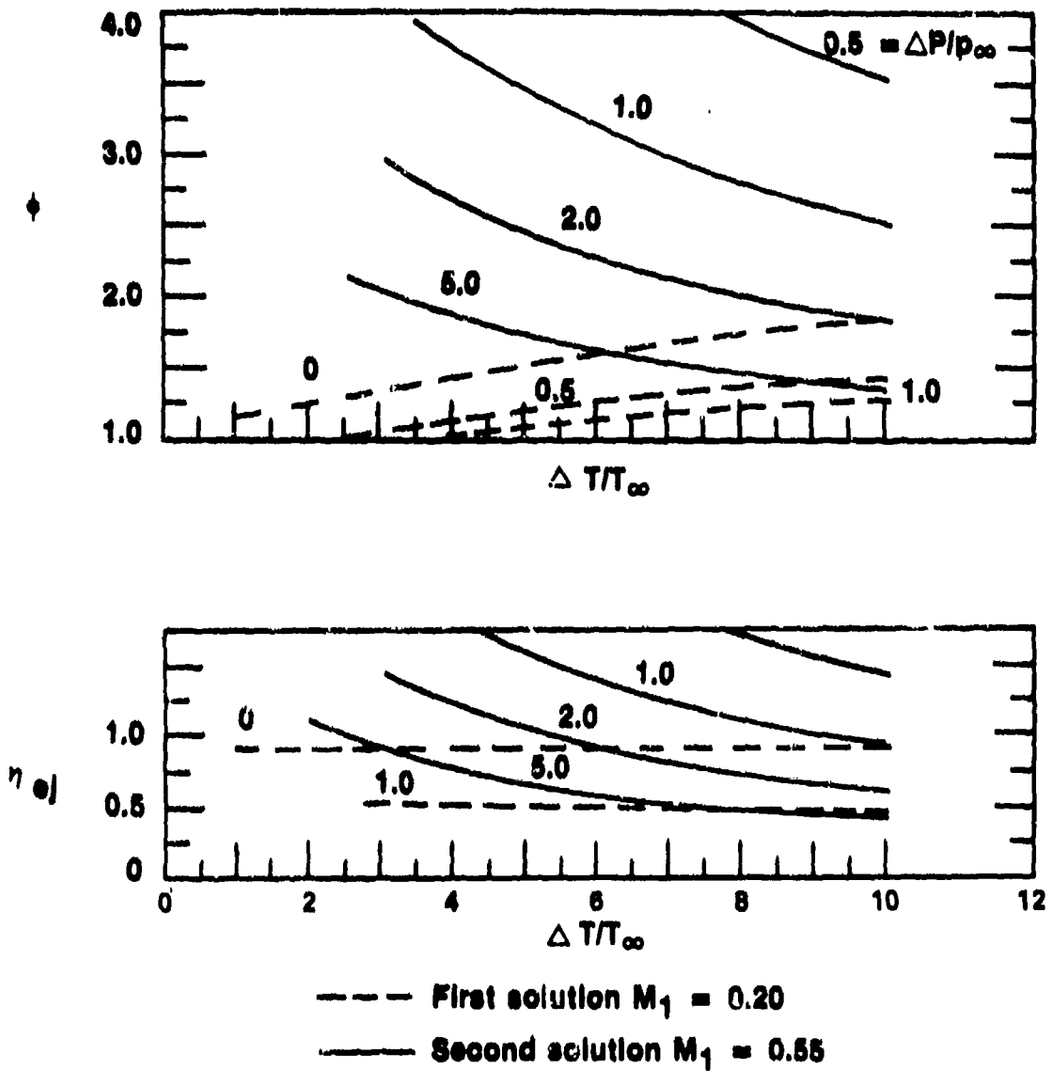

Figure 14.- Ideal high-speed ejector; $M_\infty = 0.8$, $\alpha_\infty = 20$, $s_\infty/s_\infty = 0$.

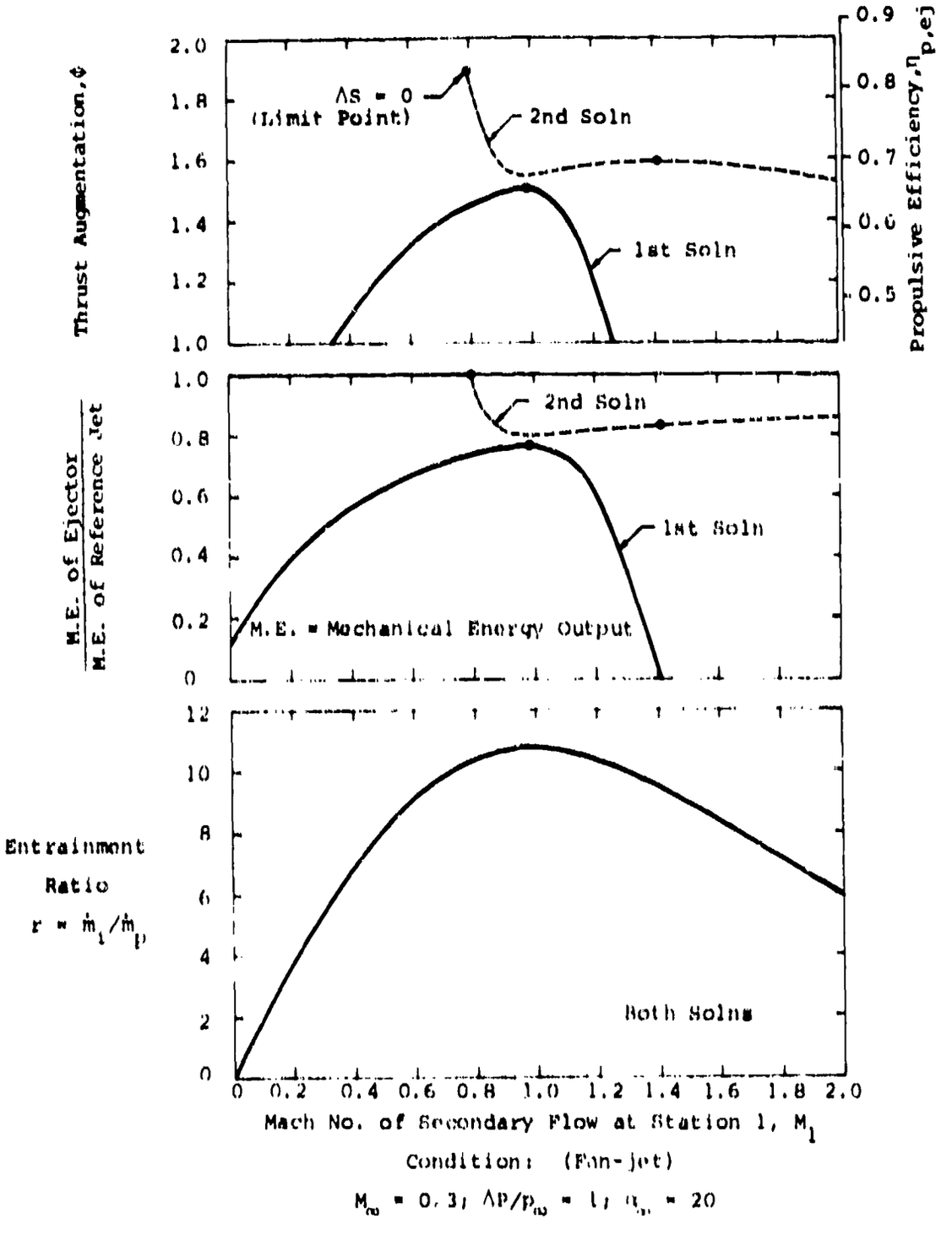

Figure 15.- Ejector in low-speed flight.

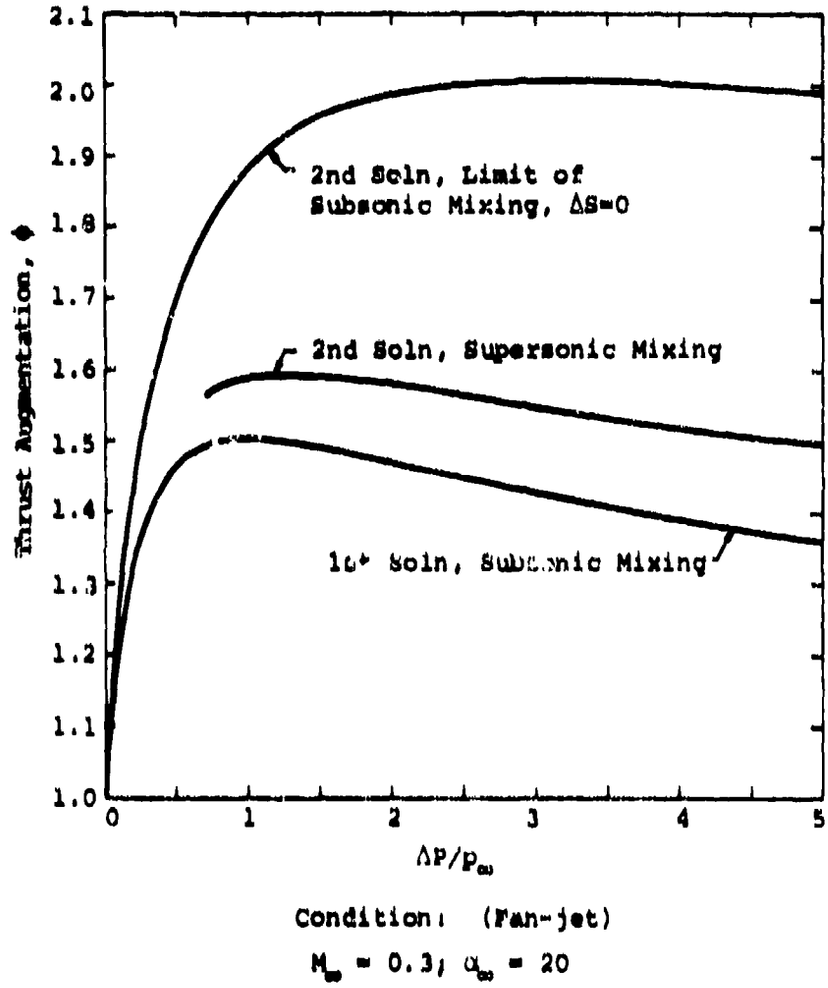

Figure 16.-Influence of pressure on low-speed ejector performance.

AD P000338

LIFTING SURFACE THEORY FOR THRUST AUGMENTING EJECTORS

by

Dr. P. M. Bevilaqua
Rockwell International
Columbus, Ohio

The circulation theory of airfoil lift has been applied to predict the static performance of thrust augmenting ejectors. The ejector shroud is considered to be "flying" in the velocity field induced by the entrainment of the primary jets, so that the thrust augmenting force is viewed as analogous to the lift on a wing. Vortex lattice methods are used to compute the augmentation from the surface pressures on the shroud. The thrust augmentation is shown to depend on the length and shape of the shroud, as well as its position and orientation. Predictions of this new theory are compared with the results of classical momentum theories for calculating the augmentation from the stream thrust.

Copyright AIAA. Reprinted with Permission.

INTRODUCTION

For their whole lives, scientists are said to have a special respect for the man who started them off. It's true; and that will always be my feeling for Dr. Hans von Ohain. My first job after college was to develop some of his ideas on ejector thrust augmentation. This experience influenced the direction of my career: his enthusiasm for the subject was contagious, and I have never lost interest in ejectors. He also influenced the theme of the paper I have selected for this volume: the existence of mechanical analogies to the augmentation process, such as the one described in the first part of this paper, was suggested by Hans.* This analogy led me to the circulation model which is the subject of the paper.

An ejector is a pneumatic device that uses entrainment by a jet of primary fluid to pump a secondary flow. Significant increases in the static thrust of turbojet engines can be obtained by diverting the exhaust jet through an ejector pump. In this application, the ejector functions like a ducted fan. Thrust is increased by accelerating a large mass of air drawn from the atmosphere. Since ejectors can be used to deflect as well as augment the engine thrust, the additional lift necessary to give an aircraft V/STOL capabilities can be developed from an engine sized for efficient cruise. When the ejector is integrated with the wing to produce a lift-propulsion system, the exhaust flow acts like a jet flap to increase the circulation lift of the wing, and thus provide good STOL performance. In addition, separate reaction jets are not required for control during hover. In order to demonstrate this technology, Rockwell International presently is constructing the XFV-12A, a Navy V/STOL aircraft employing ejectors in the wing and canard (Figure 1.).

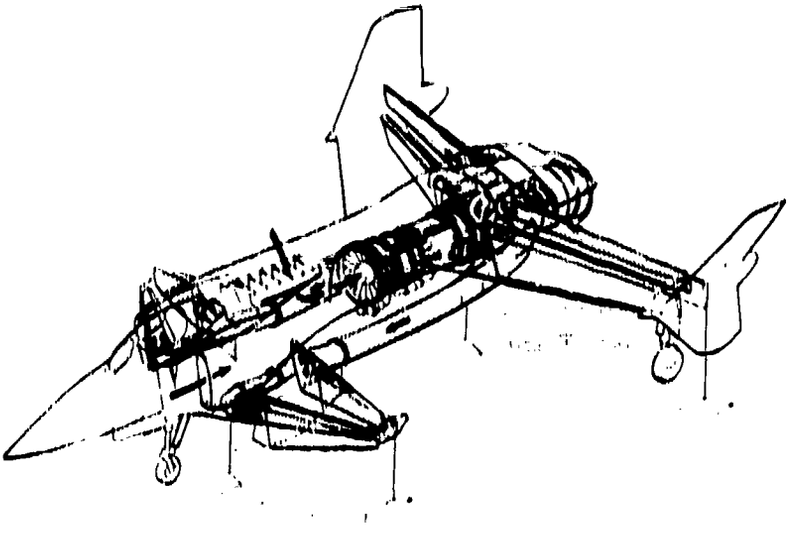

Figure 1. XFV-12A Ejector Technology Demonstrator Aircraft

*A similar analogy has been developed by our colleague, H. Viets[5].

Analytic procedures for calculating ejector performance are necessary to guide research and for preliminary design studies. The analytic methods that have been developed to date are based broadly on von Kármán's now classical momentum analysis.[1] These methods[2-4] deal only with the flow inside the ejector. The thin shear layer approximations are applied to reduce the governing elliptic equations to a parabolic set, which can be solved by marching through the ejector in the streamwise direction. This approach has been useful in identifying some of the factors that affect the level of augmentation and in predicting the results of particular changes in the ejector geometry. However, since elliptic effects are neglected, these solutions are limited to cases in which the ejector is relatively long and the diffuser angle is small.

The purpose of this paper is to demonstrate that elliptic effects can be included in the analysis of ejector performance by a relatively straightforward extension of vortex lattice methods. The ejector shroud is replaced by a distribution of bound vortices, and the primary jet is represented by a line of sinks on the ejector axis. However, the thickness of the jet is neglected, so that only performance trends are predicted. In the following section, the principle of thrust augmentation will be described. The hypothesis that a circulation is generated around the ejector shroud is used in the next section for the development of a new ejector model. In the final section, the predictions of this new model are compared with classical solutions, and the method is then used to examine the effect of changing the position and shape of the shroud.

PRINCIPLE OF THRUST AUGMENTATION

Nonconservative Collisions

All fluid propulsion devices develop thrust by imparting momentum to a fluid stream. By Newton's law of action and reaction, the propulsor experiences a force that is equal and opposite to the momentum change of the fluid, $T = \dot{m}V$. A turbojet engine draws air from the atmosphere and adds energy in the form of heat by the combustion of some fuel. The thermal energy of the hot gas is converted to the kinetic energy of an exhaust jet by accelerating the gas through a nozzle. The engine thrust is equal to the momentum change of the air drawn through it.

A thrust-augmenting ejector also adds energy to air drawn from the atmosphere, but by the direct transfer of kinetic energy from the primary jet. The mechanism of energy transfer is the turbulent mixing of the two streams. Since the mixing process is basically a collision between the jet and the surrounding fluid, the

mechanism by which the thrust is increased may be understood through the consideration of a collision between two generalized masses. Assume that a particle of mass m_1 impacts and remains embedded in a stationary mass m_2. Such a collision is said to be completely inelastic. In the absence of external forces, momentum is conserved, and the particles move off together at a speed u_{12} such that

$$m_1 u_1 = (m_1 + m_2) u_{12} \tag{1}$$

The initial kinetic energy of the first mass is $\frac{1}{2} m_1 u_1^2$, and the kinetic energy of the two-mass system after the collision is $\frac{1}{2}(m_1 + m_2)\, u_{12}^2$. Their ratio is the energy transfer efficiency.

$$\eta = \frac{\frac{1}{2}(m_1 + m_2)\, u_{12}^2}{\frac{1}{2} m_1 u_1^2} = \frac{m_1}{m_1 + m_2} \tag{2}$$

so that a fraction of the initial kinetic energy is lost to heat and other forms of random energy during the impact. The quantity of energy lost does not depend on the mechanics of the collision or the substance of which the particles are composed, but only on the ratio of their masses, as given by Eq. (2). Thus, there is no augmentation in this case, and a fraction of the kinetic energy, which depends only on the ratio of the masses, is dissipated in the collision.

However, if both particles are accelerated by an external force before the impact, the momentum is increased. Suppose, for example, that both particles are negatively charged and that the impact occurs after they have been accelerated by the attraction along the axis of a positively charged ring, as shown in Figure 2. At a distance d far from the ring, the momentum of the first mass is $m_1 u_1$, and

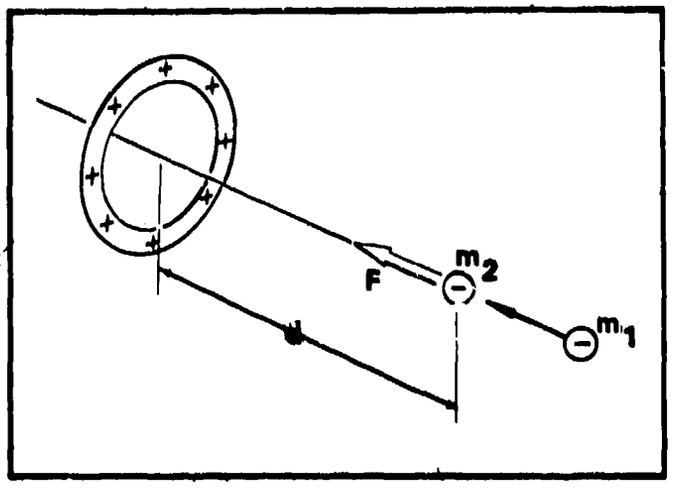

Figure 2. Attraction by the Charged Ring Produces an Augmentation of the Particle Momentum

the second mass is at rest. At the center of the ring, just before the impact, the velocities are

$$u_1^* = (u_1^2 + 2ad)^{\frac{1}{2}} \tag{3}$$

$$u_2^* = (2ad)^{\frac{1}{2}} \tag{4}$$

in which a is the average acceleration over the distance d. Momentum is conserved during the impact itself. If the two masses do not separate after the collision but become embedded or stick together, the conservation of momentum requires that

$$m_1 u_1^* + m_2 u_2^* = (m_1 + m_2) u_{12}^* \tag{5}$$

The embedded masses decelerate together behind the ring. By reason of symmetry, the average decelerating force is equal and opposite to the force of attraction. The final velocity of the embedded masses is therefore

$$u_{12} = (u_{12}^* - 2ad)^{\frac{1}{2}} \tag{6}$$

The ratio of the momentum after the collision $(m_1 + m_2)u_{12}^*$ to the initial momentum $m_1 u_1$ may be evaluated by substituting in turn for u_{12} then u_{12}^* and finally for u_1^* and u_2^*. Performing these substitutions yields, for this ratio,

$$\phi = \sqrt{1 + 2M\left[(H^2+H)^{\frac{1}{2}} - H\right]} \tag{7}$$

in which M is the ratio of the masses, $M = m_2/m_1$, and H is the ratio of the potential energy of the charge separation to the initial kinetic energy,

$$H = ad/\tfrac{1}{2}u_1^2 \tag{8}$$

The energy transfer efficiency can be evaluated by making the same substitutions for u_{12}. The result is

$$\eta = \phi^2/(1 + M) \tag{9}$$

If the charge on the ring is relatively small, then $H \ll 1$, and the collision reduces to the case of one mass striking another in the absence of an accelerating potential. There is no momentum increase, $\phi = 1$, and only a fraction of the initial kinetic energy is transferred, $\eta = 1/(1+M)$, the remainder being dissipated during the collision. Thus, in the absence of external forces, momentum is conserved, and some kinetic energy is lost. On the other hand, if the charge on the wing is large,

then H >> 1, and the momentum ratio simplifies to

$$\phi = (1 + M)^{\frac{1}{2}} \tag{10}$$

so that the momentum increases and all of the initial kinetic energy is transferred, $\eta = 1$. For example, if m_2 has three times the mass of m_1, the initial momentum is doubled. The dependence of ϕ and η on intermediate values of H is sketched in Figures 3 and 4. Thus, when the collision occurs in this kind of potential energy well, the transfer of kinetic energy and the final momentum both increase.

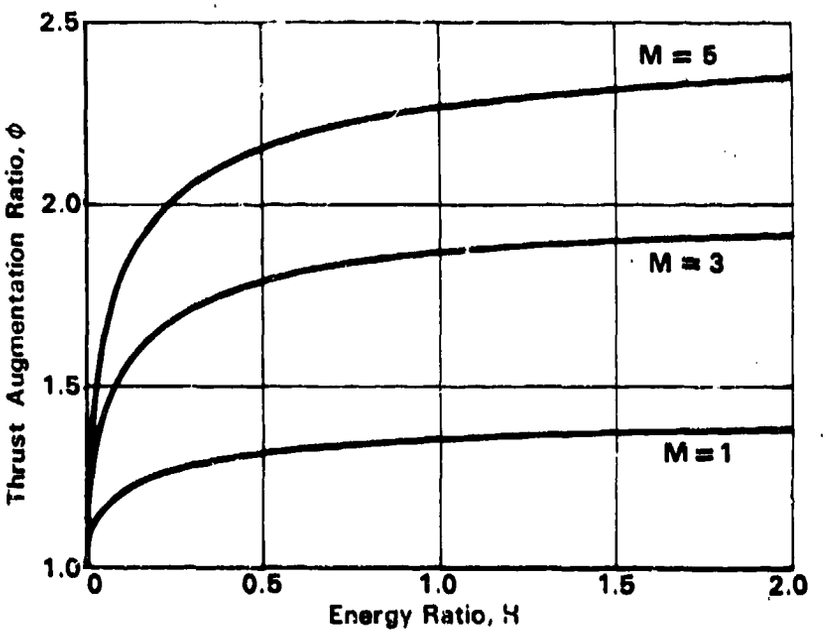

Figure 3. The Augmentation Ratio Increases with the Initial Mass and Energy Ratios

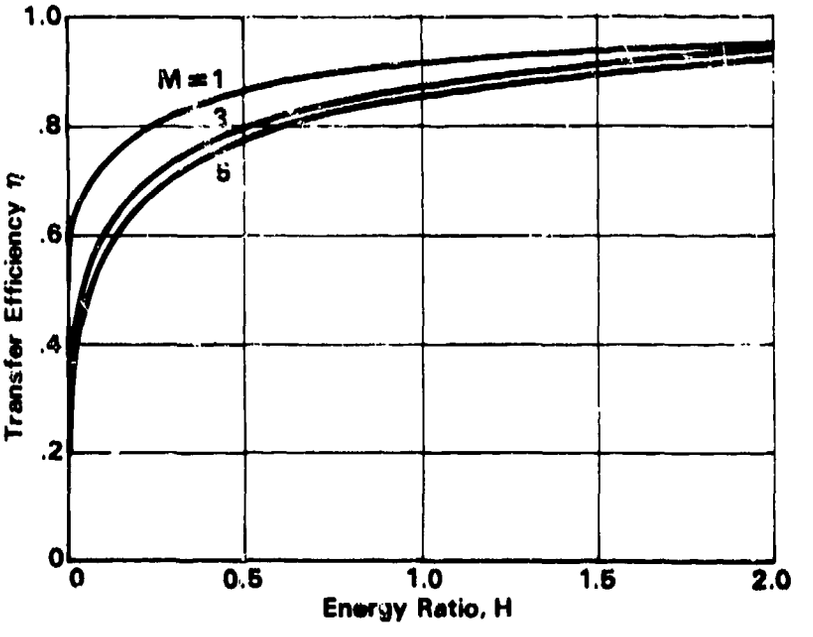

Figure 4. The Transfer of Kinetic Energy Increases with the Initial Potential Energy

The fundamental reason that momentum increases is that the transfer of kinetic energy increases. If both masses are accelerated through the same potential before impact, the absolute velocity difference between them is reduced; that is,

$$u_1^* - u_2^* \leq u_1 \tag{11}$$

and the force of the impact consequently diminishes. In the limit of an infinitely deep well, the velocity difference goes to zero, and there is no impact. Therefore, if the masses stick together, all of the initial kinetic energy is transferred, and the momentum increases accordingly. Another view of the same process is that the total time during which both masses are being accelerated is longer than the time during which they are being decelerated, because $u_{12} > 0$. Thus, over the duration of the interaction, the masses experience a net acceleration from the charged ring. This is the origin of the momentum increase.

Jet Thrust Augmentation

The jet mixing process is basically an inelastic collision between the jet and the surrounding fluid. As such, jet mixing is governed by the same laws of momentum and energy conservation as simple collisions between discrete particles. In free jet mixing, the momentum flux is conserved, and there is a corresponding loss of kinetic energy which is transformed to turbulence and heat. However, suppose that the jet passes through a region in which the static pressure is ΔP less than atmospheric pressure, as sketched in Figure 5. Both the jet and the

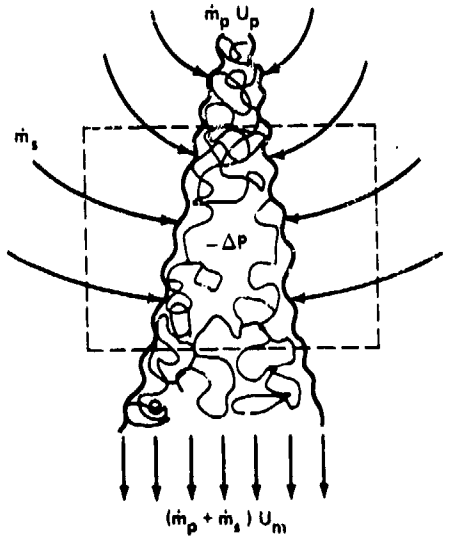

Figure 5. Jet Mixing in a Region of Reduced Pressure Increases the Initial Jet Thrust

fluid that mixes with it must accelerate upon entering the low-pressure region. Inside the region, before mixing, the flow velocities are given approximately by Bernoulli's equation,

$$U_p^* = \left[U_p^2 + (2\Delta P/\rho)\right]^{\frac{1}{2}} \tag{12}$$

$$U_s^* = (2\Delta P/\rho)^{\frac{1}{2}} \tag{13}$$

in the primary and secondary streams, respectively. Momentum is conserved during the mixing process itself, so that

$$\dot{m}_p U_p^* + \dot{m}_s U_s^* = (\dot{m}_p + \dot{m}_s) U_m^* \tag{14}$$

The mixed stream decelerates as it leaves the low-pressure region, and its final velocity is

$$U_m = \left[U_m^{*2} - (2\Delta P/\rho)\right]^{\frac{1}{2}} \tag{15}$$

By comparing these relations with those for the collision between discrete particles, it can be seen that the low-pressure region has the same role as the potential well. The velocity difference between the mixing streams is reduced in the low-pressure region, and so the transfer of kinetic energy increases. The correspo ding increase in momentum flux has the same dependence on M and H as it the simple collision; that is

$$\phi = \sqrt{1 + 2M\left[(H^2 + H)^{\frac{1}{2}} - H\right]} \tag{16}$$

except that M is defined in terms of the mass flux ratio, $M = \dot{m}_s/\dot{m}_p$, and H is the ratio of the static pressure drop to the initial kinetic energy, $H = \Delta P/\frac{1}{2}\rho U_p^2$.

If the pressure drop of negligibly small, $H \ll 1$, and the solution reduces to the case of free jet mixing. Momentum is conserved, $\phi = 1$. On the other hand, if the pressure drop is relatively large, $H \gg 1$, and the momentum ratio reduces to

$$\phi = (1 + M)^{\frac{1}{2}} \tag{17}$$

so that the thrust increases with the entrainment ratio.

Of course, low-pressure regions do not just occur; however, one can be produced by simply passing a portion of the jet through a shroud, as shown in Figure 6. The entrained flow must accelerate as it enters the shroud, and, according to Bernoulli's equation, the pressure will drop accordingly. The pumping action of the jet thus establishes its own low-pressure region within the ejector shroud. In this case, the pressure drop H is a function of the entrainment M. When the mixed stream returns to ambient pressure behind the shroud, it has greater thrust than the original jet. The ratio of the final thrust to the initial thrust is the augmentation ratio, and the shroud acts as a thrust-augmenting ejector.

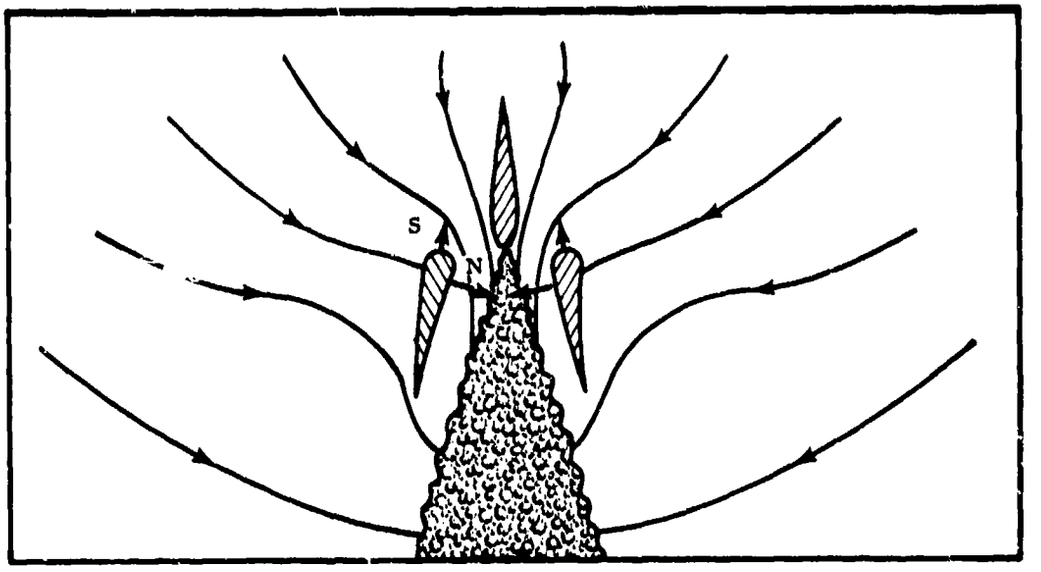

Figure 6. The Ejector Shroud Develops a Force Analogous to the Lift on a Wing

LIFTING SURFACE HYPOTHESIS

Circulation and Elliptic Effects

Except for the simple case of the long, straight shroud analyzed by von Kármán,[1] a unique solution for H in terms of M does not exist. This is because the Navier-Stokes equations for steady fluid motion are elliptic, which means that the domain of influence of a point disturbance is the entire flow volume; that is, pressure and stress gradients transmit the effect of local disturbances to every other point in the flow. Thus, the flow through the ejector, given by the values of M and H, depends on boundary conditions outside the ejector as well as inside the shroud.

In order to calculate the thrust augmentation without solving the full Navier-Stokes equations for the entire flowfield, some approximations must be made. The classical approach is based on streamwise integration of the momentum and continuity equations. If the ejector is relatively long and the diffuser angle is small, the primary direction of flow is through the ejector, so that gradients of the normal stresses and the variation of pressure across the flow can be neglected within the ejector. This thin shear layer approximation reduces the governing elliptic equations to a parabolic set. In parabolic flows, the effect of a disturbance is confined to regions downstream of the disturbance, so that the equations can be solved by marching through the ejector in the streamwise direction. The solution is obtained by iterating on the inlet velocity until the exhaust pressure matches the atmospheric pressure outside the ejector. This approach is equivalent to determining H and M as functions of the jet mixing rate and the shape of the duct.

Although the elliptic boundary value problem can thus be transformed to an initial value problem that is more easily solved, the fundamental elliptic character of the flowfield is unchanged. This means that there are configurations for which the classical thin shear layer approximation predicts the wrong performance or does not yield a solution at all. For instance, as the walls of the shroud are removed to infinity, the predicted thrust augmentation ratio does not reduce to unity,[1,3] as it must in the limit of an isolated turbulent jet. Also, when the ejector is short or the diffuser angle is large, the exhaust pressure is less than atmospheric pressure. This pressure difference is supported by the momentum of the exhaust jet, whereas the jet momentum depends, in turn, on the pressure difference. Thus, the exhaust pressure becomes a floating boundary condition, and a unique solution to the initial value problem does not exist.

In the following sections, the circulation theory of aerodynamic lift is utilized to predict the primary elliptic effects on ejector performance. The pressure and velocity of the secondary flow drawn through the ejector are controlled by the shroud. An isolated jet induces an essentially lateral flow, as seen in Figure 5. However, this induced flow is redirected through the ejector by a circulation generated around each of the shroud sections. The lifting surface hypothesis is that the shroud "flies" in the velocity field of the fluid entrained by the jet and experiences a force related to the lift developed on a wing fixed in a moving stream. The thrust augmentation is the ratio of the primary jet thrust T plus the axial force on the flaps F to the isentropic thrust of the primary mass,

$$\phi = (T + F)/\dot{m}V \tag{18}$$

The external velocity field is calculated by superpositioning a distribution of bound vortex elements, which represent the shroud, and a stream function for the flow induced by the jet. The vorticity distribution is determined by solving a system of equations which specifies that the vortex sheet must be a streamline. The force on the duct is then computed as the cross product of the bound vorticity and the velocity induced by the jet. By using vortex lattice methods for this calculation, the Kutta condition is automatically satisfied. This, in turn, sets the ejector inlet and exhaust pressures, which is the primary elliptic effect.

Entrainment Function

The stream function that describes the secondary flow induced by the isolated primary jet must be harmonic and satisfy the entrainment boundary condition on the surface of the jet. In a self-preserving turbulent jet, all velocities decay as $x^{-\frac{1}{2}}$, and so the entrainment velocity U_e was assumed to vary as

$$U_e = U_o \, (x/t)^{-\frac{1}{2}} \tag{19}$$

in which t is the nozzle gap and U_o is a free constant that depends on the entrainment rate of the jet.

Although a solution for the velocity field can be obtained numerically, by locating a line of sinks on the surface of the jet and then adding the induced velocities at each point, an analytic solution is easy to obtain. The form of the boundary condition suggests a solution in polar coordinates. Let us define a stream function $\psi(r,\theta)$ such that $U_r = -r^{-1}(\partial\psi/\partial\theta)$ and $U_e = \partial\psi/\partial r$. Any function of the form

$$\psi = r^k \, (A \sin k\theta + B \cos k\theta) \tag{20}$$

is harmonic. If it is assumed that the origin of coordinates is at the nozzle exit and the spreading angle of the jet is small, the boundary conditions on ψ become

$$\left.\frac{\partial\psi}{\partial r}\right|_{\theta=0} = -U_o \left(\frac{x}{t}\right)^{-\frac{1}{2}} \tag{21}$$

$$\left.\frac{\partial\psi}{\partial r}\right|_{\theta=\pi} = 0 \tag{22}$$

so that the stream function for the potential flow external to the jet is

$$\psi = -2U_o(rt)^{\frac{1}{2}} \cos(\theta/2) \tag{23}$$

The boundary condition on the other side of the jet is satisfied automatically. The streamlines of this solution are sketched in Figure 7.

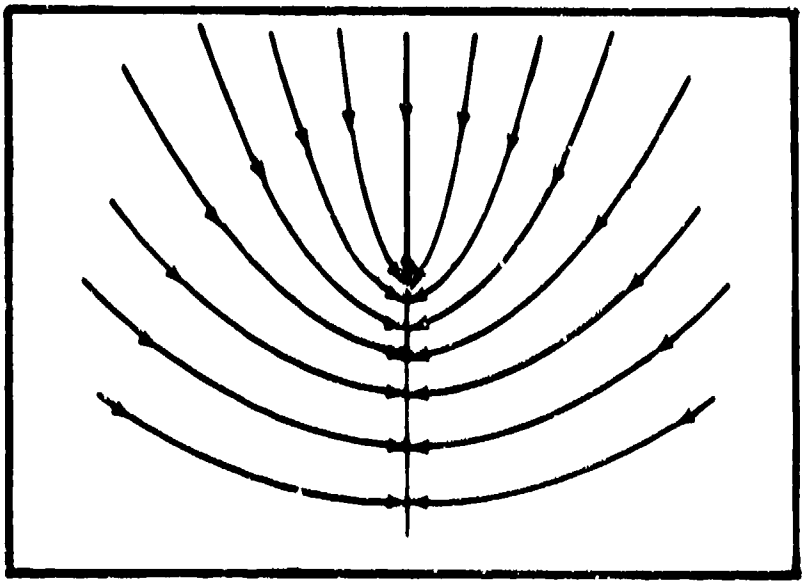

Figure 7. Streamlines of the Flow Entrained into an Isolated Jet

Vorticity Distribution

A conventional vortex lattice representation of the ejector shroud was utilized to determine the circulation generated around each section. The continuous vorticity distribution is replaced by n discrete vortices of strength γ_j located at x_j, the quarter-chord of the panels shown in Figure 8. In keeping with the

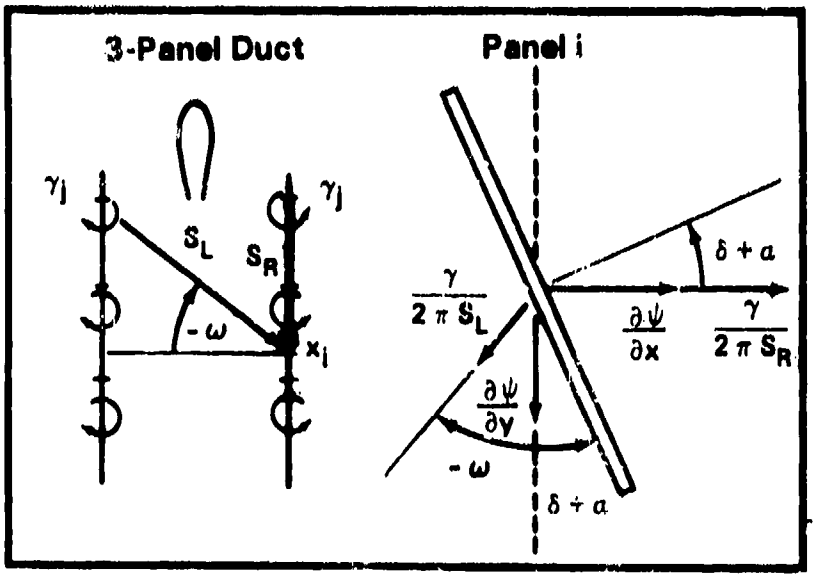

Figure 8. Vortex Panel Representation of the Ejector Shroud

assumption that the jet is thin, a planar wing approximation has been used to linearize the boundary-value problem. This approximation amounts to satisfying the boundary conditions on the chord line of the ejector shroud instead of on its surface. The appropriate boundary condition is that of zero flow through the shroud.

This boundary condition is satisfied at n control points corresponding to the three-quarter-chord station of the panels, that is, midway between the vortices. This is shown in Figure 8 also. The component of the jet-induced velocity normal to the i panel at the control point x_i is

$$U_i = \frac{\partial \psi}{\partial y} \sin(\delta + \alpha_i) + \frac{\partial \psi}{\partial x} \cos(\delta + \alpha_i) \tag{24}$$

in which δ is the mean diffuser angle determined by the chord line of the airfoil sections, and α is the angle of the i panel relative to the mean chord line. The case $\delta = \alpha_i = 0$ corresponds to a straight ejector duct.

In calculating the velocity induced by the vortex sheet, it is convenient to consider simultaneously the effect of each vortex and its image on the opposite side. The contribution to the velocity normal to the i panel by the vortex pair of strength γ_j is

$$W_i = \left[\frac{\cos(\delta + \alpha_i)}{2\pi S_{jL}} - \frac{\sin(\delta + \alpha_i - \omega_{ij})}{2\pi S_{jR}} \right] \gamma_j \tag{25}$$

The position vectors S_{jL} and S_{jR} are directed from the vortices to the control point on the panel, as shown in Figure 8. The angular position vector

$$\omega_{ij} = \tan^{-1} [(x_j - x_i)/(y_j + y_i)] \tag{26}$$

refers to the location of the image vortex on the opposite side. The total velocity induced at each panel is obtained by adding the contribution of all of the vortices from the leading edge to the trailing edge of the shroud.

The resultant of the normal velocities induced by the jet and the vortex sheet must be zero if the shroud is to be a streamline of the flow. Thus, on each panel, W_i is set equal but opposite to U_i:

$$-U_i = C_{ij} \gamma_j \tag{27}$$

The influence coefficients C_{ij} have the form given in Eq. (25). The summation convention for repeated indices is intended to apply. Thus, this expression represents a set of n simultaneous algebraic equations. This set was solved for the γ_j by traingularization of the matrix C_{ij}.

Axial Thrust

The thrust of the ejector is the sum of the initial jet thrust plus the axial thrust on the shroud. The basis of the present method is the assumption that the shroud thrust can be calculated from the normal force and leading-edge suction given for the airfoil by the vortex lattice method. These forces are shown in Figure 6. Because the inviscid leading-edge suction force is essentially independent of the leading-edge radius, the planar wing approximation does not place a restriction on the solution in this respect. However, since a contribution to the total force is determined for each panel, the vortex lattice method essentially redistributes the leading-edge suction over the entire chord. As discussed by Hancock[6] and Kalman et al.,[7] this is characteristic of the method. If a sufficient number of panels are used, the suction is concentrated near the leading edge, and satisfactory results are obtained.

The total force on each panel is determined by the interaction of the bound vortex and the velocity field induced by the jet and all of the other vortices. However, the axial component of the net thrust on the shroud is given by the cross product of the entrainment velocity component normal to the ejector axis and the vortex strength:

$$F_i = \rho \frac{\partial \psi_i}{\partial x_i} \gamma_i \tag{28}$$

The total thrust is obtained by summing the contribution of each of the panels, $F = \Sigma F_i$. Because the mutually induced forces on any two vortices are equal and opposite, the effect of the other vortices does not contribute to the net axial thrust and does not appear in Eq. (28). On the other hand, the mutually induced forces are important in determining the pressure distribution and absolute forces on each section of the shroud.

The jet thrust is calculated from the momentum flux at the origin of the jet,

$$T = \rho V_0^2 t \tag{29}$$

in which t is the nozzle gap and V_0 is the initial jet velocity. Since the static pressure in the throat of the ejector can fall several pounds per square inch

below atmospheric pressure, the nozzle thrust actually varies with the circulation. This produces a small but not insignificant contribution to the augmentation. The thrust augmentation ratio is therefore defined to be

$$\Phi = (T + \Sigma F_i)/T' \tag{30}$$

The reference thrust T' is the isentropic thrust obtained by expanding the same mass of primary fluid, $m = \rho V_0 t$, to atmospheric pressure. The reference jet thus has the same power requirements as the primary jet of the augmenter.

Because the presence of the shroud reduces the entrainment of the jet, it is necessary to iterate between the strength of the vortex sheet and the rate of jet entrainment. In the stream function for the induced velocities, the rate of entrainment is specified by the initial entrainment velocity U_0. This velocity is related to the initial jet velocity V_0 according to the relation

$$U_0 = (2/R_T)(V_0 - U_s) \tag{31}$$

The turbulent Reynolds number R_T is an empirical constant that has a value of approximately 25 in turbulent jets,[7] and U_s is the total induced velocity at the ejector inlet. The change in the entrainment was estimated by iterating between the circulation and the inlet velocity through Eq. (31). This approach is similar to that used in coupling a solution for the boundary-layer displacement thickness to a solution for the external flow.

RESULTS AND DISCUSSION

Primary Ejector Geometry

From classical ejector analysis,[1,9] it is concluded that the thrust augmentation ratio increases with the ejector inlet and diffuser area ratios, and as the mixing of the primary and secondary streams becomes more complete. The effect of length is not explicitly calculated, but insofar as mixing increases with length, it is inferred that augmentation does also. With the lifting surface method described here, the effect of varying the ejector length can be calculated directly. In Figure 9, the predicted change in augmentation with inlet area ratio for three different duct lengths is shown. All dimensions are normalized with the nozzle gap t. It can be seen that, for constant inlet area ratio, the augmentation increases with the length of the shroud.

The effect of varying the shroud length in conjunction with the throat width can also be estimated. There are two important cases to consider. The first is that in which the length of the shroud is held constant while the inlet area ratio is

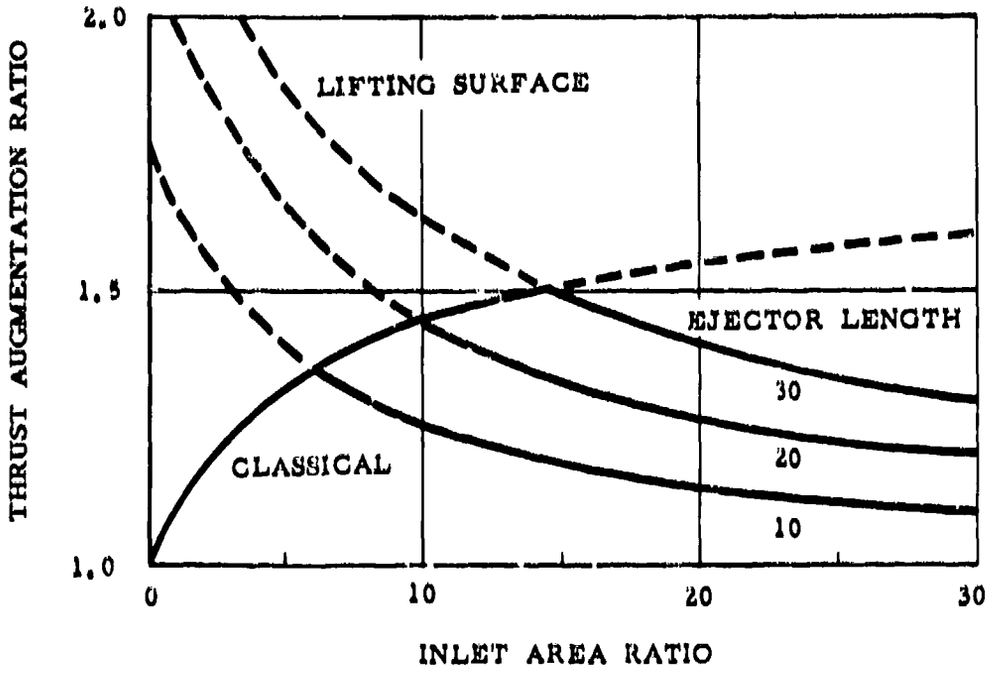

Figure 9. Variation of the Augmentation Ratio for Several Shroud Lengths

varied. It can be seen that in this case, the augmentation ratio actually decreases as the inlet area ratio increases. In the limit as the airfoils are removed to infinity, the augmentation ratio approaches unity, as it must for an isolated turbulent jet. In the opposite limit, as the inlet area ratio approaches unity, an unrealistic increase in the augmentation ratio is obtained. This is because the thickness of the jet has been neglected. The augmentation ratio actually reduces to unity in this limit, as suggested by the classical result also shown in the figure. Since it is based on global conservation of mass and momentum, the classical result puts an upper limit on the augmentation at each inlet area ratio; the intersection with a lifting surface curve is the optimum inlet area ratio for the ejector of given length and specified number of jets and rate of entrainment. The results shown are for a single slot nozzle.

The second important case is that in which the ratio of duct length to throat width L/w is kept constant as the inlet area ratio is varied. This perhaps corresponds more closely to the case implied by the classical methods. The classical result for an ejector without diffusion is a maximum augmentation ratio of $\phi=2.0$ as the inlet area ratio gets infinitely large.[1] The predictions of the present method for this case also are found in Figure 9, by reading across the curves for different duct lengths. No such limit is found; in fact, when the ejector gets very large, the augmentation ratio is not a function of the inlet area ratio at all. It depends only on the length ratio L/w. Of course, for the reasons previously given, the augmentation actually decreases at low inlet area ratios.

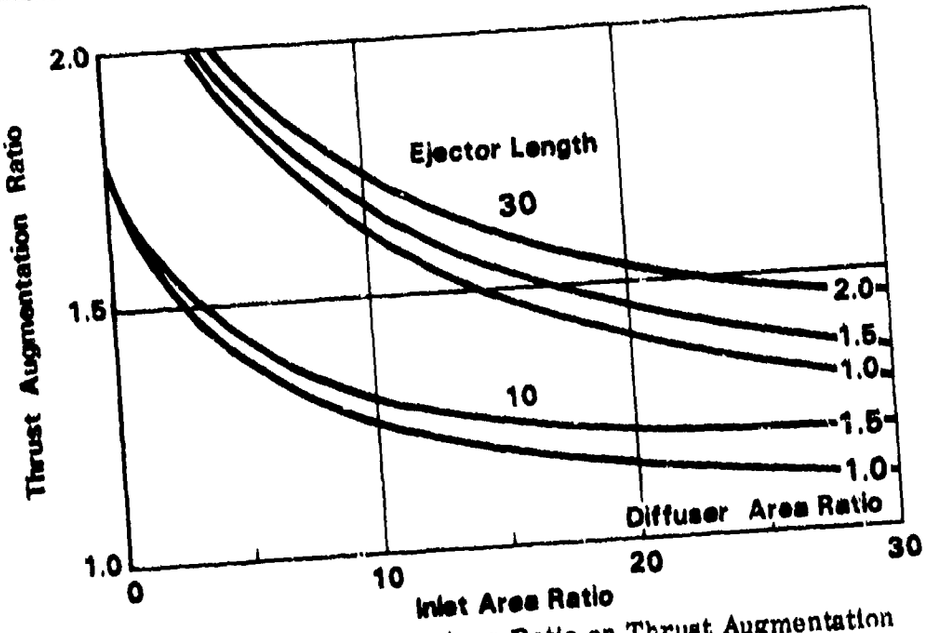

Figure 10. Effect of Diffuser Area Ratio on Thrust Augmentation

The effect of increasing the diffuser area ratio is shown in Figure 10 for two duct lengths. The increase in augmentation with diffuser angle corresponds to the increase in airfoil lift with angle of attack. The augmentation increases with diffuser area ratio over the range shown; but, as the diffusion increases, the airfoils approach 90 deg to the relative wing, and the method breaks down.

The augmentation also depends to some extent on the position of the jet within the shroud. In Figure 11, it can be seen that the optimum location for the nozzle exit

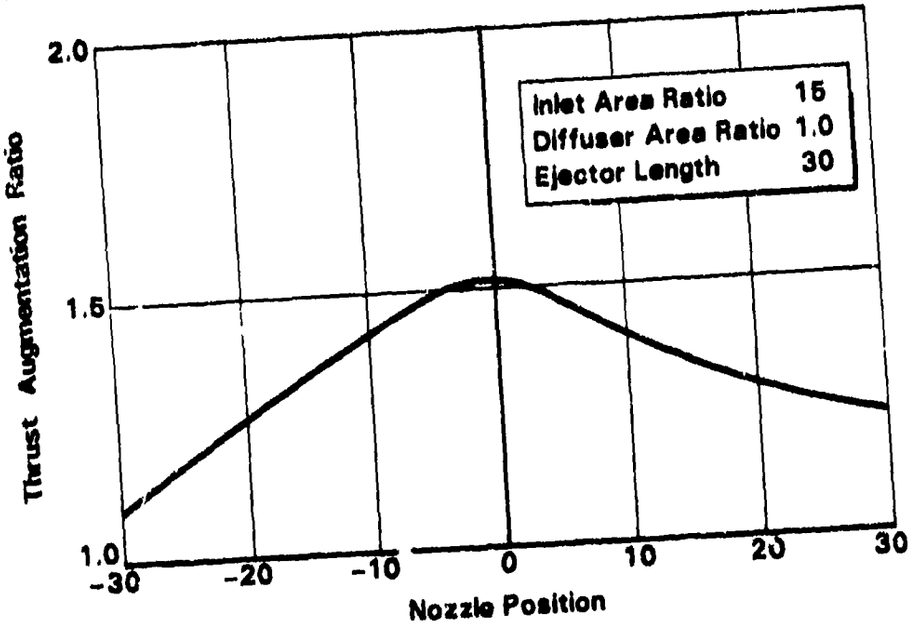

Figure 11. Effect of Nozzle Position on Thrust Augmentation

is in the ejector inlet plane, which is the 0 point in the figure. Actually, if nozzle blockage effects are taken into consideration, the optimum position may be found to be slightly above the inlet plane. The important conclusion is that, within reasonable limits, the nozzle position is not critical.

The effect of changing the rate of jet entrainment can also be estimated with the present method. By arbitrarily varying the value of the entrainment constant defined in Eq. (31), this effect can be calculated. In Figure 12, it is seen that the thrust augmentation increases with $1/R_T$, which is proportional to the von Kármán constant used in simple mixing length theories of jet mixing. The

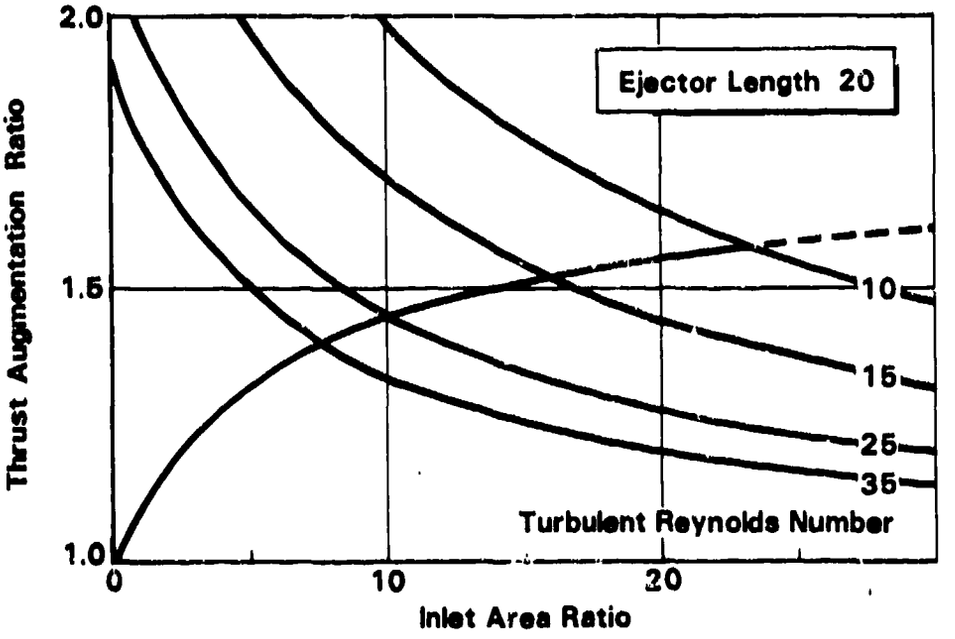

Figure 12. Effect of the Rate of Entrainment on Thrust Augmentation

significance of even small changes in the rate of entrainment is clear. In terms of the force on the shroud, increasing the entrainment corresponds to increasing the speed of the relative wind.

Thus, the present results serve to qualify the conclusions of the classical methods. For constant duct length, the augmentation initially increases with inlet area ratio; but, as the airfoils move out to large distances from the jet, the augmentation reduces to unity. On the other hand, if the duct length is increased with the inlet area ratio, the augmentation remains constant. For either case, the augmentation increases with the diffuser area ratio, up to a limit near where the airfoils become perpendicular to the relative wind. The importance of high rates of entrainment for obtaining high values of augmentation has also been confirmed.

Section Geometry

The hypothesis that the augmenting thrust is related to the lift developed on a wing suggests the use of airfoil high-lift technology to increase the augmentation. Although the ejector thrust corresponds more nearly to a leading-edge suction than to the wing normal force, as seen in Figure 6, both forces depend on the circulation that satisfies the Kutta condition at the trailing edge. Thus, the aerodynamic thrust on the ejector shroud may be expected to depend on the section geometry in the same way as the lift of an airfoil section does. The effect of adding camber and flaperons, or tabs, to the flat-plate ejector shroud will be examined with the lifting surface model in this section.

The change in γ distribution due to camber can be calculated in the planar wing approximation by specifying values of α_i which correspond to the local slope of the camber line for each panel. A simple circular arc section, for which the camber line $z(x)$ is given approximately by

$$z/c = 0.4\left[(x/c)^2 - (x/c)\right] \tag{32}$$

was investigated. This corresponds to an arc with maximum camber equal to 10% of the chord. The slope of this camber line is

$$\alpha_i = 0.8(x/c) - 0.4 \tag{33}$$

In Figure 13, it can be seen that the effect of camber on the thrust augmentation is very similar to its effect on airfoil lift. The slope of the thrust augmentation curve remains essentially the same, and the thrust at each diffuser area ratio is

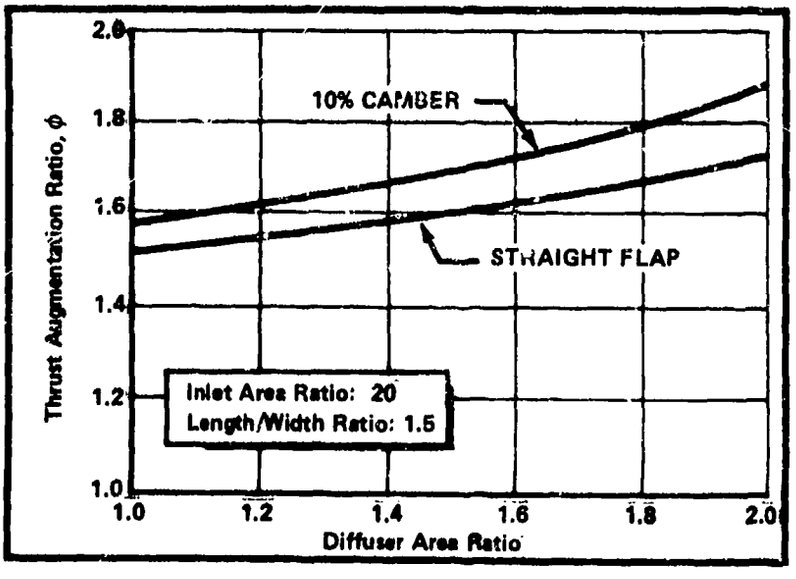

Figure 13. Effect of Camber on Thrust Augmentation

increased by the same amount. As described in the previous section, thrust augmentation is the result of jet mixing in a region of reduced pressure; expressed in these terms, the effect of camber is to further reduce the pressure within the ejector. This produces an increase in the augmentation, as given by Eq. (16).

Deflecting a trailing-edge tab has the effect of changing the camber and angle of attack of the shroud sections. The influence of small deflections can also be calculated with the lifting surface method by specifying appropriate values of α_i for panels at the trailing edge. In Figure 14, the effect of deflecting 20% of the section chord through an angle of +10 deg is shown. The results again are similar

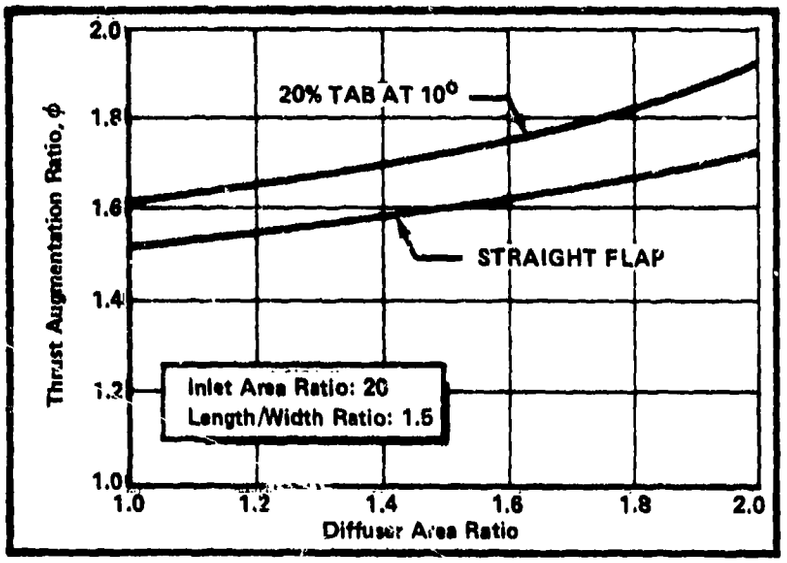

Figure 14. Effect of Trailing Edge Tab on Thrust Augmentation

to airfoil experience. There is a gain in ejector thrust at each angle of attack. However, achieving a gain in ϕ_{max} depends on keeping the flow attached at large flaperon angles. Since flow separation is a viscous phenomenon, the present inviscid analysis cannot predict the actual increase that may be obtained; but airfoil experience suggests that the stalling angle will be reduced, and the gain in $\Delta\phi$ will be less than predicted.

CONCLUSIONS

The analogy between the lift on an airfoil and the thrust on an ejector shroud provides a more intuitive understanding of the process of ejector thrust augmentation. Thus, the thrust augmentation ratio is seen as analogous to the lift/drag ratio of an airfoil, and the increase in augmentation with the shroud length and diffuser angle is understood in terms of increases in airfoil chord and angle of attack.

In addition, quantitative predictions of the thrust augmentation have been obtained from the airfoil analogy, through the use of vortex panel methods to calculate the forces induced on the ejector shroud. Because elliptic effects are included in the solution, this method of analysis has important advantages over classical methods of calculating the augmentation from the stream thrust. In particular, the effect of varying the length and position of the ejector shroud has been studied. If the ratio of shroud length to throat width is held constant as the inlet area ratio is increased, the augmentation increases slowly, but, if the shroud length is held constant as the inlet area ratio increases, the augmentation actually decreases. These results are in contrast to the classical result, which is that the augmentation increases monotonically with the inlet area ratio.

The analogy also suggests the use of airfoil high-lift technology to increase the thrust augmentation. The effect of adding camber and flaperons to the shroud was calculated with the panel method. The ejector thrust varied in the same way as airfoil lift: over the linear portion of the thrust curve, the augmentation increased the same amount at each diffuser area ratio.

At low inlet area ratios, the analytic method breaks down, because the effect of changes in the rate of entrainment and thickness of the jet is neglected. Work in progress is directed toward improving the method by coupling a parabolic solution for the flow through the ejector to an elliptic solution for the flow outside the ejector. Additional improvements will be obtained by relaxing the planar wing approximation and including the effects of jet thickness.

ACKNOWLEDGEMENT

I would like to acknowledge the contributions of J. R. Williams and J. K. McCullough, who listened to some of my first thoughts regarding this analogy and helped me to develop them.

REFERENCES

[1]von Kármán, T., "Theoretical Remarks on Thrust Augmentation," Contributions to Applied Mechanics, Reissner Anniversary Volume, J. W. Edwards, Ann Arbor, Mich., 1949, pp. 461-468.

[2]Gilbert, G. E. and Hill, P. G., "Analysis and Testing of Two-Dimensional Slot Nozzle Ejectors with Variable Area Mixing Sections," NASA CR-3351, 1973.

[3]Bevilaqua, P. M., "Evaluation of Hypermixing for Thrust Augmenting Ejectors," Journal of Aircraft, Vol. 11, June 1974, pp. 348-354.

[4]DeJoode, A. D. and Patankar, S. V., "Prediction of Three-Dimensional Turbulent Mixing in an Ejector," AIAA Journal, Vol. 16, Feb. 1978, pp. 145-150.

[5]Viets, H., "Thrust Augmenting Ejector Analogy," Journal of Aircraft, Vol. 14, April 1977, pp. 409-411.

[6]Hancock, G. J., "Comment on Spanwise Distribution of Induced Drag in Subsonic Flow by the Vortex Lattice Method," Journal of Aircraft, Vol. 8, Aug. 1971, p.681.

[7]Kalman, T. P., Giesing, J. P., and Rodden, W. P., "Reply by Authors to G. J. Hancock," Journal of Aircraft, Vol. 8, Aug. 1971, pp. 681-682.

[8]Townsend, A. A., Structure of Turbulent Shear Flow, Cambridge University Press, Cambridge, England, 1976.

[9]McCormick, B. W., Aerodynamics of V/STOL Flight, Academic Press, New York, 1967.

AD P000339

A ONE-DIMENSIONAL PROCEDURE FOR ESTIMATING THE PERFORMANCE OF EJECTOR NOZZLES

by

Kervyn D. Mach
Turbine Engine Division
Air Force Aero Propulsion Laboratory
Wright-Patterson Air Force Base, OH

The exhaust nozzles of modern turbine engines are often configured as ejectors. The turbine exit gas stream functions as the primary or driving flow, while the secondary flow may be ambient or ram air, fan discharge, or accumulated bleed and leakage flows. The procedure described in this paper was developed to provide a quick performance estimate for ejector nozzles at typical in-flight operating conditions.

The paper begins with a review of compound compressible flow theory, then shows how the choked mass flow and thereby, the ejector pumping capacity are found. Analysis of unchoked operation is described and thrust equations for choked and unchoked operation are derived.

The final section of the paper deals with the prediction of mixed flow performance for both constant pressure and constant area mixing.

Manuscript Received August 1979. The work was performed under AFAPL Work Unit No. 30660602.

A ONE DIMENSIONAL PROCEDURE FOR ESTIMATING THE PERFORMANCE OF EJECTOR NOZZLES

I. INTRODUCTION

The exhaust nozzles of modern aircraft are often required to flow more than one gas stream. Installations flowing two and three gas streams are common. The extra streams may be nozzle cooling air, a relatively small fraction of the primary flow, and/or fan discharge or ram air for thrust augmentation, which may be several times the primary flow. Proper design and accurate performance assessment of such a nozzle requires an understanding of the behavior of multiple flows. Reference 1 develops the basic theory for compound compressible flow, which will be outlined briefly in the succeeding paragraphs. To keep things simple, the discussion will consider only the primary stream and one secondary stream. Analysis of three or more streams obviously would follow the same general procedure.

For nozzle pressure ratio sufficiently high that the primary stream is supersonic, a method of characteristics solution of the primary stream coupled to a one dimensional treatment of the secondary, as outlined in Reference 2, yields results which agree well with measurements. For lower pressure ratios where the primary stream is subsonic or barely supersonic, the method of characteristics will not work and an alternative method of solution is needed. The one dimensional analysis presented herein was developed to fill this gap and serve as a supplement to the more accurate method of characteristics procedure.

II. DISCUSSION

Four concepts are fundamental to the operation of ejector nozzles - compound choking, the pumping characteristic, operation in the unchoked mode, and resultant thrust. These are presented in turn.

Consider the ejector shown in Figure 1, which consists of a primary stream at a specified total temperature and pressure and a secondary stream at some other pressure and temperature, flowing through the ejector shroud into the ambient air, whose pressure is known. Assume that the ambient pressure is just slightly lower than the primary and secondary total pressures so that both streams flow slowly through the nozzle and out the exit. The ejector at this condition is unchoked, exactly as would a single flow nozzle be. Now picture the situation as we lower the ambient pressure while holding the other parameters constant. The velocity and the mass flow of the two streams increase, just as for a single flow nozzle, until we reach a value of back pressure below which the mass flow through the nozzle does not increase. Again analogous to the single flow case, we define this to be the point of compound choking. Were there but a single stream, the Mach number at the minimum flow area would be unity. But can we expect two streams to both be sonic at the minimum area? As will be shown below, the usual case is that the primary stream is supersonic while the secondary is subsonic, yet the nozzle is choked; decreasing the back pressure yields no increase in mass flow.

The derivation of the governing one dimensional flow equations assumes (1) the two streams do not mix, and (2) the static pressures of the two streams are equal at any axial station. For any one dimensional gas flow,

$$\frac{dP}{P} = \frac{k M^2}{1 - M^2} \frac{dA}{A} \tag{1}$$

or

$$\frac{1}{P} \frac{dP}{dx} = \frac{k M^2}{1 - M^2} \frac{1}{A} \frac{dA}{dx} \tag{2}$$

solving for $\frac{dA}{dx}$

$$\frac{dA}{dx} = \frac{A}{k} \left(\frac{1 - M^2}{M^2}\right) \frac{1}{P} \frac{dP}{dx} \tag{3}$$

For the two streams with A = Ap + As and Pp = Ps = P,

$$\frac{dA}{dx} = \frac{dAp}{dx} + \frac{dAs}{dx} \tag{4}$$

$$= \left[\frac{Ap}{kp} \left(\frac{1}{Mp^2} - 1\right) + \frac{As}{ks} \left(\frac{1}{Ms^2} - 1\right)\right] \frac{1}{P} \frac{dP}{dx} \tag{5}$$

Define the compound flow indicator β:

$$\beta = \frac{Ap}{kp} \left(\frac{1}{Mp^2} - 1\right) + \frac{As}{ks} \left(\frac{1}{Ms^2} - 1\right) \tag{6}$$

In one dimensional flow, choking occurs when $\frac{dA}{dx} = 0$ and $\frac{dP}{dx} \neq 0$ (In a choked nozzle, $\frac{dP}{dx}$ is negative at the throat.); thus for two streams to be choked, β must be zero. Positive β indicates unchoked flow, sensitive to the exit pressure, while negative β indicates the opposite. Observe also that unchoked flow with a supersonic stream could exist as well as the aforementioned choked flow with a subsonic stream.

Thus far we have defined a variable, β, which is zero when $\frac{dA}{dx}$ is zero and $\frac{dP}{dx}$ is not. By analogy with the single flow case we have stated but not proven that a multiple stream flow is choked when β is zero. Before we can prove this, we need to determine which pair of Mach numbers Mp and Ms will cause β to be zero. This in turn will lead to the definition of the pumping characteristic, Pos/Pop.

Referring again to Figure 1, assume that Amin/Aop, Aex/Aop, Pamb/Pos and

W/To)s/W/To)p are known. We want to find the values of Mp and Ms and thereby the ratio Pos/Pop which will cause β to be zero. For each stream we can write

$$\frac{W}{A} = \sqrt{\frac{kg}{RTo}}\ PM\sqrt{1 + \frac{k-2}{2} M^2} \tag{7}$$

For two streams with equal static pressures

$$\frac{W\sqrt{To})s}{W\sqrt{To})p} = \frac{As}{Ap}\frac{Ms}{Mp}\sqrt{\frac{Rp}{Rs}\frac{ks}{kp}}\ \frac{\sqrt{1 + \frac{ks-1}{2} Ms^2}}{\sqrt{1 + \frac{kp-1}{2} Mp^2}} \tag{8}$$

Also for each stream we can write

$$\frac{A}{A^*} = \frac{1}{M}\left[\frac{2}{k+1}\left(1 + \frac{k-1}{2} M^2\right)\right]^{\frac{k+1}{2(k-1)}} \tag{9}$$

At the minimum area

$$\frac{Amin}{Ap^*} = \frac{Ap}{Ap^*} + \frac{As}{Ap^*} \tag{10}$$

If the primary stream is choked at Aop, Ap* = Aop.

Then

$$\frac{As}{Ap^*} = \frac{Amin}{Aop} - \frac{Ap}{Ap^*} \tag{11}$$

and

$$\frac{As}{Ap} = \frac{As}{Ap^*}\frac{Ap^*}{Ap} \tag{12}$$

thus

$$\frac{As}{Ap} = \frac{Amin}{Aop}\frac{Ap^*}{Ap} - 1 \tag{13}$$

We now have a system of two equations, (6) and (8), in two unknowns, Mp and Ms, which may be solved with the aid of equations (9) and (13). Once Ms and Mp are found, the ratio Pos/Pop is calculated from

$$\frac{Pos}{Pop} = \frac{\left(1 + \frac{ks-1}{2} Ms^2\right)^{\frac{ks}{ks-1}}}{\left(1 + \frac{kp-1}{2} Mp^2\right)^{\frac{kp}{kp-1}}} \tag{14}$$

Ms and Mp are found iteratively, by the method of false position as follows:

a. Guess two values of Mp, one just supersonic, the other around 2 or 2.5.

b. From equation (13), each Mp will yield an As/Ap.

c. These, plugged into equation (8) will give a pair of Ms.

d. Equation (6) then will yield two β, positive value corresponding to the lower Mp, and a lower value corresponding to the higher Mp. If the second β is negative, the desired value of β (zero) is bracketed and the solution can proceed as described in any text on numerical analysis. If not, repeat with a higher Mp till a negative β results, then proceed.

e. Once the Ms and Mp which make β zero are found, the pumping characteristic Pos/Pop is computed from equation (14).

III. UNCHOKED OPERATION

Unchoked operation implies that the compound flow system is sensitive to the back (ambient) pressure. The underlying assumptions are that at any axial station the static pressures of the two streams are equal to each other and at the exit plane, they are equal to the ambient pressure. Knowing the corrected flow ratio $Ws\sqrt{Tos}/Wp\sqrt{Top}$ and the overall pressure ratio Pop/Pamb, one calculates in turn

a. The exit area occupied by the primary stream,

b. The exit area available to the secondary stream,

c. The total pressure which will force Ws through the available exit area. As Pop/Pamb decreases, there comes a point where Pos falls below ambient and ejector action ceases.

These three steps are accomplished as follows, remembering that the primary stream is assumed to be always sonic at Aop:

a. Select the primary pressure ratio, Pop/Pamb. This will always be lower than the pressure ratio at which the ejector compound chokes. From the pressure ratio, calculate the primary exit Mach number, Mp, and area ratio, Ap/Ap* (=Ap/Aop), from the isentropic relations.

b. The area available to the secondary stream is found from

$$\frac{As}{Ap^*} = \frac{Ae}{Ap^*} - \frac{Ap}{Ap^*} \tag{15}$$

and equation (12).

c. Combining equations (8) and (14) yields

$$\frac{Ws}{Wp}\sqrt{\frac{Tos}{Top}} = \frac{As}{Ap}\,\frac{Pos}{Pop}\,\sqrt{\frac{ks}{Rs}}\Big/\sqrt{\frac{kp}{Rp}}\;\frac{Ms}{Mp}\;\frac{\left(1+\frac{ks-1}{2}Ms^2\right)^{-\frac{ks+1}{2(ks-1)}}}{\left(1+\frac{kp-1}{2}Mp^2\right)^{-\frac{kp+1}{2(kp-1)}}} \tag{16}$$

The only unknown is Pos/Pop, which is found iteratively. Guessing a value for Pos/Pop also gives a value for Pos/Pamb since Pop/Pamb is specified in step a. From this, Ms is Calculated and finally equation (16) yields an estimate of the corrected flow ratio. This is compared with the given value and Pos is adjusted as necessary until the estimate agrees with the specification to an acceptable degree.

IV. THRUST CALCULATION

The basic thrust equation is the nondimensional form for gross thrust,

$$\frac{F}{PoA^*} = k\sqrt{\frac{2}{k-1}\left(\frac{2}{k+1}\right)^{\frac{k+1}{k-1}}}\sqrt{1-\left(\frac{Pe}{Po}\right)^{\frac{k-1}{k}}} + \frac{Ae}{A^*}\left(\frac{Pe}{Po}-\frac{Pamb}{Po}\right) \qquad (17)$$

Equation (17) is written for each stream and the thrust of the secondary is adjusted to refer to PoA* of the primary, via

$$\text{Adjust} = \frac{Pos}{Pop}\frac{As^*}{Ap^*}$$

$$= \frac{Pos}{Pop}\frac{Ap}{Ap^*}\frac{As}{Ap}\frac{As^*}{As} = \frac{Ws\sqrt{Tos}}{Wp\sqrt{Top}} \qquad (18)$$

$$\frac{Ftotal}{PopA_p^*} = \frac{Fp}{PopA_p^*} + \frac{Fs}{PosA_s^*} \times \text{Adjust} \qquad (19)$$

Two thrust coefficients are calculated, the first being total thrust divided by the ideal total thrust, and the second being the total thrust divided by the ideal thrust of the primary, viz

$$Cv = \frac{Ftotal}{Ftotal\ ideal} \qquad (20)$$

$$Cvp = \frac{Ftotal}{Fp\ ideal} \qquad (21)$$

Where ideal thrust is obtained by setting Pe = Pamb in equation (17).

For unchoked flow, the thrust is calculated from

$$\frac{F}{PoA^*} = \frac{P}{Po}\frac{A}{A^*}kM^2 \qquad (22)$$

Which is equivalent to (17) with Pe = Pamb. Cv, Cvp, and Adjust are the same as above.

V. MIXING ANALYSIS

The foregoing discussions have assumed that the two streams pass through the ejector shroud without mingling, i.e. as if they were separated by a flexible membrane. It is possible to estimate in a similar manner the effect of complete mixing of the two streams.

5.1 Assumptions

We know the ejector geometry as before and we are given the bypass ratio B = Ws/Wp and the ratio of stagnation temperatures, Tos/Top. From these, we can form the corrected flow ratio as WR = B Tos/Top. Finally, assume that the ratio of specific heats, k, is constant and the same for both streams and that the static pressures for both streams are equal.

5.2 Analysis

As before, we shall render all quantities dimensionless by referencing them to the appropriate primary stream variable. Then, by applying the conservation laws for mass, momentum, and energy, we can develop a description of the mixed stream.

Energy: Summing the energies of the two streams yields

$$Tom = \frac{WpTop + WsTos}{Wp + Ws} \tag{23}$$

Or, in terms of WR and B

$$\frac{Tom}{Top} = \frac{B + (WR)^2}{B(1 + B)} \tag{24}$$

Momentum:

$$(1 + kM^2m)\ \frac{PmAm}{PopAp^*} = \frac{Ps}{Pop}\ \frac{As}{Ap^*}\ (1 + kM^2x) + \frac{Ap}{Ap^*}\ (1 + kM^2p) \tag{25}$$

$$= \frac{F}{PopAp^*} \tag{25a}$$

Mass: Writing equation (7) for the mixed stream yields

$$\frac{Wp(1 + B)}{PmAm}\sqrt{Tom} = \sqrt{\frac{kg}{R}}\ Mm\sqrt{1 + \frac{k - 1}{2}\ Mm^2}$$

In dimensionless form

$$\frac{Wp\sqrt{Top}}{PopAp^*}\frac{PopAp^*}{PmAm}\ (1 + B)\sqrt{\frac{Tom}{Top}} = \sqrt{\frac{kg}{R}}\ Mm\sqrt{1 + \frac{k - 1}{2}\ Mm^2} \tag{26}$$

Recall Fliegner's formula

$$\frac{W}{A^*}\sqrt{\frac{To}{Po}} = \sqrt{\frac{kg}{R}}\sqrt{\left(\frac{2}{k + 1}\right)^{\frac{k + 1}{k - 1}}} \tag{27}$$

Substituting equations (24) and (27) into (26) yields

$$\sqrt{\left(\frac{2}{k + 1}\right)^{\frac{k + 1}{k - 1}}}\ \frac{PopAp^*}{PmAm}\ (1 + B)\sqrt{\frac{B + (WR)^2}{B(1 + B)}} = Mm\sqrt{1 + \frac{k - 1}{2}\ Mm^2} \tag{28}$$

From equation (25a) we have

$$\frac{PopAp^*}{PmAm} = \frac{PopAp^*}{F}\ (1 + kMm^2)$$

Substituting this into equation (28),

$$\frac{PopAp^*}{F}\sqrt{\left(\frac{2}{k + 1}\right)^{\frac{k + 1}{k - 1}}\ \frac{(1 + B)(B + (WR)^2)}{B}}\ (1 + kMm^2) = Mm\sqrt{1 + \frac{k - 1}{2}\ Mm^2} \tag{29}$$

Define a temporary variable Q

$$Q = \left(\frac{PopAp^*}{F}\right)^2\left(\frac{2}{k + 1}\right)^{\frac{k + 1}{k - 1}}\ \frac{(1 + B)(B + (WR)^2)}{B} \tag{30}$$

Then

$$\sqrt{Q}\ (1 + kMm^2) = Mm\sqrt{1 + \frac{k - 1}{2}\ Mm^2} \tag{31}$$

If we square equation (31), we obtain a quadratic in Mm^2, from which

$$Mm^2 = \frac{1 - 2kQ + \sqrt{(2kQ - 1)^2 - 4(k^2Q - \frac{k - 1}{2})Q}}{2(k^2Q - \frac{k - 1}{2})} \tag{32}$$

The negative root yields the subsonic solution and the positive root the supersonic.

Finally, we have the choice of constant area or constant (static) pressure mixing. In either case, we use equation (25a). In the first case Am is given by the geometry, usually Ap + As. Then

$$\frac{Pm}{Pop} = \left(\frac{Pm}{Pop}\frac{Am}{Ap^*}\right)\left(\frac{Ap^*}{Am}\right) = \left(\frac{F}{PopAp^*}\right)\frac{Ap^*/Am}{(1 + kMm^2)} \tag{33}$$

In the second case, Pm = Ps and we compute Am from

$$\frac{Am}{Ap^*} = \left(\frac{PmAm}{PopAp^*}\right)\left(\frac{Pop}{Pm}\right) = \left(\frac{F}{PopAp^*}\right)\frac{(Pop/Ps)}{(1 + kMm^2)} \tag{34}$$

The thrust in either case is calculated from equation 17 and referenced to PopAp* via

$$\frac{Fm}{PopAp^*} = \left(\frac{Fm}{PomAm^*}\right)\left(\frac{Pom}{Pop}\right)\left(\frac{Am}{Ap^*}\right)\left(\frac{Am^*}{Ae}\right)\left(\frac{Ae}{Am}\right) \tag{35}$$

and we can define a thrust coefficient

$$C_{fl} = \frac{\frac{Fm}{PopAp^*}}{\frac{Fp}{PopAp^*} + \frac{Fs}{PopAp^*}} \tag{36}$$

where the denominator is calculated as described previously.

VI. RESULTS & CONCLUSIONS

The one-dimensional analysis described above has been implemented in a Fortran computer program called EFFORT. For completeness, EFFORT will also compute the performance of nozzles with no secondary flow. Copies of the source deck may be obtained from the author.

EFFORT runs very quickly (more than 20 cases per second) and the results of the compound choking analysis agree very well with the method of characteristics solution described in reference 2. Therefore one can conduct parametric studies with EFFORT, then use a more detailed analysis when the ejector configuration is better defined. EFFORT, being a one-dimensional, inviscid analysis, will yield an upper bound on expected performance.

The unchoked analysis in EFFORT extends the performance caluclation to lower pressure pressure ratios than an MOC analysis can handle, but which may still be of interest.

The mixing calculations are also estimates. They were included for completeness so that one could compare the mixed performance with the compound choked performance. In neither instance is the mechanism considered, only what the final result would be.

Constant area mixing yields thrust equal to or slightly poorer than the unmixed thrust. The constant pressure mixing results can be misleading because the area required to maintain the mixing pressure is usually smaller than the specified Amin. Therefore, the constant pressure analysis is solving a different problem. One can iterate to a solution by adjusting WR and ARmin until Amix agrees with Amin, but that iteration is not built into EFFORT.

Note that EFFORT deals with gross thrust only. Equation (20) compares

the actual gross thrust of the ejector to the thrust available from the two streams expanded ideally and therefore provides the most meaningful measure of performance. Ejector performance is sometimes quoted in terms of an "augmentation ratio," the definition of which varies from investigator to investigator. The thrust coefficient defined by equation (21) can be considered an augmentation ratio in that it compares the actual ejector thrust to the ideal thrust of the primary stream. One could also define an augmentation ratio which compares the actual ejector thrust to the thrust of the primary stream expanded to the ejector exit area. This ratio would be larger than from equation (21) except wehre the exit area is appropriate to the pressure ratio. Regardless of the measure of performance one adopts, it is important to understand that the thrust increase from the secondary mass flow is much smaller than the increase from relieving the overexpansion of the primary stream. By filling the excess area of the shroud, the secondary stream allows the primary to operate at an area ratio more suitable to the pressure ratio and reduces the PA in terms in the thrust equation.

Finally, one must clearly understand that no ejector can increase the net thrust of a propulsion system except by relieving overexpansion. Thrust is momentum. Gross thrust is the momentum of the exhaust stream(s) and net thrust is gross thrust less their incoming momentum. Consider the control volume in Figure 2. The two streams enter at the left. The primary stream gains momentum because the engine adds work to it, drawing energy from the fuel. The secondary stream, if it gains momentum at all, has to gain it from the primary stream, for there is no other source. Therefore, regardless of the amount of secondary flow, the net momentum exiting the right side of the control volume is constant.

REFERENCES

1. Bernstein, Heiser, and Hevenor, "Compound Compressible Nozzle Flow," AIAA Paper #66-663, June 1966

2. Anonymous, "User's Manual for the General Ejector Nozzle Deck," PWA-3465 Supplement A, September 1968

3. Shapir, A. H., The Dynamics and Thermodynamics of Compressible Fluid Flow, The Ronald Press, New York, 1959

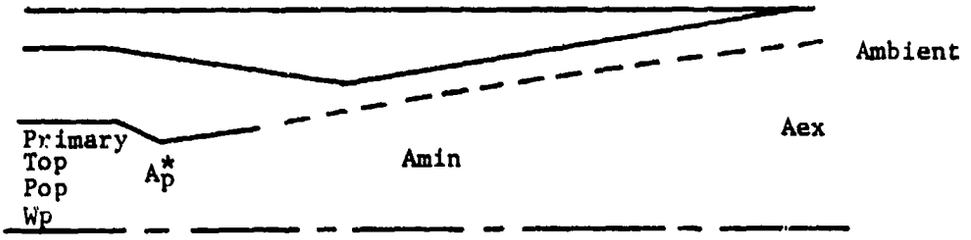

Figure 1

Ejector Nomenclature

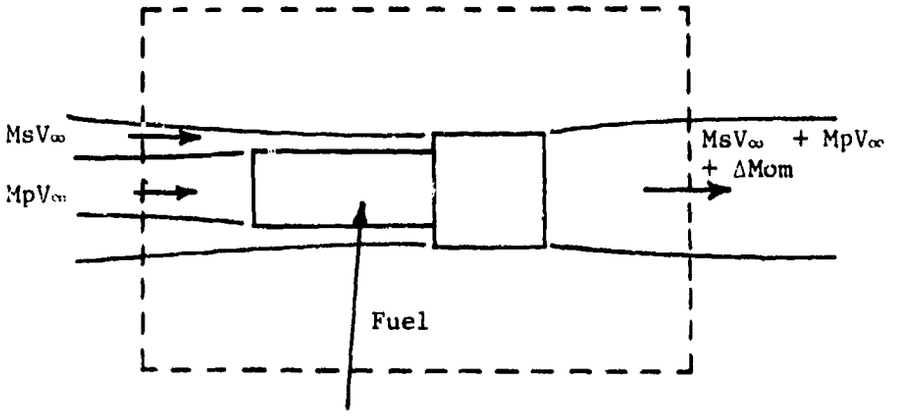

Figure 2

Control Volume

AD P000340

EFFECTS OF NON-CONSTANT ENTHALPY ADDITION ON FAN-NOZZLE COMBINATIONS

by

Gordon C. Oates
University of Washington
Seattle, Washington

Walter M. Persz, Jr.
Commercial Products Division
Pratt & Whitney Aircraft Group
East Hartford, Connecticut

It has long been recognized that a compressor or a turbine stage loading may be increased, or the efficiency improved for a given loading, by utilizing a non-constant enthalpy addition to the flow along the length of the blade. The resultant non-uniform flow at exit from the stage will itself have losses identified with it if the flow is passed through a nozzle for propulsive purposes. In order to estimate the expected effect on the thrust of the flow non-uniformities, two limiting cases are herein considered. Thus, an engine with non-constant enthalpy addition across the fan stage, but with otherwise perfect components is considered. The flow is then taken to be a) completely unmixed (isentropic), and b) fully mixed in an ideal (no sidewall friction) constant area mixer prior to expansion through the nozzle. In each case the resulting net thrust is compared to that which would exist if the same total enthalpy addition to the fluid stream was supplied uniformly.

Manuscript was received February 1979.

NOMENCLATURE

A - Area

H - Stagnation enthalpy

h - Enthalpy

M - Mach number

P - Static pressure

T_{RA} - Net thrust with variable fan blade enthalpy input

T_{RR} - Net thrust with constant fan blade enthalpy input

T_R - Ratio of net thrust $\left(\frac{T_{RA}}{T_{RR}}\right)$

u - Axial velocity

x - Axial coordinate

γ - Specific heat

ε - Constant

η - Fan efficiency

ρ - Density

τ_r - $1 + \frac{\gamma - 1}{2} M_0^2$

τ_c - Stagnation temperature ratio across the fan for constant enthalpy case

Subscripts

1 - Flow station (see Figure 1)

2 - Flow station (see Figure 1)

c - Reference constant enthalpy case

e - Flow station (see Figure 1)

o - Flow station (see Figure 1)

t - Stagnation conditions

ANALYSIS

It is assumed that the blade loading is such that the stagnation enthalpy distribution, H, is given by

$$H_1/H_c = 1 + \frac{\varepsilon}{2}(2x - 1) \qquad 1.$$

Here c refers to the reference constant enthalpy case, x is the ratio of mass flow between the hub and the given streamsurface, and the total mass flow, and ε is a (small) constant. This form of enthalpy distribution is an often used reference form.[2,3,4]

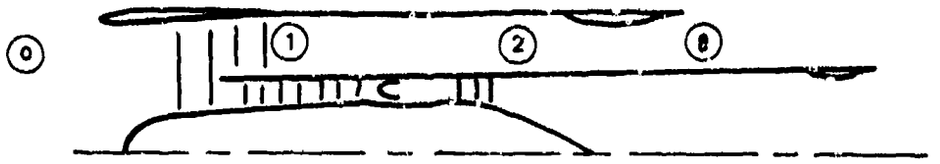

Figure 1 Definition of Engine Reference Stations

a) Isentropic flow through the nozzle.

For this case we may write

$$\int_0^1 u_e dx = \sqrt{2H_c} \int_0^1 \{1 + \frac{\varepsilon}{2}(2x - 1) - \frac{h_e}{H_c}\}^{\frac{1}{2}} dx$$

$$= \sqrt{2H_c} \left(\frac{2}{3\varepsilon}\right)\left\{\{1 - \frac{h_e}{H_c} + \frac{\varepsilon}{2}\}^{3/2}\right.$$

$$\left. - \{1 - \frac{h_e}{H_c} - \frac{\varepsilon}{2}\}^{3/2}\right) \qquad 2.$$

Now noting that for this case of ideal flow and exit pressure equal to ambient pressure, $\frac{h_e}{H_c} = \frac{1}{\tau_r \tau_c}$, where $\tau_r = 1 + \frac{\gamma-1}{2} M_o^2$ and τ_c is the stagnation temperature ratio across the fan for the constant enthalpy case, it follows that

$$\frac{\int_o^1 u_e dx}{\int_o^1 u_{ec} dx} = \frac{2}{3\varepsilon} \left[1 - \frac{1}{\tau_r \tau_c}\right]^{-\frac{1}{2}} \left[\left(1 - \frac{1}{\tau_r \tau_c} + \frac{\varepsilon}{2}\right)^{3/2} - \left(1 - \frac{1}{\tau_r \tau_c} - \frac{\varepsilon}{2}\right)^{3/2}\right] \quad 3.$$

Denoting the flight velocity as U_o, routine cycle analysis gives

$$\frac{u_{ec}}{u_o} = \left(\frac{\tau_r \tau_c - 1}{\tau_r - 1}\right)^{\frac{1}{2}} \quad 4.$$

and the ratio of net thrusts T_R is given by

$$T_R = \frac{\frac{u_{ec}}{u_o} \frac{\int_o^1 u_e dx}{\int_o^1 u_{ec} dx} - 1}{\frac{u_{ec}}{u_o} - 1} \quad 5.$$

Equations 3 - 5 may be quickly solved for example values of the parameters, but because ε must in fact be very small, we may utilize a binomial expansion to lead to the very simple approximate form

$$T_R \approx 1 - \frac{\varepsilon^2}{96} \frac{(\tau_r \tau_c)^2}{(\tau_r \tau_c - 1)^{3/2}} \frac{1}{(\sqrt{\tau_r \tau_c - 1} - \sqrt{\tau_r - 1})} \quad 6.$$

b) Fully mixed flow.

A momentum balance across the frictionless constant area mixer gives

$$\int (P + \rho u^2)_1 dA = (P + \rho u^2)_2 A \qquad 7.$$

Conservation of stagnation enthalpy gives $H_2 = H_c$, noting that since at station 1 both the entropy and pressure are constant, and hence the static temperature is constant, the continuity equation and equation 7 lead to

$$\frac{\gamma}{\frac{H_c}{H_1}} \int_0^1 \left(\frac{1}{\gamma M_1} + M_1\right) dx = \frac{(1 + \gamma M_2^2)}{M_2 (1 + \frac{\gamma-1}{2} M_2^2)^{\frac{1}{2}}} \equiv \phi^{\frac{1}{2}} \qquad 8.$$

Evaluation of the left side of this equation (and hence of the function ϕ) leads to a quadratic equation for M_2^2. Thus, noting that

$$M_1^2 = \frac{2}{\gamma-1} \left(\frac{H_1}{h_1} - 1\right) \qquad 9.$$

equation 1 leads to

$$M_1^2 = \frac{2}{\gamma-1} \left[\frac{H_c}{h_1} \{1 + \frac{\epsilon}{2}(2x - 1)\} - 1\right] \qquad 10.$$

It may be noted from equation 10, (The enthalpy distribution given by equation 1 is used here as a convenient example distribution. Other suitable forms could easily be

considered within the same formulation.) that the maximum imaginable value of ε would be that leading to $M_1 = 0$ on the hub ($x = 0$), so that

$$\varepsilon_{max} = \frac{2(\frac{H_c}{h_1} - 1)}{H_c/h_1} = \frac{(\gamma - 1)M_c^2}{1 + \frac{\gamma-1}{2}M_c^2}$$

With equation 10, the function ϕ is easily integrated to give

$$\phi = \left[\frac{1}{\varepsilon}(\frac{H_c}{h_1})^{-3/2}\left(\sqrt{2(\gamma - 1)}\ (\beta_+ - \beta_-) + \frac{2\gamma}{3}\ \frac{2}{\gamma-1}\ (\beta_+^3 - \beta_-^3)\right)\right]^2 \qquad 11.$$

in which $\beta_+ = \{\frac{H_c - h_1}{h_1} + \frac{H_c}{h_1}\frac{\varepsilon}{2}\}^{\frac{1}{2}}$

$$\beta_- = \{\frac{H_c - h_1}{h_1} - \frac{h_c}{h_1}\frac{\varepsilon}{2}\}^{\frac{1}{2}}$$

Solution of equation 8 then gives

$$M_2^2 = 2\ [\phi - 2\gamma + \{\phi^2 - 2(\gamma + 1)\ \phi\}^{\frac{1}{2}}]^{-1} \qquad 12.$$

The continuity equation may be utilized to determine the static pressure at station 2 by writing

$$A_1 = \rho_2 u_2 A_2 \int_o^1 \frac{dx}{\rho_1 u_1} = A_2$$

from which

$$\frac{P_2}{P_1} = \frac{h_2}{h_1} \frac{1}{M_2 \int_0^1 \frac{dx}{M_1}} \qquad \underline{13}.$$

The integral is easily evaluated utilizing equation 9. These equations may be summarized in a form allowing sequential solution as follows: (ε, M_c, τ_r, τ_c and γ would be prescribed)

SUMMARY

$$\frac{H_c}{h_1} = 1 + \frac{\gamma-1}{2} M_c^2$$

$$\beta_+ = \left\{\frac{H_c}{h_1} - 1 + \frac{H_c}{h_1}\frac{\varepsilon}{2}\right\}^{\frac{1}{2}}$$

$$\beta_- = \left\{\frac{H_c}{h_1} - 1 - \frac{H_c}{h_1}\frac{\varepsilon}{2}\right\}^{\frac{1}{2}}$$

$$\phi = \left[\frac{1}{\varepsilon}\left(\frac{H_c}{h_1}\right)^{-3/2}\left\{\sqrt{2(\gamma-1)}(\beta_+ - \beta_-) + \frac{2\gamma}{3}\frac{2}{\gamma-1}(\beta_+^3 - \beta_-^3)\right\}\right]^2$$

$$M_2^2 = 2\left[\phi - 2\gamma + \left\{\phi^2 - 2(\gamma+1)\phi\right\}^{\frac{1}{2}}\right]^{-1}$$

$$\frac{h_2}{h_1} = \frac{1 + \frac{\gamma-1}{2} M_c^2}{1 + \frac{\gamma-1}{2} M_2^2}$$

$$\frac{P_2}{P_1} = \frac{h_2}{h_1}\frac{M_c}{M_2}\left(\frac{H_c - h_1}{h_1}\right)^{-\frac{1}{2}} \frac{\beta_+ + \beta_-}{2}$$

$$\frac{P_{t2}}{P_{tc}} = \frac{P_2}{P_1}\left(\frac{h_2}{h_1}\right)^{-\frac{\gamma}{\gamma-1}}$$

$$\frac{\int_0^1 u_e dx}{u_{ec}} = \left(1 - \frac{1}{\tau_r \tau_c}\right)^{-\frac{1}{2}}\left[1 - \frac{1}{\tau_r \tau_c}\left(\frac{P_{t2}}{P_{tc}}\right)^{-\frac{\gamma-1}{\gamma}}\right]^{\frac{1}{2}}$$

$$\frac{u_{ec}}{u_o} = \left\{\frac{\tau_r\tau_c - 1}{\tau_r - 1}\right\}^{\frac{1}{2}}$$

$$T_R = \frac{\frac{u_{ec}}{u_o}\frac{\int_o^1 u_e dx}{u_{ec}} - 1}{\frac{u_{ec}}{u_o} - 1}$$

Though unwieldy in appearance, these equations are easily programmed on a desk calculator. We may once again utilize binomial expansions, however, to get after a great deal of algebra, the following very simple approximate form

$$T_R = 1 - \left[\sqrt{\tau_r\tau_c - 1}\left(\sqrt{\tau_r\tau_c - 1} - \sqrt{\tau_r - 1}\right)\right]^{-1} \frac{\left(1 + \frac{\gamma-1}{2} M_c^2\right)^2}{48(\gamma - 1) M_c^2} \varepsilon^2 \qquad 14.$$

Numerical verification indicates that both equations 6 and 14 are quite accurate. The largest fractional error in the perturbation terms found in the range of values considered was only about ten percent.

In order to compare the losses predicted above with a possible thrust gain due to compressor efficiency improvement, the net thrust of an otherwise perfect engine with a non-perfect compressor efficiency was obtained. Again utilizing a binomial expansion (in terms of $1 - \eta_c$) it follows simply that

$$T_R = 1 - \frac{1-\eta_c}{2}\frac{\tau_c - 1}{\tau_c}\left[\sqrt{\tau_r\tau_c - 1}\left(\sqrt{\tau_r\tau_c - 1} - \sqrt{\tau_r - 1}\right)\right]^{-1} \qquad 15.$$

Simple relationships now follow for the "break-even" efficiency improvement $\Delta\eta_c = (1 - \eta_c)$ required if the fan efficien-

cy improvement resulting from utilizing the non-constant enthalpy addition is to overcome the losses introduced. Thus equations 6, 14 and 15 give

$$(\Delta\eta_c)\text{break even} = \frac{\tau_c}{\tau_c - 1} \frac{(\tau_r \tau_c)^2}{\tau_r \tau_c - 1} \frac{\varepsilon^2}{48} \qquad \text{(non-mixing)}$$

$$(\Delta\eta_c)\text{break even} = \frac{\tau_c}{\tau_c - 1} \frac{\left(1 + \frac{\gamma-1}{2} M_c^2\right)^2}{(\gamma - 1) M_c^2} \frac{\varepsilon^2}{24} \qquad \text{(mixing)}$$

RESULTS

Example results were calculated for the case where the compressor pressure ratio is 1.5, $M_o = 0.85$ and $M_c = 0.5$. Note that in terms of the variation in stagnation pressure ratio across streamsurfaces we may write

$$\varepsilon = \frac{2}{2x-1} \left[\left(\frac{P_{t1}}{P_{tc}} \right)^{\frac{\gamma-1}{\gamma}} - 1 \right]$$

Thus if the ratio of tip stagnation pressure to P_{tc} was chosen to be 1.1, ε would be .055, and P_{t1}/P_{tc} would be .907 .

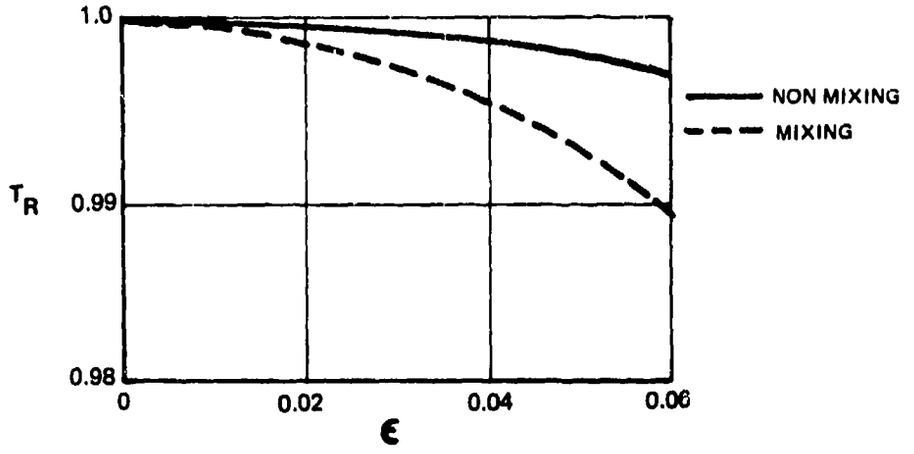

Figure 2 Effects of Fan Exit Profiles on Nozzle Thrust

Figure 2 illustrates the reduction in net thrust of the fan stream with increase in ϵ. It can be seen that the mixing losses introduce a substantial penalty. This effect is apparent also in Figure 3 where it is evident that quite substantial increases in compressor efficiency must be achieved to overcome the losses due to non-constant enthalpy distribution, if substantial mixing occurs. The quadratic nature of the losses due to non-constant enthalpy make the concept of utilizing slight variations in enthalpy quite attractive.

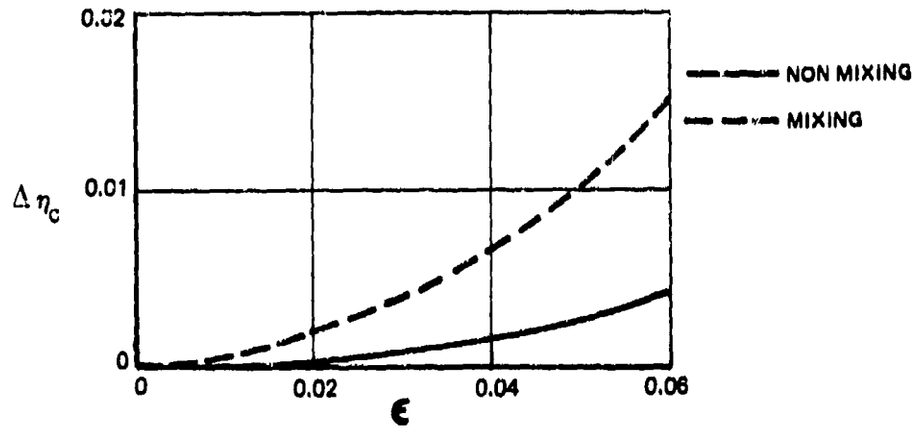

Figure 3 Breakeven Fan Efficiency Variations

As a final comment, we would like to point out that though these calculations utilized the simplified model of a perfect engine, it is expected that the predicted tendencies for the *ratio* of the net thrusts will remain quite accurate.

REFERENCES

1. Dorman, T. E., Welna, H. and Lindlauf, R. W., "The Application of Controlled-Vortex Aerodynamics to Advanced Axial Flow Turbines," Trans. ASME, J. Eng. for Power, July 1968.

2. Bragg, S. L. and Hawthorne, W. R., "Some Exact Solutions of the Flow Through Annular Cascade Actuator Discs," Journal of Aeronautical Science, Vol. 17, No. 4, 1950, pp. 243-249.

3. Oates, G. C. and Knight, C. J., "Throughflow Theory for Turbomachines," AFAPL-TR-73-61, May 1973.

4. Oates, G. C., Knight, C. J., and Carey, G. F., "A Variational Formulation of the Compressible Throughflow Problem," Trans. ASME, Series A, Vol. 98, No. 1, January 1976, pp. 1-8.

AD P000341

SOME ADVANTAGES OF UNSTEADY AERODYNAMICS

by

Hermann Viets
Wright State University
Dayton, Ohio 45435

With few exceptions, aerodynamicists have historically considered unsteady flow as detrimental to performance. Two notable examples are the problems of inlet buzz and wing flutter while the performance of the pulsed combustion missiles of the 1940's is a prominent exception. In some situations unsteady flows are unavoidable, as in the case of rotating compressors and turbines. In these and other situations, it is of interest to examine the time dependence from a positive point of view. That is; if unsteadiness is deliberately introduced or amplified, are there potential performance advantages? It is the purpose of this paper to examine several recent and ongoing experiments which involve the attempt to improve performance by utilizing unsteady flow. Two areas are described. The first is the introduction of unsteadiness into a boundary layer by mechanical means. The aim is to energize the boundary layer to avoid or lessen problems resulting from separation. A second area is the attempt to increase the mixing rate of jets by fluidically produced unsteadiness. The time dependency can be completely fluidically produced or it can be driven by a mechanical-fluidic interface.

Manuscript Received June 1980.

Some Advantages of Unsteady Aerodynamics+

Hermann Viets*
Wright State University
Dayton, Ohio 45435

I. Introduction

With few exceptions, aerodynamicists have historically considered unsteady flow as detrimental to performance. Two notable examples are the problems of inlet buzz and wing flutter while the performance of the pulsed combustion missiles of the 1940's is a prominent exception.

In some situations unsteady flows are unavoidable, as in the case of rotating compressors and turbines. In these and other situations, it is of interest to examine the time dependence from a positive point of view. That is; if unsteadiness is deliberately introduced or amplified, are there potential performance advantages? It is the purpose of this paper to examine several recent and ongoing experiments which involve the attempt to improve performance by utilizing unsteady flow.

Two areas are described. The first is the introduction of unsteadiness into a boundary layer by mechanical means. The aim is to energize the boundary layer to avoid or lessen problems resulting from separation. A second area is the attempt to increase the mixing rate of jets by fluidically produced unsteadiness. The time dependency can be completely fluidically produced or it can be driven by a mechanical-fluidic interface.

II. Induced Unsteady Boundary Layers

A. Unsteady Airfoil Flow

Time dependent flow over an airfoil has been studied by a number of investigators, often from the point of view of helicopter application. In his review, McCroskey[1] reports several experiments which show that an airfoil

+ Partially supported by AFOSR Grant No. 78-3525, Monitored by AFFDL/FXM
* Associate Professor

performing sinusoidal oscillations of angle of attack about some mean value, is able to attain higher lift than a static configuration. Apparently, the dynamics allow a delay in the onset of stall to a higher angle of attack. McAllister and Carr[2] have investigated the flow structure by flow visualization and have demonstrated the large scale vorticies existing above the airfoil.

The objective then, is to produce a similar vortex structure above the airfoil without having to oscillate the airfoil itself. The method employed[3] is shown in Figure 1 and consists of a simple rotor which turns in the counter clockwise sense and produces a vortex for each revolution. The vortex structure produced by such a configuration is shown in Figure 2 for a flat plate configuration made visible by the use of smoke streaklines. It should be noted that the top of rotor moves upstream, so the rotor <u>does not simply push</u> the flow downstream.

The same technique is employed to study the time average streamlines above a symmetrical airfoil at an angle of attack of 20°. The smoke flow is photographed and the streamlines traced to yield the results in Figure 3. The comparison between the ω = 0 rpm case (rotor withdrawn into the airfoil and the cavity taped) and that of ω = 2400 rpm clearly shows that the size of the separated flow region is dramatically reduced by the use of the rotor. In addition, a streamline which passes below the airfoil in the static case appears above the surface in the dynamic one. This indicates a reduction in the pressure above the wing and an increase in the circulation and hence in the lift produced.

The pressure variation with the use of the rotor is shown in Figure 4 at a single pressure port located at the 63% chord position. The pressure difference between the static pressure at that point, P, and the freestream

static pressure, P_{fs}, is non-dimensionalized with its own value for the static case ($\omega = 0$) and presented versus the rotor speed. Based on the single port, the optimum condition is for a minimum P which corresponds to a maximum in the pressure parameter of Figure 4. The 20° angle of attack is fully separated and as the rotor frequency is increased, the performance indicated improves by more than 35%.

B. Unsteady Rearward Facing Ramp

Another potential application of the time dependent boundary layer energization is to decrease separation problems in diffusers and rearward facing ramps. Such an arrangement is illustrated schematically in Figure 5 and discussed in detail in Reference 4. In this case, the boundary layer is turbulent and the rotor is completely submerged within it. Without the use of the rotor, the flow is fully separated at the corner at a ramp angle $\theta = 28°$. This fact may be verified by flow visualization and may also be seen in the ramp pressure distributions shown in Figure 6, where the downstream distance is measured from the corner.

In the static condition (no rotor, $\omega = 0$), the pressure distribution on the ramp deviates only slightly from the free stream value. This is a reflection of the fact that the flow separates at the corner and therefore the effective area that the flow experiences is nearly a constant area duct. The use of the rotor at 1000 rpm reduces the pressure distribution at the beginning of the ramp, indicating that the flow more easily negotiates the turn. The upstream static pressure, designated by the large solid symbols, is unchanged. This is significant since the tests are performed in an open circuit tunnel and a substantial improvement in the ramp flow would lead to an upstream static pressure reduction because the rearward facing ramp is

essentially a diffuser.

The reduction in upstream static pressure is clear as the rotational speed of the rotor is increased. Thus, at frequencies greater than 1000 rpm, the static pressure distribution on the ramp decreases while free stream static pressure also drops. The performance at rotor speeds of 4000 and 5000 rpm is virtually indistinguishable, suggesting that this frequency range may contain the maximum performance in terms of ω for the present flow geometry. This question cannot be completely answered here since 5000 rpm is the upper range of the present experimental capabilities.

C. Unsteady Dump Flow

A third potential application of the unsteady energization of the boundary layer by a mechanical technique is related to dump combustor flow fields. The dump combustor, illustrated schematically in Figure 7 (from Drewry[5]) involves a rapid enlargement of a duct flow. The recirculation region produced by the enlargement acts as a flame holder and keeps the flame from being blown downstream by the high speed flow. In order for the recirculation region to ignite the main combustor flow, there must be an interaction between the two regions.

In an effort to foster an increased interaction[6], a rotor is positioned slightly upstream of the dump (corner) station. The vortex structure shed by the rotor causes a time dependency in the length of the recirculation region. Two different lengths of the same recirculation region at different times are shown in Figure 8 for a rotor speed of 2500 rpm for a step height to half upstream channel width of 1/3. The length difference is large, indicating that a significant portion of the region is intermittently shed and swept downstream. It is this shedding and pulsing interaction with the main flow region which has potential advantages over the static configuration.

The flow visualization results shown in Figure 8 are two dimensional while the basic application, the ram jet, is axisymmetric. This problem can probably be overcome by an appropriate design, perhaps a segmented rotor.

III. Induced Unsteady Jet Flows

The general purpose for the introduction of unsteadiness into jet flows is to increase the mixing rate between the jet and its surroundings. Several different concepts have been proposed to drive the jet, including acoustical bombardment, mechanical interruption and fluidic control. The basic advantage of the fluidic control method is that the system contains no moving parts and can produce rather high nozzle efficiencies. The three nozzles discussed below are of the fluidic type, although the third includes a mechanical control for the fluidic parts.

A. Single Phase Fluidic Nozzle

A fluidically controlled jet is illustrated in Figure 9 and discussed in detail in Reference 7. Its method of operation is as follows: The jet flow passes through a contraction section and past two control ports into a wider channel. The sides of the channel are near enough for the jet to be bistable. That is, the jet must attach to one wall or the other. If the initial attachment is to the lower wall, the entrainment from the lower control port causes a relatively low pressure there. The pressure in the upper control port remains relatively high since the entrained flow can be replenished from outside.

Then a compression wave travels through the feedback loop from the upper (high pressure) control port to the lower control port, increasing the pressure there and tending to push the jet off the lower wall. Simultaneously, an expansion wave travels from the lower (low pressure) control port to the upper control port, decreasing the pressure there and tending to pull the

jet onto the upper wall. In a well designed system, the jet attaches to the upper wall and the process repeats itself, producing a flapping jet flow at the nozzle exit.

The main advantage of the flapping jet is shown in Figure 10, where the jet half width (divided by exit size) is plotted against non-dimensionalized distance downstream. The half width is the distance between the jet centerline and the position on the velocity profile where the velocity is half the centerline velocity. The half width contains most of the jet's momentum and as such is a measure of the jet's width or the rate at which it mixes with the ambient fluid. The various nozzle geometries all improve the mixing rate as compared with the growth of a 2-D jet indicated by the dashed line. The best efficiency produced by this set of nozzles is 88% by nozzle 3D while nozzle 1, which produced the most rapid half width growth, yielded an efficiency of only 70%. The precise nozzle geometries are presented in Reference 7.

B. Dual Phase Fluidic Nozzle

The nozzle described above operated consistently well for a single phase, i.e. the nozzle fluid the same as the ambient fluid. Operating the nozzle with the flow of water into air resulted in air bubble leaking into the feedback loop and acting as shock absorber there. Thus the waves could not pass through the loops and no oscillation occurred.

A solution[8] to the two phase flow problem is shown in Figure 11. The control is still fluidic, but in this case when the jet attaches to a wall, some of the flow is actually scooped off and passed back to a position just downstream of the contraction. This feedback exerts a pressure at that point and the jet moves to the opposite wall where the process repeats itself. Again, as in the air case, the jet flaps up and down.

The instantaneous flow field produced by the water jet is shown in Figure 12. The rapid mixing between the jet and ambient fluids may be clearly seen. The intimate unsteady mixing between the liquid and gas allows a potential improvement in combustion chambers employing such unsteady primary nozzles.

C. Multi-Nozzle Flows

The fluidically controlled nozzle of Figure 9 has been proposed[9] as the basic element of a gust tunnel. That is, a number of these nozzles together are capable of producing a gust environment if the phase relationship between various nozzles can be established and maintained. This cannot be accomplished totally fluidically but requires a mechanical control. The rotating valves employed to control the flow are illustrated in Figure 13. A multi-nozzle device has been constructed and is currently under investigation with a conditioned sampling hot wire instrument.

IV. Conclusions

As demonstrated by the studies cited above and also by additional investigation cited in the articles referenced, the judicious use of unsteady flow can lead to performance improvements in various fluid dynamic devices. Thus the existence of unsteady flow need not have a negative influence on aerodynamics but rather may be a strong positive factor if properly exploited.

References

1. McCroskey, W.J., "Recent Developments in Dynamic Stall," Unsteady Aerodynamics, R.B. Kinney, Ed., Univ. of Arizona, 1975.
2. McAllister, K.W. and Carr, L.W., "Water Tunnel Experiments on an Oscillating Airfoil at Re = 21,000," NASA TM 78446, March 1978.
3. Viets, H., Piatt, M. and Ball, M., "Unsteady Wing Boundary Layer Energization," U.S.A.-Germany Data Exchange Meeting, Friedrichshafen, West Germany, April 1979.
4. Viets, H., Piatt, M. and Ball, M., "Boundary Layer Control by Unsteady Vortex Generation," ASME Symposium on Aerodynamics of Transportation, Niagra Falls, New York, June 1979.
5. Drewry, J.E., "Fluid Dynamic Characterization of Sudden Expansion Ramjet Combustor Flowfields," AIAA Journal, Vol. 16, April 1978, pp. 313-319.
6. Viets, H. and Piatt, M., "Induced Unsteady Flow in a Dump Combustor," Proceedings of the 7th International Colloquium on Gasdynamics of Explosions and Reactive Systems, Göttingen, Germany, August 1979.
7. Viets, H., "Flip-Flop Jet Nozzle," AIAA Journal, Vol. 13, No. 10, Oct. 1975, pp. 1375-1379.
8. Viets, H., Balster, D. and Toms, H.L., "Time Dependent Fuel Injectors," AIAA Paper No. 75-1305, AIAA/SAE 11th Propulsion Conference, 1975.
9. Viets, H., "High Frequency Gust Tunnel," AGARD CCP-No. 174, AGARD Specialists Mtg. on Wind Tunnel Design and Testing Techniques, London, Oct. 1975.

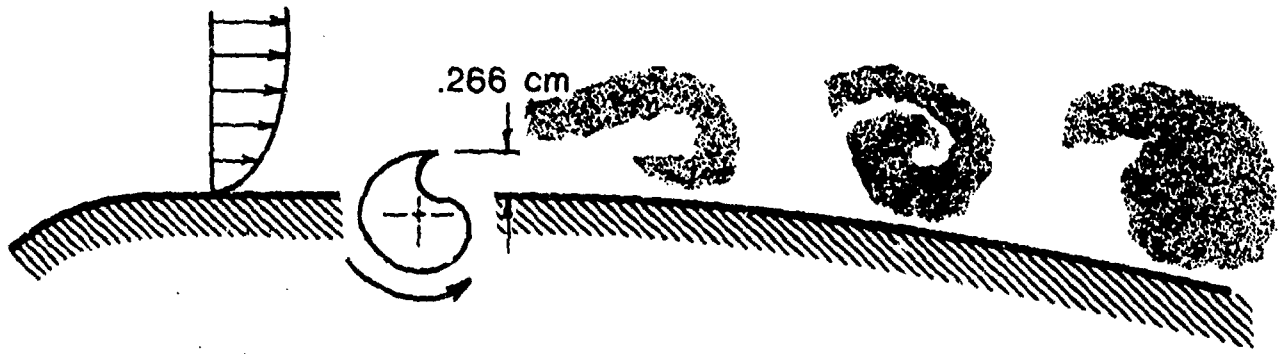

Figure 1. Vortex Generation by an Embedded Rotor[3]

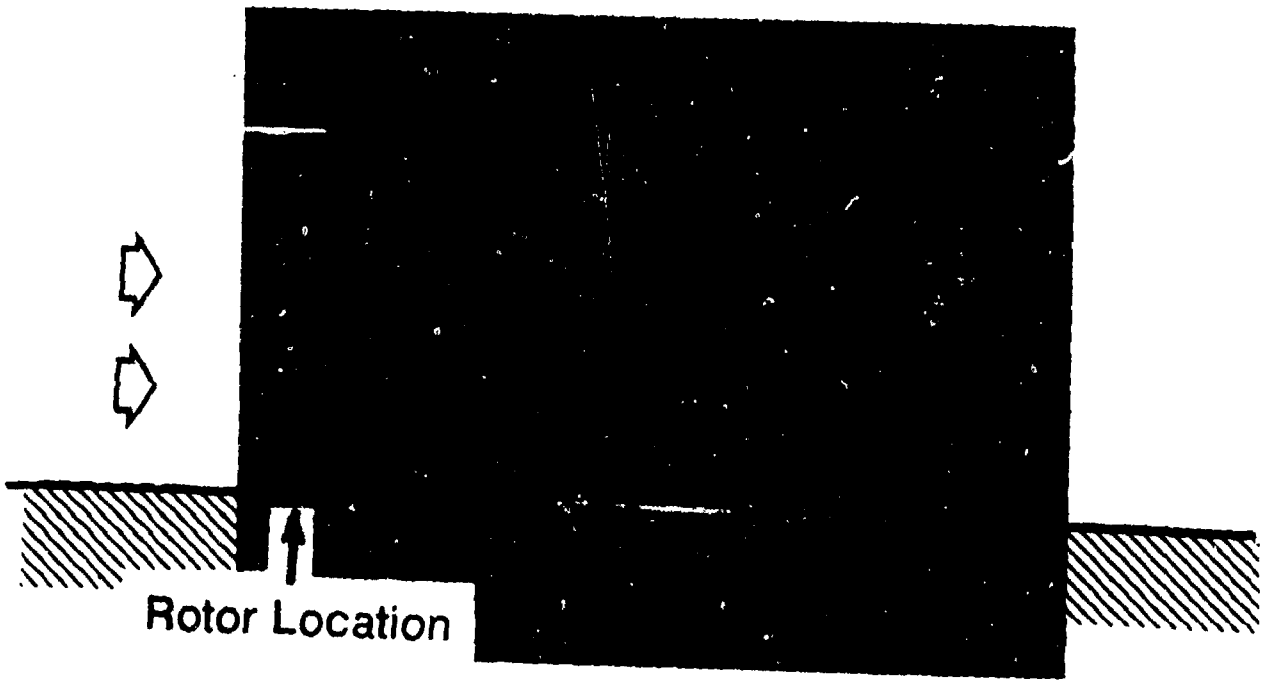

Figure 2. Vortex Structure behind the Rotor on a Flat Plate[3]

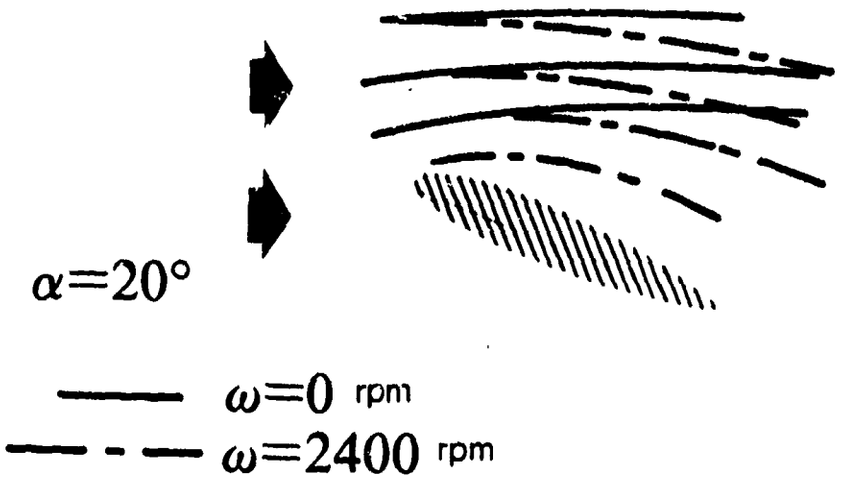

Figure 3. Effect of the Rotor Speed on the Streamline Pattern over the Airfoil[3]

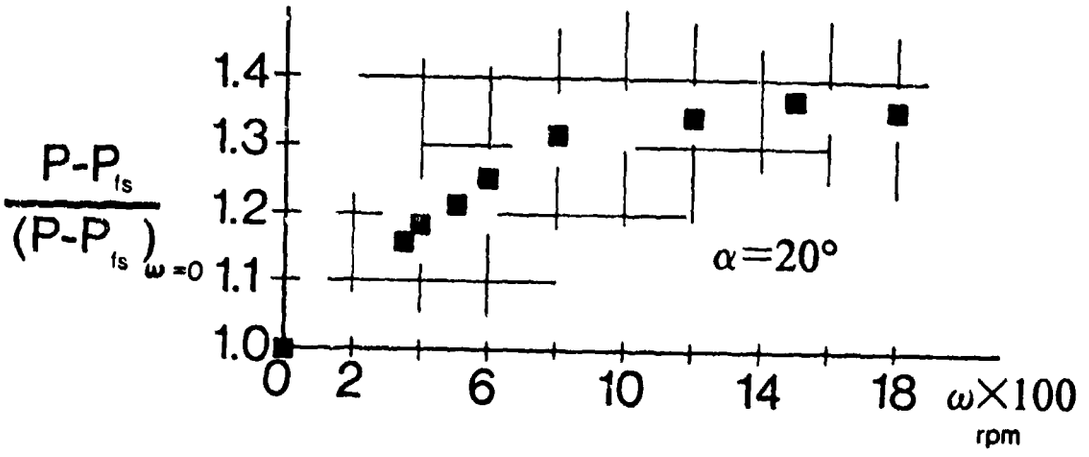

Figure 4. Pressure Variation with Rotor Speed[3]

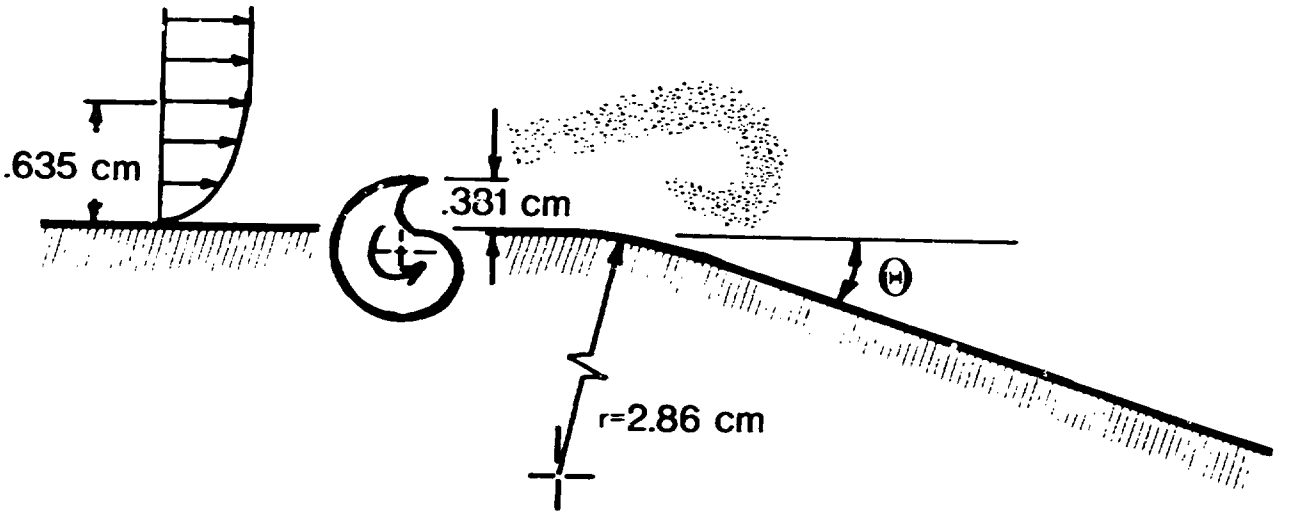

Figure 5. Unsteady Ramp Flow Configuration

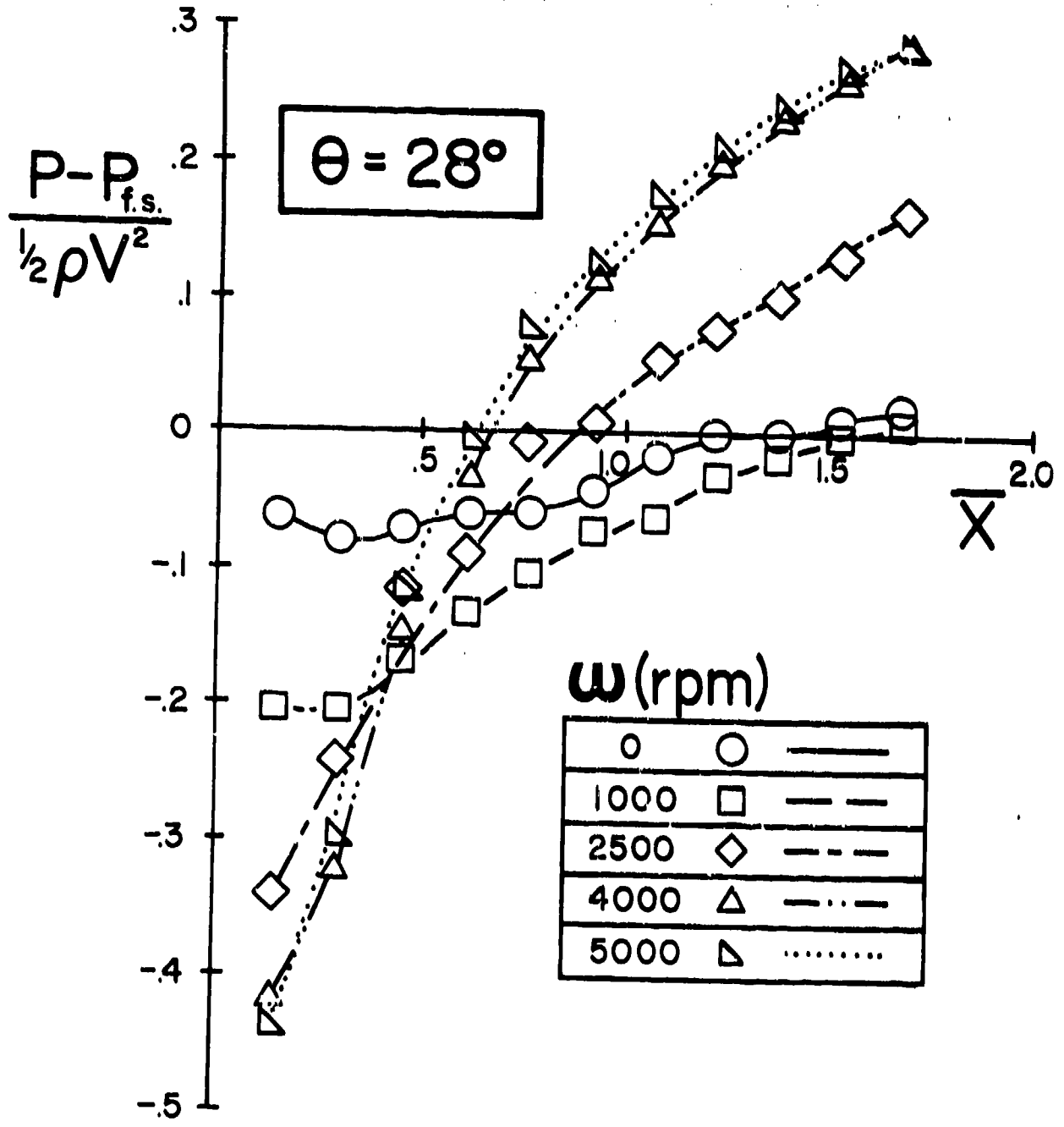

Figure 6. Ramp Pressure Distribution[4] for $\theta=28^{o}$

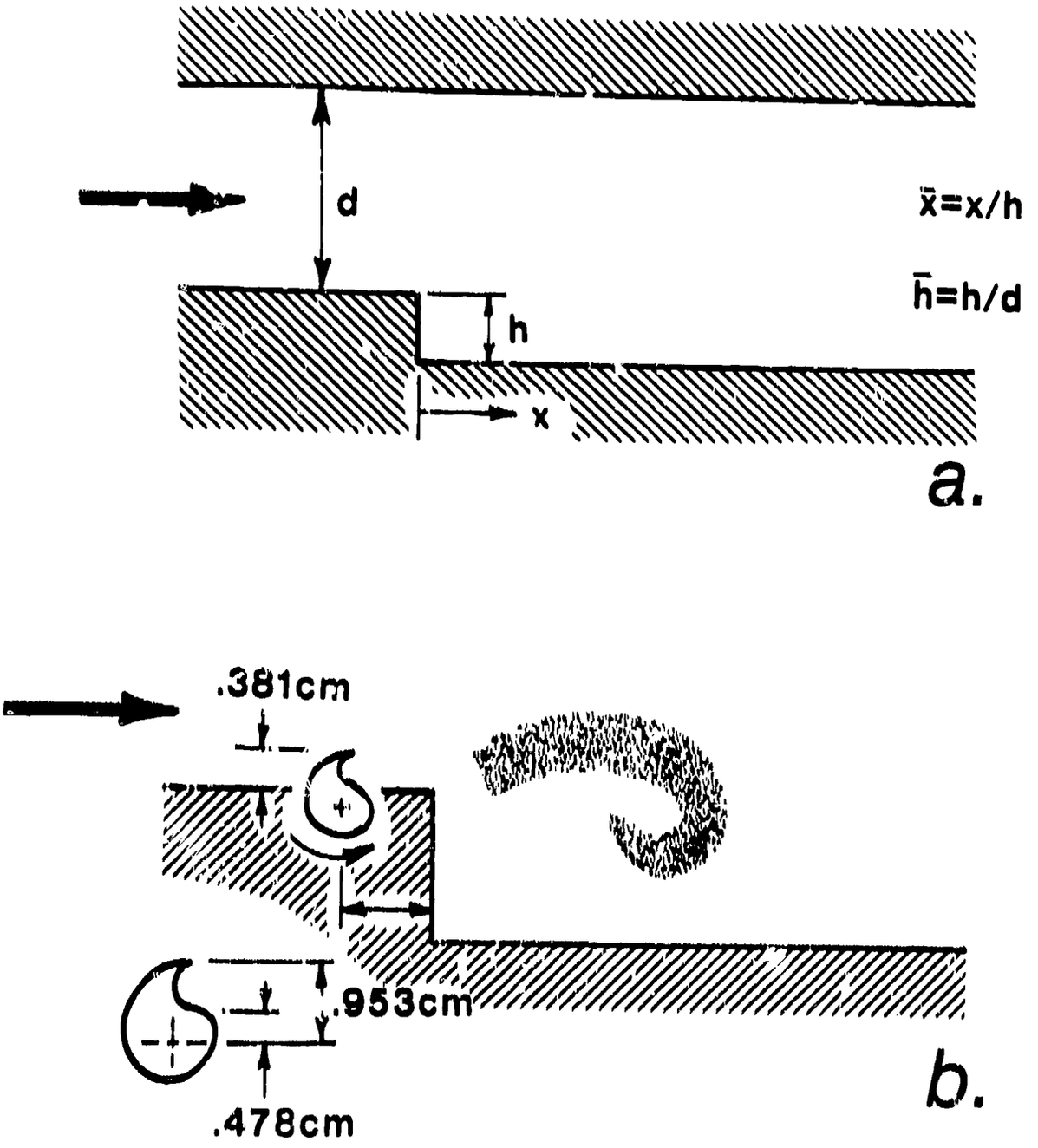

Figure 7. Schematic of Dump Combustor Flow[6]

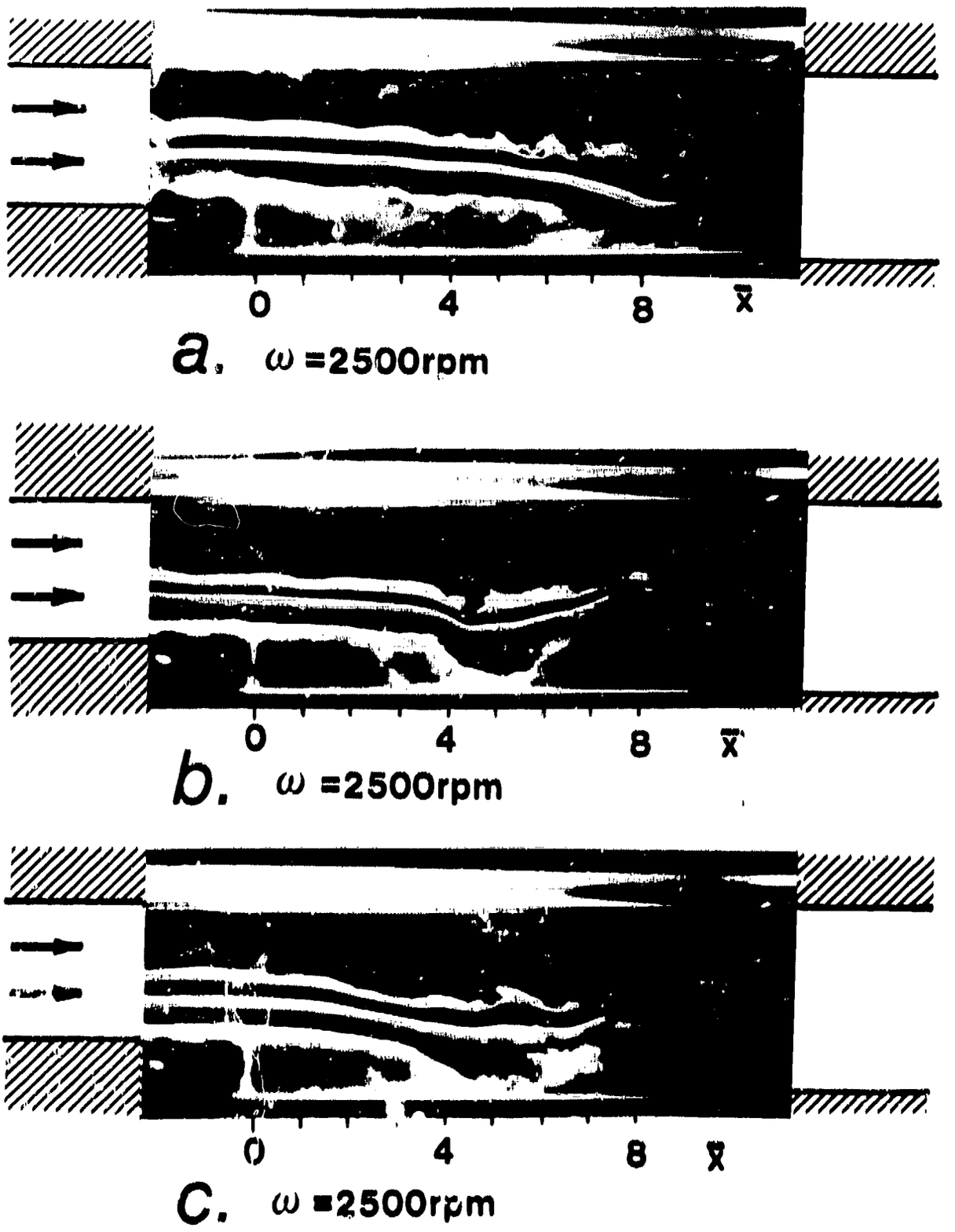

Figure 3. Time Dependent Change in the Recirculation Region Length[6]

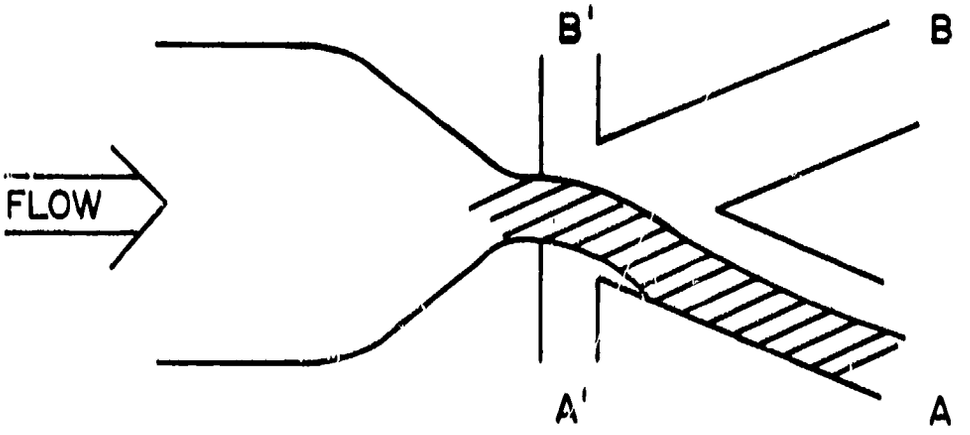

Figure 9. Schematic of a Fluidically Controlled Oscillating Jet

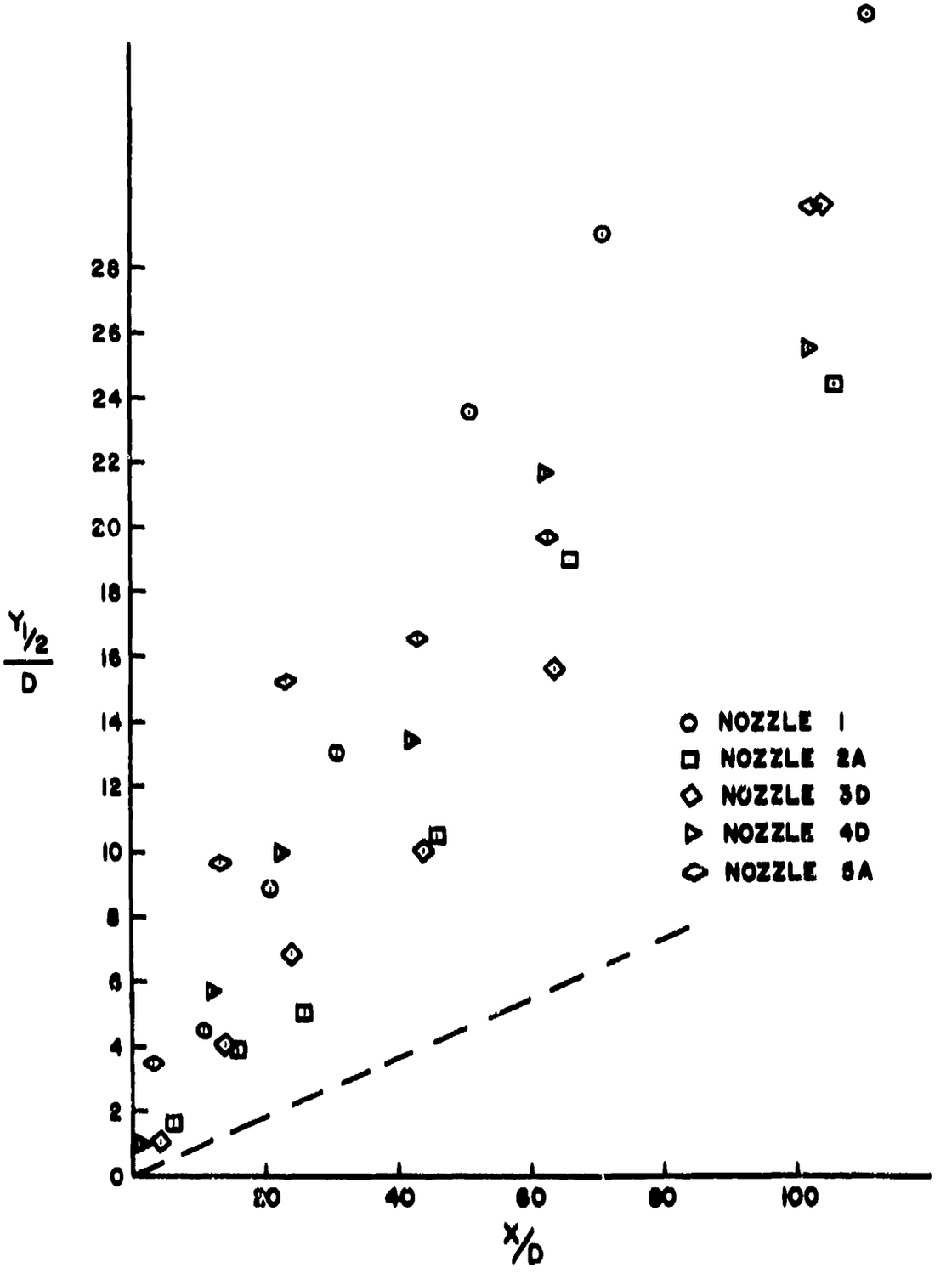

Figure 10. Half Width Growth for Oscillating Jets[7]
(dashed line represents 2-D jet growth)

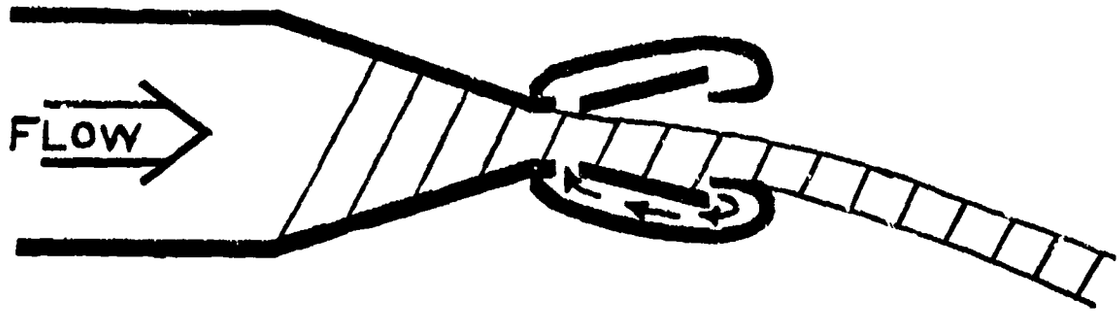

Figure 11. Schematic of the Oscillating Two Phase Jet Flowfield[8]

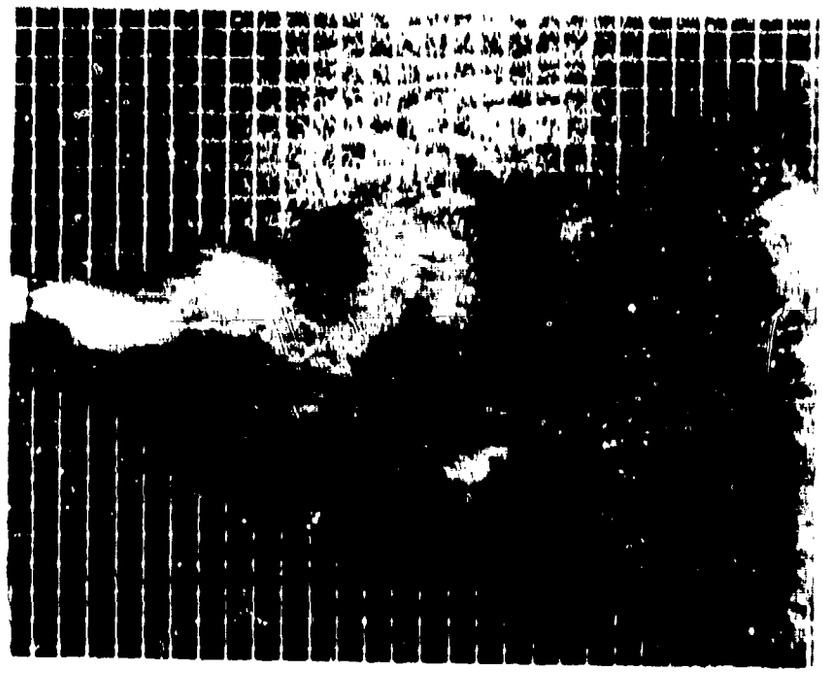

Figure 12. High Speed Photograph of Two Phase Jet[8]

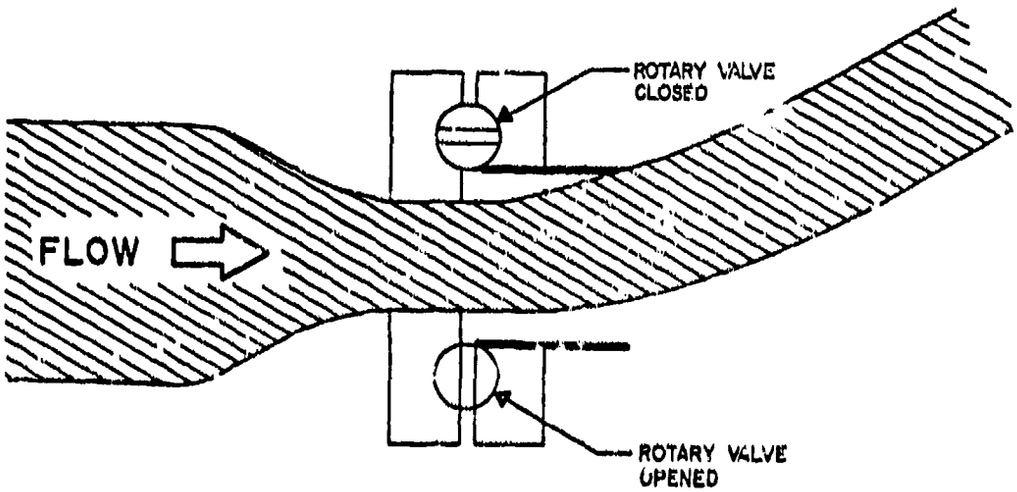

Figure 13. Rotating Value Control for Fluidic Jet[9]

AD P000342

THE BOJARSKI-LEWIS IDENTIFY FOR ELASTIC WAVE SCATTERING

by

D. A. Lee
U.S. Air Force Institute of Technology

In 1967 N. N. Bojarski published a remarkable identify, which showed that the physical optics approximation to the far-field back-scattered radiation generated by plane electromagnetic waves incident on a convex, perfectly conducting body could be processed simply to give the Fourier transform of the characteristic function of the body. (A body's characteristic function has the value 1 at all points inside the body, and is zero everywhere else.) R. M. Lewis explored the identity's implications. With the current interest in sophisticated ultrasonic inspection, it is natural to ask if an identity like the Bojarski-Lewis identity holds for elastic wave scattering. Elastic wave scattering is, of course, complicated by the existence of two different kinds of elastic waves, while electromagnetic scattering involves waves of just one kind. The present paper shows that an extension of the Bojarski-Lewis identity does indeed hold for elastic wave scattering, and discusses ways of applying this result in non-destructive testing.

Manuscript Received June 1980.

SECTION 1
INTRODUCTION

In 1967, N. N. Bojarski[1] published a remarkable identity which shows that knowledge of the far-field limit of the physical optics approximation to the electromagnetic waves back-scattered from a perfectly conducting convex body illuminated by plane waves, is equivalent to knowledge of the Fourier transform of the characteristic function of the body (a body's characteristic function has the value 1 at points of the body, and zero everywhere else). R. M. Lewis later explored the identity and some of its uses. The Bojarski-Lewis identity gives means in principle for such applications as obtaining target shape information from broad-band radars.

With current interest in non-destructive evaluation using elastic waves, it's natural to ask whether a version of the Bojarski-Lewis identity holds for elastodynamic scattering. Since elastodynamic scattering generally involves both longitudinal (dilatation) and transverse (shear) waves, while electromagnetic scattering involves only transverse waves, it is perhaps not entirely obvious that there is such a version, nor does intuition seem clearly to suggest the way to account for the conversions from waves of one type to the other which are common features of elastodynamic scattering. This assertion that there isn't an obvious answer to the question, "Is there an elastodynamic homologue to the Bojarski-Lewis identity", is of course entirely my responsibility. I make it, however, with considerable confidence because I once asked Hans von Ohain if he could see the answer intuitively, and, after a few minutes' reflection, he said he could not.

This paper gives a partial answer to the question, by establishing the following result: knowledge of the far-field limit of the physical elastodynamics approximation to the dilatation waves back-scattered from plane dilatation waves incident on a convex void in a homogeneous, isotropic, linearly elastic material, is equivalent

to knowledge of the Fourier transform of the void's characteristic function.

SECTION II
INTEGRAL REPRESENTATION FOR SCATTERED FIELD

A time-harmonic elastodynamic displacement field in an isotropic, linearly elastic material subject to an appropriate radiation condition can be expressed in terms of displacements and stresses over any sufficiently regular surface S which bounds a sufficiently large finite domain (3), as

$$u_i(\underline{x}) = \frac{1}{4\pi\rho\omega^2} \iint_S n_k(\underline{y}) [T_{jk\ell}(\underline{y}-\underline{x}) u_\ell(\underline{y}) - g_{j\ell}(\underline{y}-\underline{x})\sigma_{k\ell}(\underline{y})] d\sigma(\underline{y}) \qquad (1)$$

when $\underline{x}$ is outside the domain bounded by S. In (1), $g_{jk}(\underline{x})$ is the fundamental singular solution

$$g_{jk}(\underline{x}) = k_b^2 \frac{e^{ik_b x}}{x} \delta_{jk} - \left[\frac{e^{ik_a x}}{x} - \frac{e^{ik_b x}}{x} \right]_{,jk}$$

$$k_a = \omega/a, \quad k_b = \omega/b \qquad (2)$$

where ω is the frequency and a and b are respectively the dilatation and shear wave speeds of the material, while

$$T_{jk\ell}(\underline{x}) = \lambda g_{j,m,m}\delta_{k\ell} + \mu(g_{jk,\ell}+g_{j\ell,k}) \qquad (3)$$

and

$$\sigma_{k\ell}(\underline{x}) = \lambda u_{m,m}\delta_{k\ell} + \mu(u_{k,\ell}+u_{\ell,k}) \qquad (4)$$

The elements σ_{ij} may be called the stress field of the elastodynamic wave whose displacement field is u_i.

Equation (1) leads to the conclusion that the displacement field $U_i^s(\underline{x})$ of elastodynamic waves scattered from a void B whose (sufficiently regular) boundary is ∂B, due to an incident elastodynamic wave whose stress field is $T^o_{k\ell}(\underline{x})$, can be represented as

$$U_j^s(\underline{x}) = \frac{1}{4\pi\rho\omega^2}\iint_{\partial B} n_k(\underline{y})\left[\Gamma_{jk\ell}(\underline{y}-\underline{x})U^s_\ell(\underline{y}) + g_{j\ell}(\underline{y}-\underline{x})T^o_{k\ell}(\underline{y})\right]d\sigma(\underline{y}) \quad (5)$$

SECTION III
THE PHYSICAL ELASTODYNAMICS APPROXIMATION

Equation (5) cannot be used as it stands to evaluate the scattered field $U_i^s(\underline{x})$, because the values of U_i^s in the integral of (5) are not known. The physical elastodynamics approximation to U_i^s is obtained by replacing the unknown U_i^s on the right side of (5), with the displacement field $U_i^p(\underline{x})$, which, at "illuminated" points of ∂B, is the displacement field which would have been produced at the point $\underline{x}\in\partial B$, if the incident field were scattered by the (infinite) tangent plane of ∂B at $\underline{x}$. $U_i^p(\underline{x})$ is taken to be zero on "shadowed" parts of B.

If we take the incident field to be a plane dilatation wave,

$$\underline{U}_0 = U\underline{e}\,\exp(ik_a\underline{e}\cdot\underline{x}) \quad (6)$$

then, following Achenbach (4) we may write the displacement field U^p at illuminated points of ∂B as

$$\underline{U}^p(\underline{y}) = U[A_1\underline{d}_1 + A_2\underline{d}_2]e^{ik_a\underline{e}\cdot\underline{y}} \quad (7)$$

where A_1 and A_2 are solutions of

$$(\lambda+2\mu\cos^2\theta_0)A_1 - \kappa\mu\sin 2\theta_2 A_2 = -(\lambda+2\mu\cos^2\theta_0) \quad (8)$$

$$-\mu\sin 2\theta_0 A_1 + \kappa\mu\cos 2\theta_2 A_2 = -\mu\sin 2\theta_0 \quad (9)$$

The unit vectors $\underline{d}_1$ and $\underline{d}_2$ may be expressed as

$$\underline{d}_1 = -2(\underline{n}\cdot\underline{e})\underline{n} + \underline{e};\quad \underline{d}_2 = \frac{\cos\theta_2}{\sin\theta_0}(\underline{e}-(\underline{n}\cdot\underline{e})\underline{n}) - \sin\theta_2\,\underline{n}$$

The angle θ_2 is determined by

$$\sin\theta_2 = \frac{1}{\kappa}\sin\theta_0 \tag{11}$$

and θ_0 is the angle of incidence. The parameter κ is the ratio of the dilatation wave speed to the shear wave speed, i.e.,

$$\kappa \equiv \sqrt{\frac{\lambda+2\mu}{\mu}} > 1 \tag{12}$$

The local geometry of plane-wave scattering from a plane is sketched in Figure 1, and the global geometry of plane-wave scattering from a void is shown in Figure 2.

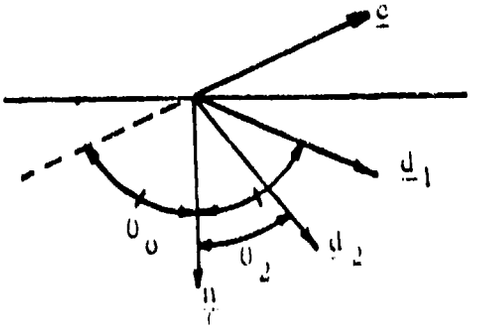

Figure 1. Local Plane-Wave Scattering.

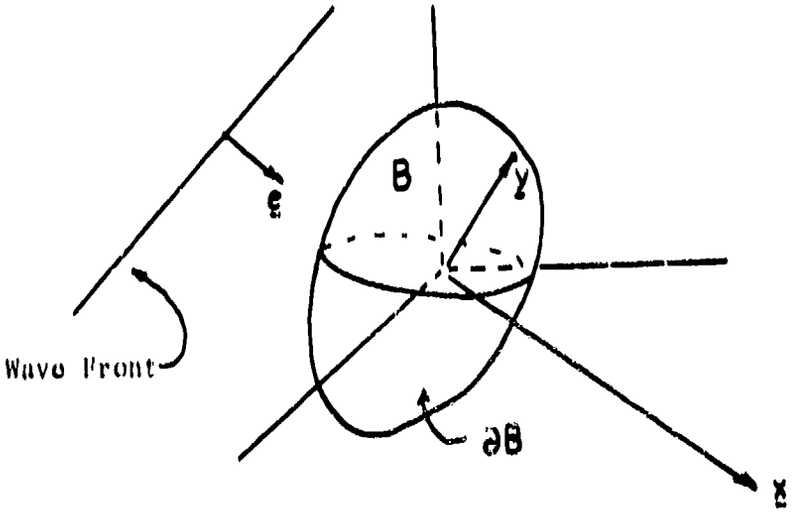

Figure 2. Global Plane-Wave Scattering.

SECTION IV
THE FAR FIELD

By "far field", we mean those $\underline{x}$ such that

$$\frac{|\underline{y}|}{|\underline{x}|} << 1, \quad k_b|\underline{y}| \cdot \frac{|\underline{y}|}{|\underline{x}|} << \pi/4, \quad \underline{y}\varepsilon\partial B \cup B \tag{13}$$

When inequalities (13) are met,

$$g_{\ell j}(\underline{y}-\underline{x}) \doteq k_a^2 \hat{x}_\ell x_j \frac{e^{ik_a x}}{x} e^{-ik_a \hat{x}\cdot\underline{y}} + k_b^2(\delta_{\ell j}-\hat{x}_\ell \hat{x}_j) \frac{e^{ik_b x}}{x} e^{-ik_b \hat{x}\cdot\underline{y}}$$

and (14)

$$T_{jk\ell}(\underline{y}-\underline{x}) \doteq -ik_a^3(\lambda \hat{x}_j \delta_{\ell k}+2\mu \hat{x}_j \hat{x}_\ell \hat{x}_k) \frac{e^{ik_a x}}{x} e^{-ik_a \hat{x}\cdot\underline{y}}$$

$$-i\mu k_b^3(\hat{x}_k \delta_{\ell j}+\hat{x}_\ell \delta_{jk}-2\hat{x}_j \hat{x}_k \hat{x}_\ell) \frac{e^{ik_b x}}{x} e^{-ik_b \hat{x}\cdot\underline{y}}$$

In (14), $\hat{x}$ denotes a unit vector in the direction of $\underline{x}$. In the back-scatter direction, where $\hat{x} = -\underline{e}$, substitution of (13) and (14) into (5), and some straightforward simplification, gives

$$U_j^s(\underline{x}) = \frac{ik_a^3}{4\pi\rho\omega^2} e_j \frac{e^{ik_a x}}{x} \iint_{\partial B} \Big[\lambda(\underline{n}\cdot\underline{U}^s(\underline{y}))+2\mu(\underline{n}\cdot\underline{e})(\underline{e}\cdot\underline{U}^s(\underline{y})) + (\lambda+2\mu)U(\underline{n}\cdot\underline{e})e^{ik_a \underline{e}\cdot\underline{y}} \Big] e^{ik_a \underline{e}\cdot\underline{y}} \, do(\underline{y})$$

$$+ Q_j \frac{e^{ik_b x}}{x} \tag{15}$$

In (15), we have used the fact that, for the dilatation wave (6),

$$T^o_{k\ell}(\underline{y}) = ik_a U(\lambda\delta_{k\ell}+2\mu e_k e_\ell) e^{ik_a \underline{y}\cdot\underline{e}} \tag{16}$$

The quantity denoted by Q_j in (15) can be expressed in terms of integrals over ∂B. The first term of (15) characterizes the dilatation-wave component of the far-field back-scattered elastic energy. If the incident pulse is sufficiently short, and if the distance from B to the surface at which the scattered field is observed is sufficiently great, it will be possible to separate the dilatation wave component from the components represented by the second term of (15).

SECTION V
PHYSICAL ELASTODYNAMICS APPROXIMATION IN THE FAR FIELD

Use of the physical elastodynamics approximation in the first term of the right side of (15) requires evaluation of

$$H \equiv \lambda(\underline{n}\cdot\underline{U}^s) + 2\mu(\underline{n}\cdot\underline{e})(\underline{e}\cdot\underline{U}^s),$$
$$= \hat{H} \exp(i\kappa_a \underline{e}\cdot\underline{y}) \qquad (17)$$

using equations (7) through (12). One finds, since $\underline{n}\cdot\underline{e} = -\cos\theta_0$,

$$\hat{H} = \lambda(A_1 \cos\theta_0 - A_2 \sin\theta_2)$$
$$- 2\mu\cos\theta_0(-A_1\cos 2\theta_0 + A_2 \sin(\theta_0+\theta_2)) \qquad (18)$$

Since

$$\lambda = (\kappa^2-2)\mu, \qquad (19)$$

$$\hat{H} = \mu\cos\theta_0\left\{A_1(\kappa^2 - 2 + 2\cos 2\theta_0)\right.$$
$$\left. - A_2\left[2\sin(\theta_0+\theta_2) + \frac{\kappa^2-2}{\cos\theta_0}\sin\theta_2\right]\right\} \qquad (20)$$

The parameters λ and μ may be eliminated from (8) and (9) by means of (19), to give

$$(\kappa^2 - 2 + 2\cos^2\theta_0)A_1$$
$$- \kappa\sin 2\theta_2 A_2 = -(\kappa^2 - 2 + 2\cos^2\theta_0) \qquad (21)$$

and

$$-2 \sin \theta_0 \cos \theta_0 A_1$$

$$- \kappa \cos 2\theta_2 A_2 = -2 \sin \theta_0 \cos \theta_0 \qquad (22)$$

If (22) is multiplied by tan θ_0 and added to (21), the sum yields

$$(\kappa^2 - 2 + 2 \cos 2\theta_0) A_1$$

$$- A_2 (\kappa \sin 2\theta_2 + \kappa \frac{\sin \theta_0}{\cos \theta_0} \cos 2\theta_2) = -\kappa^2 \qquad (23)$$

But, since $\cos 2\phi = 1 - 2 \sin^2 \phi$,

$$\cos 2\theta_2 = 1 - 2 \sin^2 \theta_2 = 1 - \frac{2 \sin^2 \theta_0}{\kappa^2} \qquad (24)$$

in view of (11). It then follows that

$$\cos 2\theta_2 = \frac{\kappa^2 - 2 \sin^2 \theta_0}{\kappa^2} = \frac{\kappa^2 - 2 + 2 \cos^2 \theta_0}{\kappa^2}$$

Thus

$$\kappa \frac{\sin \theta_0}{\cos \theta_0} \cos 2\theta_2 = \frac{\sin \theta_0}{\kappa \cos \theta_0} (\kappa^2 - 2 + 2 \cos^2 \theta_0)$$

$$= (\kappa^2 - 2) \frac{\sin \theta_0}{\kappa \cos \theta_0} + \frac{2 \sin \theta_0}{\kappa} \cos \theta_0$$

$$= (\kappa^2 - 2) \frac{\sin \theta_2}{\cos \theta_0} + 2 \sin \theta_2 \cos \theta_0 \qquad (25)$$

Substituting (25) into (23) gives

$$(\kappa^2 - 2 + 2 \cos 2\theta) A_1 - A_2 \left[2\kappa \frac{\sin \theta_0}{\kappa} \cos \theta_2 \right.$$

$$\left. + \frac{(\kappa^2 - 2)}{\cos \theta_0} \sin \theta_0 + 2 \sin \theta_2 \cos \theta_0 \right] = - \kappa^2$$

or

$$(\kappa^2 - 2 + 2\cos 2\theta)A_1$$

$$- A_2\left[2\sin(\theta_0+\theta_2) + \kappa\frac{\kappa^2-2}{\cos\theta_0}\sin\theta_0\right] = -\kappa^2 \qquad (26)$$

Substituting (26) into (20) then gives

$$\hat{H} = -\mu\cos\theta_0\kappa^2 = -(\lambda+2\mu)\cos\theta_0 = (\lambda+2\mu)(\underline{n}\cdot\underline{e}) \qquad (27)$$

Substituting (27) into (17) and using the result in (15) shows that $\tilde{U}_j^s$, the dilatation-wave component of the far-field back-scattered elastic energy, has the pleasantly simple expression

$$\tilde{U}_j^s = \frac{2ik_a^3U(\lambda+2\mu)}{4\pi\rho\omega^2}e_j\frac{e^{ik_ax}}{x}\iint_{\partial B_I(\underline{e})}(\underline{n}\cdot\underline{e})e^{2ik_a\underline{e}\cdot\underline{y}}\,d\sigma(\underline{y}) \qquad (28)$$

or

$$\tilde{U}_j^s = \frac{ik_aU}{2\pi}\frac{e^{ik_aU}}{x}e_j\iint_{\partial B_I(\underline{e})}(\underline{n}\cdot\underline{e})e^{2ik_a\underline{e}\cdot\underline{y}}\,d\sigma(\underline{y}) \qquad (29)$$

where $\partial B_I(\underline{e})$ denotes the portion of ∂B illuminated by waves propagating in the direction of $\underline{e}$.

Thus, in principle one can recover, by observing the far-field back-scattered dilatation waves, the quantity

$$\Phi(\underline{p}) \equiv \frac{i}{4\pi}\iint_{\partial B_I(\underline{e})}(\underline{n}\cdot\underline{p})e^{-i\underline{p}\cdot\underline{y}}\,d\sigma(\underline{y}) \qquad (30)$$

where

$$\underline{p} \equiv -2k_a\underline{e} \qquad (31)$$

If B is convex, then $\partial B_I(\underline{e})$ consists of those parts of ∂B for which $(\underline{n}\cdot\underline{p}) > 0$. Thus for convex B,

$$\Phi(\underline{p}) = \frac{i}{4\pi} \iint_{\underline{n}\cdot\underline{p} > 0} (\underline{n}\cdot\underline{p}) e^{-i\underline{p}\cdot\underline{\gamma}} \, d\sigma(\underline{\gamma}) \qquad (32)$$

Equation (32) may be used in general, noting that an approximation is thereby introduced, if B is not convex. Equations (30) and (31) are, apart from a constant in the definition of $\Phi(\underline{p})$, the same as Equations (5) and (6) of Reference (2), which considered electromagnetic scattering. We continue, closely following the development of Reference (2).

Since, by (32),

$$\Phi^*(-\underline{p}) = \frac{i}{4\pi} \iint_{\underline{n}\cdot\underline{p} < 0} (\underline{n}\cdot\underline{p}) e^{-i\underline{p}\cdot\underline{\gamma}} \, d\sigma(\underline{\gamma}),$$

one has

$$\Phi(\underline{p}) + \Phi^*(-\underline{p}) = \frac{i}{4\pi} \iint_{\partial B} (\underline{n}\cdot\underline{p}) e^{-i\underline{p}\cdot\underline{\gamma}} \, d\sigma(\underline{\gamma}) = \frac{p^2}{4\pi} \iiint_B e^{-i\underline{p}\cdot\underline{\gamma}} \, dv$$

so that

$$\Gamma(\underline{p}) \equiv \frac{2}{p^2} [\Phi(\underline{p}) + \Phi^*(-\underline{p})] = \frac{1}{2\pi} \iiint_B e^{i\underline{p}\cdot\underline{\gamma}} \, dv$$

$$= \frac{1}{2\pi} \iiint_{\underline{\gamma}} \gamma(\underline{\gamma}) e^{-i\underline{p}\cdot\underline{\gamma}} \, dv \qquad (33)$$

where $\gamma(\underline{\gamma})$, the characteristic function of B, is defined by

$$\gamma(\underline{\gamma}) = \begin{cases} 1, & \underline{\gamma} \in B \\ 0, & \text{otherwise} \end{cases}$$

Equation (33) shows that knowledge of the far-field limit of the physical elastodynamics approximation to the dilatation waves back-scattered from plane dilatation waves incident on a convex void in a homogeneous, isotropic, linearly-elastic material, is equivalent to knowledge of the Fourier transform of the void's characteristic function. Deriving this generalization to elastodynamic

scattering of the Bojarski-Lewis identity was the purpose of this paper.

By the Fourier integral theorem, one can reconstruct $\gamma(\underline{x})$ from $\Gamma(\underline{p})$, as

$$\gamma(\underline{x}) = \frac{1}{(2\pi)^2} \iiint_{\underline{p}} \Gamma(\underline{p}) e^{i\underline{x}\cdot\underline{p}} \, dv(\underline{p}) \qquad (34)$$

Producing the required values of $\Gamma(\underline{p})$ from observations would require observing the void at arbitrarily many look angles, for arbitrarily many frequencies. The challenging question of making rational estimates of $\gamma(\underline{x})$, together with error estimates, from noisy band-limited data restricted to a finite set of look angles, is considered to some degree in Reference (2), and also in References (5) and (6).

REFERENCES

1. Bojarski, N. N., Three-Dimensional Electromagnetic Short Pulse Inverse Scattering, Syracuse University Research Corporation, Syracuse, N.Y. (1967).
2. Lewis, R. M., IEEE Trans. Antennas and Propagation AP-17, 308 (1969).
3. Kupradze, V. D., Dynamical Problems in Elasticity, Chapter I, §6, Volume III of Progress in Solid Mechanics, I. N. Sneddon and R. Hill, Editors; North-Holland, Amsterdam; Interscience (Wiley), New York (1963).
4. Achenbach, J. D., Wave Propagation in Elastic Solids, §5.6, pp 172 et seq. North-Holland, Amsterdam; American Elsevier, New York (1973).
5. Perry, W. L., Proc. 9th Pittsburgh Conference on Modeling and Simulation, Part 3, page 865.
6. Lee, D. A., Mathematical Principles of Data Inversion, Chapter 5 of Elements of Quantitative Non-Destructive Evaluation, Buckley and Thompson, Editors, Springer-Verlag, New York, to appear.

EFFECT OF INITIAL CONFIGURATIONS ON LIBRATION POINT MOTION

by

Lynn E. Wolaver
Air Force Institute of Technology
Wright-Patterson Air Force Base, OH

In the restricted three-body problem, motion about the triangular Lagrange libration points is stable, under certain conditions, in the sense that if a particle is "slightly" disturbed it will still remain "close" to the original libration point. In the case of the earth-moon system, the sun exerts a strong perturbing influence and the equilibrium points no longer exist. To investigate stability in this case, a very restricted four-body problem is formulated and "stable" trajectories are found. Their existence is shown to be markedly influenced by the initial configuration of the three large bodies. The stable initial state conditions are found from a first-order variational solution and later refined by numerical integration of the equations of motion. Real world trajectories are shown to exhibit qualitatively the same configuration effects.

Originally published as an AIAA preprint 65-684. Reprinted with permission.

EFFECT OF INITIAL CONFIGURATION ON LIBRATION POINT MOTION

Lynn E. Wolaver

Introduction

Stability in politics, in economics, and in other fields is much admired. It is no less so in outer space. The search for stable trajectories among the planets has been going on for centuries and continued even today.

In the case of two isolated bodies, the relative motion can be determined analytically and is known to be a portion of a conic section. If a third body is introduced, an analytical solution can no longer be found in general. As the number of bodies is increased, the problem becomes more formidable.

For three massive bodies there are, however, special configuration for which a solution is known. Lagrange in 1772 discovered five exact solutions of the three-body problem in which the masses maintain a constant configuration.[4] An important specialization of this three-body problem is the restricted three-body problem. For this case one of the masses is so small that it does not affect the motion of the two larger masses. Thus the larger masses move as a two body problem and their trajectories are known. The restricted three-body problem assumes that they move in circular orbits about their common center of mass.

In a rotating coordinate system the five Lagrange solutions become five fixed points (Fig. 1). A particle placed at any of these points with zero relative velocity will remain stationary in the rotating system. These points are singularities of the equations of motion. They are equilibrium points. The vectorial addition of the attraction of the two large bodies for the small body is just balanced by the centrifugal force developed by that small body about the common barycenter.

In addition to these special solutions, various investigators have shown the existence of periodic orbits about these points in a rotating coordinate system. Accordingly, Gylden was led to call these points "centres of libration." They are more often referred to as libration points or the Lagrange libration points.

By linearizing the equations of motion, in turn, about each of the libration points, one can determine stability "in-the-small," so to speak. [9,10] The well-known results show that the triangular points L4 and L5 are stable points in the sense that for very "small" changes in the state variables the resultant trajectory will lie "close" to the libration point so long as the mass ratio of the two large bodies is less than 0.04. The collinear points are unstable for all mass ratios.

These solutions remained of purely academic interest until 1906 when the first of the Trojan asteroids was discovered. This group of asteroids oscillates around the sun-Jupiter triangular libration points. Investigation of motion about these libration points was made by a number of distinguished astronomers, including Brown,[2] Smart,[16] Willard,[18] Herz,[6] Brouwer,[3] Eckert,[5] and Wilkins[19] among others.

The study of the libration points in the earth-moon system was initiated by Klemperer and Benedikt[7] in 1958. They called the system a selenoid satellite, a term which fortunately didn't catch on. Again, as with the Trojan asteroids, it was an observational discovery, which increased interest in the earth-moon system. In 1961 a Polish astronomer named Kordylewski photoelectrically determined two bright spots, which he regarded as clouds of matter in the neighborhood of the libration point L5 in the earth-moon system, [8,15] Later (January 1962) he reported the discovery of a "cloud" near L4 (the libration point 60° ahead of the moon).[12] The cloud's very low surface brightness makes it difficult to detect. Its presence can be observed only during brief periods of time. From December to April of each year there are but three days a month when, for not more than 2 hrs at a time, the clouds are visible over the horizon at an antisolar point remote from the Milky Way, and when, also, the moon has set.[12] Thus, the configuration of the sun-earth-moon and libration point must have the proper orientation relative to the observers' horizon. This difficulty of observation may account for the lack of confirmation of such clouds. In any event, these reported observations have initiated a flood of activity into the investigation of motion about the libration points in the earth-moon system. The interested reader is referred to Refs. 20-35 for a few of these.

In a review of space research by the National Academy of Science, [11] the summer study group recommended further practical consideration be given to placing a satellite at the earth-moon triangular libration point. Because this point is free from the perturbations caused by the geomagnetic field it would provide valuable data on solar flare and charged particle measurements. Further, it enjoys a view over nearly the entire celestial sphere and has only short and infrequent solar eclipses, being in the sunlight almost continuously.[11] The study group investigated payload size and various boosters.

Whatever the virtues of such a point, the purpose of this paper is to investigate stability of motion about such a point. We shall leave its utility to others.

Any investigation of orbital stability requires that one first formulate a mathematical model. At this point we are confronted with the eternal problem of choosing a model so oversimplified, in order to make it mathematically feasible, that it is physically or realistically no longer interesting or on the other hand of choosing a realistic model, which is mathematically intractable. No mathematical model however simple or sophisticated is any good at all if it does not make physical sense.

In using a simplified model in applying mathematics to the real world we will be guided by the criterion that reasonable assurances can be given that the study of the simplified model will in some way advance us toward a physical understanding of the real world phenomenon.

It is the approach of this paper to abandon reality entirely and oversimplify the real world model. In so doing it is possible to find "stable" trajectories near the libration points in a simple planar very restricted four-body problem. Having found these stable trajectories, the severe limitations of the simplified model will be examined and the real world searched (in vain) for similar stable behavior. The same qualitative behavior will, however, be demonstrated.

The Very Restricted Four-Body Problem

Consider the system of Fig. 2 consisting of an infinitesimal body of mass m moving in a system of three bodies of masses m_S, m_E, and m_M so arranged that the center of mass (O) of m_E and m_M is revolving around the center of mass of the entire system (B) in a circular orbit, and m_E and m_M themselves are revolving likewise about their center of mass (O) in a

circular orbit. Such motion is not possible. However, if $m_S >> m_E + m_M >> m$ and if the distance R is very much greater than d, (Fig. 2), the approximation will deviate very little from the actual solution. This is the case for the real earth-moon-sun system.

We shall consider only planar motion. A rotating x-y axis system is used with the origin at the earth-moon center of mass, with the x axis through the moon. See the diagram shown in Fig. 2. The angular velocity of the earth-moon is ω while the angular velocity of the mass center o about the barycenter B is taken to be Ω. The equations of motion may then be written as follows:

$$\ddot{x} - 2\omega\dot{y} - \omega^2 x - \bar{R}\Omega^2 \cos\phi = \partial U/\partial x \qquad (1)$$

$$\ddot{y} + 2\omega\dot{x} - \omega^2 y + \bar{R}\Omega^2 \sin\phi = \partial U/\partial y$$

with

$$U = \frac{\gamma M_M}{[(x-1+\mu)^2 + y^2]^{1/2}} + \frac{\gamma M_E}{[(x+\mu)^2+y^2]^{1/2}} + \frac{\gamma M_S}{[(x+R\cos\phi)^2+(y-R\sin\phi)^2]^{1/2}}$$

$$\bar{R} = RM_S/(M_S + M_e + M_M) \qquad \mu = M_M/(M_M + M_e)$$

$$d^3 = [\gamma(M_E + M_M)]/\omega^2, \quad \omega = 2\pi/T_M \qquad T_M = 27.321661$$

$$R^3 = \gamma(M_S + M_E + M_M)\Omega^2, \ \Omega = 2\pi/T \qquad T = 365.256354$$

$\phi = \alpha + (\omega-\Omega)t$ $\quad$ α = initial configuration angle

The equations may be nondimensionalized by choosing the unit of distance to be d, the unit of mass to be $m_E + m_M$ and the unit of time such that $\gamma = 1$; then $\omega = 1$ and one time unit is equal to 4.348377 mean solar days. With these relations the equation may be written

$$\ddot{x} - 2\dot{y} - x - (M_s/R^2)\cos\phi = \partial U/\partial x \qquad (2)$$

$$\ddot{y} + 2\dot{x} - y + (M_s/R^2)\sin\phi = \partial U/\partial y$$

$$U = \frac{\mu}{[(x-1+\mu)^2+y^2]^{1/2}} + \frac{1-\mu}{[(x+\mu)+y^2]^{1/2}} + \frac{M_s}{[(x+R\cos\phi)^2+(y-R\sin\phi)^2]^{1/2}}$$

$\omega = 1 \qquad \Omega = 0.07480133$

$\omega - \Omega = 0.92519867$

These very restricted four-body equations do not admit of a singular point. The libration points are no longer equilibrium points, and it does not make good sense, mathematically speaking, to hang around these points. However, because of Kordylewski's observations one is spurred to jump into the analysis and investigate trajectories starting near the old libration points. In so doing, a new variable α has been introduced. This represents the relative initial position of the sun with respect to the earth-moon line at the time the particle is placed at the old libration point with zero relative velocity (relative to the earth-moon rotating system).

In order to investigate stability let us place the mass m at the L4 libration point with zero relative velocity and obtain its trajectory by numerically integrating the equations of motion Eqs.(2). Figures 3 and 4 indicate motion in a coordinate system centered at the old L4 libration point for the case where $\alpha = 0$ and $\alpha = 135$ degrees, respectively. Figure 5 shows the radal distance of the particle from the old libration point as a function of time. For $\alpha = 0$ the range is steadily increasing and appears to diverge from the libration point. For $\alpha = 135^0$ (and similarly for $\alpha = 315^0$) the range does not appear to diverge but seems to be stable. We must, however, emphasize that a stable orbit has not been demonstrated in the sense of any of the normal stability criteria. What has been demonstrated is that the orbit remains close to the vicinity of the old libration point for at least 250 days when the initial configuration of the earth-moon-sun is a proper one. It may well increase at some later date (as indeed it does). As a practical matter one could apply a small amount of thrust at the end of each year to return all of the state variables to their epoch values. Thus, stability for a year would suffice. But let us not yet venture into practicality from such a crude model.

It is always valid to look askance at purely numerically integrated results. In order to investigate this phenomenon closer and to verify the results, Capt. Paul Ulshafer [34] obtained a first-order solution of the linearized equations of motion. The technique is one used by deVries[24] together with a modification to allow for different initial configurations of the three large bodies.

If one linearizes Eq. (2) about the old libration point the following equations are obtained[24]:

$$\ddot{x}-2\dot{y}-C_1x-C_2y = C_4+C_6\cos2\phi+C_7\sin2\phi+C_8\cos\phi+C_9\sin\phi$$
$$+C_{11}V(x\cos2\phi-y\sin2\phi)+C_{12}V(3X_L\cos\phi-Y_L\sin\phi)X \qquad (3)$$
$$+C_{12}V(Y_L\cos\phi-X_L\sin\phi)y$$

$$\ddot{y}+2\dot{x}-C_2x-C_3y = C_5+C_7\cos2\phi-C_6\sin2\phi-C_9\cos\phi+C_{10}\sin\phi$$
$$-C_{11}V(x\sin2\phi+y\cos2\phi)+C_{12}V(Y_L\cos\phi-X_L\sin\phi)x \qquad (4)$$
$$+C_{12}V(X_L\cos\phi-3Y_L\sin\phi)y$$

$$C_1 = 3/4 + V/2 \qquad C_6 = 3VX/2$$
$$C_2 = 3\sqrt{3}(1-2\mu/4 \qquad C_7 = -3VY_L/2$$
$$C_3 = 9/4 + V/2 \qquad C_8 = -3V(3X_L^2+Y_L^2)/8R \qquad (5)$$
$$C_4 = VX_L/2 \qquad C_9 = 3VX_LY_L/4R$$
$$C_5 = VY_L/2 \qquad C_{10} = 3V(3Y_L^2+X_L^2)/8R$$
$$C_{11} = 3/2 \qquad \mu = 1/82.45$$
$$C_{12} = -3/4R \qquad V = M_s/R^3$$
$$X_L = 1/2 - \mu \qquad R = 388.9237$$

$Y_L = \sqrt{3}/2$ $\quad V = 0.00566779$

$\phi = \alpha + (1-\Omega)t = \alpha + 0.925198yt$

These eqs. (3) and (4) form a time varying linear system. To solve, one assumes a solution of the form

$$x = \sum_{i=1}^{\infty} V^i x^{(i)}(t) \qquad y = \sum_{i=1}^{\infty} V^i y^{(i)}(t) \tag{6}$$

By substituting (6) into (3) and (4) and collecting like powers of V one can form successive approximations. The equations for $x^{(i)}$ and $y^{(i)}$, which lead to the first-order solutions are just the first line of (3) and the first line of (4), with initial conditions x_0, y_0, $\dot{x}_0$, $\dot{y}_0$. These may be solved by the use of the LaPlace transform. Ulshafer[34] obtained the first-order solution in the following form:

$$x^{(1)} = K_x + (A_1+A)\cos pt + \left(\frac{B_1}{p}+B\right)\sin pt + (x_0 - A_1 + C)\cos qt + \left[(\dot{x}_0 - B_1)/q + D\right]\sin qt + E\cos 2\phi + F\sin 2\phi + G\cos\phi + H\sin\phi \tag{7}$$

$$y^{(1)} = K_y + (A_2+J)\cos pt + \left(\frac{B_2}{q}+K\right)\sin pt + (y_0 - A_2 + L)\cos qt + \left[(\dot{y}_0 - B_2)/q + M\right]\sin qt + N\cos 2\phi + P\sin 2\phi + Q\sin\phi + R\cos\phi \tag{8}$$

The coeeficients of Eqs. (7) and (8) are listed in Tables 1 ard 2. Those of Table 1 are functions of α only while those of Table 2 depend only on the initial conditions and are independent of α.

The angular frequencies p = 0.9457 and q = 0.3161 are the fundamental frequencies associated with tne left-hand sides of the pair of Eqs. (3) and (4). They differ slightly from the three-body values because of the addition of 1/2V to coefficients C_1 and C_3.

Having obtained this first-order solution one could then proceed with the perturbation analysis and obtain higher-order approximations. However, we seek only approximate starting conditions and will be quite satisfied with the first-order solution. In fact, deVries shows that the higher-order solutions suffer from the problems of the small diviscr and convergence is quite poor. The small divisor problem here is not merely mathematical but arises from the near resonance conditions of the problem. This is discussed by Schechter and Hollis[31] and by Breakwell and Pringle.[22]

Table 1 Coeeficients of first-order solution

Sum of terms in row	$x10^{-3}$	$x10^{-2}$ x cosα	$x10^{-3}$ x sinα	$x10^{-2}$ x cos2α	$x10^{-2}$ x sing2α
A	-1.745801	0.1458397	0.368662	1.87777914	-2.2473146
B	-6.532998	0.0372955	-1.462943	-2.4371739	-2.5699487
C	1.789636	0.0063482	0.024830	-1.3042055	1.4887025
D	19.54382	0.0035895	-0.064632	2.8505752	4.3308594
E				-0.5735737	0.758612
F				0.758612	0.5735737
G		-0.1521879	-0.393493		
H		-0.0393493	1.521879		
J	-3.223166	-0.0363221	-1.027686	-2.220977	-0.6394122
K	3.680373	-0.1026684	0.367632	-0.146962	2.385641
L	4.287914	-0.002455	-0.034200	1.468659	0.3618108
M	-11.010034	-0.0036398	0.035087	-1.1852334	-2.7332567
N				0.752317	0.277601
K	-0.043827				
P				0.277601	-0.752317
K	-1.06470				
Q		0.038778	1.06190		
R		0.106190	-0.38778		

Table 2 Coefficients dependent upon the initial conditions

Coefficient	Coefficient is sum of terms in each row times x_o	times y_o	times $\dot{x}_o$	times $\dot{y}_o$
A_1	-1.0734247	-1.5954815		-2.5174708
A_2	-1.5954815	-2.9615272	2.5174708	
B_1	-3.1909630	-5.6714422	3.9615168	-1.5954815
B_2	1.8952373	3.1909630	-1.5954815	2.0734144

Given the first-order solution [Eqs. (7) and (8)] together with Tables 1 and 2, one now desires to find initial conditions, which will reduce the maximum excursions of both x and y.

Careful examination of the coefficients of Eqs. (7) and (8) will show that coefficients E, F, G, and H in (7) and N, P, Q, and R in (8) are generally smaller than the other α dependent coefficients and further, $\sqrt{E^2 + F^2 + G^2 + H^2}$ and $\sqrt{N^2 + p^2 + Q^2 + R^2}$ are both small constants, which are independent of the initial conditions. We thus concentrate on reducing the coefficients of the fundamental frequency terms in (7) and (8).

Because there are eight coefficients in (7) and (8) which must be reduced to zero and only five initial conditions, it is not possible to solve the nonlinear programing problem. However, the numerical integration results indicate that the x components is always greater than the y component when zero initial conditions are used. Accordingly, we first select the initial conditions x_o, y_o, $\dot{x}_o$, $\dot{y}_o$ so that each of the four coefficients of the fundamental frequency terms in the x component [Eq. (7)] are each zero. We shall then vary α in order to make the corresponding coefficients of the y component [Eq. (8)] be as small as possible.

The four coefficients in the x component may be written in the following form:

$$A_1 + A = -\hat{C}_1 x_o - \hat{C}_2 y_o - \hat{C}_3 \dot{y}_o + k_1 + f_1(\alpha) = 0$$

$$B_1/p + B = -\hat{C}_5 x_o/p - \hat{C}_6 y_o/p + \hat{C}_7 \dot{x}_o/p - \hat{C}_2 \dot{y}_o/p + k_2 + f_2(\alpha) = 0$$

$$x_o - A_1 + C = (\hat{C}_1 + 1) x_o + \hat{C}_2 y_o + \hat{C}_3 \dot{y}_o + k_3 + f_3(\alpha) = 0 \qquad (9)$$

$$(\dot{x}_o - B_1)/q + D = \hat{C}_5 x_o/q + \hat{C}_2 y_o/q - (\hat{C}_7 - 1)\dot{x}_o/q + \hat{C}_2 \dot{y}_o/q + k_4 + f_4(\alpha) = 0$$

The $\hat{C}_n$ are listed in Table 2, k_n values are found Table 1 the $f_n(\alpha)$ values are listed separately in Table 3. By solving these four equations (9) for the initial conditions, one obtains the following relations:

$$x_o = -0.000043835 - f_1(\alpha) - f_3(\alpha) \qquad (10)$$

$$y_o = 0.56827878\, f_1(\alpha) + 0.084836931\, f_3(\alpha)$$

$$+ 0.3810187\, f_2(\alpha) + 0.17037141\, f_4(\alpha)$$

$$\dot{x}_o = -0.94572\, f_2(\alpha) - 0.31613\, f_4(\alpha)$$

$$\dot{y}_o = -0.0.0010647183 + 0.40274407\, f_1(\alpha) + 0.53873657\, f_3(\alpha) \qquad (10)$$

$$- 0.60098844\, f_2(\alpha) - 0.26872918\, f_4(\alpha)$$

These are functions of α. For a given value of α one may now obtain the initial conditions for which all four of the coefficients of the fundamental frequency terms in the x component [Eq. (7)] will be precisely zero. The four corresponding coefficients of the fundamental frequency terms in the y component (Eq. (8)] may be written as follows:

$$K_1 = A_2+J = \hat{C}_2 x_o - \hat{C}_8 y_o + \hat{C}_3 \dot{x}_o + k_5 + f_5(\alpha)$$

$$K_2 = B_2/p+K = \hat{C}_9/p\; x_o + \hat{C}_5/p\; y_o - \hat{C}_2/p\; \dot{x}_o + \hat{C}_{10}/p\; \dot{y}_o + k_6 + f_6(\alpha)$$

$$K_3 = y_o - A_2 + L = \hat{C}_2 x_o + (\hat{C}_8+1) y_o - \hat{C}_{11} \dot{x}_o + f_7(\alpha) \qquad (11)$$

$$K_4 = (\dot{y}_o - B_2)/q + M = -\hat{C}_9/q\; x_o - \hat{C}_5/q\; y_o + \hat{C}_2/q\; x_o - (\hat{C}_{10}-1) q\; \dot{y}_o$$

$$+ k_8 + f_8(\alpha)$$

These are the coefficients of the y component [Eq. (8)].

Substitution of the initial conditions from Eq. (10) into Eqs. (11) gives the y component coeeficients as a function of α alone. One can then determine say $\sqrt{K_1^2 + K_2^2 + K_3^2 + K_4^2}$ as some measure of the y amplitude. When this measure is computed as a function of α, it is found to have three relative minimum points at $\alpha = 133^\circ$, 210° and 337°. For these minimal points one obtains the following initial conditions:

I	$\alpha = 133^{\circ}$	$x_o = -0.00646$	$y_o = -0.00385$
		$\dot{x}_o = -0.01029$	$\dot{y}_o = 0.0126$
II	$\alpha = 210^{\circ}$	$x_o = 0.00517$	$y_o = 0.00424$
		$\dot{x}_o = 0.01582$	$\dot{y}_o = -0.01016$
III	$\alpha = 337^{\circ}$	$x_o = -0.01073$	$y_o = 0.00211$
		$x_o = 0.00123$	$\dot{y}_o = 0.01463$

With these initial conditions, Eqs. (3) and (4) may be numerically integrated to obtain the solutions shown in Figs. 6, 7, and 8. These represent further improvements over the best zero initial condition configurations.

These initial conditions not only reduce the coeeficients of the fundamental frequencies of the x component to zero, but the rather amazing fact is that these same initial conditions reduce the corresponding coefficients of the fundamental frequencies in the y equation [Eq. (8)] by three orders of magnitude below those obtained using zero initial conditions. It is not clear why this should occur and indeed the whole procedure described is completely without mathematical justification. These nice minimal results are a fluke of the model.

It is, of course, obvious that such an approach would not even have been attempted except for the motivating fact that some such dependence was observed numerically. It is perhaps worth mentioning that such a large reduction in the y- component coefficients, as compared with the zero initial conditions,occurs only for certain α angles. Some reduction always occurs, but it is very much greater at these critical α angles.

Table 3 $f_n(\alpha)$ functions

$f_1(\alpha) = 0.001458397\cos\alpha+0.00036866\sin\alpha+0.18777791\cos(2\alpha)$
$-0.0224473146\sin(2\alpha)$

$f_2(\alpha) = 0.00037295\cos\alpha-0.00146294\sin\alpha-0.024371739\cos(2\alpha)$
$-0.025699487\sin(2\alpha)$

$f_3(\alpha) = 0.00006348\cos\alpha+0.0000248\sin\alpha-0.01304205\cos(2\alpha)$
$+0.014887025\sin(2\alpha)$

$f_4(\alpha) = 0.000035895\cos\alpha-0.0000643\sin\alpha+0,02850575\cos(2\alpha)$
$+0.04330859\sin(2\alpha)$

$f_5(\alpha) = -0.00036322\cos\alpha-0.001027686\sin\alpha-0.02220977(2\alpha)$
$-0.00639412\sin(2\alpha)$

$f_6(\alpha) = -0.00102668\cos\alpha+0.00036763\sin\alpha-0.0014696\cos(2\alpha)$
$+0.0238564\sin(2\alpha)$

$f_7(\alpha) = -0.0000245\cos\alpha-0.0000342\sin\alpha+0.0146866\cos(2\alpha)$
$+0.003618108\sin(2\alpha)$

$f_8(\alpha) + -0.000036398\cos\alpha+0.00003509\sin\alpha-0.0118523\cos(2\alpha)$
$-0.027332567\sin(2\alpha)$

$k_1 = -0.00174580$ $k_2 = -0.006532998$ $k_3 = 0.001789636$

$k_4 = 0.0195438$ $k_5 = -0.003223166$ $k_6 = 0.00368037$

$k_7 = 0.00428791$ k_8 -0.01101003

Using these initial state values, one can once again return to the original Eqs. (2) and obtain a solution by numerical integration. With this model the initial conditions can then be systematically varied to obtain a somewhat better trajectory. One of the final best initial conditions was found to be $\alpha = 144^{\circ}$, $x_o = -0.00836$, $y_o = 0.00048668$, $\dot{x}_o = -0.001155$, $\dot{y}_o = 0.013594$. This can undoubtedly be improved. The radial distance from the initial trajectory point is given as a function of time in Fig. 9. Note that the time scale now extends for more than one Julian year.

It should be mentioned here that the first-order solution given by Eqs. (7) and (8) fits the numerically integrated results quite well for a period of about 90 days after which time it begins to differ slightly. This lends confidence to the numerically integrated results.

The trajectories and determination of the minimal α values are sensitive to the mass ratio m_E/m_M. The results shown here were computed for a ratio of 81.45. Figure 10 gives a comparison of the same initial conditions used to compute the trajectory depicted in Fig. 9 with the difference that the mass ratio in Fig. 10 was taken to be 81.375.

The method used here can be applied to find initial conditions which reduce divergent trends as well. As an example Ulshafer used the method to calculate initial conditions for $\alpha = 90^{\circ}$. In comparison with radial trajectory with zero initial conditions, that having optimum initial conditions shows quite an improvement. This is shown in Fig. 11.

Model Deficiencies

When we attempt to relate these results to the real world we are confronted with the alarming deficiencies of our model. The model is a planar one which is not even dynamically correct. The stability phenomenon observed in such a simple model is, however, of interest in its own right and the fact that this same trend is found to exist qualitatively in the real world is most encouraging. However, the real world is much more complicated in several important respects and if we are to find stable trajectories in the real world, we must study other models. Let us point out some important effects by citing examples.

In Masters' Thesis by Guffey and McKinley[27] (1962), the authors used a restricted four-body problem in three dimensions with the earth-moon plane inclined five degrees to the earth-sun plane. They found the motion was bounded and estimated empirically that the radial amplitude was given by $R = \sin^2(2\pi t/8T)$ with T the period of revolution of the earth about the sun. Actually the period is closer to 8.8T. Proceeding further they then included the effect of the sun on the orbits of the earth and moon. This is the indirect effect. Numerically integrating these orbits along with the previous equations led to unbounded orbits. Although the discovery of a few unbounded orbits does not call for the conclusion that all orbits are unbounded, nevertheless the importance of the indirect effect is quite clear. The reader is referred to Guffey and McKinley[27] and the RAND report of Schechter and Hollis[31] for further discussions of this effect. A good discussion of this important effect has been given by Danby[20].

It should be noted that these indirect results do not contradict the remarks made by Brown (Ref. 1, p. 283) concerning the indirect effect of Saturn upon the Trojan Asteroids. The mass ratios and distances involved here are decidedly different.

The three-dimensional effect by itself is an important one, particularly as a source of resonance (see, for example the discussion of Schechter and Hollis[31]). In addition, solar radiation pressure will affect small particles appreciably, although the published results (25, 31, 32) differ on the magnitude of the effect. It is not clear whether Refs. 25 and 32 include the effect of eclipsing. It also appears that the solar radiation effects are likewise sensitive to the initial configuration and this may account in part for the differences in magnitude of the effect among the published results.

Thus it is clear that our very restricted four-body model is seriously defective as a realistic model for the real world. Nevertheless, let us at least be hopeful and venture into the real world. We shall see that the stabilizing effect of the initial configuration manifests itself, but to date no truly stable real world orbits have been reported. Trajectories which are started with α corresponding to nearly optimum values diverge much more slowly and have a smaller envelope than trajectories started with $\alpha = 0^\circ$.

Real World

In order to study trajectories in the real world, a machine program for the actual solar system is used in which the ephemeris coordinates of the sun, earth, moon and all the planets save Pluto are given at discrete time intervals. The resultant force on an infinitesimal particle is summed and integrated to give its motion in a coordinate system centered at the instantaneous location of the three-body Lagrange libration point. The program used is one developed by General Electric for the Aeronautical Systems Division[17] and is the same routine employed by deVries and Pauson[25] and Guffey and McKinley.[25]

The published results of deVries and Pauson[25] show the initial configuration effects. Figures 12 and 13 show real world trajectories for the configurations of new moon and last quarter.

Tapley and Schultz[33] show the same initial configuration effects, however, they have not included the very important indirect effect mentioned before and therefore their results are not representative of real world conditions. As we discussed previously, the earth-moon ratio affects the actual value of the optimum α angle. Reference 33 uses a mass ratio of 81.51.

Figure 14 is drawn to show the relative effect in the real world. The envelopes indicate roughly the maximum excursions up to the time indicated. Figure 14 corresponds to the case shown in Fig. 13. Using the real world computer program, Robert Highfill of our summer staff computed some more nearly minimal trajectories. One of these is shown in Fig. 15. It appears possible to improve this real world trajectory by proper selection of initial conditions. Note carefully that nothing can be said here about long term stability.

Because the real world motion is not planar, there is great difficulty in computing proper initial velocity conditions which correspond to the very restricted four body model. The trajectory is very sensitive to these initial velocity values. For this reason the configuration affects, per se, become difficult to discern but the qualitative effect is there.

The particle is located on the graph of Fig. 15 by computing its radial distance from the earth and again from the moon. This value is then divided by the instantaneous earth-moon radial distance and the result is plotted in Fig. 15. It represents the three-dimensional deviation of the particle from the instantaneous three-dimensional location of the old Lagrange libration point.

Summary and Conclusion

The sun is not just a small perturbation on the restricted three-body problem but changes the very qualitative nature of the solution even in the very restricted four-body problem. The use of the over simplified very restricted four-body model has shown that a proper initial configuration leads to stable trajectories about the old libration point in a certain sense. The real world exhibits the same qualitative initial configuration effects but completely stable real world trajectories still eludes us. This, however, does not justify the conlusion that they do not exist.

The history of the study of stability in the earth-moon-sun system is an interesting one. It began with an oft referenced but apparently seldom read report by Sehnal.[14] He assumed the earth, sun, and moon all revolve at the same angular rate. Hardly a realistic assumption. He then made a mistake in applying the perturbation analysis and compounded it with an algebraic sign error. Accordingly one can surely question his conlusion that this shows the sun causes instability. In fact, with his variational equations it is possible to obtain an analytical solution by means of the LaPlace transform and thereby show that his model is stable under all conditions.

The conclusion of Schechter and Hollis[31] that "the results raise serious doubts concerning the particulate clouds," is based on the $\alpha = 0$ configuration with zero initial conditions. From the results of this paper one may at least modify the statement from "serious doubts" to at most some doubts still exist. As was aptly demonstrated by Rabe[13] in his comments on some results of Thuring, a hat full of numerically unstable orbits does not imply anything about the stability of orbits about the libration point.

References

[1] Brown, E.W. and Shook, C.A., Planetary Theory (Dover Publications, New York, 1964).

[2] Brown, E.W., "Theory of the Trojan group of asteroids," Trans. Yale Obs. 3, 1-47, 87-133 (1926).

[3] Brouwer, D., "Theory and tables of the motion of achilles," Trans. Yale Obs. 6, 177-188 (1933).

[4] Danby, J.M.A., Fundamentals of Celestial Mechanics (The MacMillan Company, New York, 1962), Chap. 8, p. 187.

[5] Eckert, W.J., "The general orbit of Hector," Trans. of Yale Obs. 6, 161-172 (1933).

[6] Herz, H.G., "On the theory of Trojan asteroids," Astron. J. 50, 1146, 121-125 (1943).

[7] Klemperer, W.B., and Benedikt, E.T., "Selenoidal satellites," Astronaut. Acta 4, 25-30 (1958)

[8] Kordylewski, K., "Photographic investigations of the libration point L5 in the earth-moon system," Acta Astron. 11, no. 3, 165-169 (1961); also Research Transl. E-T-G-64-35, Cambridge Research Labs. Office of Aerospace Research (1961).

[9] Moskowitz, S.E., "On the stability of the equilibrium solution of the plane restricted three body problem in the sense of Liapounov," Proceedings of XV International Astronaut. Congress, Warsaw, Springer-Verlag, New York (1967).

[10] McCuskey, S.W., Introduction to Celestial Mechanics (Addison-Wesley Publishing Company, Inc., Reading, Jass., 1963), p. 118.

[11] Steg, L., and Shoemaker, E.,(editors), "A review of space research," National Academy of Science, National Research Publication 1079, State University of Iowa (June 17-August 10, 1962).

[12] Pskovski, Yu. P., "Dust in circumterrestrial space," Priroda, 12, 68-73 (1962); also transl. by E.R. Hope as TR383R, Defense Research Board, Canada (1963).

[13] Rabe, E., "Determination and survey of periodic Trojan orbits in the restricted problem of three bodies," Astron. J. 66, 500-513 (1961).

[14] Sehnal, L., "The stability of the libration points L4 and L5 in the earth-moon system," Astron. Inst. Czechoslovakia 11, no. 4, 130-131 (1960).

[15] Anon, "New natural satellites of the earth?" Sky and Telescope XXII, 10 (July 1962).

[16] Smart, W., "Libration of the Trojan planets," Paper I, Mem. Royal Astron. Soc. 62, 79-112 (1918).

[17] deVries, J.P., "Generalized interplanetary trajectory study," Wright Air Development Div. TR 60-502, Wright-Patterson Air Force Base, Ohio (February 1961)

[18] Willard, H.R., "On a family of oscillating orbits of short periods," Monthly Notices of the Royal Astron. Soc. 73, 471-484 (1913).

[19] Wilkins, A., "Zur theorie der librationen in sonnen-system," Astron. Nach. 227, 337-348 (May 1926).

[20] Danby, J.M.A., "Inclusion of extra forces in the problem of three bodies," Astron. J. 66, 181 (1965).

[21] Bennett, A.G., and Citron, S.J., "On the effect of the sun on the stability of the earth-moon Lagrange triangle points," Thesis, Purdue Univ. (1964).

[22] Brakewell, J., and Pringle, R., "Resonances affecting motion near the earth-moon equilateral libration points," AIAA Preprint Paper 65-683 (September 1965).

[23] Colombo, G., Lautman, D., and Momford, C., "On the librations of a particle near the triangular point in the semi-restricted three body problem," Smithsonian Institution Special Rept. no. 108 (November 20, 1962).

[24] deVries, J.P., "The sun's perturbing effect on motion near a triangular Lagrange point," Proc. of XIII Intern. Astron. Congr., Varna, Springer-Verlag, New York (1964).

[25] deVries, J.P., Pauson, W.M., "A study of motion near libration points in the earth-moon system," General Electric Rept. R62SD5, Space Science Lab., General Electric (1962).

[26] Ellis, G.A., and Diana, A.C., "The use of the earth-moon libration points as terminals for space stations," Rome Air Development Center, RADC-TDR-82-1 (January 1962).

[27] Guffey, H.F., and McKinley, H.L., "Libration point studies by numerical techniques," M.S. Thesis, U.S. Air Force Inst. of Technology, Wright-Patterson Air Force Base, Ohio (March 1962).

[28] Michael, W.H., "Consideration of the motion of a small body in the vicinity of the stable libration points in the earth-moon system," NASA TR-R-160 (1963).

[29] Pohle, F.V., "The least density of a spherical swarm of particles in the restricted three body problem," AIAA Preprint no. 63-425 (August 1963).

[30] Rudolph, G.T., "Station keeping of a space vehicle at the earth-moon L4 libration point," U.S. Air Force Inst. of Technology, M.S. Thesis (1963).

[31] Schechter, H.B., and Hollis, W.C., "Stability of the Trojan points in the four body problem," Rand Memo. RM-3993-PR, AD-606232 (September 1964).

[32] Tapley, B.R., and Lewallen, J.M., "Solar influence on satellite motion near the stable earth-moon libration points," AIAA 2, 728-732 (April 1964).

[33] Tapley, B.R., and Schultz, B.E., "Some additional results on solar influenced libration point motion," AIAA Preprint no. 65-88 (January 1965).

[34] Ulshafer, P.M., "Libration point studies - an analytical approach," M.S. Thesis, U.S. Air Force Inst. of Technology (January 1963).

[35] Wolaver, L.E., "Stability of certain trajectories in the four-body problem," Office of Aerospace Research Review II, no. 11 (July 15, 1963), p 4.

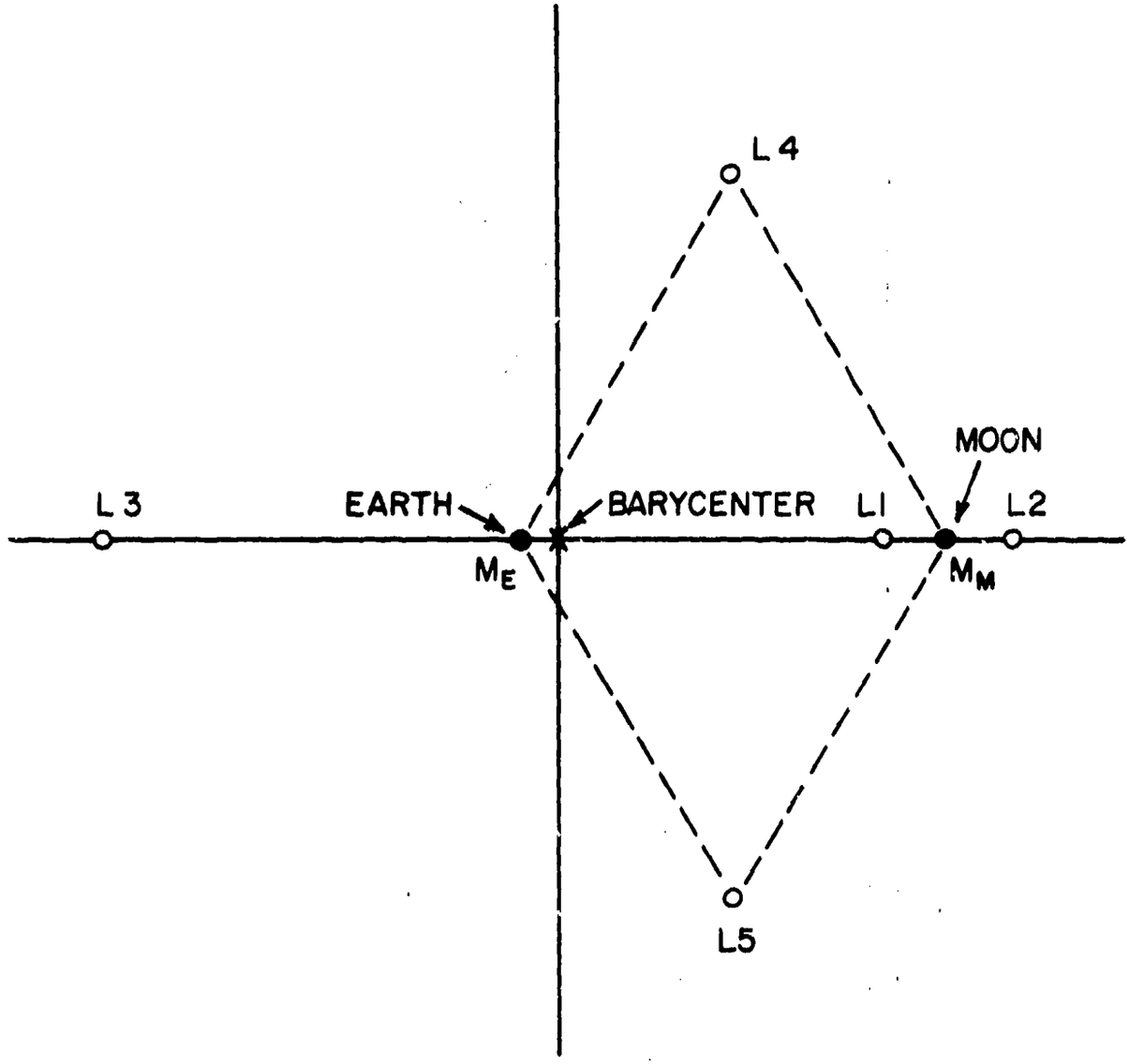

FIGURE 1. LIBRATION POINTS IN RESTRICTED THREE BODY PROBLEM

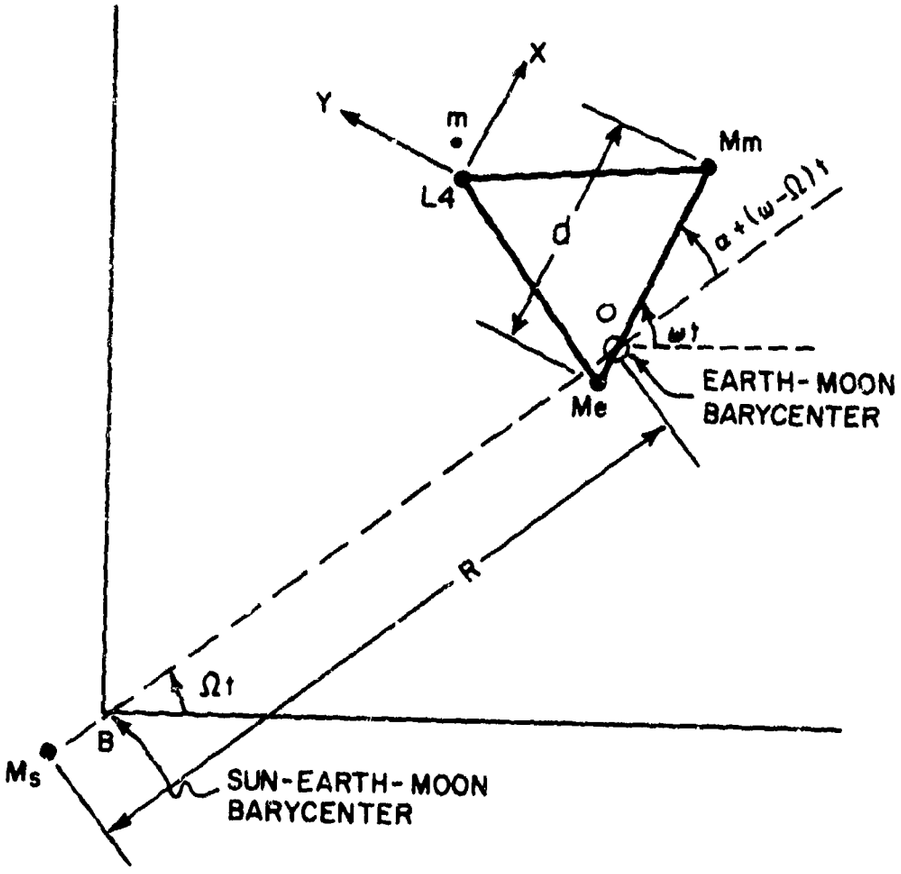

FIGURE 2. FOUR BODY PROBLEM

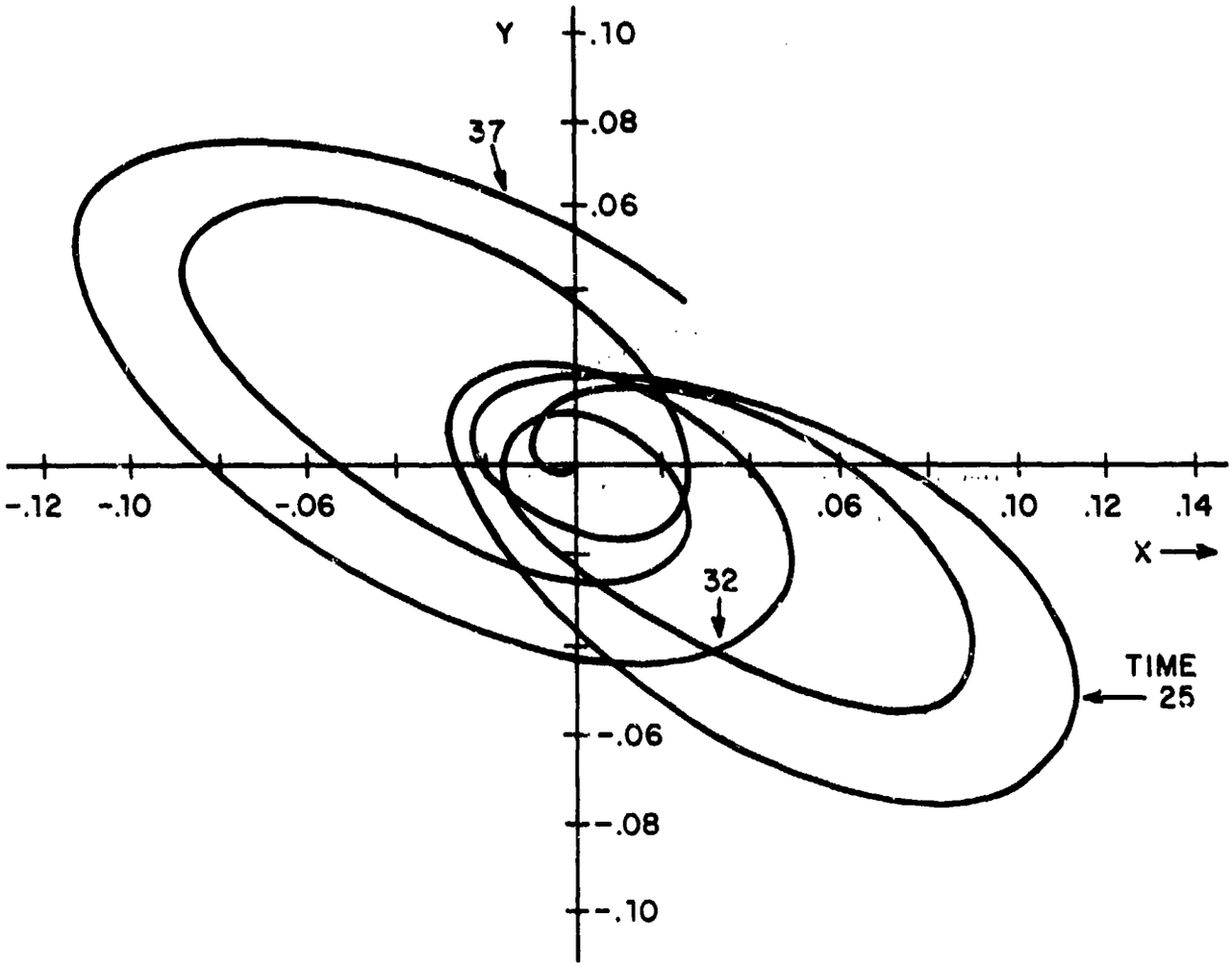

FIGURE 3

VERY RESTRICTED FOUR BODY PROBLEM
L4 LIBRATION POINT $\alpha = 0.$

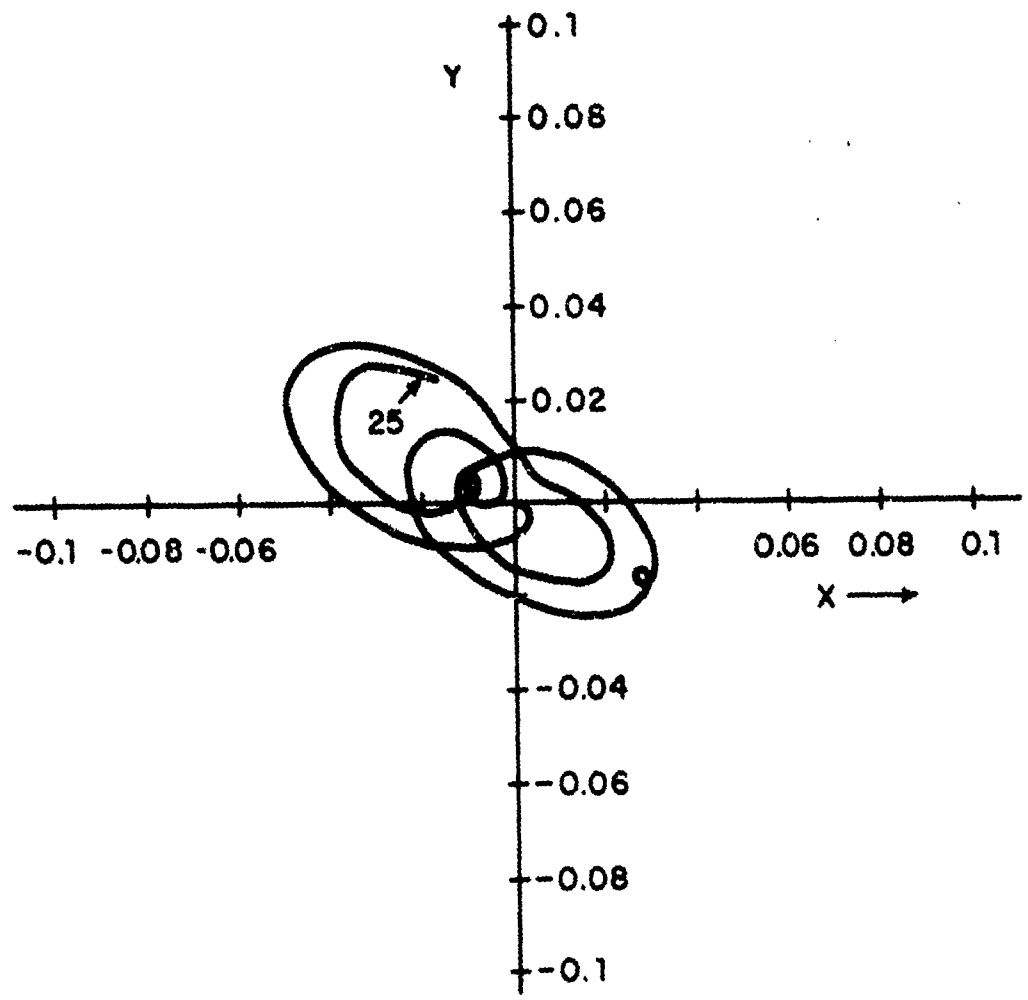

FIGURE 4

VERY RESTRICTED FOUR BODY PROBLEM
L4 LIBRATION POINT $\alpha = 135°$

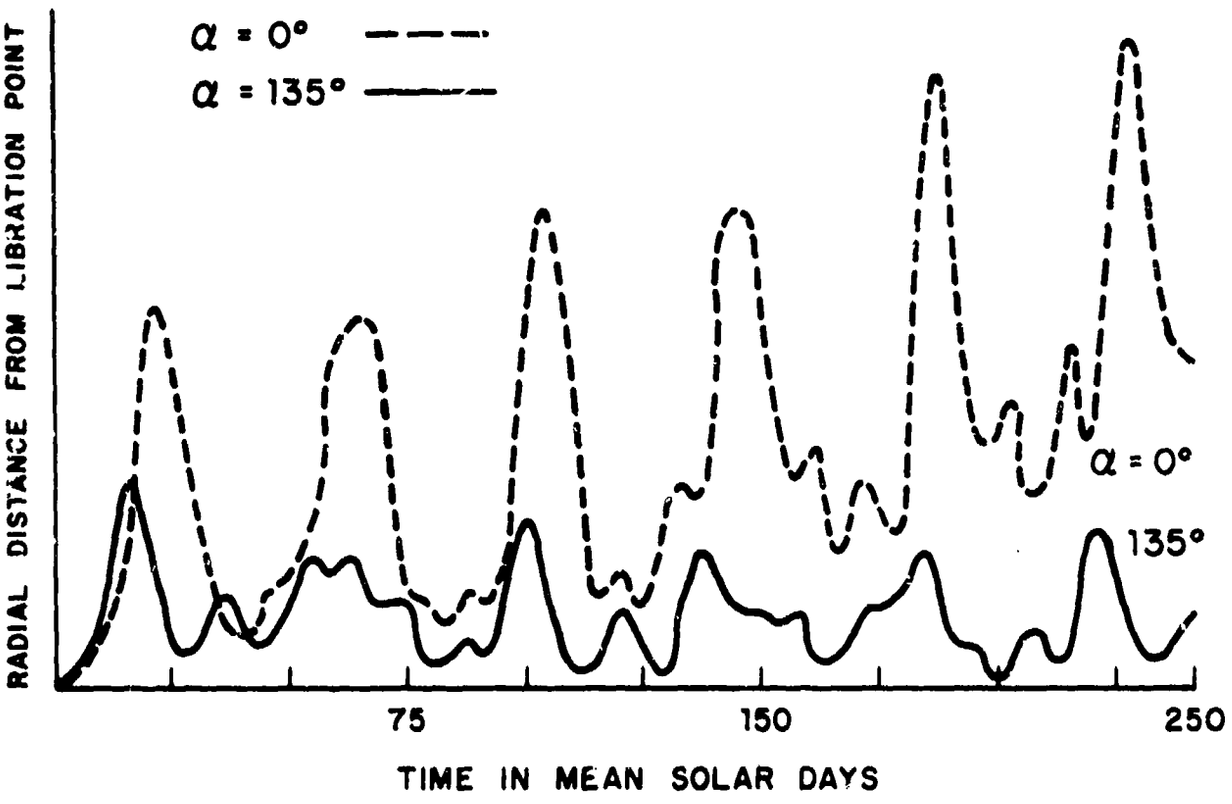

FIGURE 5. RADIAL DISTANCE VS. TIME

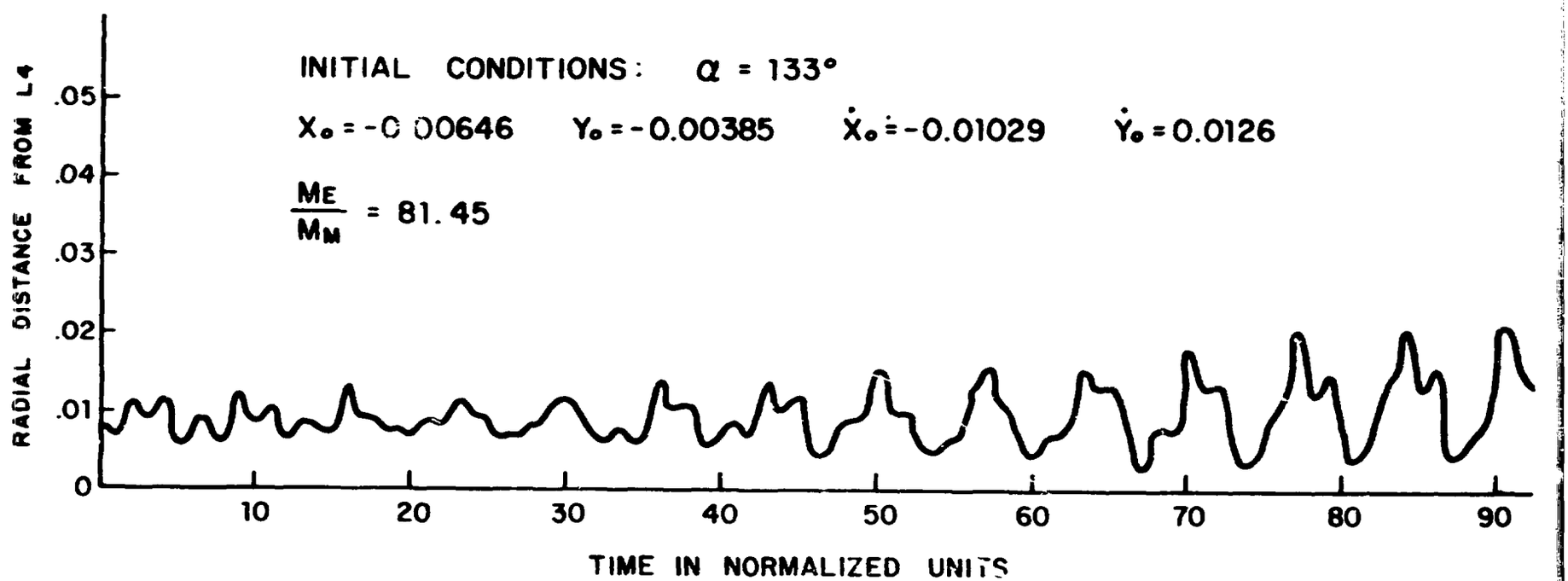

FIGURE 6. MINIMAL INITIAL CONDITIONS

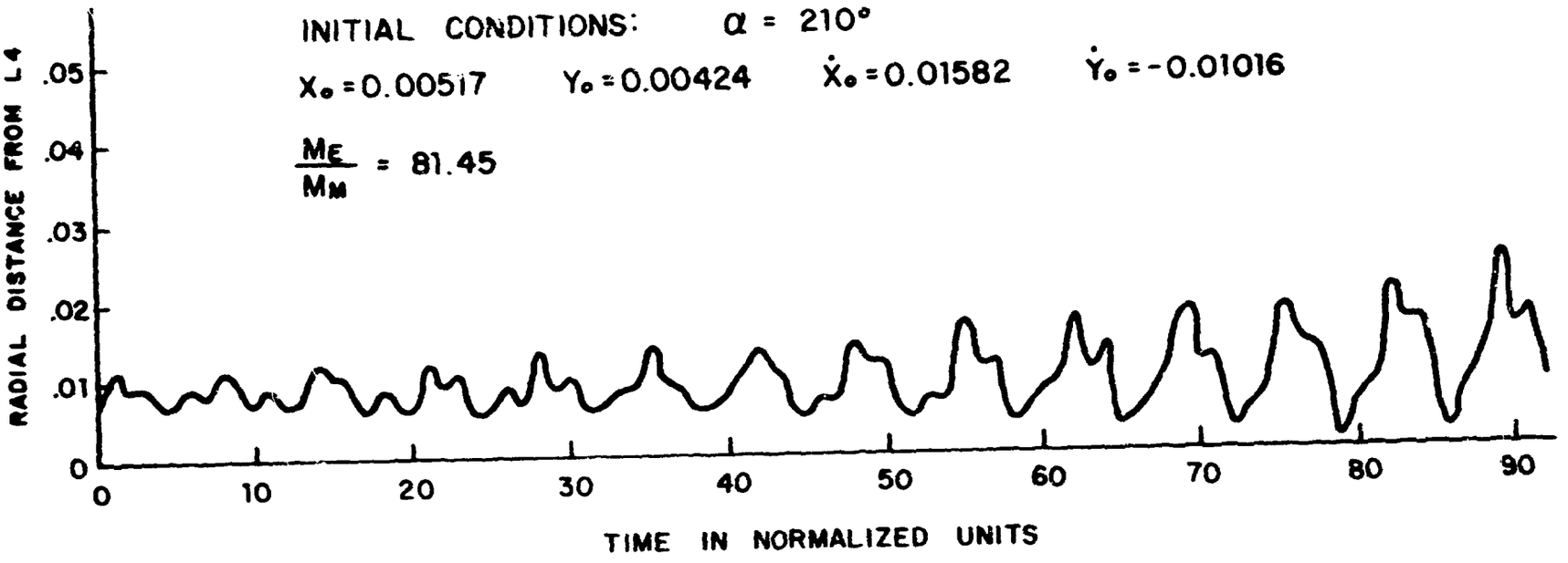

FIGURE 7. MINIMAL INITIAL CONDITIONS

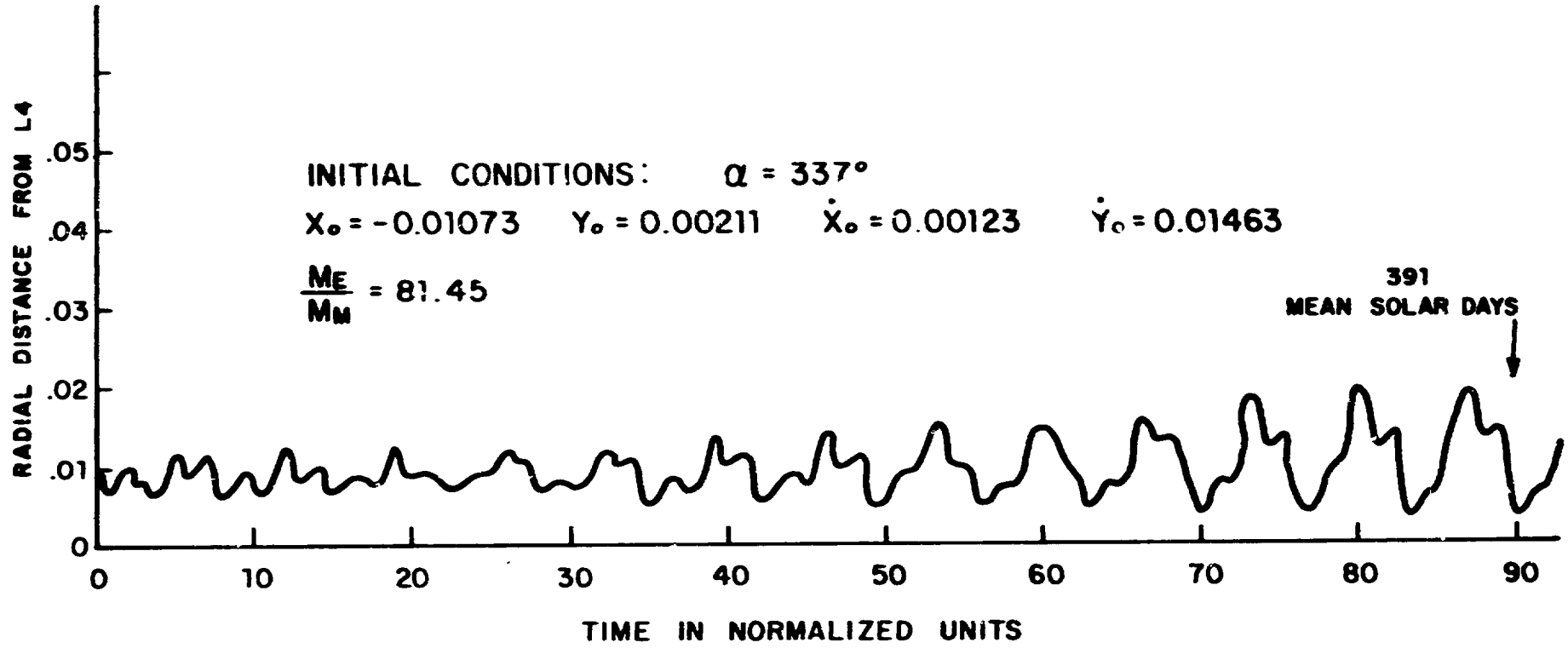

FIGURE 8. MINIMAL INITIAL CONDITIONS

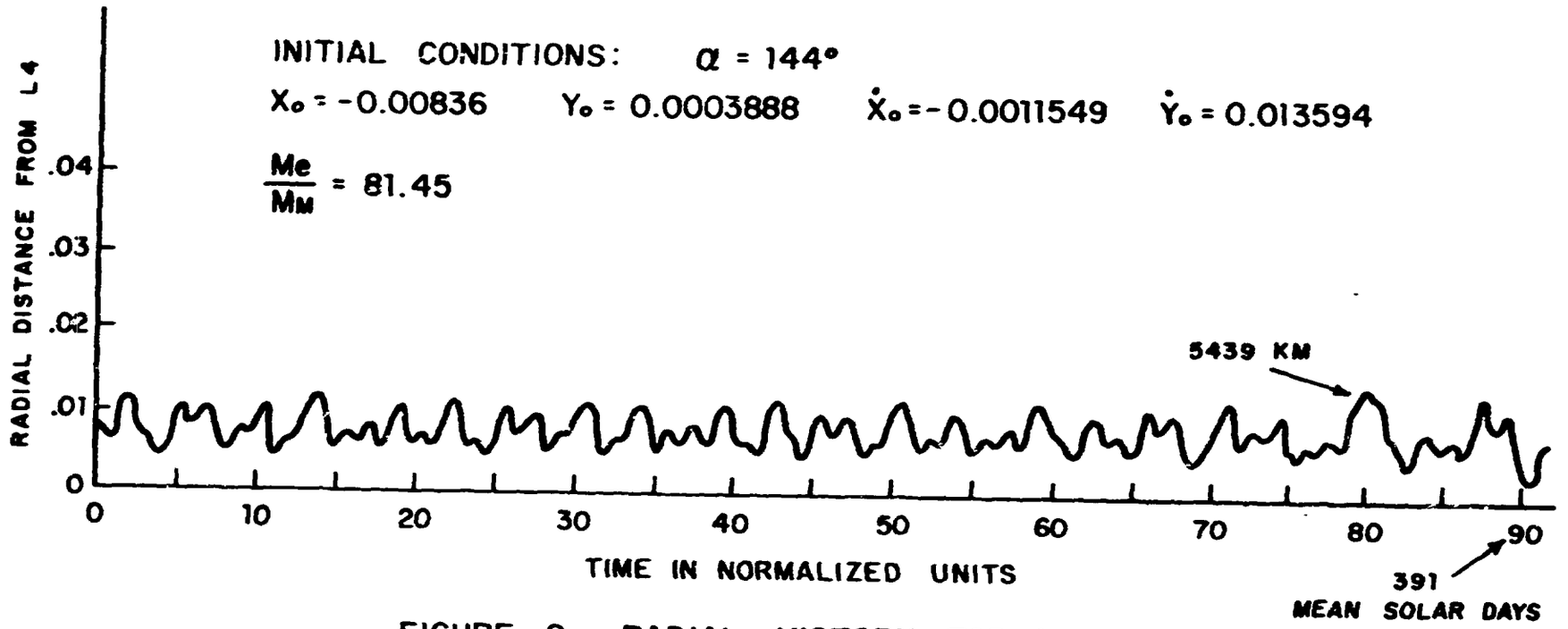

FIGURE 9. RADIAL HISTORY FOR MINIMAL $I_o C_o$

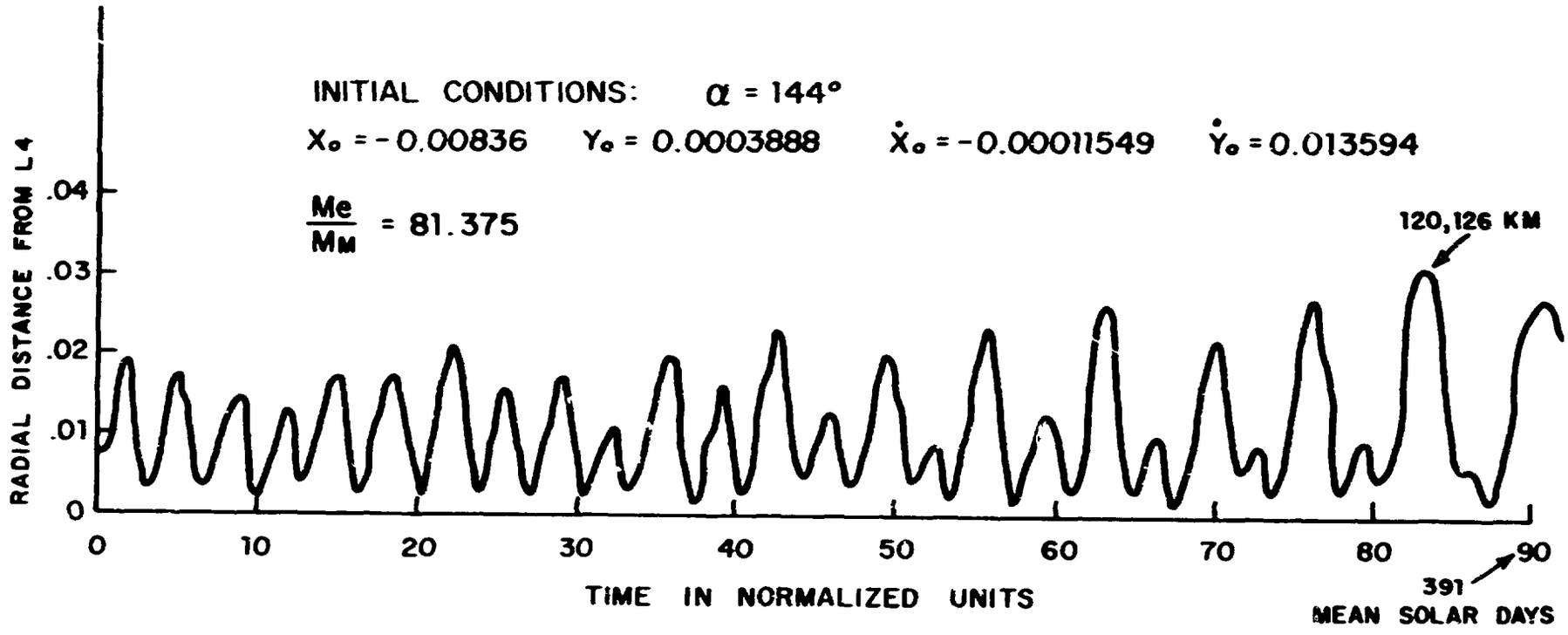

FIGURE 10. RADIAL HISTORY FOR Me/Mm = 81.375

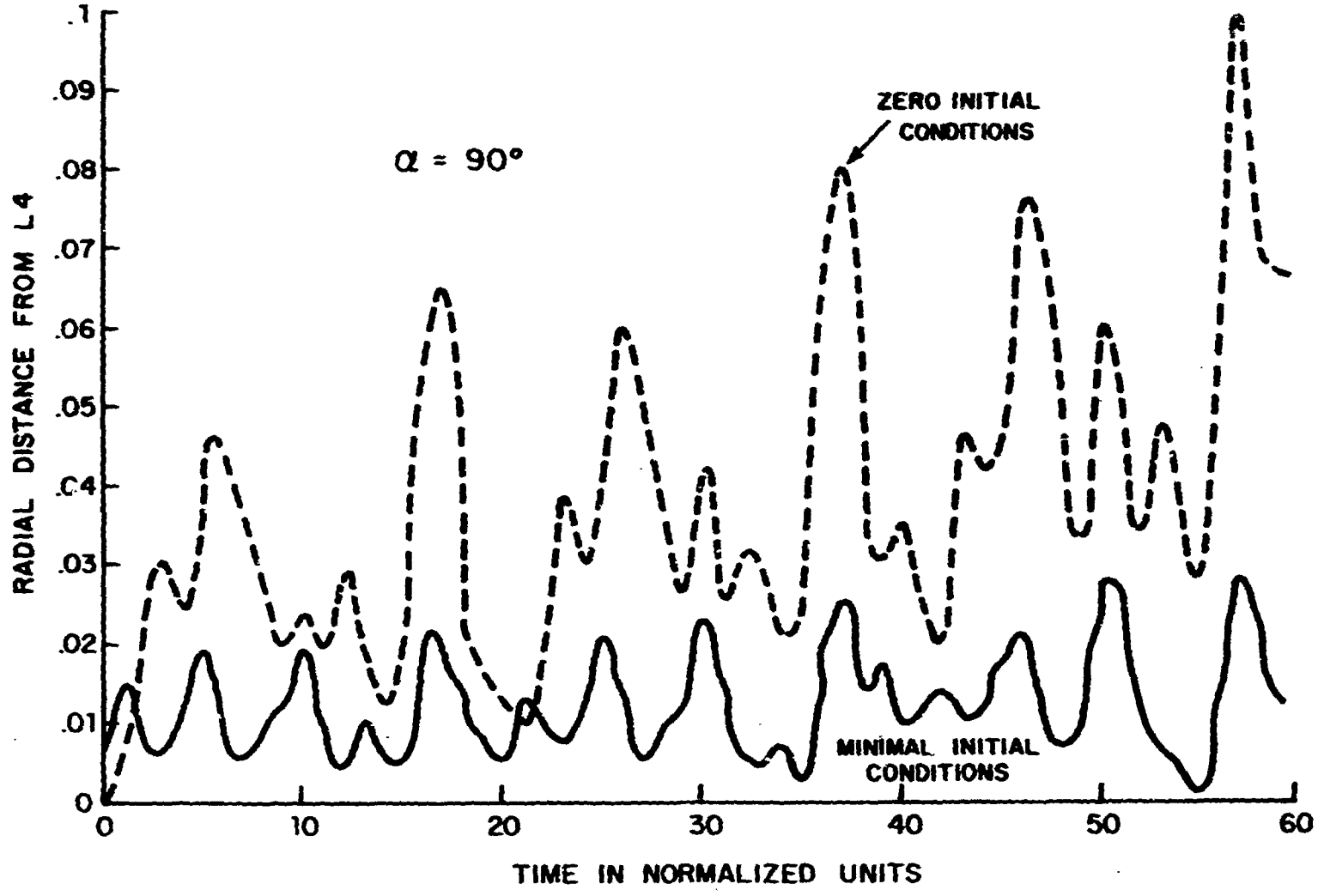

FIGURE 11. RADIAL REDUCTION WITH MINIMAL I.C.

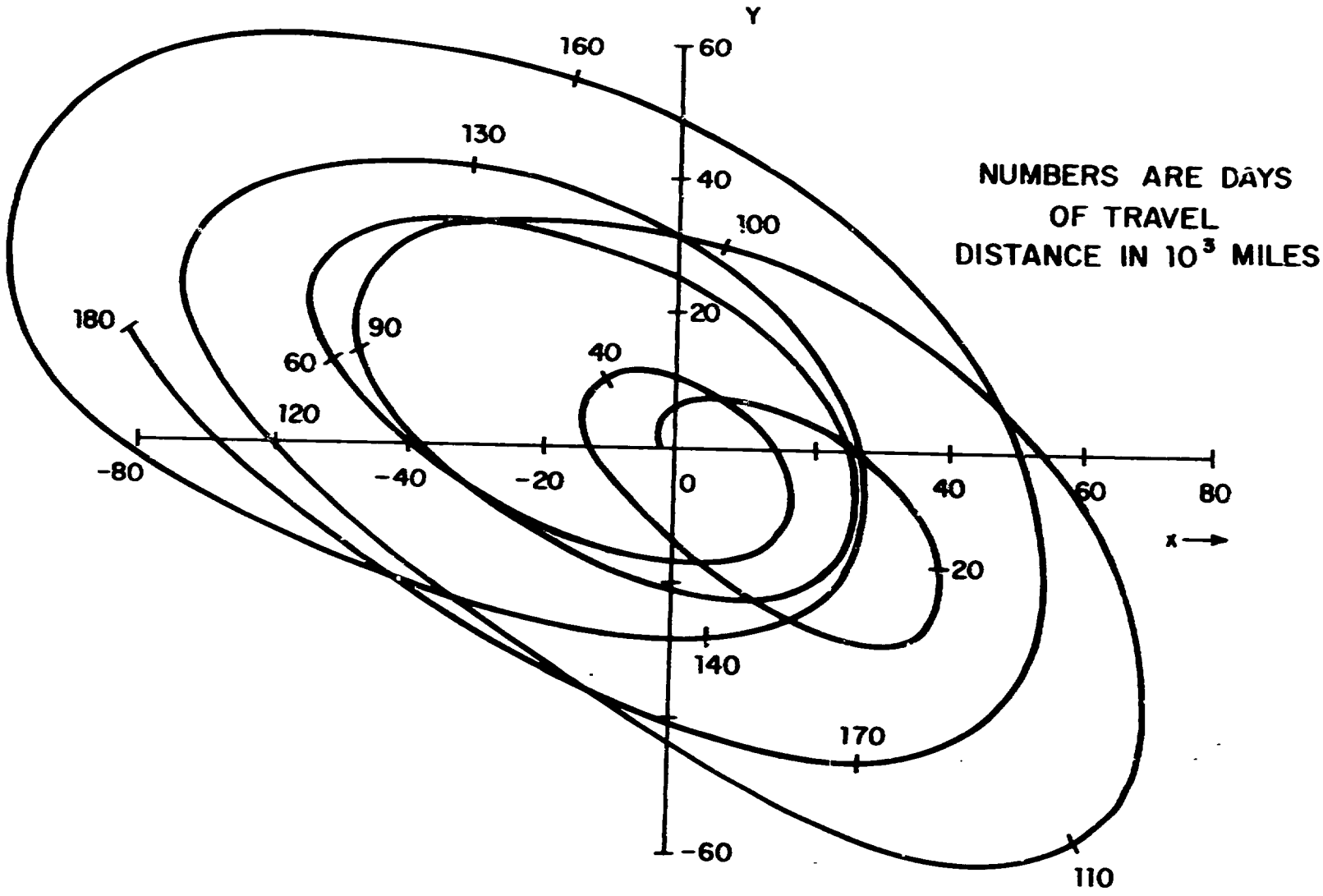

FIGURE 12 MOTION ABOUT L4 - t_o = JUNE 10, 1964 (NEW MOON).
(deVRIES AND PAUSON)

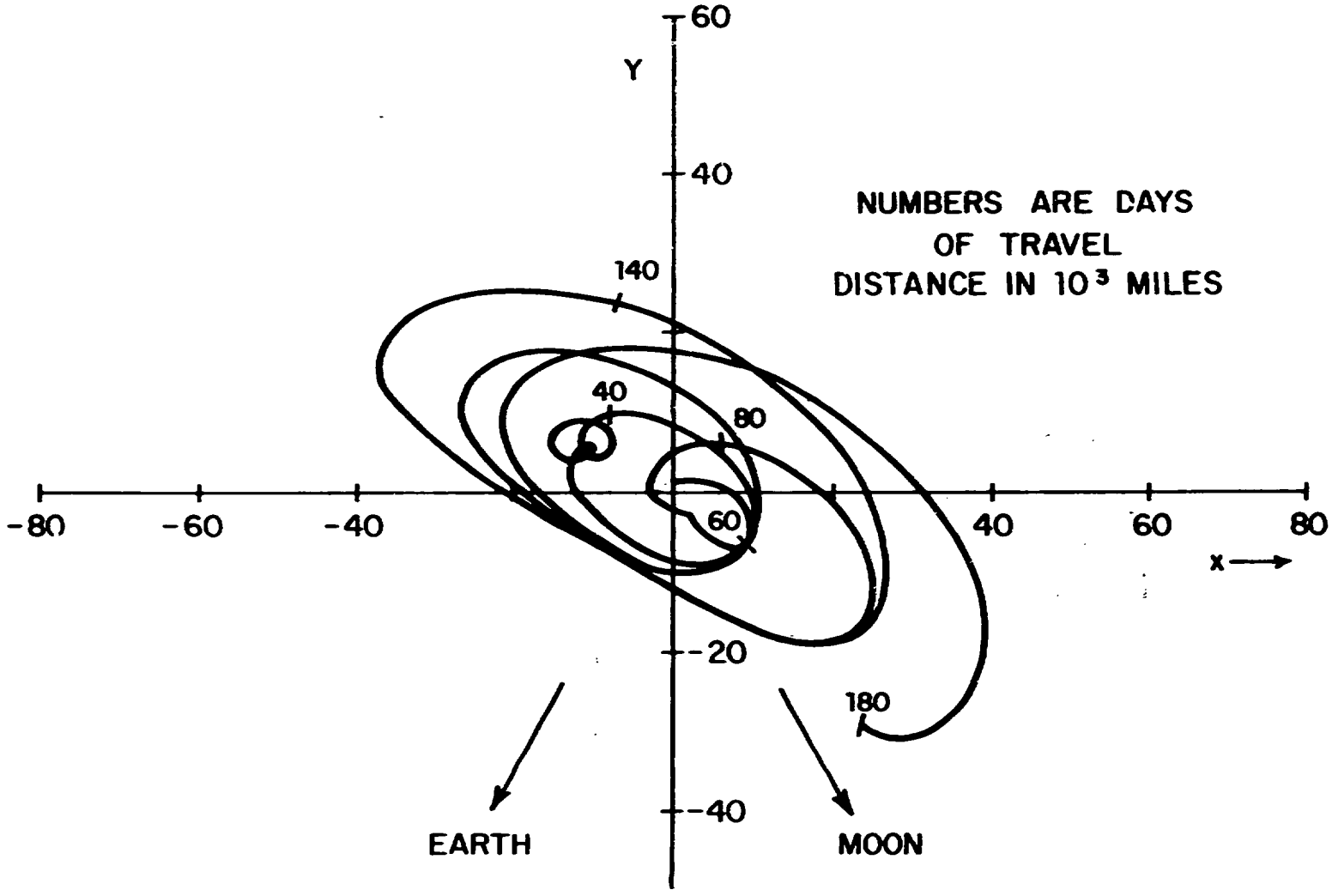

FIGURE 13 MOTION ABOUT L4 - t_o = JULY 2, 1964 (LAST QUARTER).
(de VRIES AND PAUSON)

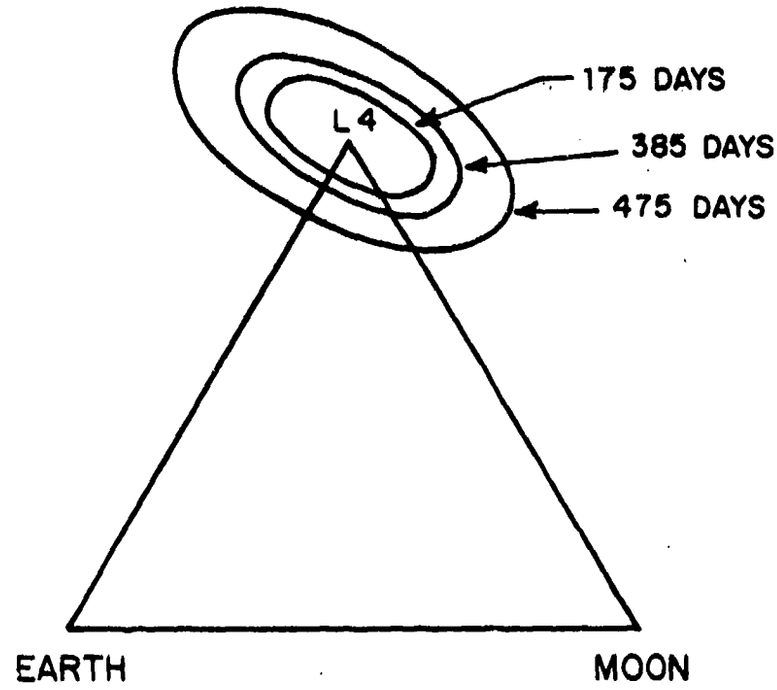

FIGURE 14

ENVELOPES OF TRAJECTORY IN FIGURE 13

LAUNCH: JULY 2, 1964 (LAST QUATER)

VELOCITY = MOONS VELOCITY.

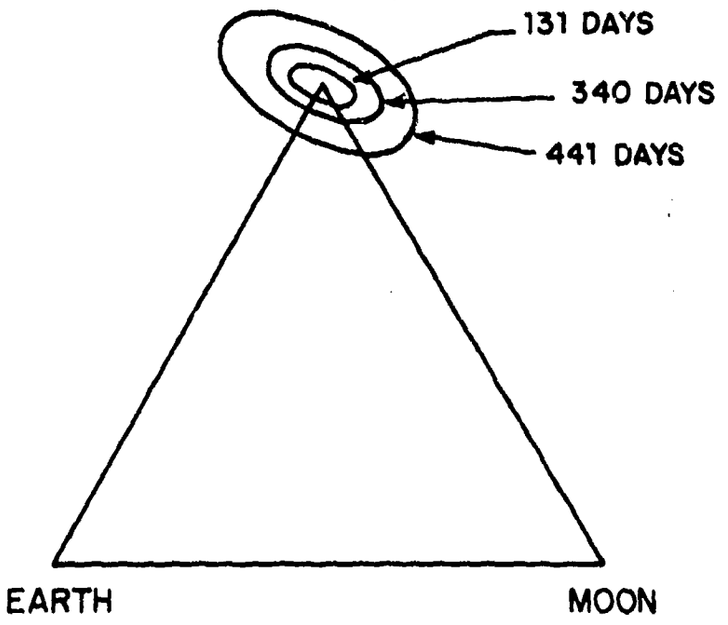

FIGURE 15

ENVELOPES OF REAL WORLD TRAJECTORY
LAUNCH: JULY 5, 1964
MINIMAL INITIAL STATE VARIABLES. (HIGHFILL)

AD P000343

THERMAL DISSOCIATION OF DIATOMIC MOLECULES

by

W. F. Bailey and A. Garscadden
Air Force Aero Propulsion Laboratory
Wright-Patterson Air Force Base, OH

A discrete collisional theory of dissociation under equilibrium and nonequilibrium conditions using a quantum kinetic approach to molecular energy transfer was investigated. The kinetic equations for molecular dissociation in a pure diatomic gas and diatomic gases in the presence of an inert diluent were formulated and solved. The incubation time was calculated and exhibited good agreement with experimental measurements. An analytic steady state form for the vibrational population and dissociation rate was developed which agreed with the time-dependent calculations. It was determined that rotational states play a significant role in the dissociation process and that the standard ladder model is inadequate. When rotational effects are properly included in the analysis, good agreement with experimental data is obtained.

This work was performed under AFAPL Work Unit No. 2301S212

Thermal Dissociation of Diatomic Molecules

W. F. Bailey, A. Garscadden

The topics of dissociation and energy transfer embrace many physical phenomena and have direct application to a wide variety of technical fields. Gas temperatures of a few thousand degrees Kelvin are encountered in the operating environment of re-entry vehicles, rocket engines, and hypersonic aircraft. The need for a detailed understanding of the processes and phenomena associated with these environments has spurred interest in the chemical kinetics of dissociation and recombination of molecules.

While numerous studies of energy transfer and dissociation in diatomic molecules have been made, recent measurements of dissociation (Refs 1, 2, 3) and relaxation rates (Refs 4, 5, 6, 7) indicate substantial deviations from previous theories. This study establishes a consistent, discrete collisional theory of thermal dissociation. A variety of gases is examined over a broad temperature range using both a time-dependent and steady-state analyses. Rotational effects have long been invoked as leading to enhanced dissociation, but few in-depth and extensive analyses have been performed. We, therefore, evaluate the contribution of the various degrees of freedom in modifying the collisional activation process and determine to what extent rotation alters the calculated dissociation rates.

The dissociation of diatomic molecule, A_2, can be represented as a simple collisional process

$$A_2 + M \underset{k_r}{\overset{k_d}{\rightleftarrows}} A + A + M \qquad (1)$$

The rate equation for the reaction (1) takes the form

$$\frac{d[A_2]}{dt} = \frac{-1}{2}\frac{d[A]}{dt} = -\left\{k_d[A_2] - k_r[A]^2\right\}[M] \qquad (2)$$

where the number densities of the particles have been denoted by their symbols. In predicting the dissociation reaction rates from the properties of the reacting molecules and/or atoms, one is concerned with the evaluation of the dissociation rate coefficient k_d. The recombination rate coefficient, k_r, is related to k_d through the law of mass action.

The physical system under consideration is that of a diatomic gas highly diluted in an inert gas, such as argon. We will model the dissociation of diatomic gases as observed under typical experimental conditions in shock tube studies. Under these conditions, the shocked gas is suddenly raised to a high temperature and maintained at constant volume. In our model analysis, chemical reactions other than dissociation and recombination will be excluded.

The dissociation process is governed by a set of coupled, nonlinear differential rate equations for each of the internal molecular states as well as the continuum. Formally each state population is governed by an equation

$$\frac{dN_l}{dt} = \sum_{i,j,k} R^{k,i}_{j,l} N_j N_k - \sum_{i,j,k} R^{l,k}_{l,j} N_l N_i \qquad (3)$$

where N_l is the concentration of molecules in state l, and the R's represent generalized rate coefficients for the population or depopulation of state l. This set of equations is commonly referred to as the Master Equation. In principle, the rate of molecular dissociation could be calculated by incorporating the detailed mechanics of the molecular collisions into the generalized rate coefficients and solving the resulting set of equation for each and every state. However, the aim in this analysis will be to obtain a simplified Master Equati while retaining only those physically important mechanisms required to understand and describe the process of dissociation. To that end, the following physically realistic assumptions were introduced: 1) the translational and rotational degrees of freedom are in complete Boltzmann equilibrium, 2) the molecules in each vibrational state are treated as separate species, 3) only single quantum vibrational exchanges occur, 4) the molecule is treated as a Morse oscillator rigid rotator system.

Much of the dissociation data from shock tube experiments has been obtained for gas mixtures in which various diatomic species are highly diluted in argon. This is an extremely simple physical situation from a collisional analysis viewpoint, in that collisional exchanges are limited to vibration-to-translation, V-T, exchanges with the argon buffer. Under these conditions, the Master Equation for a given vibrational state reduces to

$$\dot{N}_v = N_{v+1}\rho_{v+1,v} + N_{v-1}\rho_{v-1,v} - N_v(\rho_{v,v+1} + \rho_{v,v-1}) - N_v d_v \qquad v=0,1,\ldots,v^* \qquad (4)$$

with $\rho_{v+1,v}(\sec^{-1}) = ZMP_{v+1,v}$ = V-T transfer rate for v+1→v

$\rho_{v-1,v}(\sec^{-1}) = ZMP_{v,v+1}$ = V-T transfer rate for v-1→v

$d_v(\sec^{-1})$ = dissociation rate out of level v

Z represents the gas kinetic collision frequency, (cm^3 sec^{-1}), M the buffer gas number density (cm^3), and $P_{i,j}$ the VT exchange probability for a transition from state i to state j. The vibrational quantum number of the highest, bound vibrational state is denoted by v*.

For the case of a highly diluted gas mixture the formal solution of this linear set of coupled differential equations is well known, in terms of a series of exponentials in the eigenvalues (Ref 8). Numerical procedures can be utilized to determine the roots of the (v*+1)th order polynomial. However, we attack the general problem with a numerical integration of the rate equations. This time dependent approach is then complemented by two independent steady state analyses.

Recognizing the stiff nature of the set of simultaneous differential equations, we have selected the Gear (Ref 9) integration technique for their solution. This multistep, implicit, stiffly stable scheme utilizes a predictor-corrector technique to perform the integration. The predicting technique, ensuring stiff

stability, is coupled to a correcting scheme that utilizes the Jacobian to accomplish time step adjustment.

An analytic steady state solution of the coupled equations (Ref 10) yields

$$N_{v-1} = e^{\delta v}\left\{N_v + \sum_{i=v}^{v^*} \frac{[d_i - \alpha c]N_i}{\rho_{v,v-1}}\right\} \qquad (5)$$

with αc characterizing the self-similar form achieved by the vibrational distribution

$$\frac{\dot{N}_v}{N_v} = \alpha c = \text{constant} \qquad v = 0,1,\ldots v^* \qquad (6a)$$

$$\delta_v \equiv \beta(E_v - E_{v-1})$$

$$\beta \equiv (kT)^{-1}$$

E_v = energy associated with vibrational energy level v

k = Boltzmann's constant

T = gas temperature (6b)

Observe that the dissociation process causes the vibrational distribution to deviate from the equilibrium distribution. This deviation, termed dissociation induced vibrational depletion, results in a reduction in the dissociation rate below the value that would be obtained if equilibrium were maintained. The extent and character of this departure is dictated by the behavior of the summation term in (5). This term is controlled by the transfer rate, V-T, and the magnitude and bias of the dissociation rates, d . Equation (5) is a stable representation of the vibrational distribution amenable to rapid solution using iterative techniques. For a specified set of V-T rates and any distribution of dissociation rates, we can use the steady state form of (5) to calculate both the vibrational distribution and the steady state dissociation rate.

An alternate steady state solution, based on the approach of Nikitin (Ref 11) has been developed (Ref 10). This solution yields an analytic form for the dissociation rate and does not require iteration. However, no information regarding the vibrational distribution is obtained. This approach yields:

$$k_d = \frac{Z}{\sum_{i-1}^{v^*+1}\left\{\frac{e^{\beta E_i}}{\rho_{i,i-1}}\left[\sum_{s=0}^{i-1} e^{-\beta E_s}\right]\right\}} \qquad (7)$$

Having developed the formalism and numerical approaches required for time-dependent and steady-state solutions of the Master Equation, we introduce three models of collision induced dissociation. The time-dependent solution is then used to examine the temporal behavior of the dissociation process, assess the degree of vibrational dissociative coupling, and validate both steady state analyses.

All three dissociation models are based upon the ladder climbing model, the differences being in how rotational affects are treated. The essence of the ladder model of dissociation is the stepwise excitation of a molecule to a dissociating state. The activation of excited vibrational states is assumed to occur primarily through single quantum exchanges. Dissociation proceeds only from relatively high lying vibrational-rotational states.

The first model, the standard ladder model, has been used extensively in time-dependent and steady-state analysis of dissociation. The model can be understood by referring to Figure 1a which displays a typical potential energy diagram. Superimposed is the vibrational energy structure. During the relaxation process, the molecules are excited to higher and higher vibrational states and dissociate upon making a transition to the pseudolevel designated by the dashed line. Rotational structure is not considered in this model.

Figure 1b shows that the potential energy curves of a diatomic molecule actually depend on the rotational quantum number, J. The potential for J=0 is shown in the dashed curve. For the higher values of J, shown in solid lines, the potential well depth is reduced, and the minimum is shifted to a larger internuclear separation. In addition, a rotational or centrifugal barrier arises. This barrier is usually of sufficient height to result in the formation of one or more quasi-bound states which are metastable with respect to the normal dissociation limit for J=0.

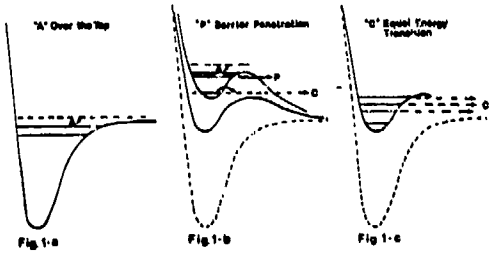

The two models describing rotational effects differ only with respect to the form of the assumed vibrational rotational coupling. The first rotational model, designated the uncoupled model, treats each J value as a distinct molecular species with its own vibrational ladder. In contrast, the second rotational model assumes that different rotational states are closely linked or strongly coupled to a given vibrational state. Under this model, designated the coupled model, dissociation proceeds from the last bound rotational state of every vibrational level.

When treating the rotational models, two types of vibrational-rotational transitions will be considered. These transitions, type A and type C, are the most efficient from an energy requirement standpoint and can be handled within reasonable computer storage requirements. An A type transition requires that the molecule surmount the rotational barrier, Figure 1a and 1b, while a C type transition is an equal energy transition (eet) involving the simultaneous reduction in J and increase in v. The C type process is not the same as barrier penetration, P, Figure 1b; it does have a similar effect. The rotational barrier is lowered below the final vibrational state and dissociational occurs. If this process is very efficient, it will proceed in a cascaded fashion to successively reduce the rotational barrier height leading ultimately to the effective disappearance of the barrier as depicted in Figure 1c. The importance of type C collisions, especially for heavy molecules, which was intuitively argued in the past (Ref 12), has been confirmed by recent trajectory calculations (Ref 13).

Prior to presenting a detailed rate/model comparison, we illustrate the typical time profiles of the molecular and atomic densities for a shock heated gas, Figure 2. We have adopted this data from the calculations of Fisher (Ref 14) and Bauer and Hilden (Ref 15). The solid lines represent the molecular and atomic densities. Superimposed on the plot is the unidirectional flux coefficient, k_d, where

$$k_d = \frac{\sum_{V=0}^{V^*} d_V N_V(t)}{\sum_{V=0}^{V^*} N_V(t)}$$

Note that the dissociation process can be divided into three characteristic time regimes: (1) the vibrational relaxation regime in which the molecule is "heated" through collisional energy exchanges and where insignificant dissociation occure, (2) the quasi-steaty-state regime (Q.S.S.) which onsets at the incubation time, τ_{inc}, (3) the chemical equilibrium regime where atomic and molecular concentrations have achieved their equilibrium values and state populations are Boltzmann.

The relaxation/excitation of the vibrational distribution and the temporal evolution of the dissociation reaction shown in Figure 3, were calculated through a numerical integration of the coupled vibrational rate equations using the SSH exchange rates as modified by Keck and Carrier (Ref 16) and fitted to the data of Millikan and White (Ref 17) and of Hancock and Smith (Ref 18).

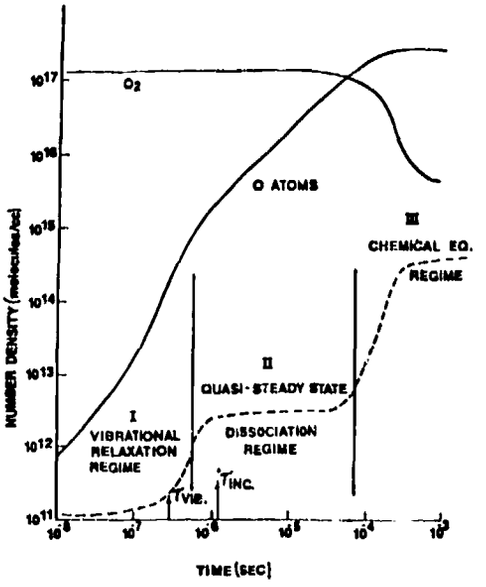

FIG. 2 Time Profiles and Uni-Directional Flux

These results established the existence of the quasi-steady-state vibrational distribution and validated the steady-state calculations. They also defined the extent of vibrational depletion resulting from vibrational dissociative coupling, and identified the associated incubation time. A comparison of the calculated incubation times with the experimental data of Watt (Ref 19) and Wray (Ref 20) is presented in Figure 4. The results have been normalized to an argon density of 1.28×10^{17} cm^{-3}. Good agreement is obtained from 3000°K to 10,000°K; however, at

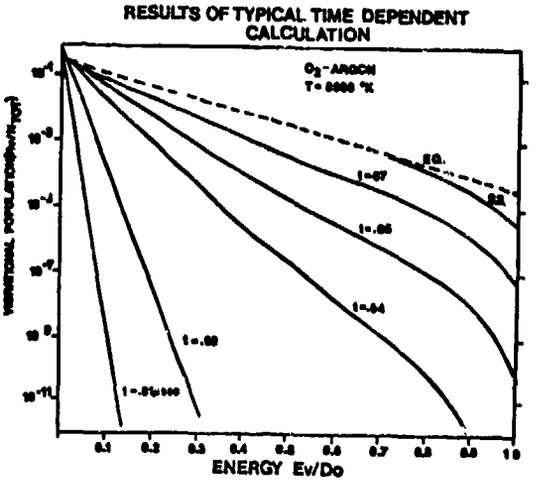

FIG.3 Time Dependent Results for O_2-Ar
$\left([O_2] = 2.67 \times 10^{16}\,cm^{-3},\ [Ar] = 2.67 \times 10^{18}\,cm^{-3}\right)$

higher temperatures the calculated incubation times were too long. This disparity may be attributed to the increased importance of multiple-quantum transitions at these temperatures. Wengle's analysis (Ref 21), dashed curve, establishes what may be considered to be an upper bound to the magnitude of the effect of these processes.

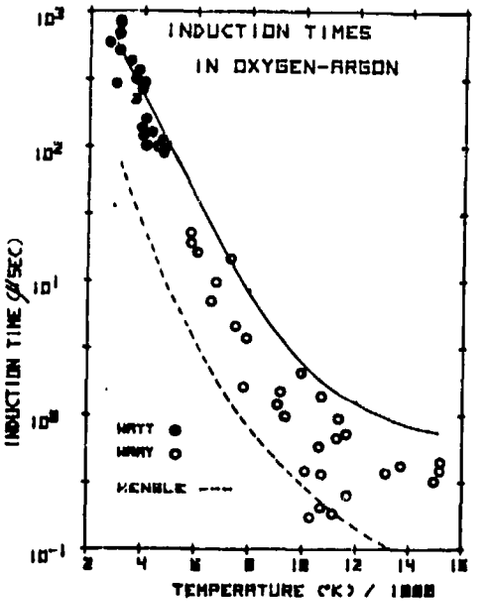

FIG. 4 Induction Times in O_2-Ar

Let us now compare the dissociation and recombination coefficients calculated for the three different models: 1) the standard ladder, 2) coupled rotational, 3) uncoupled rotational, to the experimental data for mixtures of a diatomic gas highly diluted in argon. Within the rotational models, the influence of the two types of vibrational rotational transitions, A and C, will be assessed. Calculations were performed for H_2, O_2, N_2, Br_2, CO, and I_2. The results presented here

for N_2 and I_2 are representative and illustrate the failure of the standard ladder model, the enhancement resulting from rotational effects, and the importance of equal energy transitions.

A comparison of experimental and theoretical values for N_2 is presented in Figure 5. The standard ladder, model L, is over a factor of 10 low. All of the rotational models: 1) coupled, Type C, CC; 2) coupled, Type A, CA; 3) uncoupled, Type C, UC; 4) uncoupled, Type A, UA; yield a rate enhancement and improved agreement with experiment. As the molecular weight of the diatomic gas increases the standard ladder results more severely underestimate the dissociation coefficient, being over a factor of 100 too low in Br_2 and I_2. The inclusion of equal energy transitions (type C) leads to a substantial enhancement of the dissociation rate. This is especially marked in I_2, Figure 6, where the rate constant is increased by almost an order of magnitude.

We conclude that the standard ladder model is inadequate, yielding rate coefficients that are unacceptably low. When rotational effects are included, better agreement with experimental data is obtained. The comparison becomes very good when equal energy transitions involving quasi-bound vibrational rotational levels are included.

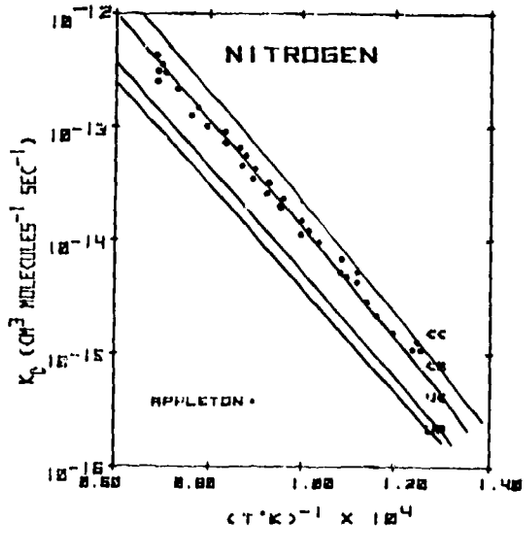

FIG.5 Arrhenius Plot of Nitrogen Dissociation

We have also examined the recombination coefficient, k_r, that would be inferred from the dissociation coefficient through the equilibrium constant. This aspect elucidates the pre-exponential temperature dependence of the dissociation coefficient and expands the temperature range for available data comparisons. When considering recombination, we will examine only the UA and UC models, since these models behaved similarly to the CC and CA models differing mainly in magnitude.

The predicted k_r's for N_2 and I_2 are compared with recombination coefficients inferred from high temperature dissociation rate measurements and direct rate measurements in Figures 7 and 8. The agreement obtained in N_2 is good. Figure 7 illustrates the comparison with the low temperature point measurements of Campbell and Thrush (CT), Ref 22, and Clyne and Steadman (CS), Ref 23, and the high temperature data of Appleton (A), Ref 24, Byron (b), Ref 25, and Cary, (C), Ref 26. Observe that at low temperatures, the UC

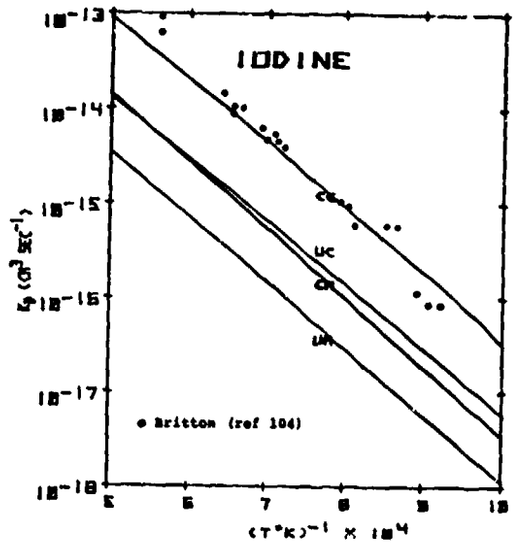

FIG.6 Dissociation of Iodine Diluted in Argon

curve, incorporating eet's, exhibits a stronger temperature dependence than the UA curve, and yields substantially better agreement with experiment. This behavior suggests the eet's play a major role in enhancing the reaction rate. The magnitude of this enhancement increases at lower temperatures. The predicted rate coefficients for I_2 confirm the eet trend established in N_2 and also evident in Br_2.

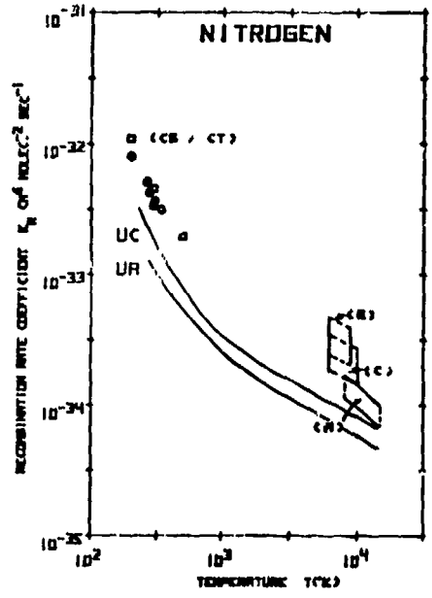

FIG. 7 N_2 Recombination Coefficient

Illustrated in Figure 8 are the point data of Porter and Smith, Ref 27, at low temperatures along with the data of Bunker, Ref 28. The high temperature data are those of Britton et al, Ref 29, and Troe, Ref 30. The eet rotational model not only yields a more reasonable magnitude for the rate coefficient but yields a temperature dependence consistent with the data over the entire temperature range.

To summarize, we have shown that the standard, and popular, ladder model is inadequate to describe

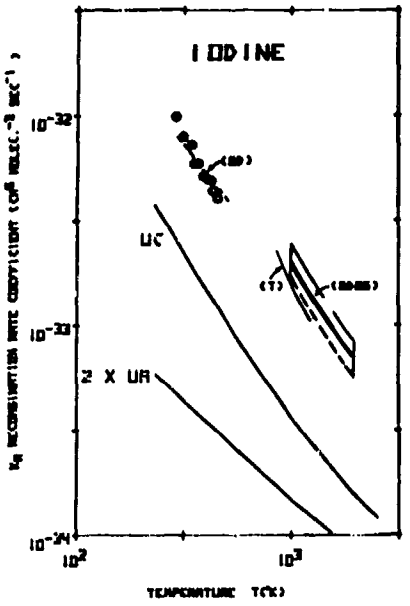

FIG.8 I_2 Recombination Coefficient

dissociation and recombination. The effects of rotation must be included. Our time dependent and steady-state analysis incorporating rotational effects and equal energy transitions give good agreement with experimental data at both high and low temperatures for a variety of gases. At very high temperatures (>10,000°K) it appears that multiquantum transitions begin to play a role. We observe throughout the recombination comparisons that the predicted temperature dependence is extremely good, especially when one considers the temperature range, rate scaling, and variety of gases considered. We conclude that our discrete collisional model accounts for the most important physical effects and permits a relatively simple and reliable computation of dissociation and recombination of diatomic gases for many situations of scientific and technical interest.

References

1. Breshears, W. D. and P. F. Bird. Symposium on Combustion 14th Univ. Park, D. A. (1973), p. 211; "Density Gradient Measurements of HCl Dissociation in Shock Waves." Journal of Chemical Physics, 58:5176 (1973).

2. Hanson, R. K. and D. Baganoff. "Shock Tube Study of Nitrogen Dissociation Using Pressure Measurements." AIAA Journal, 10:211 (1972).

3. Appleton, J. P., M. Steinberg, and D. J. Liquornik. "Shock Tube Study of Carbon Monoxide Dissociation Using Vacuum-Ultraviolet Absorption." Journal of Chemical Physics, 52:2205 (1970).

4. Millikan, R. C. and D. R. White. "Systematics of Vibrational Relaxation." Journal of Chemical Physics, 44:668 (1966).

5. Kiefer, J. H. and P. W. Lutz. "Vibrational Relaxation of Hydrogen." Journal of Chemical Physics, 44:668 (1966).

6. Breshears, W. P. and P. F. Bird. "Effect of Oxygen Atoms on the Vibrational Relaxation of Nitrogen." Journal of Chemical Physics, 48:4768 (1968).

7. Serry, D. J. "Vibrational Relaxation in HCl with Inert Gas Collision Partners." Journal of Chemical Physics, 58:1796 (1973).

8. Benson, S. W. The Foundations of Chemical Kinetics. New York: McGraw Hill (1960).

9. Gear, C. W. "The Automatic Integration of Stiff Ordinary Differential Equations." Communications in ACM, 14:176 (1971).

10. Bailey, W. F., "Collision Induced Dissociation of Diatomic Molecules," AFAPL-TR-78-105, November 1978.

11. Nikitin, E. E. "Theory of Thermal Second Order Decomposition of Molecules." Journal of Chemical Physics, 31:1371 (1959).

12. Bauer, S. H. and S. C. Tsang. "Mechanisms for Vibrational Relaxation at High Temperatures." Physics of Fluids, 6:182 (1963). Pritchard, H. O. "Reacting Kinetics." Vol. I. Specialist Periodical Reports. London: The Chemical Society (1975), pp. 243-290.

13. Wong, W. H. and G. Burne. "Dynamics of Collisional Dissociation: I_2 in Ar and Xe." Proceedings of the Royal Society, London, A, 341:105 (1974).

14. Kummler, R. H., E. R. Fisher, et al. "Analytical and Laboratory Studies on Upper Atmospheric Energy Transfer Processes." AFCRL-TR-73-0605, pp. 20-54 (1973).

15. Bauer, S. H., D. Hilden, and P. Jeffers. "Relative Roles of Ensemble Constraints vs Cross Sections in Hydrogen Dissociation." Journal of Chemical Physics, 80:922 (1976).

16. Keck, J. and G. Carrier. "Diffusion Theory of Nonequilibrium Dissociation and Recombination." Journal of Chemical Physics, 43:2284 (1965).

17. Millikan, R. C. and D. R. White. "Systematics of Vibrational Relaxation." Journal of Chemical Physics, 44:668 (1966).

18. Hancock, G. and I. W. M. Smith. "Quenching of Infrared Chemiluminescence. 1: The Rates of De-Excitation of CO ($4<v<13$) by He, CO, NO, N_2, O_2, OCS, N_2O, and CO_2." Applied Optics, 10:1827 (1971).

19. Watt, W. S. and A. L. Myerson. "Atom Formation Rates Behind Shock Waves in Oxygen." Journal of Chemical Physics, 51:1638 (1969).

20. Wray, K. L. "Shock Tube Study of the Coupling of O_2-Ar Rates of Dissociation and Relaxation." Journal of Chemical Physics, 37:1254 (1962).

21. Wengle, H. "Vibrational Relaxation and Dissociation of Diatomic Molecules." Zeitschrift Fur angewante Mathematik und Physik (SAMP), 26:377 (1975).

22. Campbell, I. M. and B. A. Thrush. "The Recombination of Nitrogen Atoms and the Nitrogen Afterglow." Proceedings of the Royal Society, A, 296:201 (1967).

23. Clyne, M. A. and D. Stedman. "Rate of Recombination of Nitrogen Atoms." Journal of Physical Chemistry, 71:307 (1967).

24. Appleton, J. P., M. Steinberg, and D. J. Liquornik. "Shock Tube Study of Nitrogen Dissociation Using Vacuum Ultraviolet Light Absorption." Journal of Chemical Physics, 48:599 (1968).

25. Byron, S. J. "Measurement of the Dissociation Rate of Oxygen." Journal of Chemical Physics, 44:1378 (1966).

26. Cary, B. Physics of Fluids, 8:26 (1965); K. L. Wray and S. Byron. "Shock Tube Study of the Thermal Dissociation of Nitrogen." Ibid, 9:1046 (1966); B. Cary, "Comments on 'Shock Tube Study of the Thermal Dissociation of Nitrogen.'" Ibid, 9:1047 (1966).

27. Porter, G. and J. A. Smith. "The Recombination of Atoms III. Temperature Coefficients of Iodine Atom Recombination." Proceedings of the Royal Society, A, 261:28 (1961).

28. Bunker, D. L. and N. Davidson. A Further Study of the Flash Photolysis of Iodine." Journal of the American Chemical Society, 80:5085 (1958).

29. Britton, D. L., N. Davidson, W. Gehman, and G. Schott. "Shock Waves in Chemical Kinetics: Further Studies on the Rate of Dissociation of Molecular Iodine." Journal of Chemical Physics, 25:804 (1956).

30. Troe, J. and H. G. Wagner. Zeitschrift Physik Chem, 55:326 (1967).

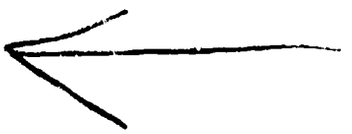

AD P000344

VIBRATION ANALYSIS OF A SPINNING DISK USING IMAGE DEROTATED HOLOGRAPHIC INTERFEROMETRY

by

J. C. MacBain, J. E. Horner, W. A. Stange
Air Force Aero Propulsion Laboratory
Wright-Patterson Air Force Base, OH

J. S. Ogg
Aeronautical Systems Division
Wright-Patterson Air Force Base, OH

The present work reports on the application of image derotated holographic interferometry to study the resonant response of a rotating steel disk at speeds up to 8000 RPM. The rotational motion of the disk is optically removed by passing the image of the rotating disk through a prism that is traveling at half the rotational speed of the disk. Off-axis double-pulsed laser holography is then used to record the disk resonant vibratory response. The first five diametrical modes and one complex mode of disk vibration are obtained at various RPM. The effects of disk imbalance, misalignment of optical and mechanical axes of rotation and system-excited modes of vibration are also addressed. Selected experimental results are compared to those obtained using finite element analysis.

Copyright 1979 Society for Experimental Stress Analysis. Reprinted with Permission.

Vibration Analysis of a Spinning Disk Using Image-derotated Holographic Interferometry

A disk rotating at speeds up to 8000 rpm is analyzed for its resonant modes of vibration as a function of rpm using pulsed-laser holography in conjunction with an image derotator

by J.C. MacBain, J.E. Horner, W.A. Stange and J.S. Ogg

ABSTRACT--This paper reports on the application of image-derotated holographic interferometry to study the resonant response of a rotating steel disk at speeds up to 8000 rpm. The rotational motion of the disk is optically removed by passing the image of the rotating disk through a prism that is traveling at half the rotational speed of the disk. Off-axis, double-pulsed, laser holography is then used to record the disk resonant-vibratory response. The first five diametrical modes and one complex mode of disk vibration are obtained at various rpm. The effects of disk imbalance, misalignment of optical and mechanical axes of rotation and system-excited modes of vibration are also addressed. Selected experimental results are compared to those obtained using finite element analysis.

Introduction

The structural dynamic response of bladed disks rotating at high speeds in turbomachinery has been an object of study beginning with the advent of the steam turbine.[1] Blade-disk structural dynamics plays a particularly important role in today's advanced turbine engines because of the emphasis on light-weight, high-strength bladed disks. The combination of light-weight disks and low-aspect-ratio blades greatly increases the chance for strong coupled blade-disk vibration phenomena, a type of vibratory response that is highly complex in nature and is often difficult to characterize using standard strain-gage techniques. This difficulty is due to the fact that strain-gage data are localized, being limited in number and area of coverage of the bladed-disk system. The vibration of such systems is highly complex and often nonsymmetric in nature.

A recently developed technique that shows great promise for studying the structural dynamic response of rotating objects, such as bladed disks, is image-derotated holographic interferometry. The technique consists of optically removing the rotational motion of a disk by passing the image of the rotating disk through a prism that is rotating at half the disk's angular velocity. The prism has the effect of causing the disk image to rotate in the opposite sense and at the same speed as the actual disk, thus cancelling out the rotational motion. Standard double-pulsed holographic interferometry can then be used to record the rotating disk's resonant response. The successful application of the image-derotator technique was first demonstrated by Waddell[2] when he carried out a photoelastic analysis on a spinning disk. In 1977, Stetson and Elkins[3,4] successfully developed and utilized a highly sophisticated image derotator to carry out holographic interferometry on a spinning disk. This study reports on the application of the image-derotator system designed built by Stetson and Elkins to the structural dynamic analysis of a disk rotating at speeds up to 8000 rpm.

An internally clamped annular disk was rotated at speeds ranging from 2000 to 8000 rpm while its resonant modes of vibration were excited using an electromagnet driven by an oscillator. Using the image derotator in conjunction with a double-pulsed ruby laser, the first five diametrical modes and one complex mode of vibration were determined for specified rotational speeds.

The resulting holographic interferograms were typically quite good in quality normally having 4 to 5 bias fringes across the unexcited disk surface, a bias fringe being representative of the optical and mechanical misalignment between the disk and derotator axes of rotation.

While the derotator operated quite well at high rotational speeds (approximately 8000 rpm), it was found that the electromagnetic excitation could be overpowered by the excitation forces generated by the disk drive motor and shaft rotordynamics, a phenomenon verified by spectrum analysis of the drive system. Hence, care had to be exercised in order to get pure disk mode shapes as opposed to modes excited by the rotor system.

The work represents a successful first-phase effort that will eventually be addressing coupled bladed-disk vibration phenomena.

Experimental Setup and Procedure

The experimental setup for carrying out image-derotated

J.C. MacBain, J.E. Horner and W.A. Stange are Project Engineers at the Air Force Aero Propulsion Laboratory, Turbine Engine Division, Wright-Patterson AFB, OH 45433. J.S. Ogg is a Project Engineer with the Aeronautical Systems Division, Structural Durability Division, Wright-Patterson AFB, OH 45433

Paper was presented at 1978 SESA Spring Meeting held in Wichita, KS on May 14-19

holographic interferometry on a rotating disk is shown in Fig. 1. The light from a Q-switched, double-pulsed, ruby laser (Apollo Model 22HD) is divided by a 50-50 beam splitter and illuminates the disk via a mirror system M_1, and, by virtue of the retroflective paint on the disk, is reflected back along the same path where it is reflected by the beam splitter through the derotator to the holographic film (Agva-Gevaert 10E75). The reference beam is reflected by the 50-50 beam splitter to Mirror M_2 and on to the holographic film via Mirror M_3.

It is important to note two factors[3] that affect the execution of holographic interferometry with this system. First, the reference beam does not pass through the derotator and, hence, remains linearly polarized throughout its travel. The object beam, on the other hand, undergoes a change in polarization because it passes through the image derotator. As noted by Stetson,[3] a half-wave retardation takes place as the object beam passes through the derotator. This is compensated for by converting the linearly polarized light to circular polarized light at the derotator entrance using a quarter-wave plate and then converting back to linearly polarized light at the derotator exit using a second quarter-wave plate. Secondly, while the image of the rotating disk is held stationary, the linearly polarized laser beam is not and, hence, rotates at the disk angular velocity relative to the derotated image of the disk. This could present a problem if the disk were allowed to rotate 90 deg between the two laser pulses. This was easily overcome in the present study by keeping the laser-pulse separation to less than 50 μs. This amounts to less than 3 deg of disk rotation at 10,000 rpm.

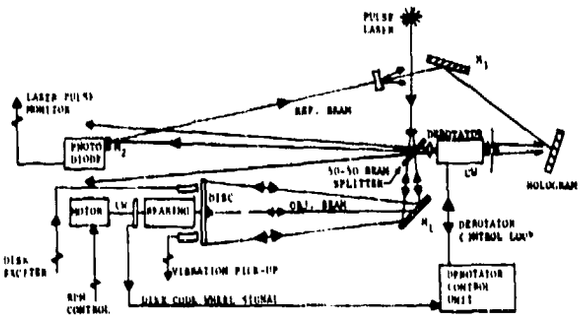

Fig. 1—Experimental setup for image-derotated holographic interferometry (CW—code wheel; M—mirror)

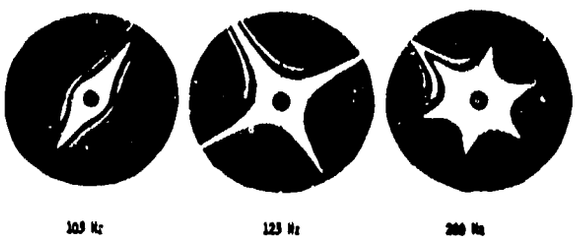

Fig. 2—Time-average holograms of resonant mode shapes 1N, 2N and 3N for the stationary disk

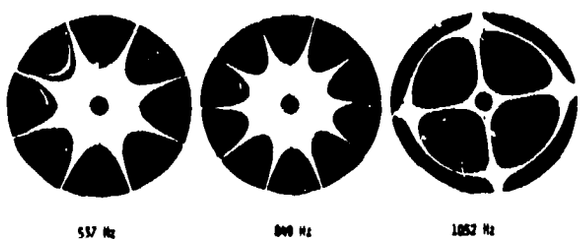

Fig. 3—Time-average holograms of resonant mode shapes 4N, 5N and (2N, 1S) for the stationary disk

The disk was driven by means of ¼ HP tool-post-grinder motor connected by a belt to a two-bearing internal grinding spindle. The disk was attached to one end of the spindle and the disk-code wheel to the other end. This drive system was more than adequate to achieve a true center of rotation of the disk, a requirement necessary in order to provide continuous alignment between the disk axis of rotation and the derotator optical axis of rotation. The rotational speed of the disk was controlled by means of a simple rheostat.

While the disk was either rotating or stationary, it was excited into one of its resonant modes of vibration by an electromagnet or siren (denoted as 'disk exciter' in Fig. 1) placed at some point on its outer circumference. A stationary vibration pickup, typically a capacitance probe, was placed near the disk's back face and used to detect the resonant condition. Upon detection of a resonant response, a holographic interferogram was made of the resonant-mode shape and its natural frequency and disk rpm were recorded. In this way, the disk's resonant response as a function of excitation frequency and rpm were determined.

Prior to recording double-exposure holograms of the disk resonant response under rotating conditions, a double-exposure hologram was taken of the rotating disk without any resonant excitation. This was done in order to check the optical-mechanical alignment between the disk and derotator axes of rotation. If the disk's mechanical axes of rotation are not collinear with the optical axis of the derotator, a double-exposure hologram will yield a raster of parallel fringes across the disk surface whose spacing is proportional to the misalignment of the two aforementioned axes of rotation. If the spatial frequency of this fringe spacing is of the same order as that of the normal-displacement fringes resulting from resonant excitation, a confusing double-explosure hologram will result. Hence, care was taken to properly align[4] the optical axis of rotation of the derotator with the mechanical axis

of rotation of the disk. With the system properly aligned, a double-exposure hologram of the rotating disk with no resonant excitation would typically have four or five parallel interference fringes across its surface. This degree of alignment was more than adequate to achieve distinctly defined resonant mode shapes under rotating conditions.

The disk in this study was made of 1018 cold-rolled steel, was .0625 in. (1.587 mm) thick, 10.0 in. (254.0 mm) in diameter, with a 1.0-in. (25.4-mm)-diam center hub that was 1.0 in. (25.4 mm) thick. The juncture between the center hub and disk surface was joined by an .0625-in. (1.59-mm)-radius fillet. The center hub had a .500-in. (12.70-mm)-diam hole bored in it for sliding onto the half-inch-diam shaft of the drive spindle. The disk was then butted up against the drive spindle lip by applying 100-in.-lb (11.3 N-m)-torque to a 3/8 in.-16 NC nut.

Experimental Findings and Analysis

In order to have a reference for the disk mode shapes obtained under rotating conditions, the first five diametrical modes of vibration, (1N, OS) through (5N, OS), and the second coupled mode of vibration (2N, 1S) for a stationary disk fixed at its center were determined by means of time-average holography. In classifying the different disk modes of vibration, 'N' refers to the number of nodal diameters and 'S' refers to the number of nodal circles not including the inner fixed boundary. Except when noted, the 'OS' part of mode notation shall be implied in what follows.

Figures 2 and 3 show the six resonant modes described above obtained using siren excitation and a standard off-axis holographic setup with a 50-mw HeNe laser (Spectra-Physics 125A). Because of the disk's high degree of radial symmetry, the nodal-line orientation was governed primarily by the location of the siren excitation. [The siren had a 1.0-in. (25.4-mm)-diam opening so that its point of excitement could be localized to approximately a 1.0-in. (25.4-mm)-diam circle]. Each mode of vibration actually consisted of two pairs of resonant frequencies and mode shapes; only one mode of each pair is shown in Figs. 2 and 3. The disk's normal displacement relative to its thickness was such that nonlinear effects could be avoided.

The mode pairs were essentially the inverse of each other with the nodal lines of one becoming the anti-nodal lines of the other. Their resonant frequencies were separated by .5 to 1.5 Hz. The small difference in the natural frequency for each mode pair is indicative of the high degree of radial symmetry present in the disk's mass and stiffness characteristics. In the case of a disk with perfect radial symmetry, it can be shown that each of the mode pairs will degenerate to a single-mode shape and corresponding resonant frequency.[4]

Before discussing the test results of the disk resonant response under rotation conditions, it is instructive to look at the equations describing disk resonant response under nonrotating conditions resulting from a nonrotating force varying sinusoidally in time, $P \cos \omega t$. The normal displacement, W, for a stationary disk vibrating in its nth diametrical mode shape can be represented by

$$W(\theta_0, t) = A \sin n\theta_0 \cos p_n t \qquad (1)$$

where p_n is the resonant frequency of the nth mode, θ_0 is the absolute angular coordinate, and A is the resonant amplitude. The resonant amplitude is some function of the disk radius, r, and is proportional to the magnitude of excitation force, P. Since eq (1) represents a disk resonance, $\omega = \pm p_n$.

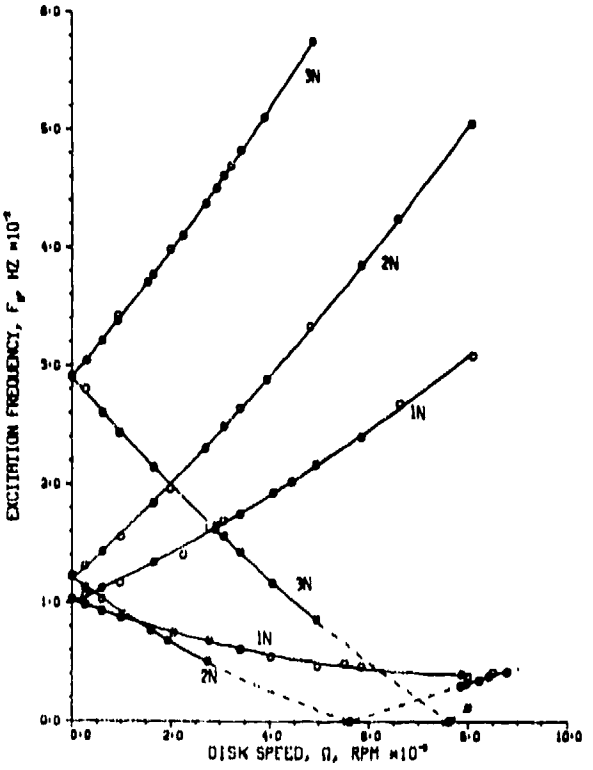

Fig. 4—Resonant-excitation frequency as a function of disk speed, modes 1N, 2N and 3N

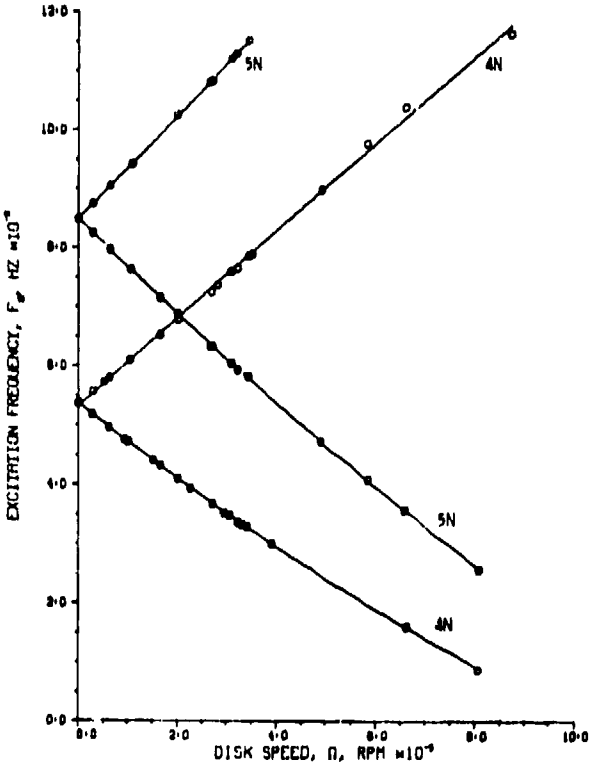

Fig. 5—Resonant-excitation frequency as a function of disk speed, modes 4N and 5N

Using a trigonometric identity, eq (1) can be put in the form

$$W(\theta_0, t) = \frac{A}{2}\sin(n\theta_0 - p_n t) + \frac{A}{2}\sin(n\theta_0 + p_n t) \tag{2}$$

Now for a disk rotating at an angular velocity, Ω, the absolute angular coordinate, θ_0, is related to an angular position on the disk, θ, by $\theta_0 = \theta - \Omega t$. Equation (2) thus becomes:

$$W(\theta, t) = \frac{A}{2}\sin[n\theta - (p_n + n\Omega)t] + \frac{A}{2}\sin[n\theta + (p_n - \Omega n)t] \tag{3}$$

Looking at eq (3), it is seen that for the case of a rotating disk, resonance occurs when the excitation frequency, ω, is such that $\omega = p_n \pm n\,\Omega$. Two excitation frequencies will excite the same resonant mode. In other words, at a specific disk speed, the 2N mode of vibration, for example, will be excited into resonance at two different excitation frequencies, one that is 2Ω greater than the 2N natural frequency and one that is 2Ω less than the 2N natural frequency. Figures 4 and 5 demonstrate this phenomenon for resonant modes 1N, 2N, 3N, and 4N, 5N, respectively. Shown in the figures is a plot of the frequency of an electromagnetic exciter required to generate a resonant disk mode as a function of disk speed. The data points represent a maximum response indication from a capacitance probe placed near the disk's back face (see Fig. 1, 'Vibration Pickup'). The curve joining each set of data points is a second-order least-squares fit. As discussed above, the upper curve for each mode of vibration is a plot of $p_n + n\,\Omega$ and the lower curve that of $p_n - n\,\Omega$. As the disk speed decreases to zero, the upper and lower branches of the excitation frequency converge to the corresponding resonant frequency for the stationary disk. The dashed lines in Fig. 4 represent extrapolated data and show the 2N and 3N modes crossing the abscissa at 5600 and 7600 rpm, respectively. At these points, a resonant mode can be excited by a static force. This would be a particularly dangerous region of operation for a turbine-engine disk since a circumferential variation in the existing pressure field could generate a resonant response. In terms of the so-called 'Campbell Diagram' used by turbine engine designers, these two points correspond to the disk speed at which the 2E and 3E engine orders of excitation (two and three static-pressure pulses per disk revolution) intersect the 2N and 3N disk resonant modes of vibration, respectively.

Figures 6 and 7 show the same disk resonant mode shapes that were obtained under stationary conditions (Figs. 2 and 3) obtained using image-derotated holographic interferometry at specified disk speeds. The mode shapes shown in the figures are double-exposure holograms made using the pulsed ruby laser with a pulse separation of 20 μs. It is seen that the fringe contrast is quite good and almost entirely proportional to disk out-of-plane displacement with very little distortion introduced from bias fringes caused by opto-mechanical misalignment. Each mode shape in Figs. 6 and 7 corresponds to some point on one of the excitation frequency-disk speed curves in Figs. 4 or 5. For example, the 5N mode shape in Fig. 7 was excited at 1193 Hz when the disk was rotating at 3910 rpm. This point lies on the upper branch of the 5N curve in Fig. 5. The actual natural frequency for the mode at this rpm would thus be:

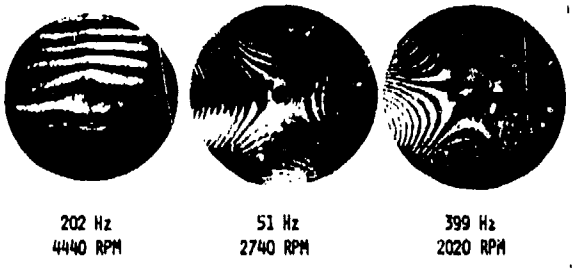

Fig. 6—Double-exposure holograms of disk modes 1N, 2N and 3N at specified excitation frequency and disk speed

Fig. 7—Double-exposure holograms of disk modes 4N, 5N and (2N, 1S) at specified excitation frequency and disk speed

Fig. 8—Distorted resonant disk mode at excitation frequency of 765 Hz and disk speed of 3210 rpm

$$P_s = \omega - 5\Omega = 1193 - (5)(3910)/60 = 867 \text{ Hz}.$$

This is an increase of 18 Hz over the 5N natural frequency for the nonrotating disk. Note that Fig. 7 shows the 4N mode shape obtained while the disk was running at 7920 rpm. The very minor contribution of bias fringes, i.e., the two fringes running approximately across the disk's diameter, demonstrates the stability of the system even at speeds near the upper design limit of the derotator (10,000 rpm).

Figures 6 and 7 show modes of vibration that are fairly pure in their nature, i.e., mode shapes characteristic of classical disk-vibration theory. Disk mode shapes were

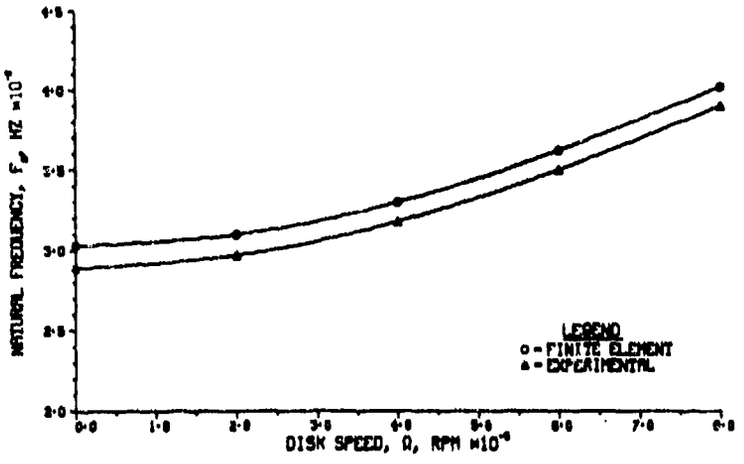

Fig. 9--Disk resonant frequency as a function of rpm or 3N mode

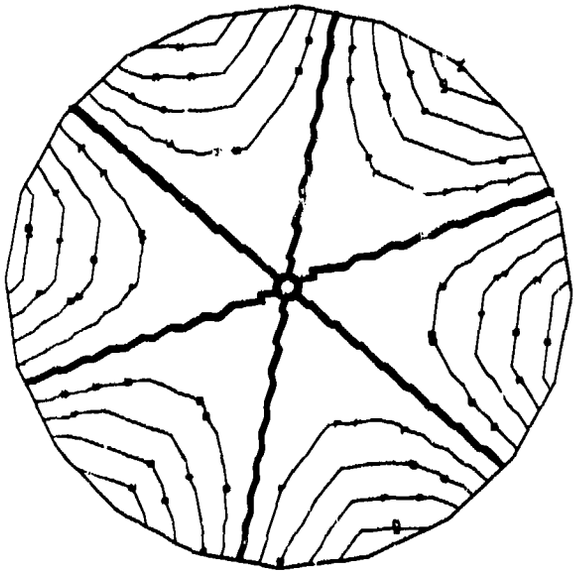

Fig. 10—Normal-displacement contour plot of disk finite-element model (3N mode)

also recorded that were apparently combinations of more than one resonant mode shape. This type of response would manifest itself as the symmetrical resonant mode shape being distorted, typically by the 1N mode shape. An example of this is shown in Fig. 8. This type of response was thought to be caused by an additional disk-excitation force resulting from rotor dynamic imbalance of the disk shaft. This phenomenon was subsequently verified by carrying out a power-spectral-density analysis of the vibration-transducer signal with and without disk excitation. The excitation component due to shaft imbalance was not found to present a problem provided that the amplitude of the electromagnetic excitation was made an order of magnitude larger than the force from the dynamic shaft imbalance. There was no added complication in increasing the electromagnetic-force amplitude since the laser-pulse separation could be decreased proportionally in order to avoid 'wash out' of the holographic fringes from too large a disk displacement.

Finite-element Model of Disk

A parallel study using finite-element analysis was carried out in order to provide an analytical check on the effect of centrifugal loading on the disk's resonant frequencies. The general-purpose finite-element computer program, NASTRAN (Rigid Format 13) was used to compute the natural frequencies and mode shapes of the disk. Figure 9 shows a plot of the disk 3N resonant frequency as a function of RPM. The experimental resonant frequencies lie approximately 4 percent below those computed from the finite-element model. This can be attributed to differences in boundary constraints imposed on the finite-element model and the experimental disk. The numerical solution assumed constraints in all six degrees of freedom around the inner circumference resulting in a very 'stiff' model. The disk used in the experiment was constrained by an integral hub whose circumference matched that of the finite-element model. However, it is probable that some deflections occurred around the hub, thus changing the system's stiffening characteristics and resulting in natural frequencies slightly lower than the numerical calculations. This boundary effect would be even greater for the lower modes because fewer nodal lines pass through the hub, allowing more deflections to occur in an area which is assumed rigidly constrained in the finite-element model. Figure 10 shows the 3N mode shape generated by NASTRAN. The figure presents a contour plot of the mode shape's normal displacement. The contour lines having a value of zero and, thus, representing the nodal lines for the 3N mode, have been highlighted.

Discussion and Conclusion

The purpose of this paper was to report on the first phase of a research effort addressing the dynamic structural response of rotating disks, the eventual goal being that of studying bladed-disk assemblies under controlled laboratory conditions. Emphasis was placed on: (a) the description and application of image-derotated holographic interferometry; and (b) the graphic results that can be obtained with the technique. Bearing this in mind, it is noted that the detailed physical characteristics of the disk mode

Fig. 11— Time-average holograc. complex mode shape of a small bladed disk

shapes recorded under rotating conditions require a much more detailed analysis than was possible within the confines of this paper. For example, while Figs. 6 and 7 show clearly defined disk modes of vibration, they do not provide information as to the motion of the modes relative to the disk rotation. Are the modes fixed in the disk and, hence, rotating with it; are they stationary in inertial space with the disk rotating through them; or is their relative movement some combination of the two cases? The derotator and pulsed laser combination permits disk mode shapes to be recorded under any of these conditions as one can verify by sketching a series of sinusoidal wave trains that are traveling around the disk and then looking at the increment of normal displacement occurring on the disk's surface in the 20 μs separating the two laser pulses. It is highly likely that the last condition, that of relative rotational motion between the rotating disk and resonant mode shape, is what actually occurs and what was recorded in the holograms shown in Figs. 6 and 7. Stetson[3] found this condition to be the case when he made a triple-pulsed interferogram of a rotating disk. This hypothesis is also supported by the results of a series of tests where the same mode shape was consecutively recorded in a series of interferograms while keeping the disk rpm and vibration-excitation amplitude constant. The resulting nodal lines of the mode shapes did not seem to be fixed in the disk or in inertial space. Tobias[6] carried out a detailed study of the vibration characteristics of elastically imperfect rotating disks and analytically demonstrated the presence of a spatial phase change in the disk mode shape as the rotating disk passes through a resonant point. He also emphasized the very complicated nature of rotating-disk vibration characteristics.

The above questic ·d others still need to be addressed in order to provide . ased assurance as to the structural integrity of bladed-disk resonant structural response. While rotating disk vibration phenomenon is complex in itself, the addition of blades to the structure adds even further complication to the problem. This fact is demonstrated by Fig. 11 which shows a complex mode shape of a nonrotating bladed disk obtained using time-average holography. The astute observer will recognize a form of the 5N mode shape of a solid circular disk in the figure. The questions posed above and the complex vibratory behavior exemplified by Fig. 11 will be addressed in future phases of the present research effort with the aid of image derotated holographic interferometry.

References

1. Campbell, W.E., "The Protection of Steam-Turbine Disc Wheels from Axial Vibration," presented ASME Meeting, Cleveland (May 1924).

2. Weddell, P., "Strain Pattern Examination," Engrg. and Mats. Design, 17 (3) (1973).

3. Stetson, K.A., "The Use of Image Derotation in Holographic Interferometry and Speckly Photography of Rotating Objects," EXPERIMENTAL MECHANICS, 18 (2), 67-73 (Feb. 1978).

4. Stetson, K.A. and Elkins, J.N., "Optical System for Dynamic Analysis of Rotating Structures," Air Force Aero Propulsion Lab. Contract F33615-75-C-2013, AFAPL-TR-77-51 (Oct. 1977).

5. Zenneck, J., "Uber die freien Schwingungen nur angenahernd vollkommener kreisformigir Platten," Annal der Physik, 67, 167 (1889).

6. Tobias, S.A. and Arnold, R.N., "The Influence of Dynamical Imperfection on the Vibration of Rotating Disks," Proc. Inst. Mech. Engrs., 171, 669-690 (1957).

AD P000345

STATISTICAL EXPERIMENTAL DESIGNS IN COMPUTER AIDED OPTIMAL AIRCRAFT DESIGN

by

K. S. Nagaraja
Air Force Flight Dynamics Laboratory
Wright-Patterson Air Force Base, OH

Ram B. Ram
Department of Mathematics, State University of New York
Oneonta, New York

A review of the statistical experimental designs which are relevant to the selection process of the design variables is made. Although several aerospace industries still use Latin Square techniques, the inherent shortcomings of the approach are not recognized. Optimal aircraft designs which are derived from such a deficient method become suspect, and reliability and cost saving can both become unattainable. An alternate approach, called D-optimal design, which has several advantages due to its reliability and efficiency, is discussed.

The statistical design techniques which have great usefulness in the computer aided design of systems such as aircraft made a great deal of impression on the imagination of Hans von Ohain. His interest and support in this area not only provided much inspiration to the work performed at AFFDL, but also demonstrated the extraordinary openess of his mind to many new and innovative ideas which he cherishes with great interest and enthusiasm.

This work was performed under AFFDL Work Unit No. 24041024 in 1978.

STATISTICAL EXPERIMENTAL DESIGNS IN COMPUER AIDED OPTIMAL AIRCRAFT DESIGN

by

K. S. Nagaraja

Air Force Flight Dynamics Laboratory
Wright-Patterson Air Force Base, OH

and

Ram B. Ram
State University of New York
Oneonta, New York

Computer aided aircraft designs involve consideration of several airframe, propulsion and mission related variables. Such engine or propulsion system variables as cycle pressure ratio, turbine temperature, engine bypass ratio, engine size, engine thrust to weight ratio, etc. together with airframe variables such as wing loading, wing aspect ratio, leading edge sweep, wing cross sectional characteristics, etc. constitute the design variables. Mission variables which the designer will be required to work with can be range, take-off gross weight, payload, fuel consumption, etc. Computer aided design will consider relevant engine and airframe variables, and by appropriate application of aircraft performance evaluation codes, the designer will arrive at several configurations which then is narrowed down to optimal design configuration capable of fulfilling the mission requirements. Constraints may be imposed on the variables in order to reflect the limits which the design conditions may impose.

The number of design variables and combinations thereof which the designer will have to deal with may be so large that even with the available computer capabilities, evaluation of the performance parameters as well as the task of

optimizing the configuration may (and usually will) become mathematically cumbersome and prohibitive. The time required for carrying out the computations will be very expensive, and oftentimes the procedure will be generating lots of data points that may prove to be unnecessary.

If all possible combinations of applicable design variables are chosen - and this leads to a large number of aircraft designs - the designer will be overspecifying the requirements for carrying out a regressional analysis and establishing functional relationships between engine and airframe design variables and performance characteristics. A common practice among aerospace companies has been to obtain quadratic polynomial approximations to the functional relationships and use these approximations in lieu of the more expensive computer programs while performing their design optimizations and trade studies.

The approximations are obtained by using first a screening procedure for generating an acceptable subset of the design vectors (each design vector being defined by one combination of the values of the design variables). The screening is done both by an application of an appropriate statistical experimental design and by an imposition of structural and other aircraft design requirements, if any.

In the statistical screening of the design vectors, several aerospace industries and other systems design engineers have been generally using the Latin square design methodlogy (central composite designs have also been used; however, the Latin square approach requires fewer computer runs.).

Recent research has indicated that the use of Latin square can yield poor approximations, and that there exist statistical experimental designs which yield better approximations using no more than 60% of the computer runs required by Latin squares. These statistical experimental designs are

known as D-optimal designs. This report gives an analysis of these statistical design methods and show how D-optimal designs can serve effectively the needs of computer aided aircraft design methods.

Flow chart of the several operations which comprise the aircraft design cycle is given below.

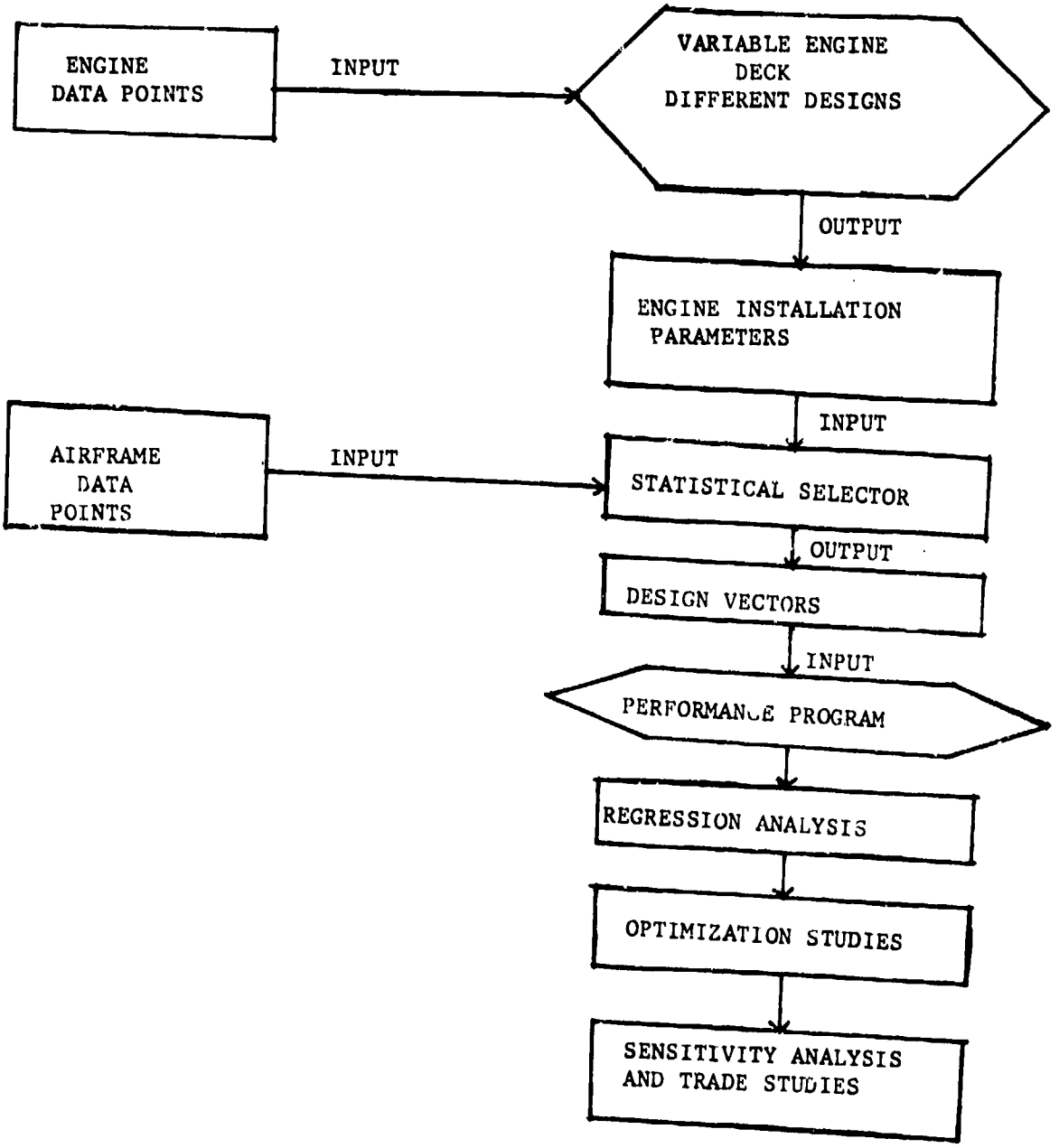

Aircraft design variables are represented by independent variables $\underline{\xi} \equiv \xi_1, \xi_2, \ldots, \xi_n$, and the functional relation $y_K = f_K(\underline{\xi})$ represents aircraft performance or response parameter $(K = 1, \ldots, N)$.

Taylor series expansion of the function f around the point $\underline{\xi} = \underline{\omega}$ where $\underline{\xi} = \omega_1, \ldots, \omega_n$ is given by

$$f_K(\underline{\xi}) \simeq f_K(\underline{\omega}) + \sum_{i=1}^{n} (\xi_i - \omega_i) \left.\frac{\partial f_K(\underline{\xi})}{\partial \xi_i}\right|_{\underline{\xi} = \underline{\omega}} + \sum_{i=1}^{n}\sum_{j=1}^{n} (\xi_i - \omega_i)(\xi_j - \omega_j) \left.\frac{\partial^2 f_K(\underline{\xi})}{\partial \xi_i \partial \xi_j}\right|_{\underline{\xi} = \underline{\omega}} \quad (1)$$

Independent variables are normalized in the range (-1, + 1):

$$x_i = \frac{\xi_i - \frac{1}{2}(\xi_{i,max.} + \xi_{i,min.})}{\frac{1}{2}(\xi_{i,max.} - \xi_{i,min.})}$$

Therefore, $x_i \in [-1, +1]$,

and $$\xi_{i,min.} \leq \xi_i \leq \xi_{i,max.}$$

The unknown function y_{JK} can be written as

$$y_K = b_o + \sum_{i=1}^{n} b_i x_{Ki} + \sum_{i=1}^{n}\sum_{j=1}^{n} b_{ij} x_{Ki} x_{Kj} + \varepsilon_K, (K = 1, \ldots, N) \quad (2)$$

where the co-efficients b_o, b_i and b_{ij} can easily be sorted out from equation (1). An error term ε is also introduced. This term arises due to the approximation in fitting the estimated responses with the quadratic expression.

In matrix notation, equation (2) is represented by

$$\underline{Y} = \bar{\underline{X}}\,\underline{b} + \underline{\varepsilon}$$

where $\underline{Y} \equiv (y_1 \;\; y_2 \;\; \cdots \;\; y_N)'$ (3)

$$\bar{\underline{X}} \equiv [\phi(\underline{x}_1) \;\; \phi(\underline{x}_2) \;\; \cdots \;\; \phi(\underline{x}_N)]'$$

$$\phi(\underline{x}_k) = (1 \;\; x_{k1} \;\; x_{k2} \;\cdots\; x_{kn} \;\; x_{k1}^2 \;\; x_{k1}x_{k2} \;\cdots\; x_{kn}^2)$$

$$\underline{b} = (b_0 \;\; b_1 \;\cdots\; b_n \;\; b_{11} \;\; b_{12} \;\cdots\; b_{nn})'$$

and $\underline{\varepsilon} = (\varepsilon_1 \;\; \varepsilon_2 \;\cdots\; \varepsilon_N)'$

(Note the dashed superscript indicates that the transpose of the matrix is being considered actually).

For example, vector elements of $\phi(\underline{x}_k)$ when substituted in the expression for $\bar{\underline{X}}$ give the matrix

$$\bar{\underline{X}} = \begin{bmatrix} 1 & x_{11} & x_{12} & \cdots & x_{1n} & x_{11}^2 & x_{11}x_{12} & \cdots & x_{1n}^2 \\ 1 & x_{21} & x_{22} & \cdots & x_{2n} & x_{21}^2 & x_{21}x_{22} & \cdots & x_{2n}^2 \\ \cdots & \cdots & \cdots & \cdots & \cdots & \cdots & \cdots & \cdots & \cdots \\ \cdots & \cdots & \cdots & \cdots & \cdots & \cdots & \cdots & \cdots & \cdots \\ \cdots & \cdots & \cdots & \cdots & \cdots & \cdots & \cdots & \cdots & \cdots \\ \cdots & \cdots & \cdots & \cdots & \cdots & \cdots & \cdots & \cdots & \cdots \\ 1 & x_{N1} & x_{N2} & \cdots & x_{Nn} & x_{N1}^2 & x_{N1}x_{N2} & \cdots & x_{Nn}^2 \end{bmatrix} \quad (4)$$

The number of coefficients in the quadratic polynomial and hence the number or columns in $\bar{\underline{X}}$ is $\tilde{K} = \frac{(n+1)(n+2)}{2}$.

The $N \times \tilde{K}$ matrix $\bar{\underline{X}}$ is called the experimental design matrix. Also $\underline{b}$ is a $\tilde{K} \times 1$ vector of unknown parameters to be estimated, and ε is an vector of errors with mean zero and variance σ^2.

The error sum of squares, in matrix notation is:

$$\underline{\varepsilon}'\underline{\varepsilon} = (\underline{Y} - \bar{\underline{X}}\,\underline{b})'(\underline{Y} - \bar{\underline{X}}\,b)$$

$$= \underline{Y}'\underline{Y} - 2\underline{b}\,\bar{\underline{X}}'\underline{Y} + \underline{b}'\bar{\underline{X}}'\bar{\underline{X}}\,\underline{b} \qquad (5)$$

The least square estimate of $\underline{b}$ is the value $\hat{\underline{b}}$ which minimizes $\underline{\varepsilon}'\underline{\varepsilon}$. This is determined by differentiating with respect to $\underline{b}$, and setting the resultant matrix equation equal to zero, and at the same time replacing $\underline{b}$ by $\hat{\underline{b}}$. This provides the normal equations

$$(\bar{\underline{X}}'\bar{\underline{X}})\hat{b} = \bar{\underline{X}}'\underline{Y} \; . \qquad (6)$$

If the $\tilde{K}$ normal equations are independent, $\bar{\underline{X}}'\bar{\underline{X}}$ is non-singular, and its inverse exists. In this case, the solution of the normal equations can be written as

$$\hat{\underline{b}} = (\bar{\underline{X}}'\bar{\underline{X}})^{-1}\,\bar{\underline{X}}'\underline{Y} \qquad (7)$$

This requires that $\bar{\underline{X}}$ has at least $\tilde{K} = \frac{(n+1)(n+2)}{2}$ rows. A design matrix is saturated if it has exactly $\tilde{K} = \frac{(n+1)(n+2)}{2}$ rows, and the row vectors are linearly independent.

The solution $\hat{\underline{b}}$ has the following properties:

1. It is an estimate of $\underline{b}$ which minimized the error sum of squares $\underline{\varepsilon}'\underline{\varepsilon}$ irrespective of any distribution properties of the error.
2. The elements of $\hat{\underline{b}}$ are functions of the observations $y_1, \ldots, y_N$, and provide unbiased estimates of the elements of $\underline{b}$ which have the minimum variances irrespective of the distribution properties of the error.

3. If the errors are independent and $\underline{\varepsilon} \sim N(\underline{0}, I\sigma^2)$, then $\hat{\underline{b}}$ is the maximum likelihood estimate of $\underline{b}$. For a fixed value of σ, maximizing the likelihood function is equivalent to minimizing the quantity $\underline{\varepsilon}'\underline{\varepsilon}$. This fact provides a justification for the least squares procedure (i.e., for minimizing the sum of squares of errors).

Since the primary purpose of obtaining $\hat{\underline{b}}$ is to estimate the response $y(\underline{x})$ for a given design vector $\underline{x}$, we define the estimated response $\hat{y}(\underline{x})$ at $\underline{x}$ by

$$\hat{y}(\underline{x}) = \phi(\underline{x})\underline{b} .$$

Since $\hat{\underline{b}}$ is, in general a random variable, so is the estimated response. The variance of this response if given by

$$V[\hat{y}(\underline{x})] = \sigma^2 \phi(\underline{x})(\bar{\underline{x}}'\bar{\underline{x}})^{-1}\phi'(\underline{x}) .$$

If χ denotes the experimental design region, then the design problem consists of selecting design vectors $\underline{x}_i (i = 1, \cdots N)$ from the n - dimensional region χ such that the design defined by these N vectors is, in some defined snese, optimal.

In the case of the linear surface fit (e.e., the regression is carried out with a linear model), the response surface is given by

$$y_j = b_0 + \sum_{i=1}^{n} b_i x_{ji} + \varepsilon_j , \qquad (8)$$

and this can be expressed in the matrix notation as

$$\underline{Y} = \underline{x}\,\underline{b} + \underline{\varepsilon} \qquad (9)$$

where

$$\underline{X} = \begin{bmatrix} 1 & x_{11} & \cdots & x_{1n} \\ 1 & x_{21} & \cdots & x_{2n} \\ \cdot & \cdot & \cdots & \cdot \\ \cdot & \cdot & \cdots & \cdot \\ \cdot & \cdot & \cdots & \cdot \\ 1 & x_{N1} & \cdots & x_{Nn} \end{bmatrix}, \quad \underline{Y} = \begin{bmatrix} y_1 \\ y_2 \\ \cdot \\ \cdot \\ \cdot \\ y_N \end{bmatrix}, \quad \underline{b} = \begin{bmatrix} b_0 \\ b_1 \\ \cdot \\ \cdot \\ \cdot \\ b_N \end{bmatrix}, \quad \underline{\varepsilon} = \begin{bmatrix} \varepsilon_1 \\ \varepsilon_2 \\ \cdot \\ \cdot \\ \cdot \\ \varepsilon_N \end{bmatrix}.$$

This information matrix M is

$$M = \underline{X}'\underline{X} = \begin{bmatrix} N & \sum_{j=1}^{N} x_{j1} & \sum_{j=1}^{N} x_{j2} & \cdots & \sum_{j=1}^{N} x_{jn} \\ \sum x_{j1} & \sum x_{j1}^2 & \sum x_{j1}x_{j2} & \cdots & \sum x_{j1}x_{jn} \\ \sum x_{j2} & \sum x_{j2}x_{j1} & \sum x_{j2}^2 & \cdots & \sum x_{j2}x_{jn} \\ \cdot & \cdot & \cdot & \cdots & \cdot \\ \cdot & \cdot & \cdot & \cdots & \cdot \\ \sum x_{jn} & \sum x_{jn}x_{j1} & \sum x_{jn}x_{j2} & \cdots & \sum x_{jn}^2 \end{bmatrix} \qquad (10)$$

The variances are given

$$V(b_0) = \frac{\sum \underline{X}_i^2}{|\sum \underline{X}'\underline{X}|}\,\sigma^2 \qquad (11a)$$

$$V(b_1) = \frac{n\sigma^2}{|\underline{X}'\underline{X}|} \qquad (11b)$$

$$V(b_p) = \frac{\sigma^2}{N}\left(1 + \frac{Q}{|\underline{X}'\underline{X}|}\right) \qquad (11c)$$

$$|\underline{X}'\underline{X}| = \omega_{pp} A_{pp} - \sum_{i} \sum_{j} \omega_{pi}\omega_{pj} A_{ij;pp} \quad (p=0,1,\ldots,\tilde{K}) \quad (i,j) \neq p$$

$$= \omega_{pp} A_{pp} - Q \,, \tag{11d}$$

Q being a positive definite form obtained from the matrix elements, and N being the number of experimental runs.

Minimum variance, therefore, requires that the value of the determinant be maximized. Indeed, when the determinant is maximized, the diagonal terms are the only non-zero terms in the matrix. In fact, even Q becomes zero. (Detailed discussion of several of these aspects will be made in a later report).

We assume that maximization of the determinant $|\bar{X}'\bar{X}|$ plays a similar role in the case of the quadratic response surface model.

We note that in the case of the linear regression model, if the design variables are functionally independent, then the information matrix $[\bar{X}'\bar{X}]$ is non-singular and the model coefficients b_i have the smallest variance, when the information matrix is diagonal. Conversely, it can be shown that in the case of a linear regression model, the information matrix can be diagonalized, and consequently the coefficients in the surface fit equation are uncorrelated with one another (i.e., the correlation coefficient will be zero ideally; it is enough, in practice, to ensure that the correlation coefficient lie within a confidence band of values near zero). If the correlation coefficient is zero or near zero, the design variables are statiscically as well as functionally independent.

Experimental designs in which the information matrix can be diagonalized, and thus, the coefficients in the surface fit equation are uncorrelated with one another, are called diagonal designs.

A proper experimental design should allow choice of such design points that under the information matrix $\underline{\bar{X}}'\underline{\bar{X}}$ which is non-singular (and diagonal), the least square estimates of the coefficients of the regression equation will have minimum variance property (thus ensuring the independence of the design variables). Also, the design points should be saturated.

It is worth pointing out that in the case of the non-linear regression model, the entries in the matrix $\underline{\bar{X}}$ are not functionally independent, and because of this, there is no assurance that the rank of $\underline{\bar{X}}$ is equal to $\tilde{K}$ ($\tilde{K}$ being the number of coefficients in the regression model). Closer N is to $\tilde{K}$ such that $|\underline{\bar{X}}'\underline{\bar{X}}|$ remains non-singular, closer is the design to being orthogonal. This is a desirable feature of a proper design. If the matrix $\underline{\bar{X}}'\underline{\bar{X}}$ can be diagonalized, then the variance of the coefficients will be minimized.

In practice, trial values for the design point combinations $(x_{j1} \cdots x_{jn})$ can be realized as follows prior to actually using these points as input to an engine airframe simulator program. Design points can be added and discarded until the desired number N of points satisfy the desirable characteristics of proper or good designs. However, this procedure can be a time consuming procedure unless a computer algorithm is formulated for the purpose of adding and deleting a large number of data points while testing the correlation coefficient, the information matrix, etc. Therefore, a reliable aprori choice of experimental design is needed instead which may possess the above desired properties, can minimize the cost of the approximations and enhance the accuracy and yield flyable aircraft. Recent studies on experimental designs show that a considerable enhancement of the screening methodology based on the number of design points needed and the efficiencies of the designs involved can be realized. There are a hierarchy of optimal designs proposed, and one such design - called D-optimal design - in the hierarchy will be discussed.

D - Optimal design maximizes the determinant of the information matrix $[\bar{X}'\bar{X}]$.

The statistics of D - optimal designs show the following important characteristics.

1. D - optimal designs are unique.

2. For a linear response surface, the information matrix of a normalized D - optimal design is diagonal. In other words, the D - optimal design for a linear response surface is orthogonal.

3. D - optimal designs for quadratic response are not orthogonal.

Discussion of the nature and characteristics of D - optimal as well as other generalized designs will be made in a different paper.

Following is a discussion of an algorithm for generating saturated D - optimal designs.

A function $d(\underline{x})$ of the design vector $\underline{x}$ is defined as follows:

$$d(\underline{x}) = \phi(\underline{x})(\bar{X}'\bar{X})^{-1}\phi'(\underline{x}). \tag{12}$$

Step 1. An arbitrary saturated design $\bar{X}$, where $(\bar{X}'\bar{X})^{-1}$ exists, is selected subject to the vectors $\underline{x}$ satisfying whatever constraints are required to yield responses $y(\underline{x})$. Here the number of runs (and the number of design vectors) is equal to the number of unknown parameters to be estimated which is $\frac{(n+1)(n+2)}{2}$ for a quadratic approximating polynomial in variables.

Step 2. A vector $\underline{x}_{k+1}$ satisfying the constraints is determined such that

$$d(\underline{x}_{k+1}) = \max_{\underline{x}} d(\underline{x}), \tag{13}$$

where maximum is taken over all vectors $\underline{x}$ satisfying the constraints, and

not in the current design $\underline{\bar{X}}$. That vector $\underline{x}_{K+1}$ is added to the original K-point design. Now we have a $K+1$ point design $\underline{\overset{*}{X}}$.

Step 3. Find a vector $\underline{x}_j$ from among resulting $(K+1)$ vectors such that

$$d(\underline{x}_j) = \min_{1 \le i \le K+1} d(\underline{x}_i) \tag{14}$$

and remove this vector $\underline{x}_j$ from the set of $K+1$ vectors. This process reestablishes a K-point design $\underline{\bar{X}}$. In this step, the new information matrix $\underline{\overset{*}{X}}', \underline{\overset{*}{X}}$ is used for calculation.

Step 4. Steps 2 and 3 are repeated to obtain a maximum value of the determinant $|\underline{\bar{X}}'\underline{\bar{X}}|$.

Following are some mathematical details which illustrate the algorithm process.

Let $\underline{A} = \underline{\bar{X}}'\underline{\bar{X}}$ and $\underline{\overset{*}{A}} = \underline{\overset{*}{X}}'\underline{\overset{*}{X}}$, where $\underline{\overset{*}{X}}$ is the design of the $K+1$ point design. We find the inverse the matrix $\underline{\overset{*}{A}}$:

$$\left(\underline{A} + \phi'(\underline{x}_{K+1})\phi(\underline{x}_{K+1})\right)^{-1} = \underline{\overset{*}{A}}^{-1}$$

$$= \underline{A}^{-1} - \frac{\underline{A}^{-1}\phi'(\underline{x}_{K+1})\phi(\underline{x}_{K+1})\underline{A}^{-1}}{1+\phi(\underline{x}_{K+1})\underline{A}^{-1}\phi'(\underline{x}_{K+1})}$$

Multiplying both sides by $\underline{A}$, we obtain

$$\left(\underline{A} + \phi'(\underline{x}_{K+1})\phi(\underline{x}_{K+1})\right)^{-1}\left[\underline{A} + \phi'(\underline{x}_{K+1})\phi(\underline{x}_{K+1}) - \phi'(\underline{x}_{K+1})\phi(\underline{x}_{K+1})\right]$$

$$= I - \frac{\underline{A}^{-1}\phi'(\underline{x}_{K+1})\phi(\underline{x}_{K+1})}{1+\phi(\underline{x}_{K+1})\underline{A}^{-1}\phi'(\underline{x}_{K+1})} .$$

This gives

$$I - \left(\underline{A} + \phi'(\underline{x}_{K+1})\phi(\underline{x}_{K+1})\right)^{-1} \phi'(\underline{x}_{K+1})\phi(\underline{x}_{K+1})$$

$$= I - \frac{\underline{A}^{-1}\phi'(\underline{x}_{K+1})\phi(\underline{x}_{K+1})}{1 + \phi(\underline{x}_{K+1})\,\underline{A}^{-1}\phi'(\underline{x}_{K+1})} .$$

Noting that $|A^{-1}| = \frac{1}{|A|}$ and $|BA| = |AB|$, we obtain

$$\frac{|\underline{A} + \phi'(\underline{x}_{K+1})\phi(\underline{x}_{K+1})|}{|A|} = 1 + \phi(\underline{x}_{K+1})\underline{A}^{-1}\phi'(\underline{x}_{K+1}) .$$

Further noting that

$$\underline{A} + \phi'(\underline{x}_{K+1})\phi(\underline{x}_{K+1}) = \overset{*}{\underline{A}}$$

and

$$\phi(\underline{x}_{K+1})A^{-1}\phi'(\underline{x}_{K+1}) = d(\underline{x}_{K+1}) ,$$

we have

$$|\overset{*}{\underline{A}}| = |A|\{1 + d(\underline{x}_{K+1})\}$$

i.e.

$$|\overset{*}{\underline{X}}'\overset{*}{\underline{X}}| = |\underline{X}'\underline{X}|\{1 + d(\underline{x}_{K+1})\} .$$

Thus to maximize $|\overset{*}{\underline{X}}'\overset{*}{\underline{X}}|$, we must choose that vector $\underline{x}_{K+1}$, which maximizes the value of the function $d(\underline{x})$ as required in Step 2 of the algorithm.

The goal is to achieve the maximum value of the determinant $|\underline{X}'\underline{X}|$. The vector chosen for removal must result in the minimum possible decrease in $|\overset{*}{\underline{X}}'\overset{*}{\underline{X}}|$. The difference $\{|\overset{*}{\underline{X}}'\overset{*}{\underline{X}}| - |\underline{X}'\underline{X}|\}$ can be minimized by maximizing

the determinant $|\underline{X}'\underline{X}|$ for the resulting K - point design $\underline{X}$. We note that the relation

$$|\underline{X}'\underline{X}| = \frac{|\underline{X}^{*\prime}\underline{X}^{*}|}{1 + d(\underline{x}_{K+1})} ,$$

indicates that the maximization of $|\underline{X}'\underline{X}|$ for the optimal K - point design is equivalent to minimzing the value of the function $d(\underline{x})$ over the set of $K+1$ vectors under consideration. This is what is realized in Step 3.

The discussions so far point out that the D-optimal design method is a proper screening procedure for selecting the design variables. However, most aerospace companies have been using (or have used so far without exploring any other method such as D-optimal method) Latin square method. Therefore, some comments are worth making in regard to the characteristics of latin squares.

A latin square of order n is defined as an $n \times n$ square, the n^2 cells of which are occupied by n distinct symbols (which may be Greek or Latin letters or Hindu numerals) such that each symbol occurs once on each row and in each column.

Two Latin squares are said to be orthogonal if on superposition each symbol of the first square occurs exactly once with each symbol of the second square. There may exist more than two Latin squares such that any pair is orthogonal. A set of Latin squares such that any two of them are orthogonal is called an orthogonal set. There cannot be more than $n-1$ orthogonal Latin squares of order n in any orthogonal set. When n equals a prime power p^r, p a prime number, r a positive integer, then a complete set of $(n-1)$ orthogonal Latin squares can be constructed. But it is not known whether a complete set of orthogonal Latin squares exists when n is not a prime power.

Several authors discuss the properties of Latin squares in detail and two appropriate ones are shown in the reference list (i.e., references 5 & 6).

Following are some of the important features of Latin squares.

1. The order of the squares is determined by the number of levels assigned to each variable.

2. The number of levels should at least be greater by unity than the number of design variables in a problem. This is due to the fact that the number of orthogonal Latin squares of order p is less than or equal to $p - 1$. When p is a prime number or the power of a prime, the equality holds.

3. The design space consists of $n^2+n(n-1)$ design points, and the minimum number of points which Latin square design provides is $(n+1)^2$, n being the number of design variables.

4. The design vectors will not necessarily yield the matrix $|\underline{\bar{X}}'\underline{\bar{X}}|$ such that its determinant is not zero. In other words, $|\underline{\bar{X}}'\underline{\bar{X}}|$ can be zero or be very close to zero.

5. Reliability is reduced in Latin square designs if the number of variables become large. Also, when the number of variables become less than or equal to four, Latin square designs will not maintain reliability in error estimates. On the other hand, if the number of variables exceeds eight, row and column interactions (i.e, confounding of the variables) become noticeable. The design will not be orthogonal.

A point of comparison between D - optimal and Latin square experimental design concerns the estimation of regression coefficients. In order to calculate the least squares estimate of the unknown coefficients, we must have an experimental design that yields a non-singular matrix $[\underline{\bar{X}}'\underline{\bar{X}}]$. The Latin square experimental design generating algorithm sometimes yields a non-singular matrix $\underline{\bar{X}}'\underline{\bar{X}}$ only by adding more design vectors than are required. For example, in reference 2, Boeing used mutually orthogonal Latin square

designs to obtain 91 design vectors for a six variable problem. A six variable quadratic polynomial has 28 unknown regression coefficients. It is possible to find 28 vector experimental designs which yield non-singular matrices $\underline{\bar{X}}' \underline{\bar{X}}$. The smallest possible six variable Latin square design would have 59 points and these designs can be singular for 7 and 8 variable designs.

D - optimal designs ensure that $|\underline{\bar{X}}' \underline{\bar{X}}|$ will have high value.

Second point of comparison between D - optimal and Latin square designs concerns the accuracy of the approximations. This point is the most important because the polynomial approximations are used in lieu of the aircraft sizing and performance synthesis programs. Table 3 shows prediction accuracy comparison between regression equations derived using the D - optimal design and those derived using Latin square designs. This clearly demonstrates the superiority of the D - optimal design. Table 3 has been generated for the case of an advanced tactical fighter design study made by General Dynamics.* the comparison is made by using the design points not used to derive the quadratic approximation.

The third point of comparison relates to the computer time required for an "n" variable problem $(n \geq 4)$. We know that Latin square design requires at least $(n+1)^2$ points, whereas the D - optimal design requires $\frac{(n+1)(n+2)}{2}$ points. Thus, for $n = 4$, D - optimal design requires 40% fewer computer runs than the minimum possible run required by Latin square design. As the number of design variables increases, the efficiency of D - optimal design over Latin square design increases up to 50%, thus resulting in cost savings of up to 50%. In reference 2, the orthogonal Latin square design for 6 variables required 91 points whereas saturated D - optimal design would require only

* The authors thank Dr James A. Craig, General Dynamics, Fort Worth, Texas for providing the information shown in Table 3, as well as the information contained in the fourth point of comparison between the designs.

28 points, a savings of almost 70%.

The fourth point of comparison is in regard to the derivation of realistic aircraft designs.

Latin square design generates aircraft designs according to algebraic algorithm. Therefore, it is quite possible that the levels of the independent variables so chosen may result in such design vectors which may not yield a realistic response. An example of this is again demonstrated in the close-coupled canard design study (Ref. 2). A close study of the designs generated by the Latin square algorithm showed that only 37 of the 91 design vectors represented aircraft with flyable wings.

Inclusion or exclusion of improper designs generated by Latin squares may make the information matrix singular or near singular, and as a result, the quadratic approximation will be poorer.

D - optimal designs affords the designer to screen the improper designs (such as unflyable aircraft) in the design cycle.

In conclusion, it can be stated that the central composite design yields the most accurate results in terms of mean percent absolute error, whereas the Latin square design is the worst of all. However, D - optimal design's accuracy is very close to that of the central composite design. This becomes particularly significant if one looks at the significantly less number of points required under the D - optimal design.

Some additional studies are required in the area of D - optimal designs. The following areas need to be further explored.

1. Analysis of variance and co-variance pertaining to D - optimal design.

2. Properties of D - optimal design relating to orthoganility of the design, confounding of effects, interactions of the variables, etc.

3. Significance tests on model coefficeints obtained by using D - optimal designs.

Further, instead of least squares estimation, other procedures such as ridge regression should be explored. The alternative regression procedure works better in case D - optimal designs are non-orthogonal.

Higher order polynomials such as cubic should be considered also for enhancing efficiencies and accuracies in the event that a quadratic representation is a poor approximation for the response characteristics.

A computer aided aircraft design with D - optimal design as a module should be checked out in the case of existing aircraft for comparison purposes. Constrained D - optimal designs should be well investigated.

Cost effectiveness can also be considered in the D - optimally generated optimal aircraft designs. D - optimal desings based on cost cycle iterations should be explored.

TABLE 1

Number of Design Points Required Under Applicable Experimental Designs

Number of Independent Variables, n	Modified Central Composite Design $2^n + 2n + 1$	Latin Square Design $(n+1)^2$	D - Optimal Design $\frac{1}{2}(n+1)(n+2)$
2	9	9	6
3	15	16	10
4	25	25	15
5	43	36	21
6	77	49	28
7	143	64	36
8	273	81	45
9	531	100	55
10	1045	121	66
11	2071	144	78
12	4121	169	91
13	8219	196	105

TABLE 2

Comparison of Latin Square and D-Optimal Designs

Number of Independent Variables	Number of Regression Coefficients	Number of Design Points Required		Determinant of	
		Latin Squares	D-Optimal	Latin Squares	D-Optimal
4	15	25	15	$2 \cdot 2 \times 10^{12}$	$2 \cdot 7 \times 10^{12}$
5	21	36	21	$8 \cdot 7 \times 10^{4}$	$2 \cdot 6 \times 10^{6}$
6	28	49	28	$8 \cdot 2 \times 10^{25}$	$2 \cdot 4 \times 10^{29}$
7	36	64	36	$3 \cdot 2 \times 10^{-17}$	$1 \cdot 2 \times 10^{38}$
8	45	81	45	$1 \cdot 8 \times 10^{-16}$	$6 \cdot 4 \times 10^{32}$

TABLE 3

Accuracy of Approximations

RESPONSE	CORRELATION			MEAN PERCENT ERROR		
	D-OPTIMAL	LATIN SQUARE	CENTRAL COMPOSITE	D-OPTIMAL	LATIN SQUARE	CENTRAL COMPOSITE
1	.999873	.998268	.999964	0.19	0.78	0.12
2	.999888	.999565	.999908	0.08	0.20	0.07
3	.999961	.999727	.999970	0.07	0.21	0.06
4	.997253	.981523	.997785	0.41	1.21	0.29
5	.984867	.978733	.979529	1.59	2.80	1.24
6	.999765	.994042	.999878	0.12	0.78	0.12
7	.999915	.999853	.999941	0.12	0.16	0.08
8	.999961	.999732	.99970	0.07	0.21	0.06
9	.995152	.953276	.996785	0.52	1.91	0.36
10	.797345	.419518	.846973	7.19	8.21	3.51
11	.989825	.974936	.990520	1.47	3.48	2.04
12	.999588	.986647	.999342	0.10	1.41	0.11
13	.999774	.994538	.999902	0.15	0.83	0.12
14	.960110	.617250	.953537	4.56	11.47	2.80
15	.950842	.711151	.955383	3.50	8.70	2.08

REFERENCES

1. "Airplane Responsive Engine Selection (ARES)", Boeing Document, prepared by G. J. Eckard, et al (Aug 1975), Document No. DI 80-18895-1.

2. "Light Experimental Supercruiser Conceptual Design," Nelson, B. D.; The Boeing Co, April 1976, USAF Contract F33615-75-C-3150, AFFDL, WPAFB.

3. "Airplane Engine Selection By Optimization on Surface Fit Approximations," Healy, M. J., Kowalik, J. S., and Ramsay, J. W., Journal of Aircraft, Vol 12, No 7, July 1975.

4. "An Application of D-Optimal Regression Analysis Designs to D-Optimal Aircraft Design," Craig, Jr., J. A., and Hoffman, R. A., Presented at Symposium on Applications of Statistics, Sponsored by AFFDL, WAPFB, June 14-16, 1976.

5. "Construction of Some Sets of Mutually Orthogonal Latin Squares," Proc American Mathematical Society, Vol 10 (1959), pp 946-951.

6. "On Complete Sets of Latin Squares," Bose, R. C., and Nair, K. R., Sankhya, Vol (5), 1941, pp 361-382.

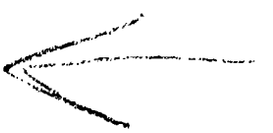

MTBF CONFIDENCE BOUNDS BASED ON MIL-STD-781C FIXED-LENGTH TEST RESULTS

H. Leon Harter

Air Force Flight Dynamics Laboratory
Wright-Patterson Air Force Base, OH

ABSTRACT

Exact confidence bounds are available for the parameter θ of an exponential distribution in the case of Type II (failure) censored samples, but not in the case of Type I (time) censored samples. In the latter case, the conventional confidence bounds are conservative; Cox has proposed approximate confidence bounds which may not be conservative, but have other advantages. For MIL-STD-781C fixed-length tests, we have a mixture of the two types of censoring, Type II for rejected lots and Type I for accepted lots. Epstein proposes combining the exact bounds for rejected lots with the conventional bounds for accepted lots. We propose replacing the latter by Cox's approximate bounds, and show that this gives true confidence levels closer to the nominal levels.

Reprinted with permission from the Journal of Quality Technology, 1978.

MTBF Confidence Bounds Based on MIL-STD-781C Fixed-Length Test Results

H. LEON HARTER

Air Force Flight Dynamics Laboratory, Wright-Patterson Air Force Base, Ohio 45433

Exact confidence bounds are available for the parameter θ of an exponential distribution in the case of Type II (failure) censored samples, but not in the case of Type I (time) censored samples. In the latter case, the conventional confidence bounds are conservative; Cox has proposed approximate confidence bounds which may not be conservative, but have other advantages. For MIL-STD-781C fixed-length tests, we have a mixture of the two types of censoring, Type II for rejected lots and Type I for accepted lots. Epstein proposes combining the exact bounds for rejected lots with the conventional bounds for accepted lots. We propose replacing the latter by Cox's approximate bounds, and show that this gives true confidence levels closer to the nominal levels.

Introduction

MIL-STD-781C is a complete revision of MIL-STD-781B [8] in which some new terminology is introduced. For example, θ_1 is called simply the lower test MTBF (mean time between failures) instead of the minimum acceptable MTBF, and θ_0 is called simply the upper test MTBF instead of the specified MTBF. Times are expressed as multiples of θ_1 instead of θ_0. The ratio θ_0/θ_1 is still called the discrimination ratio, as in MIL-STD-781B. MIL-STD-781C gives eight sequential test plans and twelve fixed-length test plans for specified values of the producer's risk α (the probability of rejecting a lot whose true MTBF is θ_0), the consumer's risk β (the probability of accepting a lot whose true MTBF is θ_1), and the discrimination ratio θ_0/θ_1. The values of the risks α and β, the discrimination ratio θ_0/θ_1, the test duration T (multiples of θ_1), and the acceptance number c for the twelve fixed-length tests are given in Table 1.

In carrying out the fixed-length tests of MIL-STD-781C, one places at least three items (assumed to be a random sample from a lot whose life distribution is exponential) on life test (not necessarily simultaneously). As the test proceeds, items that fail are removed and repaired (after which they are assumed to be as good as new), then returned to test. For each item, a record is kept of the number of failures and the time on test. It is required that each item shall operate at least one half the average operating time of all items on the test. The test terminates when the total number of failures exceeds c (the acceptance number) or when the total test time equals T (the test duration), whichever occurs first. In the former case, the lot is rejected; in the latter case, it is accepted.

The question has arisen (see, for example, a recent paper by Blondin [1]) as to how one can use the results of MIL-STD-781C acceptance tests to set confidence bounds on the true MTBF, θ. Bryant and Schmee [2] have studied this question in the case of the sequential tests of MIL-STD-781C. The question is somewhat simpler, though by no means trivial, in the case of fixed-length tests. If a fixed-length test results in rejection of the lot, the test is Type II (failure) censored. If, however, the test

Dr. Harter is a mathematician in the applied mathematics group of the Analysis and Optimization Branch, Structural Mechanics Division at the Air Force Flight Dynamics Laboratory located in Wright-Patterson Air Force Base, Ohio. He was formerly a senior mathematical statistics scientist at Aerospace Research Laboratories.

TABLE 1. Summary of MIL-STD-781C Fixed-Length Test Plans

Test Plan	Producer's Risk, α	Consumer's Risk, β	Discrimination Ratio, θ_0/θ_1	Test Duration, T (Multiples of θ_1)	Acceptance Number, c
IXC	10%	10%	1.5	45.0	36
XC	10%	20%	1.5	29.9	25
XIC	20%	20%	1.5	21.1	17
XIIC	10%	10%	2.0	18.8	13
XIIIC	10%	20%	2.0	12.4	9
XIVC	20%	20%	2.0	7.8	5
XVC	10%	10%	3.0	9.3	5
XVIC	10%	20%	3.0	5.4	3
XVIIC	20%	20%	3.0	4.3	2
XIXC	30%	30%	1.5	8.0	6
XXC	30%	30%	2.0	3.7	2
XXIC	30%	30%	3.0	1.1	0

results in acceptance of the lot, the test is Type I (time) censored so in MIL-STD-781 tests one has a mixture of the two types of censoring. For pure Type II censoring, exact confidence bounds for θ are known, but for pure Type I censoring, exact confidence bounds are not available and the conventional confidence bounds are conservative. The difference arises because of the facts that (1) in the former case, the number of failures r is known, and the total test time T_r to the r^{th} failure is a (continuous) random variable, and (2) in the latter case, the total test time T is known, while the number of failures $r = 0,1,2,\cdots$ is a (discrete) random variable. The details for these two cases are discussed in the next two sections of this paper. Later sections are devoted to a discussion of combination of the two sets of results to obtain a system of confidence bounds for the hybrid case encountered in MIL-STD-781 tests, numerical examples illustrating computation of the confidence bounds, and the results of a Monte Carlo simulation for three representative test plans from MIL-STD-781C.

Case 1: Pure Type II Censoring

If the life distribution is exponential, it is well known (see, for example, Epstein [4]) that if the test always terminates at total test time T_r, the total observed life up to the time of occurrence of the r^{th} failure, then $2T_r/\theta$, where θ is the true MTBF, is distributed as $\chi^2(2r)$. Hence a $100(1-\alpha)$ per cent lower confidence bound for θ is given by

$$\theta^E_{1-\alpha} = \frac{2T_r}{\chi^2_{1-\alpha}(2r)} \tag{1}$$

and a $100(1-\alpha)$ per cent upper confidence bound for θ is given by

$$\bar{\theta}^E_{1-\alpha} = \frac{2T_r}{\chi^2_{\alpha}(2r)}, \tag{2}$$

where $\chi^2_\gamma(f)$, is the 100γ per cent point (γ fractile) of the chi-square distribution with f degrees of freedom. A $100(1-2\alpha)$ per cent central confidence interval for θ is given by

$$(\theta^E_{1-\alpha}, \bar{\theta}^E_{1-\alpha}), \tag{3}$$

where $\theta^E_{1-\alpha}$ and $\bar{\theta}^E_{1-\alpha}$ are given by equations (1) and (2), respectively.

Case 2: Pure Type I Censoring

Conventional Confidence Bounds

If the life distribution is assumed to be exponential with parameter θ, the number of observed failures, K, in a fixed time T is a random variable whose distribution is Poisson with parameter $\lambda = T/\theta$. Then it is well known (see, for example, Mann, Schafer, and Singpurwalla [7], p. 181) that $P(K \leq r) = \text{Prob}[\chi^2(2r+2) > 2T/\theta]$. It follows that if r failures have been observed in time T, then, with probability at least $1-\alpha$ (*at least* because K is discrete), $2T/\theta < \chi^2_{1-\alpha}(2r+2)$, so that a conservative $100(1-\alpha)$ per cent lower confidence bound for θ is given by

$$\theta^C_{1-\alpha} = \frac{2T}{\chi^2_{1-\alpha}(2r+2)}. \tag{4}$$

Similarly, it can be shown that $\text{Prob}(K > r) = \text{Prob}[\chi^2(2r) < 2T/\theta]$, so that a conservative $100(1-\alpha)$ per cent upper confidence bound for θ is given by

$$\bar{\theta}^C_{1-\alpha} = \frac{2T}{\chi^2_{\alpha}(2r)}. \tag{5}$$

Finally, a conservative $100(1-2\alpha)$ per cent central confidence interval for θ is given by

$$(\theta^C_{1-\alpha}, \bar{\theta}^C_{1-\alpha}), \tag{6}$$

where $\theta^C_{1-\alpha}$ and $\bar{\theta}^C_{1-\alpha}$ are given by equations (4) and (5), respectively.

Cox's Approximate Confidence Bounds

Cox [3] has proposed approximate confidence bounds for Poisson parameters, based on the number of events that are observed in a fixed time. His method, applied to the case of acceptance of a lot on the basis of a fixed-length test, yields the following results: An approximate $100(1 - \alpha)$ per cent lower confidence bound for θ, the true MTBF, is given by

$$\theta^{\wedge}_{1-\alpha} = \frac{2T}{\chi^2_{1-\alpha}(2r + 1)}, \tag{7}$$

and an approximate $100(1 - \alpha)$ per cent upper confidence bound for θ is given by

$$\theta^{\wedge}_{1-\alpha} = \frac{2T}{\chi^2_{\alpha}(2r + 1)}. \tag{8}$$

An approximate $100(1 - 2\alpha)$ per cent central confidence interval for θ is given by

$$(\theta^{\wedge}_{1-\alpha}, \theta^{\wedge}_{1-\alpha}), \tag{9}$$

where $\theta^{\wedge}_{1-\alpha}$ and $\theta^{\wedge}_{1-\alpha}$ are given by equations (7) and (8), respectively.

Heuristic Justification for Cox's Approximate Bounds

The conventional lower confidence bounds are conservative, since they are what we would obtain if we were to assume that, instead of Type I censoring at time T, we have Type II censoring with the occurrence of the $(r + 1)^{th}$ failure at time T. Actually, the $(r + 1)^{th}$ failure might occur at any time $T_{r+1} > T$, but the earliest it could occur is at time $T + \epsilon$ ($\epsilon \to 0^+$). The conventional upper confidence bounds are also conservative, since they are what we would obtain if we were to assume that, instead of Type I censoring at time T, we have Type II censoring with the occurrence of the r^{th} failure at time T. Actually, the r^{th} failure might have occurred at any time $T_r < T$, but the latest it could have occurred is at time $T - \epsilon$ ($\epsilon \to 0^+$). In practice, we do not know the time of occurrence of the $(r + 1)^{th}$ failure, but (if the life test is monitored continuously) we do know that of the r^{th} failure. If we assume that we have Type II censoring with the occurrence of *half* a failure at time T, r failures having occurred earlier (which is roughly equivalent to assuming that T_r and T_{r+1} are such that T lies midway between them), we obtain Cox's approximate bounds. These bounds may be either conservative or nonconservative, but, averaged over a large number of trials, the proportion of cases in which the approximate confidence intervals (one-sided or two-sided) contain the true MTBF, θ, can be expected to be closer to the nominal confidence level than the proportion of cases in which the corresponding conventional confidence intervals contain θ.

Hybrid Case: MIL-STD-781 Tests

Epstein's Procedure

Epstein [5], pp. 3.23–3.24, has combined the results for pure Type II censoring and for pure Type I censoring to obtain a confidence procedure for the hybrid case encountered in tests of the type found in MIL-STD-781C. If the test results in rejection, with Type II censoring at time T_{c+1}, his $100(1 - \alpha)$ per cent lower and upper confidence bounds for θ are found by setting $r = c + 1$ in equations (1) and (2), which yields

$$\theta^{E}_{1-\alpha} = \frac{2T_{c+1}}{\chi^2_{1-\alpha}(2c + 2)} \tag{10}$$

and

$$\theta^{E}_{1-\alpha} = \frac{2T_{c+1}}{\chi^2_{\alpha}(2c + 2)}. \tag{11}$$

His $100(1 - 2\alpha)$ per cent central confidence interval for θ is given by

$$(\theta^{E}_{1-\alpha}, \theta^{E}_{1-\alpha}), \tag{12}$$

where $\theta^{E}_{1-\alpha}$ and $\theta^{E}_{1-\alpha}$ are given by equations (10) and (11), respectively. If, however, the test results in acceptance, with Type I censoring at time T and $r = 0,1,2,\cdots,c$ failures, his $100(1 - \alpha)$ per cent lower and upper confidence bounds for θ are the conservative bounds given by equations (4) and (5), respectively, and his $100(1 - 2\alpha)$ per cent central confidence interval for θ is the conservative interval given by equation (6). Epstein [5], Appendix 3E (pp. 3.63–3.66), has shown that his system of one-sided confidence intervals (from the lower confidence bound to ∞) is conservative, and has conjectured that the same is true for his system of two-sided intervals. It should be borne in mind, however, that it is the a priori confidence before the test has been run (and, thus, before one knows whether acceptance or rejection will occur) that equals or exceeds the nominal level. Hence, in judging the performance of Epstein's procedure, one should average the results for a large number of accepted and rejected lots, not for accepted lots and rejected lots separately.

Harter's Procedure

We propose a modification of Epstein's procedure in which the confidence intervals remain the

same when the test results in rejection, with Type II censoring at time T_{c+1}. However, if the test results in acceptance, with Type I censoring at time T and $r = 0,1,2,\cdots,c$ failures, the conservative lower and upper $100(1-\alpha)$ per cent confidence bounds for θ are replaced by Cox's approximate confidence bounds, which are given by equations (7) and (8), respectively, and the conservative $100(1-2\alpha)$ per cent central confidence interval for θ is replaced by Cox's approximate central confidence interval, which is given by equation (9). The resulting system of approximate confidence intervals (one-sided or two-sided) may be either conservative or nonconservative, but, averaged over a large number of trials involving both accepted and rejected lots, their true confidence levels may be expected to be closer than those for Epstein's system of conservative intervals to the nominal levels.

Numerical Examples

Suppose we have two lots, A and B, from two different vendors of an electronic device. We wish to reject a lot 20 per cent of the time (producer's risk, α) if its true MTBF is 1000 hours, and accept it 20 per cent of the time (consumer's risk, β) if its true MTBF is only 500 hours. Thus, the appropriate MIL-STD-781C fixed-length test plan is plan XIVC (see Table 1) with $\alpha = \beta = 20\%$, discrimination ratio $\theta_0/\theta_1 = 1000/500 = 2.0$, test duration $T = 7.8\theta_1 = 3900$ hours, and acceptance number $c = 5$. Regardless of whether the lot is accepted or rejected, we wish to set 90 per cent lower and upper confidence bounds and an 80 per cent central confidence interval on the MTBF of the lot.

Example 1 (Rejected Lot)

A random sample of three or more devices from lot A is placed on test as outlined in the Introduction. The sixth failure occurs when the total test time T_6 is 3510 hours, so the lot is rejected. From equations (10) through (12), with the aid of a table of percentage points of the chi-square distribution (see, for example, Harter [6]), we find that the 90 per cent lower confidence bound, according to both Epstein's and Harter's procedures, is $\hat{\theta}^E_{.90} = 2T_6/\chi^2_{.90}(12) = 2(3510)/18.55 = 378$ hours, the corresponding 90 per cent upper confidence bound is $\hat{\theta}^E_{.90} = 2T_6/\chi^2_{.10}(12) = 2(3510)/6.304 = 1114$ hours, and hence the 80 per cent central confidence interval for the true MTBF, θ, is (378 hours, 1114 hours).

Example 2 (Accepted Lot)

The same test is performed on a random sample from lot B. The test continues for a total test time $T = 3900$ hours, during which $r = 4$ failures oc-

TABLE 2. Monte Carlo Results for All Lots (Rejected and Accepted) and All u's (Proportion of Cases in which Confidence Intervals Contain u)

		Epstein's Procedure			Harter's Procedure		
Interval Type	Nominal Level	Plan IXC	Plan XIVC	Plan XXIC	Plan IXC	Plan XIVC	Plan XXIC
(LB, ∞)	.9900	.9934	.9969	1.0000	.9899	.9912	1.0000
	.9500	.9637	.9736	1.0000	.9470	.9606	.9815
	.9000	.9157	.9391	1.0000	.8918	.8859	.9815
	.8000	.8328	.8693	.9666	.8003	.7747	.9110
	.7000	.7325	.7433	.9499	.7038	.7433	.7989
	.6000	.6399	.7108	.8667	.5926	.5554	.6545
	.5000	.5311	.5648	.8335	.5174	.4934	.4913
(0, UB)	.9900	.9908	.9901	.9901	.9901	.9901	.9901
	.9500	.9570	.9525	.9501	.9507	.9525	.9501
	.9000	.9102	.9091	.9001	.9049	.8966	.9001
	.8000	.8218	.8302	.8060	.8020	.7819	.8060
	.7000	.7372	.7330	.7357	.6858	.7080	.7357
	.6000	.6414	.6571	.6838	.5925	.5762	.6838
	.5000	.5329	.5844	.6471	.4826	.5066	.5087
(LB, UB)	.9800	.9842	.9870	.9901	.9801	.9812	.9901
	.9000	.9207	.9261	.9501	.8977	.9132	.9316
	.8000	.8260	.8482	.9001	.7967	.7825	.8816
	.6000	.6546	.6996	.7726	.6022	.5566	.7170
	.4000	.4697	.4763	.6856	.3895	.4513	.5346
	.2000	.2813	.3679	.5505	.1852	.1316	.3383
	.0000	.0640	.1491	.4806	.0000	.0000	.0000

cur, so the lot is accepted. According to Epstein's procedure, we use equations (4) through (6) and a table of chi-square percentage points to find that the 90 per cent lower confidence bound is $\theta^C_{.90} = 2T/\chi^2_{.90}(10) = 2(3900)/15.99 = 488$ hours, the corresponding 90 per cent upper confidence bound is $\bar{\theta}^C_{.90} = 2T/\chi^2_{.10}(8) = 2(3900)/3.490 = 2235$ hours, and hence the 80 per cent central confidence interval for the true MTBF, θ, is (488 hours, 2235 hours). According to Harter's procedure, we use equations (7) through (9) and a table of chi-square percentage points to find that the 90 per cent lower confidence bound is $\theta^A_{.90} = 2T/\chi^2_{.90}(9) = 2(3900)/14.68 = 531$ hours, the corresponding 90 per cent upper confidence bound is $\bar{\theta}^A_{.90} = 2T/\chi^2_{.10}(9) = 2(3900)/4.168 = 1871$ hours, and hence the 80 per cent central confidence interval for the true MTBF, θ, is (531 hours, 1871 hours).

Monte Carlo Study

A Monte Carlo simulation was performed for a few representative cases in order to compare the proportions of cases in which Epstein's and Harter's systems of confidence intervals contain the true

TABLE 3. Summary of Theoretical and Monte Carlo Results

Test Procedures (all give same test decision, but different confidence intervals)	Confidence Intervals for MTBF, θ Nominal level = $1 - \alpha$ (one-sided) = $1 - 2\alpha$ (two-sided)		Characterization: Rej. Lots	Acc. Lots	All Lots
PURE TYPE II CENSORING:	$(\underline{\theta}^C_{1-\alpha}, \infty) = (2T_{c+1}/\chi^2_{1-\alpha}(2c+2), \infty)$		C	N	E
Test each lot until $(c+1)^{th}$ failure occurs (at total test time T_{c+1})	$(0, \bar{\theta}^C_{1-\alpha}) = (0, 2T_{c+1}/\chi^2_{\alpha}(2c+2))$		N	C	E
Reject lot if $T_{c+1} \le T$	$(\underline{\theta}^A_{1-\alpha}, \bar{\theta}^A_{1-\alpha})$		PN	PC	E
Accept lot if $T_{c+1} > T$					
PURE TYPE I CENSORING:	$(\underline{\theta}^C_{1-\alpha}, \infty) = (2T/\chi^2_{1-\alpha}(2r+2), \infty)$		C	PC	C
Test each lot until total test time T is accumulated	$(0, \bar{\theta}^C_{1-\alpha}) = (0, 2T/\chi^2_{\alpha}(2r))$		A-PC	C	C
Let r = no. of failures in time T	$(\underline{\theta}^A_{1-\alpha}, \bar{\theta}^A_{1-\alpha})$		C-PC	PC	C
Reject lot if $r \ge c+1$	$(\underline{\theta}^C_{1-\alpha}, \infty) = (2T/\chi^2_{1-\alpha}(2T+1), \infty)$		PC	PN	A
Accept lot if $r \le c$	$(0, \bar{\theta}^C_{1-\alpha}) = (0, 2T/\chi^2_{\alpha}(2r+1))$		PN	PC	A
	$(\underline{\theta}^A_{1-\alpha}, \bar{\theta}^A_{1-\alpha})$		A	A	A
HYBRID CENSORING (MIL-STD-781C):	$(\underline{\theta}^{HC}_{1-\alpha}, \infty) =$	$(\underline{\theta}^C_{1-\alpha}, \infty)$ for rej. lots	C		C
Test each lot until $(c+1)^{th}$ failure occurs (at total test time T_{c+1}) or until total test time T is accumulated (with r failures in time T), whichever occurs first		$(\underline{\theta}^C_{1-\alpha}, \infty)$ for acc. lots		PC	
Reject lot if $T_{c+1} \le T$	$(0, \bar{\theta}^{HC}_{1-\alpha}) =$	$(0, \bar{\theta}^C_{1-\alpha})$ for rej. lots	N		C
Accept lot if $r \le c$		$(0, \theta^C_{1-\alpha})$ for acc. lots		C	
	$(\underline{\theta}^{HC}_{1-\alpha}, \bar{\theta}^{HC}_{1-\alpha})$		PN	PC	C
	$(\underline{\theta}^{HA}_{1-\alpha}, \infty) =$	$(\underline{\theta}^A_{1-\alpha}, \infty)$ for rej. lots	C		A
		$(\underline{\theta}^A_{1-\alpha}, \infty)$ for acc. lots		PN	
	$(0, \bar{\theta}^{HA}_{1-\alpha}) =$	$(0, \bar{\theta}^A_{1-\alpha})$ for rej. lots	N		A
		$(0, \theta^A_{1-\alpha})$ for acc. lots		PC	
	$(\underline{\theta}^{HA}_{1-\alpha}, \bar{\theta}^{HA}_{1-\alpha})$		PN	A	A

Characterizations: E = exact; C = conservative; N = nonconservative; A = approximate*; PC = predominantly conservative (averaged over θ); PN = predominantly nonconservative (averaged over θ).

* May be either conservative or nonconservative, but tends to have true levels closer to the nominal level than do purely conservative or nonconservative intervals.

MTBF, θ, with each other and with the nominal confidence levels. The cases chosen for study were test plans IXC and XIVC, each with $\theta = .5\theta_1, \theta_1, 1.5\theta_1, 2\theta_1, 3\theta_1, 4.5\theta_1$, and test plan XXIC, with $\theta = .5\theta_1, \theta_1, 2\theta_1, 3\theta_1, 4.5\theta_1, 6\theta_1$. In each case the Monte Carlo sample size was $N = 10{,}000$. A computer was used to generate exponential random numbers with parameter θ, perform the tests, calculate the confidence intervals, and count the number of intervals containing θ. For each plan, the results were tabulated separately for rejected lots, accepted lots, and all lots, for each of the six values of θ. A summary of the results for all lots and all θ's is given in Table 2. These results verify Epstein's conjecture that his system of two-sided confidence intervals is conservative when considered over all lots (rejected and accepted), and indicate that the same is true for the system of one-sided intervals from 0 to his upper bounds, as he proved for the system of one-sided intervals from his lower bounds to ∞. The results also show, as expected, that the true confidence levels for Harter's systems of confidence intervals (one-sided and two-sided) are closer than those for Epstein's systems to the nominal levels.

A summary of the main theoretical and Monte Carlo results is given in Table 3. In that table, an attempt is made to characterize the exact confidence intervals for pure Type II censoring, the conventional confidence intervals and Cox's approximate confidence intervals for pure Type I censoring and the Epstein and Harter systems of confidence intervals for hybrid censoring (as in MIL-STD-781C fixed-length tests). The various confidence intervals are characterized as exact, conservative, nonconservative, or approximate, not only for all lots, but for rejected and accepted lots separately.

Acknowledgments

The author wishes to thank Lt. Michael Himmelberg and Sharon Foley of the ASD Computer Center for performing the Monte Carlo study on a CDC 6600 computer, and Rhonda Baab and Lynn Curtis for typing the original and revised manuscripts, respectively.

References

1. Blondin, Roger A., "Analysis of MIL-STD-781B Test Data: Fixed Length and Probability Ratio Sequential Tests versus Constant Confidence Tests." Unpublished manuscript.
2. Bryant, Clifford M., and Schmee, Josef, "Confidence Limits on MTBF for Sequential and Fixed Length Test Plans of MIL-STD-781," *Technometrics*, Vol. 21, No. 1, February 1979 (to appear).
3. Cox, D. R., "Some Simple Approximate Tests for Poisson Variates," *Biometrika*, Vol. 40, Parts 3 and 4, December 1953, pp. 354-360.
4. Epstein, Benjamin, "Estimation from Life Test Data," *Technometrics*, Vol. 2, No. 4, November 1960, pp. 447-454.
5. Epstein, Benjamin, "Statistical Techniques in Life Testing, Chapter III: Problems of Estimation," Technical Report No. 4, prepared under Contract Nonr-2163(00)(NR-042-018) for Office of Naval Research, January 1959, Department of Mathematics, Wayne State University, Detroit, Michigan. AD 211458 (Available from NTIS, United States Department of Commerce, Springfield, Virginia 22161).
6. Harter, H. Leon, *New Tables of the Incomplete Gamma-Function Ratio and of Percentage Points of the Chi-Square and Beta Distributions*, United States Government Printing Office, Washington, DC, 1964.
7. Mann, Nancy R., Schafer, Ray E., and Singpurwalla, Nozer D., *Methods for Statistical Analysis of Reliability and Life Data*, Wiley, New York, 1974.
8. "Reliability Tests: Exponential Distribution," MIL-STD-781B, November 1967, United States Department of Defense, Washington DC Revision "Reliability Design Qualification and Production Acceptance Tests: Exponential Distribution," MIL-STD-781C, October 1977.